

Second Edition

The **Rock Physics Handbook**

Tools for Seismic Analysis of Porous Media

**Gary Mavko,
Tapan Mukerji
and Jack Dvorkin**

CAMBRIDGE

CAMBRIDGE

www.cambridge.org/9780521861366

This page intentionally left blank

The Rock Physics Handbook, Second Edition

Tools for Seismic Analysis of Porous Media

The science of rock physics addresses the relationships between geophysical observations and the underlying physical properties of rocks, such as composition, porosity, and pore fluid content. The *Rock Physics Handbook* distills a vast quantity of background theory and laboratory results into a series of concise, self-contained chapters, which can be quickly accessed by those seeking practical solutions to problems in geophysical data interpretation.

In addition to the wide range of topics presented in the First Edition (including wave propagation, effective media, elasticity, electrical properties, and pore fluid flow and diffusion), this Second Edition also presents major new chapters on granular material and velocity–porosity–clay models for clastic sediments. Other new and expanded topics include anisotropic seismic signatures, nonlinear elasticity, wave propagation in thin layers, borehole waves, models for fractured media, poroelastic models, attenuation models, and cross-property relations between seismic and electrical parameters. This new edition also provides an enhanced set of appendices with key empirical results, data tables, and an atlas of reservoir rock properties expanded to include carbonates, clays, and gas hydrates.

Supported by a website hosting MATLAB routines for implementing the various rock physics formulas presented in the book, the Second Edition of *The Rock Physics Handbook* is a vital resource for advanced students and university faculty, as well as in-house geophysicists and engineers working in the petroleum industry. It will also be of interest to practitioners of environmental geophysics, geomechanics, and energy resources engineering interested in quantitative subsurface characterization and modeling of sediment properties.

Gary Mavko received his Ph.D. in Geophysics from Stanford University in 1977 where he is now Professor (Research) of Geophysics. Professor Mavko co-directs the Stanford Rock Physics and Borehole Geophysics Project (SRB), a group of approximately 25 researchers working on problems related to wave propagation in earth materials. Professor Mavko is also a co-author of *Quantitative Seismic Interpretation* (Cambridge University Press, 2005), and has been an invited instructor for numerous industry courses on rock physics for seismic reservoir characterization. He received the Honorary Membership award from the Society of Exploration Geophysicists (SEG) in 2001, and was the SEG Distinguished Lecturer in 2006.

Tapan Mukerji received his Ph.D. in Geophysics from Stanford University in 1995 and is now an Associate Professor (Research) in Energy Resources Engineering and

a member of the Stanford Rock Physics Project at Stanford University. Professor Mukerji co-directs the Stanford Center for Reservoir Forecasting (SCRF) focusing on problems related to uncertainty and data integration for reservoir modeling. His research interests include wave propagation and statistical rock physics, and he specializes in applied rock physics and geostatistical methods for seismic reservoir characterization, fracture detection, time-lapse monitoring, and shallow subsurface environmental applications. Professor Mukerji is also a co-author of *Quantitative Seismic Interpretation*, and has taught numerous industry courses. He received the Karcher award from the Society of Exploration Geophysicists in 2000.

Jack Dvorkin received his Ph.D. in Continuum Mechanics in 1980 from Moscow University in the USSR. He has worked in the Petroleum Industry in the USSR and USA, and is currently a Senior Research Scientist with the Stanford Rock Physics Project at Stanford University. Dr Dvorkin has been an invited instructor for numerous industry courses throughout the world, on rock physics and quantitative seismic interpretation. He is a member of American Geophysical Union, Society of Exploration Geophysicists, American Association of Petroleum Geologists, and the Society of Petroleum Engineers.

The Rock Physics Handbook, Second Edition

Tools for Seismic Analysis of Porous Media

Gary Mavko

Stanford University, USA

Tapan Mukerji

Stanford University, USA

Jack Dvorkin

Stanford University, USA



CAMBRIDGE
UNIVERSITY PRESS

CAMBRIDGE UNIVERSITY PRESS
Cambridge, New York, Melbourne, Madrid, Cape Town, Singapore,
São Paulo, Delhi, Dubai, Tokyo

Cambridge University Press
The Edinburgh Building, Cambridge CB2 8RU, UK

Published in the United States of America by Cambridge University Press, New York

www.cambridge.org

Information on this title: www.cambridge.org/9780521861366

© G. Mavko, T. Mukerji, and J. Dvorkin 2009

This publication is in copyright. Subject to statutory exception and to the provision of relevant collective licensing agreements, no reproduction of any part may take place without the written permission of Cambridge University Press.

First published in print format 2009

ISBN-13 978-0-511-65062-8 eBook (NetLibrary)

ISBN-13 978-0-521-86136-6 Hardback

Cambridge University Press has no responsibility for the persistence or accuracy of urls for external or third-party internet websites referred to in this publication, and does not guarantee that any content on such websites is, or will remain, accurate or appropriate.

Contents

Preface

page xi

1	Basic tools	1
1.1	The Fourier transform	1
1.2	The Hilbert transform and analytic signal	6
1.3	Statistics and probability	9
1.4	Coordinate transformations	18
2	Elasticity and Hooke's law	21
2.1	Elastic moduli: isotropic form of Hooke's law	21
2.2	Anisotropic form of Hooke's law	23
2.3	Thomsen's notation for weak elastic anisotropy	35
2.4	Tsvankin's extended Thomsen parameters for orthorhombic media	39
2.5	Third-order nonlinear elasticity	40
2.6	Effective stress properties of rocks	43
2.7	Stress-induced anisotropy in rocks	47
2.8	Strain components and equations of motion in cylindrical and spherical coordinate systems	54
2.9	Deformation of inclusions and cavities in elastic solids	56
2.10	Deformation of a circular hole: borehole stresses	68
2.11	Mohr's circles	74
2.12	Static and dynamic moduli	76
3	Seismic wave propagation	81
3.1	Seismic velocities	81
3.2	Phase, group, and energy velocities	83

3.3	NMO in isotropic and anisotropic media	86
3.4	Impedance, reflectivity, and transmissivity	93
3.5	Reflectivity and amplitude variations with offset (AVO) in isotropic media	96
3.6	Plane-wave reflectivity in anisotropic media	105
3.7	Elastic impedance	115
3.8	Viscoelasticity and Q	121
3.9	Kramers–Kronig relations between velocity dispersion and Q	127
3.10	Waves in layered media: full-waveform synthetic seismograms	129
3.11	Waves in layered media: stratigraphic filtering and velocity dispersion	134
3.12	Waves in layered media: frequency-dependent anisotropy, dispersion, and attenuation	138
3.13	Scale-dependent seismic velocities in heterogeneous media	146
3.14	Scattering attenuation	150
3.15	Waves in cylindrical rods: the resonant bar	155
3.16	Waves in boreholes	160

4 Effective elastic media: bounds and mixing laws 169

4.1	Hashin–Shtrikman–Walpole bounds	169
4.2	Voigt and Reuss bounds	174
4.3	Wood’s formula	175
4.4	Voigt–Reuss–Hill average moduli estimate	177
4.5	Composite with uniform shear modulus	178
4.6	Rock and pore compressibilities and some pitfalls	179
4.7	Kuster and Toksöz formulation for effective moduli	183
4.8	Self-consistent approximations of effective moduli	185
4.9	Differential effective medium model	190
4.10	Hudson’s model for cracked media	194
4.11	Eshelby–Cheng model for cracked anisotropic media	203
4.12	T -matrix inclusion models for effective moduli	205
4.13	Elastic constants in finely layered media: Backus average	210
4.14	Elastic constants in finely layered media: general layer anisotropy	215
4.15	Poroelectric Backus average	216
4.16	Seismic response to fractures	219
4.17	Bound-filling models	224

5 Granular media 229

5.1	Packing and sorting of spheres	229
5.2	Thomas–Stieber model for sand–shale systems	237

5.3	Particle size and sorting	242
5.4	Random spherical grain packings: contact models and effective moduli	245
5.5	Ordered spherical grain packings: effective moduli	264

6 Fluid effects on wave propagation 266

6.1	Biot's velocity relations	266
6.2	Geertsma–Smit approximations of Biot's relations	272
6.3	Gassmann's relations: isotropic form	273
6.4	Brown and Korrington's generalized Gassmann equations for mixed mineralogy	282
6.5	Fluid substitution in anisotropic rocks	284
6.6	Generalized Gassmann's equations for composite porous media	287
6.7	Generalized Gassmann equations for solid pore-filling material	290
6.8	Fluid substitution in thinly laminated reservoirs	292
6.9	BAM: Marion's bounding average method	295
6.10	Mavko–Jizba squirt relations	297
6.11	Extension of Mavko–Jizba squirt relations for all frequencies	298
6.12	Biot–squirt model	302
6.13	Chapman <i>et al.</i> squirt model	304
6.14	Anisotropic squirt	306
6.15	Common features of fluid-related velocity dispersion mechanisms	310
6.16	Dvorkin–Mavko attenuation model	315
6.17	Partial and multiphase saturations	320
6.18	Partial saturation: White and Dutta–Odé model for velocity dispersion and attenuation	326
6.19	Velocity dispersion, attenuation, and dynamic permeability in heterogeneous poroelastic media	331
6.20	Waves in a pure viscous fluid	338
6.21	Physical properties of gases and fluids	339

7 Empirical relations 347

7.1	Velocity–porosity models: critical porosity and Nur's modified Voigt average	347
7.2	Velocity–porosity models: Geertsma's empirical relations for compressibility	350
7.3	Velocity–porosity models: Wyllie's time-average equation	350
7.4	Velocity–porosity models: Raymer–Hunt–Gardner relations	353

7.5	Velocity–porosity–clay models: Han’s empirical relations for shaley sandstones	355
7.6	Velocity–porosity–clay models: Tosaya’s empirical relations for shaley sandstones	357
7.7	Velocity–porosity–clay models: Castagna’s empirical relations for velocities	358
7.8	V_P – V_S –density models: Brocher’s compilation	359
7.9	V_P – V_S relations	363
7.10	Velocity–density relations	380
7.11	Eaton and Bowers pore-pressure relations	383
7.12	Kan and Swan pore-pressure relations	383
7.13	Attenuation and quality factor relations	384
7.14	Velocity–porosity–strength relations	386

8 Flow and diffusion 389

8.1	Darcy’s law	389
8.2	Viscous flow	394
8.3	Capillary forces	396
8.4	Kozeny–Carman relation for flow	401
8.5	Permeability relations with S_{wi}	407
8.6	Permeability of fractured formations	410
8.7	Diffusion and filtration: special cases	411

9 Electrical properties 414

9.1	Bounds and effective medium models	414
9.2	Velocity dispersion and attenuation	418
9.3	Empirical relations	421
9.4	Electrical conductivity in porous rocks	424
9.5	Cross-property bounds and relations between elastic and electrical parameters	429

Appendices 437

A.1	Typical rock properties	437
A.2	Conversions	452
A.3	Physical constants	456
A.4	Moduli and density of common minerals	457
A.5	Velocities and moduli of ice and methane hydrate	457

ix	Contents	
A.6	Physical properties of common gases	468
A.7	Velocity, moduli, and density of carbon dioxide	474
A.8	Standard temperature and pressure	474
	<i>References</i>	479
	<i>Index</i>	503

Preface to the Second Edition

In the decade since publication of the *Rock Physics Handbook*, research and use of rock physics has thrived. We hope that the First Edition has played a useful role in this era by making the scattered and eclectic mass of rock physics knowledge more accessible to experts and nonexperts, alike.

While preparing this Second Edition, our objective was still to summarize in a convenient form many of the commonly needed theoretical and empirical relations of rock physics. Our approach was to present *results*, with a few of the key assumptions and limitations, and almost never any derivations. Our intention was to create a quick reference and not a textbook. Hence, we chose to encapsulate a broad range of topics rather than to give in-depth coverage of a few. Even so, there are many topics that we have not addressed. While we have summarized the assumptions and limitations of each result, we hope that the brevity of our discussions does not give the impression that application of any rock physics result to real rocks is free of pitfalls. We assume that the reader will be generally aware of the various topics, and, if not, we provide a few references to the more complete descriptions in books and journals.

The handbook contains 101 sections on basic mathematical tools, elasticity theory, wave propagation, effective media, elasticity and poroelasticity, granular media, and pore-fluid flow and diffusion, plus overviews of dispersion mechanisms, fluid substitution, and V_P – V_S relations. The book also presents empirical results derived from reservoir rocks, sediments, and granular media, as well as tables of mineral data and an atlas of reservoir rock properties. The emphasis still focuses on elastic and seismic topics, though the discussion of electrical and cross seismic-electrical relations has grown. An associated website (<http://srb.stanford.edu/books>) offers MATLAB codes for many of the models and results described in the Second Edition.

In this Second Edition, [Chapter 2](#) has been expanded to include new discussions on elastic anisotropy including the Kelvin notation and eigenvalues for stiffnesses, effective stress behavior of rocks, and stress-induced elasticity anisotropy. [Chapter 3](#) includes new material on anisotropic normal moveout (NMO) and reflectivity, amplitude variation with offset (AVO) relations, plus a new section on elastic impedance (including anisotropic forms), and updates on wave propagation in stratified media, and borehole waves. [Chapter 4](#) includes updates of inclusion-based effective media models, thinly layered media, and fractured rocks. [Chapter 5](#) contains

extensive new sections on granular media, including packing, particle size, sorting, sand–clay mixture models, and elastic effective medium models for granular materials. [Chapter 6](#) expands the discussion of fluid effects on elastic properties, including fluid substitution in laminated media, and models for fluid-related velocity dispersion in heterogeneous poroelastic media. [Chapter 7](#) contains new sections on empirical velocity–porosity–mineralogy relations, V_P – V_S relations, pore-pressure relations, static and dynamic moduli, and velocity–strength relations. [Chapter 8](#) has new discussions on capillary effects, irreducible water saturation, permeability, and flow in fractures. [Chapter 9](#) includes new relations between electrical and seismic properties. [The Appendices](#) has new tables of physical constants and properties for common gases, ice, and methane hydrate.

This *Handbook* is complementary to a number of other excellent books. For in-depth discussions of specific rock physics topics, we recommend *Fundamentals of Rock Mechanics, 4th Edition*, by Jaeger, Cook, and Zimmerman; *Compressibility of Sandstones*, by Zimmerman; *Physical Properties of Rocks: Fundamentals and Principles of Petrophysics*, by Schon; *Acoustics of Porous Media*, by Bourbié, Coussy, and Zinszner; *Introduction to the Physics of Rocks*, by Guéguen and Palciauskas; *A Geoscientist's Guide to Petrophysics*, by Zinszner and Pellerin; *Theory of Linear Poroelasticity*, by Wang; *Underground Sound*, by White; *Mechanics of Composite Materials*, by Christensen; *The Theory of Composites*, by Milton; *Random Heterogeneous Materials*, by Torquato; *Rock Physics and Phase Relations*, edited by Ahrens; and *Offset Dependent Reflectivity – Theory and Practice of AVO Analysis*, edited by Castagna and Backus. For excellent collections and discussions of classic rock physics papers we recommend *Seismic and Acoustic Velocities in Reservoir Rocks*, Volumes 1, 2 and 3, edited by Wang and Nur; *Elastic Properties and Equations of State*, edited by Shankland and Bass; *Seismic Wave Attenuation*, by Toksöz and Johnston; and *Classics of Elastic Wave Theory*, edited by Pelissier *et al.*

We wish to thank the students, scientific staff, and industrial affiliates of the Stanford Rock Physics and Borehole Geophysics (SRB) project for many valuable comments and insights. While preparing the Second Edition we found discussions with Tiziana Vanorio, Kaushik Bandyopadhyay, Ezequiel Gonzalez, Youngseuk Keehm, Robert Zimmermann, Boris Gurevich, Juan-Mauricio Florez, Anyela Marcote-Rios, Mike Payne, Mike Batzle, Jim Berryman, Pratap Sahay, and Tor Arne Johansen, to be extremely helpful. Li Teng contributed to the chapter on anisotropic AVOZ, and Ran Bachrach contributed to the chapter on dielectric properties. Dawn Burgess helped tremendously with editing, graphics, and content. We also wish to thank the readers of the First Edition who helped us to track down and fix errata.

And as always, we are indebted to Amos Nur, whose work, past and present, has helped to make the field of rock physics what it is today.

Gary Mavko, Tapan Mukerji, and Jack Dvorkin.

1 Basic tools

1.1 The Fourier transform

Synopsis

The **Fourier transform** of $f(x)$ is defined as

$$F(s) = \int_{-\infty}^{\infty} f(x)e^{-i2\pi xs} dx$$

The inverse Fourier transform is given by

$$f(x) = \int_{-\infty}^{\infty} F(s)e^{+i2\pi xs} ds$$

Evenness and oddness

A function $E(x)$ is *even* if $E(x) = E(-x)$. A function $O(x)$ is *odd* if $O(x) = -O(-x)$.

The Fourier transform has the following properties for even and odd functions:

- *Even functions.* The Fourier transform of an even function is even. A *real even* function transforms to a *real even* function. An *imaginary even* function transforms to an *imaginary even* function.
- *Odd functions.* The Fourier transform of an odd function is odd. A *real odd* function transforms to an *imaginary odd* function. An *imaginary odd* function transforms to a *real odd* function (i.e., the “realness” flips when the Fourier transform of an odd function is taken).

real even (RE) \rightarrow real even (RE)

imaginary even (IE) \rightarrow imaginary even (IE)

real odd (RO) \rightarrow imaginary odd (IO)

imaginary odd (IO) \rightarrow real odd (RO)

Any function can be expressed in terms of its even and odd parts:


$$f(x) = E(x) + O(x)$$

where

$$E(x) = \frac{1}{2}[f(x) + f(-x)]$$

$$O(x) = \frac{1}{2}[f(x) - f(-x)]$$

Then, for an arbitrary complex function we can summarize these relations as (Bracewell, 1965)

$$f(x) = \text{re}(x) + i \text{ie}(x) + \text{ro}(x) + i \text{io}(x)$$


$$F(s) = \text{RE}(s) + i \text{IE}(s) + \text{RO}(s) + i \text{IO}(s)$$

As a consequence, a real function $f(x)$ has a Fourier transform that is *hermitian*, $F(s) = F^*(-s)$, where $*$ refers to the complex conjugate.

For a more general complex function, $f(x)$, we can tabulate some additional properties (Bracewell, 1965):

$$\begin{aligned} f(x) &\Leftrightarrow F(s) \\ f^*(x) &\Leftrightarrow F^*(-s) \\ f^*(-x) &\Leftrightarrow F^*(s) \\ f(-x) &\Leftrightarrow F(-s) \\ 2 \text{Re} f(x) &\Leftrightarrow F(s) + F^*(-s) \\ 2 \text{Im} f(x) &\Leftrightarrow F(s) - F^*(-s) \\ f(x) + f^*(-x) &\Leftrightarrow 2 \text{Re} F(s) \\ f(x) - f^*(-x) &\Leftrightarrow 2 \text{Im} F(s) \end{aligned}$$

The **convolution** of two functions $f(x)$ and $g(x)$ is

$$f(x) * g(x) = \int_{-\infty}^{+\infty} f(z) g(x - z) dz = \int_{-\infty}^{+\infty} f(x - z) g(z) dz$$

Convolution theorem

If $f(x)$ has the Fourier transform $F(s)$, and $g(x)$ has the Fourier transform $G(s)$, then the Fourier transform of the convolution $f(x) * g(x)$ is the product $F(s)G(s)$.

The **cross-correlation** of two functions $f(x)$ and $g(x)$ is

$$f^*(x) \star g(x) = \int_{-\infty}^{+\infty} f^*(z - x) g(z) dz = \int_{-\infty}^{+\infty} f^*(z) g(z + x) dz$$

where f^* refers to the complex conjugate of f . When the two functions are the same, $f^*(x) \star f(x)$ is called the **autocorrelation** of $f(x)$.

Energy spectrum

The modulus squared of the Fourier transform $|F(s)|^2 = F(s)F^*(s)$ is sometimes called the **energy spectrum** or simply the **spectrum**.

If $f(x)$ has the Fourier transform $F(s)$, then the autocorrelation of $f(x)$ has the Fourier transform $|F(s)|^2$.

Phase spectrum

The Fourier transform $F(s)$ is most generally a complex function, which can be written as

$$F(s) = |F|e^{i\varphi} = \text{Re } F(s) + i \text{Im } F(s)$$

where $|F|$ is the modulus and φ is the **phase**, given by

$$\varphi = \tan^{-1}[\text{Im } F(s)/\text{Re } F(s)]$$

The function $\varphi(s)$ is sometimes also called the **phase spectrum**.

Obviously, both the modulus and phase must be known to completely specify the Fourier transform $F(s)$ or its transform pair in the other domain, $f(x)$. Consequently, an infinite number of functions $f(x) \Leftrightarrow F(s)$ are consistent with a given spectrum $|F(s)|^2$.

The **zero-phase** equivalent function (or zero-phase equivalent wavelet) corresponding to a given spectrum is

$$F(s) = |F(s)|$$

$$f(x) = \int_{-\infty}^{\infty} |F(s)| e^{+i2\pi xs} ds$$

which implies that $F(s)$ is real and $f(x)$ is hermitian. In the case of zero-phase *real* wavelets, then, both $F(s)$ and $f(x)$ are real even functions.

The **minimum-phase** equivalent function or wavelet corresponding to a spectrum is the unique one that is both *causal* and *invertible*. A simple way to compute the minimum-phase equivalent of a spectrum $|F(s)|^2$ is to perform the following steps (Claerbout, 1992):

- (1) Take the logarithm, $B(s) = \ln |F(s)|$.
- (2) Take the Fourier transform, $B(s) \Rightarrow b(x)$.
- (3) Multiply $b(x)$ by zero for $x < 0$ and by 2 for $x > 0$. If done numerically, leave the values of b at zero and the Nyquist frequency unchanged.
- (4) Transform back, giving $B(s) + i\varphi(s)$, where φ is the desired phase spectrum.
- (5) Take the complex exponential to yield the minimum-phase function: $F_{\text{mp}}(s) = \exp[B(s) + i\varphi(s)] = |F(s)|e^{i\varphi(s)}$.
- (6) The causal minimum-phase wavelet is the Fourier transform of $F_{\text{mp}}(s) \Rightarrow f_{\text{mp}}(x)$. Another way of saying this is that the phase spectrum of the minimum-phase equivalent function is the Hilbert transform (see Section 1.2 on the Hilbert transform) of the log of the energy spectrum.

Sampling theorem

A function $f(x)$ is said to be *band limited* if its Fourier transform is nonzero only within a finite range of frequencies, $|s| < s_c$, where s_c is sometimes called the *cut-off frequency*. The function $f(x)$ is fully specified if sampled at equal spacing not exceeding $\Delta x = 1/(2s_c)$. Equivalently, a time series sampled at interval Δt adequately describes the frequency components out to the *Nyquist frequency* $f_N = 1/(2\Delta t)$.

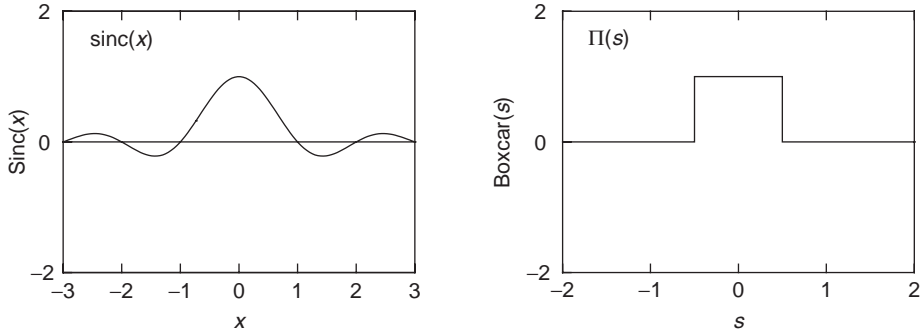


Figure 1.1.1 Plots of the function $\text{sinc}(x)$ and its Fourier transform $\Pi(s)$.

The numerical process to recover the intermediate points between samples is to convolve with the *sinc function*:

$$2s_c \text{sinc}(2s_c x) = 2s_c \sin(\pi 2s_c x) / \pi 2s_c x$$

where

$$\text{sinc}(x) \equiv \frac{\sin(\pi x)}{\pi x}$$

which has the properties:

$$\left. \begin{array}{l} \text{sinc}(0) = 1 \\ \text{sinc}(n) = 0 \end{array} \right\} n = \text{nonzero integer}$$

The Fourier transform of $\text{sinc}(x)$ is the boxcar function $\Pi(s)$:

$$\Pi(s) = \begin{cases} 0 & |s| > \frac{1}{2} \\ \frac{1}{2} & |s| = \frac{1}{2} \\ 1 & |s| < \frac{1}{2} \end{cases}$$

Plots of the function $\text{sinc}(x)$ and its Fourier transform $\Pi(s)$ are shown in [Figure 1.1.1](#).

One can see from the convolution and similarity theorems below that convolving with $2s_c \text{sinc}(2s_c x)$ is equivalent to multiplying by $\Pi(s/2s_c)$ in the frequency domain (i.e., zeroing out all frequencies $|s| > s_c$ and passing all frequencies $|s| < s_c$).

Numerical details

Consider a band-limited function $g(t)$ sampled at N points at equal intervals: $g(0)$, $g(\Delta t)$, $g(2\Delta t)$, ..., $g((N-1)\Delta t)$. A typical fast Fourier transform (FFT) routine will yield N equally spaced values of the Fourier transform, $G(f)$, often arranged as

$$\begin{array}{cccccccc} 1 & 2 & 3 & \cdots & \left(\frac{N}{2} + 1\right) & \left(\frac{N}{2} + 2\right) & \cdots & (N-1) & N \\ G(0) & G(\Delta f) & G(2\Delta f) & \cdots & G(\pm f_N) & G(-f_N + \Delta f) & \cdots & G(-2\Delta f) & G(-\Delta f) \end{array}$$

time domain sample rate Δt

Nyquist frequency $f_N = 1/(2\Delta t)$

frequency domain sample rate $\Delta f = 1/(N\Delta t)$

Note that, because of “wraparound,” the sample at $(N/2 + 1)$ represents both $\pm f_N$.

Spectral estimation and windowing

It is often desirable in rock physics and seismic analysis to estimate the spectrum of a wavelet or seismic trace. The most common, easiest, and, in some ways, the worst way is simply to chop out a piece of the data, take the Fourier transform, and find its magnitude. The problem is related to sample length. If the true data function is $f(t)$, a small sample of the data can be thought of as

$$f_{\text{sample}}(t) = \begin{cases} f(t), & a \leq t \leq b \\ 0, & \text{elsewhere} \end{cases}$$

or

$$f_{\text{sample}}(t) = f(t) \Pi\left(\frac{t - \frac{1}{2}(a+b)}{b-a}\right)$$

where $\Pi(t)$ is the boxcar function discussed above. Taking the Fourier transform of the data sample gives

$$F_{\text{sample}}(s) = F(s) * [|b-a| \text{sinc}((b-a)s) e^{-i\pi(a+b)s}]$$

More generally, we can “window” the sample with some other function $\omega(t)$:

$$f_{\text{sample}}(t) = f(t) \omega(t)$$

yielding

$$F_{\text{sample}}(s) = F(s) * W(s)$$

Thus, the estimated spectrum can be highly contaminated by the Fourier transform of the window, often with the effect of smoothing and distorting the spectrum due to the convolution with the window spectrum $W(s)$. This can be particularly severe in the analysis of ultrasonic waveforms in the laboratory, where often only the first 1 to $1\frac{1}{2}$ cycles are included in the window. The solution to the problem is not easy, and there is an extensive literature (e.g., Jenkins and Watts, 1968; Marple, 1987) on spectral estimation. Our advice is to be aware of the artifacts of windowing and to experiment to determine the sensitivity of the results, such as the spectral ratio or the phase velocity, to the choice of window size and shape.

Fourier transform theorems

Tables 1.1.1 and 1.1.2 summarize some useful theorems (Bracewell, 1965). If $f(x)$ has the Fourier transform $F(s)$, and $g(x)$ has the Fourier transform $G(s)$, then the Fourier

Table 1.1.1 *Fourier transform theorems.*

Theorem	x -domain		s -domain
Similarity	$f(ax)$	\Leftrightarrow	$\frac{1}{ a } F\left(\frac{s}{a}\right)$
Addition	$f(x) + g(x)$	\Leftrightarrow	$F(s) + G(s)$
Shift	$f(x - a)$	\Leftrightarrow	$e^{-i2\pi as} F(s)$
Modulation	$f(x) \cos \omega x$	\Leftrightarrow	$\frac{1}{2} F\left(s - \frac{\omega}{2\pi}\right) + \frac{1}{2} F\left(s + \frac{\omega}{2\pi}\right)$
Convolution	$f(x) * g(x)$	\Leftrightarrow	$F(s) G(s)$
Autocorrelation	$f(x) * f^*(-x)$	\Leftrightarrow	$ F(s) ^2$
Derivative	$f'(x)$	\Leftrightarrow	$i2\pi s F(s)$

Table 1.1.2 *Some additional theorems.*

Derivative of convolution	$\frac{d}{dx} [f(x) * g(x)] = f'(x) * g(x) = f(x) * g'(x)$
Rayleigh	$\int_{-\infty}^{\infty} f(x) ^2 dx = \int_{-\infty}^{\infty} F(s) ^2 ds$
Power	$\int_{-\infty}^{\infty} f(x) g^*(x) dx = \int_{-\infty}^{\infty} F(s) G^*(s) ds$
(f and g real)	$\int_{-\infty}^{\infty} f(x) g(-x) dx = \int_{-\infty}^{\infty} F(s) G(s) ds$

transform pairs in the x -domain and the s -domain are as shown in the tables. [Table 1.1.3](#) lists some useful Fourier transform pairs.

1.2 The Hilbert transform and analytic signal

Synopsis

The **Hilbert transform** of $f(x)$ is defined as

$$F_{\text{Hi}}(x) = \frac{1}{\pi} \int_{-\infty}^{\infty} \frac{f(x')}{x' - x} dx'$$

which can be expressed as a convolution of $f(x)$ with $(-1/\pi x)$ by

$$F_{\text{Hi}} = -\frac{1}{\pi x} * f(x)$$

The Fourier transform of $(-1/\pi x)$ is $(i \operatorname{sgn}(s))$, that is, $+i$ for positive s and $-i$ for negative s . Hence, applying the Hilbert transform keeps the Fourier amplitudes or spectrum the same but changes the phase. Under the Hilbert transform, $\sin(kx)$ is converted to $\cos(kx)$, and $\cos(kx)$ is converted to $-\sin(kx)$. Similarly, the Hilbert transforms of even functions are odd functions and vice versa.

Table 1.1.3 Some Fourier transform pairs.

	$\sin \pi x$	$\frac{i}{2} \left[\delta \left(s + \frac{1}{2} \right) - \delta \left(s - \frac{1}{2} \right) \right]$	$\begin{matrix} \uparrow \\ \downarrow \end{matrix}$
	$\cos \pi x$	$\frac{1}{2} \left[\delta \left(s + \frac{1}{2} \right) + \delta \left(s - \frac{1}{2} \right) \right]$	$\begin{matrix} \uparrow & \uparrow \end{matrix}$
	$\delta(x)$	1	
	$\text{sinc}(x)$	$\Pi(s)$	
	$\text{sinc}^2(x)$	$\Lambda(s)$	
	$e^{-\pi x^2}$	$e^{-\pi s^2}$	
	$-1/\pi x$	$i \operatorname{sgn}(s)$	
	$\frac{x_0}{x_0^2 + x^2}$	$\pi \exp(-2\pi x_0 s)$	
	$e^{- x }$	$\frac{2}{1 + (2\pi s)^2}$	
	$ x ^{-1/2}$	$ s ^{-1/2}$	

The inverse of the Hilbert transform is itself the Hilbert transform with a change of sign:

$$f(x) = -\frac{1}{\pi} \int_{-\infty}^{\infty} \frac{F_{\text{Hi}}(x')}{x' - x} dx'$$

or

$$f(x) = -\left(-\frac{1}{\pi x}\right) * F_{\text{Hi}}$$

The **analytic signal** associated with a real function, $f(t)$, is the complex function $S(t) = f(t) - i F_{\text{Hi}}(t)$

As discussed below, the Fourier transform of $S(t)$ is zero for negative frequencies.

The **instantaneous envelope** of the analytic signal is

$$E(t) = \sqrt{f^2(t) + F_{\text{Hi}}^2(t)}$$

The **instantaneous phase** of the analytic signal is

$$\begin{aligned}\varphi(t) &= \tan^{-1}[-F_{\text{Hi}}(t)/f(t)] \\ &= \text{Im}[\ln(S(t))]\end{aligned}$$

The **instantaneous frequency** of the analytic signal is

$$\omega = \frac{d\varphi}{dt} = \text{Im}\left[\frac{d}{dt}\ln(S)\right] = \text{Im}\left(\frac{1}{S}\frac{dS}{dt}\right)$$

Claerbout (1992) has suggested that ω can be numerically more stable if the denominator is rationalized and the functions are locally smoothed, as in the following equation:

$$\bar{\omega} = \text{Im}\left[\frac{\left\langle S^*(t) \frac{dS(t)}{dt} \right\rangle}{\left\langle S^*(t) S(t) \right\rangle}\right]$$

where $\langle \cdot \rangle$ indicates some form of running average or smoothing.

Causality

The **impulse response**, $I(t)$, of a real physical system must be causal, that is,

$$I(t) = 0, \quad \text{for } t < 0$$

The Fourier transform $T(f)$ of the impulse response of a causal system is sometimes called the **transfer function**:

$$T(f) = \int_{-\infty}^{\infty} I(t) e^{-i2\pi ft} dt$$

$T(f)$ must have the property that the real and imaginary parts are Hilbert transform pairs, that is, $T(f)$ will have the form

$$T(f) = G(f) + iB(f)$$

where $B(f)$ is the Hilbert transform of $G(f)$:

$$B(f) = \frac{1}{\pi} \int_{-\infty}^{\infty} \frac{G(f') df'}{f' - f}$$

$$G(f) = -\frac{1}{\pi} \int_{-\infty}^{\infty} \frac{B(f') df'}{f' - f}$$

Similarly, if we reverse the domains, an analytic signal of the form

$$S(t) = f(t) - iF_{\text{Hi}}(t)$$

must have a Fourier transform that is zero for negative frequencies. In fact, one convenient way to implement the Hilbert transform of a real function is by performing the following steps:

- (1) Take the Fourier transform.
- (2) Multiply the Fourier transform by zero for $f < 0$.
- (3) Multiply the Fourier transform by 2 for $f > 0$.
- (4) If done numerically, leave the samples at $f = 0$ and the Nyquist frequency unchanged.
- (5) Take the inverse Fourier transform.

The imaginary part of the result will be the negative Hilbert transform of the real part.

1.3 Statistics and probability

Synopsis

The **sample mean**, m , of a set of n data points, x_i , is the arithmetic average of the data values:

$$m = \frac{1}{n} \sum_{i=1}^n x_i$$

The **median** is the midpoint of the observed values if they are arranged in increasing order. The **sample variance**, σ^2 , is the average squared difference of the observed values from the mean:

$$\sigma^2 = \frac{1}{n} \sum_{i=1}^n (x_i - m)^2$$

(An unbiased estimate of the **population variance** is often found by dividing the sum given above by $(n - 1)$ instead of by n .)

The **standard deviation**, σ , is the square root of the variance, while the **coefficient of variation** is σ/m . The **mean deviation**, α , is

$$\alpha = \frac{1}{n} \sum_{i=1}^n |x_i - m|$$

Regression

When trying to determine whether two different data variables, x and y , are related, we often estimate the **correlation coefficient**, ρ , given by (e.g., Young, 1962)

$$\rho = \frac{\frac{1}{n} \sum_{i=1}^n (x_i - m_x)(y_i - m_y)}{\sigma_x \sigma_y}, \quad \text{where } |\rho| \leq 1$$

where σ_x and σ_y are the standard deviations of the two distributions and m_x and m_y are their means. The correlation coefficient gives a measure of how close the points come to falling along a straight line in a scatter plot of x versus y . $|\rho| = 1$ if the points lie perfectly along a line, and $|\rho| < 1$ if there is scatter about the line. The numerator of this expression is the **sample covariance**, C_{xy} , which is defined as

$$C_{xy} = \frac{1}{n} \sum_{i=1}^n (x_i - m_x)(y_i - m_y)$$

It is important to remember that the correlation coefficient is a measure of the *linear* relation between x and y . If they are related in a nonlinear way, the correlation coefficient will be misleadingly small.

The simplest recipe for estimating the linear relation between two variables, x and y , is **linear regression**, in which we assume a relation of the form:

$$y = ax + b$$

The coefficients that provide the best fit to the measured values of y , in the least-squares sense, are

$$a = \rho \frac{\sigma_y}{\sigma_x}, \quad b = m_y - am_x$$

More explicitly,

$$a = \frac{n \sum x_i y_i - (\sum x_i)(\sum y_i)}{n \sum x_i^2 - (\sum x_i)^2}, \quad \text{slope}$$

$$b = \frac{(\sum y_i)(\sum x_i^2) - (\sum x_i y_i)(\sum x_i)}{n \sum x_i^2 - (\sum x_i)^2}, \quad \text{intercept}$$

The scatter or variation of y -values around the regression line can be described by the sum of the squared errors as

$$E^2 = \sum_{i=1}^n (y_i - \hat{y}_i)^2$$

where \hat{y}_i is the value predicted from the regression line. This can be expressed as a variance around the regression line as

$$\hat{\sigma}_y^2 = \frac{1}{n} \sum_{i=1}^n (y_i - \hat{y}_i)^2$$

The square of the correlation coefficient ρ is the **coefficient of determination**, often denoted by r^2 , which is a measure of the regression variance relative to the total variance in the variable y , expressed as

$$r^2 = \rho^2 = 1 - \frac{\text{variance of } y \text{ around the linear regression}}{\text{total variance of } y}$$

$$= 1 - \frac{\sum_{i=1}^n (y_i - \hat{y}_i)^2}{\sum_{i=1}^n (y_i - m_y)^2} = 1 - \frac{\hat{\sigma}_y^2}{\sigma_y^2}$$

The inverse relation is

$$\hat{\sigma}_y^2 = \sigma_y^2(1 - r^2)$$

Often, when doing a linear regression the choice of dependent and independent variables is arbitrary. The form above treats x as independent and exact and assigns errors to y . It often makes just as much sense to reverse their roles, and we can find a regression of the form

$$x = a'y + b'$$

Generally $a \neq 1/a'$ unless the data are perfectly correlated. In fact, the correlation coefficient, ρ , can be written as $\rho = \sqrt{aa'}$.

The coefficients of the linear regression among three variables of the form

$$z = a + bx + cy$$

are given by

$$b = \frac{C_{xz}C_{yy} - C_{xy}C_{yz}}{C_{xx}C_{yy} - C_{xy}^2}$$

$$c = \frac{C_{xz}C_{yz} - C_{xy}C_{xz}}{C_{xx}C_{yy} - C_{xy}^2}$$

$$a = m_z - m_x b - m_y c$$

The coefficients of the n -dimensional linear regression of the form

$$z = c_0 + c_1 x_1 + c_2 x_2 + \cdots + c_n x_n$$

are given by

$$\begin{bmatrix} c_0 \\ c_1 \\ c_2 \\ \vdots \\ c_n \end{bmatrix} = (M^T M)^{-1} M^T \begin{bmatrix} z^{(1)} \\ z^{(2)} \\ \vdots \\ z^{(k)} \end{bmatrix}$$

where the k sets of independent variables form columns 2:($n + 1$) in the matrix M :

$$M = \begin{bmatrix} 1 & x_1^{(1)} & x_2^{(1)} & \cdots & x_n^{(1)} \\ 1 & x_1^{(2)} & x_2^{(2)} & \cdots & x_n^{(2)} \\ \vdots & \vdots & \vdots & & \vdots \\ 1 & x_1^{(k)} & x_2^{(k)} & \cdots & x_n^{(k)} \end{bmatrix}$$

Variogram and covariance function

In geostatistics, variables are modeled as random fields, $X(\mathbf{u})$, where \mathbf{u} is the spatial position vector. Spatial correlation between two random fields $X(\mathbf{u})$ and $Y(\mathbf{u})$ is described by the cross-covariance function $C_{XY}(\mathbf{h})$, defined by

$$C_{XY}(\mathbf{h}) = E\{[X(\mathbf{u}) - m_X(\mathbf{u})][Y(\mathbf{u} + \mathbf{h}) - m_Y(\mathbf{u} + \mathbf{h})]\}$$

where $E\{\}$ denotes the expectation operator, m_X and m_Y are the means of X and Y , and \mathbf{h} is called the lag vector. For stationary fields, m_X and m_Y are independent of position. When X and Y are the same function, the equation represents the auto-covariance function $C_{XX}(\mathbf{h})$. A closely related measure of two-point spatial variability is the semivariogram, $\gamma(\mathbf{h})$. For stationary random fields $X(\mathbf{u})$ and $Y(\mathbf{u})$, the cross-variogram $2\gamma_{XY}(\mathbf{h})$ is defined as

$$2\gamma_{XY}(\mathbf{h}) = E\{[X(\mathbf{u} + \mathbf{h}) - X(\mathbf{u})][Y(\mathbf{u} + \mathbf{h}) - Y(\mathbf{u})]\}$$

When X and Y are the same, the equation represents the variogram of $X(\mathbf{h})$. For a stationary random field, the variogram and covariance function are related by

$$\gamma_{XX}(\mathbf{h}) = C_{XX}(0) - C_{XX}(\mathbf{h})$$

where $C_{XX}(0)$ is the stationary variance of X .

Distributions

A population of n elements possesses $\binom{n}{r}$ (pronounced “ n choose r ”) different subpopulations of size $r \leq n$, where

$$\binom{n}{r} = \frac{(n)_r}{r!} = \frac{n(n-1) \cdots (n-r+1)}{1 \cdot 2 \cdots (r-1)r} = \frac{n!}{r!(n-r)!}$$

Expressions of this kind are called **binomial coefficients**. Another way to say this is that a subset of r elements can be chosen in $\binom{n}{r}$ different ways from the original set.

The **binomial distribution** gives the probability of n successes in N independent trials, if p is the probability of success in any one trial. The binomial distribution is given by

$$f_{N,p}(n) = \binom{N}{n} p^n (1-p)^{N-n}$$

The mean of the binomial distribution is given by

$$m_b = Np$$

and the variance of the binomial distribution is given by

$$\sigma_b^2 = Np(1-p)$$

The **Poisson distribution** is the limit of the binomial distribution as $N \rightarrow \infty$ and $p \rightarrow 0$ so that $\lambda = Np$ remains finite. The Poisson distribution is given by

$$f_{\lambda}(n) = \frac{\lambda^n e^{-\lambda}}{n!}$$

The Poisson distribution is a discrete probability distribution and expresses the probability of n events occurring during a given interval of time if the events have an average (positive real) rate λ , and the events are independent of the time since the previous event. n is a non-negative integer.

The mean of the Poisson distribution is given by

$$m_P = \lambda$$

and the variance of the Poisson distribution is given by

$$\sigma_P^2 = \lambda$$

The **uniform** distribution is given by

$$f(x) = \begin{cases} \frac{1}{b-a}, & a \leq x \leq b \\ 0, & \text{elsewhere} \end{cases}$$

The mean of the uniform distribution is

$$m = \frac{(a+b)}{2}$$

and the standard deviation of the uniform distribution is

$$\sigma = \frac{|b-a|}{\sqrt{12}}$$

The **Gaussian** or **normal** distribution is given by

$$f(x) = \frac{1}{\sigma\sqrt{2\pi}} e^{-(x-m)^2/2\sigma^2}$$

where σ is the standard deviation and m is the mean. The mean deviation for the Gaussian distribution is

$$\alpha = \sigma\sqrt{\frac{2}{\pi}}$$

When m measurements are made of n quantities, the situation is described by the n -dimensional **multivariate Gaussian** probability density function (pdf):

$$f_n(x) = \frac{1}{(2\pi)^{n/2} |\mathbf{C}|^{1/2}} \exp \left[-\frac{1}{2} (\mathbf{x} - \mathbf{m})^T \mathbf{C}^{-1} (\mathbf{x} - \mathbf{m}) \right]$$

where $\mathbf{x}^T = (x_1, x_2, \dots, x_n)$ is the vector of observations, $\mathbf{m}^T = (m_1, m_2, \dots, m_n)$ is the vector of means of the individual distributions, and \mathbf{C} is the covariance matrix:

$$\mathbf{C} = [C_{ij}]$$

where the individual covariances, C_{ij} , are as defined above. Notice that this reduces to the single variable normal distribution when $n = 1$.

When the natural logarithm of a variable, $x = \ln(y)$, is normally distributed, it belongs to a **lognormal distribution** expressed as

$$f(y) = \frac{1}{\sqrt{2\pi} \beta y} \exp \left[-\frac{1}{2} \left(\frac{\ln(y) - \alpha}{\beta} \right)^2 \right]$$

where α is the mean and β^2 is the variance. The relations among the arithmetic and logarithmic parameters are

$$\begin{aligned} m &= e^{\alpha + \beta^2/2}, & \alpha &= \ln(m) - \beta^2/2 \\ \sigma^2 &= m^2(e^{\beta^2} - 1), & \beta^2 &= \ln(1 + \sigma^2/m^2) \end{aligned}$$

The **truncated exponential distribution** is given by

$$P(x) = \begin{cases} \frac{1}{X} \exp(-x/X), & x \geq 0 \\ 0, & x < 0 \end{cases}$$

The mean m and variance σ^2 of the exponential distribution are given by

$$\begin{aligned} m &= X \\ \sigma^2 &= X^2 \end{aligned}$$

The **truncated exponential distribution** and the **Poisson distribution** are closely related. Many random events in nature are described by the Poisson distribution. For example, in a well log, consider that the occurrence of a flooding surface is a random event. Then in every interval of log of length D , the probability of finding exactly n flooding surfaces is

$$P_{\lambda D}(n) = \frac{(\lambda D)^n}{n!} \exp(-\lambda D)$$

The mean number of occurrences is λD , where λ is the mean number of occurrences per unit length. The mean thickness between events is $D/(\lambda D) = 1/\lambda$. The interval thicknesses d between flooding events are governed by the truncated exponential

$$P(d) = \begin{cases} \lambda \exp(-\lambda d), & d \geq 0 \\ 0, & d < 0 \end{cases}$$

the mean of which is $1/\lambda$.

The **logistic distribution** is a continuous distribution with probability density function given by

$$P(x) = \frac{e^{-(x-\mu)/s}}{s[1 + e^{-(x-\mu)/s}]^2} = \frac{1}{4s} \operatorname{sech}^2\left(\frac{x-\mu}{2s}\right)$$

The mean m and variance σ^2 of the logistic distribution are given by

$$m = \mu$$

$$\sigma^2 = \frac{\pi^2 s^2}{3}$$

The **Weibull distribution** is a continuous distribution with probability density function

$$P(x) = \begin{cases} \frac{k}{\lambda} \left(\frac{x}{\lambda}\right)^{k-1} e^{-(x/\lambda)^k}, & x \geq 0 \\ 0, & x < 0 \end{cases}$$

where $k > 0$ is the *shape* parameter and $\lambda > 0$ is the *scale* parameter for the distribution. The mean m and variance σ^2 of the logistic distribution are given by

$$m = \lambda \Gamma\left(1 + \frac{1}{k}\right)$$

$$\sigma^2 = \lambda^2 \Gamma\left(1 + \frac{2}{k}\right) - m^2$$

where Γ is the gamma function. The Weibull distribution is often used to describe failure rates. If the failure rate decreases over time, $k < 1$; if the failure rate is constant $k = 1$; and if the failure rate increases over time, $k > 1$. When $k = 3$, the Weibull distribution is a good approximation to the normal distribution, and when $k = 1$, the Weibull distribution reduces to the exponential distribution.

Monte Carlo simulations

Statistical simulation is a powerful numerical method for tackling many probabilistic problems. One of the steps is to draw samples X_i from a desired probability distribution function $F(x)$. This procedure is often called *Monte Carlo simulation*, a term made popular by physicists working on the bomb during the Second World War. In general, Monte Carlo simulation can be a very difficult problem, especially when X is multivariate with correlated components, and $F(x)$ is a complicated function. For the simple case of a univariate X and a completely known $F(x)$ (either analytically or numerically), drawing X_i amounts to first drawing *uniform* random variates U_i between 0 and 1, and then evaluating the inverse of the desired cumulative distribution function (CDF) at these U_i : $X_i = F^{-1}(U_i)$. The inverse of the CDF is called the quantile function. When $F^{-1}(X)$ is not known analytically, the inversion can be easily done by

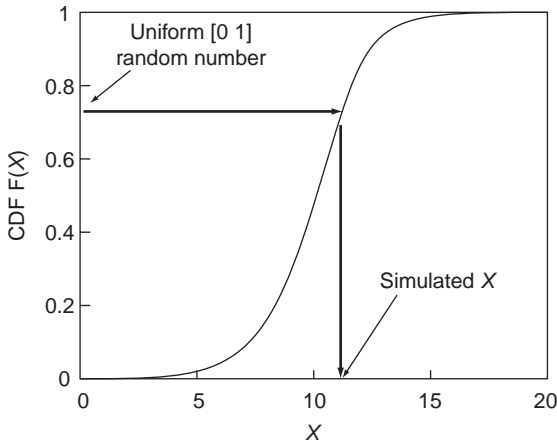


Figure 1.3.1 Schematic of a univariate Monte Carlo simulation.

table-lookup and interpolation from the numerically evaluated or nonparametric CDF derived from data. A graphical description of univariate Monte Carlo simulation is shown in Figure 1.3.1.

Many modern computer packages have random number generators not only for uniform and normal (Gaussian) distributions, but also for a large number of well-known, analytically defined statistical distributions.

Often Monte Carlo simulations require simulating correlated random variables (e.g., V_P , V_S). Correlated random variables may be simulated sequentially, making use of the chain rule of probability, which expresses the joint probability density in terms of the conditional and marginal densities: $P(V_P, V_S) = P(V_S|V_P)P(V_P)$.

A simple procedure for correlated Monte Carlo draws is as follows:

- draw a V_P sample from the V_P distribution;
- compute a V_S from the drawn V_P and the V_P – V_S regression;
- add to the computed V_S a random Gaussian error with zero mean and variance equal to the variance of the residuals from the V_P – V_S regression.

This gives a random, correlated (V_P , V_S) sample. A better approach is to draw V_S from the conditional distributions of V_S for each given V_P value, instead of using a simple V_P – V_S regression. Given sufficient V_P – V_S training data, the conditional distributions of V_S for different V_P can be computed.

Bootstrap

“Bootstrap” is a very powerful computational statistical method for assigning measures of accuracy to statistical estimates (e.g., Efron and Tibshirani, 1993). The general idea is to make multiple replicates of the data by drawing from the original data *with replacement*. Each of the bootstrap data replicates has the *same number* of samples as the original data set, but since they are drawn with replacement, some of the data may be represented more than once in the replicate data sets, while others might be

missing. Drawing with replacement from the data is equivalent to Monte Carlo realizations from the empirical CDF. The statistic of interest is computed on all of the replicate bootstrap data sets. The distribution of the bootstrap replicates of the statistic is a measure of uncertainty of the statistic.

Drawing bootstrap replicates from the empirical CDF in this way is sometimes termed **nonparametric bootstrap**. In **parametric bootstrap** the data are first modeled by a parametric CDF (e.g., a multivariate Gaussian), and then bootstrap data replicates are drawn from the modeled CDF. Both simple bootstrap techniques described above assume the data are independent and identically distributed. More sophisticated bootstrap techniques exist that can account for data dependence.

Statistical classification

The goal in statistical classification problems is to predict the class of an unknown sample based on observed attributes or features of the sample. For example, the observed attributes could be P and S impedances, and the classes could be lithofacies, such as sand and shale. The classes are sometimes also called states, outcomes, or responses, while the observed features are called the predictors. Discussions concerning many modern classification methods may be found in Fukunaga (1990), Duda *et al.* (2000), Hastie *et al.* (2001), and Bishop (2006).

There are two general types of statistical classification: **supervised classification**, which uses a training data set of samples for which both the attributes and classes have been observed; and **unsupervised learning**, for which only the observed attributes are included in the data. Supervised classification uses the training data to devise a classification rule, which is then used to predict the classes for new data, where the attributes are observed but the outcomes are unknown. Unsupervised learning tries to cluster the data into groups that are statistically different from each other based on the observed attributes.

A fundamental approach to the supervised classification problem is provided by Bayesian decision theory. Let x denote the univariate or multivariate input attributes, and let c_j , $j = 1, \dots, N$ denote the N different states or classes. The Bayes formula expresses the probability of a particular class given an observed x as

$$P(c_j | x) = \frac{P(x, c_j)}{P(x)} = \frac{P(x | c_j) P(c_j)}{P(x)}$$

where $P(x, c_j)$ denotes the joint probability of x and c_j ; $P(x | c_j)$ denotes the conditional probability of x given c_j ; and $P(c_j)$ is the prior probability of a particular class. Finally, $P(x)$ is the marginal or unconditional pdf of the attribute values across all N states. It can be written as

$$P(X) = \sum_{j=1}^N P(X | c_j) P(c_j)$$

and serves as a normalization constant. The class-conditional pdf, $P(x | c_j)$, is estimated from the training data or from a combination of training data and forward models.

The Bayes classification rule says:

classify as class c_k if $P(c_k | x) > P(c_j | x)$ for all $j \neq k$.

This is equivalent to choosing c_k when $P(x | c_k)P(c_k) > P(x | c_j)P(c_j)$ for all $j \neq k$.

The Bayes classification rule is the optimal one that minimizes the misclassification error and maximizes the posterior probability. Bayes classification requires estimating the complete set of class-conditional pdfs $P(x | c_j)$. With a large number of attributes, getting a good estimate of the highly multivariate pdf becomes difficult.

Classification based on traditional **discriminant analysis** uses only the means and covariances of the training data, which are easier to estimate than the complete pdfs. When the input features follow a multivariate Gaussian distribution, discriminant classification is equivalent to Bayes classification, but with other data distribution patterns, the discriminant classification is not guaranteed to maximize the posterior probability. Discriminant analysis classifies new samples according to the minimum Mahalanobis distance to each class cluster in the training data. The Mahalanobis distance is defined as follows:

$$M^2 = (\mathbf{x} - \boldsymbol{\mu}_j)^T \Sigma^{-1} (\mathbf{x} - \boldsymbol{\mu}_j)$$

where \mathbf{x} is the sample feature vector (measured attribute), $\boldsymbol{\mu}_j$ are the vectors of the attribute means for the different categories or classes, and Σ is the training data covariance matrix. The Mahalanobis distance can be interpreted as the usual Euclidean distance scaled by the covariance, which decorrelates and normalizes the components of the feature vector. When the covariance matrices for all the classes are taken to be identical, the classification gives rise to linear discriminant surfaces in the feature space. More generally, with different covariance matrices for each category, the discriminant surfaces are quadratic. If the classes have unequal prior probabilities, the term $\ln[P(\text{class})_j]$ is added to the right-hand side of the equation for the Mahalanobis distance, where $P(\text{class})_j$ is the prior probability for the j th class. Linear and quadratic discriminant classifiers are simple, robust classifiers and often produce good results, performing among the top few classifier algorithms.

1.4 Coordinate transformations

Synopsis

It is often necessary to transform vector and tensor quantities in one coordinate system to another more suited to a particular problem. Consider two right-hand rectangular Cartesian coordinates (x, y, z) and (x', y', z') with the same origin, but

with their axes rotated arbitrarily with respect to each other. The relative orientation of the two sets of axes is given by the direction cosines β_{ij} , where each element is defined as the cosine of the angle between the new i' -axis and the original j -axis. The variables β_{ij} constitute the elements of a 3×3 rotation matrix $[\beta]$. Thus, β_{23} is the cosine of the angle between the 2-axis of the primed coordinate system and the 3-axis of the unprimed coordinate system.

The general transformation law for tensors is

$$M'_{ABCD\dots} = \beta_{Aa}\beta_{Bb}\beta_{Cc}\beta_{Dd}\dots M_{abcd\dots}$$

where summation over repeated indices is implied. The left-hand subscripts (A, B, C, D, \dots) on the β s match the subscripts of the transformed tensor \mathbf{M}' on the left, and the right-hand subscripts (a, b, c, d, \dots) match the subscripts of \mathbf{M} on the right. Thus vectors, which are first-rank tensors, transform as

$$v'_i = \beta_{ij}v_j$$

or, in matrix notation, as

$$\begin{pmatrix} v'_1 \\ v'_2 \\ v'_3 \end{pmatrix} = \begin{pmatrix} \beta_{11} & \beta_{12} & \beta_{13} \\ \beta_{21} & \beta_{22} & \beta_{23} \\ \beta_{31} & \beta_{32} & \beta_{33} \end{pmatrix} \begin{pmatrix} v_1 \\ v_2 \\ v_3 \end{pmatrix}$$

whereas second-rank tensors, such as stresses and strains, obey

$$\sigma'_{ij} = \beta_{ik}\beta_{jl}\sigma_{kl}$$

or

$$[\sigma'] = [\beta][\sigma][\beta]^T$$

in matrix notation. Elastic stiffnesses and compliances are, in general, fourth-order tensors and hence transform according to

$$c'_{ijkl} = \beta_{ip}\beta_{jq}\beta_{kr}\beta_{ls}c_{pqrs}$$

Often c_{ijkl} and s_{ijkl} are expressed as the 6×6 matrices C_{ij} and S_{ij} , using the abbreviated 2-index notation, as defined in [Section 2.2](#) on anisotropic elasticity. In this case, the usual tensor transformation law is no longer valid, and the change of coordinates is more efficiently performed with the 6×6 **Bond transformation matrices** \mathbf{M} and \mathbf{N} , as explained below (Auld, 1990):

$$[C'] = [M][C][M]^T$$

$$[S'] = [N][S][N]^T$$

The elements of the 6×6 **M** and **N** matrices are given in terms of the direction cosines as follows:

$$\mathbf{M} = \begin{bmatrix} \beta_{11}^2 & \beta_{12}^2 & \beta_{13}^2 & 2\beta_{12}\beta_{13} & 2\beta_{13}\beta_{11} & 2\beta_{11}\beta_{12} \\ \beta_{21}^2 & \beta_{22}^2 & \beta_{23}^2 & 2\beta_{22}\beta_{23} & 2\beta_{23}\beta_{21} & 2\beta_{21}\beta_{22} \\ \beta_{31}^2 & \beta_{32}^2 & \beta_{33}^2 & 2\beta_{32}\beta_{33} & 2\beta_{33}\beta_{31} & 2\beta_{31}\beta_{32} \\ \beta_{21}\beta_{31} & \beta_{22}\beta_{32} & \beta_{23}\beta_{33} & \beta_{22}\beta_{33} + \beta_{23}\beta_{32} & \beta_{21}\beta_{33} + \beta_{23}\beta_{31} & \beta_{22}\beta_{31} + \beta_{21}\beta_{32} \\ \beta_{31}\beta_{11} & \beta_{32}\beta_{12} & \beta_{33}\beta_{13} & \beta_{12}\beta_{33} + \beta_{13}\beta_{32} & \beta_{11}\beta_{33} + \beta_{13}\beta_{31} & \beta_{11}\beta_{32} + \beta_{12}\beta_{31} \\ \beta_{11}\beta_{21} & \beta_{12}\beta_{22} & \beta_{13}\beta_{23} & \beta_{22}\beta_{13} + \beta_{12}\beta_{23} & \beta_{11}\beta_{23} + \beta_{13}\beta_{21} & \beta_{22}\beta_{11} + \beta_{12}\beta_{21} \end{bmatrix}$$

and

$$\mathbf{N} = \begin{bmatrix} \beta_{11}^2 & \beta_{12}^2 & \beta_{13}^2 & \beta_{12}\beta_{13} & \beta_{13}\beta_{11} & \beta_{11}\beta_{12} \\ \beta_{21}^2 & \beta_{22}^2 & \beta_{23}^2 & \beta_{22}\beta_{23} & \beta_{23}\beta_{21} & \beta_{21}\beta_{22} \\ \beta_{31}^2 & \beta_{32}^2 & \beta_{33}^2 & \beta_{32}\beta_{33} & \beta_{33}\beta_{31} & \beta_{31}\beta_{32} \\ 2\beta_{21}\beta_{31} & 2\beta_{22}\beta_{32} & 2\beta_{23}\beta_{33} & \beta_{22}\beta_{33} + \beta_{23}\beta_{32} & \beta_{21}\beta_{33} + \beta_{23}\beta_{31} & \beta_{22}\beta_{31} + \beta_{21}\beta_{32} \\ 2\beta_{31}\beta_{11} & 2\beta_{32}\beta_{12} & 2\beta_{33}\beta_{13} & \beta_{12}\beta_{33} + \beta_{13}\beta_{32} & \beta_{11}\beta_{33} + \beta_{13}\beta_{31} & \beta_{11}\beta_{32} + \beta_{12}\beta_{31} \\ 2\beta_{11}\beta_{21} & 2\beta_{12}\beta_{22} & 2\beta_{13}\beta_{23} & \beta_{22}\beta_{13} + \beta_{12}\beta_{23} & \beta_{11}\beta_{23} + \beta_{13}\beta_{21} & \beta_{22}\beta_{11} + \beta_{12}\beta_{21} \end{bmatrix}$$

The advantage of the Bond method for transforming stiffnesses and compliances is that it can be applied directly to the elastic constants given in 2-index notation, as they almost always are in handbooks and tables.

Assumptions and limitations

Coordinate transformations presuppose right-handed rectangular coordinate systems.

2 Elasticity and Hooke's law

2.1 Elastic moduli: isotropic form of Hooke's law

Synopsis

In an isotropic, linear elastic material, the stress and strain are related by **Hooke's law** as follows (e.g., Timoshenko and Goodier, 1934):

$$\sigma_{ij} = \lambda \delta_{ij} \varepsilon_{\alpha\alpha} + 2\mu \varepsilon_{ij}$$

or

$$\varepsilon_{ij} = \frac{1}{E} [(1 + \nu) \sigma_{ij} - \nu \delta_{ij} \sigma_{\alpha\alpha}]$$

where

ε_{ij} = elements of the strain tensor

σ_{ij} = elements of the stress tensor

$\varepsilon_{\alpha\alpha}$ = volumetric strain (sum over repeated index)

$\sigma_{\alpha\alpha}$ = mean stress times 3 (sum over repeated index)

$\delta_{ij} = 0$ if $i \neq j$ and $\delta_{ij} = 1$ if $i = j$

In an isotropic, linear elastic medium, only two constants are needed to specify the stress–strain relation completely (for example, $[\lambda, \mu]$ in the first equation or $[E, \nu]$, which can be derived from $[\lambda, \mu]$, in the second equation). Other useful and convenient moduli can be defined, but they are always relatable to just two constants. The three moduli that follow are examples.

The Bulk modulus, K , is defined as the ratio of the hydrostatic stress, σ_0 , to the volumetric strain:

$$\sigma_0 = \frac{1}{3} \sigma_{\alpha\alpha} = K \varepsilon_{\alpha\alpha}$$

The bulk modulus is the reciprocal of the **compressibility**, β , which is widely used to describe the volumetric compliance of a liquid, solid, or gas:

$$\beta = \frac{1}{K}$$

Caution

Occasionally in the literature authors have used the term *incompressibility* as an alternate name for Lamé's constant, λ , even though λ is *not the reciprocal of the compressibility*.

The shear modulus, μ , is defined as the ratio of the shear stress to the shear strain:

$$\sigma_{ij} = 2\mu\epsilon_{ij}, \quad i \neq j$$

Young's modulus, E , is defined as the ratio of the extensional stress to the extensional strain in a *uniaxial stress* state:

$$\sigma_{zz} = E\epsilon_{zz}, \quad \sigma_{xx} = \sigma_{yy} = \sigma_{xy} = \sigma_{xz} = \sigma_{yz} = 0$$

Poisson's ratio, which is defined as minus the ratio of the lateral strain to the axial strain in a *uniaxial stress* state:

$$\nu = -\frac{\epsilon_{xx}}{\epsilon_{zz}}, \quad \sigma_{xx} = \sigma_{yy} = \sigma_{xy} = \sigma_{xz} = \sigma_{yz} = 0$$

P-wave modulus, $M = \rho V_p^2$, defined as the ratio of the axial stress to the axial strain in a *uniaxial strain* state:

$$\sigma_{zz} = M\epsilon_{zz}, \quad \epsilon_{xx} = \epsilon_{yy} = \epsilon_{xy} = \epsilon_{xz} = \epsilon_{yz} = 0$$

Note that the moduli (λ , μ , K , E , M) all have the same units as stress (force/area), whereas Poisson's ratio is dimensionless.

Energy considerations require that the following relations always hold. If they do not, one should suspect experimental errors or that the material is not isotropic:

$$K = \lambda + \frac{2\mu}{3} \geq 0; \quad \mu \geq 0$$

or

$$-1 < \nu \leq \frac{1}{2}; \quad E \geq 0$$

In rocks, we seldom, if ever, observe a Poisson's ratio of less than 0. Although permitted by this equation, a negative measured value is usually treated with suspicion. A Poisson's ratio of 0.5 can mean an infinitely incompressible rock (not possible) or a liquid. A suspension of particles in fluid, or extremely soft, water-saturated sediments under essentially zero effective stress, such as pelagic ooze, can have a Poisson's ratio approaching 0.5.

Although any one of the isotropic constants (λ , μ , K , M , E , and ν) can be derived in terms of the others, μ and K have a special significance as *eigenelastic* constants (Mehrabadi and Cowin, 1989) or *principal elasticities* of the material (Kelvin, 1856). The stress and strain eigentensors associated with μ and K are orthogonal, as discussed in Section 2.2. Such an orthogonal significance does not hold for the pair λ and μ .

Table 2.1.1 Relationships among elastic constants in an isotropic material (after Birch, 1961).

K	E	λ	ν	M	μ
$\lambda + 2\mu/3$	$\mu \frac{3\lambda+2\mu}{\lambda+\mu}$	—	$\frac{\lambda}{2(\lambda+\mu)}$	$\lambda + 2\mu$	—
—	$9K \frac{K-\lambda}{3K-\lambda}$	—	$\frac{\lambda}{3K-\lambda}$	$3K - 2\lambda$	$3(K - \lambda)/2$
—	$\frac{9K\mu}{3K+\mu}$	$K - 2\mu/3$	$\frac{3K-2\mu}{2(3K+\mu)}$	$K + 4\mu/3$	—
$\frac{E\mu}{3(3\mu-E)}$	—	$\mu \frac{E-2\mu}{(3\mu-E)}$	$E/(2\mu) - 1$	$\mu \frac{4\mu-E}{3\mu-E}$	—
—	—	$3K \frac{3K-E}{9K-E}$	$\frac{3K-E}{6K}$	$3K \frac{3K+E}{9K-E}$	$\frac{3KE}{9K-E}$
$\lambda \frac{1+\nu}{3\nu}$	$\lambda \frac{(1+\nu)(1-2\nu)}{\nu}$	—	—	$\lambda \frac{1-\nu}{\nu}$	$\lambda \frac{1-2\nu}{2\nu}$
$\mu \frac{2(1+\nu)}{3(1-2\nu)}$	$2\mu(1 + \nu)$	$\mu \frac{2\nu}{1-2\nu}$	—	$\mu \frac{2-2\nu}{1-2\nu}$	—
—	$3K(1 - 2\nu)$	$3K \frac{\nu}{1+\nu}$	—	$3K \frac{1-\nu}{1+\nu}$	$3K \frac{1-2\nu}{2+2\nu}$
$\frac{E}{3(1-2\nu)}$	—	$\frac{E\nu}{(1+\nu)(1-2\nu)}$	—	$\frac{E(1-\nu)}{(1+\nu)(1-2\nu)}$	$\frac{E}{2+2\nu}$
$M - \frac{4}{3}\mu$	—	$M - 2\mu$	$\frac{M-2\mu}{2(M-\mu)}$	—	—

Table 2.1.1 summarizes useful relations among the constants of linear isotropic elastic media.

Assumptions and limitations

The preceding equations assume isotropic, linear elastic media.

2.2 Anisotropic form of Hooke's law

Synopsis

Hooke's law for a general anisotropic, linear, elastic solid states that the stress σ_{ij} is linearly proportional to the strain ε_{ij} , as expressed by

$$\sigma_{ij} = c_{ijkl}\varepsilon_{kl}$$

in which summation (over 1, 2, 3) is implied over the repeated subscripts k and l . The **elastic stiffness tensor**, with elements c_{ijkl} , is a fourth-rank tensor obeying the laws of tensor transformation and has a total of 81 components. However, not all 81 components are independent. The symmetry of stresses and strains implies that

$$c_{ijkl} = c_{jikl} = c_{ijlk} = c_{jilk}$$

reducing the number of independent constants to 36. In addition, the existence of a unique strain energy potential requires that

$$c_{ijkl} = c_{klij}$$

further reducing the number of independent constants to 21. This is the maximum number of independent elastic constants that any homogeneous linear elastic medium can have. Additional restrictions imposed by symmetry considerations reduce the number much further. **Isotropic**, linear elastic materials, which have maximum symmetry, are completely characterized by two independent constants, whereas materials with **triclinic** symmetry (the minimum symmetry) require all 21 constants.

Alternatively, the strains may be expressed as a linear combination of the stresses by the following expression:

$$\varepsilon_{ij} = s_{ijkl}\sigma_{kl}$$

In this case s_{ijkl} are elements of the **elastic compliance tensor** which has the same symmetry as the corresponding stiffness tensor. The compliance and stiffness are tensor inverses, denoted by

$$c_{ijkl}s_{klmn} = I_{ijmn} = \frac{1}{2}(\delta_{im}\delta_{jn} + \delta_{in}\delta_{jm})$$

The stiffness and compliance tensors must always be positive definite. One way to express this requirement is that all of the eigenvalues of the elasticity tensor (described below) must be positive.

Voigt notation

It is a standard practice in elasticity to use an abbreviated *Voigt* notation for the stresses, strains, and stiffness and compliance tensors, for doing so simplifies some of the key equations (Auld, 1990). In this abbreviated notation, the stresses and strains are written as six-element column vectors rather than as nine-element square matrices:

$$\mathbf{T} = \begin{bmatrix} \sigma_1 = \sigma_{11} \\ \sigma_2 = \sigma_{22} \\ \sigma_3 = \sigma_{33} \\ \sigma_4 = \sigma_{23} \\ \sigma_5 = \sigma_{13} \\ \sigma_6 = \sigma_{12} \end{bmatrix} \quad \mathbf{E} = \begin{bmatrix} e_1 = \varepsilon_{11} \\ e_2 = \varepsilon_{22} \\ e_3 = \varepsilon_{33} \\ e_4 = 2\varepsilon_{23} \\ e_5 = 2\varepsilon_{13} \\ e_6 = 2\varepsilon_{12} \end{bmatrix}$$

Note the factor of 2 in the definitions of strains, but not in the definition of stresses.

With the Voigt notation, four subscripts of the stiffness and compliance tensors are reduced to two. Each pair of indices $ij(kl)$ is replaced by one index $I(J)$ using the following convention:

$ij(kl)$	$I(J)$
11	1
22	2
33	3
23, 32	4
13, 31	5
12, 21	6

The relation, therefore, is $c_{IJ} = c_{ijkl}$ and $s_{IJ} = s_{ijkl} \mathbf{N}$, where

$$N = \begin{cases} 1 & \text{for } I \text{ and } J = 1, 2, 3 \\ 2 & \text{for } I \text{ or } J = 4, 5, 6 \\ 4 & \text{for } I \text{ and } J = 4, 5, 6 \end{cases}$$

Note how the definition of s_{IJ} differs from that of c_{IJ} . This results from the factors of 2 introduced in the definition of strains in the abbreviated notation. Hence the Voigt matrix representation of the elastic stiffness is

$$\begin{pmatrix} c_{11} & c_{12} & c_{13} & c_{14} & c_{15} & c_{16} \\ c_{12} & c_{22} & c_{23} & c_{24} & c_{25} & c_{26} \\ c_{13} & c_{23} & c_{33} & c_{34} & c_{35} & c_{36} \\ c_{14} & c_{24} & c_{34} & c_{44} & c_{45} & c_{46} \\ c_{15} & c_{25} & c_{35} & c_{45} & c_{55} & c_{56} \\ c_{16} & c_{26} & c_{36} & c_{46} & c_{56} & c_{66} \end{pmatrix}$$

and similarly, the Voigt matrix representation of the elastic compliance is

$$\begin{pmatrix} s_{11} & s_{12} & s_{13} & s_{14} & s_{15} & s_{16} \\ s_{12} & s_{22} & s_{23} & s_{24} & s_{25} & s_{26} \\ s_{13} & s_{23} & s_{33} & s_{34} & s_{35} & s_{36} \\ s_{14} & s_{24} & s_{34} & s_{44} & s_{45} & s_{46} \\ s_{15} & s_{25} & s_{35} & s_{45} & s_{55} & s_{56} \\ s_{16} & s_{26} & s_{36} & s_{46} & s_{56} & s_{66} \end{pmatrix}$$

The Voigt stiffness and compliance matrices are symmetric. The upper triangle contains 21 constants, enough to contain the maximum number of independent constants that would be required for the least symmetric linear elastic material.

Using the Voigt notation, we can write Hooke's law as

$$\begin{pmatrix} \sigma_1 \\ \sigma_2 \\ \sigma_3 \\ \sigma_4 \\ \sigma_5 \\ \sigma_6 \end{pmatrix} = \begin{pmatrix} c_{11} & c_{12} & c_{13} & c_{14} & c_{15} & c_{16} \\ c_{12} & c_{22} & c_{23} & c_{24} & c_{25} & c_{26} \\ c_{13} & c_{23} & c_{33} & c_{34} & c_{35} & c_{36} \\ c_{14} & c_{24} & c_{34} & c_{44} & c_{45} & c_{46} \\ c_{15} & c_{25} & c_{35} & c_{45} & c_{55} & c_{56} \\ c_{16} & c_{26} & c_{36} & c_{46} & c_{56} & c_{66} \end{pmatrix} \begin{pmatrix} \varepsilon_1 \\ \varepsilon_2 \\ \varepsilon_3 \\ \varepsilon_4 \\ \varepsilon_5 \\ \varepsilon_6 \end{pmatrix}$$

It is very important to note that the stress (strain) vector and stiffness (compliance) matrix in Voigt notation are not tensors.

Caution

Some forms of the abbreviated notation adopt different definitions of strains, moving the factors of 2 and 4 from the compliances to the stiffnesses. However, the form given above is the more common convention. In the two-index notation, c_{IJ} and s_{IJ} can conveniently be represented as 6×6 matrices. However, these matrices no longer follow the laws of tensor transformation. Care must be taken when transforming from one coordinate system to another. One way is to go back to the four-index notation and then use the ordinary laws of coordinate transformation. A more efficient method is to use the **Bond transformation matrices**, which are explained in [Section 1.4](#) on coordinate transformations.

Voigt stiffness matrix structure for common anisotropy classes

The nonzero components of the more symmetric anisotropy classes commonly used in modeling rock properties are given below in Voigt notation.

Isotropic: two independent constants

The structure of the Voigt elastic stiffness matrix for an isotropic linear elastic material has the following form:

$$\begin{bmatrix} c_{11} & c_{12} & c_{12} & 0 & 0 & 0 \\ c_{12} & c_{11} & c_{12} & 0 & 0 & 0 \\ c_{12} & c_{12} & c_{11} & 0 & 0 & 0 \\ 0 & 0 & 0 & c_{44} & 0 & 0 \\ 0 & 0 & 0 & 0 & c_{44} & 0 \\ 0 & 0 & 0 & 0 & 0 & c_{44} \end{bmatrix}, \quad c_{12} = c_{11} - 2c_{44}$$

The relations between the elements c and Lamé's parameters λ and μ of isotropic linear elasticity are

$$c_{11} = \lambda + 2\mu, \quad c_{12} = \lambda, \quad c_{44} = \mu$$

The corresponding nonzero isotropic compliance tensor elements can be written in terms of the stiffnesses:

$$s_{11} = \frac{c_{11} + c_{12}}{(c_{11} - c_{12})(c_{11} + 2c_{12})}, \quad s_{44} = \frac{1}{c_{44}}$$

Energy considerations require that for an isotropic linear elastic material the following conditions must hold:

$$K = c_{11} - \frac{4}{3}c_{44} > 0, \quad \mu = c_{44} > 0$$

Cubic: three independent constants

When each Cartesian coordinate plane is aligned with a symmetry plane of a material with cubic symmetry, the Voigt elastic stiffness matrix has the following form:

$$\begin{bmatrix} c_{11} & c_{12} & c_{12} & 0 & 0 & 0 \\ c_{12} & c_{11} & c_{12} & 0 & 0 & 0 \\ c_{12} & c_{12} & c_{11} & 0 & 0 & 0 \\ 0 & 0 & 0 & c_{44} & 0 & 0 \\ 0 & 0 & 0 & 0 & c_{44} & 0 \\ 0 & 0 & 0 & 0 & 0 & c_{44} \end{bmatrix}$$

The corresponding nonzero cubic compliance tensor elements can be written in terms of the stiffnesses:

$$s_{11} = \frac{c_{11} + c_{12}}{(c_{11} - c_{12})(c_{11} + 2c_{12})}, \quad s_{12} = \frac{-c_{12}}{(c_{11} - c_{12})(c_{11} + 2c_{12})}, \quad s_{44} = \frac{1}{c_{44}}$$

Energy considerations require that for a linear elastic material with cubic symmetry the following conditions must hold:

$$c_{44} \geq 0, \quad c_{11} > |c_{12}|, \quad c_{11} + 2c_{12} > 0$$

Hexagonal or transversely isotropic: five independent constants

When the axis of symmetry of a transversely isotropic material lies along the x_3 -axis, the Voigt stiffness matrix has the form:

$$\begin{bmatrix} c_{11} & c_{12} & c_{13} & 0 & 0 & 0 \\ c_{12} & c_{11} & c_{13} & 0 & 0 & 0 \\ c_{13} & c_{13} & c_{33} & 0 & 0 & 0 \\ 0 & 0 & 0 & c_{44} & 0 & 0 \\ 0 & 0 & 0 & 0 & c_{44} & 0 \\ 0 & 0 & 0 & 0 & 0 & c_{66} \end{bmatrix}, \quad c_{66} = \frac{1}{2}(c_{11} - c_{12})$$

The corresponding nonzero hexagonal compliance tensor elements can be written in terms of the stiffnesses:

$$s_{11} + s_{12} = \frac{c_{33}}{c_{33}(c_{11} + c_{12}) - 2c_{13}^2}, \quad s_{11} - s_{12} = \frac{1}{c_{11} - c_{12}}$$

$$s_{13} = -\frac{c_{13}}{c_{33}(c_{11} + c_{12}) - 2c_{13}^2}, \quad s_{33} = \frac{c_{11} + c_{12}}{c_{33}(c_{11} + c_{12}) - 2c_{13}^2}, \quad s_{44} = \frac{1}{c_{44}}$$

Energy considerations require that for a linear elastic material with transversely isotropic symmetry the following conditions must hold:

$$c_{44} \geq 0, \quad c_{11} > |c_{12}|, \quad (c_{11} + c_{12})c_{33} > 2c_{13}^2$$

Orthorhombic: nine independent constants

When each Cartesian coordinate plane is aligned with a symmetry plane of a material with orthorhombic symmetry, the Voigt elastic stiffness matrix has the following form:

$$\begin{bmatrix} c_{11} & c_{12} & c_{13} & 0 & 0 & 0 \\ c_{12} & c_{22} & c_{23} & 0 & 0 & 0 \\ c_{13} & c_{23} & c_{33} & 0 & 0 & 0 \\ 0 & 0 & 0 & c_{44} & 0 & 0 \\ 0 & 0 & 0 & 0 & c_{55} & 0 \\ 0 & 0 & 0 & 0 & 0 & c_{66} \end{bmatrix}$$

Monoclinic: 13 independent constants

When the symmetry plane of a monoclinic medium is orthogonal to the x_3 -axis, the Voigt elastic stiffness matrix has the following form:

$$\begin{bmatrix} c_{11} & c_{12} & c_{13} & 0 & c_{15} & 0 \\ c_{12} & c_{22} & c_{23} & 0 & c_{25} & 0 \\ c_{13} & c_{23} & c_{33} & 0 & c_{35} & 0 \\ 0 & 0 & 0 & c_{44} & 0 & c_{46} \\ c_{15} & c_{25} & c_{35} & 0 & c_{55} & 0 \\ 0 & 0 & 0 & c_{46} & 0 & c_{66} \end{bmatrix}$$

Phase velocities for several elastic symmetry classes

For *isotropic* symmetry, the phase velocity of wave propagation is given by

$$V_P = \sqrt{\frac{c_{11}}{\rho}} \quad V_S = \sqrt{\frac{c_{44}}{\rho}}$$

where ρ is the density.

In *anisotropic* media there are, in general, three modes of propagation (quasi-longitudinal, quasi-shear, and pure shear) with mutually orthogonal polarizations.

For a medium with **transversely isotropic** (hexagonal) symmetry, the wave slowness surface is always rotationally symmetric about the axis of symmetry. The phase velocities of the three modes in any plane containing the symmetry axis are given as

quasi-longitudinal mode (transversely isotropic):

$$V_P = (c_{11} \sin^2 \theta + c_{33} \cos^2 \theta + c_{44} + \sqrt{M})^{1/2} (2\rho)^{-1/2}$$

quasi-shear mode (transversely isotropic):

$$V_{SV} = (c_{11} \sin^2 \theta + c_{33} \cos^2 \theta + c_{44} - \sqrt{M})^{1/2} (2\rho)^{-1/2}$$

pure shear mode (transversely isotropic):

$$V_{SH} = \left(\frac{c_{66} \sin^2 \theta + c_{44} \cos^2 \theta}{\rho} \right)^{1/2}$$

where

$$M = [(c_{11} - c_{44}) \sin^2 \theta - (c_{33} - c_{44}) \cos^2 \theta]^2 + (c_{13} + c_{44})^2 \sin^2 2\theta$$

and θ is the angle between the wave vector and the x_3 -axis of symmetry ($\theta = 0$ for propagation along the x_3 -axis). The five components of the stiffness tensor for a transversely isotropic material are obtained from five velocity measurements: $V_P(0^\circ)$, $V_P(90^\circ)$, $V_P(45^\circ)$, $V_{SH}(90^\circ)$, and $V_{SH}(0^\circ) = V_{SV}(0^\circ)$:

$$c_{11} = \rho V_P^2(90^\circ)$$

$$c_{12} = c_{11} - 2\rho V_{SH}^2(90^\circ)$$

$$c_{33} = \rho V_P^2(0^\circ)$$

$$c_{44} = \rho V_{SH}^2(0^\circ)$$

and

$$c_{13} = -c_{44} + \sqrt{4\rho^2 V_{P(45^\circ)}^4 - 2\rho V_{P(45^\circ)}^2 (c_{11} + c_{33} + 2c_{44}) + (c_{11} + c_{44})(c_{33} + c_{44})}$$

For the more general **orthorhombic** symmetry, the phase velocities of the three modes propagating in the three symmetry planes (XZ , YZ , and XY) are given as follows:

quasi-longitudinal mode (orthorhombic, XZ plane):

$$V_P = \left(c_{55} + c_{11} \sin^2 \theta + c_{33} \cos^2 \theta + \sqrt{(c_{55} + c_{11} \sin^2 \theta + c_{33} \cos^2 \theta)^2 - 4A} \right)^{1/2} (2\rho)^{-1/2}$$

quasi-shear mode (orthorhombic, XZ plane):

$$V_{SV} = \left(c_{55} + c_{11} \sin^2 \theta + c_{33} \cos^2 \theta - \sqrt{(c_{55} + c_{11} \sin^2 \theta + c_{33} \cos^2 \theta)^2 - 4A} \right)^{1/2} (2\rho)^{-1/2}$$

pure shear mode (orthorhombic, XZ plane):

$$V_{SH} = \left(\frac{c_{66} \sin^2 \theta + c_{44} \cos^2 \theta}{\rho} \right)^{1/2}$$

where

$$A = (c_{11} \sin^2 \theta + c_{55} \cos^2 \theta)(c_{55} \sin^2 \theta + c_{33} \cos^2 \theta) - (c_{13} + c_{55})^2 \sin^2 \theta \cos^2 \theta$$

quasi-longitudinal mode (orthorhombic, YZ plane):

$$V_P = \left(c_{44} + c_{22} \sin^2 \theta + c_{33} \cos^2 \theta + \sqrt{(c_{44} + c_{22} \sin^2 \theta + c_{33} \cos^2 \theta)^2 - 4B} \right)^{1/2} (2\rho)^{-1/2}$$

quasi-shear mode (orthorhombic, YZ plane):

$$V_{SV} = \left(c_{44} + c_{22} \sin^2 \theta + c_{33} \cos^2 \theta - \sqrt{(c_{44} + c_{22} \sin^2 \theta + c_{33} \cos^2 \theta)^2 - 4B} \right)^{1/2} (2\rho)^{-1/2}$$

pure shear mode (orthorhombic, YZ plane):

$$V_{SH} = \left(\frac{c_{66} \sin^2 \theta + c_{55} \cos^2 \theta}{\rho} \right)^{1/2}$$

where

$$B = (c_{22} \sin^2 \theta + c_{44} \cos^2 \theta)(c_{44} \sin^2 \theta + c_{33} \cos^2 \theta) - (c_{23} + c_{44})^2 \sin^2 \theta \cos^2 \theta$$

quasi-longitudinal mode (orthorhombic, XY plane):

$$V_P = \left(c_{66} + c_{22} \sin^2 \varphi + c_{11} \cos^2 \varphi + \sqrt{(c_{66} + c_{22} \sin^2 \varphi + c_{11} \cos^2 \varphi)^2 - 4C} \right)^{1/2} (2\rho)^{-1/2}$$

quasi-shear mode (orthorhombic, XY plane):

$$V_{SH} = \left(c_{66} + c_{22} \sin^2 \varphi + c_{11} \cos^2 \varphi - \sqrt{(c_{66} + c_{22} \sin^2 \varphi + c_{11} \cos^2 \varphi)^2 - 4C} \right)^{1/2} (2\rho)^{-1/2}$$

pure shear mode (orthorhombic, XY plane):

$$V_{SV} = \left(\frac{c_{55} \cos^2 \varphi + c_{44} \sin^2 \varphi}{\rho} \right)^{1/2}$$

where

$$C = (c_{66} \sin^2 \varphi + c_{11} \cos^2 \varphi)(c_{22} \sin^2 \varphi + c_{66} \cos^2 \varphi) - (c_{12} + c_{66})^2 \sin^2 \varphi \cos^2 \varphi$$

and θ and φ are the angles of the wave vector relative to the x_3 and x_1 axes, respectively.

Kelvin notation

In spite of its almost exclusive use in the geophysical literature, the abbreviated Voigt notation has several mathematical disadvantages. For example, certain norms of the fourth-rank stiffness tensor are not equal to the corresponding norms of the Voigt stiffness matrix (Thomson, 1878; Helbig, 1994; Dellinger *et al.*, 1998), and the eigenvalues of the Voigt stiffness matrix are not the eigenvalues of the stress tensor.

The lesser-known **Kelvin notation** is very similar to the Voigt notation, except that each element of the 6×6 matrix is weighted according to how many elements of the actual stiffness tensor it represents. Kelvin matrix elements having indices 1, 2, or 3 each map to only a single index pair in the fourth-rank notation, 11, 22, and 33,

respectively, so any matrix stiffness element with index 1, 2, or 3 is given a weight of 1. Kelvin elements with indices 4, 5, or 6 each represent two index pairs (23, 32), (13, 31), and (12, 21), respectively, so each element containing 4, 5, or 6 receives a weight of $\sqrt{2}$. The weighting must be applied for each Kelvin index. For example, the Kelvin notation would map $\hat{c}_{11} = c_{1111}$, $\hat{c}_{14} = \sqrt{2}c_{1123}$, $\hat{c}_{66} = 2c_{1212}$. One way to convert a Voigt stiffness matrix into a Kelvin stiffness matrix is to pre- and post-multiply by the following weighting matrix (Dellinger *et al.*, 1998):

$$\begin{bmatrix} 1 & 0 & 0 & 0 & 0 & 0 \\ 0 & 1 & 0 & 0 & 0 & 0 \\ 0 & 0 & 1 & 0 & 0 & 0 \\ 0 & 0 & 0 & \sqrt{2} & 0 & 0 \\ 0 & 0 & 0 & 0 & \sqrt{2} & 0 \\ 0 & 0 & 0 & 0 & 0 & \sqrt{2} \end{bmatrix}$$

yielding

$$\begin{pmatrix} \hat{c}_{11} & \hat{c}_{12} & \hat{c}_{13} & \hat{c}_{14} & \hat{c}_{15} & \hat{c}_{16} \\ \hat{c}_{12} & \hat{c}_{22} & \hat{c}_{23} & \hat{c}_{24} & \hat{c}_{25} & \hat{c}_{26} \\ \hat{c}_{13} & \hat{c}_{23} & \hat{c}_{33} & \hat{c}_{34} & \hat{c}_{35} & \hat{c}_{36} \\ \hat{c}_{14} & \hat{c}_{24} & \hat{c}_{34} & \hat{c}_{44} & \hat{c}_{45} & \hat{c}_{46} \\ \hat{c}_{15} & \hat{c}_{25} & \hat{c}_{35} & \hat{c}_{45} & \hat{c}_{55} & \hat{c}_{56} \\ \hat{c}_{16} & \hat{c}_{26} & \hat{c}_{36} & \hat{c}_{46} & \hat{c}_{56} & \hat{c}_{66} \end{pmatrix} = \begin{pmatrix} c_{11} & c_{12} & c_{13} & \sqrt{2}c_{14} & \sqrt{2}c_{15} & \sqrt{2}c_{16} \\ c_{12} & c_{22} & c_{23} & \sqrt{2}c_{24} & \sqrt{2}c_{25} & \sqrt{2}c_{26} \\ c_{13} & c_{23} & c_{33} & \sqrt{2}c_{34} & \sqrt{2}c_{35} & \sqrt{2}c_{36} \\ \sqrt{2}c_{14} & \sqrt{2}c_{24} & \sqrt{2}c_{34} & 2c_{44} & 2c_{45} & 2c_{46} \\ \sqrt{2}c_{15} & \sqrt{2}c_{25} & \sqrt{2}c_{35} & 2c_{45} & 2c_{55} & 2c_{56} \\ \sqrt{2}c_{16} & \sqrt{2}c_{26} & \sqrt{2}c_{36} & 2c_{46} & 2c_{56} & 2c_{66} \end{pmatrix}$$

where the \hat{c}_{ij} are the Kelvin elastic elements and c_{ij} are the Voigt elements.

Similarly, the stress and strain elements take on the following weights in the Kelvin notation:

$$\hat{T} = \begin{bmatrix} \hat{\sigma}_1 = \sigma_{11} \\ \hat{\sigma}_2 = \sigma_{22} \\ \hat{\sigma}_3 = \sigma_{33} \\ \hat{\sigma}_4 = \sqrt{2}\sigma_{23} \\ \hat{\sigma}_5 = \sqrt{2}\sigma_{13} \\ \hat{\sigma}_6 = \sqrt{2}\sigma_{12} \end{bmatrix}; \quad \hat{E} = \begin{bmatrix} \hat{\epsilon}_1 = \epsilon_{11} \\ \hat{\epsilon}_2 = \epsilon_{22} \\ \hat{\epsilon}_3 = \epsilon_{33} \\ \hat{\epsilon}_4 = \sqrt{2}\epsilon_{23} \\ \hat{\epsilon}_5 = \sqrt{2}\epsilon_{13} \\ \hat{\epsilon}_6 = \sqrt{2}\epsilon_{12} \end{bmatrix}$$

Hooke's law again takes on the familiar form in the Kelvin notation:

$$\begin{pmatrix} \hat{\sigma}_1 \\ \hat{\sigma}_2 \\ \hat{\sigma}_3 \\ \hat{\sigma}_4 \\ \hat{\sigma}_5 \\ \hat{\sigma}_6 \end{pmatrix} = \begin{pmatrix} \hat{c}_{11} & \hat{c}_{12} & \hat{c}_{13} & \hat{c}_{14} & \hat{c}_{15} & \hat{c}_{16} \\ \hat{c}_{12} & \hat{c}_{22} & \hat{c}_{23} & \hat{c}_{24} & \hat{c}_{25} & \hat{c}_{26} \\ \hat{c}_{13} & \hat{c}_{23} & \hat{c}_{33} & \hat{c}_{34} & \hat{c}_{35} & \hat{c}_{36} \\ \hat{c}_{14} & \hat{c}_{24} & \hat{c}_{34} & \hat{c}_{44} & \hat{c}_{45} & \hat{c}_{46} \\ \hat{c}_{15} & \hat{c}_{25} & \hat{c}_{35} & \hat{c}_{45} & \hat{c}_{55} & \hat{c}_{56} \\ \hat{c}_{16} & \hat{c}_{26} & \hat{c}_{36} & \hat{c}_{46} & \hat{c}_{56} & \hat{c}_{66} \end{pmatrix} \begin{pmatrix} \hat{\varepsilon}_1 \\ \hat{\varepsilon}_2 \\ \hat{\varepsilon}_3 \\ \hat{\varepsilon}_4 \\ \hat{\varepsilon}_5 \\ \hat{\varepsilon}_6 \end{pmatrix}$$

The **Kelvin notation** for the stiffness matrix has a number of advantages. The Kelvin elastic matrix is a tensor. It preserves the norm of the $3 \times 3 \times 3 \times 3$ notation:

$$\sum_{i,j=1,\dots,6} \hat{c}_{ij}^2 = \sum_{i,j,k,l=1,\dots,3} c_{ijkl}^2$$

The eigenvalues and eigenvectors (or eigentensors) of the Kelvin 6×6 C -matrix are geometrically meaningful (Kelvin, 1856; Mehrabadi and Cowin, 1989; Dellinger *et al.*, 1998). Each Kelvin eigentensor corresponds to a state of the medium where the stress and strain ellipsoids are aligned and have the same aspect ratios. Furthermore, a stiffness matrix is physically realizable if and only if all of the Kelvin eigenvalues are non-negative, which is useful for inferring elastic constants from laboratory data.

Elastic eigentensors and eigenvalues

The eigenvectors of the three-dimensional fourth-rank anisotropic elasticity tensor are called *eigentensors* when projected into three-dimensional space. The maximum number of eigentensors for any elastic symmetry is six (Kelvin, 1856; Mehrabadi and Cowin, 1989). In the case of isotropic linear elasticity, there are two unique eigentensors. The total stress tensor $\tilde{\sigma}$ and the total strain tensor $\tilde{\varepsilon}$ for the isotropic case can be decomposed in terms of the deviatoric second-rank tensors ($\tilde{\sigma}_{\text{dev}}$ and $\tilde{\varepsilon}_{\text{dev}}$) and scaled unit tensors $[\frac{1}{3} \text{tr}(\tilde{\sigma})\tilde{I}]$ and $[\frac{1}{3} \text{tr}(\tilde{\varepsilon})\tilde{I}]$:

$$\begin{aligned} \tilde{\sigma} &= \tilde{\sigma}_{\text{dev}} + \frac{1}{3} \text{tr}(\tilde{\sigma})\tilde{I} \\ \tilde{\varepsilon} &= \tilde{\varepsilon}_{\text{dev}} + \frac{1}{3} \text{tr}(\tilde{\varepsilon})\tilde{I} \end{aligned}$$

For an isotropic material, Hooke's law can be written as

$$\tilde{\sigma} = \lambda \text{tr}(\tilde{\varepsilon})\tilde{I} + 2\mu\tilde{\varepsilon}$$

where λ is Lamé's constant and μ is the shear modulus. However, if expressed in terms of the stress and strain eigentensors, Hooke's law becomes two uncoupled equations:

$$\text{tr}(\tilde{\sigma})\tilde{I} = 3K \text{tr}(\tilde{\varepsilon})\tilde{I}, \quad \tilde{\sigma}_{\text{dev}} = 2\mu\tilde{\varepsilon}_{\text{dev}}$$

Table 2.2.1 *Eigenelastic constants for several different symmetries.*

Symmetry	Eigenvalue	Multiplicity of eigenvalue
Isotropic	$c_{11} + 2c_{12} = 3K$	1
	$2c_{44} = 2\mu$	5
Cubic	$c_{11} + 2c_{12}$	1
	$c_{11} - c_{12}$	2
	$2c_{44}$	3
Transverse Isotropy	$c_{33} + \sqrt{2}c_{13}\left(\beta + \sqrt{\beta^2 + 1}\right), \beta = \frac{\sqrt{2}}{4c_{13}}(c_{11} + c_{12} - c_{33})$	1
	$c_{33} + \sqrt{2}c_{13}\left(\beta - \sqrt{\beta^2 + 1}\right)$	1
	$c_{11} - c_{12}$	2
	$2c_{44}$	2

where K is the bulk modulus. Similarly, the strain energy U for an isotropic material can be written as

$$2U = 2\mu \operatorname{tr}(\tilde{\epsilon}_{\text{dev}}^2) + K [\operatorname{tr}(\tilde{\epsilon})]^2$$

where μ and K scale two energy modes that do not interact.

Hence we can see that, although any two of the isotropic constants (λ , μ , K , Young's modulus, and Poisson's ratio) can be derived in terms of the others, μ and K have a special significance as *eigenelastic* constants (Mehrabadi and Cowin, 1989) or *principal elasticities* of the material (Kelvin, 1856). The stress and strain eigentensors associated with μ and K are orthogonal, as shown above. Such an orthogonal significance does not hold for the pair λ and μ . Eigenelastic constants for a few other symmetries are shown in Table 2.2.1, expressed in terms of the Voigt constants (Mehrabadi and Cowin, 1989).

Poisson's ratio defined for anisotropic elastic materials

Familiar isotropic definitions for elastic constants are sometimes extended to anisotropic materials. For example, consider a transversely isotropic (TI) material with uniaxial stress, applied along the symmetry (x_3 -) axis, such that

$$\sigma_{33} \neq 0 \quad \sigma_{11} = \sigma_{12} = \sigma_{13} = \sigma_{22} = \sigma_{23} = 0$$

One can define a transversely isotropic Young's modulus associated with this experiment as

$$E_{33} = \frac{\sigma_{33}}{\epsilon_{33}} = c_{33} - \frac{2c_{31}^2}{c_{11} + c_{12}}$$

where the c_{ij} are the elastic stiffnesses in Voigt notation. A pair of TI Poisson ratios can similarly be defined in terms of the same experiment:

$$\nu_{31} = \nu_{32} = -\frac{\varepsilon_{11}}{\varepsilon_{33}} = \frac{c_{31}}{c_{11} + c_{12}}$$

If the uniaxial stress field is rotated normal to the symmetry axis, such that

$$\sigma_{11} \neq 0 \quad \sigma_{12} = \sigma_{13} = \sigma_{22} = \sigma_{23} = \sigma_{33} = 0$$

then one can define another TI Young's modulus and pair of Poisson ratios as

$$\begin{aligned} E_{11} &= \frac{\sigma_{11}}{\varepsilon_{11}} = c_{11} + \frac{c_{31}^2(-c_{11} + c_{12}) + c_{12}(-c_{33}c_{12} + c_{31}^2)}{c_{33}c_{11} - c_{31}^2} \\ \nu_{13} &= \nu_{23} = -\frac{\varepsilon_{33}}{\varepsilon_{11}} = \frac{c_{31}(c_{11} - c_{12})}{c_{33}c_{11} - c_{31}^2} \\ \nu_{12} &= \nu_{21} = -\frac{\varepsilon_{22}}{\varepsilon_{11}} = \frac{c_{33}c_{12} - c_{31}^2}{c_{33}c_{11} - c_{31}^2} \end{aligned}$$

Caution

Just as with the isotropic case, definitions of Young's modulus and Poisson ratio in terms of stresses and strains are only true for the uniaxial stress state. Definitions in terms of elastic stiffnesses are independent of stress state.

In spite of their similarity to their isotropic analogs, these TI Poisson ratios have several distinct differences. For example, the bounds on the isotropic Poisson ratio require that

$$-1 \leq \nu_{\text{isotropic}} \leq \frac{1}{2}$$

In contrast, the bounds on the TI Poisson ratios defined here are (Christensen, 2005)

$$|\nu_{12}| \leq 1; \quad |\nu_{31}| \leq \left(\frac{E_{33}}{E_{11}}\right)^{1/2}; \quad |\nu_{13}| \leq \left(\frac{E_{11}}{E_{33}}\right)^{1/2}$$

Another distinct difference is the relation of Poisson's ratio to seismic velocities. In an isotropic material, Poisson's ratio is directly related to the V_P/V_S ratio as follows:

$$(V_P/V_S)^2 = \frac{2(1 - \nu)}{(1 - 2\nu)}$$

or, equivalently,

$$\nu = \frac{(V_P/V_S)^2 - 2}{2[(V_P/V_S)^2 - 1]}$$

However, in the TI material, the ratio of velocities propagating along the symmetry (x_3 -) axis is

$$\left(\frac{V_P}{V_S}\right)^2 = \frac{c_{33}}{c_{44}}$$

and is not simply related to the ν_{31} Poisson ratio.

Caution

The definition of Young's modulus and Poisson's ratio for anisotropic materials, while possible, can be misinterpreted, especially when compared with isotropic formulas.

For *orthorhombic* and higher symmetries, the “engineering” parameters—Poisson ratios, ν_{ij} , shear moduli, G_{ij} , and Young's moduli, E_{ij} —can be conveniently defined in terms of elastic *compliances* (Jaeger *et al.*, 2007):

$$\begin{aligned} E_{11} &= 1/s_{11} & E_{22} &= 1/s_{22} & E_{33} &= 1/s_{33} \\ \nu_{21} &= -s_{12}E_{22} & \nu_{31} &= -s_{13}E_{33} & \nu_{32} &= -s_{23}E_{33} \\ G_{12} &= 1/s_{66} & G_{13} &= 1/s_{55} & G_{23} &= 1/s_{44} \end{aligned}$$

Existence of a strain energy leads to the following constraints:

$$\begin{aligned} G_{12}, G_{13}, G_{23}, E_{11}, E_{22}, E_{33} &> 0 \\ \frac{E_{11}}{E_{22}}(\nu_{21})^2 &< 1, \quad \frac{E_{11}}{E_{33}}(\nu_{31})^2 < 1, \quad \frac{E_{22}}{E_{33}}(\nu_{32})^2 < 1 \end{aligned}$$

Assumptions and limitations

The preceding equations assume anisotropic, linear elastic media.

2.3 Thomsen's notation for weak elastic anisotropy

Synopsis

A transversely isotropic elastic material is completely specified by five independent constants. In terms of the abbreviated Voigt notation (see Section 2.2 on elastic anisotropy) the elastic constants can be represented as

$$\begin{bmatrix} c_{11} & c_{12} & c_{13} & 0 & 0 & 0 \\ c_{12} & c_{11} & c_{13} & 0 & 0 & 0 \\ c_{13} & c_{13} & c_{33} & 0 & 0 & 0 \\ 0 & 0 & 0 & c_{44} & 0 & 0 \\ 0 & 0 & 0 & 0 & c_{44} & 0 \\ 0 & 0 & 0 & 0 & 0 & c_{66} \end{bmatrix}, \quad \text{where } c_{66} = \frac{1}{2}(c_{11} - c_{12})$$

and where the axis of symmetry lies along the x_3 -axis.

Thomsen (1986) suggested the following convenient notation for a TI material that is only weakly anisotropic. His notation uses the P- and S-wave velocities (denoted by α and β , respectively) propagating along the symmetry axis, plus three additional constants:

$$\alpha = \sqrt{c_{33}/\rho}, \quad \beta = \sqrt{c_{44}/\rho}, \quad \varepsilon = \frac{c_{11} - c_{33}}{2c_{33}}$$

$$\gamma = \frac{c_{66} - c_{44}}{2c_{44}}, \quad \delta = \frac{(c_{13} + c_{44})^2 - (c_{33} - c_{44})^2}{2c_{33}(c_{33} - c_{44})}$$

In terms of these constants, the three phase velocities can be approximated conveniently as

$$V_P(\theta) \approx \alpha(1 + \delta \sin^2 \theta \cos^2 \theta + \varepsilon \sin^4 \theta)$$

$$V_{SV}(\theta) \approx \beta \left[1 + \frac{\alpha^2}{\beta^2} (\varepsilon - \delta) \sin^2 \theta \cos^2 \theta \right]$$

$$V_{SH}(\theta) \approx \beta(1 + \gamma \sin^2 \theta)$$

where θ is the angle of the wave vector relative to the x_3 -axis; V_{SH} is the wavefront velocity of the pure shear wave, which has no component of polarization in the symmetry axis direction; V_{SV} is the pseudo-shear wave polarized normal to the pure shear wave; and V_P is the pseudo-longitudinal wave.

Berryman (2008) extends the validity of Thomsen's expressions for P- and quasi-SV-wave velocities to wider ranges of angles and stronger anisotropy with the following expressions:

$$V_P(\theta) \approx \alpha \left[1 + \varepsilon \sin^2 \theta - (\varepsilon - \delta) \frac{2 \sin^2 \theta_m \sin^2 \theta \cos^2 \theta}{1 - \cos 2\theta_m \cos 2\theta} \right]$$

$$V_{SV}(\theta) \approx \beta \left[1 + \left(\frac{\alpha^2}{\beta^2} \right) (\varepsilon - \delta) \frac{2 \sin^2 \theta_m \sin^2 \theta \cos^2 \theta}{1 - \cos 2\theta_m \cos 2\theta} \right]$$

where

$$\tan^2 \theta_m = \frac{c_{33} - c_{44}}{c_{11} - c_{44}}$$

Berryman's formulas give more accurate velocities at larger angles. They are designed to give the angular location of the peak (or trough) of the quasi-SV-velocity closer to the correct location; hence, the quasi-SV-velocities are more accurate than those from Thomsen's equations. Thomsen's P-wave velocities will sometimes be more accurate than Berryman's at small θ and sometimes worse.

For weak anisotropy, the constant ε can be seen to describe the fractional difference between the P-wave velocities parallel and orthogonal to the symmetry axis (in the weak anisotropy approximation):

$$\varepsilon \approx \frac{V_P(90^\circ) - V_P(0^\circ)}{V_P(0^\circ)}$$

Therefore, ε best describes what is usually called the “P-wave anisotropy.”

Similarly, for weak anisotropy the constant γ can be seen to describe the fractional difference between the SH-wave velocities parallel and orthogonal to the symmetry axis, which is equivalent to the difference between the velocities of S-waves polarized parallel and normal to the symmetry axis, both propagating normal to the symmetry axis:

$$\gamma \approx \frac{V_{SH}(90^\circ) - V_{SV}(90^\circ)}{V_{SV}(90^\circ)} = \frac{V_{SH}(90^\circ) - V_{SH}(0^\circ)}{V_{SH}(0^\circ)}$$

The small-offset normal moveout velocity is affected by VTI (transversely isotropic with vertical symmetry axis) anisotropy. In terms of the Thomsen parameters, NMO (normal moveout) velocities, $V_{NMO,P}$, $V_{NMO,SV}$, and $V_{NMO,SH}$ for P-, SV-, and SH-modes are (Tsvankin, 2001):

$$V_{NMO,P} = \alpha \sqrt{1 + 2\delta}$$

$$V_{NMO,SV} = \beta \sqrt{1 + 2\sigma}, \quad \sigma = \left(\frac{\alpha}{\beta}\right)^2 (\varepsilon - \delta)$$

$$V_{NMO,SH} = \beta \sqrt{1 + 2\gamma}$$

An additional *anellipticity* parameter, η , was introduced by Alkhalifah and Tsvankin (1995):

$$\eta = \frac{\varepsilon - \delta}{1 + 2\delta}$$

η is important in quantifying the effects of anisotropy on nonhyperbolic moveout and P-wave time-processing steps (Tsvankin, 2001), including NMO, DMO (dip moveout), and time migration.

The Thomsen parameters can be inverted for the elastic constants as follows:

$$c_{33} = \rho \alpha^2, \quad c_{44} = \rho \beta^2$$

$$c_{11} = c_{33}(1 + 2\varepsilon), \quad c_{66} = c_{44}(1 + 2\gamma)$$

$$c_{13} = \pm \sqrt{2c_{33}(c_{33} - c_{44})\delta + (c_{33} - c_{44})^2} - c_{44}$$

Note the nonuniqueness in c_{13} that results from uncertainty in the sign of $(c_{13} + c_{44})$. Tsvankin (2001, p. 19) argues that for most cases, it can be assumed that $(c_{13} + c_{44}) > 0$, and therefore, the +sign in the equation for c_{13} is usually appropriate.

Tsvankin (2001) summarizes some bounds on the values of the Thomsen parameters:

- the lower bound for δ : $\delta \geq -(1 - \beta^2/\alpha^2)/2$;
- an *approximate* upper bound for δ : $\delta \leq 2/(\alpha^2/\beta^2 - 1)$; and
- in VTI materials resulting from thin layering, $\varepsilon > \delta$ and $\gamma > 0$.

Table 2.3.1 Ranges of Thomsen parameters expected for thin laminations of isotropic materials (Berryman *et al.*, 1999).

	$\mu = \text{const}$	$\lambda = \text{const}$ $\mu \neq \text{const}$	$\lambda + \mu = \text{const}$ $\mu \neq \text{const}$	$\lambda + 2\mu = \text{const}$ $\mu \neq \text{const}$	$\nu = \text{const}$ $\lambda, \mu \neq \text{const}$
ε	0	≥ 0	0	≤ 0	≥ 0
δ	0	≤ 0	≤ 0	≤ 0	0
γ	0	≥ 0	≥ 0	≥ 0	≥ 0
$\varepsilon - \delta$	0	≥ 0	≥ 0	≥ 0	≥ 0

Transversely isotropic media consisting of thin isotropic layers always have Thomsen (1986) parameters, such that $\varepsilon - \delta \geq 0$ and $\gamma \geq 0$ (Tsvankin, 2001). Berryman *et al.* (1999) find the additional conditions summarized in Table 2.3.1, based on Backus (1962) average analysis and Monte Carlo simulations of thinly laminated media. Although all of the cases in the table have $\delta \leq 0$, Berryman *et al.* find that δ can be positive if the layers have significantly varying and positively correlated shear modulus, μ , and Poisson ratio, ν .

Bakulin *et al.* (2000) studied the Thomsen parameters for anisotropic HTI (transversely isotropic with horizontal symmetry axis) media resulting from aligned vertical fractures with crack normals along the horizontal x_1 -axis in an isotropic background. For example, when the Hudson (1980) penny-shaped crack model (Section 4.10) is used to estimate weak anisotropy resulting from crack density, e , the dry-rock Thomsen parameters in the vertical plane containing the x_1 -axis can be approximated as

$$\begin{aligned}
 \varepsilon_{\text{dry}}^{(V)} &= \frac{c_{11} - c_{33}}{2c_{33}} = -\frac{8}{3}e \leq 0; \\
 \delta_{\text{dry}}^{(V)} &= \frac{(c_{13} + c_{55})^2 - (c_{33} - c_{55})^2}{2c_{33}(c_{33} - c_{55})} = -\frac{8}{3}e \left[1 + \frac{g(1-2g)}{(3-2g)(1-g)} \right] \leq 0; \\
 \gamma_{\text{dry}}^{(V)} &= \frac{c_{66} - c_{44}}{2c_{44}} = -\frac{8e}{3(3-2g)} \leq 0; \\
 \eta_{\text{dry}}^{(V)} &= \frac{\varepsilon_{\text{dry}}^{(V)} - \delta_{\text{dry}}^{(V)}}{1 + 2\delta_{\text{dry}}^{(V)}} = \frac{8}{3}e \left[\frac{g(1-2g)}{(3-2g)(1-g)} \right] \geq 0
 \end{aligned}$$

where $g = V_S^2/V_P^2$ is a property of the unfractured background rock. In the case of fluid-saturated penny-shaped cracks, such that the crack aspect, α , is much less than the ratio of the fluid bulk modulus to the mineral bulk modulus, $K_{\text{fluid}}/K_{\text{mineral}}$, then the weak-anisotropy Thomsen parameters can be approximated as

$$\begin{aligned}
 \varepsilon_{\text{saturated}}^{(V)} &= \frac{c_{11} - c_{33}}{2c_{33}} = 0 \\
 \delta_{\text{saturated}}^{(V)} &= \frac{(c_{13} + c_{55})^2 - (c_{33} - c_{55})^2}{2c_{33}(c_{33} - c_{55})} = -\frac{32ge}{3(3-2g)} \leq 0
 \end{aligned}$$

$$\gamma_{\text{saturated}}^{(\text{V})} = \frac{c_{66} - c_{44}}{2c_{44}} = -\frac{8e}{3(3-2g)} \leq 0$$

$$\eta_{\text{saturated}}^{(\text{V})} = -\delta_{\text{saturated}}^{(\text{V})} = \frac{32ge}{3(3-2g)} \geq 0$$

In intrinsically anisotropic shales, Sayers (2004) finds that δ can be positive or negative, depending on the contact stiffness between microscopic clay domains and on the distribution of clay domain orientations. He shows, via modeling, that distributions of clays domains, each having $\delta \leq 0$, can yield a composite with $\delta > 0$ overall if the domain orientations vary significantly from parallel.

Rasolofosaon (1998) shows that under the assumptions of third-order elasticity an isotropic rock obtains ellipsoidal symmetry with respect to the propagation of qP waves. Hence $\varepsilon = \delta$ in the symmetry planes (see Section 2.4) on Tsvankin's extended Thomsen parameters.

Uses

Thomsen's notation for weak elastic anisotropy is useful for conveniently characterizing the elastic constants of a transversely isotropic linear elastic medium.

Assumptions and limitations

The preceding equations are based on the following assumptions:

- material is linear, elastic, and transversely isotropic;
- anisotropy is weak, so that $\varepsilon, \gamma, \delta \ll 1$.

2.4 Tsvankin's extended Thomsen parameters for orthorhombic media

The well-known Thomsen (1986) parameters for weak anisotropy are well suited for transversely isotropic media (see Section 2.3). They allow the five independent elastic constants c_{11} , c_{33} , c_{12} , c_{13} , and c_{44} to be expressed in terms of the more intuitive P-wave velocity, α , and S-wave velocity, β , along the symmetry axis, plus additional constants ε , γ , and δ . For orthorhombic media, requiring nine independent elastic constants, the conventional Thomsen parameters are insufficient.

Analogous of the Thomsen parameters suitable for orthorhombic media can be defined (Tsvankin, 1997), recognizing that wave propagation in the x_1 – x_3 and x_2 – x_3 symmetry planes (pseudo-P and pseudo-S polarized in each plane and SH polarized normal to each plane) is analogous to propagation in two different VTI media. We once again define vertically propagating (along the x_3 -axis) P- and S-wave velocities, α and β , respectively:

$$\alpha = \sqrt{c_{33}/\rho}, \quad \beta = \sqrt{c_{55}/\rho}$$

Unlike in a VTI medium, S-waves propagating along the x_3 -axis in an orthorhombic medium can have two different velocities, $\beta_{x_2} = \sqrt{c_{44}/\rho}$ and $\beta_{x_1} = \sqrt{c_{55}/\rho}$, for waves polarized in the x_2 and x_1 directions, respectively. Either polarization can be chosen as a reference, though here we take $\beta = \sqrt{c_{55}/\rho}$ following the definitions of Tsvankin (1997). Some results shown in later sections will use redefined polarizations in the definition of β .

For the seven constants, we can write

$$\begin{aligned} \varepsilon^{(2)} &= \frac{c_{11} - c_{33}}{2c_{33}} & \varepsilon^{(1)} &= \frac{c_{22} - c_{33}}{2c_{33}} \\ \delta^{(2)} &= \frac{(c_{13} + c_{55})^2 - (c_{33} - c_{55})^2}{2c_{33}(c_{33} - c_{55})} & \delta^{(1)} &= \frac{(c_{23} + c_{44})^2 - (c_{33} - c_{44})^2}{2c_{33}(c_{33} - c_{44})} \\ \gamma^{(2)} &= \frac{c_{66} - c_{44}}{2c_{44}} & \gamma^{(1)} &= \frac{c_{66} - c_{55}}{2c_{55}} \\ \delta^{(3)} &= \frac{(c_{12} + c_{66})^2 - (c_{11} - c_{66})^2}{2c_{11}(c_{11} - c_{66})} \end{aligned}$$

Here, the superscripts (1), (2), and (3) refer to the TI-analog parameters in the symmetry planes normal to x_1 , x_2 , and x_3 , respectively. These definitions assume that one of the symmetry planes of the orthorhombic medium is horizontal and that the vertical symmetry axis is along the x_3 direction.

These Thomsen–Tsvankin parameters play a useful role in modeling wave propagation and reflectivity in anisotropic media.

Uses

Tsvankin's notation for weak elastic anisotropy is useful for conveniently characterizing the elastic constants of an orthorhombic elastic medium.

Assumptions and limitations

The preceding equations are based on the following assumptions:

- material is linear, elastic, and has orthorhombic or higher symmetry;
- the constants are definitions. They sometimes appear in expressions for anisotropy of arbitrary strength, but at other times the applications assume that the anisotropy is weak, so that $\varepsilon, \gamma, \delta \ll 1$.

2.5 Third-order nonlinear elasticity

Synopsis

Seismic velocities in crustal rocks are almost always sensitive to stress. Since so much of geophysics is based on *linear* elasticity, it is common to extend the familiar linear elastic terminology and refer to the “stress-dependent linear elastic moduli” – which can

have meaning for the local slope of the strain-curves at a given static state of stress. If the relation between stress and strain has no hysteresis and no dependence on rate, then it is more accurate to say that the rocks are **nonlinearly elastic** (e.g., Truesdell, 1965; Helbig, 1998; Rasolofosaon, 1998). Nonlinear elasticity (i.e., stress-dependent velocities) in rocks is due to the presence of compliant mechanical defects, such as cracks and grain contacts (e.g., Walsh, 1965; Jaeger and Cook, 1969; Bourbié *et al.*, 1987).

In a material with **third-order nonlinear elasticity**, the strain energy function E (for arbitrary anisotropy) can be expressed as (Helbig, 1998)

$$E = \frac{1}{2} c_{ijkl} \varepsilon_{ij} \varepsilon_{kl} + \frac{1}{6} c_{ijklmn} \varepsilon_{ij} \varepsilon_{kl} \varepsilon_{mn}$$

where c_{ijkl} and c_{ijklmn} designate the components of the second- and third-order elastic tensors, respectively, and repeated indices in a term imply summation from 1 to 3. The components c_{ijkl} are the usual elastic constants in Hooke's law, discussed earlier. Hence, linear elasticity is often referred to as **second-order elasticity**, because the strain energy in a linear elastic material is second order in strain. The linear elastic tensor (c_{ijkl}) is fourth rank, having a minimum of two independent constants for a material with the highest symmetry (isotropic) and a maximum of 21 independent constants for a material with the lowest symmetry (triclinic). The additional tensor of third-order elastic coefficients (c_{ijklmn}) is rank six, having a minimum of three independent constants (isotropic) and a maximum of 56 independent constants (triclinic) (Rasolofosaon, 1998).

Third-order elasticity is sometimes used to describe the stress-sensitivity of seismic velocities and apparent elastic constants in rocks. The apparent fourth-rank stiffness tensor, \tilde{c}^{eff} , which determines the speeds of infinitesimal-amplitude waves in a rock under applied static stress can be written as

$$\tilde{c}_{ijkl}^{\text{eff}} = c_{ijkl} + c_{ijklmn} \varepsilon_{mn}$$

where ε_{mn} are the principal strains associated with the applied static stress.

Approximate expressions, in Voigt notation, for the effective elastic constants of a stressed VTI (transversely isotropic with a vertical axis of symmetry) solid can be written as (Rasolofosaon, 1998; Sarkar *et al.*, 2003; Prioul *et al.*, 2004)

$$\begin{aligned} c_{11}^{\text{eff}} &\approx c_{11}^0 + c_{111} \varepsilon_{11} + c_{112} (\varepsilon_{22} + \varepsilon_{33}) \\ c_{22}^{\text{eff}} &\approx c_{11}^0 + c_{111} \varepsilon_{22} + c_{112} (\varepsilon_{11} + \varepsilon_{33}) \\ c_{33}^{\text{eff}} &\approx c_{33}^0 + c_{111} \varepsilon_{33} + c_{112} (\varepsilon_{11} + \varepsilon_{22}) \\ c_{12}^{\text{eff}} &\approx c_{12}^0 + c_{112} (\varepsilon_{11} + \varepsilon_{22}) + c_{123} \varepsilon_{33} \\ c_{13}^{\text{eff}} &\approx c_{13}^0 + c_{112} (\varepsilon_{11} + \varepsilon_{33}) + c_{123} \varepsilon_{22} \\ c_{23}^{\text{eff}} &\approx c_{13}^0 + c_{112} (\varepsilon_{22} + \varepsilon_{33}) + c_{123} \varepsilon_{11} \\ c_{66}^{\text{eff}} &\approx c_{66}^0 + c_{144} \varepsilon_{33} + c_{155} (\varepsilon_{11} + \varepsilon_{22}) \\ c_{55}^{\text{eff}} &\approx c_{44}^0 + c_{144} \varepsilon_{22} + c_{155} (\varepsilon_{11} + \varepsilon_{33}) \\ c_{44}^{\text{eff}} &\approx c_{44}^0 + c_{144} \varepsilon_{11} + c_{155} (\varepsilon_{22} + \varepsilon_{33}) \end{aligned}$$

Table 2.5.1 Experimentally determined third-order elastic constants c_{111} , c_{112} , and c_{123} and derived constants c_{144} , c_{155} , and c_{456} , determined by Prioul and Lebrat (2004), using laboratory data from Wang (2002). Six different sandstone and six different shale samples are shown.

	c_{111} (GPa)	c_{112} (GPa)	c_{123} (GPa)	c_{144} (GPa)	c_{155} (GPa)	c_{456} (GPa)
Sandstones						
	-10 245	-966	-966	0	-2320	-1160
	-9 482	-1745	-1745	0	-1934	-967
	-6 288	-1744	-1744	0	-1136	-568
	-8 580	-527	-527	0	-2013	-1006
	-8 460	-1162	-1162	0	-1825	-912
	-12 440	-3469	-3094	-188	-2243	-1027
Shales						
	-6 903	-976	-976	0	-1482	-741
	-4 329	-2122	-1019	-552	-552	0
	-7 034	-2147	296	-1222	-1222	0
	-4 160	-2013	-940	-536	-536	0
	1 294	-510	-119	-196	-196	0
	-1 203	-637	-354	-141	-141	0

where the constants c_{11}^0 , c_{33}^0 , c_{13}^0 , c_{44}^0 , c_{66}^0 are the VTI elastic constants at the unstressed reference state, with $c_{12}^0 = c_{11}^0 - 2c_{66}^0$. ε_{11} , ε_{22} , and ε_{33} are the principal strains, computed from the applied stress using the conventional Hooke's law, $\varepsilon_{ij} = s_{ijkl}\sigma_{kl}$. For these expressions, it is assumed that the direction of the applied principal stress is aligned with the VTI symmetry (x_3 -) axis. Furthermore, for these expressions it is assumed that the stress-sensitive third-order tensor is isotropic, defined by the three independent constants, c_{111} , c_{112} , and c_{123} with $c_{144} = (c_{112} - c_{123})/2$, $c_{155} = (c_{111} - c_{112})/4$, and $c_{456} = (c_{111} - 3c_{112} + 2c_{123})/8$. It is generally observed (Prioul *et al.*, 2004) that $c_{111} < c_{112} < c_{123}$, $c_{155} < c_{144}$, $c_{155} < 0$, and $c_{456} < 0$. A sample of experimentally determined values from Prioul and Lebrat (2004) using laboratory data from Wang (2002) are shown in the Table 2.5.1.

The third-order elasticity as used in most of geophysics and rock physics (Bakulin and Bakulin, 1999; Prioul *et al.*, 2004) is called the **Murnaghan (1951)** formulation of finite deformations, and the third-order constants are also called the **Murnaghan constants**.

Various representations of the third-order constants that can be found in the literature (Rasolofosaon, 1998) include the **crystallographic set** (c_{111} , c_{112} , c_{123}) presented here, the Murnaghan (1951) constants (l , m , n), and **Landau's set** (A , B , C) (Landau and Lifschitz, 1959). The relations among these are (Rasolofosaon, 1998)

$$c_{111} = 2A + 6B + 2C = 2l + 4m$$

$$c_{112} = 2B + 2C = 2l$$

$$c_{123} = 2C = 2l - 2m + n$$

Chelam (1961) and Krishnamurty (1963) looked at fourth-order elastic coefficients, based on an extension of Murnaghan's theory. It turns out from group theory that there will only be n independent n th-order coefficients for isotropic solids, and $n^2 - 2n + 3$ independent n th-order constants for cubic systems. Triclinic solids have 126 fourth-order elastic constants.

Uses

Third-order elasticity provides a way to parameterize the stress dependence of seismic velocities. It also allows for a compact description of stress-induced anisotropy, which is discussed later.

Assumptions and limitations

- The above equations assume that the material is **hyperelastic**, i.e., there is no hysteresis or rate dependence in the relation between stress and strain, and there exists a unique strain energy function.
- This formalism assumes that strains are infinitesimal. When strains become finite, an additional source of nonlinearity, called **geometrical** or **kinetic** nonlinearity, appears, related to the difference between Lagrangian and Eulerian descriptions of motion (Zarembko and Krasil'nikov, 1971; Johnson and Rasolofosaon, 1996).
- Third-order elasticity is often not general enough to describe the shapes of real stress–strain curves over large ranges of stress and strain. Third-order elasticity is most useful when describing stress–strain within a small range around a reference state of stress and strain.

2.6 Effective stress properties of rocks

Synopsis

Because rocks are deformable, many rock properties are sensitive to applied stresses and pore pressure. Stress-sensitive properties include porosity, permeability, electrical resistivity, sample volume, pore-space volume, and elastic moduli. Empirical evidence (Hicks and Berry, 1956; Wyllie *et al.*, 1958; Todd and Simmons, 1972; Christensen and Wang, 1985; Prasad and Manghnani, 1997; Siggins and Dewhurst, 2003, Hoffman *et al.*, 2005) and theory (Brandt, 1955; Nur and Byerlee, 1971; Zimmerman, 1991a; Gangi and Carlson, 1996; Berryman, 1992a, 1993; Gurevich, 2004) suggest that the pressure dependence of each of these rock properties, X , can be

represented as a function, f_X , of a linear combination of the hydrostatic confining stress, P_C , and the pore pressure, P_P :

$$X = f_X(P_C - nP_P); \quad n \leq 1$$

The combination $P_{\text{eff}} = P_C - nP_P$ is called the **effective pressure**, or more generally, the tensor $\sigma_{ij}^{\text{eff}} = \sigma_{ij}^C - nP_P\delta_{ij}$ is the **effective stress**. The parameter n is called the “effective-stress coefficient,” which can itself be a function of stress. The negative sign on the pore pressure indicates that the pore pressure approximately counteracts the effect of the confining pressure. An expression such as $X = f_X(P_C - nP_P)$ is sometimes called the **effective-stress law** for the property X . It is important to point out that each rock property might have a different function f_i and a different value of n_i (Zimmerman, 1991a; Berryman, 1992a, 1993; Gurevich, 2004). Extensive discussions on the effective-stress behavior of elastic moduli, permeability, resistivity, and thermoelastic properties can be found in Berryman (1992a, 1993). Zimmerman (1991a) gives a comprehensive discussion of effective-stress behavior for strain and elastic constants.

Zimmerman (1991a) points out the distinction between the effective-stress behavior for finite pressure changes versus the effective-stress behavior for infinitesimal increments of pressure. For example, increments of the bulk-volume strain, ε_b , and the pore-volume strain, ε_p , can be written as

$$\begin{aligned} \varepsilon_b(P_C, P_P) &= -C_{bc}(P_C - m_b P_P)(\delta P_C - n_b \delta P_P); & C_{bc} &= -\frac{1}{V_T} \left(\frac{\partial V_T}{\partial P_C} \right)_{P_P} \\ \varepsilon_p(P_C, P_P) &= -C_{pc}(P_C - m_p P_P)(\delta P_C - n_p \delta P_P); & C_{pc} &= -\frac{1}{V_P} \left(\frac{\partial V_P}{\partial P_C} \right)_{P_P} \end{aligned}$$

where the compressibilities C_{bc} and C_{pc} are functions of $P_C - mP_P$. The coefficients m_b and m_p govern the way that the compressibilities vary with P_C and P_P . In contrast, the coefficients n_b and n_p describe the relative increments of additional strain resulting from pressure *increments* δP_C and δP_P . For example, in a laboratory experiment, ultrasonic velocities will depend on the values of C_{pc} , the local slope of the stress–strain curve at the static values of P_C and P_P . On the other hand, the sample length change monitored within the pressure vessel is the total strain, obtained by integrating the strain over the entire stress path.

The existence of an effective-stress law, i.e., that a rock property depends only on the state of stress, requires that the rock be elastic – possibly nonlinearly elastic. The deformation of an elastic material depends only on the state of stress, and is independent of the stress history and the rate of loading. Furthermore, the existence of an effective-stress law requires that there is no hysteresis in stress–strain cycles. Since no rock is perfectly elastic, all effective-stress laws for rocks are approximations. In fact, deviation from elasticity makes estimating the effective-stress coefficient from laboratory data sometimes ambiguous. Another condition required for the existence of an effective-pressure law is that the pore pressure is well defined and uniform throughout the pore space. Todd and Simmons (1972) show that the effect of pore

pressure on velocities varies with the *rate* of pore-pressure change and whether the pore pressure has enough time to equilibrate in thin cracks and poorly connected pores. Slow changes in pore pressure yield more stable results, describable with an effective-stress law, and with a larger value of n for velocity.

Much discussion focuses on the value of the effective-stress constants, n (and m). Biot and Willis (1957) predicted theoretically that the pressure-induced *volume* increment, δV_T , of a sample of linear poroelastic material depends on pressure increments ($\delta P_C - n\delta P_P$). For this special case, $n = \alpha = 1 - K/K_S$, where α is known as the Biot coefficient or Biot–Willis coefficient. K is the dry-rock (drained) bulk modulus and K_S is the mineral bulk modulus (or some appropriate average of the moduli if there is mixed mineralogy), defined below. Explicitly,

$$\frac{\delta V_T}{V_T} = -\frac{1}{K} \left[\delta P_C - \left(1 - \frac{K}{K_S} \right) \delta P_P \right]$$

where δV_T , δP_C , and δP_P signify increments relative to a reference state.

Pitfall

A common error is to assume that the Biot–Willis effective-stress coefficient α for volume change also applies to other deformation-related rock properties. For example, although rock elastic moduli vary with crack and pore deformation, there is no theoretical justification for extrapolating α to elastic moduli and seismic velocities.

Other factors determining the apparent effective-stress coefficient observed in the laboratory include the rate of change of pore pressure, the connectivity of the pore space, the presence or absence of hysteresis, heterogeneity of the rock mineralogy, and variation of pore-fluid compressibility with pore pressure.

Table 2.6.1, compiled from Zimmerman (1984), Berryman (1992a, 1993), and H. F. Wang (2000), summarizes the theoretically expected effective *incremental* stress laws for a variety of rock properties. These depend on four defined rock moduli:

$$\begin{aligned} \frac{1}{K} &= -\frac{1}{V_T} \left(\frac{\partial V_T}{\partial P_d} \right)_{P_p}; & K &= \text{modulus of the drained porous frame,} \\ \frac{1}{K_S} &= -\frac{1}{V_T} \left(\frac{\partial V_T}{\partial P_P} \right)_{P_d}; & K_S &= \text{unjacketed modulus; if monomineralic,} \\ & & K_S &= K_{\text{mineral}}, \text{ otherwise } K_S \text{ is a poorly understood} \\ & & & \text{average of the mixed mineral moduli} \\ \frac{1}{K_{\phi\phi}} &= -\frac{1}{V_\phi} \left(\frac{\partial V_\phi}{\partial P_P} \right)_{P_d}; & \text{if monomineralic, } & K_S = K_{\phi\phi} = K_{\text{mineral}} \\ \frac{1}{K_P} &= -\frac{1}{V_\phi} \left(\frac{\partial V_\phi}{\partial P_d} \right)_{P_p} = \frac{1}{\phi} \left(\frac{1}{K} - \frac{1}{K_S} \right) \end{aligned}$$

Table 2.6.1 *Theoretically predicted effective-stress laws for incremental changes in confining and pore pressures (from Berryman, 1992a).*

Property	General mineralogy
Sample volume ^a	$\frac{\delta V_T}{V_T} = -\frac{1}{K}(\delta P_C - \alpha \delta P_P)$
Pore volume ^b	$\frac{\delta V_\phi}{V_\phi} = -\frac{1}{K_P}(\delta P_C - \beta \delta P_P)$
Porosity ^c	$\frac{\delta \phi}{\phi} = -\left(\frac{\alpha - \phi}{\phi K}\right)(\delta P_C - \chi \delta P_P)$
Solid volume ^d	$\frac{\delta V_S}{V_S} = -\frac{1}{(1-\phi)K_S}(\delta P_C - \sigma \delta P_P)$
Permeability ^e	$\frac{\delta k}{k} = -\left[h\left(\frac{\alpha - \phi}{\phi K}\right) + \frac{2}{3K}\right](\delta P_C - \kappa \delta P_P)$
Velocity/elastic moduli ^f	$\frac{\delta V_P}{V_P} = f(\delta P_C - \theta P_P)$

Notes:

^a V_T is the total volume. $\alpha = 1 - K/K_S$, Biot coefficient; usually in the range $\phi \leq \alpha \leq 1$;

if monomineralic, $\alpha = 1 - K/K_{\text{mineral}}$. ^b $V_\phi = \phi V_T$, pore volume. $\beta = 1 - K_P/K_{\phi\phi}$, usually,

$\phi \leq \beta \leq 1$, but it is possible that $\beta > 1$. ^c $\chi = \left(\frac{\beta - \phi}{\alpha - \phi}\right)\alpha$; if monomineralic, $\chi = 1$.

^d $\sigma = \alpha - \left(\frac{\chi - \alpha}{1 - \alpha}\right)(\alpha - \phi)$; if monomineralic, $\sigma = \phi$. $\sigma \leq \alpha \leq \beta$. ^e $\kappa = 1 - \frac{2\phi(1-\alpha)}{3h(\alpha-\phi)+2\phi} \leq 1$.

$h \approx 2 + m \approx 4$, where m is Archie's cementation exponent. ^f $\theta = 1 - \frac{\partial(1/K_S)/\partial P_C}{\partial(1/K)/\partial P_C}$; if monomineralic, $\theta = 1$.

where $P_d = P_C - P_P$ is the differential pressure, V_T is the sample bulk (i.e., total) volume, and V_ϕ is the pore volume. The negative sign for each of these rock properties follows from defining pressures as being positive in compression and volumes positive in expansion.

There is still a need to reconcile theoretical predictions of effective stress with certain laboratory data. For example, simple, yet rigorous, theoretical considerations (Zimmerman, 1991a; Berryman, 1992a; Gurevich, 2004) predict that $n_{\text{velocity}} = 1$ for monomineralic, elastic rocks. Experimentally observed values for n_{velocity} are sometimes close to 1, and sometimes less than one. Speculations for the variations have included mineral heterogeneity, poorly connected pore space, pressure-related changes in pore-fluid properties, incomplete correction for fluid-related velocity dispersion in ultrasonic measurements, poorly equilibrated or characterized pore pressure, and inelastic deformation.

Uses

Characterization of the stress sensitivity of rock properties makes it possible to invert for rock-property changes from changes in seismic or electrical measurements. It also provides a means of understanding how rock properties might change in response to tectonic stresses or pressure changes resulting from reservoir or aquifer production.

Assumptions and limitations

- The existence of effective-pressure laws assumes that the rocks are *hyperelastic*, i.e., there is no hysteresis or rate dependence in the relation between stress and strain.
- Rocks are extremely variable, so effective-pressure behavior can likewise be variable.

2.7 Stress-induced anisotropy in rocks

Synopsis

The closing of cracks under compressive stress (or, equivalently, the stiffening of compliant grain contacts) tends to increase the effective elastic moduli of rocks (see also [Section 2.5](#) on third-order elasticity).

When the crack population is anisotropic, either in the original unstressed condition or as a result of the stress field, then this condition can impact the overall elastic anisotropy of the rock. Laboratory demonstrations of stress-induced anisotropy have been reported by numerous authors (Nur and Simmons, 1969a; Lockner *et al.*, 1977; Zamora and Poirier, 1990; Sayers *et al.*, 1990; Yin, 1992; Cruts *et al.*, 1995).

The simplest case to understand is a rock with a random (isotropic) distribution of cracks embedded in an isotropic mineral matrix. In the initial unstressed state, the rock is elastically isotropic. If a *hydrostatic* compressive stress is applied, cracks in all directions respond similarly, and the rock remains isotropic but becomes stiffer. However, if a *uniaxial* compressive stress is applied, cracks with normals parallel or nearly parallel to the applied-stress axis will tend to close preferentially, and the rock will take on an axial or transversely isotropic symmetry.

An initially isotropic rock with arbitrary stress applied will have at least orthorhombic symmetry (Nur, 1971; Rasolofosaon, 1998), provided that the stress-induced changes in moduli are small relative to the absolute moduli.

[Figure 2.7.1](#) illustrates the effects of stress-induced crack alignment on seismic-velocity anisotropy discovered in the laboratory by Nur and Simmons (1969a). The crack porosity of the dry granite sample is essentially isotropic at low stress.

As uniaxial stress is applied, crack anisotropy is induced. The velocities (compressional and two polarizations of shear) clearly vary with direction relative to the stress-induced crack alignment. [Table 2.7.1](#) summarizes the elastic symmetries that result when various applied-stress fields interact with various initial crack symmetries (Paterson and Weiss, 1961; Nur, 1971).

A rule of thumb is that a wave is most sensitive to cracks when its direction of propagation or direction of polarization is perpendicular (or nearly so) to the crack faces.

The most common approach to modeling the stress-induced anisotropy is to assume angular distributions of idealized penny-shaped cracks (Nur, 1971; Sayers, 1988a, b; Gibson and Toksöz, 1990). The stress dependence is introduced by assuming or inferring distributions or spectra of crack aspect ratios with various orientations.

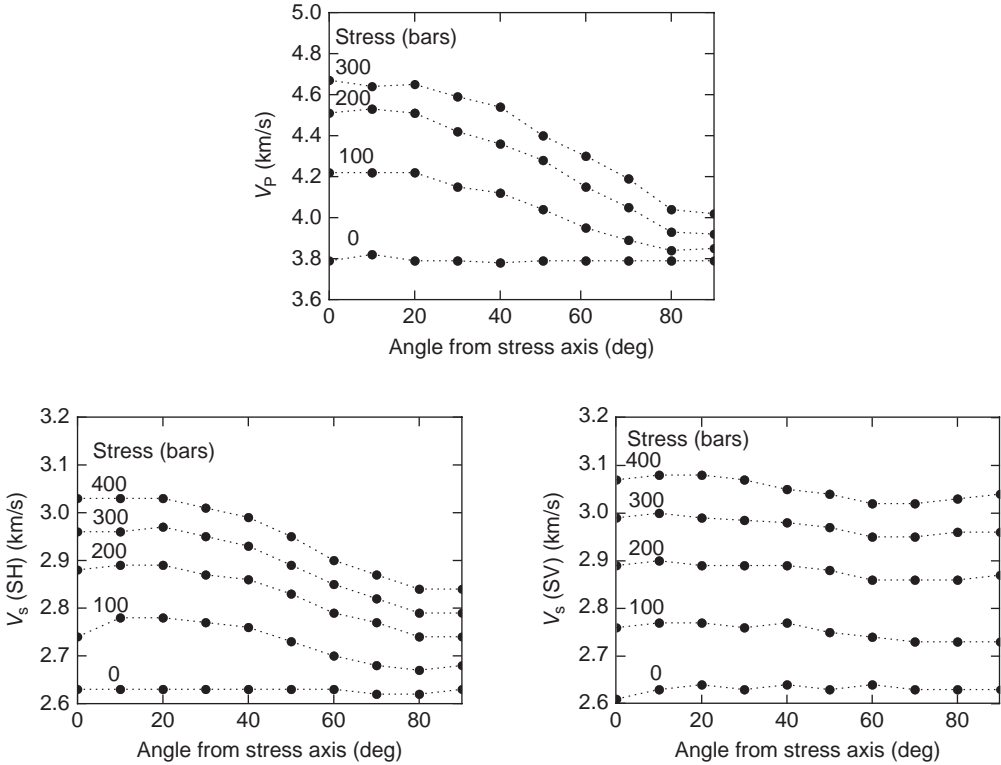


Figure 2.7.1 The effects of stress-induced crack alignment on seismic-velocity anisotropy measured in the laboratory (Nur and Simmons, 1969a).

The assumption is that a crack will close when the component of applied compressive stress normal to the crack faces causes a normal displacement of the crack faces equal to the original half-width of the crack. This allows us to estimate the crack **closing stress** as follows:

$$\sigma_{\text{close}} = \frac{3\pi(1-2\nu)}{4(1-\nu^2)} \alpha K_0 = \frac{\pi}{2(1-\nu)} \alpha \mu_0$$

where α is the aspect ratio of the crack, and ν , μ_0 , and K_0 are the Poisson ratio, shear modulus, and bulk modulus of the mineral, respectively (see Section 2.9 on the deformation of inclusions and cavities in elastic solids). Hence, the thinnest cracks will close first, followed by thicker ones. This allows one to estimate, for a given aspect-ratio distribution, how many cracks remain open in each direction for any applied stress field. These inferred crack distributions and their orientations can be put into one of the popular crack models (e.g., Hudson, 1981) to estimate the resulting effective elastic moduli of the rock. Although these penny-shaped crack models have been relatively successful and provide a useful physical interpretation, they are limited to low crack concentrations and may not effectively represent a broad range of crack geometries (see Section 4.10 on Hudson's model for cracked media).

Table 2.7.1 *Dependence of symmetry of induced velocity anisotropy on initial crack distribution and applied stress and its orientation.*

Symmetry of initial crack distribution	Applied stress	Orientation of applied stress	Symmetry of induced velocity anisotropy	Number of elastic constants
Random	Hydrostatic		Isotropic	2
	Uniaxial		Axial	5
	Triaxial ^a		Orthorhombic	9
Axial	Hydrostatic		Axial	5
	Uniaxial	Parallel to axis of symmetry	Axial	5
	Uniaxial	Normal to axis of symmetry	Orthorhombic	9
	Uniaxial	Inclined	Monoclinic	13
	Triaxial ^a	Parallel to axis of symmetry	Orthorhombic	9
	Triaxial ^a	Inclined	Monoclinic	13
	Triaxial ^a	Inclined	Triclinic	21
Orthorhombic	Hydrostatic		Orthorhombic	9
	Uniaxial	Parallel to axis of symmetry	Orthorhombic	9
	Uniaxial	Inclined in plane of symmetry	Monoclinic	13
	Uniaxial	Inclined	Triclinic	21
	Triaxial ^a	Parallel to axis of symmetry	Orthorhombic	9
	Triaxial ^a	Inclined in plane of symmetry	Monoclinic	13
	Triaxial ^a	Inclined	Triclinic	21

Note:

^aThree generally unequal principal stresses.

As an alternative, Mavko *et al.* (1995) presented a simple recipe for estimating stress-induced velocity anisotropy directly from measured values of isotropic V_P and V_S versus hydrostatic pressure. This method differs from the inclusion models, because it is relatively independent of any assumed crack geometry and is not limited to small crack densities. To invert for a particular crack distribution, one needs to assume crack shapes and aspect-ratio spectra. However, if rather than inverting for a crack distribution, we instead directly transform hydrostatic velocity–pressure data to stress-induced velocity anisotropy, we can avoid the need for parameterization in terms of ellipsoidal cracks and the resulting limitations to low crack densities. In this sense, the method of Mavko *et al.* (1995) provides not only a simpler but also a more general solution to this problem, for ellipsoidal cracks are just one particular case of the general formulation.

The procedure is to estimate the generalized pore-space compliance from the measurements of isotropic V_P and V_S . The physical assumption that the compliant part of the pore space is crack-like means that the pressure dependence of the generalized compliances is governed primarily by *normal* tractions resolved across cracks and defects. These defects can include grain boundaries and contact regions between clay platelets (Sayers, 1995). This assumption allows the measured pressure dependence to be mapped from the hydrostatic stress state to any applied nonhydrostatic stress.

The method applies to rocks that are approximately isotropic under hydrostatic stress and in which the anisotropy is caused by *crack closure* under stress. Sayers (1988b) also found evidence for some stress-induced *opening* of cracks, which is ignored in this method. The potentially important problem of stress–strain hysteresis is also ignored.

The anisotropic elastic compliance tensor $S_{ijkl}(\sigma)$ at any given stress state σ may be expressed as

$$\begin{aligned}\Delta S_{ijkl}(\sigma) &= S_{ijkl}(\sigma) - S_{ijkl}^0 \\ &= \int_{\theta=0}^{\pi/2} \int_{\phi=0}^{2\pi} [W'_{3333}(\hat{\mathbf{m}}^T \sigma \hat{\mathbf{m}}) - 4W'_{2323}(\hat{\mathbf{m}}^T \sigma \hat{\mathbf{m}})] m_i m_j m_k m_l \sin \theta \, d\theta \, d\phi \\ &\quad + \int_{\theta=0}^{\pi/2} \int_{\phi=0}^{2\pi} W'_{2323}(\hat{\mathbf{m}}^T \sigma \hat{\mathbf{m}}) [\delta_{ik} m_j m_l + \delta_{il} m_j m_k + \delta_{jk} m_i m_l \\ &\quad \quad \quad + \delta_{jl} m_i m_k] \sin \theta \, d\theta \, d\phi\end{aligned}$$

where

$$\begin{aligned}W'_{3333}(p) &= \frac{1}{2\pi} \Delta S_{jjkk}^{\text{iso}}(p) \\ W'_{2323}(p) &= \frac{1}{8\pi} [\Delta S_{\alpha\beta\alpha\beta}^{\text{iso}}(p) - \Delta S_{\alpha\alpha\beta\beta}^{\text{iso}}(p)]\end{aligned}$$

The tensor S_{ijkl}^0 denotes the reference compliance at some very large confining hydrostatic pressure when all of the compliant parts of the pore space are closed. The expression $\Delta S_{ijkl}^{\text{iso}}(p) = S_{ijkl}^{\text{iso}}(p) - S_{ijkl}^0$ describes the difference between the compliance under a hydrostatic effective pressure p and the reference compliance at high pressure. These are determined from measured P- and S-wave velocities versus the hydrostatic pressure. The tensor elements W'_{3333} and W'_{2323} are the *measured* normal and shear crack compliances and include all interactions with neighboring cracks and pores. These could be approximated, for example, by the compliances of idealized ellipsoidal cracks, interacting or not, but this would immediately reduce the generality. The expression $\hat{\mathbf{m}} \equiv (\sin \theta \cos \phi, \sin \theta \sin \phi, \cos \theta)^T$ denotes the unit normal to the crack face, where θ and ϕ are the polar and azimuthal angles in a spherical coordinate system, respectively.

An important physical assumption in the preceding equations is that, for thin cracks, the *crack compliance tensor* W'_{ijkl} is *sparse*, and thus only W'_{3333} , W'_{1313} , and W'_{2323} are nonzero. This is a general property of planar crack formulations and reflects an approximate decoupling of normal and shear deformation of the crack and decoupling of the in-plane and out-of-plane deformations. This allows us to write $W'_{jjkk} \approx W'_{3333}$. Furthermore, it is assumed that the two unknown shear compliances are approximately equal: $W'_{1313} \approx W'_{2323}$. A second important physical assumption is that for a thin crack under any stress field, it is primarily the *normal* component of stress, $\sigma = \hat{\mathbf{m}}^T \boldsymbol{\sigma} \hat{\mathbf{m}}$, resolved on the faces of a crack, that causes it to close and to have a stress-dependent compliance. Any open crack will have both normal and shear deformation under normal and shear loading, but it is only the normal stress that determines crack closure.

For the case of uniaxial stress σ_0 applied along the 3-axis to an initially isotropic rock, the normal stress in any direction is $\sigma_n = \sigma_0 \cos^2 \theta$. The rock takes on a transversely isotropic symmetry, with five independent elastic constants. The five independent components of ΔS_{ijkl} become

$$\begin{aligned} \Delta S_{3333}^{\text{uni}} &= 2\pi \int_0^{\pi/2} [W'_{3333}(\sigma_0 \cos^2 \theta) - 4W'_{2323}(\sigma_0 \cos^2 \theta)] \cos^4 \theta \sin \theta d\theta \\ &\quad + 2\pi \int_0^{\pi/2} 4W'_{2323}(\sigma_0 \cos^2 \theta) \cos^2 \theta \sin \theta d\theta \\ \Delta S_{1111}^{\text{uni}} &= 2\pi \int_0^{\pi/2} \frac{3}{8} [W'_{3333}(\sigma_0 \cos^2 \theta) - 4W'_{2323}(\sigma_0 \cos^2 \theta)] \sin^4 \theta \sin \theta d\theta \\ &\quad + 2\pi \int_0^{\pi/2} 2W'_{2323}(\sigma_0 \cos^2 \theta) \sin^2 \theta \sin \theta d\theta \\ \Delta S_{1122}^{\text{uni}} &= 2\pi \int_0^{\pi/2} \frac{1}{8} [W'_{3333}(\sigma_0 \cos^2 \theta) - 4W'_{2323}(\sigma_0 \cos^2 \theta)] \sin^4 \theta \sin \theta d\theta \\ \Delta S_{1133}^{\text{uni}} &= 2\pi \int_0^{\pi/2} \frac{1}{2} [W'_{3333}(\sigma_0 \cos^2 \theta) - 4W'_{2323}(\sigma_0 \cos^2 \theta)] \sin^2 \theta \cos^2 \theta \sin \theta d\theta \\ \Delta S_{2323}^{\text{uni}} &= 2\pi \int_0^{\pi/2} \frac{1}{2} [W'_{3333}(\sigma_0 \cos^2 \theta) - 4W'_{2323}(\sigma_0 \cos^2 \theta)] \sin^2 \theta \cos^2 \theta \sin \theta d\theta \\ &\quad + 2\pi \int_0^{\pi/2} \frac{1}{2} W'_{2323}(\sigma_0 \cos^2 \theta) \sin^2 \theta \sin \theta d\theta \\ &\quad + 2\pi \int_0^{\pi/2} W'_{2323}(\sigma_0 \cos^2 \theta) \cos^2 \theta \sin \theta d\theta \end{aligned}$$

Note that in the above equations, the terms in parentheses with $W'_{2323}(\cdot)$ and $W'_{3333}(\cdot)$ are arguments to the W'_{2323} and W'_{3333} pressure functions, and not multiplicative factors.

Sayers and Kachanov (1991, 1995) have presented an equivalent formalism for stress-induced anisotropy. The elastic compliance S_{ijkl} is once again written in the form

$$\Delta S_{ijkl} = S_{ijkl}(\sigma) - S_{ijkl}^0$$

where S_{ijkl}^0 is the compliance in the absence of compliant cracks and grain boundaries and ΔS_{ijkl} is the excess compliance due to the cracks. ΔS_{ijkl} can be written as

$$\Delta S_{ijkl} = \frac{1}{4} (\delta_{ik}\alpha_{jl} + \delta_{il}\alpha_{jk} + \delta_{jk}\alpha_{il} + \delta_{jl}\alpha_{ik}) + \beta_{ijkl}$$

where α_{ij} is a second-rank tensor and β_{ijkl} is a fourth-rank tensor defined by

$$\alpha_{ij} = \frac{1}{V} \sum_r B_T^{(r)} n_i^{(r)} n_j^{(r)} A^{(r)}$$

$$\beta_{ijkl} = \frac{1}{V} \sum_r \left(B_N^{(r)} - B_T^{(r)} \right) n_i^{(r)} n_j^{(r)} n_k^{(r)} n_l^{(r)} A^{(r)}$$

In these expressions, the summation is over all grain contacts and microcracks within the rock volume V . $B_N^{(r)}$ and $B_T^{(r)}$ are the normal and shear compliances of the r th discontinuity, which relate the displacement discontinuity across the crack to the applied traction across the crack faces; $n_i^{(r)}$ is the i th component of the normal to the discontinuity, and $A^{(r)}$ is the area of the discontinuity.

A completely different strategy for quantifying stress-induced anisotropy is to use the formalism of third-order elasticity, described in [Section 2.5](#) (e.g., [Helbig, 1994](#); [Johnson and Rasolofosaon, 1996](#); [Prioul *et al.*, 2004](#)). The third-order elasticity approach is phenomenological, avoiding the physical mechanisms of stress sensitivity, but providing a compact notation. For example, [Prioul *et al.* \(2004\)](#) found that for a stressed VTI (transversely isotropic with vertical symmetry axis) material, the effective elastic constants can be approximated in Voigt notation as

$$\begin{aligned} c_{11}^{\text{eff}} &\approx c_{11}^0 + c_{111}\varepsilon_{11} + c_{112}(\varepsilon_{22} + \varepsilon_{33}) \\ c_{22}^{\text{eff}} &\approx c_{11}^0 + c_{111}\varepsilon_{22} + c_{112}(\varepsilon_{11} + \varepsilon_{33}) \\ c_{33}^{\text{eff}} &\approx c_{33}^0 + c_{111}\varepsilon_{33} + c_{112}(\varepsilon_{11} + \varepsilon_{22}) \\ c_{12}^{\text{eff}} &\approx c_{12}^0 + c_{112}(\varepsilon_{11} + \varepsilon_{22}) + c_{123}\varepsilon_{33} \\ c_{13}^{\text{eff}} &\approx c_{13}^0 + c_{112}(\varepsilon_{11} + \varepsilon_{33}) + c_{123}\varepsilon_{22} \\ c_{23}^{\text{eff}} &\approx c_{13}^0 + c_{112}(\varepsilon_{22} + \varepsilon_{33}) + c_{123}\varepsilon_{11} \\ c_{66}^{\text{eff}} &\approx c_{66}^0 + c_{144}\varepsilon_{33} + c_{155}(\varepsilon_{11} + \varepsilon_{22}) \\ c_{55}^{\text{eff}} &\approx c_{44}^0 + c_{144}\varepsilon_{22} + c_{155}(\varepsilon_{11} + \varepsilon_{33}) \\ c_{44}^{\text{eff}} &\approx c_{44}^0 + c_{144}\varepsilon_{11} + c_{155}(\varepsilon_{22} + \varepsilon_{33}) \end{aligned}$$

where the constants c_{11}^0 , c_{33}^0 , c_{13}^0 , c_{44}^0 , c_{66}^0 are the VTI elastic constants at the unstressed reference state, with $c_{12}^0 = c_{11}^0 - 2c_{66}^0$. The quantities ε_{11} , ε_{22} , and ε_{33} are the principal strains, computed from the applied stress using the conventional Hooke's law, $\varepsilon_{ij} = s_{ijkl}\sigma_{kl}$. For these expressions, it is assumed that the direction of

the applied principal stress is aligned with the VTI symmetry (x_3 -) axis. Furthermore, for these expressions it is assumed that the stress-sensitive third-order tensor is isotropic, defined by the three independent constants, c_{111} , c_{112} , and c_{123} with $c_{144} = (c_{112} - c_{123})/2$ and $c_{155} = (c_{111} - c_{112})/4$.

In practice, the elastic constants (five for the unstressed VTI rock and three for the third-order elasticity) can be estimated from laboratory measurements, as illustrated by Sarkar *et al.* (2003) and Prioul *et al.* (2004). For an intrinsically VTI rock, hydrostatic loading experiments provide sufficient information to invert for all three of the third-order constants, provided that the anisotropy is not too weak. However, for an intrinsically isotropic rock, nonhydrostatic loading is required in order to provide enough independent information to determine the constants. Once the constants are determined, the stress-induced elastic constants corresponding to any (aligned) stress field can be determined. The full expressions for stress-induced anisotropy of an originally VTI rock are given by Sarkar *et al.* (2003) and Prioul *et al.* (2004).

Sarkar *et al.* (2003) give expressions for stress-induced changes in Thomsen parameters of an originally VTI rock, provided that both the original and stress-induced anisotropies are weak:

$$\begin{aligned} \varepsilon^{(1)} &= \varepsilon^0 + \frac{c_{155}}{c_{33}^0 c_{55}^0} (\sigma_{22} - \sigma_{33}); & \varepsilon^{(2)} &= \varepsilon^0 + \frac{c_{155}}{c_{33}^0 c_{55}^0} (\sigma_{11} - \sigma_{33}) \\ \delta^{(1)} &= \delta^0 + \frac{c_{155}}{c_{33}^0 c_{55}^0} (\sigma_{22} - \sigma_{33}); & \delta^{(2)} &= \delta^0 + \frac{c_{155}}{c_{33}^0 c_{55}^0} (\sigma_{11} - \sigma_{33}) \\ \gamma^{(1)} &= \gamma^0 + \frac{c_{456}}{2c_{55}^0 c_{55}^0} (\sigma_{22} - \sigma_{33}); & \gamma^{(2)} &= \gamma^0 + \frac{c_{456}}{2c_{55}^0 c_{55}^0} (\sigma_{11} - \sigma_{33}) \\ \delta^{(3)} &= \frac{c_{155}}{c_{33}^0 c_{55}^0} (\sigma_{22} - \sigma_{11}) \\ c_{155} &= \frac{1}{4} (c_{111} - c_{112}); & c_{456} &= \frac{1}{8} (c_{111} - 3c_{112} + 2c_{123}) \end{aligned}$$

The results are shown in terms of Tsvankin's extended Thomsen parameters (Section 2.4). Orthorhombic symmetry occurs when $\sigma_{11} \neq \sigma_{22}$. (Strictly speaking, three different principal stresses applied to a VTI rock do not result in perfect orthorhombic symmetry. However, orthorhombic parameters are adequate in the case of weak anisotropy.)

Uses

Understanding or, at least, empirically describing the stress dependence of velocities is useful for quantifying the change of velocities in seismic time-lapse data due to changes in reservoir pressure, as well as in certain types of naturally occurring overpressure. Since the state of stress *in situ* is seldom hydrostatic, quantifying the impact of stress on anisotropy can often improve on the usual isotropic analysis.

Assumptions and limitations

- Most models for predicting or describing stress-induced anisotropy that are based on cracks and crack-like flaws assume an isotropic, linear, elastic solid mineral material.
- Methods based on ellipsoidal cracks or spherical contacts are limited to idealized geometries and to low crack densities.
- The method of Mavko *et al.* (1995) has been shown to sometimes under predict stress-induced anisotropy when the maximum stress difference is comparable to the mean stress magnitude. More generally, there is evidence (Johnson and Rasolofosaon, 1996) that classical elastic formulations (nonlinear elasticity) can fail to describe the behavior of rocks at low stresses.
- The methods presented here assume that the strains are infinitesimal. When strains become finite, an additional source of nonlinearity, called *geometrical* or *kinetic* nonlinearity, appears, related to the difference between Lagrangian and Eulerian descriptions of motion (Zarembko and Krasil'nikov, 1971; Johnson and Rasolofosaon, 1996).

2.8 Strain components and equations of motion in cylindrical and spherical coordinate systems

Synopsis

The equations of motion and the expressions for small-strain components in cylindrical and spherical coordinate systems differ from those in a rectangular coordinate system. Figure 2.8.1 shows the variables used in the equations that follow.

In the **cylindrical** coordinate system (r, ϕ, z) , the coordinates are related to those in the rectangular coordinate system (x, y, z) as

$$r = \sqrt{x^2 + y^2}, \quad \tan(\phi) = \frac{y}{x}$$

$$x = r \cos(\phi), \quad y = r \sin(\phi), \quad z = z$$

The small-strain components can be expressed through the displacements u_r , u_ϕ , and u_z (which are in the directions r , ϕ , and z , respectively) as

$$e_{rr} = \frac{\partial u_r}{\partial r}, \quad e_{\phi\phi} = \frac{1}{r} \frac{\partial u_\phi}{\partial \phi} + \frac{u_r}{r}, \quad e_{zz} = \frac{\partial u_z}{\partial z}$$

$$e_{r\phi} = \frac{1}{2} \left(\frac{1}{r} \frac{\partial u_r}{\partial \phi} + \frac{\partial u_\phi}{\partial r} - \frac{u_\phi}{r} \right)$$

$$e_{\phi z} = \frac{1}{2} \left(\frac{\partial u_\phi}{\partial z} + \frac{1}{r} \frac{\partial u_z}{\partial \phi} \right), \quad e_{zr} = \frac{1}{2} \left(\frac{\partial u_z}{\partial r} + \frac{\partial u_r}{\partial z} \right)$$

The equations of motion are

$$\frac{\partial \sigma_{rr}}{\partial r} + \frac{1}{r} \frac{\partial \sigma_{r\phi}}{\partial \phi} + \frac{\partial \sigma_{zr}}{\partial z} + \frac{\sigma_{rr} - \sigma_{\phi\phi}}{r} = \rho \frac{\partial^2 u_r}{\partial t^2}$$

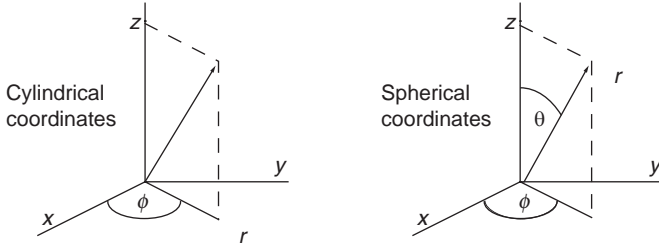


Figure 2.8.1 The variables used for converting between Cartesian, spherical, and cylindrical coordinates.

$$\frac{\partial \sigma_{r\phi}}{\partial r} + \frac{1}{r} \frac{\partial \sigma_{\phi\phi}}{\partial \phi} + \frac{\partial \sigma_{\phi z}}{\partial z} + \frac{2\sigma_{r\phi}}{r} = \rho \frac{\partial^2 u_\phi}{\partial t^2}$$

$$\frac{\partial \sigma_{rz}}{\partial r} + \frac{1}{r} \frac{\partial \sigma_{\phi z}}{\partial \phi} + \frac{\partial \sigma_{zz}}{\partial z} + \frac{\sigma_{rz}}{r} = \rho \frac{\partial^2 u_z}{\partial t^2}$$

where ρ denotes density and t time.

In the **spherical** coordinate system (r, ϕ, θ) the coordinates are related to those in the rectangular coordinate system (x, y, z) as

$$r = \sqrt{x^2 + y^2 + z^2}, \quad \tan(\phi) = \frac{y}{x}, \quad \cos(\theta) = \frac{z}{\sqrt{x^2 + y^2 + z^2}}$$

$$x = r \sin(\theta) \cos(\phi), \quad y = r \sin(\theta) \sin(\phi), \quad z = r \cos(\theta)$$

The small-strain components can be expressed through the displacements u_r, u_ϕ , and u_θ (which are in the directions r, ϕ , and θ , respectively) as

$$e_{rr} = \frac{\partial u_r}{\partial r}, \quad e_{\phi\phi} = \frac{1}{r \sin(\theta)} \frac{\partial u_\phi}{\partial \phi} + \frac{u_r}{r} + \frac{u_\theta}{r \tan(\theta)}, \quad e_{\theta\theta} = \frac{1}{r} \frac{\partial u_\theta}{\partial \theta} + \frac{u_r}{r}$$

$$e_{r\phi} = \frac{1}{2} \left[\frac{1}{r \sin(\theta)} \frac{\partial u_r}{\partial \phi} + \frac{\partial u_\phi}{\partial r} - \frac{u_\phi}{r} \right]$$

$$e_{\phi\theta} = \frac{1}{2} \left[\frac{1}{r} \frac{\partial u_\phi}{\partial \theta} - \frac{u_\phi}{r \tan(\theta)} + \frac{1}{r \sin(\theta)} \frac{\partial u_\theta}{\partial \phi} \right]$$

$$e_{r\theta} = \frac{1}{2} \left(\frac{\partial u_\theta}{\partial r} - \frac{u_\theta}{r} + \frac{1}{r} \frac{\partial u_r}{\partial \theta} \right)$$

The equations of motion are

$$\frac{\partial \sigma_{rr}}{\partial r} + \frac{1}{r \sin(\theta)} \frac{\partial \sigma_{r\phi}}{\partial \phi} + \frac{1}{r} \frac{\partial \sigma_{r\theta}}{\partial \theta} + \frac{2\sigma_{rr} + \sigma_{r\theta} \cot(\theta) - \sigma_{\phi\phi} - \sigma_{\theta\theta}}{r} = \rho \frac{\partial^2 u_r}{\partial t^2}$$

$$\frac{\partial \sigma_{r\phi}}{\partial r} + \frac{1}{r \sin(\theta)} \frac{\partial \sigma_{\phi\phi}}{\partial \phi} + \frac{1}{r} \frac{\partial \sigma_{\phi\theta}}{\partial \theta} + \frac{3\sigma_{r\phi} + \sigma_{\phi\theta} \cot(\theta)}{r} = \rho \frac{\partial^2 u_\phi}{\partial t^2}$$

$$\frac{\partial \sigma_{r\theta}}{\partial r} + \frac{1}{r \sin(\theta)} \frac{\partial \sigma_{\phi\phi}}{\partial \phi} + \frac{1}{r} \frac{\partial \sigma_{\phi\theta}}{\partial \theta} + \frac{3\sigma_{r\theta} + (\sigma_{\theta\theta} - \sigma_{\phi\phi}) \cot(\theta)}{r} = \rho \frac{\partial^2 u_\theta}{\partial t^2}$$

Uses

The foregoing equations are used to solve elasticity problems where cylindrical or spherical geometries are most natural.

Assumptions and limitations

The equations presented assume that the strains are small.

2.9 Deformation of inclusions and cavities in elastic solids

Synopsis

Many problems in effective-medium theory and poroelasticity can be solved or estimated in terms of the elastic behavior of cavities and inclusions. Some **static** and **quasistatic** results for cavities are presented here. It should be remembered that often these are also valid for certain limiting cases of dynamic problems. Excellent treatments of cavity deformation and pore compressibility are given by Jaeger and Cook (1969) and by Zimmerman (1991a).

General pore deformation

Effective dry compressibility

Consider a homogeneous linear elastic solid that has an arbitrarily shaped pore space – either a single cavity or a collection of pores. The effective dry compressibility (i.e., the reciprocal of the dry bulk modulus) of the porous solid can be written as

$$\frac{1}{K_{\text{dry}}} = \frac{1}{K_0} + \frac{\phi}{v_p} \frac{\partial v_p}{\partial \sigma} \Big|_{\text{dry}}$$

where K_{dry} is the effective bulk modulus of the dry porous solid, K_0 is the bulk modulus of the solid mineral material, ϕ is the porosity, v_p is the pore volume, $\partial v_p / \partial \sigma|_{\text{dry}}$ is the derivative of the pore volume with respect to the externally applied hydrostatic stress. We also assume that no inelastic effects such as friction or viscosity are present. This is strictly true, regardless of the pore geometry and the pore concentration. The preceding equation can be rewritten slightly as

$$\frac{1}{K_{\text{dry}}} = \frac{1}{K_0} + \frac{\phi}{K_\phi}$$

where $K_\phi = v_p / (\partial v_p / \partial \sigma)|_{\text{dry}}$ is defined as the dry pore-space stiffness. These equations state simply that the porous rock compressibility is equal to the intrinsic mineral compressibility plus an additional compressibility caused by the pore space.

Caution: “Dry rock” is not the same as gas-saturated rock

The dry-frame modulus refers to the incremental bulk deformation resulting from an increment of applied confining pressure with pore pressure held constant. This corresponds to a “drained” experiment in which pore fluids can flow freely in or out of the sample to ensure constant pore pressure. Alternatively, the dry-frame modulus can correspond to an undrained experiment in which the pore fluid has zero bulk modulus, and in which pore compressions therefore do not induce changes in pore pressure. This is approximately the case for an air-filled sample at standard temperature and pressure. However, at reservoir conditions, the gas takes on a non-negligible bulk modulus and should be treated as a saturating fluid.

An equivalent expression for the dry rock compressibility or bulk modulus is

$$K_{\text{dry}} = K_0(1 - \beta)$$

where β is sometimes called the **Biot coefficient**, which describes the ratio of pore-volume change Δv_p to total bulk-volume change ΔV under dry or drained conditions:

$$\beta = \left. \frac{\Delta v_p}{\Delta V} \right|_{\text{dry}} = \frac{\phi K_{\text{dry}}}{K_\phi}$$

Stress-induced pore pressure: Skempton’s coefficient

If this arbitrary pore space is filled with a pore fluid with bulk modulus, K_{fl} , the saturated solid is stiffer under compression than the dry solid, because an increment of pore-fluid pressure is induced that resists the volumetric strain. The ratio of the induced pore pressure, dP , to the applied compressive stress, $d\sigma$, is sometimes called **Skempton’s coefficient** and can be written as

$$\begin{aligned} B &\equiv \frac{dP}{d\sigma} = \frac{1}{1 + K_\phi(1/K_{\text{fl}} - 1/K_0)} \\ &= \frac{1}{1 + \phi(1/K_{\text{fl}} - 1/K_0)(1/K_{\text{dry}} - 1/K_0)^{-1}} \end{aligned}$$

where K_ϕ is the dry pore-space stiffness defined earlier in this section. For this definition to be true, the pore pressure must be uniform throughout the pore space, as will be the case if:

- (1) there is only one pore,
- (2) all pores are well connected and the frequency and viscosity are low enough for any pressure differences to equilibrate, or
- (3) all pores have the same dry pore stiffness.

Given these conditions, there is no additional limitation on pore geometry or concentration. All of the necessary information concerning pore stiffness and geometry is contained in the parameter K_ϕ .

Saturated stress-induced pore-volume change

The corresponding change in fluid-saturated pore volume, v_p , caused by the remote stress is

$$\left. \frac{1}{v_p} \frac{dv_p}{d\sigma} \right|_{\text{sat}} = \frac{1}{K_\phi} \frac{dP}{d\sigma} = \frac{1/K_\phi}{1 + K_\phi(1/K_\phi - 1/K_0)}$$

Low-frequency saturated compressibility

The low-frequency saturated bulk modulus, K_{sat} , can be derived from Gassmann's equation (see [Section 6.3](#) on Gassmann). One equivalent form is

$$\frac{1}{K_{\text{sat}}} = \frac{1}{K_0} + \frac{\phi}{K_\phi + \frac{K_0 K_\phi}{K_0 - K_\phi}} \approx \frac{1}{K_0} + \frac{\phi}{K_\phi + K_\phi}$$

where, again, all of the necessary information concerning pore stiffness and geometry is contained in the dry pore stiffness K_ϕ , and we must ensure that the stress-induced pore pressure is uniform throughout the pore space.

Three-dimensional ellipsoidal cavities

Many effective media models are based on ellipsoidal inclusions or cavities. These are mathematically convenient shapes and allow quantitative estimates of, for example, K_ϕ , which was defined earlier in this section. Eshelby (1957) discovered that the strain, ε_{ij} , inside an ellipsoidal inclusion is homogeneous when a homogeneous strain, ε_{ij}^0 , (or stress) is applied at infinity. Because the inclusion strain is homogeneous, operations such as determining the inclusion stress or integrating to obtain the displacement field are straightforward.

It is very important to remember that the following results assume a single isolated cavity in an infinite medium. Therefore, substituting them directly into the preceding formulas for dry and saturated moduli gives estimates that are strictly valid only for low concentrations of pores (see also [Section 4.8](#) on self-consistent theories).

Spherical cavity

For a single spherical cavity with volume $v_p = \frac{4}{3}\pi R^3$ and a hydrostatic stress, $d\sigma$, applied at infinity, the radial strain of the cavity is

$$\frac{dR}{R} = \frac{1}{K_0} \frac{(1-\nu)}{2(1-2\nu)} d\sigma$$

where ν and K_0 are the Poisson ratio and bulk modulus of the solid material, respectively. The change of pore volume is

$$dv_p = \frac{1}{K_0} \frac{3(1-\nu)}{2(1-2\nu)} v_p d\sigma$$

Then, the volumetric strain of the sphere is

$$\varepsilon_{ii} = \frac{dv_p}{v_p} = \frac{1}{K_0} \frac{3(1-\nu)}{2(1-2\nu)} d\sigma$$

and the single-pore stiffness is

$$\frac{1}{K_\phi} = \frac{1}{v_p} \frac{dv_p}{d\sigma} = \frac{1}{K_0} \frac{3(1-\nu)}{2(1-2\nu)}$$

Remember that this estimate of K_ϕ assumes a single isolated spherical cavity in an infinite medium.

Under a remotely applied homogeneous *shear stress*, τ_0 , corresponding to remote shear strain $\varepsilon_0 = \tau_0/2\mu_0$, the effective *shear strain* in the spherical cavity is

$$\varepsilon = \frac{15(1-\nu)}{2\mu_0(7-5\nu)} \tau_0$$

where μ_0 is the shear modulus of the solid. Note that this results in approximately twice the strain that would occur without the cavity.

Penny-shaped crack: oblate spheroid

Consider a dry penny-shaped ellipsoidal cavity with semiaxes $a \ll b = c$. When a remote uniform tensional stress, $d\sigma$, is applied normal to the plane of the crack, each crack face undergoes an outward displacement, U , normal to the plane of the crack, given by the radially symmetric distribution

$$U(r) = \frac{4(1-\nu^2)c\sqrt{1-(r/c)^2}}{3\pi K_0(1-2\nu)} d\sigma$$

where r is the radial distance from the axis of the crack. For any arbitrary homogeneous remote stress, $d\sigma$ is the component of stress *normal* to the plane of the crack. Thus, $d\sigma$ can also be thought of as a remote hydrostatic stress field.

This displacement function is also an ellipsoid with semiminor axis, $U(r=0)$, and semimajor axis, c . Therefore the volume change, dv , which is simply the

integral of $U(r)$ over the faces of the crack, is just the volume of the displacement ellipsoid:

$$dv_p = \frac{4}{3} \pi U(0) c^2 = \frac{16c^3}{9K_0} \frac{(1 - \nu^2)}{(1 - 2\nu)} d\sigma$$

Then the volumetric strain of the cavity is

$$\varepsilon_{ii} = \frac{dv_p}{v_p} = \frac{4(c/a)}{3\pi K_0} \frac{(1 - \nu^2)}{(1 - 2\nu)} d\sigma$$

and the pore stiffness is

$$\frac{1}{K_\phi} = \frac{1}{v_p} \frac{dv_p}{d\sigma} = \frac{4(c/a)}{3\pi K_0} \frac{(1 - \nu^2)}{(1 - 2\nu)}$$

An interesting case is an applied compressive stress causing a displacement, $U(0)$, equal to the original half-width of the crack, thus closing the crack. Setting $U(0) = a$ allows one to compute the **closing stress**:

$$\sigma_{\text{close}} = \frac{3\pi(1 - 2\nu)}{4(1 - \nu^2)} \alpha K_0 = \frac{\pi}{2(1 - \nu)} \alpha \mu_0$$

where $\alpha = (a/c)$ is the aspect ratio.

Now, under a remotely applied homogeneous *shear stress*, τ_0 , corresponding to remote shear strain $\varepsilon_0 = \tau_0/2\mu_0$, the effective **shear strain** in the cavity is

$$\varepsilon = \tau_0 \frac{2(c/a)}{\pi\mu_0} \frac{(1 - \nu)}{(2 - \nu)}$$

Needle-shaped pore: prolate spheroid

Consider a dry needle-shaped ellipsoidal cavity with semiaxes $a \gg b = c$ and with pore volume $v = \frac{4}{3}\pi a c^2$. When a remote hydrostatic stress, $d\sigma$, is applied, the pore volume change is

$$dv_p = \frac{(5 - 4\nu)}{3K_0(1 - 2\nu)} v_p d\sigma$$

The volumetric strain of the cavity is then

$$\varepsilon_{ii} = \frac{dv_p}{v_p} = \frac{(5 - 4\nu)}{3K_0(1 - 2\nu)} d\sigma$$

and the pore stiffness is

$$\frac{1}{K_\phi} = \frac{1}{v_p} \frac{dv_p}{d\sigma} = \frac{(5 - 4\nu)}{3K_0(1 - 2\nu)}$$

Note that in the limit of very large a/c , these results are exactly the same as for a two-dimensional circular cylinder.

Estimate the increment of pore pressure induced in a water-saturated rock when a 1 bar increment of hydrostatic confining pressure is applied. Assume that the rock consists of stiff, spherical pores in a quartz matrix. Compare this with a rock with thin, penny-shaped cracks (aspect ratio $\alpha = 0.001$) in a quartz matrix. The moduli of the individual constituents are $K_{\text{quartz}} = 36 \text{ GPa}$, $K_{\text{water}} = 2.2 \text{ GPa}$, and $\nu_{\text{quartz}} = 0.07$.

The pore-space stiffnesses are given by

$$K_{\phi\text{-sphere}} = K_{\text{quartz}} \frac{2(1 - 2\nu_{\text{quartz}})}{3(1 - \nu_{\text{quartz}})} = 22.2 \text{ GPa}$$

$$K_{\phi\text{-crack}} = \frac{3\pi\alpha K_{\text{quartz}}}{4} \frac{(1 - 2\nu_{\text{quartz}})}{(1 - \nu_{\text{quartz}}^2)} = 0.0733 \text{ GPa}$$

The pore-pressure increment is computed from Skempton's coefficient:

$$\frac{\Delta P_{\text{pore}}}{\Delta P_{\text{confining}}} = B = \frac{1}{1 + K_{\phi}(K_{\text{water}}^{-1} - K_{\text{quartz}}^{-1})}$$

$$B_{\text{sphere}} = \frac{1}{1 + 22.2[(1/2.2) - (1/36)]} = 0.095$$

$$B_{\text{crack}} = \frac{1}{1 + 0.0733[(1/2.2) - (1/36)]} = 0.970$$

Therefore, the pore pressure induced in the spherical pores is 0.095 bar and the pore pressure induced in the cracks is 0.98 bar.

Two-dimensional tubes

A special two-dimensional case of long, tubular pores was treated by Mavko (1980) to describe melt or fluids arranged along the edges of grains. The cross-sectional shape is described by the equations

$$x = R \left(\cos \theta + \frac{1}{2 + \gamma} \cos 2\theta \right)$$

$$y = R \left(-\sin \theta + \frac{1}{2 + \gamma} \sin 2\theta \right)$$

where γ is a parameter describing the roundness (Figure 2.9.1).

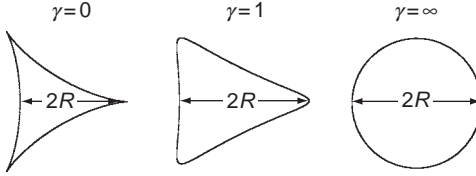


Figure 2.9.1 The cross-sectional shapes of various two-dimensional tubes.

Consider, in particular, the case on the left, $\gamma = 0$. The pore volume is $\frac{1}{2}\pi aR^2$, where $a \gg R$ is the length of the tube. When a remote hydrostatic stress, $d\sigma$, is applied, the pore volume change is

$$dv_p = \frac{(13 - 4\nu - 8\nu^2)}{3K_0(1 - 2\nu)} v_p d\sigma$$

The volumetric strain of the cavity is then

$$\varepsilon_{ii} = \frac{dv_p}{v_p} = \frac{(13 - 4\nu - 8\nu^2)}{3K_0(1 - 2\nu)} d\sigma$$

and the pore stiffness is

$$\frac{1}{K_\phi} = \frac{1}{v_p} \frac{dv_p}{d\sigma} = \frac{(13 - 4\nu - 8\nu^2)}{3K_0(1 - 2\nu)}$$

In the extreme, $\gamma \rightarrow \infty$, the shape becomes a circular cylinder, and the expression for pore stiffness, K_ϕ , is exactly the same as that derived for the needle-shaped pores above. Note that the triangular cavity ($\gamma = 0$) has about half the pore stiffness of the circular one; that is, the triangular tube can give approximately the same effective modulus as the circular tube with about half the porosity.

Caution

These expressions for K_ϕ , dv_p , and ε_{ii} include an estimate of tube shortening as well as a reduction in pore cross-sectional area under hydrostatic stress. Hence, the deformation is neither plane stress nor plane strain.

Plane strain

The **plane-strain** compressibility in terms of the reduction in cross-sectional area A is given by

$$\frac{1}{K'_\phi} = \frac{1}{A} \frac{dA}{d\sigma} = \begin{cases} \frac{6(1-\nu)}{\mu_0}, & \gamma \rightarrow 0 \\ \frac{2(1-\nu)}{\mu_0}, & \gamma \rightarrow \infty \end{cases}$$

The latter case ($\gamma \rightarrow \infty$) corresponds to a tube with a circular cross-section and agrees (as it should) with the expression given below for the limiting case of a tube with an elliptical cross-section with aspect ratio unity.

A general method of determining K'_ϕ for nearly arbitrarily shaped two-dimensional cavities under *plane-strain* deformation was developed by Zimmerman (1986, 1991a) and involves conformal mapping of the tube shape into circular pores. For example, pores with cross-sectional shapes that are n -sided hypotrochoids given by

$$x = \cos(\theta) + \frac{1}{(n-1)} \cos(n-1)\theta$$

$$y = -\sin(\theta) + \frac{1}{(n-1)} \sin(n-1)\theta$$

(see the examples labeled (1) in Table 2.9.1) have plane-strain compressibilities

$$\frac{1}{K'_\phi} = \frac{1}{A} \frac{dA}{d\sigma} = \frac{1}{K'^{\text{cir}}_\phi} \frac{1 + (n-1)^{-1}}{1 - (n-1)^{-1}}$$

where $1/K'^{\text{cir}}_\phi$ is the plane-strain compressibility of a circular tube given by

$$\frac{1}{K'^{\text{cir}}_\phi} = \frac{2(1-\nu)}{\mu_0}$$

Table 2.9.1 summarizes a few plane-strain pore compressibilities.

Two-dimensional thin cracks

A convenient description of very thin two-dimensional cracks is in terms of elastic line dislocations. Consider a crack lying along $-c < x < c$ in the $y = 0$ plane and very long in the z direction. The **total relative displacement** of the crack faces $u(x)$, defined as the displacement of the negative face ($y = 0^-$) relative to the positive face ($y = 0^+$), is related to the dislocation density function by

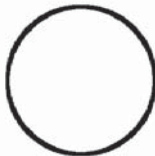







$$B(x) = -\frac{\partial u}{\partial x}$$

where $B(x)dx$ represents the total length of the Burger vectors of the dislocations lying between x and $x + dx$. The stress change in the plane of the crack that results from introduction of a dislocation line with unit Burger vector at the origin is

$$\sigma = \frac{\mu_0}{2\pi D x}$$

where $D = 1$ for screw dislocations and $D = (1 - \nu)$ for edge dislocations (ν is Poisson's ratio and μ_0 is the shear modulus). Edge dislocations can be used to describe mode I and mode II cracks; screw dislocations can be used to describe mode III cracks.

Table 2.9.1 Plane-strain compressibility normalized by the compressibility of a circular tube.

	(1)	(1)	(1)	(1)	(2)	(3)		
$\frac{\mu_0}{2(1-\nu)K'_\phi}$	1	1.581	3	1.188	2	$\pi/8\alpha$	$1/2\alpha$	$2/3\alpha$
								

Notes:

(1) $x = \cos(\theta) + \frac{1}{(n-1)}\cos((n-1)\theta)$, where n = number of sides; $y = -\sin(\theta) + \frac{1}{(n-1)}\sin((n-1)\theta)$. (2) $y = 2b\sqrt{1 - (x/c)^2}$ (ellipse). (3) $y = 2b\left[1 - (x/c)^2\right]^{3/2}$ (nonelliptical, “tapered” crack).

The stress here is the component of traction in the crack plane parallel to the displacement: normal stress for mode I deformation, in-plane shear for mode II deformation, and out-of-plane shear for mode III deformation.

Then the stress resulting from the distribution $B(x)$ is given by the convolution

$$\sigma(x) = \frac{\mu_0}{2\pi D} \int_{-c}^c \frac{B(x') dx'}{x - x'}$$

The special case of interest for nonfrictional cavities is the deformation for stress-free crack faces under a remote uniform tensional stress, $d\sigma$, acting normal to the plane of the crack. The outward displacement distribution of *each* crack face is given by (using edge dislocations)

$$U(x) = \frac{c\sigma(1-\nu)\sqrt{1-(x/c)^2}}{\mu_0} = \frac{2c\sigma(1-\nu^2)\sqrt{1-(x/c)^2}}{3K_0(1-2\nu)}$$

The volume change is then given by

$$\frac{dv_p}{d\sigma} = \pi U(0)ca = \frac{2\pi c^2 a (1-\nu^2)}{3K_0 (1-2\nu)}$$

It is important to note that *these results for displacement and volume change apply to any two-dimensional crack of arbitrary cross-section* as long as it is very thin and approximately planar. They are not limited to cracks of elliptical cross-section.

For the special case in which the very thin crack is elliptical in cross-section with half-width b in the thin direction, the volume is $v = \pi abc$, and the pore stiffness under plane-strain deformation is given by

$$\frac{1}{K'_\phi} = \frac{1}{A} \frac{dA}{d\sigma} = \frac{(c/b)(1-\nu)}{\mu_0} = \frac{2(c/b)(1-\nu^2)}{3K_0 (1-2\nu)}$$

Another special case is a crack of *nonelliptical* form (Mavko and Nur, 1978) with initial shape given by

$$U_0(x) = 2b \left[1 - \left(\frac{x}{c_0} \right)^2 \right]^{3/2}$$

where c_0 is the crack half-length and $2b$ is the maximum crack width. This crack is plotted in Figure 2.9.2. Note that unlike elliptical cracks that have rounded or blunted ends, this crack has tapered tips where faces make a smooth, tangent contact. If we apply a pressure, P , the crack shortens as well as thins, and the pressure-dependent length is given by

$$c = c_0 \left[1 - \frac{2(1-\nu)}{3\mu_0(b/c_0)} P \right]^{1/2}$$

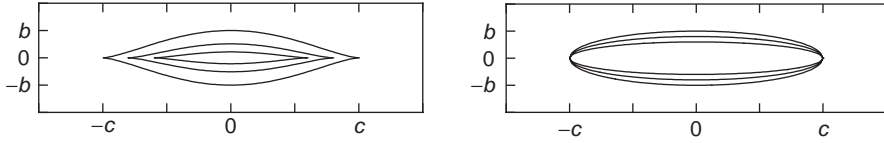


Figure 2.9.2 A nonelliptical crack shortens as well as narrows under compression. An elliptical crack only narrows.

Then the deformed shape is

$$U(x, P) = 2b \left(\frac{c}{c_0} \right)^3 \left[1 - \left(\frac{x}{c} \right)^2 \right]^{3/2}, \quad |x| \leq c$$

An important consequence of the smoothly tapered crack tips and the gradual crack shortening is that there is no stress singularity at the crack tips. In this case, crack closure occurs (i.e., $U \rightarrow 0$) as the crack length goes to zero ($c \rightarrow 0$). The closing stress is

$$\sigma_{\text{close}} = \frac{3}{2(1-\nu)} \alpha_0 \mu_0 = \frac{3}{4(1-\nu^2)} \alpha_0 E_0$$

where $\alpha_0 = b/c_0$ is the original crack aspect ratio, and μ_0 and E_0 are the shear and Young's moduli of the solid material, respectively. This expression is consistent with the usual rule of thumb that the crack-closing stress is numerically $\sim \alpha_0 E_0$. The exact factor depends on the details of the original crack shape. In comparison, the pressure required to close a two-dimensional elliptical crack of aspect ratio α_0 is

$$\sigma_{\text{close}} = \frac{1}{2(1-\nu^2)} \alpha_0 E_0$$

Ellipsoidal cracks of finite thickness

The pore compressibility under plane-strain deformation of a *two-dimensional* elliptical cavity of arbitrary aspect ratio α is given by (Zimmerman, 1991a)

$$\frac{1}{K'_\phi} = \frac{1}{A} \frac{dA}{d\sigma} = \frac{1-\nu}{\mu_0} \left(\alpha + \frac{1}{\alpha} \right) = \frac{2(1-\nu^2)}{3K_0(1-2\nu)} \left(\alpha + \frac{1}{\alpha} \right)$$

where μ_0 , K_0 , and ν are the shear modulus, bulk modulus, and Poisson's ratio of the mineral material, respectively. Circular pores (tubes) correspond to aspect ratio $\alpha = 1$ and the pore compressibility is given as

$$\frac{1}{K'_\phi} = \frac{1}{A} \frac{dA}{d\sigma} = \frac{2(1-\nu)}{\mu_0} = \frac{4(1-\nu^2)}{3K_0(1-2\nu)}$$

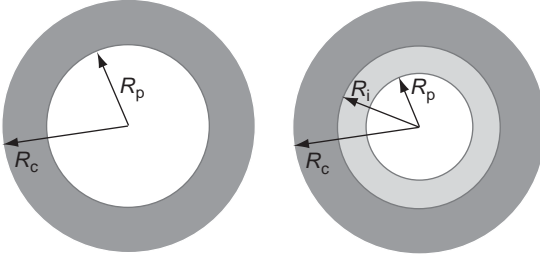


Figure 2.9.3 Deformation of a single- and double-layer spherical shell.

Deformation of spherical shells

The radial displacement u_r of a spherical elastic shell (Figure 2.9.3) with inner pore radius R_p and outer radius R_c under applied confining pressure P_c and pore pressure P_p is given by (Ciz *et al.*, 2008)

$$u_r = \frac{r}{3K(1-\phi)} (\phi P_p - P_c) + \frac{R_p^3}{4r^2\mu(1-\phi)} (P_p - P_c)$$

where r is the radial distance from the center of the sphere, K is the bulk modulus of the solid elastic material, μ is the shear modulus of the solid elastic material, and ϕ is the porosity. The associated volume change of the inner spherical pore is

$$dV_\phi = \frac{3V_\phi}{1-\phi} \left[\left(\frac{\phi}{3K} + \frac{1}{4\mu} \right) dP_p - \left(\frac{1}{3K} + \frac{1}{4\mu} \right) dP_c \right].$$

The volume change of the total sphere (shell plus pore) is

$$dV = \frac{3V}{1-\phi} \left[\phi \left(\frac{1}{3K} + \frac{1}{4\mu} \right) dP_p - \left(\frac{1}{3K} + \frac{\phi}{4\mu} \right) dP_c \right].$$

Similarly, the radial displacement of a double-layer sphere (Figure 2.9.3) is given by (Ciz *et al.*, 2008)

$$u_r = \frac{A_n r}{3} + \frac{B_n}{r^2}$$

where R_p is the pore radius, R_c is the outer sphere radius, and R_i is the radius at the boundary between the inner and outer elastic shells. The elastic moduli of the inner solid shell are K_1 and μ_1 , and the moduli of the outer shell are K_2 and μ_2 :

$$A_1 = \frac{1}{\Delta} \left\{ [(4\mu_1\mu_2 + 3K_2\mu_2)R_i^3 + (3K_2\mu_1 - 3K_2\mu_2)R_c^3] R_p^3 P_p - (3K_2\mu_1 + 4\mu_1\mu_2) R_c^3 R_i^3 P_c \right\}$$

$$\begin{aligned}
B_1 &= \frac{1}{\Delta} \left\{ \left[\left(\frac{3}{4} K_1 K_2 + K_2 \mu_2 \right) R_c^3 + (K_1 \mu_2 + K_2 \mu_2) R_i^3 \right] R_p^3 R_i^3 P_p \right. \\
&\quad \left. - \left(\frac{3}{4} K_1 K_2 + K_1 \mu_2 \right) R_c^3 R_i^3 R_p^3 P_c \right\} \\
A_2 &= \frac{1}{\Delta} \left\{ \left[(3K_1 \mu_1 - 3K_1 \mu_2) R_p^3 - (3K_1 \mu_2 + 4\mu_1 \mu_2) R_i^3 \right] R_c^3 P_c \right. \\
&\quad \left. + (3K_1 \mu_2 - 4\mu_1 \mu_2) R_i^3 R_p^3 P_p \right\} \\
B_2 &= \frac{1}{\Delta} \left\{ \left[(K_1 \mu_1 - K_2 \mu_1) R_i^3 - \left(\frac{3}{4} K_1 K_2 + K_2 \mu_1 \right) R_p^3 \right] R_c^3 R_i^3 P_c \right. \\
&\quad \left. + \left(\frac{3}{4} K_1 K_2 + K_1 \mu_1 \right) R_c^3 R_i^3 R_p^3 P_p \right\} \\
\Delta &= K_2 \mu_1 (3K_1 + 4\mu_2) R_c^3 R_i^3 - K_1 \mu_2 (3K_2 + 4\mu_1) R_i^3 R_p^3 \\
&\quad + 4\mu_1 \mu_2 (K_1 - K_2) R_i^6 + 3K_1 K_2 (\mu_2 - \mu_1) R_c^3 R_p^3
\end{aligned}$$

Uses

The equations presented in this section are useful for computing deformation of cavities in elastic solids and estimating effective moduli of porous solids.

Assumptions and limitations

The equations presented in this section are based on the following assumptions.

- Solid material must be homogeneous, isotropic, linear, and elastic.
- Results for specific geometries, such as spheres and ellipsoids, are derived for single isolated cavities. Therefore, estimates of effective moduli based on these are limited to relatively low pore concentrations where pore elastic interaction is small.
- Pore-pressure computations assume that the induced pore pressure is uniform throughout the pore space, which will be the case if (1) there is only one pore, (2) all pores are well connected and the frequency and viscosity are low enough for any pressure differences to equilibrate, or (3) all pores have the same dry pore stiffness.

2.10 Deformation of a circular hole: borehole stresses

Synopsis

Presented here are some solutions related to a circular hole in a stressed, linear, elastic, and poroelastic isotropic medium.

Hollow cylinder with internal and external pressures

The cylinder's internal radius is R_1 and the external radius is R_2 . Hydrostatic stress p_1 is applied at the interior surface at R_1 and hydrostatic stress p_2 is applied at the exterior surface at R_2 . The resulting (plane-strain) outward displacement U and radial and tangential stresses are

$$U = \frac{(p_2 R_2^2 - p_1 R_1^2)}{2(\lambda + \mu)(R_2^2 - R_1^2)} r + \frac{(p_2 - p_1) R_1^2 R_2^2}{2\mu(R_2^2 - R_1^2)} \frac{1}{r}$$

$$\sigma_{rr} = \frac{(p_2 R_2^2 - p_1 R_1^2)}{(R_2^2 - R_1^2)} - \frac{(p_2 - p_1) R_1^2 R_2^2}{(R_2^2 - R_1^2)} \frac{1}{r^2}$$

$$\sigma_{\theta\theta} = \frac{(p_2 R_2^2 - p_1 R_1^2)}{(R_2^2 - R_1^2)} + \frac{(p_2 - p_1) R_1^2 R_2^2}{(R_2^2 - R_1^2)} \frac{1}{r^2}$$

where λ and μ are the Lamé coefficient and shear modulus, respectively.

If $R_1 = 0$, we have the case of a **solid cylinder** under external pressure, with displacement and stress denoted by the following:

$$U = \frac{p_2 r}{2(\lambda + \mu)}$$

$$\sigma_{rr} = \sigma_{\theta\theta} = p_2$$

If, instead, $R_2 \rightarrow \infty$, then

$$U = \frac{p_2 r}{2(\lambda + \mu)} + \frac{(p_2 - p_1) R_1^2}{2\mu r}$$

$$\sigma_{rr} = p_2 \left(1 - \frac{R_1^2}{r^2} \right) + \frac{p_1 R_1^2}{r^2}$$

$$\sigma_{\theta\theta} = p_2 \left(1 + \frac{R_1^2}{r^2} \right) - \frac{p_1 R_1^2}{r^2}$$

These results for **plane strain** can be converted to **plane stress** by replacing ν by $\nu/(1 + \nu)$, where ν is the Poisson ratio.

Circular hole with principal stresses at infinity

The circular hole with radius R lies along the z -axis. A principal stress, σ_{xx} , is applied at infinity. The stress solution is then

$$\sigma_{rr} = \frac{\sigma_{xx}}{2} \left(1 - \frac{R^2}{r^2} \right) + \frac{\sigma_{xx}}{2} \left(1 - \frac{4R^2}{r^2} + \frac{3R^4}{r^4} \right) \cos 2\theta$$

$$\sigma_{\theta\theta} = \frac{\sigma_{xx}}{2} \left(1 + \frac{R^2}{r^2} \right) - \frac{\sigma_{xx}}{2} \left(1 + \frac{3R^4}{r^4} \right) \cos 2\theta$$

$$\begin{aligned}\sigma_{r\theta} &= -\frac{\sigma_{xx}}{2} \left(1 + \frac{2R^2}{r^2} - \frac{3R^4}{r^4} \right) \sin 2\theta \\ \frac{8\mu U_r}{R\sigma_{xx}} &= (\chi - 1 + 2 \cos 2\theta) \frac{r}{R} + \frac{2R}{r} \left[1 + \left(\chi + 1 - \frac{R^2}{r^2} \right) \cos 2\theta \right] \\ \frac{8\mu U_\theta}{R\sigma_{xx}} &= \left[-\frac{2r}{R} + \frac{2R}{r} \left(1 - \chi - \frac{R^2}{r^2} \right) \right] \sin 2\theta\end{aligned}$$

where θ is measured from the x -axis, and

$$\begin{aligned}\chi &= 3 - 4\nu, & \text{for plane strain} \\ \chi &= \frac{3 - \nu}{1 + \nu}, & \text{for plane stress}\end{aligned}$$

At the cavity surface, $r = R$,

$$\begin{aligned}\sigma_{rr} &= \sigma_{r\theta} = 0 \\ \sigma_{\theta\theta} &= \sigma_{xx}(1 - 2 \cos 2\theta)\end{aligned}$$

Thus, we see the well-known result that the borehole creates a stress concentration of $\sigma_{\theta\theta} = 3\sigma_{xx}$ at $\theta = 90^\circ$.

Stress concentration around an elliptical hole

If, instead, the borehole is elliptical in cross-section with a shape denoted by (Lawn and Wilshaw, 1975)

$$\frac{x^2}{b^2} + \frac{y^2}{c^2} = 1$$

where b is the semiminor axis and c is the semimajor axis, and the principal stress σ_{xx} is applied at infinity, then the largest stress concentration occurs at the tip of the long axis ($y = c$; $x = 0$). This is the same location at $\theta = 90^\circ$ as for the circular hole. The stress concentration is

$$\sigma_{\theta\theta} = \sigma_{xx}[1 + 2(c/\rho)^{1/2}]$$

where ρ is the radius of curvature at the tip given by

$$\rho = \frac{b^2}{c}$$

When $b \ll c$, the stress concentration is approximately

$$\frac{\sigma_{\theta\theta}}{\sigma_{xx}} \approx \frac{2c}{b} = 2\sqrt{\frac{c}{\rho}}$$

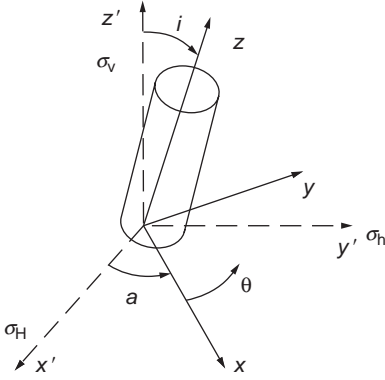


Figure 2.10.1 The coordinate system for the remote stress field around an inclined, cylindrical borehole.

Stress around an inclined cylindrical hole

We now consider the case of a cylindrical borehole of radius R inclined at an angle i to the vertical axis, in a linear, isotropic elastic medium with Poisson ratio ν in a nonhydrostatic remote stress field (Jaeger and Cook, 1969; Bradley, 1979; Fjaer *et al.*, 2008). The borehole coordinate system is denoted by (x, y, z) with the z -axis along the axis of the borehole. The remote principal stresses are denoted by

- σ_v , the vertical stress,
- σ_H , the maximum horizontal stress, and
- σ_h , the minimum horizontal stress

The coordinate system for the remote stress field (shown in Figure 2.10.1) is denoted by (x', y', z') with x' along the direction of the maximum horizontal stress, and z' along the vertical. The angle a represents the azimuth of the borehole x -axis with respect to the x' -axis, while θ is the azimuthal angle around the borehole measured from the x -axis. Assuming plane-strain conditions with no displacements along the z -axis, the stresses as a function of radial distance r and azimuthal angle θ are given by (Fjaer *et al.*, 2008):

$$\begin{aligned}\sigma_{rr} = & \left(\frac{\sigma_{xx}^0 + \sigma_{yy}^0}{2} \right) \left(1 - \frac{R^2}{r^2} \right) + \left(\frac{\sigma_{xx}^0 - \sigma_{yy}^0}{2} \right) \left(1 + 3 \frac{R^4}{r^4} - 4 \frac{R^2}{r^2} \right) \cos 2\theta \\ & + \sigma_{xy}^0 \left(1 + 3 \frac{R^4}{r^4} - 4 \frac{R^2}{r^2} \right) \sin 2\theta + p_w \frac{R^2}{r^2} \\ \sigma_{\theta\theta} = & \left(\frac{\sigma_{xx}^0 + \sigma_{yy}^0}{2} \right) \left(1 + \frac{R^2}{r^2} \right) - \left(\frac{\sigma_{xx}^0 - \sigma_{yy}^0}{2} \right) \left(1 + 3 \frac{R^4}{r^4} \right) \cos 2\theta \\ & - \sigma_{xy}^0 \left(1 + 3 \frac{R^4}{r^4} \right) \sin 2\theta - p_w \frac{R^2}{r^2}\end{aligned}$$

$$\begin{aligned}
\sigma_{zz} &= \sigma_{zz}^0 - \nu \left[2 \left(\sigma_{xx}^0 - \sigma_{yy}^0 \right) \frac{R^2}{r^2} \cos 2\theta + 4 \sigma_{xy}^0 \frac{R^2}{r^2} \sin 2\theta \right] \\
\sigma_{r\theta} &= \left(\frac{\sigma_{yy}^0 - \sigma_{xx}^0}{2} \right) \left(1 - 3 \frac{R^4}{r^4} + 2 \frac{R^2}{r^2} \right) \sin 2\theta + \sigma_{xy}^0 \left(1 - 3 \frac{R^4}{r^4} + 2 \frac{R^2}{r^2} \right) \cos 2\theta \\
\sigma_{\theta z} &= \left(-\sigma_{xz}^0 \sin \theta + \sigma_{yz}^0 \cos \theta \right) \left(1 + \frac{R^2}{r^2} \right) \\
\sigma_{rz} &= \left(\sigma_{xz}^0 \cos \theta + \sigma_{yz}^0 \sin \theta \right) \left(1 - \frac{R^2}{r^2} \right)
\end{aligned}$$

In the above equations p_w represents the well-bore pressure and σ_{ij}^0 is the remote stress tensor expressed in the borehole coordinate system through the usual coordinate transformation (see [Section 1.4](#) on coordinate transformations) involving the direction cosines of the angles between the (x', y', z') axes and the (x, y, z) axes as follows:

$$\begin{aligned}
\sigma_{xx}^0 &= \beta_{xx'}^2 \sigma_H + \beta_{xy'}^2 \sigma_h + \beta_{xz'}^2 \sigma_v \\
\sigma_{yy}^0 &= \beta_{yx'}^2 \sigma_H + \beta_{yy'}^2 \sigma_h + \beta_{yz'}^2 \sigma_v \\
\sigma_{zz}^0 &= \beta_{zx'}^2 \sigma_H + \beta_{zy'}^2 \sigma_h + \beta_{zz'}^2 \sigma_v \\
\sigma_{xy}^0 &= \beta_{xx'} \beta_{yx'} \sigma_H + \beta_{xy'} \beta_{yy'} \sigma_h + \beta_{xz'} \beta_{yz'} \sigma_v \\
\sigma_{yz}^0 &= \beta_{yx'} \beta_{zx'} \sigma_H + \beta_{yy'} \beta_{zy'} \sigma_h + \beta_{yz'} \beta_{zz'} \sigma_v \\
\sigma_{zx}^0 &= \beta_{zx'} \beta_{xx'} \sigma_H + \beta_{zy'} \beta_{xy'} \sigma_h + \beta_{zz'} \beta_{xz'} \sigma_v
\end{aligned}$$

and

$$\begin{aligned}
\beta_{xx'} &= \cos a \cos i, & \beta_{xy'} &= \sin a \cos i, & \beta_{xz'} &= -\sin i \\
\beta_{yx'} &= -\sin a, & \beta_{yy'} &= \cos a, & \beta_{yz'} &= 0 \\
\beta_{zx'} &= \cos a \sin i, & \beta_{zy'} &= \sin a \sin i, & \beta_{zz'} &= \cos i
\end{aligned}$$

Stress around a vertical cylindrical hole in a poroelastic medium

The circular hole with radius R_i lies along the z -axis. Pore pressure, p_f , at the permeable borehole wall equals the pressure in the well bore, p_w . At a remote boundary $R_0 \gg R_i$ the stresses and pore pressure are

$$\begin{aligned}
\sigma_{zz}(R_0) &= \sigma_v \\
\sigma_{rr}(R_0) &= \sigma_{\theta\theta}(R_0) = \sigma_h \\
p_f(R_0) &= p_{f0}
\end{aligned}$$

The stresses as a function of radial distance r from the hole are given by (Risnes *et al.*, 1982; Bratli *et al.*, 1983; Fjaer *et al.*, 2008)

$$\begin{aligned}\sigma_{rr} &= \sigma_h + (\sigma_h - p_w) \frac{R_i^2}{R_0^2 - R_i^2} \left[1 - \left(\frac{R_0}{r} \right)^2 \right] - (p_{f0} - p_w) \frac{1 - 2\nu}{2(1 - \nu)} \\ &\quad \times \alpha \left\{ \frac{R_i^2}{R_0^2 - R_i^2} \left[1 - \left(\frac{R_0}{r} \right)^2 \right] + \frac{\ln(R_0/r)}{\ln(R_0/R_i)} \right\} \\ \sigma_{\theta\theta} &= \sigma_h + (\sigma_h - p_w) \frac{R_i^2}{R_0^2 - R_i^2} \left[1 + \left(\frac{R_0}{r} \right)^2 \right] - (p_{f0} - p_w) \frac{1 - 2\nu}{2(1 - \nu)} \\ &\quad \times \alpha \left\{ \frac{R_i^2}{R_0^2 - R_i^2} \left[1 + \left(\frac{R_0}{r} \right)^2 \right] + \frac{\ln(R_0/r) - 1}{\ln(R_0/R_i)} \right\} \\ \sigma_{zz} &= \sigma_v + 2\nu(\sigma_h - p_w) \frac{R_i^2}{R_0^2 - R_i^2} - (p_{f0} - p_w) \frac{1 - 2\nu}{2(1 - \nu)} \\ &\quad \times \alpha \left[\nu \frac{2R_i^2}{R_0^2 - R_i^2} + \frac{2 \ln(R_0/r) - \nu}{\ln(R_0/R_i)} \right]\end{aligned}$$

where ν is the dry (drained) Poisson ratio of the poroelastic medium, $\alpha = 1 - K_{\text{dry}}/K_0$ is the Biot coefficient, K_{dry} is effective bulk modulus of dry porous solid, and K_0 is the bulk modulus of solid mineral material. In the limit $R_0/R_i \rightarrow \infty$ the expressions simplify to (Fjaer *et al.*, 2008)

$$\begin{aligned}\sigma_{rr} &= \sigma_h - (\sigma_h - p_w) \left(\frac{R_i}{r} \right)^2 + (p_{f0} - p_w) \frac{1 - 2\nu}{2(1 - \nu)} \alpha \left[\left(\frac{R_i}{r} \right)^2 - \frac{\ln(R_0/r)}{\ln(R_0/R_i)} \right] \\ \sigma_{\theta\theta} &= \sigma_h + (\sigma_h - p_w) \left(\frac{R_i}{r} \right)^2 - (p_{f0} - p_w) \frac{1 - 2\nu}{2(1 - \nu)} \alpha \left[\left(\frac{R_i}{r} \right)^2 + \frac{\ln(R_0/r)}{\ln(R_0/R_i)} \right] \\ \sigma_{zz} &= \sigma_v - (p_{f0} - p_w) \frac{1 - 2\nu}{2(1 - \nu)} \alpha \frac{2 \ln(R_0/r) - \nu}{\ln(R_0/R_i)}\end{aligned}$$

Uses

The equations presented in this section can be used for the following:

- estimating the stresses around a borehole resulting from tectonic stresses;
- estimating the stresses and deformation of a borehole caused by changes in borehole fluid pressure.

Assumptions and limitations

The equations presented in this section are based on the following assumptions:

- the material is linear, isotropic, and elastic or poroelastic.

Extensions

More complicated remote stress fields can be constructed by superimposing the solutions for the corresponding principal stresses.

2.11 Mohr's circles

Synopsis

Mohr's circles provide a graphical representation of how the tractions on a plane depend on the angular orientation of the plane within a given stress field. Consider a stress state with principal stresses $\sigma_1 \geq \sigma_2 \geq \sigma_3$ and coordinate axes defined along the corresponding principal directions x_1, x_2, x_3 . The traction vector, \mathbf{T} , acting on a plane with outward unit normal vector, $\mathbf{n} = (n_1, n_2, n_3)$, is given by Cauchy's formula as

$$\mathbf{T} = \boldsymbol{\sigma} \mathbf{n}$$

where $\boldsymbol{\sigma}$ is the stress tensor. The components of \mathbf{n} are the direction cosines of \mathbf{n} relative to the coordinate axes and are denoted by

$$n_1 = \cos \phi, \quad n_2 = \cos \gamma, \quad n_3 = \cos \theta$$

and

$$n_1^2 + n_2^2 + n_3^2 = 1$$

where ϕ, γ , and θ are the angles between \mathbf{n} and the axes x_1, x_2, x_3 (Figure 2.11.1).

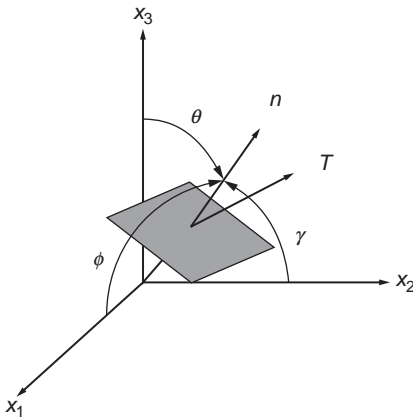


Figure 2.11.1 Angle and vector conventions for Mohr's circles.

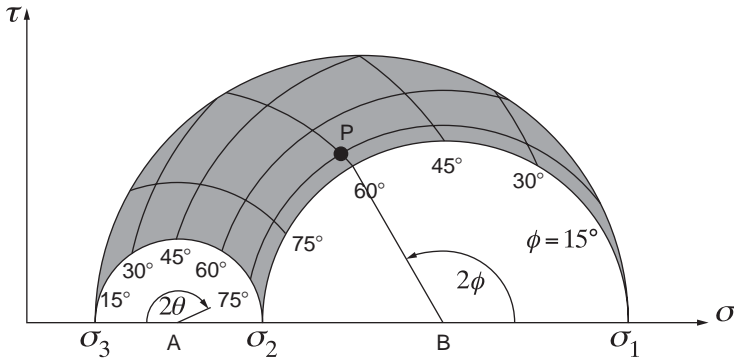


Figure 2.11.2 Three-dimensional Mohr's circle.

The normal component of traction, σ , and the *magnitude* of the shear component, τ , acting on the plane are given by

$$\sigma = n_1^2 \sigma_1 + n_2^2 \sigma_2 + n_3^2 \sigma_3$$

$$\tau^2 = n_1^2 \sigma_1^2 + n_2^2 \sigma_2^2 + n_3^2 \sigma_3^2 - \sigma^2$$

Three-dimensional Mohr's circle

The numerical values of σ and τ can be read graphically from the three-dimensional Mohr's circle shown in Figure 2.11.2. All permissible values of σ and τ must lie in the shaded area.

To determine σ and τ from the orientation of the plane (ϕ , γ , and θ), perform the following procedure.

- (1) Plot $\sigma_1 \geq \sigma_2 \geq \sigma_3$ on the horizontal axis and construct the three circles, as shown. The outer circle is centered at $(\sigma_1 + \sigma_3)/2$ and has radius $(\sigma_1 - \sigma_3)/2$. The left-hand inner circle is centered at $(\sigma_2 + \sigma_3)/2$ and has radius $(\sigma_2 - \sigma_3)/2$. The right-hand inner circle is centered at $(\sigma_1 + \sigma_2)/2$ and has radius $(\sigma_1 - \sigma_2)/2$.
- (2) Mark angles 2θ and 2ϕ on the small circles centered at **A** and **B**. For example, $\phi = 60^\circ$ plots at $2\phi = 120^\circ$ from the horizontal, and $\theta = 75^\circ$ plots at $2\theta = 150^\circ$ from the horizontal, as shown. Be certain to include the factor of 2, and note the different directions defined for the positive angles.
- (3) Draw a circle centered at point **A** that intersects the right-hand small circle at the mark for ϕ .
- (4) Draw another circle centered at point **B** that intersects the left-hand small circle at the point for θ .
- (5) The intersection of the two constructed circles at point **P** gives the values of σ and τ .

Reverse the procedure to determine the orientation of the plane having particular values of σ and τ .

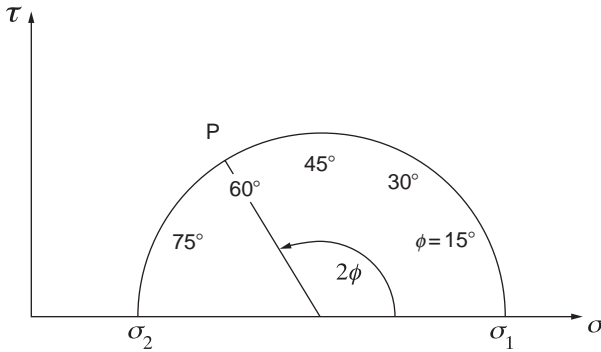


Figure 2.11.3 Two-dimensional Mohr's circle.

Two-dimensional Mohr's circle

When the plane of interest contains one of the principal axes, the tractions on the plane depend only on the two remaining principal stresses, and using Mohr's circle is therefore simplified. For example, when $\theta = 90^\circ$ (i.e., the x_3 -axis lies in the plane of interest), all stress states lie on the circle centered at **B** in Figure 2.11.2. The stresses then depend only on σ_1 and σ_2 and on the angle ϕ , and we need only draw the single circle, as shown in Figure 2.11.3.

Uses

Mohr's circle is used for graphical determination of normal and shear tractions acting on a plane of arbitrary orientation relative to the principal stresses.

2.12 Static and dynamic moduli

In a uniaxial stress experiment (Figure 2.12.1), Young's modulus E is defined as the ratio of the axial stress σ to the axial strain ε_a , while Poisson's ratio ν is defined as the (negative) ratio of the radial strain ε_r to the axial strain:

$$E = \frac{\sigma}{\varepsilon_a}, \quad \nu = -\frac{\varepsilon_r}{\varepsilon_a}$$

It follows from these definitions that Poisson's ratio is zero if the sample does not expand radially during axial loading and Poisson's ratio is 0.5 if the radial strain is half the axial strain, which is the case for fluids and incompressible solids. Poisson's ratio must lie within the range $-1 < \nu \leq 0.5$.

The speeds of elastic waves in the solid are linked to the elastic moduli and the bulk density ρ by the wave equation. The corresponding expressions for Poisson's ratio and Young's modulus are:

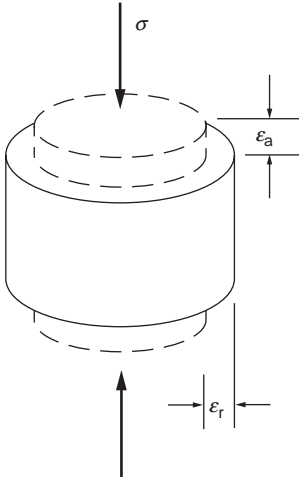


Figure 2.12.1 Uniaxial loading experiment. Dashed lines show undeformed sample, and solid lines show deformed sample.

$$v = \frac{1}{2} \frac{(V_P/V_S)^2 - 2}{(V_P/V_S)^2 - 1}, \quad E = 2\rho V_S^2(1 + v)$$

where V_P and V_S are the P- and S-wave velocities, respectively. The elastic moduli calculated from the elastic-wave velocities and density are the **dynamic moduli**. In contrast, the elastic moduli calculated from deformational experiments, such as the one shown in [Figure 2.12.1](#), are the **static moduli**.

In most cases the static moduli are different from the dynamic moduli for the same sample of rock. There are several reasons for this. One is that stress–strain relations for rocks are often nonlinear. As a result, the ratio of stress to strain over a large-strain measurement is different from the ratio of stress to strain over a very small-strain measurement. Another reason is that rocks are often inelastic, affected, for example, by frictional sliding across microcracks and grain boundaries. More internal deformation can occur over a large-strain experiment than over very small-strain cycles. The strain magnitude relevant to geomechanical processes, such as hydrofracturing, is of the order of 10^{-2} , while the strain magnitude due to elastic-wave propagation is of the order of 10^{-7} or less. This large strain difference affects the difference between the static and dynamic moduli.

Relations between the dynamic and static moduli are not simple and universal because:

- (a) the elastic-wave velocity in a sample and the resulting dynamic elastic moduli depend on the conditions of the measurement, specifically on the effective pressure and pore fluid; and
- (b) the static moduli depend on details of the loading experiment. Even for the same type of experiment – axial loading – the static Young’s modulus may be strongly

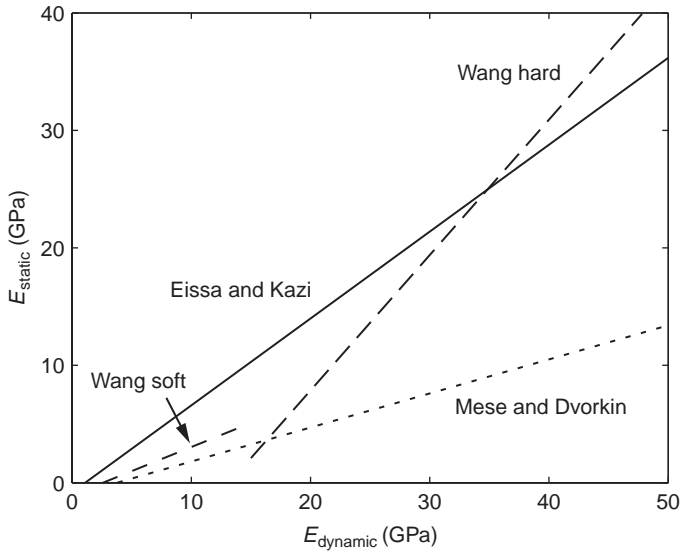


Figure 2.12.2 Comparison of selected relations between dynamic and static Young's moduli.

affected by the overall pressure applied to the sample, as well as by the axial deformation magnitude.

Some results have been reviewed by Schön (1996) and Wang and Nur (2000). Presented below and in Figure 2.12.2 are some of their equations, where the moduli are in GPa and the impedance is in km/s g/cc. In all the examples, E_{stat} is the static Young's modulus and E_{dyn} is the dynamic Young's modulus.

Data on microcline-granite, by Belikov *et al.* (1970):

$$E_{\text{stat}} = 1.137E_{\text{dyn}} - 9.685$$

Igneous and metamorphic rocks from the Canadian Shield, by King (1983):

$$E_{\text{stat}} = 1.263E_{\text{dyn}} - 29.5$$

Granites and Jurassic sediments in the UK, by McCann and Entwisle (1992):

$$E_{\text{stat}} = 0.69E_{\text{dyn}} + 6.4$$

A wide range of rock types, by Eissa and Kazi (1988):

$$E_{\text{stat}} = 0.74E_{\text{dyn}} - 0.82$$

Shallow soil samples, by Gorjainov and Ljachowickij (1979) for clay:

$$E_{\text{stat}} = 0.033E_{\text{dyn}} + 0.0065$$

and for sandy, wet soil:

$$E_{\text{stat}} = 0.061E_{\text{dyn}} + 0.00285$$

Table 2.12.1 Empirical relations between static and dynamic bulk moduli in dry tight sandstones from the Travis Peak formation.

Pressure (MPa)	$K_{\text{stat}} = a + bK_{\text{dyn}}$ (GPa)	
	a (GPa)	b
5	0.98	0.490
20	3.16	0.567
40	1.85	0.822
125	-1.85	1.13

Wang and Nur (2000) for soft rocks (defined as rocks with the static Young's modulus < 15 GPa):

$$E_{\text{stat}} = 0.41E_{\text{dyn}} - 1.06$$

Wang and Nur (2000) for hard rocks (defined as rocks with the static Young's modulus > 15 GPa):

$$E_{\text{stat}} = 1.153E_{\text{dyn}} - 15.2$$

Mese and Dvorkin (2000) related the static Young's modulus and static Poisson's ratio (ν_{stat}) to the dynamic shear modulus calculated from the shear-wave velocity in shales and shaley sands:

$$E_{\text{stat}} = 0.59\mu_{\text{dyn}} - 0.34, \quad \nu_{\text{stat}} = -0.0208\mu_{\text{dyn}} + 0.37$$

where μ_{dyn} is the dynamic shear modulus $\mu_{\text{dyn}} = \rho V_S^2$.

The same data were used to obtain relations between the static moduli and the dynamic S-wave impedance, $I_{S\text{-dyn}}$:

$$E_{\text{stat}} = 1.99I_{S\text{-dyn}} - 3.84, \quad \nu_{\text{stat}} = -0.07I_{S\text{-dyn}} + 0.5$$

as well as between the static moduli and the dynamic Young's modulus:

$$E_{\text{stat}} = 0.29E_{\text{dyn}} - 1.1, \quad \nu_{\text{stat}} = -0.00743E_{\text{dyn}} + 0.34$$

Jizba (1991) compared the static bulk modulus, K_{stat} and the dynamic bulk modulus, K_{dyn} , and found the following empirical relations as a function of confining pressure in dry tight sandstones from the Travis Peak formation (Table 2.12.1).

Assumptions and limitations

There are only a handful of well-documented experimental data where large-strain deformational experiments have been conducted with simultaneous measurement of the dynamic P- and S-wave velocity. One of the main uncertainties in applying

laboratory static moduli data *in situ* comes from the fact that the *in-situ* loading conditions are often unknown. Moreover, in most cases, the *in-situ* conditions are so complex that they are virtually impossible to reproduce in the laboratory. In most cases, static data exhibit a *strongly nonlinear stress dependence*, so that it is never clear which data point to use as the static modulus at *in-situ* conditions. Because of the strongly nonlinear dependence of static moduli on the strain magnitude, the isotropic linear elasticity equations that relate various elastic moduli to each other might not be applicable to static moduli.

Finally, this section refers only to isotropic descriptions of static and dynamic moduli.

3 Seismic wave propagation

3.1 Seismic velocities

Synopsis

The velocities of various types of seismic waves in homogeneous, isotropic, elastic media are given by

$$V_P = \sqrt{\frac{K + \frac{4}{3}\mu}{\rho}} = \sqrt{\frac{\lambda + 2\mu}{\rho}}$$

$$V_S = \sqrt{\frac{\mu}{\rho}}$$

$$V_E = \sqrt{\frac{E}{\rho}}$$

where V_P is the P-wave velocity, V_S is the S-wave velocity, and V_E is the extensional wave velocity in a narrow bar.

In addition, ρ is the density, K is the bulk modulus, μ is the shear modulus, λ is Lamé's coefficient, E is Young's modulus, and ν is Poisson's ratio.

In terms of Poisson's ratio one can also write

$$\frac{V_P^2}{V_S^2} = \frac{2(1 - \nu)}{(1 - 2\nu)}$$

$$\frac{V_E^2}{V_P^2} = \frac{(1 + \nu)(1 - 2\nu)}{(1 - \nu)}$$

$$\frac{V_E^2}{V_S^2} = 2(1 + \nu)$$

$$\nu = \frac{V_P^2 - 2V_S^2}{2(V_P^2 - V_S^2)} = \frac{V_E^2 - 2V_S^2}{2V_S^2}$$

The various wave velocities are related by

$$\frac{V_P^2}{V_S^2} = \frac{4 - V_E^2/V_S^2}{3 - V_E^2/V_S^2}$$

$$\frac{V_E^2}{V_S^2} = \frac{3V_P^2/V_S^2 - 4}{V_P^2/V_S^2 - 1}$$

The elastic moduli can be extracted from measurements of density and any two wave velocities. For example,

$$\mu = \rho V_S^2$$

$$K = \rho(V_P^2 - \frac{4}{3}V_S^2)$$

$$E = \rho V_E^2$$

$$\nu = \frac{V_P^2 - 2V_S^2}{2(V_P^2 - V_S^2)}$$

The **Rayleigh wave** phase velocity V_R at the surface of an isotropic homogeneous elastic half-space is given by the solution to the equation (White, 1983)

$$\left(2 - \frac{V_R^2}{V_S^2}\right)^2 - 4\left(1 - \frac{V_R^2}{V_P^2}\right)^{1/2} \left(1 - \frac{V_R^2}{V_S^2}\right)^{1/2} = 0$$

(Note that the equivalent equation given in Bourbié *et al.* (1987) is in error.) The wave speed is plotted in Figure 3.1.1 and is given by

$$\frac{V_R^2}{V_S^2} = \left[-\frac{q}{2} + \left(\frac{q^2}{4} + \frac{p^3}{27}\right)^{1/2}\right]^{1/3} + \left[-\frac{q}{2} - \left(\frac{q^2}{4} + \frac{p^3}{27}\right)^{1/2}\right]^{1/3} + \frac{8}{3}$$

$$\text{for } \left(\frac{q^2}{4} + \frac{p^3}{27}\right) > 0$$

$$\frac{V_R^2}{V_S^2} = -2\left(\frac{-p}{3}\right)^{1/2} \cos\left[\frac{\pi - \cos^{-1}(-27q^2/4p^3)^{1/2}}{3}\right] + \frac{8}{3}$$

$$\text{for } \left(\frac{q^2}{4} + \frac{p^3}{27}\right) < 0$$

$$p = \frac{8}{3} - \frac{16V_S^2}{V_P^2}; \quad q = \frac{272}{27} - \frac{80V_S^2}{3V_P^2}$$

The Rayleigh velocity at the surface of a homogeneous elastic half-space is non-dispersive (i.e., independent of frequency).

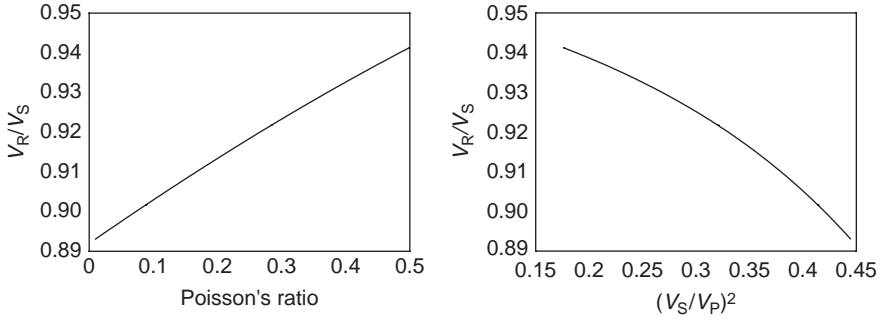


Figure 3.1.1 Rayleigh wave phase velocity normalized by shear velocity.

Assumptions and limitations

These equations assume isotropic, linear, elastic media.

3.2 Phase, group, and energy velocities

Synopsis

In the physics of wave propagation we often talk about different velocities (the **phase**, **group**, and **energy** velocities: V_p , V_g , and V_e , respectively) associated with the wave phenomenon. In laboratory measurements of core sample velocities using finite bandwidth signals and finite-sized transducers, the velocity given by the first arrival does not always correspond to an easily identified velocity.

A general time-harmonic wave may be defined as

$$U(\mathbf{x}, t) = U_0(\mathbf{x}) \cos[\omega t - p(\mathbf{x})]$$

where ω is the angular frequency and U_0 and p are functions of position \mathbf{x} ; U can be any field of interest such as pressure, stress, or electromagnetic fields. The surfaces given by $p(\mathbf{x}) = \text{constant}$ are called cophasal or wave surfaces. In particular, for plane waves, $p(\mathbf{x}) = \mathbf{k} \cdot \mathbf{x}$, where \mathbf{k} is the wave vector, or the propagation vector, and is in the direction of propagation. For the phase to be the same at (\mathbf{x}, t) and $(\mathbf{x} + d\mathbf{x}, t + dt)$ we must have

$$\omega dt - (\text{grad } p) \cdot d\mathbf{x} = 0$$

from which the **phase velocity** is defined as

$$V_p = \frac{\omega}{|\text{grad } p|}$$

For *plane waves* $\text{grad } p = \mathbf{k}$, and hence $V_p = \omega/k$. The reciprocal of the phase velocity is often called the **slowness**, and a polar plot of slowness versus the direction of propagation is termed the slowness surface. Phase velocity is the speed of advance

of the cophasal surfaces. Born and Wolf (1980) consider the phase velocity to be devoid of any physical significance because it does not correspond to the velocity of propagation of any signal and cannot be directly determined experimentally.

Waves encountered in rock physics are rarely perfectly monochromatic but instead have a finite bandwidth, $\Delta\omega$, centered around some mean frequency $\bar{\omega}$. The wave may be regarded as a superposition of monochromatic waves of different frequencies, which then gives rise to the concept of wave packets or wave groups. Wave packets, or modulation on a wave containing a finite band of frequencies, propagate with the **group velocity** defined as

$$V_g = \frac{1}{|\text{grad}(\partial p / \partial \omega)_{\bar{\omega}}|}$$

which for plane waves becomes

$$V_g = \left(\frac{\partial \omega}{\partial k} \right)_{\bar{\omega}}$$

The group velocity may be considered to be the velocity of propagation of the envelope of a modulated carrier wave. The group velocity can also be expressed in various equivalent ways as

$$V_g = V_p - \lambda \frac{dV_p}{d\lambda}$$

$$V_g = V_p + k \frac{dV_p}{dk}$$

or

$$\frac{1}{V_g} = \frac{1}{V_p} - \frac{\omega}{V_p^2} \frac{dV_p}{d\omega}$$

where λ is the wavelength. These equations show that the group velocity is different from the phase velocity when the phase velocity is *frequency dependent*, *direction dependent*, or both. When the phase velocity is frequency dependent (and hence different from the group velocity), the medium is said to be **dispersive**. Dispersion is termed *normal* if the group velocity decreases with frequency and *anomalous* or *inverse* if it increases with frequency (Elmore and Heald, 1985; Bourbié *et al.*, 1987). In elastic, isotropic media, dispersion can arise as a result of geometric effects such as propagation along waveguides. As a rule such geometric dispersion (Rayleigh waves, waveguides) is *normal* (i.e., the group velocity decreases with frequency). In a homogeneous viscoelastic medium, on the other hand, dispersion is *anomalous* or *inverse* and arises owing to intrinsic dissipation.

The **energy velocity** V_e represents the velocity at which energy propagates and may be defined as

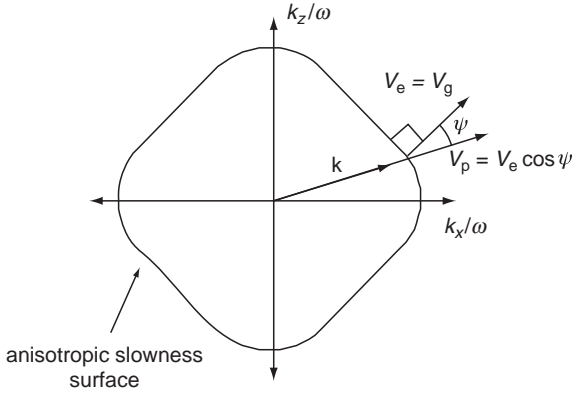


Figure 3.2.1 In anisotropic media, energy propagates along V_e , which is always normal to the slowness surface and in general is deflected by the angle ψ away from V_p and the wave vector \mathbf{k} .

$$V_e = \frac{P_{av}}{E_{av}}$$

where P_{av} is the average power flow density and E_{av} is the average total energy density.

In *isotropic, homogeneous, elastic media* all three velocities are the same. In a *lossless homogeneous* medium (of arbitrary symmetry), V_g and V_e are identical, and energy propagates with the group velocity. In this case the energy velocity may be obtained from the group velocity, which is usually somewhat easier to compute. If the medium is not strongly dispersive and a wave group can travel a measurable distance without appreciable “smearing” out, the group velocity *may* be considered to represent the velocity at which the energy is propagated (though this is not strictly true in general).

In *anisotropic, homogeneous, elastic media*, the phase velocity, in general, differs from the group velocity (which is equal to the energy velocity because the medium is elastic) except along certain symmetry directions, where they coincide. The direction in which V_e is deflected away from \mathbf{k} (which is also the direction of V_p) is obtained from the slowness surface (shown in Figure 3.2.1), for $V_e (= V_g$ in elastic media) must always be normal to the slowness surface (Auld, 1990).

The group velocity in anisotropic media may be calculated by differentiation of the dispersion relation obtained in an implicit form from the Christoffel equation given by

$$|\mathbf{k}^2 c_{ijkl} n_j n_l - \rho \omega^2 \delta_{ik}| = \Phi(\omega, k_x, k_y, k_z) = 0$$

where c_{ijkl} is the stiffness tensor, n_i are the direction cosines of \mathbf{k} , ρ is the density, and δ_{ij} is the Kronecker delta function. The group velocity is then evaluated as

$$V_g = - \frac{\nabla_k \Phi}{\partial \Phi / \partial \omega}$$

where the gradient is with respect to k_x , k_y , and k_z .

The concept of group velocity is not strictly applicable to attenuating viscoelastic media, but the energy velocity is still well defined (White, 1983). The energy propagation velocity in a dissipative medium is neither the group velocity nor the phase velocity *except* when

- (1) the medium is infinite, homogeneous, linear, and viscoelastic, and
- (2) the wave is monochromatic and homogeneous, i.e., planes of equal phase are parallel to planes of equal amplitude, or, in other words, the real and imaginary parts of the complex wave vector point in the same direction (in general they do not), in which case the energy velocity is equal to the phase velocity (Ben-Menahem and Singh, 1981; Bourbié *et al.*, 1987).

For the special case of a Voigt solid (see Section 3.8 on viscoelasticity) the energy transport velocity is equal to the phase velocity at all frequencies. For wave propagation in dispersive, viscoelastic media, one sometimes defines the limit

$$V_{\infty} = \lim_{\omega \rightarrow \infty} V_p(\omega)$$

which describes the propagation of a well-defined wavefront and is referred to as the **signal velocity** (Beltzer, 1988).

Sometimes it is not clear which velocities are represented by the recorded travel times in laboratory ultrasonic core sample measurements, especially when the sample is anisotropic. For elastic materials, there is no ambiguity for propagation along symmetry directions because the phase and group velocities are identical. For non-symmetry directions, the energy does not necessarily propagate straight up the axis of the core from the transducer to the receiver. Numerical modeling of laboratory experiments (Dellinger and Vernik, 1992) indicates that, for typical transducer widths (10 mm), the recorded travel times correspond closely to the *phase velocity*. Accurate measurement of group velocity along nonsymmetry directions would essentially require point transducers of less than 2 mm width.

According to Bourbié *et al.* (1987), the velocity measured by a resonant-bar standing-wave technique corresponds to the phase velocity.

Assumptions and limitations

In general, phase, group, and energy velocities may differ from each other in both magnitude and direction. Under certain conditions two or more of them may become identical. For homogeneous, linear, isotropic, elastic media all three are the same.

3.3 NMO in isotropic and anisotropic media

Synopsis

The two-way seismic travel time, t , of a pure (nonconverted) mode from the surface, through a homogeneous, isotropic, elastic layer, to a horizontal reflector is hyperbolic

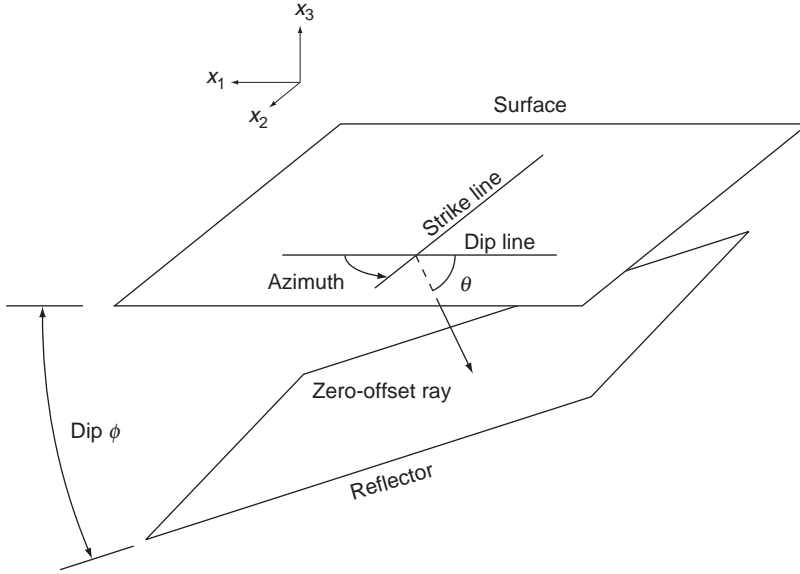


Figure 3.3.1 Schematic showing the geometry for NMO with a dipping reflector.

$$t^2 = t_0^2 + \frac{x^2}{V^2}$$

where x is the *offset* between the source and the receiver, t_0 is the zero-offset, two-way travel time, and V is the velocity of the layer. The increase in travel time with distance, specifically the extra travel time relative to t_0 , is called **normal moveout** (or NMO), and the velocity that determines the NMO, is called the **NMO velocity**, V_{NMO} . In the case of a homogeneous layer above a horizontal reflector, $V_{\text{NMO}} = V$.

When the reflector is dipping with angle ϕ from the horizontal (Figure 3.3.1), the travel time equation in the vertical plane along dip becomes (Levin, 1971)

$$t^2 = t_0^2 + \frac{x^2}{(V/\cos \phi)^2}$$

or $V_{\text{NMO}}(\phi) = V/\cos \phi$. Again, t_0 is the zero-offset, two-way travel time. More generally, the azimuthally varying NMO velocity is (Levin, 1971)

$$V_{\text{NMO}}^2(\zeta, \phi) = \frac{V^2}{1 - \cos^2 \zeta \sin^2 \phi}$$

where ϕ is the reflector dip and ζ is the azimuth relative to a horizontal axis in the dip direction. Note that in the strike direction $V_{\text{NMO}} = V$.

When the Earth consists of horizontal, homogeneous, isotropic layers down to the reflector, the two-way travel time equation is approximately hyperbolic, with the approximation being best for small offsets:

$$t^2 \approx t_0^2 + \frac{x^2}{V_{\text{NMO}}^2}$$

At zero dip, the NMO velocity is often approximated as the **root mean squared (RMS) velocity**, $V_{\text{NMO}} \approx V_{\text{RMS}}$, where

$$V_{\text{RMS}}^2 = \sum_{i=1}^N V_i^2 t_i / \sum_{i=1}^N t_i$$

where V_i is the velocity of the i th layer and t_i is the two-way, zero-offset travel time of the i th layer. The summations are over all layers from the surface to the reflector. The approximation $V_{\text{NMO}} \approx V_{\text{RMS}}$ is best at offsets that are small relative to the reflector depth.

If the NMO velocity is estimated at two horizontal reflectors (e.g., $V_{\text{NMO}-(n)}$ at the base of layer n and $V_{\text{NMO}-(n-1)}$ at the base of layer $(n-1)$), then the RMS equation can be inverted to yield the **Dix equation** (Dix, 1955) for the **interval velocity**, V_n , of the n th layer:

$$V_n^2 \approx \frac{1}{t_n} \left(V_{\text{NMO}-(n)}^2 \sum_{i=1}^n t_i - V_{\text{NMO}-(n-1)}^2 \sum_{i=1}^{n-1} t_i \right)$$

It is important to remember that this model assumes: (1) flat, homogeneous, isotropic layers; (2) the offsets are small enough for the RMS velocity to be a reasonable estimate of the moveout velocity; and (3) the estimated interval velocities are themselves averages over velocities of thinner layers lying below the resolution of the seismic data.

The equivalent of the Dix equation for anisotropic media is shown below.

NMO in an anisotropic Earth

For a heterogeneous elastic Earth with arbitrary anisotropy and arbitrary dip, the NMO velocity of pure modes (at offsets generally less than the depth) can be written as (Grechka and Tsvankin, 1998; Tsvankin, 2001)

$$\frac{1}{V_{\text{NMO}}^2(\zeta)} = W_{11} \cos^2 \zeta + 2W_{12} \sin \zeta \cos \zeta + W_{22} \sin^2 \zeta$$

where ζ is the azimuth relative to the x_1 -axis. The components W_{ij} are elements of a symmetric matrix $\tilde{\mathbf{W}}$ and are defined as $W_{ij} = \tau_0 (\partial p_i / \partial x_j)$, where $p_i = \partial \tau / \partial x_i$ are horizontal components of the slowness vector for rays between the zero-offset reflection point and the surface location $[x_i, x_j]$, $\tau(x_1, x_2)$ is the one-way travel time

from the zero-offset reflection point, and τ_0 is the one-way travel time to the CMP (common midpoint) location $x_1 = x_2 = 0$. The derivatives are evaluated at the CMP location. This result assumes a sufficiently smooth reflector and sufficiently smooth lateral velocity heterogeneity, such that the travel time field exists (e.g., no shadow zones) at the CMP point and the derivatives can be evaluated. This can be rewritten as

$$\frac{1}{V_{\text{NMO}}^2(\zeta)} = \lambda_1 \cos^2(\zeta - \psi) + \lambda_2 \sin^2(\zeta - \psi)$$

where λ_1 and λ_2 are the eigenvalues of $\tilde{\mathbf{W}}$, and ψ is the rotation of the eigenvectors of $\tilde{\mathbf{W}}$ relative to the coordinate system. λ_1 and λ_2 are typically positive, in which case $V_{\text{NMO}}(\zeta)$ is an ellipse in the horizontal plane. The elliptical form allows the exact expression for $V_{\text{NMO}}(\zeta)$ to be determined by only three parameters, the values of the NMO velocity at the axes of the ellipse, and the orientation of the ellipse relative to the coordinate axes. The elliptical form simplifies modeling of azimuthally varying NMO for various geometries and anisotropies, since only $V_{\text{NMO}}(\zeta)$ along the ellipse axes needs to be derived. For example, we can write

$$\frac{1}{V_{\text{NMO}}^2(\zeta)} = \frac{\cos^2 \zeta}{V_{\text{NMO}}^2(\zeta = 0)} + \frac{\sin^2 \zeta}{V_{\text{NMO}}^2(\zeta = \pi/2)}$$

where the axes of the ellipse are at $\zeta = 0$ and $\zeta = \pi/2$.

A simple example of the elliptical form is the azimuthally varying moveout velocity for a homogeneous, isotropic layer above a dipping reflector, given above, which can be written as (Grechka and Tsvankin, 1998)

$$\frac{1}{V_{\text{NMO}}^2(\zeta, \phi)} = \frac{\sin^2 \zeta}{V^2} + \frac{\cos^2 \zeta}{(V/\cos \phi)^2}$$

where ϕ is the dip and ζ is the azimuth relative to a horizontal axis in the dip direction.

VTI symmetry with horizontal reflector

NMO velocities in a **VTI medium** (vertical symmetry axis) overlying a horizontal reflector are given for P, SV, and SH modes (Tsvankin, 2001) by

$$V_{\text{NMO,P}}(0) = V_{\text{P0}} \sqrt{1 + 2\delta}$$

$$V_{\text{NMO,SV}}(0) = V_{\text{S0}} \sqrt{1 + 2\sigma}; \quad \sigma = \left(\frac{V_{\text{P0}}}{V_{\text{S0}}} \right)^2 (\varepsilon - \delta)$$

$$V_{\text{NMO,SH}}(0) = V_{\text{S0}} \sqrt{1 + 2\gamma}$$

where V_{P0} and V_{S0} are the vertical P- and S-wave velocities, and ε , δ , and γ are the Thomsen parameters for VTI media. In this case, the NMO ellipse is a circle, giving

an azimuthally independent NMO velocity. These expressions for NMO velocity hold for anisotropy of arbitrary strength (Tsvankin, 2001).

In the special case of **elliptical anisotropy**, with vertical symmetry axis, $\varepsilon = \delta$, the expressions for NMO velocity become (Tsvankin, 2001):

$$V_{\text{NMO,P}}(0) = V_{\text{P0}}\sqrt{1 + 2\varepsilon}$$

$$V_{\text{NMO,SV}}(0) = V_{\text{S0}}$$

$$V_{\text{NMO,SH}}(0) = V_{\text{S0}}\sqrt{1 + 2\gamma}$$

Vertical symmetry axis with dipping reflector

A dipping reflector creates an azimuthal dependence for the NMO velocity, even with a VTI medium. For general VTI symmetry (vertical symmetry axis) and assuming weak anisotropy, the NMO velocities overlying a dipping reflector are given for P and SV modes by Tsvankin (2001). In the dip direction,

$$V_{\text{NMO,P}}(0, \phi) = \frac{V_{\text{P0}}(1 + \delta)}{\cos \phi} [1 + \delta \sin^2 \phi + 3(\varepsilon - \delta) \sin^2 \phi (2 - \sin^2 \phi)]$$

$$V_{\text{NMO,SV}}(0, \phi) = \frac{V_{\text{S0}}(1 + \sigma)}{\cos \phi} [1 - 5\sigma \sin^2 \phi + 3\sigma \sin^4 \phi]; \quad \sigma = \left(\frac{V_{\text{P0}}}{V_{\text{S0}}}\right)^2 (\varepsilon - \delta)$$

where ϕ is the dip, V_{P0} and V_{S0} are the vertical P- and S-wave velocities, and ε , δ , and γ are the Thomsen parameters for VTI media. In the strike direction with VTI symmetry:

$$V_{\text{NMO,P}}\left(\frac{\pi}{2}, \phi\right) = V_{\text{P0}}(1 + \delta) [1 + (\varepsilon - \delta) \sin^2 \phi (2 - \sin^2 \phi)]$$

$$V_{\text{NMO,SV}}\left(\frac{\pi}{2}, \phi\right) = V_{\text{S0}}(1 + \sigma) [1 - \sigma \sin^2 \phi (2 - \sin^2 \phi)]; \quad \sigma = \left(\frac{V_{\text{P0}}}{V_{\text{S0}}}\right)^2 (\varepsilon - \delta)$$

The complete azimuthal dependence can be easily written as an ellipse, where the strike and dip NMO velocities are the semiaxes.

For the special case of **elliptical symmetry** ($\varepsilon = \delta$) of arbitrary strength anisotropy, the dip-direction NMO velocities are (Tsvankin, 2001):

$$V_{\text{NMO,P}}(0, \phi) = \frac{V_{\text{P0}}\sqrt{1 + 2\varepsilon}}{\cos \phi} \sqrt{1 + 2\varepsilon \sin^2 \phi}$$

$$V_{\text{NMO,SV}}(0, \phi) = \frac{V_{\text{S0}}}{\cos \phi}$$

$$V_{\text{NMO,SH}}(0, \phi) = \frac{V_{\text{S0}}\sqrt{1 + 2\gamma}}{\cos \phi} \sqrt{1 + 2\gamma \sin^2 \phi}$$

where ϕ is the layer dip angle. In the strike direction,

$$V_{\text{NMO,P}}\left(\frac{\pi}{2}, \phi\right) = V_{\text{P0}}\sqrt{1 + 2\varepsilon}$$

$$V_{\text{NMO,SV}}\left(\frac{\pi}{2}, \phi\right) = V_{\text{S0}}$$

$$V_{\text{NMO,SH}}\left(\frac{\pi}{2}, \phi\right) = V_{\text{S0}}\sqrt{1 + 2\gamma}$$

Tilted TI symmetry with dipping reflector

For TI symmetry with symmetry axis tilting an angle ν from the vertical and assuming weak anisotropy, the NMO velocities are given by Tsvankin (2001). In the dip direction

$$\begin{aligned} V_{\text{NMO,P}}(0, \phi) &= \frac{V_{\text{P0}}}{\cos \phi} \left\{ 1 + \delta + \delta \sin^2(\phi - \nu) + 3(\varepsilon - \delta) \sin^2(\phi - \nu) [2 - \sin^2(\phi - \nu)] \right. \\ &\quad \left. + \frac{2 \sin \nu \sin(\phi - \nu)}{\cos \phi} [\delta + 2(\varepsilon - \delta) \sin^2(\phi - \nu)] \right\} \\ V_{\text{NMO,SV}}(0, \phi) &= \frac{V_{\text{S0}}}{\cos \phi} \left\{ 1 + \sigma + \sigma \sin^2(\phi - \nu) - 3\sigma \sin^2(\phi - \nu) [2 - \sin^2(\phi - \nu)] \right. \\ &\quad \left. + 2\sigma \frac{\sin \nu \sin(\phi - \nu) \cos 2(\phi - \nu)}{\cos \phi} \right\} \end{aligned}$$

where ϕ is the reflector dip, V_{P0} and V_{S0} are the symmetry axis P- and S-wave velocities, and ε , δ , and γ are the Thomsen parameters for TI media. It is assumed that the azimuth of the symmetry axis tilt is the same as the azimuth of the reflector dip. In the strike direction, for weak tilted TI symmetry

$$\begin{aligned} V_{\text{NMO,P}}\left(\frac{\pi}{2}, \phi\right) &= V_{\text{P0}}(1 + \delta) \{ 1 + (\varepsilon - \delta) \sin^2(\phi - \nu) [2 - \sin^2(\phi - \nu)] \} \\ V_{\text{NMO,SV}}\left(\frac{\pi}{2}, \phi\right) &= V_{\text{S0}}(1 + \sigma) \{ 1 - \sigma \sin^2(\phi - \nu) [2 - \sin^2(\phi - \nu)] \} \\ \sigma &= \left(\frac{V_{\text{P0}}}{V_{\text{S0}}} \right)^2 (\varepsilon - \delta) \end{aligned}$$

In the special case of **tilted elliptical symmetry** with a tilted symmetry axis, the NMO velocity in the dip direction is

$$\begin{aligned} V_{\text{NMO,P}}(0, \phi) &= \frac{V_{\text{P0}}}{\cos \phi} \sqrt{1 + 2\delta} \sqrt{1 + 2\delta \sin^2(\phi - \nu)} \left[1 - 2\delta \frac{\sin \nu \sin(\phi - \nu)}{\cos \phi} \right]^{-1} \\ V_{\text{NMO,SV}}(\phi) &= \frac{V_{\text{S0}}}{\cos \phi} \\ V_{\text{NMO,SH}}(0, \phi) &= \frac{V_{\text{S0}}}{\cos \phi} \sqrt{1 + 2\gamma} \sqrt{1 + 2\gamma \sin^2(\phi - \nu)} \left[1 - 2\gamma \frac{\sin \nu \sin(\phi - \nu)}{\cos \phi} \right]^{-1} \end{aligned}$$

In the strike direction for **tilted elliptical symmetry**

$$V_{\text{NMO,P}}\left(\frac{\pi}{2}, \phi\right) = V_{\text{P0}}(1 + \delta)$$

$$V_{\text{NMO,SV}}\left(\frac{\pi}{2}, \phi\right) = V_{\text{S0}}$$

Orthorhombic symmetry with horizontal reflector

We now consider an orthorhombic layer of arbitrary strength anisotropy over a horizontal reflector. A symmetry plane of the orthorhombic medium is also horizontal. The vertically propagating (along the x_3 -axis) P-wave velocity (V_{P0}) and vertically propagating S-wave velocities, polarized in the x_1 (V_{S0}) and x_2 (V_{S1}) directions are

$$V_{\text{P0}} = \sqrt{c_{33}/\rho}; \quad V_{\text{S0}} = \sqrt{c_{55}/\rho}; \quad V_{\text{S1}} = \sqrt{c_{44}/\rho}$$

where ρ is the density. Additional constants necessary for this discussion are

$$\varepsilon^{(2)} = \frac{c_{11} - c_{33}}{2c_{33}}$$

$$\varepsilon^{(1)} = \frac{c_{22} - c_{33}}{2c_{33}}$$

$$\delta^{(2)} = \frac{(c_{13} + c_{55})^2 - (c_{33} - c_{55})^2}{2c_{33}(c_{33} - c_{55})}$$

$$\delta^{(1)} = \frac{(c_{23} + c_{44})^2 - (c_{33} - c_{44})^2}{2c_{33}(c_{33} - c_{44})}$$

$$\gamma^{(2)} = \frac{c_{66} - c_{44}}{2c_{44}}$$

$$\gamma^{(1)} = \frac{c_{66} - c_{55}}{2c_{55}}$$

$$\sigma^{(2)} = \left(\frac{V_{\text{P0}}}{V_{\text{S0}}}\right)^2 [\varepsilon^{(2)} - \delta^{(2)}]$$

$$\sigma^{(1)} = \left(\frac{V_{\text{P0}}}{V_{\text{S1}}}\right)^2 [\varepsilon^{(1)} - \delta^{(1)}]$$

For a CMP line in the x_1 direction, the NMO velocities are

$$V_{\text{NMO,P}}(\zeta = 0, \phi = 0) = V_{\text{P0}}\sqrt{1 + 2\delta^{(2)}}$$

$$V_{\text{NMO,SV}}(\zeta = 0, \phi = 0) = V_{\text{S0}}\sqrt{1 + 2\sigma^{(2)}}$$

$$V_{\text{NMO,SH}}(\zeta = 0, \phi = 0) = V_{\text{S1}}\sqrt{1 + 2\gamma^{(2)}}$$

where ϕ is the dip and ζ is the azimuth measured from the x_1 -axis. For a line in the x_2 direction,

$$V_{\text{NMO,P}}\left(\zeta = \frac{\pi}{2}, \phi = 0\right) = V_{\text{P0}}\sqrt{1 + 2\delta^{(1)}}$$

$$V_{\text{NMO,SV}}\left(\zeta = \frac{\pi}{2}, \phi = 0\right) = V_{\text{S1}}\sqrt{1 + 2\sigma^{(1)}}$$

$$V_{\text{NMO,SH}}\left(\zeta = \frac{\pi}{2}, \phi = 0\right) = V_{\text{S0}}\sqrt{1 + 2\gamma^{(1)}}$$

NMO in a horizontally layered anisotropic Earth

The effective NMO for a stack of horizontal homogeneous layers above a dipping reflector can be written as (Tsvankin, 2001)

$$V_{\text{NMO}}^2 = \frac{1}{t_0} \sum_{i=1}^N \left[V_{\text{NMO}}^{(i)}(p) \right]^2 t_0^i(p)$$

where $t_0^i(p)$ is the interval travel time in layer i computed along the zero-offset ray, $t_0 = \sum_{i=1}^N t_0^i$ is the total zero-offset time, and $V_{\text{NMO}}^{(i)}(p)$ is the interval NMO velocity for the ray parameter p of the zero-offset ray. The ray parameter for the zero-offset ray is

$$p = \frac{\sin \phi}{V_N(\phi)}$$

where ϕ is the reflector dip, and $V_N(\phi)$ is the velocity at angle ϕ from the vertical in the N th layer at the reflector.

Synopsis

The expressions for NMO in a layered and/or anisotropic elastic medium generally work best for small offsets.

3.4 Impedance, reflectivity, and transmissivity

Synopsis

The impedance, I , of an elastic medium is the ratio of the stress to the particle velocity (Aki and Richards, 1980) and is given by ρV , where ρ is the density and V is the wave propagation velocity. At a plane interface between two thick, homogeneous, isotropic, elastic layers, the normal incidence reflectivity for waves traveling from medium 1 to medium 2 is the ratio of the displacement amplitude, A_r , of the reflected wave to that of the incident wave, A_i , and is given by

$$R_{12} = \frac{A_r}{A_i} = \frac{I_2 - I_1}{I_2 + I_1} = \frac{\rho_2 V_2 - \rho_1 V_1}{\rho_2 V_2 + \rho_1 V_1}$$

$$\approx \frac{1}{2} \ln(I_2/I_1)$$

The logarithmic approximation is reasonable for $|R| < 0.5$ (Castagna, 1993). A normally incident P-wave generates only reflected and transmitted P-waves. A normally incident S-wave generates only reflected and transmitted S-waves. There is no mode conversion.

The above expression for the reflection coefficient is obtained when the *particle displacements are measured with respect to the direction of the wave vector* (equivalent to the slowness vector or the direction of propagation). A displacement is taken to be positive when its component along the interface has the same phase (or the same direction) as the component of the wave vector along the interface. For P-waves, this means that positive displacement is along the direction of propagation. Thus, a positive reflection coefficient implies that a compression is reflected as a compression, whereas a negative reflection coefficient implies a phase inversion (Sheriff, 1991). When the *displacements are measured with respect to a space-fixed coordinate system*, and not with respect to the wave vector, the reflection coefficient is given by

$$R_{12} = \frac{A_r}{A_i} = \frac{I_1 - I_2}{I_2 + I_1} = \frac{\rho_1 V_1 - \rho_2 V_2}{\rho_2 V_2 + \rho_1 V_1}$$

The normal incidence transmissivity in both coordinate systems is

$$T_{12} = \frac{A_t}{A_i} = \frac{2I_1}{I_2 + I_1} = \frac{2\rho_1 V_1}{\rho_2 V_2 + \rho_1 V_1}$$

where A_t is the displacement amplitude of the transmitted wave. Continuity at the interface requires

$$\begin{aligned} A_i + A_r &= A_t \\ 1 + R &= T \end{aligned}$$

This choice of signs for A_i and A_r is for a space-fixed coordinate system. Note that the transmission coefficient for wave amplitudes can be greater than 1. Sometimes the reflection and transmission coefficients are defined in terms of scaled displacements A' , which are proportional to the square root of energy flux (Aki and Richards, 1980; Kennett, 1983). The scaled displacements are given by

$$A' = A\sqrt{\rho V \cos \theta}$$

where θ is the angle between the wave vector and the normal to the interface. The normal incidence reflection and transmission coefficients in terms of these scaled displacements are

$$\begin{aligned} R'_{12} &= \frac{A'_r}{A'_i} = R_{12} \\ T'_{12} &= \frac{A'_t}{A'_i} = T_{12} \frac{\sqrt{\rho_2 V_2}}{\sqrt{\rho_1 V_1}} = \frac{2\sqrt{\rho_1 V_1 \rho_2 V_2}}{\rho_2 V_2 + \rho_1 V_1} \end{aligned}$$

Reflectivity and transmissivity for energy fluxes, R^e and T^e , respectively, are given by the squares of the reflection and transmission coefficients for scaled displacements. For normal incidence they are

$$R_{12}^e = \frac{E_r}{E_i} = (R'_{12})^2 = \frac{(\rho_1 V_1 - \rho_2 V_2)^2}{(\rho_2 V_2 + \rho_1 V_1)^2}$$

$$T_{12}^e = \frac{E_t}{E_i} = (T'_{12})^2 = \frac{4\rho_1 V_1 \rho_2 V_2}{(\rho_2 V_2 + \rho_1 V_1)^2}$$

where E_i , E_r , and E_t are the incident, reflected, and transmitted energy fluxes, respectively. Energy reflection coefficients were first given by Knott (1899). Conservation of energy at an interface where no trapping of energy occurs requires that

$$E_i = E_r + E_t$$

$$1 = R^e + T^e$$

The reflection and transmission coefficients for energy fluxes can never be greater than 1.

Simple band-limited inverse of reflectivity time series

Consider a flat-layered Earth, with an impedance time series $I_n = \rho(n\Delta t)V(n\Delta t)$, where ρ is density, V is velocity (either P or S), and $t = n\Delta t$, where $n = 0, 1, 2, \dots, N$ is the normal incidence two-way travel time, equally sampled in intervals Δt . In these expressions, $n\Delta t$ is the argument of $\rho(\cdot)$ and $V(\cdot)$, not a factor multiplying ρ and V . The reflectivity time series can be approximated as

$$R_{n+1} = \frac{I_{n+1} - I_n}{I_{n+1} + I_n}$$

Solving for I_{n+1} yields a simple recursive algorithm

$$I_{n+1} = I_n \frac{(1 + R_{n+1})}{(1 - R_{n+1})}; \quad n = 0: N - 1$$

where I_0 , the impedance at time $t = 0$, must be supplied. For small Δt and small R_n , this equation can be written as

$$I_n \approx I_0 \exp \left[\sum_{i=1}^n \left(2R_i + \frac{2}{3} R_i^3 + \frac{2}{5} R_i^5 + \dots \right) \right]$$

In contrast, a simple running summation of R_n leads to

$$I_n \approx I_0 \exp \left[\sum_{i=1}^n (2R_i) \right]$$

which is a low-order approximation of the first algorithm.

Rough surfaces

Random interface roughness at scales smaller than the wavelength causes incoherent scattering and a decrease in amplitude of the coherent reflected and transmitted waves. This could be one of the explanations for the observation that amplitudes of multiples in synthetic seismograms are often larger than the amplitudes of corresponding multiples in the data (Frazer, 1994). Kuperman (1975) gives results that modify the reflectivity and transmissivity to include scattering losses at the interface. With the mean-squared departure from planarity of the rough interface denoted by σ^2 , the modified coefficients are

$$\tilde{R}_{12} = R_{12}(1 - 2k_1^2\sigma^2) = R_{12}[1 - 8\pi^2(\sigma/\lambda_1)^2]$$

$$\tilde{T}_{12} = T_{12} \left[1 - \frac{1}{2}(k_1 - k_2)^2\sigma^2 \right] = T_{12} \left[1 - 2\pi^2(\lambda_2 - \lambda_1)^2 \left(\frac{\sigma}{\lambda_1\lambda_2} \right)^2 \right]$$

where $k_1 = \omega/V_1$, $k_2 = \omega/V_2$ are the wavenumbers, and λ_1 and λ_2 are the wavelengths in media 1 and 2, respectively.

Uses

The equations presented in this section can be used for the following purposes:

- to calculate amplitudes and energy fluxes of reflected and transmitted waves at interfaces in elastic media;
- to estimate the decrease in wave amplitude caused by scattering losses during reflection and transmission at rough interfaces.

Assumptions and limitations

The equations presented in this section apply only under the following conditions:

- normal incidence, plane-wave, time-harmonic propagation in isotropic, linear, elastic media with a single interface, or multiple interfaces well separated by thick layers with thickness much greater than the wavelength;
- no energy losses or trapping at the interface; and
- rough surface results are valid for small deviations from planarity (small σ).

3.5 Reflectivity and amplitude variations with offset (AVO) in isotropic media

Synopsis

The **seismic impedance** is the product of velocity and density (see Section 3.4), as expressed by

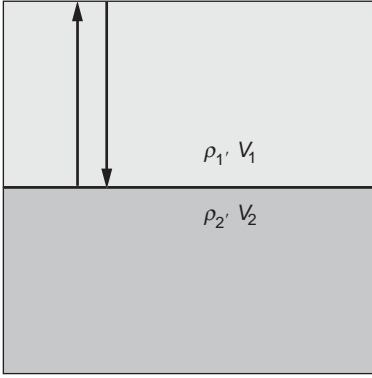


Figure 3.5.1 Reflection of a normal-incidence wave at an interface between two thick homogeneous, isotropic, elastic layers.

$$I_P = \rho V_P \quad I_S = \rho V_S$$

where I_P , I_S are P- and S-wave impedances, V_P , V_S are P- and S-wave velocities, and ρ is density.

At an interface between two thick homogeneous, isotropic, elastic layers, the **normal incidence reflectivity**, defined as the ratio of the reflected wave amplitude to the incident wave amplitude, is

$$\begin{aligned} R_{PP} &= \frac{\rho_2 V_{P2} - \rho_1 V_{P1}}{\rho_2 V_{P2} + \rho_1 V_{P1}} = \frac{I_{P2} - I_{P1}}{I_{P2} + I_{P1}} \\ &\approx \frac{1}{2} \ln(I_{P2}/I_{P1}) \\ R_{SS} &= \frac{\rho_2 V_{S2} - \rho_1 V_{S1}}{\rho_2 V_{S2} + \rho_1 V_{S1}} = \frac{I_{S2} - I_{S1}}{I_{S2} + I_{S1}} \\ &\approx \frac{1}{2} \ln(I_{S2}/I_{S1}) \end{aligned}$$

where R_{PP} is the normal incidence P-to-P reflectivity, R_{SS} is the S-to-S reflectivity, and the subscripts 1 and 2 refer to the first and second media, respectively (Figure 3.5.1). The logarithmic approximation is reasonable for $|R| < 0.5$ (Castagna, 1993). A normally incident P-wave generates only reflected and transmitted P-waves. A normally incident S-wave generates only reflected and transmitted S-waves. There is no mode conversion.

AVO: amplitude variations with offset

For non-normal incidence, the situation is more complicated. An incident P-wave generates reflected P- and S-waves and transmitted P- and S-waves. The reflection

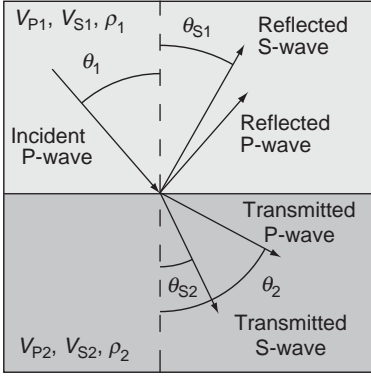


Figure 3.5.2 The angles of the incident, reflected, and transmitted rays of a P-wave with non-normal incidence.

and transmission coefficients depend on the angle of incidence as well as on the material properties of the two layers. An excellent review is given by Castagna (1993).

The angles of the incident, reflected, and transmitted rays (Figure 3.5.2) are related by Snell's law as follows:

$$p = \frac{\sin \theta_1}{V_{P1}} = \frac{\sin \theta_2}{V_{P2}} = \frac{\sin \theta_{S1}}{V_{S1}} = \frac{\sin \theta_{S2}}{V_{S2}}$$

where p is the **ray parameter**. θ and θ_S are the angles of P- and S-wave propagation, respectively, relative to the reflector normal. Subscripts 1 and 2 indicate angles or material properties of layers 1 and 2, respectively.

The complete solution for the amplitudes of transmitted and reflected P- and S-waves for both incident P- and S-waves is given by the Knott–Zoeppritz equations (Knott, 1899; Zoeppritz, 1919; Aki and Richards, 1980; Castagna, 1993).

Aki and Richards (1980) give the results in the following convenient matrix form:

$$\begin{pmatrix} \begin{matrix} \downarrow\uparrow & \downarrow\uparrow & \uparrow\uparrow & \uparrow\uparrow \\ \text{PP} & \text{SP} & \text{PP} & \text{SP} \end{matrix} \\ \begin{matrix} \downarrow\uparrow & \downarrow\uparrow & \uparrow\uparrow & \uparrow\uparrow \\ \text{PS} & \text{SS} & \text{PS} & \text{SS} \end{matrix} \\ \begin{matrix} \downarrow\downarrow & \downarrow\downarrow & \uparrow\downarrow & \uparrow\downarrow \\ \text{PP} & \text{SP} & \text{PP} & \text{SP} \end{matrix} \\ \begin{matrix} \downarrow\downarrow & \downarrow\downarrow & \uparrow\downarrow & \uparrow\downarrow \\ \text{PS} & \text{SS} & \text{PS} & \text{SS} \end{matrix} \end{pmatrix} = \mathbf{M}^{-1}\mathbf{N}$$

where each matrix element is a reflection or transmission coefficient for displacement amplitudes. The first letter designates the type of incident wave, and the second letter designates the type of reflected or transmitted wave. The arrows indicate downward \downarrow and upward \uparrow propagation, so that a combination $\downarrow\uparrow$ indicates a reflection coefficient, while a combination $\downarrow\downarrow$ indicates a transmission coefficient. The matrices \mathbf{M} and \mathbf{N} are given by

$$\mathbf{M} = \begin{pmatrix} -\sin \theta_1 & -\cos \theta_{S1} & \sin \theta_2 & \cos \theta_{S2} \\ \cos \theta_1 & -\sin \theta_{S1} & \cos \theta_2 & -\sin \theta_{S2} \\ 2\rho_1 V_{S1} \sin \theta_{S1} \cos \theta_1 & \rho_1 V_{S1} (1 - 2 \sin^2 \theta_{S1}) & 2\rho_2 V_{S2} \sin \theta_{S2} \cos \theta_2 & \rho_2 V_{S2} (1 - 2 \sin^2 \theta_{S2}) \\ -\rho_1 V_{P1} (1 - 2 \sin^2 \theta_{S1}) & \rho_1 V_{S1} \sin 2\theta_{S1} & -\rho_2 V_{P2} (1 - 2 \sin^2 \theta_{S2}) & -\rho_2 V_{S2} \sin 2\theta_{S2} \end{pmatrix}$$

$$\mathbf{N} = \begin{pmatrix} \sin \theta_1 & \cos \theta_{S1} & -\sin \theta_2 & -\cos \theta_{S2} \\ \cos \theta_1 & -\sin \theta_{S1} & \cos \theta_2 & -\sin \theta_{S2} \\ 2\rho_1 V_{S1} \sin \theta_{S1} \cos \theta_1 & \rho_1 V_{S1} (1 - 2 \sin^2 \theta_{S1}) & 2\rho_2 V_{S2} \sin \theta_{S2} \cos \theta_2 & \rho_2 V_{S2} (1 - 2 \sin^2 \theta_{S2}) \\ \rho_1 V_{P1} (1 - 2 \sin^2 \theta_{S1}) & -\rho_1 V_{S1} \sin 2\theta_{S1} & -\rho_2 V_{P2} (1 - 2 \sin^2 \theta_{S2}) & \rho_2 V_{S2} \sin 2\theta_{S2} \end{pmatrix}$$

Results for incident P and incident S, given explicitly by Aki and Richards (1980), are as follows, where $R_{PP} = \overset{\uparrow\uparrow}{PP}$, $R_{PS} = \overset{\uparrow\uparrow}{PS}$, $T_{PP} = \overset{\downarrow\downarrow}{PP}$, $T_{PS} = \overset{\downarrow\downarrow}{PS}$, $R_{SS} = \overset{\uparrow\uparrow}{SS}$, $R_{SP} = \overset{\downarrow\downarrow}{SP}$, $T_{SP} = \overset{\downarrow\downarrow}{SP}$, $T_{SS} = \overset{\downarrow\downarrow}{SS}$:

$$R_{PP} = \left[\left(b \frac{\cos \theta_1}{V_{P1}} - c \frac{\cos \theta_2}{V_{P2}} \right) F - \left(a + d \frac{\cos \theta_1}{V_{P1}} \frac{\cos \theta_{S2}}{V_{S2}} \right) H p^2 \right] / D$$

$$R_{PS} = \left[-2 \frac{\cos \theta_1}{V_{P1}} \left(ab + cd \frac{\cos \theta_2}{V_{P2}} \frac{\cos \theta_{S2}}{V_{S2}} \right) p V_{P1} \right] / (V_{S1} D)$$

$$T_{PP} = 2\rho_1 \frac{\cos \theta_1}{V_{P1}} F V_{P1} / (V_{P2} D)$$

$$T_{PS} = 2\rho_1 \frac{\cos \theta_1}{V_{P1}} H p V_{P1} / (V_{S2} D)$$

$$R_{SS} = - \left[\left(b \frac{\cos \theta_{S1}}{V_{S1}} - c \frac{\cos \theta_{S2}}{V_{S2}} \right) E - \left(a + d \frac{\cos \theta_2}{V_{P2}} \frac{\cos \theta_{S1}}{V_{S1}} \right) G p^2 \right] / D$$

$$R_{SP} = -2 \frac{\cos \theta_{S1}}{V_{S1}} \left(ab + cd \frac{\cos \theta_2}{V_{P2}} \frac{\cos \theta_{S2}}{V_{S2}} \right) p V_{S1} / (V_{P1} D)$$

$$T_{SP} = -2\rho_1 \frac{\cos \theta_{S1}}{V_{S1}} G p V_{S1} / (V_{P2} D)$$

$$T_{SS} = 2\rho_1 \frac{\cos \theta_{S1}}{V_{S1}} E V_{S1} / (V_{S2} D)$$

where

$$a = \rho_2(1 - 2 \sin^2 \theta_{S2}) - \rho_1(1 - 2 \sin^2 \theta_{S1})$$

$$b = \rho_2(1 - 2 \sin^2 \theta_{S2}) + 2\rho_1 \sin^2 \theta_{S1}$$

$$c = \rho_1(1 - 2 \sin^2 \theta_{S1}) + 2\rho_2 \sin^2 \theta_{S2}$$

$$d = 2(\rho_2 V_{S2}^2 - \rho_1 V_{S1}^2)$$

$$D = EF + GHp^2 = (\det \mathbf{M}) / (V_{P1} V_{P2} V_{S1} V_{S2})$$

$$E = b \frac{\cos \theta_1}{V_{P1}} + c \frac{\cos \theta_2}{V_{P2}}$$

$$F = b \frac{\cos \theta_{S1}}{V_{S1}} + c \frac{\cos \theta_{S2}}{V_{S2}}$$

$$G = a - d \frac{\cos \theta_1}{V_{P1}} \frac{\cos \theta_{S2}}{V_{S2}}$$

$$H = a - d \frac{\cos \theta_2}{V_{P2}} \frac{\cos \theta_{S1}}{V_{S1}}$$

and p is the ray parameter.

Approximate forms

Although the complete Zoeppritz equations can be evaluated numerically, it is often useful and more insightful to use one of the simpler approximations.

Bortfeld (1961) linearized the Zoeppritz equations by assuming small contrasts between layer properties as follows:

$$R_{PP}(\theta_1) \approx \frac{1}{2} \ln \left(\frac{V_{P2} \rho_2 \cos \theta_1}{V_{P1} \rho_1 \cos \theta_2} \right) + \left(\frac{\sin \theta_1}{V_{P1}} \right)^2 (V_{S1}^2 - V_{S2}^2) \left[2 + \frac{\ln(\rho_2/\rho_1)}{\ln(V_{S2}/V_{S1})} \right]$$

Aki and Richards (1980) also derived a simplified form by assuming small layer contrasts. The results are conveniently expressed in terms of contrasts in V_P , V_S , and ρ as follows:

$$R_{PP}(\theta) \approx \frac{1}{2} (1 - 4p^2 \bar{V}_S^2) \frac{\Delta \rho}{\bar{\rho}} + \frac{1}{2 \cos^2 \theta} \frac{\Delta V_P}{\bar{V}_P} - 4p^2 \bar{V}_S^2 \frac{\Delta V_S}{\bar{V}_S}$$

$$R_{PS}(\theta) \approx \frac{-p \bar{V}_P}{2 \cos \theta \bar{V}_S} \left[\left(1 - 2 \bar{V}_S^2 p^2 + 2 \bar{V}_S^2 \frac{\cos \theta \cos \theta_S}{\bar{V}_P \bar{V}_S} \right) \frac{\Delta \rho}{\bar{\rho}} \right. \\ \left. - \left(4p^2 \bar{V}_S^2 - 4 \bar{V}_S^2 \frac{\cos \theta \cos \theta_S}{\bar{V}_P \bar{V}_S} \right) \frac{\Delta V_S}{\bar{V}_S} \right]$$

$$T_{PP}(\theta) \approx 1 - \frac{1}{2} \frac{\Delta \rho}{\bar{\rho}} + \left(\frac{1}{2 \cos^2 \theta} - 1 \right) \frac{\Delta V_P}{\bar{V}_P}$$

$$T_{PS}(\theta) \approx \frac{p\bar{V}_P}{2\cos\theta_S} \left[\left(1 - 2\bar{V}_S^2 p^2 - 2\bar{V}_S^2 \frac{\cos\theta}{\bar{V}_P} \frac{\cos\theta_S}{\bar{V}_S} \right) \frac{\Delta\rho}{\bar{\rho}} - \left(4p^2\bar{V}_S^2 + 4\bar{V}_S^2 \frac{\cos\theta}{\bar{V}_P} \frac{\cos\theta_S}{\bar{V}_S} \right) \frac{\Delta V_S}{\bar{V}_S} \right]$$

$$R_{SP}(\theta) \approx \frac{\cos\theta_S}{\bar{V}_P} \frac{\bar{V}_S}{\cos\theta} R_{PS}(\theta)$$

$$R_{SS}(\theta) \approx -\frac{1}{2} (1 - 4p^2\bar{V}_S^2) \frac{\Delta\rho}{\bar{\rho}} - \left(\frac{1}{2\cos^2\theta_S} - 4p^2\bar{V}_S^2 \right) \frac{\Delta V_S}{\bar{V}_S}$$

$$T_{SP}(\theta) \approx -\frac{\cos\theta_S}{\bar{V}_P} \frac{\bar{V}_S}{\cos\theta} T_{PS}$$

$$T_{SS}(\theta) \approx 1 - \frac{1}{2} \frac{\Delta\rho}{\bar{\rho}} + \left(\frac{1}{2\cos^2\theta_S} - 1 \right) \frac{\Delta V_S}{\bar{V}_S}$$

where

$$p = \frac{\sin\theta_1}{V_{P1}} = \frac{\sin\theta_{S1}}{V_{S1}} \quad \theta = (\theta_2 + \theta_1)/2$$

$$\theta_S = (\theta_{S2} + \theta_{S1})/2$$

$$\Delta\rho = \rho_2 - \rho_1 \quad \bar{\rho} = (\rho_2 + \rho_1)/2$$

$$\Delta V_P = V_{P2} - V_{P1} \quad \bar{V}_P = (V_{P2} + V_{P1})/2$$

$$\Delta V_S = V_{S2} - V_{S1} \quad \bar{V}_S = (V_{S2} + V_{S1})/2$$

Often, the mean P-wave angle θ is approximated as θ_1 , the P-wave angle of incidence.

The result for P-wave reflectivity can be rewritten in the familiar form:

$$R_{PP}(\theta) \approx R_{P0} + B \sin^2\theta + C(\tan^2\theta - \sin^2\theta)$$

or

$$R_{PP}(\theta) \approx \frac{1}{2} \left(\frac{\Delta V_P}{\bar{V}_P} + \frac{\Delta\rho}{\bar{\rho}} \right) + \left[\frac{1}{2} \frac{\Delta V_P}{\bar{V}_P} - 2 \frac{\bar{V}_S^2}{\bar{V}_P^2} \left(2 \frac{\Delta V_S}{\bar{V}_S} + \frac{\Delta\rho}{\bar{\rho}} \right) \right] \sin^2\theta$$

$$+ \frac{1}{2} \frac{\Delta V_P}{\bar{V}_P} (\tan^2\theta - \sin^2\theta)$$

This form can be interpreted in terms of different angular ranges (Castagna, 1993). In the above equations R_{P0} is the normal incidence reflection coefficient as expressed by

$$R_{P0} = \frac{I_{P2} - I_{P1}}{I_{P2} + I_{P1}} \approx \frac{\Delta I_P}{2I_P} \approx \frac{1}{2} \left(\frac{\Delta V_P}{\bar{V}_P} + \frac{\Delta \rho}{\bar{\rho}} \right)$$

The parameter B describes the variation at intermediate offsets and is often called the **AVO gradient**, and C dominates at far offsets near the critical angle.

Shuey (1985) presented a similar approximation where the AVO gradient is expressed in terms of the Poisson ratio ν as follows:

$$R_{PP}(\theta_1) \approx R_{P0} + \left[ER_{P0} + \frac{\Delta \nu}{(1 - \bar{\nu})^2} \right] \sin^2 \theta_1 + \frac{1}{2} \frac{\Delta V_P}{\bar{V}_P} (\tan^2 \theta_1 - \sin^2 \theta_1)$$

where

$$R_{P0} \approx \frac{1}{2} \left(\frac{\Delta V_P}{\bar{V}_P} + \frac{\Delta \rho}{\bar{\rho}} \right)$$

$$E = F - 2(1 + F) \left(\frac{1 - 2\bar{\nu}}{1 - \bar{\nu}} \right)$$

$$F = \frac{\Delta V_P / \bar{V}_P}{\Delta V_P / \bar{V}_P + \Delta \rho / \bar{\rho}}$$

and

$$\Delta \nu = \nu_2 - \nu_1$$

$$\bar{\nu} = (\nu_2 + \nu_1)/2$$

The coefficients E and F used here in Shuey's equation are not the same as those defined earlier in the solutions to the Zoeppritz equations.

Smith and Gidlow (1987) offered a further simplification to the Aki–Richards equation by removing the dependence on density using Gardner's equation (see Section 7.10) as follows:

$$\rho \propto V^{1/4}$$

giving

$$R_{PP}(\theta) \approx c \frac{\Delta V_P}{\bar{V}_P} + d \frac{\Delta V_S}{\bar{V}_S}$$

where

$$c = \frac{5}{8} - \frac{1}{2} \frac{\bar{V}_S^2}{\bar{V}_P^2} \sin^2 \theta + \frac{1}{2} \tan^2 \theta$$

$$d = -4 \frac{\bar{V}_S^2}{\bar{V}_P^2} \sin^2 \theta$$

Wiggins *et al.* (1983) showed that when $V_P \approx 2V_S$, the AVO gradient is approximately (Spratt *et al.*, 1993)

$$B \approx R_{P0} - 2R_{S0}$$

given that the P and S normal incident reflection coefficients are

$$R_{P0} \approx \frac{1}{2} \left(\frac{\Delta V_P}{\bar{V}_P} + \frac{\Delta \rho}{\bar{\rho}} \right)$$

$$R_{S0} \approx \frac{1}{2} \left(\frac{\Delta V_S}{\bar{V}_S} + \frac{\Delta \rho}{\bar{\rho}} \right)$$

Hilterman (1989) suggested the following slightly modified form:

$$R_{PP}(\theta) \approx R_{P0} \cos^2 \theta + PR \sin^2 \theta$$

where R_{P0} is the normal incidence reflection coefficient and

$$PR = \frac{v_2 - v_1}{(1 - \bar{v})^2}$$

This modified form has the interpretation that the near-offset traces reveal the P-wave impedance, and the intermediate-offset traces image contrasts in Poisson ratio (Castagna, 1993).

Gray *et al.* (1999) derived linearized expressions for P–P reflectivity in terms of the angle of incidence, θ , and the contrast in bulk modulus, K , shear modulus, μ , and bulk density, ρ :

$$\begin{aligned} R(\theta) = & \left(\frac{1}{4} - \frac{1}{3} \frac{\bar{V}_S^2}{\bar{V}_P^2} \right) (\sec^2 \theta) \frac{\Delta K}{K} + \left(\frac{\bar{V}_S^2}{\bar{V}_P^2} \right) \left(\frac{1}{3} \sec^2 \theta - 2 \sin^2 \theta \right) \frac{\Delta \mu}{\mu} \\ & + \left(\frac{1}{2} - \frac{1}{4} \sec^2 \theta \right) \frac{\Delta \rho}{\rho} \end{aligned}$$

Similarly, their expression in terms of Lamé's coefficient, λ , shear modulus, and bulk density is

$$\begin{aligned} R(\theta) = & \left(\frac{1}{4} - \frac{1}{2} \frac{\bar{V}_S^2}{\bar{V}_P^2} \right) (\sec^2 \theta) \frac{\Delta \lambda}{\lambda} + \left(\frac{\bar{V}_S^2}{\bar{V}_P^2} \right) \left(\frac{1}{2} \sec^2 \theta - 2 \sin^2 \theta \right) \frac{\Delta \mu}{\mu} \\ & + \left(\frac{1}{2} - \frac{1}{4} \sec^2 \theta \right) \frac{\Delta \rho}{\rho} \end{aligned}$$

In the same assumptions of small layer contrast and limited angle of incidence, we can write the linearized SV-to-SV reflection (Rüger, 2001):

$$R_{SV\text{-iso}}(\theta_S) \approx -\frac{1}{2} \frac{\Delta I_S}{\bar{I}_S} + \left(\frac{7}{2} \frac{\Delta V_S}{\bar{V}_S} + 2 \frac{\Delta \rho}{\bar{\rho}} \right) \sin^2 \theta_S - \frac{1}{2} \frac{\Delta V_S}{\bar{V}_S} \sin^2 \theta_S \tan^2 \theta_S$$

where θ_S is the SV-wave phase angle of incidence and $I_S = \rho V_S$ is the shear impedance.

Similarly, for SH-to-SH reflection (Rüger, 2001):

$$R_{SH}(\theta_S) = -\frac{1}{2} \frac{\Delta I_S}{I_S} + \frac{1}{2} \left(\frac{\Delta V_S}{V_S} \right) \tan^2 \theta_S$$

where θ_S is the SH-wave phase angle of incidence.

For P-to-SV converted shear-wave reflection (Aki and Richards, 1980):

$$R_{PS}(\theta_S) \approx \frac{-\tan \theta_S}{2\bar{V}_S/\bar{V}_P} \left(1 - 2 \sin^2 \theta_S + 2 \cos \theta_S \sqrt{\left(\frac{\bar{V}_S}{\bar{V}_P} \right)^2 - \sin^2 \theta_S} \right) \frac{\Delta \rho}{\bar{\rho}} \\ + \frac{\tan \theta_S}{2\bar{V}_S/\bar{V}_P} \left(4 \sin^2 \theta_S - 4 \cos \theta_S \sqrt{\left(\frac{\bar{V}_S}{\bar{V}_P} \right)^2 - \sin^2 \theta_S} \right) \frac{\Delta V_S}{\bar{V}_S}$$

where θ_S is the S-wave phase angle of reflection. This can be rewritten as (González, 2006)

$$R_{PS}(\theta) \approx \frac{-\sin \theta}{(\bar{V}_P/\bar{V}_S) \sqrt{(\bar{V}_P/\bar{V}_S)^2 - \sin^2 \theta}} \\ \times \left\{ \left[\frac{1}{2} \left(\frac{\bar{V}_P}{\bar{V}_S} \right)^2 - \sin^2 \theta + \cos \theta \sqrt{\left(\frac{\bar{V}_P}{\bar{V}_S} \right)^2 - \sin^2 \theta} \right] \frac{\Delta \rho}{\bar{\rho}} \right. \\ \left. - \left[2 \sin^2 \theta - 2 \cos \theta \sqrt{\left(\frac{\bar{V}_P}{\bar{V}_S} \right)^2 - \sin^2 \theta} \right] \frac{\Delta V_S}{\bar{V}_S} \right\}$$

where θ is the P-wave phase angle of incidence.

For small angles, Duffaut *et al.* (2000) give the following expression for $R_{PS}(\theta)$:

$$R_{PS}(\theta) \approx \left[-\frac{1}{2} \left(1 + 2 \frac{\bar{V}_S}{\bar{V}_P} \right) \frac{\Delta \rho}{\bar{\rho}} - 2 \frac{\bar{V}_S}{\bar{V}_P} \frac{\Delta V_S}{\bar{V}_S} \right] \sin \theta \\ + \frac{\bar{V}_S}{\bar{V}_P} \left[\left(\frac{\bar{V}_S}{\bar{V}_P} + \frac{1}{2} \right) \left(\frac{\Delta \rho}{\bar{\rho}} + \frac{2 \Delta V_S}{\bar{V}_S} \right) - \frac{1}{4} \frac{\bar{V}_S}{\bar{V}_P} \frac{\Delta \rho}{\bar{\rho}} \right] \sin^3 \theta$$

which can be simplified further (Jílek, 2002b) to

$$R_{PS}(\theta) \approx \left[-\frac{1}{2} \left(1 + 2 \frac{\bar{V}_S}{\bar{V}_P} \right) \frac{\Delta \rho}{\bar{\rho}} - 2 \frac{\bar{V}_S}{\bar{V}_P} \frac{\Delta V_S}{\bar{V}_S} \right] \sin \theta$$

Assumptions and limitations

The equations presented in this section apply in the following cases:

- the rock is linear, isotropic, and elastic;
- plane-wave propagation is assumed; and
- most of the simplified forms assume small contrasts in material properties across the boundary and angles of incidence of less than about 30° . The simplified form for P-to-S reflection given by González (2006) is valid for large angles of incidence.

3.6 Plane-wave reflectivity in anisotropic media

Synopsis

An incident wave at a boundary between two anisotropic media (Figure 3.6.1) can generate reflected quasi-P-waves and quasi-S-waves as well as transmitted quasi-P-waves and quasi-S-waves (Auld, 1990). In general, the reflection and transmission coefficients vary with offset and azimuth. The AVOA (amplitude variation with offset and azimuth) can be detected by three-dimensional seismic surveys and is a useful seismic attribute for reservoir characterization.

Brute-force modeling of AVOA by solving the Zoeppritz (1919) equations can be complicated and unintuitive for several reasons: for anisotropic media in general, the two shear waves are separate (shear-wave birefringence); the slowness surfaces are nonspherical and are not necessarily convex; and the polarization vectors are neither parallel nor perpendicular to the propagation vectors.

Schoenberg and Protázio (1992) give explicit solutions for the plane-wave reflection and transmission problem in terms of submatrices of the coefficient matrix of the Zoeppritz equations. The most general case of the explicit solutions is applicable to

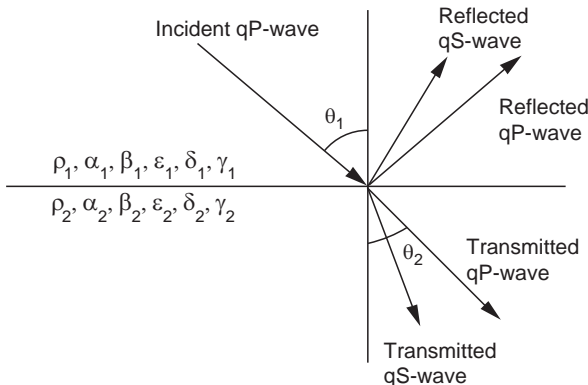


Figure 3.6.1 Reflected and transmitted rays caused by a P-wave incident at a boundary between two anisotropic media.

monoclinic media with a mirror plane of symmetry parallel to the reflecting plane. Let \mathbf{R} and \mathbf{T} represent the **reflection** and **transmission matrices**, respectively,

$$\mathbf{R} = \begin{bmatrix} R_{PP} & R_{SP} & R_{TP} \\ R_{PS} & R_{SS} & R_{TS} \\ R_{PT} & R_{ST} & R_{TT} \end{bmatrix}$$

$$\mathbf{T} = \begin{bmatrix} T_{PP} & T_{SP} & T_{TP} \\ T_{PS} & T_{SS} & T_{TS} \\ T_{PT} & T_{ST} & T_{TT} \end{bmatrix}$$

where the first subscript denotes the type of incident wave and the second subscript denotes the type of reflected or transmitted wave. For “weakly” anisotropic media, the subscript P denotes the P-wave, S denotes one quasi-S-wave, and T denotes the other quasi-S-wave (i.e., the tertiary or third wave). As a convention for real s_{3P}^2 , s_{3S}^2 , and s_{3T}^2 ,

$$s_{3P}^2 < s_{3S}^2 < s_{3T}^2$$

where s_{3i} is the vertical component of the phase slowness of the i th wave type when the reflecting plane is horizontal. An imaginary value for any of the vertical slownesses implies that the corresponding wave is inhomogeneous or evanescent. The impedance matrices are defined as

$$\mathbf{X} = \begin{bmatrix} e_{P1} & e_{S1} & e_{T1} \\ e_{P2} & e_{S2} & e_{T2} \\ \{-(C_{13}e_{P1} + C_{36}e_{P2})s_1 \\ -(C_{23}e_{P2} + C_{36}e_{P1})s_2 \\ -C_{33}e_{P3}s_{3P}\} & \{-(C_{13}e_{S1} + C_{36}e_{S2})s_1 \\ -(C_{23}e_{S2} + C_{36}e_{S1})s_2 \\ -C_{33}e_{S3}s_{3S}\} & \{-(C_{13}e_{T1} + C_{36}e_{T2})s_1 \\ -(C_{23}e_{T2} + C_{36}e_{T1})s_2 \\ -C_{33}e_{T3}s_{3T}\} \end{bmatrix}$$

$$\mathbf{Y} = \begin{bmatrix} \{-(C_{55}s_1 + C_{45}s_2)e_{P3} \\ -(C_{55}e_{P1} + C_{45}e_{P2})s_{3P}\} & \{-(C_{55}s_1 + C_{45}s_2)e_{S3} \\ -(C_{55}e_{S1} + C_{45}e_{S2})s_{3S}\} & \{-(C_{55}s_1 + C_{45}s_2)e_{T3} \\ -(C_{55}e_{T1} + C_{45}e_{T2})s_{3T}\} \\ e_{P3} & e_{S3} & e_{T3} \end{bmatrix}$$

where s_1 and s_2 are the horizontal components of the phase slowness vector; \mathbf{e}_P , \mathbf{e}_S , and \mathbf{e}_T are the associated eigenvectors evaluated from the Christoffel equations (see [Section 3.2](#)), and C_{IJ} denotes elements of the stiffness matrix of the incident medium. \mathbf{X}' and \mathbf{Y}' are the same as above except that primed parameters (transmission medium) replace unprimed parameters (incidence medium). When neither \mathbf{X} nor \mathbf{Y} is singular and $(\mathbf{X}^{-1}\mathbf{X}' + \mathbf{Y}^{-1}\mathbf{Y}')$ is invertible, the reflection and transmission coefficients can be written as

$$\mathbf{T} = 2(\mathbf{X}^{-1}\mathbf{X}' + \mathbf{Y}^{-1}\mathbf{Y}')^{-1}$$

$$\mathbf{R} = (\mathbf{X}^{-1}\mathbf{X}' - \mathbf{Y}^{-1}\mathbf{Y}')(\mathbf{X}^{-1}\mathbf{X}' + \mathbf{Y}^{-1}\mathbf{Y}')^{-1}$$

Schoenberg and Protázio (1992) point out that a singularity occurs at a horizontal slowness for which an interface wave (e.g., a Stoneley wave) exists. When \mathbf{Y} is singular, straightforward matrix manipulations yield

$$\mathbf{T} = 2\mathbf{Y}'^{-1}\mathbf{Y}(\mathbf{X}^{-1}\mathbf{X}'\mathbf{Y}'^{-1}\mathbf{Y} + \mathbf{I})^{-1}$$

$$\mathbf{R} = (\mathbf{X}^{-1}\mathbf{X}'\mathbf{Y}'^{-1}\mathbf{Y} + \mathbf{I})^{-1}(\mathbf{X}^{-1}\mathbf{X}'\mathbf{Y}'^{-1}\mathbf{Y} - \mathbf{I})$$

Similarly, \mathbf{T} and \mathbf{R} can also be written without \mathbf{X}^{-1} when \mathbf{X} is singular as

$$\mathbf{T} = 2\mathbf{X}'^{-1}\mathbf{X}(\mathbf{I} + \mathbf{Y}^{-1}\mathbf{Y}'\mathbf{X}'^{-1}\mathbf{X})^{-1}$$

$$\mathbf{R} = (\mathbf{I} + \mathbf{Y}^{-1}\mathbf{Y}'\mathbf{X}'^{-1}\mathbf{X})^{-1}(\mathbf{I} - \mathbf{Y}^{-1}\mathbf{Y}'\mathbf{X}'^{-1}\mathbf{X})$$

Alternative solutions can be found by assuming that \mathbf{X}' and \mathbf{Y}' are invertible

$$\mathbf{R} = (\mathbf{Y}'^{-1}\mathbf{Y} + \mathbf{X}'^{-1}\mathbf{X})^{-1}(\mathbf{Y}'^{-1}\mathbf{Y} - \mathbf{X}'^{-1}\mathbf{X})$$

$$\mathbf{T} = 2\mathbf{X}'^{-1}\mathbf{X}(\mathbf{Y}'^{-1}\mathbf{Y} + \mathbf{X}'^{-1}\mathbf{X})^{-1}\mathbf{Y}'^{-1}\mathbf{Y}$$

$$= 2\mathbf{Y}'^{-1}\mathbf{Y}(\mathbf{Y}'^{-1}\mathbf{Y} + \mathbf{X}'^{-1}\mathbf{X})^{-1}\mathbf{X}'^{-1}\mathbf{X}$$

These formulas allow more straightforward calculations when the media have at least monoclinic symmetry with a horizontal symmetry plane.

For a wave traveling in anisotropic media, there will generally be out-of-plane motion unless the wave path is in a symmetry plane. These symmetry planes include all vertical planes in VTI (transversely isotropic with vertical symmetry axis) media and the symmetry planes in HTI (transversely isotropic with horizontal symmetry axis) and orthorhombic media. In this case, the quasi-P- and the quasi-S-waves in the symmetry plane uncouple from the quasi-S-wave polarized transversely to the symmetry plane. For weakly anisotropic media, we can use simple analytical formulas (Banik, 1987; Thomsen, 1993; Chen, 1995; Rüger, 1995, 1996) to compute AVOA (amplitude variation with offset and azimuth) responses at the interface of anisotropic media that can be either VTI, HTI, or orthorhombic. The analytical formulas give more insight into the dependence of AVOA on anisotropy. Vavryčuk and Pšenčík (1998) and Pšenčík and Martins (2001) provide formulas for arbitrary weak anisotropy.

Transversely isotropic media: VTI

Thomsen (1986) introduced the following notation for weakly anisotropic VTI media with density ρ :

$$\alpha = \sqrt{\frac{C_{33}}{\rho}}; \quad \varepsilon = \frac{C_{11} - C_{33}}{2C_{33}}$$

$$\beta = \sqrt{\frac{C_{44}}{\rho}}; \quad \gamma = \frac{C_{66} - C_{44}}{2C_{44}}$$

$$\delta = \frac{(C_{13} + C_{44})^2 - (C_{33} - C_{44})^2}{2C_{33}(C_{33} - C_{44})}$$

In this chapter we use $\alpha = \sqrt{C_{33}/\rho}$ to refer to the P-wave velocity along the x_3 - (vertical) axis in anisotropic media. We use β to refer to the S-wave velocity along the x_3 -axis. The P-wave reflection coefficient for weakly anisotropic VTI media in the limit of small impedance contrast was derived by Thomsen (1993) and corrected by Rüger (1997):

$$R_{PP}(\theta) = R_{PP\text{-iso}}(\theta) + R_{PP\text{-aniso}}(\theta)$$

$$R_{PP\text{-iso}}(\theta) \approx \frac{1}{2} \left(\frac{\Delta Z}{\bar{Z}} \right) + \frac{1}{2} \left[\frac{\Delta \alpha}{\bar{\alpha}} - \left(\frac{2\bar{\beta}}{\bar{\alpha}} \right)^2 \frac{\Delta \mu}{\bar{\mu}} \right] \sin^2 \theta$$

$$+ \frac{1}{2} \left(\frac{\Delta \alpha}{\bar{\alpha}} \right) \sin^2 \theta \tan^2 \theta$$

$$R_{PP\text{-aniso}}(\theta) \approx \frac{\Delta \delta}{2} \sin^2 \theta + \frac{\Delta \varepsilon}{2} \sin^2 \theta \tan^2 \theta$$

where

$$\theta = (\theta_1 + \theta_2)/2 \quad \Delta \varepsilon = \varepsilon_2 - \varepsilon_1$$

$$\bar{\rho} = (\rho_1 + \rho_2)/2 \quad \Delta \rho = \rho_2 - \rho_1 \quad \Delta \gamma = \gamma_2 - \gamma_1$$

$$\bar{\alpha} = (\alpha_1 + \alpha_2)/2 \quad \Delta \alpha = \alpha_2 - \alpha_1 \quad \Delta \delta = \delta_2 - \delta_1$$

$$\bar{\beta} = (\beta_1 + \beta_2)/2 \quad \Delta \beta = \beta_2 - \beta_1 \quad \mu = \rho \beta^2$$

$$\bar{Z} = (Z_1 + Z_2)/2 \quad \Delta Z = Z_2 - Z_1 \quad Z = \rho \alpha$$

$$\bar{Z}_S = (Z_{S1} + Z_{S2})/2 \quad \Delta Z_S = Z_{S2} - Z_{S1} \quad Z_S = \rho \beta$$

$$\bar{\mu} = (\mu_1 + \mu_2)/2 \quad \Delta \mu = \mu_2 - \mu_1$$

In the preceding and following equations, Δ indicates a difference in properties between layer 1 (above) and layer 2 (below) and an overbar indicates an average of

the corresponding quantities in the two layers. θ is the P-wave phase angle of incidence, $Z = \rho\alpha$ is the vertical P-wave impedance, $Z_S = \rho\beta$ is the vertical S-wave impedance, and $\mu = \rho\beta^2$ is the vertical shear modulus. Note that the VTI anisotropy causes perturbations of both the AVO gradient and far-offset terms.

Rüger (2001) derived the corresponding SV-to-SV reflectivity in VTI media, again under the assumption of weak anisotropy and small-layer contrast:

$$R_{SV}(\theta_S) = R_{SV\text{-iso}}(\theta_S) + R_{SV\text{-aniso}}(\theta_S)$$

$$R_{SV\text{-iso}}(\theta_S) \approx -\frac{1}{2} \frac{\Delta Z_S}{Z_S} + \left(\frac{7}{2} \frac{\Delta\beta}{\bar{\beta}} + 2 \frac{\Delta\rho}{\bar{\rho}} \right) \sin^2 \theta_S - \frac{1}{2} \frac{\Delta\beta}{\bar{\beta}} \tan^2 \theta_S \sin^2 \theta_S$$

$$R_{SV\text{-aniso}}(\theta_S) = \frac{1}{2} \frac{\bar{\alpha}^2}{\bar{\beta}^2} (\Delta\varepsilon - \Delta\delta) \sin^2 \theta_S$$

In the S-wave reflectivity equations, note that θ_S is the S-wave angle of incidence and $Z_S = \rho\beta$ is the shear impedance. The weak anisotropy, weak contrast SH-to-SH reflectivity is (Rüger, 2001)

$$R_{SH}(\theta_S) = -\frac{1}{2} \frac{\Delta Z_S}{Z_S} + \frac{1}{2} \left(\frac{\Delta\beta}{\bar{\beta}} + \Delta\gamma \right) \tan^2 \theta_S$$

The P–S converted wave reflectivity in VTI media is given by (Rüger, 2001)

$$R_{PS}(\theta_S) = R_{PS\text{-iso}}(\theta_S) + R_{PS\text{-aniso}}(\theta_S)$$

$$R_{PS\text{-iso}}(\theta_S) \approx -\frac{1}{2} \frac{\Delta\rho}{\bar{\rho}} \frac{\sin \theta_P}{\sin \theta_S} - \frac{\bar{\beta}}{\bar{\alpha}} \left(2 \frac{\Delta\beta}{\bar{\beta}} + \frac{\Delta\rho}{\bar{\rho}} \right) \sin \theta_P \cos \theta_P$$

$$+ \left(\frac{\bar{\beta}}{\bar{\alpha}} \right)^2 \left(2 \frac{\Delta\beta}{\bar{\beta}} + \frac{\Delta\rho}{\bar{\rho}} \right) \frac{\sin^3 \theta_P}{\cos \theta_S}$$

$$R_{PS\text{-aniso}}(\theta_S) = \left[\left(\frac{\bar{\alpha}^2}{2(\bar{\alpha}^2 - \bar{\beta}^2) \cos \theta_S} - \frac{\bar{\alpha}\bar{\beta} \cos \theta_P}{2(\bar{\alpha}^2 - \bar{\beta}^2)} \right) (\delta_2 - \delta_1) \right] \sin \theta_P$$

$$+ \left[\frac{\bar{\alpha}\bar{\beta} \cos \theta_P}{(\bar{\alpha}^2 - \bar{\beta}^2)} (\delta_2 - \delta_1 + \varepsilon_1 - \varepsilon_2) \right] \sin^3 \theta_P$$

$$- \left[\frac{\bar{\alpha}^2}{(\bar{\alpha}^2 - \bar{\beta}^2) \cos \theta_S} (\delta_2 - \delta_1 + \varepsilon_1 - \varepsilon_2) \right] \sin^3 \theta_P$$

$$+ \left[\frac{\bar{\beta}^2}{2(\bar{\alpha}^2 - \bar{\beta}^2) \cos \theta_S} (\delta_1 - \delta_2) \right] \sin^3 \theta_P$$

$$+ \left[\frac{\bar{\beta}^2}{(\bar{\alpha}^2 - \bar{\beta}^2) \cos \theta_S} (\delta_2 - \delta_1 + \varepsilon_1 - \varepsilon_2) \right] \sin^5 \theta_P$$

Transversely isotropic media: HTI

In HTI (transversely isotropic with horizontal symmetry axis) media, reflectivity will vary with azimuth, ζ , as well as offset or incident angle θ . Rüger (1995, 1996) and Chen (1995) derived the P-wave reflection coefficient in the symmetry planes for reflections at the boundary of two HTI media sharing the same symmetry axis. At a horizontal interface between two HTI media with horizontal symmetry axis x_1 and vertical axis x_3 , the P-wave reflectivity for propagation in the vertical symmetry axis plane (x_1 - x_3 plane) parallel to the x_1 symmetry axis can be written as

$$\begin{aligned}
 R_{PP}(\zeta = 0, \theta) &\approx \frac{1}{2} \frac{\Delta Z}{\bar{Z}} + \frac{1}{2} \left[\frac{\Delta \alpha}{\bar{\alpha}} - \left(\frac{2\bar{\beta}^\perp}{\bar{\alpha}} \right)^2 \frac{\Delta \mu^\perp}{\bar{\mu}^\perp} + \Delta \delta^{(v)} \right] \\
 &\quad \times \sin^2 \theta + \frac{1}{2} \left[\frac{\Delta \alpha}{\bar{\alpha}} + \Delta \varepsilon^{(v)} \right] \sin^2 \theta \tan^2 \theta \\
 &\approx \frac{1}{2} \frac{\Delta Z}{\bar{Z}} + \frac{1}{2} \left[\frac{\Delta \alpha}{\bar{\alpha}} - \left(\frac{2\bar{\beta}}{\bar{\alpha}} \right)^2 \left(\frac{\Delta \mu}{\bar{\mu}} - 2\Delta \gamma \right) + \Delta \delta^{(v)} \right] \\
 &\quad \times \sin^2 \theta + \frac{1}{2} \left[\frac{\Delta \alpha}{\bar{\alpha}} + \Delta \varepsilon^{(v)} \right] \sin^2 \theta \tan^2 \theta
 \end{aligned}$$

where the azimuth angle ζ is measured from the x_1 -axis and the incident angle θ is defined with respect to x_3 . The isotropic part $R_{PP\text{-iso}}(\theta)$ is the same as before. In the preceding expression

$$\begin{aligned}
 \alpha &= \sqrt{\frac{C_{33}}{\rho}}; \quad \varepsilon^{(v)} = \frac{C_{11} - C_{33}}{2C_{33}} \\
 \beta &= \sqrt{\frac{C_{44}}{\rho}}; \quad \delta^{(v)} = \frac{(C_{13} + C_{55})^2 - (C_{33} - C_{55})^2}{2C_{33}(C_{33} - C_{55})} \\
 \beta^\perp &= \sqrt{\frac{C_{55}}{\rho}}; \quad \gamma^{(v)} = \frac{C_{66} - C_{44}}{2C_{44}} = -\frac{\gamma}{1 + 2\gamma} \\
 \gamma &= \frac{C_{44} - C_{66}}{2C_{66}}
 \end{aligned}$$

where β is the velocity of a vertically propagating shear wave polarized in the x_2 direction and β^\perp is the velocity of a vertically propagating shear wave polarized in the x_1 direction. $\mu = c_{44}$ and $\mu^\perp = c_{55}$ are the shear moduli corresponding to the shear velocities β and β^\perp . In the vertical symmetry plane (x_2 - x_3 plane), perpendicular to the symmetry axis, the P-wave reflectivity resembles the isotropic solution:

$$R_{PP}\left(\zeta = \frac{\pi}{2}, \theta\right) \approx \frac{1}{2} \left(\frac{\Delta Z}{\bar{Z}} \right) + \frac{1}{2} \left[\frac{\Delta \alpha}{\bar{\alpha}} - \left(\frac{2\bar{\beta}}{\bar{\alpha}} \right)^2 \frac{\Delta \mu}{\bar{\mu}} \right] \sin^2 \theta + \frac{1}{2} \left(\frac{\Delta \alpha}{\bar{\alpha}} \right) \sin^2 \theta \tan^2 \theta$$

In nonsymmetry planes, Rüger (1996) derived the P-wave reflectivity $R_{PP}(\zeta, \theta)$ using a perturbation technique as follows:

$$R_{PP}(\zeta, \theta) \approx \frac{1}{2} \frac{\Delta Z}{\bar{Z}} + \frac{1}{2} \left[\frac{\Delta \alpha}{\bar{\alpha}} - \left(\frac{2\bar{\beta}}{\bar{\alpha}} \right)^2 \frac{\Delta \mu}{\mu} + \left(\Delta \delta^{(V)} + 2 \left(\frac{2\bar{\beta}}{\bar{\alpha}} \right)^2 \Delta \gamma \right) \cos^2 \zeta \right] \sin^2 \theta \\ + \frac{1}{2} \left[\frac{\Delta \alpha}{\bar{\alpha}} + \Delta \varepsilon^{(V)} \cos^4 \zeta + \Delta \delta^{(V)} \sin^2 \zeta \cos^2 \zeta \right] \sin^2 \theta \tan^2 \theta$$

where ζ is the azimuth relative to the x_1 -axis.

The reflectivity for SV- and SH-waves in the symmetry axis plane (x_1 - x_3 plane) of the HTI medium is given by (Rüger, 2001)

$$R_{SV}(\theta_S) \approx R_{SV\text{-iso}}(\theta_S) + \frac{1}{2} \left(\frac{\bar{\alpha}}{\bar{\beta}^\perp} \right)^2 \left(\Delta \varepsilon^{(V)} - \Delta \delta^{(V)} \right) \sin^2 \theta_S$$

$$R_{SH}(\theta_S) \approx R_{SH\text{-iso}}(\theta_S) + \frac{1}{2} \Delta \gamma^{(V)} \tan^2 \theta_S$$

where

$$R_{SV\text{-iso}}(\theta_S) \approx -\frac{1}{2} \frac{\Delta Z_S^\perp}{\bar{Z}_S^\perp} + \left(\frac{7}{2} \frac{\Delta \beta^\perp}{\bar{\beta}^\perp} + 2 \frac{\Delta \rho}{\bar{\rho}} \right) \sin^2 \theta_S - \frac{1}{2} \frac{\Delta \beta^\perp}{\bar{\beta}^\perp} \tan^2 \theta_S \sin^2 \theta_S$$

$$R_{SH\text{-iso}}(\theta_S) = -\frac{1}{2} \frac{\Delta Z_S}{\bar{Z}_S} + \frac{1}{2} \left(\frac{\Delta \beta}{\bar{\beta}} \right) \tan^2 \theta_S$$

For waves propagating in the (x_2 - x_3) plane

$$R_{SV}(\theta_S) \approx -\frac{1}{2} \frac{\Delta Z_S}{\bar{Z}_S} + \left(\frac{7}{2} \frac{\Delta \beta}{\bar{\beta}} + 2 \frac{\Delta \rho}{\bar{\rho}} \right) \sin^2 \theta_S - \frac{1}{2} \frac{\Delta \beta}{\bar{\beta}} \tan^2 \theta_S \sin^2 \theta_S$$

$$R_{SH}(\theta_S) = -\frac{1}{2} \frac{\Delta Z_S^\perp}{\bar{Z}_S^\perp} + \frac{1}{2} \left(\frac{\Delta \beta^\perp}{\bar{\beta}^\perp} \right) \tan^2 \theta_S$$

Orthorhombic media

The anisotropic parameters in orthorhombic media are given by Chen (1995) and Tsvankin (1997) as follows:

$$\alpha = \sqrt{\frac{C_{33}}{\rho}}; \quad \beta = \sqrt{\frac{C_{44}}{\rho}}; \quad \beta^\perp = \sqrt{\frac{C_{55}}{\rho}}$$

$$\varepsilon^{(1)} = \frac{C_{22} - C_{33}}{2C_{33}}; \quad \varepsilon^{(2)} = \frac{C_{11} - C_{33}}{2C_{33}}$$

$$\delta^{(1)} = \frac{(C_{23} + C_{44})^2 - (C_{33} - C_{44})^2}{2C_{33}(C_{33} - C_{44})}$$

$$\delta^{(2)} = \frac{(C_{13} + C_{55})^2 - (C_{33} - C_{55})^2}{2C_{33}(C_{33} - C_{55})}$$

$$\gamma = \frac{C_{44} - C_{55}}{2C_{55}}; \quad \gamma^{(1)} = \frac{C_{66} - C_{55}}{2C_{55}}; \quad \gamma^{(2)} = \frac{C_{66} - C_{44}}{2C_{44}}$$

The parameters $\varepsilon^{(1)}$ and $\delta^{(1)}$ are Thomsen's parameters for the equivalent TIV media in the x_2 – x_3 plane. Similarly, $\varepsilon^{(2)}$ and $\delta^{(2)}$ are Thomsen's parameters for the equivalent TIV media in the x_1 – x_3 plane; γ_2 represents the velocity anisotropy between two shear-wave modes traveling along the z -axis. The difference in the approximate P-wave reflection coefficient in the two vertical symmetry planes (with x_3 as the vertical axis) of orthorhombic media is given by Rüger (1995, 1996) in the following form:

$$R_{PP}^{(x_1, x_3)}(\theta) - R_{PP}^{(x_2, x_3)}(\theta) \approx \left[\frac{\Delta\delta^{(2)} - \Delta\delta^{(1)}}{2} + \left(\frac{2\bar{\beta}}{\bar{\alpha}} \right)^2 \Delta\gamma \right] \sin^2 \theta + \left[\frac{\Delta\varepsilon^{(2)} - \Delta\varepsilon^{(1)}}{2} \right] \sin^2 \theta \tan^2 \theta$$

The equations are good approximations for angles of incidence of up to 30° – 40° .

Rüger (2001) gives the following expressions for P-wave reflectivity in the orthorhombic symmetry planes:

$$R_{PP}^{(x_1, x_3)}(\theta) \approx \frac{1}{2} \frac{\Delta Z}{Z} + \frac{1}{2} \left[\frac{\Delta\alpha}{\bar{\alpha}} - \left(\frac{2\bar{\beta}^\perp}{\bar{\alpha}} \right)^2 \frac{\Delta\mu^\perp}{\bar{\mu}^\perp} + \Delta\delta^{(2)} \right] \sin^2 \theta + \frac{1}{2} \left(\frac{\Delta\alpha}{\bar{\alpha}} + \Delta\varepsilon^{(2)} \right) \sin^2 \theta \tan^2 \theta$$

$$R_{PP}^{(x_2, x_3)}(\theta) \approx \frac{1}{2} \frac{\Delta Z}{Z} + \frac{1}{2} \left[\frac{\Delta\alpha}{\bar{\alpha}} - \left(\frac{2\bar{\beta}}{\bar{\alpha}} \right)^2 \frac{\Delta\mu}{\bar{\mu}} + \Delta\delta^{(1)} \right] \sin^2 \theta + \frac{1}{2} \left(\frac{\Delta\alpha}{\bar{\alpha}} + \Delta\varepsilon^{(1)} \right) \sin^2 \theta \tan^2 \theta$$

Jílek (2002a, b) derived expressions for P-to-SV reflectivity for arbitrary weak anisotropy and weak layer contrasts. In the case of orthorhombic and higher symmetries with aligned vertical symmetry planes, the expressions for P–SV in the vertical symmetry planes simplify to

$$R_{P-SV} = B_1 \frac{\sin \phi_P}{\cos \phi_S} + B_2 \cos \phi_P \sin \phi_P + B_3 \frac{\sin^3 \phi_P}{\cos \phi_S} + B_4 \cos \phi_P \sin^3 \phi_P + B_5 \frac{\sin^5 \phi_P}{\cos \phi_S}$$

where ϕ_P is the P-wave incident phase angle and ϕ_S is the converted S-wave reflection phase angle.

In the x – z symmetry plane (the z -axis is vertical), the coefficients B_i are

$$B_1 = -\frac{1}{2} \frac{\Delta\rho}{\bar{\rho}} + \frac{\bar{\alpha}^2}{2(\bar{\alpha}^2 - \bar{\beta}^2)} \left(\tilde{\delta}_2^{(2)} - \tilde{\delta}_1^{(2)} \right)$$

$$B_2 = -\frac{\bar{\beta}}{\bar{\alpha}} \frac{\Delta\rho}{\bar{\rho}} - 2 \frac{\bar{\beta}}{\bar{\alpha}} \frac{\Delta\beta}{\bar{\beta}} - \frac{\bar{\alpha}\bar{\beta}}{2(\bar{\alpha}^2 - \bar{\beta}^2)} \left(\tilde{\delta}_2^{(2)} - \tilde{\delta}_1^{(2)} \right)$$

$$B_3 = \frac{\bar{\beta}^2}{\bar{\alpha}^2} \frac{\Delta \rho}{\bar{\rho}} + 2 \frac{\bar{\beta}^2}{\bar{\alpha}^2} \frac{\Delta \beta}{\bar{\beta}} + \frac{\bar{\beta}^2}{2(\bar{\alpha}^2 - \bar{\beta}^2)} \left(\tilde{\delta}_1^{(2)} - \tilde{\delta}_2^{(2)} \right)$$

$$+ \frac{\bar{\alpha}^2}{(\bar{\alpha}^2 - \bar{\beta}^2)} \left[\left(\varepsilon_2^{(2)} - \varepsilon_1^{(2)} \right) + \left(\tilde{\delta}_1^{(2)} - \tilde{\delta}_2^{(2)} \right) \right]$$

$$B_4 = - \frac{\bar{\alpha} \bar{\beta}}{(\bar{\alpha}^2 - \bar{\beta}^2)} \left[\left(\varepsilon_2^{(2)} - \varepsilon_1^{(2)} \right) + \left(\tilde{\delta}_1^{(2)} - \tilde{\delta}_2^{(2)} \right) \right]$$

$$B_5 = - \frac{\bar{\beta}^2}{(\bar{\alpha}^2 - \bar{\beta}^2)} \left[\left(\varepsilon_2^{(2)} - \varepsilon_1^{(2)} \right) + \left(\tilde{\delta}_1^{(2)} - \tilde{\delta}_2^{(2)} \right) \right]$$

and in the y - z symmetry plane, the coefficients are

$$B_1 = - \frac{1}{2} \frac{\Delta \rho}{\bar{\rho}} + \frac{\bar{\alpha}^2}{2(\bar{\alpha}^2 - \bar{\beta}^2)} \left(\tilde{\delta}_2^{(1)} - \tilde{\delta}_1^{(1)} \right)$$

$$B_2 = - \frac{\bar{\beta}}{\bar{\alpha}} \frac{\Delta \rho}{\bar{\rho}} - 2 \frac{\bar{\beta}}{\bar{\alpha}} \frac{\Delta \beta}{\bar{\beta}} - \frac{\bar{\alpha} \bar{\beta}}{2(\bar{\alpha}^2 - \bar{\beta}^2)} \left(\tilde{\delta}_2^{(1)} - \tilde{\delta}_1^{(1)} \right) - 2 \frac{\bar{\beta}}{\bar{\alpha}} \left(\gamma_2^{(s)} - \gamma_1^{(s)} \right)$$

$$B_3 = \frac{\bar{\beta}^2}{\bar{\alpha}^2} \frac{\Delta \rho}{\bar{\rho}} + 2 \frac{\bar{\beta}^2}{\bar{\alpha}^2} \frac{\Delta \beta}{\bar{\beta}} + \frac{\bar{\beta}^2}{2(\bar{\alpha}^2 - \bar{\beta}^2)} \left(\tilde{\delta}_1^{(1)} - \tilde{\delta}_2^{(1)} \right)$$

$$+ \frac{\bar{\alpha}^2}{(\bar{\alpha}^2 - \bar{\beta}^2)} \left[\left(\varepsilon_2^{(1)} - \varepsilon_1^{(1)} \right) + \left(\tilde{\delta}_1^{(1)} - \tilde{\delta}_2^{(1)} \right) + 2 \frac{\bar{\beta}^2}{\bar{\alpha}^2} \left(\gamma_2^{(s)} - \gamma_1^{(s)} \right) \right]$$

$$B_4 = - \frac{\bar{\alpha} \bar{\beta}}{(\bar{\alpha}^2 - \bar{\beta}^2)} \left[\left(\varepsilon_2^{(1)} - \varepsilon_1^{(1)} \right) + \left(\tilde{\delta}_1^{(1)} - \tilde{\delta}_2^{(1)} \right) \right]$$

$$B_5 = - \frac{\bar{\beta}^2}{(\bar{\alpha}^2 - \bar{\beta}^2)} \left[\left(\varepsilon_2^{(1)} - \varepsilon_1^{(1)} \right) + \left(\tilde{\delta}_1^{(1)} - \tilde{\delta}_2^{(1)} \right) \right]$$

In these expressions, a subscript 1 on $\varepsilon_1^{(m)}$, $\tilde{\delta}_1^{(m)}$, and $\gamma_1^{(s)}$ refers to properties of the incident layer and a subscript 2 on $\varepsilon_2^{(m)}$, $\tilde{\delta}_2^{(m)}$, and $\gamma_2^{(s)}$ refers to properties of the reflecting layer. “Background” isotropic P- and S-wave velocities are defined within each layer ($I = 1, 2$ refer to the incident and reflecting layers, respectively) and can be taken to be equal to the actual vertical velocities within those layers:

$$\alpha_I = \sqrt{A_{33}^{(I)}}; \quad \beta_I = \sqrt{A_{55}^{(I)}}$$

In addition, the overall isotropic “background” P-wave velocity, S-wave velocity, and density are defined as averages over the two layers:

$$\bar{\alpha} = \frac{1}{2}(\alpha_1 + \alpha_2); \quad \bar{\beta} = \frac{1}{2}(\beta_1 + \beta_2); \quad \bar{\rho} = \frac{1}{2}(\rho_1 + \rho_2)$$

and contrasts across the boundary are defined as

$$\Delta\alpha = \alpha_2 - \alpha_1; \quad \Delta\beta = \beta_2 - \beta_1; \quad \Delta\rho = \rho_2 - \rho_1$$

The anisotropic parameters of each layer are defined as

$$\begin{aligned} \varepsilon_I^{(1)} &= \frac{A_{22}^{(I)} - A_{33}^{(I)}}{2A_{33}^{(I)}}; & \tilde{\delta}_I^{(1)} &= \frac{A_{23}^{(I)} + 2A_{44}^{(I)} - A_{33}^{(I)}}{A_{33}^{(I)}} \\ \varepsilon_I^{(2)} &= \frac{A_{11}^{(I)} - A_{33}^{(I)}}{2A_{33}^{(I)}}; & \tilde{\delta}_I^{(2)} &= \frac{A_{13}^{(I)} + 2A_{55}^{(I)} - A_{33}^{(I)}}{A_{33}^{(I)}} \\ \gamma_I^{(S)} &= \frac{A_{44}^{(I)} - A_{55}^{(I)}}{2A_{55}^{(I)}}; & \tilde{\delta}_I^{(3)} &= \frac{A_{12}^{(I)} + 2A_{66}^{(I)} - A_{11}^{(I)}}{A_{11}^{(I)}} \end{aligned}$$

where $A_{jk}^{(I)}$ are the density-normalized Voigt-notation elastic constants of each layer.

In the approximation of weak anisotropy and weak layer contrasts, ϕ_S can be related approximately to ϕ_P using the linearized isotropic Snell's law:

$$\frac{1}{\cos \phi_S} \approx \frac{1}{\sqrt{1 - (\beta^2/\alpha^2) \sin^2 \phi_P}} \approx 1 + \frac{1}{2} \frac{\bar{\beta}^2}{\bar{\alpha}^2} \sin^2 \phi_P$$

Arbitrary anisotropy

Vavryčuk and Pšenčík (1998) derived P-wave reflectivity for arbitrary weak anisotropy and weak layer contrast:

$$\begin{aligned} R_{PP}(\zeta, \theta_P) &= \frac{1}{2} \frac{\Delta Z}{\bar{Z}} + \frac{1}{2} \left[\frac{\Delta\alpha}{\bar{\alpha}} - 4 \left(\frac{\bar{\beta}}{\bar{\alpha}} \right)^2 \frac{\Delta\mu}{\bar{\mu}} \right] \sin^2 \theta_P + \frac{1}{2} \frac{\Delta\alpha}{\bar{\alpha}} \tan^2 \theta_P \sin^2 \theta_P \\ &\quad + \frac{1}{2} \left\{ \Delta \left(\frac{A_{13} + 2A_{55} - A_{33}}{A_{33}} \right) \cos^2 \zeta \right. \\ &\quad + \left[\Delta \left(\frac{A_{23} + 2A_{44} - A_{33}}{A_{33}} \right) - 8\Delta \left(\frac{A_{44} - A_{55}}{2A_{33}} \right) \right] \sin^2 \zeta \\ &\quad + 2 \left[\Delta \left(\frac{A_{36} + 2A_{45}}{A_{33}} \right) - 4\Delta \left(\frac{A_{45}}{A_{33}} \right) \right] \cos \zeta \sin \zeta \left. \right\} \sin^2 \theta_P \\ &\quad + \frac{1}{2} \left[\Delta \left(\frac{A_{11} - A_{33}}{2A_{33}} \right) \cos^4 \zeta + \Delta \left(\frac{A_{22} - A_{33}}{2A_{33}} \right) \sin^4 \zeta \right. \\ &\quad + \Delta \left(\frac{A_{12} + 2A_{66} - A_{33}}{A_{33}} \right) \cos^2 \zeta \sin^2 \zeta + 2\Delta \left(\frac{A_{16}}{A_{33}} \right) \cos^3 \zeta \sin \zeta \\ &\quad \left. + 2\Delta \left(\frac{A_{26}}{A_{33}} \right) \cos \zeta \sin^3 \zeta \right] \sin^2 \theta_P \tan^2 \theta_P \end{aligned}$$

where $A_{ij} = c_{ij}/\rho$ is the Voigt-notation elastic constant divided by density. θ_P is the P-wave angle of incidence and ζ is the azimuth relative to the x_1 -axis. Δ signifies the contrast of any parameter across the reflector, e.g., $\Delta\psi = \psi_2 - \psi_1$. $\bar{\alpha}$, $\bar{\beta}$, and $\bar{\rho}$ are the background average isotropic P-wave velocity, S-wave velocity, and density, respectively. The accuracy of the result varies slightly with the choice of the background values, but a reasonable choice is the average of the vertical P-wave velocities across the two layers for $\bar{\alpha}$, the average of the vertical S-wave velocities across the reflector for $\bar{\beta}$, and the average of the densities across the two layers for $\bar{\rho}$. The corresponding expression for the P-wave transmission coefficient for arbitrary anisotropy is given by Pšenčík and Vavryčuk (1998).

Jílek (2002a,b) derived expressions for P-to-SV reflectivities for arbitrary weak anisotropy and weak layer contrasts.

Assumptions and limitations

The equations presented in this section apply under the following conditions:

- the rock is linear elastic;
- approximate forms apply to the P–P reflection at near offset for slightly contrasting, weakly anisotropic media.

3.7 Elastic impedance

The elastic impedance is a **pseudo-impedance attribute** (Connolly, 1998; Mukerji *et al.*, 1998) and is a far-offset equivalent of the more conventional zero-offset acoustic impedance. This far-offset impedance has been called the “elastic impedance” (EI), as it contains information about the V_P/V_S ratio. One can obtain the elastic impedance cube from a far-offset stack using the same trace-based one-dimensional inversion algorithm used to invert the near-offset stack. Though only approximate, the inversion for elastic impedance is economical and simple compared to full prestack inversion. As with any impedance inversion, the key to effectively using this extracted attribute for quantitative reservoir characterization is calibration with log data.

The acoustic impedance, $I_a = \rho V_P$, can be expressed as

$$I_a = \exp\left(2 \int R_{PP}(0) dt\right)$$

where $R_{PP}(0)$ is the time sequence of normal-incidence P-to-P reflection coefficients. Similarly, the **elastic impedance** may be defined in terms of the sequence of non-normal P–P reflection coefficients, $R_{PP}(\theta)$, at incidence angle θ as

$$I_e(\theta) = \exp\left(2 \int R_{PP}(\theta) dt\right)$$

Substituting into this equation one of the well-known approximations for $R_{PP}(\theta)$ (e.g., Aki and Richards, 1980),

$$R_{PP}(\theta) \approx R_{PP}(0) + M \sin^2 \theta + N \tan^2 \theta$$

$$R_{PP}(0) = \frac{1}{2} \left(\frac{\Delta V_P}{\bar{V}_P} + \frac{\Delta \rho}{\bar{\rho}} \right)$$

$$M = -2 \left(\frac{\bar{V}_S}{\bar{V}_P} \right)^2 \left(\frac{2\Delta V_S}{\bar{V}_S} + \frac{\Delta \rho}{\bar{\rho}} \right)$$

$$N = \frac{1}{2} \frac{\Delta V_P}{\bar{V}_P}$$

leads to the following expression for I_e :

$$I_e(\theta) = \rho V_P \exp \left[\tan^2 \theta \int d(\ln V_P) \right] \exp \left[-4 \sin^2 \theta (\bar{V}_S/\bar{V}_P)^2 \int 2d(\ln V_S) \right] \\ \times \exp \left[-4 \sin^2 \theta (\bar{V}_S/\bar{V}_P)^2 \int d(\ln \rho) \right]$$

or

$$I_e(\theta) = V_P^{(1+\tan^2 \theta)} \rho^{(1-4K \sin^2 \theta)} V_S^{(-8K \sin^2 \theta)}$$

where $K = (\bar{V}_S/\bar{V}_P)^2$ is taken to be a constant. The elastic impedance reduces to the usual acoustic impedance, $I_a = \rho V_P$, when $\theta = 0$. Unlike the acoustic impedance, the elastic impedance is not a function of the rock properties alone but also depends on the angle of incidence. Using only the first two terms in the approximation for $R(\theta)$ gives a similar expression for I_e with the $\tan^2 \theta$ terms being replaced by $\sin^2 \theta$,

$$I_e(\theta) = V_P^{(1+\sin^2 \theta)} \rho^{(1-4K \sin^2 \theta)} V_S^{(-8K \sin^2 \theta)}$$

This last expression has been referred to as the **first-order elastic impedance** (Connolly, 1999), and it goes to $(V_P/V_S)^2$ at $\theta = 90^\circ$, assuming $K = \frac{1}{4}$. Expressions for P-to-S converted-wave elastic impedance have been given by Duffaut *et al.* (2000) and González (2006). The elastic impedance has strange units and dimensions

that change with angle. Whitcombe (2002) defines a useful normalization for the elastic impedance:

$$I_e(\theta) = [V_{P0}\rho_0] \left(\frac{V_P}{V_{P0}} \right)^{(1+\tan^2 \theta)} \left(\frac{\rho}{\rho_0} \right)^{(1-4K \sin^2 \theta)} \left(\frac{V_S}{V_{S0}} \right)^{(-8K \sin^2 \theta)}$$

where the normalizing constants V_{P0} , V_{S0} , and ρ_0 may be taken to be either the average values of velocities and densities over the zone of interest, or the values at the top of the target zone. With this normalization, the elastic impedance has the same dimensionality as the acoustic impedance. The **extended elastic impedance** (EEI) (Whitcombe *et al.*, 2002) is defined over an angle χ , ranging from -90° to $+90^\circ$. The angle χ should not be interpreted as the actual reflection angle, but rather as the independent input variable in the definition of EEI. The EEI is expressed as

$$I_e(\chi) = [V_{P0}\rho_0] \left(\frac{V_P}{V_{P0}} \right)^{(\cos \chi + \sin \chi)} \left(\frac{\rho}{\rho_0} \right)^{(\cos \chi - 4K \sin \chi)} \left(\frac{V_S}{V_{S0}} \right)^{(-8K \sin \chi)}$$

Under certain approximations, the EEI for specific values of χ becomes proportional to rock elastic parameters such as the bulk modulus and the shear modulus.

In applications to reservoir characterization, care must be taken to filter the logs to match the seismic frequencies, as well as to account for the differences in frequency content in near- and far-offset data. Separate wavelets should be extracted for the near- and far-offset angle stacks. The inverted acoustic and elastic impedances co-located at the wells must be calibrated with the known facies and fluid types in the well, before classifying the seismic cube in the interwell region.

Major limitations in using partial-stack elastic-impedance inversion arise from the assumptions of the one-dimensional convolutional model for far offsets, the assumption of a constant value for K , and errors in estimates of the incidence angle. The convolutional model does not properly handle all the reflections at far offsets, because the primary reflections get mixed with other events. The approximations used to derive the expressions for elastic impedance become less accurate at larger angles. The first-order, two-term elastic impedance has been found to give stabler results than the three-term elastic impedance (Mallick, 2001). Mallick compares prestack inversion versus partial-stack elastic impedance inversions and recommends a hybrid approach. In this approach, full prestack inversion is done at a few control points to get reliable estimates of P and S impedance. These prestack inversions are used as anchors for cheaper, one-dimensional, trace-based inversions over large data volumes. Based on these results, small zones may be selected for detailed analysis by prestack inversions.

Elastic impedance expressions: isotropic

Table 3.7.1 Exponents in expressions for elastic impedance of an isotropic, flat-layered Earth, $EI \approx V_P^A V_S^B \rho^C$. In all expressions, θ is the P-wave angle of incidence and θ_S is the shear-wave angle of incidence. Expressions are given for P–P reflection, converted wave reflections P–S and S–P, and shear-wave reflections SV–SV and SH–SH. $\langle \bar{V}_S^2 / \bar{V}_P^2 \rangle$ and $\langle \bar{V}_S / \bar{V}_P \rangle$ are assumed to be constant, often taken as the average of the corresponding quantities.

P–P	A	$1 + \tan^2 \theta$
	B	$-8 \left\langle \frac{\bar{V}_S^2}{\bar{V}_P^2} \right\rangle \sin^2 \theta$
	C	$1 - 4 \left\langle \frac{\bar{V}_S^2}{\bar{V}_P^2} \right\rangle \sin^2 \theta$
P–SV	A	0
	B	$\frac{\sin \theta}{\sqrt{1 - \langle \bar{V}_S^2 / \bar{V}_P^2 \rangle \sin^2 \theta}} \left(4 \sin^2 \theta \left\langle \frac{\bar{V}_S^2}{\bar{V}_P^2} \right\rangle - 4 \left\langle \frac{\bar{V}_S}{\bar{V}_P} \right\rangle \cos \theta \sqrt{1 - \left\langle \frac{\bar{V}_S^2}{\bar{V}_P^2} \right\rangle \sin^2 \theta} \right)$
	C	$-\frac{\sin \theta}{\sqrt{1 - \langle \bar{V}_S^2 / \bar{V}_P^2 \rangle \sin^2 \theta}} \left(1 - 2 \left\langle \frac{\bar{V}_S^2}{\bar{V}_P^2} \right\rangle \sin^2 \theta + 2 \left\langle \frac{\bar{V}_S}{\bar{V}_P} \right\rangle \cos \theta \sqrt{1 - \left\langle \frac{\bar{V}_S^2}{\bar{V}_P^2} \right\rangle \sin^2 \theta} \right)$
SV–P	A	0
	B	$\frac{\sin \theta_S}{\sqrt{1 - \langle \bar{V}_S^2 / \bar{V}_P^2 \rangle^{-1} \sin^2 \theta_S}} \left(4 \sin^2 \theta_S - 4 \left\langle \frac{\bar{V}_S}{\bar{V}_P} \right\rangle \cos \theta_S \sqrt{1 - \left\langle \frac{\bar{V}_S^2}{\bar{V}_P^2} \right\rangle^{-1} \sin^2 \theta_S} \right)$
	C	$-\frac{\sin \theta_S}{\sqrt{1 - \langle \bar{V}_S^2 / \bar{V}_P^2 \rangle^{-1} \sin^2 \theta_S}} \left(1 - 2 \sin^2 \theta_S + 2 \left\langle \frac{\bar{V}_S}{\bar{V}_P} \right\rangle \cos \theta_S \sqrt{1 - \left\langle \frac{\bar{V}_S^2}{\bar{V}_P^2} \right\rangle^{-1} \sin^2 \theta_S} \right)$
SV–SV	A	0
	B	$-\frac{1}{\cos^2 \theta_S} + 8 \sin^2 \theta_S$
	C	$-1 + 4 \sin^2 \theta_S$
SH–SH	A	0
	B	$-1 + \tan^2 \theta_S$
	C	-1

Elastic impedance expressions: VTI anisotropic

Table 3.7.2 Exponents in expressions for elastic impedance of a VTI, flat-layered Earth, $EI \approx V_P^A V_S^B \rho^C \exp(D\varepsilon + E\delta + F\gamma^{(V)})$. θ is the P-wave angle of incidence, and θ_S is the shear-wave angle of incidence. Expressions are given for P–P reflection, and shear-wave reflections SV–SV and SH–SH. $\langle \bar{V}_S^2 / \bar{V}_P^2 \rangle$ is assumed to be constant, often taken as the average of the squared velocity ratio.

P–P	A	$1 + \tan^2 \theta$
	B	$-8 \left\langle \frac{\bar{V}_S^2}{\bar{V}_P^2} \right\rangle \sin^2 \theta$
	C	$1 - 4 \left\langle \frac{\bar{V}_S^2}{\bar{V}_P^2} \right\rangle \sin^2 \theta$
	D	$\sin^2 \theta \tan^2 \theta$
	E	$\sin^2 \theta$
	F	0
SV–SV	A	0
	B	$-\frac{1}{\cos^2 \theta_S} + 8 \sin^2 \theta_S$
	C	$-1 + 4 \sin^2 \theta_S$
	D	$\sin^2 \theta_S / \left\langle \frac{\bar{V}_S^2}{\bar{V}_P^2} \right\rangle$
	E	$-\sin^2 \theta_S / \left\langle \frac{\bar{V}_S^2}{\bar{V}_P^2} \right\rangle$
	F	0
SH–SH	A	0
	B	$-1 + \tan^2 \theta_S$
	C	-1
	D	0
	E	0
	F	$\tan^2 \theta_S$

$$V_P = \alpha = \sqrt{c_{33}/\rho}; \quad V_S = \beta = \sqrt{c_{44}/\rho}$$

$$\varepsilon = \frac{c_{11} - c_{33}}{2c_{33}}; \quad \gamma^{(V)} = \frac{c_{66} - c_{44}}{2c_{44}}; \quad \delta = \frac{(c_{13} + c_{44})^2 - (c_{33} - c_{44})^2}{2c_{33}(c_{33} - c_{44})}$$

Elastic impedance expressions: orthorhombic x_1 – x_3 symmetry plane

Table 3.7.3 Exponents in expressions for P–P elastic impedance of an orthorhombic, flat-layered Earth, $EI \approx V_P^A V_S^{\perp B} \rho^C \exp(D\varepsilon^{(2)} + E\delta^{(2)})$. θ is the P-wave angle of incidence. $\langle \bar{V}_S^2 / \bar{V}_P^2 \rangle$ is assumed to be constant, often taken as the average of the squared velocity ratio. $V_P = \sqrt{c_{33}/\rho}$; $V_S^{\perp} = \beta^{\perp} = \sqrt{c_{55}/\rho}$

P–P	A	$1 + \tan^2 \theta$
	B	$-8 \left\langle \frac{\bar{V}_S^{\perp 2}}{\bar{V}_P^2} \right\rangle \sin^2 \theta$
	C	$1 - 4 \left\langle \frac{\bar{V}_S^{\perp 2}}{\bar{V}_P^2} \right\rangle \sin^2 \theta$
	D	$\sin^2 \theta \tan^2 \theta$
	E	$\sin^2 \theta$

Elastic impedance expressions: orthorhombic x_2 – x_3 symmetry plane

Table 3.7.4 Exponents in expressions for P–P elastic impedance of an orthorhombic, flat-layered Earth, $EI \approx V_P^A V_S^B \rho^C \exp(D\varepsilon^{(1)} + E\delta^{(1)})$. θ is the P-wave angle of incidence. $\langle \bar{V}_S^{\perp 2} / \bar{V}_P^2 \rangle$ is assumed to be constant, often taken as the average of the squared velocity ratio. $V_P = \sqrt{c_{33}/\rho}$; $V_S = \beta = \sqrt{c_{44}/\rho}$

P–P	A	$1 + \tan^2 \theta$
	B	$-8 \left\langle \frac{\bar{V}_S^2}{\bar{V}_P^2} \right\rangle \sin^2 \theta$
	C	$1 - 4 \left\langle \frac{\bar{V}_S^2}{\bar{V}_P^2} \right\rangle \sin^2 \theta$
	D	$\sin^2 \theta \tan^2 \theta$
	E	$\sin^2 \theta$

$$\begin{aligned}\varepsilon^{(2)} &= \frac{c_{11} - c_{33}}{2c_{33}}; & \varepsilon^{(1)} &= \frac{c_{22} - c_{33}}{2c_{33}} \\ \delta^{(2)} &= \frac{(c_{13} + c_{55})^2 - (c_{33} - c_{55})^2}{2c_{33}(c_{33} - c_{55})}; & \delta^{(1)} &= \frac{(c_{23} + c_{44})^2 - (c_{33} - c_{44})^2}{2c_{33}(c_{33} - c_{44})} \\ \gamma^{(2)} &= \frac{c_{66} - c_{44}}{2c_{44}}; & \gamma^{(1)} &= \frac{c_{66} - c_{55}}{2c_{55}} \\ \delta^{(3)} &= \frac{(c_{12} + c_{66})^2 - (c_{11} - c_{66})^2}{2c_{11}(c_{11} - c_{66})}\end{aligned}$$

Uses

The elastic impedance provides an alternative for interpreting far-offset data. As with any inversion, the elastic impedance removes some wavelet effects and attempts to determine interval properties from the band-limited reflectivity (seismic traces).

Assumptions and limitations

Limitations of using partial-stack elastic impedance inversion arise from the assumptions of the one-dimensional convolutional model for far offsets, the assumption of a constant value for $K = (V_S/V_P)^2$, and errors in estimates of the incidence angle. The convolutional model does not properly handle all the reflections at far offsets because the primary reflections get mixed with other events. Furthermore, approximations used to derive the expressions for elastic impedance get worse at larger angles. The first-order two-term elastic impedance has been found to give more stable results than the three-term elastic impedance (Mallick, 2001).

3.8 Viscoelasticity and Q

Synopsis

Materials are **linear elastic** when the stress is proportional to the strain:

$$\frac{\sigma_{11} + \sigma_{22} + \sigma_{33}}{3} = K(\varepsilon_{11} + \varepsilon_{22} + \varepsilon_{33}) \quad \text{volumetric}$$

$$\sigma_{ij} = 2\mu\varepsilon_{ij}, \quad i \neq j \quad \text{shear}$$

$$\sigma_{ij} = \lambda\delta_{ij}\varepsilon_{kk} + 2\mu\varepsilon_{ij} \quad \text{general isotropic}$$

where σ_{ij} and ε_{ij} are the stress and strain, K is the bulk modulus, μ is the shear modulus, and λ is Lamé's coefficient.

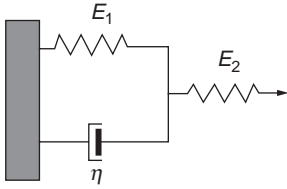


Figure 3.8.1 Schematic of a spring and dashpot system for which the force – displacement relation is described by the same equation as the standard linear solid.

In contrast, **linear, viscoelastic** materials also depend on rate or history, which can be incorporated by using time derivatives. For example, shear stress and shear strain may be related by using one of the following simple models:

$$\dot{\epsilon}_{ij} = \frac{\dot{\sigma}_{ij}}{2\mu} + \frac{\sigma_{ij}}{2\eta} \quad \text{Maxwell solid} \quad (3.8.1)$$

$$\sigma_{ij} = 2\eta\dot{\epsilon}_{ij} + 2\mu\epsilon_{ij} \quad \text{Voigt solid} \quad (3.8.2)$$

$$\eta\dot{\sigma}_{ij} + (E_1 + E_2)\sigma_{ij} = E_2(\eta\dot{\epsilon}_{ij} + E_1\epsilon_{ij}) \quad \text{standardlinearsolid} \quad (3.8.3)$$

where E_1 and E_2 are additional elastic moduli and η is a material constant resembling viscosity.

More generally, one can incorporate higher-order derivatives, as follows:

$$\sum_{i=0}^N a_i \frac{\partial^i \epsilon}{\partial t^i} = \sum_{j=0}^M b_j \frac{\partial^j \sigma}{\partial t^j}$$

Similar equations would be necessary to describe the generalizations of other elastic constants such as K .

It is customary to represent these equations with mechanical spring and dashpot models such as that for the standard linear solid shown in [Figure 3.8.1](#).

Consider a wave propagating in a viscoelastic solid so that the displacement, for example, is given by

$$u(x, t) = u_0 \exp[-\alpha(\omega)x] \exp[i(\omega t - kx)] \quad (3.8.4)$$

Then at any point in the solid the stress and strain are out of phase

$$\sigma = \sigma_0 \exp[i(\omega t - kx)] \quad (3.8.5)$$

$$\epsilon = \epsilon_0 \exp[i(\omega t - kx - \varphi)] \quad (3.8.6)$$

The ratio of stress to strain at the point is the complex modulus, $M(\omega)$.

The **quality factor**, Q , is a measure of how dissipative the material is. The lower Q , the larger the dissipation is. There are several ways to express Q . One precise way is as the ratio of the imaginary and real parts of the complex modulus:

$$\frac{1}{Q} = \frac{M_I}{M_R}$$

In terms of energies, Q can be expressed as

$$\frac{1}{Q} = \frac{\Delta W}{2\pi W}$$

where ΔW is the energy dissipated per cycle of oscillation and W is the peak strain energy during the cycle. In terms of the spatial attenuation factor, α , in [equation \(3.8.4\)](#),

$$\frac{1}{Q} \approx \frac{\alpha V}{\pi f}$$

where V is the velocity and f is the frequency. In terms of the wave amplitudes of an oscillatory signal with period τ ,

$$\frac{1}{Q} \approx \frac{1}{\pi} \ln \left[\frac{u(t)}{u(t + \tau)} \right]$$

which measures the amplitude loss per cycle. This is sometimes called the **logarithmic decrement**. Finally, in terms of the phase delay φ between the stress and strain, as in [equations \(3.8.5\) and \(3.8.6\)](#)

$$\frac{1}{Q} \approx \tan(\varphi)$$

Winkler and Nur (1979) showed that if we define $Q_E = E_R/E_I$, $Q_K = K_R/K_I$, and $Q_\mu = \mu_R/\mu_I$, where the subscripts R and I denote real and imaginary parts of the Young, bulk, and shear moduli, respectively, and if the attenuation is small, then the various Q factors can be related through the following equations:

$$\begin{aligned} \frac{(1 - \nu)(1 - 2\nu)}{Q_P} &= \frac{(1 + \nu)}{Q_E} - \frac{2\nu(2 - \nu)}{Q_S}; & \frac{Q_P}{Q_S} &= \frac{\mu_I}{K_I + \frac{4}{3}\mu_I} \frac{V_P^2}{V_S^2} \\ \frac{(1 + \nu)}{Q_K} &= \frac{3(1 - \nu)}{Q_P} - \frac{2(1 - 2\nu)}{Q_S}; & \frac{3}{Q_E} &= \frac{(1 - 2\nu)}{Q_K} + \frac{2(1 + \nu)}{Q_S} \end{aligned}$$

One of the following relations always occurs (Bourbié *et al.*, 1987):

$$Q_K > Q_P > Q_E > Q_S \quad \text{for high } V_P/V_S \text{ ratios}$$

$$Q_K < Q_P < Q_E < Q_S \quad \text{for low } V_P/V_S \text{ ratios}$$

$$Q_K = Q_P = Q_E = Q_S$$

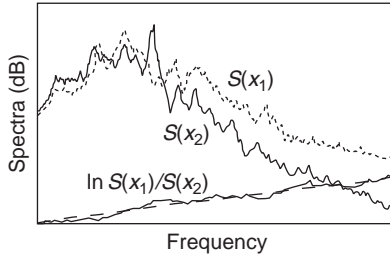


Figure 3.8.2 The slope of the log of the spectral ratio (difference of the spectra in dB) can be interpreted in terms of Q .

The **spectral ratio** method is a popular way to estimate Q in both the laboratory and the field. Because $1/Q$ is a measure of the fractional loss of energy per cycle of oscillation, after a fixed distance of propagation there is a tendency for shorter wavelengths to be attenuated more than longer wavelengths. If the amplitude of the propagating wave is

$$u(x, t) = u_0 \exp[-\alpha(\omega)x] = u_0 \exp\left(-\frac{\pi f}{VQ}x\right)$$

we can compare the spectral amplitudes at two different distances and determine Q from the slope of the logarithmic decrement (Figure 3.8.2):

$$\ln \left[\frac{S(f, x_2)}{S(f, x_1)} \right] = -\frac{\pi f}{QV}(x_2 - x_1)$$

A useful illustrative example is the **standard linear solid** (Zener, 1948) in equation (3.8.3). If we assume sinusoidal motion

$$\varepsilon = \varepsilon_0 e^{i\omega t}$$

$$\sigma = \sigma_0 e^{i\omega t}$$

and substitute into equation (3.8.3), we can write

$$\sigma_0 = M(\omega)\varepsilon_0$$

with the complex frequency-dependent modulus

$$M(\omega) = \frac{E_2(E_1 + i\omega\eta)}{E_1 + E_2 + i\omega\eta}$$

In the limits of low frequency and high frequency, we obtain the limiting moduli

$$M_0 = \frac{E_2 E_1}{E_1 + E_2}, \quad \omega \rightarrow 0$$

$$M_\infty = E_2, \quad \omega \rightarrow \infty$$

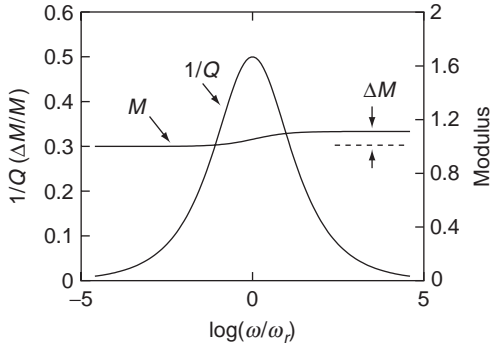


Figure 3.8.3 Schematic of the standard linear solid in the frequency domain.

Note that at very low frequencies and very high frequencies the moduli are real and independent of frequency, and thus in these limits the material behaves elastically. It is useful to rewrite the frequency-dependent complex modulus in terms of these limits:

$$M(\omega) = \frac{M_\infty \left[M_0 + i \frac{\omega}{\omega_r} (M_\infty M_0)^{1/2} \right]}{M_\infty + i \frac{\omega}{\omega_r} (M_\infty M_0)^{1/2}}$$

and

$$\begin{aligned} \text{Re}[M(\omega)] &= \frac{M_0 M_\infty \left[1 + (\omega/\omega_r)^2 \right]}{M_\infty + (\omega/\omega_r)^2 M_0} \\ \text{Im}[M(\omega)] &= \frac{(\omega/\omega_r) \sqrt{M_0 M_\infty} (M_\infty - M_0)}{M_\infty + (\omega/\omega_r)^2 M_0} \end{aligned}$$

where

$$\omega_r = \frac{\sqrt{E_1(E_1 + E_2)}}{\eta}$$

Similarly we can write Q as a function of frequency (Figure 3.8.3):

$$\begin{aligned} \frac{1}{Q} &= \frac{M_I(\omega)}{M_R(\omega)} \\ \frac{1}{Q} &= \frac{E_2}{\sqrt{E_1(E_1 + E_2)}} \frac{(\omega/\omega_r)}{1 + (\omega/\omega_r)^2} \end{aligned}$$

The maximum attenuation

$$\left(\frac{1}{Q} \right)_{\max} = \frac{1}{2} \frac{E_2}{\sqrt{E_1(E_1 + E_2)}}$$

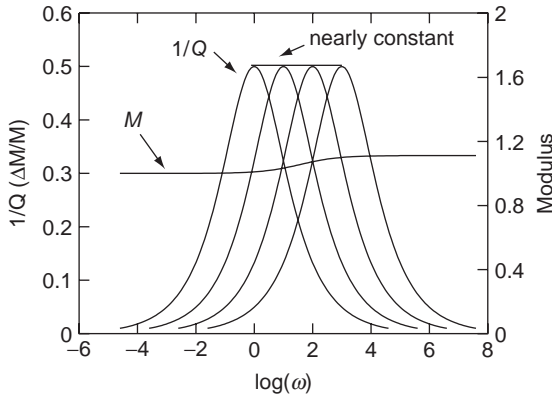


Figure 3.8.4 Schematic of the nearly constant Q model in the frequency domain.

$$\left(\frac{1}{Q}\right)_{\max} = \frac{1}{2} \frac{M_{\infty} - M_0}{\sqrt{M_{\infty} M_0}}$$

occurs at $\omega = \omega_r$. This is sometimes written as

$$\left(\frac{1}{Q}\right)_{\max} = \frac{1}{2} \frac{\Delta M}{\bar{M}} \quad (3.8.7)$$

where $\Delta M/\bar{M} = (M_{\infty} - M_0)/\bar{M}$ is the **modulus defect** and $\bar{M} = \sqrt{M_{\infty} M_0}$.

Liu *et al.* (1976) considered the **nearly constant Q model** in which simple attenuation mechanisms are combined so that the attenuation is nearly a constant over a finite range of frequencies (Figure 3.8.4). One can then write

$$\frac{V(\omega)}{V(\omega_0)} = 1 + \frac{1}{\pi Q} \ln\left(\frac{\omega}{\omega_0}\right)$$

which relates the velocity dispersion within the band of constant Q to the value of Q and the frequency. For large Q , this can be approximated as

$$\left(\frac{1}{Q}\right)_{\max} \approx \frac{\pi}{\log(\omega/\omega_0)} \left(\frac{1}{2} \frac{M - M_0}{M_0}\right) \quad (3.8.8)$$

where M and M_0 are the moduli at two different frequencies ω and ω_0 within the band where Q is nearly constant. Note the resemblance of this expression to equation (3.8.7) for the standard linear solid.

Kjartansson (1979) considered the **constant Q model** in which Q is strictly constant (Figure 3.8.5). In this case the complex modulus and Q are related by

$$M(\omega) = M_0 \left(\frac{i\omega}{\omega_0}\right)^{2\gamma}$$

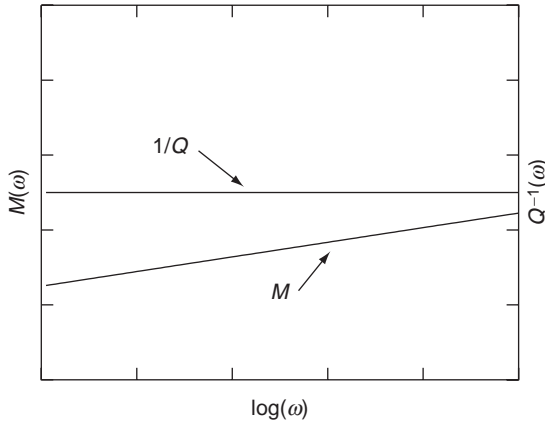


Figure 3.8.5 Schematic of the constant Q model in the frequency domain.

where

$$\gamma = \frac{1}{\pi} \tan^{-1} \left(\frac{1}{Q} \right)$$

For large Q , this can be approximated as

$$\left(\frac{1}{Q} \right)_{\max} \approx \frac{\pi}{\log(\omega/\omega_0)} \left(\frac{1}{2} \frac{M - M_0}{M_0} \right)$$

where M and M_0 are the moduli at two different frequencies ω and ω_0 . Note the resemblance of this expression to [equation \(3.8.7\)](#) for the standard linear solid and [equation \(3.8.8\)](#) for the nearly constant Q model.

Uses

The equations presented in this section are used for phenomenological modeling of attenuation and velocity dispersion of seismic waves.

Assumptions and limitations

The equations presented in this section assume that the material is linear, dissipative, and causal.

3.9 Kramers–Kronig relations between velocity dispersion and Q

Synopsis

For linear viscoelastic systems, causality requires that there be a very specific relation between velocity or modulus dispersion and Q ; that is, if the dispersion is

completely characterized for all frequencies then Q is known for all frequencies and vice versa.

We can write a viscoelastic constitutive law between the stress and strain components as

$$\sigma(t) = \frac{dr}{dt} * \varepsilon(t)$$

where $r(t)$ is the relaxation function and $*$ denotes convolution. Then in the Fourier domain we can write

$$\tilde{\sigma}(\omega) = M(\omega) \tilde{\varepsilon}(\omega)$$

where $M(\omega)$ is the complex modulus. For $r(t)$ to be causal, in the frequency domain the real and imaginary parts of $M(\omega)/(i\omega)$ must be Hilbert transform pairs (Bourbié *et al.*, 1987):

$$M_I(\omega) = \frac{\omega}{\pi} \int_{-\infty}^{+\infty} \frac{M_R(\alpha) - M_R(0)}{\alpha} \frac{d\alpha}{\alpha - \omega}$$

$$M_R(\omega) - M_R(0) = -\frac{\omega}{\pi} \int_{-\infty}^{+\infty} \frac{M_I(\alpha)}{\alpha} \frac{d\alpha}{\alpha - \omega}$$

where $M_R(0)$ is the real part of the modulus at zero frequency, which results because there is an instantaneous elastic response from a viscoelastic material. If we express this in terms of

$$Q^{-1} = \frac{M_I(\omega) \operatorname{sgn}(\omega)}{M_R(\omega)}$$

then we obtain

$$Q^{-1}(\omega) = \frac{|\omega|}{\pi M_R(\omega)} \int_{-\infty}^{+\infty} \frac{M_R(\alpha) - M_R(0)}{\alpha} \frac{d\alpha}{\alpha - \omega} \quad (3.9.1)$$

and its inverse

$$M_R(\omega) - M_R(0) = \frac{-\omega}{\pi} \int_{-\infty}^{+\infty} \frac{Q^{-1}(\alpha) M_R(\alpha)}{|\alpha|} \frac{d\alpha}{(\alpha - \omega)} \quad (3.9.2)$$

From these we see the expected result that a larger attenuation is generally associated with larger dispersion. Zero attenuation requires zero velocity dispersion.

One never has more than partial information about the frequency dependence of velocity and Q , but the Kramers–Kronig relation allows us to put some constraints on the material behavior. For example, Lucet (1989) measured velocity and attenuation at two frequencies (≈ 1 kHz and 1 MHz) and used the Kramers–Kronig relations to compare the differences with various viscoelastic models, as shown schematically in Figure 3.9.1. Using equation (3.9.1), we can determine the expected ratio of

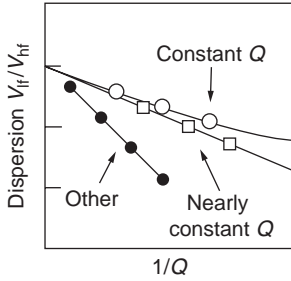


Figure 3.9.1 Lucet's (1989) use of the Kramers–Kronig relations to compare high- and low-frequency measured velocities and Q with various viscoelastic models.

low-frequency modulus or velocity, V_{lf} , and high-frequency modulus or velocity, V_{hf} , for various functional forms of Q (for example, constant Q or nearly constant Q). In all cases, linear viscoelastic behavior should lead to an intercept of $V_{lf}/V_{hf} = 1$ at $1/Q = 0$. Mechanisms with peaked attenuation curves between the measurement points will generally cause a larger dispersion, which appears as a steeper negative slope.

Uses

The Kramers–Kronig equations can be used to relate velocity dispersion and Q in linear viscoelastic materials.

Assumptions and limitations

The Kramers–Kronig equations apply when the material is linear and causal.

3.10 Waves in layered media: full-waveform synthetic seismograms

Synopsis

One of the approaches for computing wave propagation in layered media is the use of propagator matrices (Aki and Richards, 1980; Claerbout, 1985). The wave variables of interest (usually stresses and particle velocity or displacements) at the top and bottom of the stack of layers are related by a product of propagator matrices, one for each layer. The calculations are done in the frequency domain and include the effects of all multiples. For waves traveling perpendicularly to n layers with layer velocities, densities, and thicknesses V_k , ρ_k , and d_k , respectively

$$\begin{bmatrix} S \\ W \end{bmatrix}_n = \prod_{k=1}^n \mathbf{A}_k \begin{bmatrix} S \\ W \end{bmatrix}_1$$

where S and W are the Fourier transforms of the wave variables σ and w , respectively. For normal-incidence P-waves, σ is interpreted as the normal stress across each interface, and w is the normal component of the particle velocity. For normal-incidence

S-waves, σ is the shear traction across each interface, and w is the tangential component of the particle velocity. Each layer matrix \mathbf{A}_k has the form

$$\mathbf{A}_k = \begin{bmatrix} \cos\left(\frac{\omega d_k}{V_k}\right) & i\rho_k V_k \sin\left(\frac{\omega d_k}{V_k}\right) \\ \frac{i}{\rho_k V_k} \sin\left(\frac{\omega d_k}{V_k}\right) & \cos\left(\frac{\omega d_k}{V_k}\right) \end{bmatrix}$$

where ω is the angular frequency.

Kennett (1974, 1983) used the invariant imbedding method to generate the response of a layered medium recursively by adding one layer at a time (Figure 3.10.1). The overall reflection and transmission matrices, $\hat{\mathbf{R}}_D$ and $\hat{\mathbf{T}}_D$, respectively, for downgoing waves through a stack of layers are given by the following recursion relations:

$$\hat{\mathbf{R}}_D^{(k)} = \mathbf{R}_D^{(k)} + \mathbf{T}_U^{(k)} \mathbf{E}_D^{(k)} \hat{\mathbf{R}}_D^{(k+1)} \mathbf{E}_D^{(k)} \left[\mathbf{I} - \mathbf{R}_U^{(k)} \mathbf{E}_D^{(k)} \hat{\mathbf{R}}_D^{(k+1)} \mathbf{E}_D^{(k)} \right]^{-1} \mathbf{T}_D^{(k)}$$

$$\hat{\mathbf{T}}_D^{(k)} = \hat{\mathbf{T}}_D^{(k+1)} \mathbf{E}_D^{(k)} \left[\mathbf{I} - \mathbf{R}_U^{(k)} \mathbf{E}_D^{(k)} \hat{\mathbf{R}}_D^{(k+1)} \mathbf{E}_D^{(k)} \right]^{-1} \mathbf{T}_D^{(k)}$$

where $\mathbf{R}_D^{(k)}$, $\mathbf{T}_D^{(k)}$, $\mathbf{R}_U^{(k)}$, and $\mathbf{T}_U^{(k)}$ are just the single-interface downward and upward reflection and transmission matrices for the k th interface:

$$\begin{aligned} \mathbf{R}_D^{(k)} &= \begin{bmatrix} \downarrow\uparrow & \downarrow\uparrow \left(\frac{V_{P(k-1)} \cos \theta_{k-1}}{V_{S(k-1)} \cos \phi_{k-1}} \right)^{1/2} \\ \downarrow\uparrow \left(\frac{V_{S(k-1)} \cos \phi_{k-1}}{V_{P(k-1)} \cos \theta_{k-1}} \right)^{1/2} & \downarrow\uparrow \end{bmatrix} \\ \mathbf{T}_D^{(k)} &= \begin{bmatrix} \downarrow\downarrow \left(\frac{\rho_k V_{P(k)} \cos \theta_k}{\rho_{k-1} V_{P(k-1)} \cos \theta_{k-1}} \right)^{1/2} & \downarrow\downarrow \left(\frac{\rho_k V_{P(k)} \cos \theta_k}{\rho_{k-1} V_{S(k-1)} \cos \phi_{k-1}} \right)^{1/2} \\ \downarrow\downarrow \left(\frac{\rho_k V_{S(k)} \cos \phi_k}{\rho_{k-1} V_{P(k-1)} \cos \theta_{k-1}} \right)^{1/2} & \downarrow\downarrow \left(\frac{\rho_k V_{S(k)} \cos \phi_k}{\rho_{k-1} V_{S(k-1)} \cos \phi_{k-1}} \right)^{1/2} \end{bmatrix} \\ \mathbf{R}_U^{(k)} &= \begin{bmatrix} \uparrow\downarrow & \uparrow\downarrow \left(\frac{V_{P(k)} \cos \theta_k}{V_{S(k)} \cos \phi_k} \right)^{1/2} \\ \uparrow\downarrow \left(\frac{V_{S(k)} \cos \phi_k}{V_{P(k)} \cos \theta_k} \right)^{1/2} & \uparrow\downarrow \end{bmatrix} \\ \mathbf{T}_U^{(k)} &= \begin{bmatrix} \uparrow\uparrow \left(\frac{\rho_{k-1} V_{P(k-1)} \cos \theta_{k-1}}{\rho_k V_{P(k)} \cos \theta_k} \right)^{1/2} & \uparrow\uparrow \left(\frac{\rho_{k-1} V_{P(k-1)} \cos \theta_{k-1}}{\rho_k V_{S(k)} \cos \phi_k} \right)^{1/2} \\ \uparrow\uparrow \left(\frac{\rho_{k-1} V_{S(k-1)} \cos \phi_{k-1}}{\rho_k V_{P(k)} \cos \theta_k} \right)^{1/2} & \uparrow\uparrow \left(\frac{\rho_{k-1} V_{S(k-1)} \cos \phi_{k-1}}{\rho_k V_{S(k)} \cos \phi_k} \right)^{1/2} \end{bmatrix} \end{aligned}$$

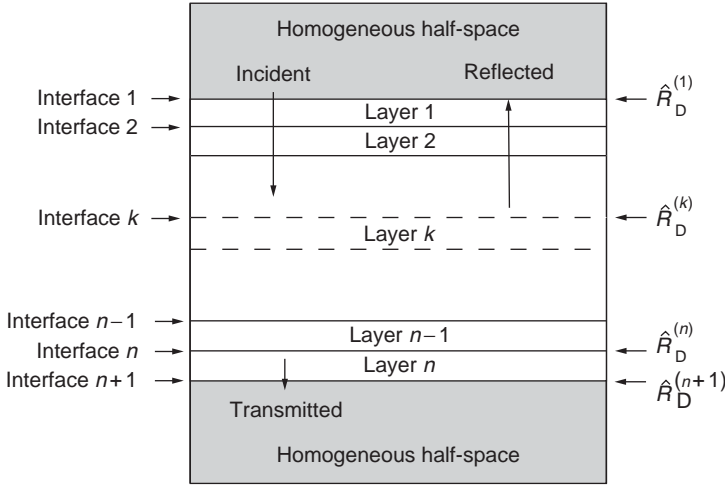


Figure 3.10.1 Recursively determined transfer functions in a layered medium.

with

$$\begin{pmatrix} \begin{matrix} \downarrow \uparrow & \downarrow \uparrow & \uparrow \uparrow & \uparrow \uparrow \\ \text{PP} & \text{SP} & \text{PP} & \text{SP} \\ \downarrow \uparrow & \downarrow \uparrow & \uparrow \uparrow & \uparrow \uparrow \\ \text{PS} & \text{SS} & \text{PS} & \text{SS} \\ \downarrow \downarrow & \downarrow \downarrow & \uparrow \downarrow & \uparrow \downarrow \\ \text{PP} & \text{SP} & \text{PP} & \text{SP} \\ \downarrow \downarrow & \downarrow \downarrow & \uparrow \downarrow & \uparrow \downarrow \\ \text{PS} & \text{SS} & \text{PS} & \text{SS} \end{matrix} \end{pmatrix} = \mathbf{M}^{-1} \mathbf{N}$$

$$\mathbf{M} = \begin{bmatrix} -\sin \theta_{k-1} & -\cos \phi_{k-1} & \sin \theta_k & \cos \phi_k \\ \cos \theta_{k-1} & -\sin \phi_{k-1} & \cos \theta_k & -\sin \phi_k \\ 2I_{S(k-1)} \sin \phi_{k-1} \cos \theta_{k-1} & I_{S(k-1)}(1 - 2 \sin^2 \phi_{k-1}) & 2I_{S(k)} \sin \phi_k \cos \theta_k & I_{S(k)}(1 - 2 \sin^2 \phi_k) \\ -I_{P(k-1)}(1 - 2 \sin^2 \phi_{k-1}) & I_{S(k-1)} \sin 2\phi_{k-1} & I_{P(k)}(1 - 2 \sin^2 \phi_k) & -I_{S(k)} \sin 2\phi_k \end{bmatrix}$$

$$\mathbf{N} = \begin{bmatrix} \sin \theta_{k-1} & \cos \phi_{k-1} & -\sin \theta_k & -\cos \phi_k \\ \cos \theta_{k-1} & -\sin \phi_{k-1} & \cos \theta_k & -\sin \phi_k \\ 2I_{S(k-1)} \sin \phi_{k-1} \cos \theta_{k-1} & I_{S(k-1)}(1 - 2 \sin^2 \phi_{k-1}) & 2I_{S(k)} \sin \phi_k \cos \theta_k & I_{S(k)}(1 - 2 \sin^2 \phi_k) \\ I_{P(k-1)}(1 - 2 \sin^2 \phi_{k-1}) & -I_{S(k-1)} \sin 2\phi_{k-1} & -I_{P(k)}(1 - 2 \sin^2 \phi_k) & I_{S(k)} \sin 2\phi_k \end{bmatrix}$$

where $I_{P(k)} = \rho_k V_{P(k)}$ and $I_{S(k)} = \rho_k V_{S(k)}$ are the P and S impedances, respectively, of the k th layer, and θ_k and ϕ_k are the angles made by the P- and S-wave vectors with the normal to the k th interface. The elements of the reflection and transmission matrices $\mathbf{R}_D^{(k)}$, $\mathbf{T}_D^{(k)}$, $\mathbf{R}_U^{(k)}$, and $\mathbf{T}_U^{(k)}$ are the reflection and transmission coefficients for scaled displacements, which are proportional to the square root of the energy flux. The scaled displacement u' is related to the displacement u by $u' = u\sqrt{\rho V \cos \theta}$.

For normal-incidence wave propagation with no mode conversions, the reflection and transmission matrices reduce to the scalar coefficients:

$$R_D^{(k)} = \frac{\rho_{k-1}V_{k-1} - \rho_k V_k}{\rho_{k-1}V_{k-1} + \rho_k V_k}, \quad R_U^{(k)} = -R_D^{(k)}$$

$$T_U^{(k)} = \frac{2\sqrt{\rho_{k-1}V_{k-1}\rho_k V_k}}{\rho_{k-1}V_{k-1} + \rho_k V_k}, \quad T_U^{(k)} = T_D^{(k)}$$

The phase shift operator for propagation across each new layer is given by $\mathbf{E}_D^{(k)}$

$$\mathbf{E}_D^{(k)} = \begin{bmatrix} \exp(i\omega d_k \cos \theta_k / V_{P(k)}) & 0 \\ 0 & \exp(i\omega d_k \cos \phi_k / V_{S(k)}) \end{bmatrix}$$

where θ_k and ϕ_k are the angles between the normal to the layers and the directions of propagation of P- and S-waves, respectively. The terms $\hat{\mathbf{R}}_D$ and $\hat{\mathbf{T}}_D$ are functions of ω and represent the overall transfer functions of the layered medium in the frequency domain. Time-domain seismograms are obtained by multiplying the overall transfer function by the Fourier transform of the source wavelet and then performing an inverse transform. The recursion starts at the base of the layering at interface $n + 1$ (Figure 3.10.1). Setting $\mathbf{R}_D^{(n+1)} = \hat{\mathbf{R}}_D^{(n+1)} = 0$ and $\mathbf{T}_D^{(n+1)} = \hat{\mathbf{T}}_D^{(n+1)} = \mathbf{I}$ simulates a stack of layers overlying a semi-infinite homogeneous half-space with properties equal to those of the last layer, layer n . The recursion relations are stepped up through the stack of layers one at a time to finally give $\hat{\mathbf{R}}_D^{(1)}$ and $\hat{\mathbf{T}}_D^{(1)}$, the overall reflection and transmission response for the whole stack.

Calculate the P-wave normal-incidence overall reflection and transmission functions $\hat{R}_D^{(1)}$ and $\hat{T}_D^{(1)}$ recursively for a three-layered medium with layer properties as follows:

$$V_{P(1)} = 4000 \text{ m/s}, \quad \rho_1 = 2300 \text{ kg/m}^3, \quad d_1 = 100 \text{ m}$$

$$V_{P(2)} = 3000 \text{ m/s}, \quad \rho_2 = 2100 \text{ kg/m}^3, \quad d_2 = 50 \text{ m}$$

$$V_{P(3)} = 5000 \text{ m/s}, \quad \rho_3 = 2500 \text{ kg/m}^3, \quad d_3 = 200 \text{ m}$$

The recursion starts with $\hat{R}_D^{(4)} = 0$ and $\hat{T}_D^{(4)} = 1$. The normal-incidence reflection and transmission coefficients at interface 3 are

$$R_D^{(3)} = \frac{\rho_2 V_{P(2)} - \rho_3 V_{P(3)}}{\rho_2 V_{P(2)} + \rho_3 V_{P(3)}} = -0.33, \quad R_U^{(3)} = -R_D^{(3)}$$

$$T_D^{(3)} = \frac{2\sqrt{\rho_2 V_{P(2)} \rho_3 V_{P(3)}}}{\rho_2 V_{P(2)} + \rho_3 V_{P(3)}} = 0.94, \quad T_U^{(3)} = T_D^{(3)}$$

and the phase factor for propagation across layer 3 is

$$E_D^{(3)} = \exp(i2\pi f d_3 / V_{P(3)}) = \exp(i2\pi f 200 / 5000)$$

where f is the frequency. The recursion relations give

$$\hat{R}_D^{(3)} = R_D^{(3)} + \frac{T_U^{(3)} E_D^{(3)} \hat{R}_D^{(4)} E_D^{(3)}}{1 - R_U^{(3)} E_D^{(3)} \hat{R}_D^{(4)} E_D^{(3)}} T_D^{(3)}$$

$$\hat{T}_D^{(3)} = \frac{\hat{T}_D^{(4)} E_D^{(3)}}{1 - R_U^{(3)} E_D^{(3)} \hat{R}_D^{(4)} E_D^{(3)}} T_D^{(3)}$$

The recursion is continued in a similar manner until finally we obtain $\hat{R}_D^{(1)}$ and $\hat{T}_D^{(1)}$.

The matrix inverse

$$[\mathbf{I} - \mathbf{R}_U^{(k)} \mathbf{E}_D^{(k)} \hat{\mathbf{R}}_D^{(k+1)} \mathbf{E}_D^{(k)}]^{-1}$$

is referred to as the reverberation operator and includes the response caused by all internal reverberations. In the series expansion of the matrix inverse

$$\begin{aligned} [\mathbf{I} - \mathbf{R}_U^{(k)} \mathbf{E}_D^{(k)} \hat{\mathbf{R}}_D^{(k+1)} \mathbf{E}_D^{(k)}]^{-1} &= \mathbf{I} + \mathbf{R}_U^{(k)} \mathbf{E}_D^{(k)} \hat{\mathbf{R}}_D^{(k+1)} \mathbf{E}_D^{(k)} \\ &\quad + \mathbf{R}_U^{(k)} \mathbf{E}_D^{(k)} \hat{\mathbf{R}}_D^{(k+1)} \mathbf{E}_D^{(k)} \mathbf{R}_U^{(k)} \mathbf{E}_D^{(k)} \hat{\mathbf{R}}_D^{(k+1)} \mathbf{E}_D^{(k)} + \dots \end{aligned}$$

the first term represents the primaries and each successive term corresponds to higher-order multiples. Truncating the expansion to $m + 1$ terms includes m internal multiples in the approximation. The full multiple sequence is included with the exact matrix inverse.

Uses

The methods described in this section can be used to compute full-wave seismograms, which include the effects of multiples for wave propagation in layered media.

Assumptions and limitations

The algorithms described in this section assume the following:

- layered medium with no lateral heterogeneities;
- layers are isotropic, linear, elastic; and
- plane-wave, time-harmonic propagation.

3.11 Waves in layered media: stratigraphic filtering and velocity dispersion

Synopsis

Waves in layered media undergo attenuation and velocity dispersion caused by multiple scattering at the layer interfaces. The effective phase slowness of normally incident waves through layered media depends on the relative scales of the wavelength and layer thicknesses and may be written as $S_{\text{eff}} = S_{\text{rt}} + S_{\text{st}}$. The term S_{rt} is the ray theory slowness of the direct ray that does not undergo any reflections and is just the thickness-weighted average of the individual layer slownesses. The individual slownesses may be complex to account for intrinsic attenuation. The excess slowness S_{st} (sometimes called the stratigraphic slowness) arises because of multiple scattering within the layers. A flexible approach to calculating the effective slowness and travel time follows from Kennett's (1974) invariant imbedding formulation for the transfer function of a layered medium. The layered medium, of total thickness L , consists of layers with velocities (inverse slownesses), densities, and thicknesses, V_j , ρ_j , and l_j , respectively.

The complex stratigraphic slowness is frequency dependent and can be calculated recursively (Frazer, 1994) by

$$S_{\text{st}} = \frac{1}{i\omega L} \sum_{j=1}^n \ln \left(\frac{t_j}{1 - R_j \theta_j^2 r_j} \right)$$

As each new layer $j + 1$ is added to the stack of j layers, R is updated according to

$$R_{j+1} = -r_{j+1} + \frac{R_j \theta_{j+1}^2 t_{j+1}^2}{1 - R_j \theta_{j+1}^2 r_{j+1}}$$

(with $R_0 = 0$) and the term

$$\ln[t_{j+1}(1 - R_{j+1} \theta_{j+1}^2 r_{j+1})^{-1}]$$

is accumulated in the sum. In the above expressions, t_j and r_j are the transmission and reflection coefficients defined as

$$t_j = \frac{2\sqrt{\rho_j V_j \rho_{j+1} V_{j+1}}}{\rho_j V_j + \rho_{j+1} V_{j+1}}$$

$$r_j = \frac{\rho_{j+1} V_{j+1} - \rho_j V_j}{\rho_j V_j + \rho_{j+1} V_{j+1}}$$

whereas $\theta_j = \exp(i\omega l_j / V_j)$ is the phase shift for propagation across layer j and ω is the angular frequency. The total travel time is $T = T_{\text{rt}} + T_{\text{st}}$, where T_{rt} is the ray theory travel time given by

$$T_{\text{rt}} = \sum_{j=1}^n \frac{l_j}{V_j}$$

and T_{st} is given by

$$T_{\text{st}} = \text{Re} \left[\frac{1}{i\omega} \sum_{j=1}^n \ln \left(\frac{t_j}{1 - R_j \theta_j^2 r_j} \right) \right]$$

The deterministic results given above are not restricted to small perturbations in the material properties or statistically stationary geology.

Calculate the excess stratigraphic travel time caused by multiple scattering for a normally incident P-wave traveling through a three-layered medium with layer properties as follows:

$$V_{\text{P}(1)} = 4000 \text{ m/s}, \quad \rho_1 = 2300 \text{ kg/m}^3, \quad l_1 = 100 \text{ m}$$

$$V_{\text{P}(2)} = 3000 \text{ m/s}, \quad \rho_2 = 2100 \text{ kg/m}^3, \quad l_2 = 50 \text{ m}$$

$$V_{\text{P}(3)} = 5000 \text{ m/s}, \quad \rho_3 = 2500 \text{ kg/m}^3, \quad l_3 = 200 \text{ m}$$

The excess travel time is given by

$$T_{\text{st}} = \text{Re} \left[\frac{1}{i\omega} \sum_{j=1}^n \ln \left(\frac{t_j}{1 - R_j \theta_j^2 r_j} \right) \right]$$

The recursion begins with $R_0 = 0$,

$$R_1 = -r_1 + \frac{R_0 \theta_1^2 t_1^2}{1 - R_0 \theta_1^2 r_1}$$

where

$$t_1 = \frac{2\sqrt{\rho_1 V_1 \rho_2 V_2}}{\rho_1 V_1 + \rho_2 V_2} = 0.98$$

$$r_1 = \frac{\rho_2 V_2 - \rho_1 V_1}{\rho_1 V_1 + \rho_2 V_2} = -0.19$$

$\theta_1 = \exp(i2\pi f l_1 / V_1) = \exp(i2\pi f 100 / 4000)$ with f as the frequency.

The recursion is continued to obtain R_2 and R_3 . Setting $t_3 = 1$ and $r_3 = 0$ simulates an impedance-matching homogeneous infinite half-space beneath layer 3.

Finally, the excess travel time, which is a function of the frequency, is obtained by taking the real part of the sum as follows:

$$T_{\text{st}} = \text{Re} \left\{ \frac{1}{i2\pi f} \left[\ln \left(\frac{t_1}{1 - R_1 \theta_1^2 r_1} \right) + \ln \left(\frac{t_2}{1 - R_2 \theta_2^2 r_2} \right) + \ln \left(\frac{t_3}{1 - R_3 \theta_3^2 r_3} \right) \right] \right\}$$

The effect of the layering can be thought of as a filter that attenuates the input wavelet and introduces a delay. The function

$$A(\omega) = \exp(i\omega x S_{\text{st}}) = \exp(i\omega T_{\text{rt}} S_{\text{st}}/S_{\text{rt}})$$

(where S_{rt} is assumed to be real in the absence of any intrinsic attenuation) is sometimes called the stratigraphic filter.

The **O'Doherty–Anstey formula** (O'Doherty and Anstey, 1971; Banik *et al.*, 1985)

$$|A(\omega)| \approx \exp(-\hat{R}(\omega)T_{\text{rt}})$$

approximately relates the amplitude of the stratigraphic filter to the power spectrum $\hat{R}(\omega)$ of the reflection coefficient time series $r(\tau)$ where

$$\tau(x) = \int_0^x dx' / V(x')$$

is the one-way travel time. Initially the O'Doherty–Anstey formula was obtained by a heuristic approach (O'Doherty and Anstey, 1971). Later, various authors substantiated the result using statistical ensemble averages of wavefields (Banik *et al.*, 1985), deterministic formulations (Resnick *et al.*, 1986), and the concepts of self-averaged values and wave localization (Shapiro and Zien, 1993). Resnick *et al.* (1986) showed that the O'Doherty–Anstey formula is obtained as an approximation from the exact frequency-domain theory of Resnick *et al.* by neglecting quadratic terms in the Riccati equation of Resnick *et al.* Another equivalent way of expressing the O'Doherty–Anstey relation is

$$\frac{\text{Im}(S_{\text{st}})}{S_{\text{rt}}} \approx \frac{1}{2Q} \approx \frac{\hat{R}(\omega)}{\omega} = \frac{1}{2} \omega \hat{M}(2\omega)$$

Here $1/Q$ is the scattering attenuation caused by the multiples, and $\hat{M}(\omega)$ is the power spectrum of the logarithmic impedance fluctuations of the medium, $\ln[\rho(\tau)V(\tau)] - \langle \ln[\rho(\tau)V(\tau)] \rangle$, where $\langle \cdot \rangle$ denotes a stochastic ensemble average. Because the filter is minimum phase, $\omega \text{Re}(S_{\text{st}})$ and $\omega \text{Im}(S_{\text{st}})$ are a Hilbert transform pair,

$$\frac{\text{Re}(S_{\text{st}})}{S_{\text{rt}}} \approx \frac{\delta t}{T_{\text{rt}}} \approx \frac{H\{\hat{R}(\omega)\}}{\omega}$$

where $H\{\cdot\}$ denotes the Hilbert transform and δt is the excess travel caused by multiple reverberations.

Shapiro and Zien (1993) generalized the O'Doherty–Anstey formula for non-normal incidence. The derivation is based on a small perturbation analysis and requires the fluctuations of material parameters to be small (<30%). The generalized formula for plane pressure (scalar) waves in an acoustic medium incident at an angle θ with respect to the layer normal is

$$|A(\omega)| \approx \exp \left[-\frac{\hat{R}(\omega \cos \theta)}{\cos^4 \theta} T_{\text{rt}} \right]$$

whereas

$$|A(\omega)| \approx \exp \left[-\frac{(2 \cos^2 \theta - 1)^2 \hat{R}(\omega \cos \theta)}{\cos^4 \theta} T_{\text{rt}} \right]$$

for SH-waves in an elastic medium (Shapiro *et al.*, 1994).

For a perfectly periodic stratified medium made up of two constituents with phase velocities V_1, V_2 ; densities ρ_1, ρ_2 ; and thicknesses l_1, l_2 , the velocity dispersion relation may be obtained from the **Floquet solution** (Christensen, 1991) for periodic media:

$$\cos \left[\frac{\omega(l_1 + l_2)}{V} \right] = \cos \left(\frac{\omega l_1}{V_1} \right) \cos \left(\frac{\omega l_2}{V_2} \right) - \chi \sin \left(\frac{\omega l_1}{V_1} \right) \sin \left(\frac{\omega l_2}{V_2} \right)$$

$$\chi = \frac{(\rho_1 V_1)^2 + (\rho_2 V_2)^2}{2\rho_1 \rho_2 V_1 V_2}$$

The Floquet solution is valid for arbitrary contrasts in the layer properties. If the spatial period ($l_1 + l_2$) is an integer multiple of one-half wavelength, multiple reflections are in phase and add constructively, resulting in a large total accumulated reflection. The frequency at which this **Bragg scattering** condition is satisfied is called the Bragg frequency. Waves cannot propagate within a stop-band around the Bragg frequency.

Uses

The results described in this section can be used to estimate velocity dispersion and attenuation caused by scattering for normal-incidence wave propagation in layered media.

Assumptions and limitations

The methods described in this section apply under the following conditions:

- layers are isotropic, linear elastic with no lateral variation;
- propagation is normal to the layers except for the generalized O'Doherty–Anstey formula; and
- plane-wave, time-harmonic propagation is assumed.

3.12 Waves in layered media: frequency-dependent anisotropy, dispersion, and attenuation

Synopsis

Waves in layered media undergo attenuation and velocity dispersion caused by multiple scattering at the layer interfaces. Thinly layered media also give rise to velocity anisotropy. At low frequencies this phenomenon is usually described by the Backus average. Velocity anisotropy and dispersion in a multilayered medium are two aspects of the same phenomenon and are related to the frequency- and angle-dependent transmissivity resulting from multiple scattering in the medium. Shapiro *et al.* (1994) and Shapiro and Hubral (1995, 1996, 1999) have presented a whole-frequency-range statistical theory for the angle-dependent transmissivity of layered media for scalar waves (pressure waves in fluids) and elastic waves. The theory encompasses the Backus average in the low-frequency limit and ray theory in the high-frequency limit. The formulation avoids the problem of ensemble averaging versus measurements for a single realization by working with parameters that are averaged by the wave-propagation process itself for sufficiently long propagation paths. The results are obtained in the limit when the path length tends to infinity. Practically, this means the results are applicable when path lengths are very much longer than the characteristic correlation lengths of the medium.

The slowness (s) and density (ρ) distributions of the stack of layers (or a continuous inhomogeneous one-dimensional medium) are assumed to be realizations of random stationary processes. The fluctuations of the physical parameters are small (<30%) compared with their constant mean values (denoted by subscripts 0):

$$s^2(z) = \frac{1}{c_0^2} [1 + \varepsilon_s(z)]$$

$$\rho(z) = \rho_0 [1 + \varepsilon_\rho(z)]$$

where the fluctuating parts $\varepsilon_s(z)$ (the squared slowness fluctuation) and $\varepsilon_\rho(z)$ (the density fluctuation) have zero means by definition. The depth coordinate is denoted by z , and the x - and y -axes lie in the plane of the layers. The velocity

$$c_0 = \langle s^2 \rangle^{-1/2}$$

corresponds to the average squared slowness of the medium. Instead of the squared slowness fluctuations, the random medium may also be characterized by the P- and S-velocity fluctuations, α and β , respectively, as follows:

$$\alpha(z) = \langle \alpha \rangle [1 + \varepsilon_\alpha(z)] = \alpha_0 [1 + \varepsilon_\alpha(z)]$$

$$\beta(z) = \langle \beta \rangle [1 + \varepsilon_\beta(z)] = \beta_0 [1 + \varepsilon_\beta(z)]$$

In the case of small fluctuations $\varepsilon_\alpha \approx -\varepsilon_s/2$ and $\langle \alpha \rangle \approx c_0(1 + 3\sigma_{\alpha\alpha}^2/2)$, where $\sigma_{\alpha\alpha}^2$ is the normalized variance (the variance divided by the square of the mean)

of the velocity fluctuations. The horizontal wavenumber k_x is related to the incidence angle θ by

$$k_x = k_0 \sin \theta = \omega p$$

where $k_0 = \omega/c_0$, $p = \sin \theta/c_0$ is the horizontal component of the slowness (also called the ray parameter), and ω is the angular frequency. For elastic media, depending on the type of the incident wave, $p = \sin \theta/\alpha_0$ or $p = \sin \theta/\beta_0$. The various autocorrelation and cross-correlation functions of the density and velocity fluctuations are denoted by

$$B_{\rho\rho}(\xi) = \langle \varepsilon_\rho(z) \varepsilon_\rho(z + \xi) \rangle$$

$$B_{\alpha\alpha}(\xi) = \langle \varepsilon_\alpha(z) \varepsilon_\alpha(z + \xi) \rangle$$

$$B_{\beta\beta}(\xi) = \langle \varepsilon_\beta(z) \varepsilon_\beta(z + \xi) \rangle$$

$$B_{\alpha\beta}(\xi) = \langle \varepsilon_\alpha(z) \varepsilon_\beta(z + \xi) \rangle$$

$$B_{\alpha\rho}(\xi) = \langle \varepsilon_\alpha(z) \varepsilon_\rho(z + \xi) \rangle$$

$$B_{\beta\rho}(\xi) = \langle \varepsilon_\beta(z) \varepsilon_\rho(z + \xi) \rangle$$

These correlation functions can often be obtained from sonic and density logs. The corresponding normalized variances and cross-variances are given by

$$\sigma_{\rho\rho}^2 = B_{\rho\rho}(0), \quad \sigma_{\alpha\alpha}^2 = B_{\alpha\alpha}(0), \quad \sigma_{\beta\beta}^2 = B_{\beta\beta}(0),$$

$$\sigma_{\alpha\beta}^2 = B_{\alpha\beta}(0), \quad \sigma_{\alpha\rho}^2 = B_{\alpha\rho}(0), \quad \sigma_{\beta\rho}^2 = B_{\beta\rho}(0)$$

The real part of the effective vertical wavenumber for pressure waves in acoustic media is (neglecting higher than second-order powers of the fluctuations)

$$k_z = k_z^{\text{stat}} - k_0^2 \cos^2 \theta \int_0^\infty d\xi B(\xi) \sin(2k_0\xi \cos \theta)$$

$$k_z^{\text{stat}} = k_0 \cos \theta (1 + \sigma_{\rho\rho}^2/2 + \sigma_{\rho\alpha}^2/\cos^2 \theta)$$

$$B(\xi) = B_{\rho\rho}(\xi) + 2B_{\rho\alpha}(\xi)/\cos^2 \theta + B_{\alpha\alpha}(\xi)/\cos^4 \theta$$

For waves in an elastic layered medium, the real part of the vertical wavenumber for P-, SV-, and SH-waves is given by

$$k_z^{\text{P}} = \lambda_a + \omega \hat{A}_{\text{P}} - \omega^2 \int_0^\infty d\xi [B_{\text{P}}(\xi) \sin(2\xi \lambda_a) + B_{\text{BB}}(\xi) \sin(\xi \lambda_-) + B_{\text{DD}}(\xi) \sin(\xi \lambda_+)]$$

$$k_z^{\text{SV}} = \lambda_b + \omega \hat{A}_{\text{SV}} - \omega^2 \int_0^\infty d\xi [B_{\text{SV}}(\xi) \sin(2\xi \lambda_b) - B_{\text{BB}}(\xi) \sin(\xi \lambda_-) + B_{\text{DD}}(\xi) \sin(\xi \lambda_+)]$$

$$k_z^{\text{SH}} = \lambda_b + \omega \hat{A}_{\text{SH}} - \omega^2 \int_0^\infty d\xi [B_{\text{SH}}(\xi) \sin(2\xi \lambda_b)]$$

and the imaginary part of the vertical wavenumber (which is related to the attenuation coefficient due to scattering) is

$$\gamma_P = \omega^2 \int_0^\infty d\xi [B_P(\xi) \cos(2\xi\lambda_a) + B_{BB}(\xi) \cos(\xi\lambda_-) + B_{DD}(\xi) \cos(\xi\lambda_+)]$$

$$\gamma_{SV} = \omega^2 \int_0^\infty d\xi [B_{SV}(\xi) \cos(2\xi\lambda_b) + B_{BB}(\xi) \cos(\xi\lambda_-) + B_{DD}(\xi) \cos(\xi\lambda_+)]$$

$$\gamma_{SH} = \omega^2 \int_0^\infty d\xi [B_{SH}(\xi) \cos(2\xi\lambda_b)]$$

where $\lambda_a = \omega\sqrt{1/\alpha_0^2 - p^2}$, $\lambda_b = \omega\sqrt{1/\beta_0^2 - p^2}$, $\lambda_+ = \lambda_a + \lambda_b$, and $\lambda_- = \lambda_b - \lambda_a$ (only real-valued $\lambda_{a,b}$ are considered). The other quantities in the preceding expressions are

$$B_P(\xi) = (X^2\alpha_0^2)^{-1}[B_{\rho\rho}(\xi)C_1^2 + 2B_{\alpha\rho}(\xi)C_1 + 2B_{\beta\rho}(\xi)C_1C_2 \\ + 2B_{\alpha\beta}(\xi)C_2 + B_{\alpha\alpha}(\xi) + B_{\beta\beta}(\xi)C_2^2]$$

$$B_{SV}(\xi) = (Y^2\beta_0^2)^{-1}[B_{\rho\rho}(\xi)C_7^2 + 2B_{\beta\rho}(\xi)C_7C_8 + B_{\beta\beta}(\xi)C_8^2]$$

$$B_{SH}(\xi) = (Y^2\beta_0^2)^{-1}[B_{\rho\rho}(\xi)Y^4 + 2B_{\beta\rho}(\xi)C_{10}Y^2 + 2B_{\beta\beta}(\xi)C_{10}^2]$$

$$B_{BB}(\xi) = p^2\beta_0(4XY\alpha_0)^{-1}[B_{\rho\rho}(\xi)C_3^2 + 2B_{\beta\rho}(\xi)C_3C_4 + B_{\beta\beta}(\xi)C_4^2]$$

$$B_{DD}(\xi) = p^2\beta_0(4XY\alpha_0)^{-1}[B_{\rho\rho}(\xi)C_5^2 + 2B_{\beta\rho}(\xi)C_5C_6 + B_{\beta\beta}(\xi)C_6^2]$$

$$\hat{A}_P = (2X\alpha_0)^{-1}A_P, \quad \hat{A}_{SV} = (2Y\beta_0)^{-1}A_{SV}, \quad \hat{A}_{SH} = (2Y\beta_0)^{-1}A_{SH}$$

$$A_P = \sigma_{\rho\rho}^2(1 - 4p^2\beta_0^2Z) + 2\sigma_{\alpha\rho}^2(1 - 4p^2\beta_0^2) + 8\sigma_{\beta\rho}^2p^2\beta_0^2(1 - 2Z) \\ + 3\sigma_{\alpha\alpha}^2 - 16p^2\beta_0^2\sigma_{\alpha\beta}^2 + 16p^2\beta_0^2\sigma_{\beta\beta}^2(1 - Z)$$

$$A_{SV} = \sigma_{\rho\rho}^2(1 - C_9) + \sigma_{\beta\rho}^2(2 - 4C_9) + \sigma_{\beta\beta}^2(3 - 4C_9)$$

$$A_{SH} = \sigma_{\rho\rho}^2Y^2 + 2\sigma_{\beta\rho}^2(2Y^2 - 1) + \sigma_{\beta\beta}^2(4Y^2 - 1)$$

where

$$X = \sqrt{(1 - p^2\alpha_0^2)}, \quad Y = \sqrt{(1 - p^2\beta_0^2)}, \quad Z = p^2(\alpha_0^2 - \beta_0^2)$$

$$C_1 = X^2(1 - 4p^2\beta_0^2), \quad C_2 = -8p^2\beta_0^2X^2$$

$$C_3 = X(3 - 4\beta_0^2p^2) - Y[(\alpha_0/\beta_0) + (2\beta_0/\alpha_0) - 4\alpha_0\beta_0p^2]$$

$$C_4 = 4X(1 - 2\beta_0^2p^2) - 4Y[(\beta_0/\alpha_0) - 2\alpha_0\beta_0p^2]$$

$$C_5 = X(4\beta_0^2p^2 - 3) - Y[(\alpha_0/\beta_0) + (2\beta_0/\alpha_0) - 4\alpha_0\beta_0p^2]$$

$$C_6 = 4X(2\beta_0^2p^2 - 1) - 4Y[(\beta_0/\alpha_0) - 2\alpha_0\beta_0p^2], \quad C_7 = Y^2(1 - 4p^2\beta_0^2)$$

$$C_8 = 1 - 8p^2\beta_0^2Y^2, \quad C_9 = 4Y^2Z\beta_0^2/\alpha_0^2, \quad C_{10} = 1 - 2p^2\beta_0^2$$

For multimode propagation (P–SV), neglecting higher-order terms restricts the range of applicable pathlengths L . This range is approximately given as

$$\max\{\lambda, a\} < L < Y^2 \max\{\lambda, a\}/\sigma^2$$

where λ is the wavelength, a is the correlation length of the medium, and σ^2 is the variance of the fluctuations. The equations are valid for the whole frequency range, and there is no restriction on the wavelength to correlation length ratio.

The angle- and frequency-dependent phase and group velocities are given by

$$c^{\text{phase}} = \frac{\omega}{\sqrt{k_x^2 + k_z^2}} = \frac{1}{\sqrt{p^2 + k_z^2/\omega^2}}$$

$$c^{\text{group}} = \sqrt{\left(\frac{\partial\omega}{\partial k_x}\right)^2 + \left(\frac{\partial\omega}{\partial k_z}\right)^2}$$

In the low- and high-frequency limits the phase and group velocities are the same. The low-frequency limit for pressure waves in acoustic media is

$$c_{\text{fluid}}^{\text{low freq}} \approx c_0 \left[1 - \left(\sigma_{\rho\rho}^2/2 \right) \cos^2 \theta - \sigma_{\rho\alpha}^2 \right]$$

and for elastic waves

$$c_{\text{P}}^{\text{low freq}} = \alpha_0 (1 - A_{\text{P}}/2)$$

$$c_{\text{SV}}^{\text{low freq}} = \beta_0 (1 - A_{\text{SV}}/2)$$

$$c_{\text{SH}}^{\text{low freq}} = \beta_0 (1 - A_{\text{SH}}/2)$$

These limits are the same as the result obtained from Backus averaging with higher-order terms in the medium fluctuations neglected. The high-frequency limit of phase and group velocities is

$$c_{\text{fluid}}^{\text{high freq}} = c_0 \left[1 + \left(\sigma_{\alpha\alpha}^2/2 \cos^2 \theta \right) \right]$$

for fluids, and

$$c_{\text{P}}^{\text{high freq}} = \alpha_0 \left[1 - \sigma_{\alpha\alpha}^2 (1 - 3p^2 \alpha_0^2/2) / (1 - p^2 \alpha_0^2) \right]$$

$$c_{\text{SV,SH}}^{\text{high freq}} = \beta_0 \left[1 - \sigma_{\beta\beta}^2 (1 - 3p^2 \beta_0^2/2) / (1 - p^2 \beta_0^2) \right]$$

for elastic media, which are in agreement with ray theory predictions, again neglecting higher-order terms.

Shear-wave splitting or birefringence and its frequency dependence can be characterized by

$$S(\omega, p) = \frac{c_{SV}(\omega, p) - c_{SH}(\omega, p)}{c_{SV}(\omega, p)} \approx \frac{c_{SV}(\omega, p) - c_{SH}(\omega, p)}{\beta_0}$$

In the low-frequency limit $S^{\text{low freq}}(\omega, p) \approx (A_{SH} - A_{SV})/2$, which is the shear-wave splitting in the transversely isotropic medium obtained from a Backus average of the elastic moduli. In the high-frequency limit $S^{\text{high freq}}(\omega, p) = 0$.

For a medium with exponential correlation functions $\sigma^2 \exp(-\xi/a)$ (where a is the correlation length) for the velocity and density fluctuations with different variances σ^2 but the same correlation length a , the complete frequency dependence of the phase and group velocities is expressed as

$$c_{\text{fluid}}^{\text{phase}} = c_0 \left(1 + \frac{(2k_0^2 a^2 \sigma_{\alpha\alpha}^2 - \sigma_{\rho\alpha}^2 - \frac{1}{2} \cos^2 \theta \sigma_{\rho\rho}^2)}{1 + 4k_0^2 a^2 \cos^2 \theta} \right)$$

$$c_{\text{fluid}}^{\text{group}} = c_0 \left[1 + \frac{N}{(1 + 4k_0^2 a^2 \cos^2 \theta)^2} \right]$$

$$N = 2k_0^2 a^2 \sigma_{\alpha\alpha}^2 (3 + 4k_0^2 a^2 \cos^2 \theta) + \left(\frac{\sigma_{\rho\rho}^2 \cos^2 \theta}{2} + \sigma_{\rho\alpha}^2 \right) (4k_0^2 a^2 \cos^2 \theta - 1)$$

for pressure waves in acoustic media. For elastic P-, SV-, and SH-waves in a randomly layered medium with exponential spatial autocorrelation with correlation length a , the real part of the vertical wavenumber (obtained by Fourier sine transforms) is given as (Shapiro and Hubral, 1995, 1996, 1999)

$$k_z^P = \lambda_a + \omega A_P - \omega^2 a^2 \left[B_P(0) \frac{2\lambda_a}{1 + 4a^2 \lambda_a^2} + B_{BB}(0) \frac{\lambda_-}{1 + a^2 \lambda_-^2} + B_{DD}(0) \frac{\lambda_+}{1 + a^2 \lambda_+^2} \right]$$

$$k_z^{SV} = \lambda_b + \omega A_{SV} - \omega^2 a^2 \left[B_{SV}(0) \frac{2\lambda_b}{1 + 4a^2 \lambda_b^2} - B_{BB}(0) \frac{\lambda_-}{1 + a^2 \lambda_-^2} + B_{DD}(0) \frac{\lambda_+}{1 + a^2 \lambda_+^2} \right]$$

$$k_z^{SH} = \lambda_b + \omega A_{SH} - \omega^2 a^2 B_{SH}(0) \frac{2\lambda_b}{1 + 4a^2 \lambda_b^2}$$

and the imaginary part of the vertical wavenumber (which is related to the attenuation coefficient due to scattering) is

$$\gamma_P = \omega^2 a \left[B_P(0) \frac{1}{1 + 4a^2 \lambda_a^2} + B_{BB}(0) \frac{1}{1 + a^2 \lambda_-^2} + B_{DD}(0) \frac{1}{1 + a^2 \lambda_+^2} \right]$$

$$\gamma_{SV} = \omega^2 a \left[B_{SV}(0) \frac{1}{1 + 4a^2 \lambda_b^2} + B_{BB}(0) \frac{1}{1 + a^2 \lambda_-^2} + B_{DD}(0) \frac{1}{1 + a^2 \lambda_+^2} \right]$$

$$\gamma_{SH} = \omega^2 a B_{SH}(0) \frac{1}{1 + 4a^2 \lambda_b^2}$$

The shear-wave splitting for exponentially correlated randomly layered media is

$$S(\omega, p) \approx S^{\text{low freq}} + \omega a^2 \beta_0 Y \left\{ \frac{2\lambda_b}{1 + 4a^2 \lambda_b^2} [B_{SV}(0) - B_{SH}(0)] \right. \\ \left. - \frac{\lambda_+}{1 + a^2 \lambda_+^2} B_{DD}(0) + \frac{\lambda_-}{1 + a^2 \lambda_-^2} B_{BB}(0) \right\}$$

These equations reveal the general feature that the *anisotropy* (change in velocity with angle) *depends on the frequency*, and the *dispersion* (change in velocity with frequency) *depends on the angle*. Stratigraphic filtering causes the transmitted amplitudes to decay as $\exp(-\gamma L)$, where L is the path length and γ is the attenuation coefficient for the different wave modes as described in the equations above.

One-dimensional layered poroelastic medium

The small-perturbation statistical theory has been extended to one-dimensional layered poroelastic media (Gurevich and Lopatnikov, 1995; Gelinsky and Shapiro, 1997b; Gelinsky *et al.*, 1998). In addition to the attenuation due to multiple scattering in random elastic media, waves in a random porous saturated media cause inter-layer flow of pore fluids, leading to additional attenuation and velocity dispersion. The constituent poroelastic layers are governed by the Biot equations (see Section 6.1), and can support two P-waves, the fast and the slow P-wave. The poroelastic parameters of the random one-dimensional medium consist of a homogeneous background (denoted by subscript 0) upon which is superposed a zero-mean fluctuation. The fluctuations are characterized by their variance and a normalized spatial correlation function $B(r/a)$, such that $B(0) = 1$, where a is the correlation length. All parameters of the medium are assumed to have the same normalized correlation function and the same correlation length, but can have different variances. The poroelastic material parameters include:

ϕ , porosity; ρ , saturated bulk rock density; κ , permeability; ρ_f , fluid density; η , fluid viscosity, and K_f , fluid bulk modulus. $P_d = K_d + \frac{4}{3}\mu_d$ is the dry (drained) P-wave modulus, with K_d and μ_d being the dry bulk and shear moduli, respectively. $\alpha = 1 - K_d/K_0$ is the Biot coefficient (note that in this section, α denotes the Biot coefficient, not the P-wave velocity). K_0 is the mineral bulk modulus; $M = [\phi/K_f + (\alpha - \phi)/K_0]^{-1}$; $H = P_d + \alpha^2 M$ is the saturated P-wave modulus

(equivalent to Gassmann's equation). $N = MP_d/H$; $\omega_0 = \kappa N/\eta a^2$ is the characteristic frequency separating inter-layer-flow and no-flow regimes. $\omega_c = \eta\phi/\kappa\rho_f$ is the Biot critical frequency.

Plane P-waves are assumed to be propagating vertically (along the z -direction) normal to the stack of horizontal layers. The fast P-wavenumber ψ and attenuation coefficient γ are given by (Gelinsky *et al.*, 1998):

$$\begin{aligned}\psi &= k_1^R + A \\ &\quad - \int_0^\infty B(z/a) \left[\sqrt{2}D \exp(-zk_-^I) \cos(zk_-^R - \pi/4) \right. \\ &\quad \left. + \sqrt{2}D \exp(-zk_+^I) \cos(zk_+^R - \pi/4) + C \exp(-2zk_1^I) \sin(2zk_1^R) \right] dz \\ \gamma &= k_1^I \\ &\quad + \int_0^\infty B(z/a) \left[\sqrt{2}D \exp(-zk_-^I) \cos(zk_-^R + \pi/4) \right. \\ &\quad \left. - \sqrt{2}D \exp(-zk_+^I) \cos(zk_+^R + \pi/4) + C \exp(-2zk_1^I) \cos(2zk_1^R) \right] dz\end{aligned}$$

where superscripts R and I denote real and imaginary parts; $\tilde{k}_1 = k_1^R + ik_1^I$ and $\tilde{k}_2 = k_2^R + ik_2^I$ are the complex wavenumbers for the Biot fast and slow P-waves in the homogeneous background medium; $\tilde{k}_+ = k_+^R + ik_+^I = \tilde{k}_2 + \tilde{k}_1$; $\tilde{k}_- = k_-^R + ik_-^I = \tilde{k}_2 - \tilde{k}_1$. The quantities A , C , and D involve complicated functions of frequency and linear combinations of the variances and covariances of the medium fluctuations. Approximations for these quantities are discussed below. The above expressions assume small fluctuations in the poroelastic parameters but are not limited by any restriction on the relation between wavelength and the correlation length of the medium fluctuations. The phase velocity for the fast P-wave is given as $V_P = \omega/\psi$. For a medium with an exponential correlation function with correlation length a , the expressions after carrying out the integrations are (Gelinsky *et al.*, 1998):

$$\begin{aligned}\frac{\omega}{V_P} &= k_1^R + A - \frac{Da[1 + a(k_-^R + k_-^I)]}{1 + 2ak_-^I + a^2[(k_-^R)^2 + (k_-^I)^2]} \\ &\quad - \frac{Da[1 + a(k_+^R + k_+^I)]}{1 + 2ak_+^I + a^2(k_+^R^2 + k_+^I^2)} - \frac{2Ca^2k_1^R}{1 + 4ak_1^I + 4a^2(k_1^R^2 + k_1^I^2)} \\ \gamma &= k_1^I + \frac{Da[1 - a(k_-^R - k_-^I)]}{1 + 2ak_-^I + a^2(k_-^R^2 + k_-^I^2)} \\ &\quad + \frac{Da[1 - a(k_+^R - k_+^I)]}{1 + 2ak_+^I + a^2(k_+^R^2 + k_+^I^2)} + \frac{Ca(1 + 2ak_1^I)}{1 + 4ak_1^I + 4a^2(k_1^R^2 + k_1^I^2)}\end{aligned}$$

Gelinsky *et al.* (1998) introduce approximate expressions for A , C , and D , valid in the frequency range below Biot's critical frequency. Other approximations used are: $\tilde{k}_+ \approx \tilde{k}_- \approx \tilde{k}_2$; $\tilde{k}_2 \approx (1+i)k_2$; $\tilde{k}_1 \approx k_1^R = k_1$; $k_1 = \omega\sqrt{\rho/H}$; and $k_2 = \sqrt{\omega\omega_c\rho_f/(2\phi N)}$:

$$A = \frac{\omega}{2} \sqrt{\frac{\rho}{H_0}} \frac{P_{d0}}{H_0} \left[\sigma_{PP}^2 + \frac{\alpha_0^2 M_0}{P_{d0}} (\sigma_{MM}^2 + 2\sigma_{P\alpha}^2) + \frac{\alpha_0^4 M_0^2}{P_{d0}^2} \sigma_{\alpha\alpha}^2 \right]$$

$$\begin{aligned} \frac{2D}{k_2} = \frac{\omega}{2} \sqrt{\frac{\rho}{H_0}} \frac{P_{d0}\alpha_0^2 M_0}{H_0^2} & \left[\sigma_{PP}^2 - 2\sigma_{PM}^2 + \sigma_{MM}^2 - 2\frac{P_{d0} - \alpha_0^2 M_0}{P_{d0}} (\sigma_{P\alpha}^2 - \sigma_{M\alpha}^2) \right. \\ & \left. + \frac{(P_{d0} - \alpha_0^2 M_0)^2}{P_{d0}^2} \sigma_{\alpha\alpha}^2 \right] \end{aligned}$$

$$\frac{C}{2k_1} = \frac{\omega}{8} \sqrt{\frac{\rho}{H_0}} \frac{P_{d0}^2}{H_0^2} \left[\sigma_{PP}^2 + 2\frac{\alpha_0^2 M_0}{P_{d0}} (\sigma_{PM}^2 + 2\sigma_{P\alpha}^2) + \frac{\alpha_0^4 M_0^2}{P_{d0}^2} (\sigma_{MM}^2 + 4\sigma_{\alpha\alpha}^2 + 4\sigma_{M\alpha}^2) \right]$$

The phase velocity has three limiting values: a quasi-static value for $\omega \ll \omega_0$ and $\omega \rightarrow 0$, $V_{qs} = \omega[k_1 + A]^{-1}$; an intermediate no-flow velocity for $\omega \gg \omega_0$, $V_{nf} = \omega[k_1 + A - 2D/k_2]^{-1}$, and a ray-theoretical limit $V_{ray} = \omega[k_1 + A - 2D/k_2 - C/(2k_1)]^{-1}$. The quasi-static limit is equivalent to the poroelastic Backus average (see Section 4.15). The inter-layer flow effect contributes significantly to the total attenuation in the seismic frequency range for highly permeable thin layers with correlation lengths of a few centimeters.

Uses

The equations described in this section can be used to estimate velocity dispersion and frequency-dependent anisotropy for plane-wave propagation at any angle in randomly layered, one-dimensional media. They can also be used to apply angle-dependent amplitude corrections to correct for the effect of stratigraphic filtering in amplitude-versus-offset (AVO) modeling of a target horizon below a thinly layered overburden. The corrected amplitudes are obtained by multiplying the transmissivity by $\exp(\gamma L)$ for the down-going and up-going ray paths (Widmaier *et al.*, 1996). The equations for poroelastic media can be used to compute velocity dispersion and attenuation in heterogeneous, fluid-saturated one-dimensional porous media.

Assumptions and limitations

The results described in this section are based on the following assumptions:

- layers are isotropic, linear elastic or poroelastic with no lateral variation;
- the layered medium is statistically stationary with small fluctuations ($<30\%$) in the material properties;

- the propagation path is very much longer than any characteristic correlation length of the medium; and
- incident plane-wave propagation is assumed. The expressions for poroelastic media assume plane waves along the normal to the layers (0° angle of incidence). Numerical calculations (Gelinsky *et al.*, 1998) indicate that the expressions give reasonable results for angles of incidence up to 20° .

3.13 Scale-dependent seismic velocities in heterogeneous media

Synopsis

Measurable travel times of seismic events propagating in heterogeneous media depend on the scale of the seismic wavelength relative to the scale of the geological heterogeneities. In general, the velocity inferred from arrival times is slower when the wavelength, λ , is longer than the scale of the heterogeneity, a , and faster when the wavelength is shorter (Mukerji *et al.*, 1995b).

Layered (one-dimensional) media

For normal-incidence propagation in stratified media, in the long-wavelength limit ($\lambda/a \gg 1$), where a is the scale of the layering, the stratified medium behaves as a homogeneous effective medium with a velocity given by effective medium theory as

$$V_{\text{EMT}} = \left(\frac{M_{\text{EMT}}}{\rho_{\text{av}}} \right)^{1/2}$$

The effective modulus M_{EMT} is obtained from the Backus average. For normal-incidence plane-wave propagation, the effective modulus is given by the harmonic average

$$M_{\text{EMT}} = \left(\sum_k \frac{f_k}{M_k} \right)^{-1}$$

$$\frac{1}{\rho_{\text{av}} V_{\text{EMT}}^2} = \sum_k \frac{f_k}{\rho_k V_k^2}$$

$$\rho_{\text{av}} = \sum_k f_k \rho_k$$

where f_k , ρ_k , M_k , and V_k are the volume fractions, densities, moduli, and velocities of each constituent layer, respectively. The modulus M can be interpreted as C_{3333} or $K + 4\mu/3$ for P-waves and as C_{2323} or μ for S-waves (where K and μ are the bulk and shear moduli, respectively).

In the short-wavelength limit $\lambda/a \ll 1$, the travel time for plane waves traveling perpendicularly to the layers is given by ray theory as the sum of the travel times through each layer. The ray theory or short-wavelength velocity through the medium is, therefore,

$$\frac{1}{V_{\text{RT}}} = \sum_k \frac{f_k}{V_k}$$

The ray theory velocity involves averaging slownesses, whereas the effective medium velocity involves averaging compliances (slownesses squared). The result is that V_{RT} is always faster than V_{EMT} .

In **two- and three-dimensional heterogeneous media**, there is also the path effect as a result of Fermat's principle. Shorter wavelengths tend to find fast paths and diffract around slower inhomogeneities, thus biasing the travel times to lower values (Nolet, 1987; Müller *et al.* 1992). This is sometimes referred to as the “Wielandt effect,” “fast path effect,” or “velocity shift.” The velocity shift was quantified by Boyse (1986) and by Roth *et al.* (1993) using an asymptotic ray-theoretical approach. The heterogeneous random medium is characterized by a spatially varying, statistically stationary slowness field

$$n(\mathbf{r}) = n_0 + \varepsilon n_1(\mathbf{r})$$

where \mathbf{r} is the position vector, $n_1(\mathbf{r})$ is a zero-mean small fluctuation superposed on the constant background slowness n_0 , and $\varepsilon \ll 1$ is a small perturbation parameter. The spatial structure of the heterogeneities is described by the isotropic spatial autocorrelation function:

$$\langle \varepsilon n_1(\mathbf{r}_1) \varepsilon n_1(\mathbf{r}_2) \rangle = \varepsilon^2 \langle n_1^2 \rangle N(|\mathbf{r}_1 - \mathbf{r}_2|)$$

and the coefficient of variation (normalized standard deviation) is given by

$$\sigma_n = \frac{\varepsilon \sqrt{\langle n_1^2 \rangle}}{n_0}$$

where $\langle \cdot \rangle$ denotes the expectation operator. For short-wavelength, $\lambda/a \ll 1$, initially plane waves traveling along the x -direction, the expected travel time (spatial average of the travel time over a plane normal to x) at distance X is given as (Boyse, 1986)

$$\langle T \rangle = n_0 \left[X + \alpha \sigma_n^2 \int_0^X (X - \xi)^2 \frac{N'(\xi)}{\xi} d\xi \right] + O(\varepsilon^3)$$

where $\alpha = 1, \frac{1}{2}$, and 0 for three, two, and one dimension(s), respectively, and the prime denotes differentiation. When the wave has traveled a large distance compared

with the correlation length a of the medium $X \gg a$, and when the autocorrelation function is such that $N(\xi) \ll N(0)$ for $\xi > a$, then

$$\langle T \rangle \approx n_0 (X - \alpha X^2 \sigma_n^2 D)$$

$$D = - \int_0^\infty \frac{N'(\xi)}{\xi} d\xi > 0$$

The ray-theory slowness calculated from the average ray-theory travel time is given by $n_{\text{RT}} = \langle T \rangle / X$. Scaling the distance by the correlation length, a , results in the following equation:

$$\frac{n_{\text{RT}}}{n_0} = 1 - \alpha \sigma_n^2 \left(\frac{X}{a} \right) \hat{D}$$

where \hat{D} is defined similarly to D but with the autocorrelation function being of unit correlation length ($a = 1$). For a Gaussian autocorrelation function $\hat{D} = \sqrt{\pi}$. In one dimension $\alpha = 0$, and the ray-theory slowness is just the average slowness. In two and three dimensions the path effect is described by the term $\alpha \sigma_n^2 (X/a) \hat{D}$. In this case, the wave arrivals are on average faster in the random medium than in a uniform medium having the same mean slowness. The expected travel time in three dimensions is less than that in two dimensions, which in turn is less than that in one dimension. This is because in higher dimensions more admissible paths are available to minimize the travel time.

Müller *et al.* (1992) have established ray-theoretical results relating $N(|r|)$ to the spatial autocorrelation function $\phi(|r|)$ of the travel time fluctuations around the mean travel time. Using first-order straight-ray theory, they show

$$\phi(\zeta) = 2X \int_\zeta^\infty N(\xi) \frac{\xi}{\sqrt{\xi^2 - \zeta^2}} d\xi$$

For a medium with a Gaussian slowness autocorrelation function, $N(r) = \exp(-r^2/a^2)$, the variance of travel time fluctuations $\phi(0)$ is related to the variance of the slowness fluctuations by

$$\phi(0) = \sqrt{\pi} X a n_0^2 \sigma_n^2$$

The expected travel time $\langle T \rangle$ of the wavefield $U(n)$ in the heterogeneous medium with random slowness n is distinct from the travel time T of the expected wavefield $\langle U(n) \rangle$ in the random medium. The expected wave, which is an ensemble average of the wavefield over all possible realizations of the random medium, travels slower than the wavefield in the average medium $\langle n \rangle$ (Keller, 1964).

Thus,

$$\langle T(U(n)) \rangle \leq T(U(\langle n \rangle)) \leq T(\langle U(n) \rangle)$$

Gold *et al.* (2000) analyzed wave propagation in random heterogeneous elastic media in the limit of small fluctuations and low frequencies (low-frequency limit of the elastic Bourret approximation) to obtain the effective P- and S-wave slownesses for the coherent wavefield. The random medium is characterized by zero-mean fluctuations of Lamé parameters and density superposed on a homogeneous background with constant mean values of Lamé parameters (λ_0, μ_0) and density (ρ_0) :

$$\lambda(\mathbf{r}) = \lambda_0(1 + \varepsilon_\lambda(\mathbf{r})); \quad \langle \varepsilon_\lambda \rangle = 0$$

$$\mu(\mathbf{r}) = \mu_0(1 + \varepsilon_\mu(\mathbf{r})); \quad \langle \varepsilon_\mu \rangle = 0$$

$$\rho(\mathbf{r}) = \rho_0(1 + \varepsilon_\rho(\mathbf{r})); \quad \langle \varepsilon_\rho \rangle = 0$$

The effective slownesses for P- and S-waves for three-dimensional random media in the low-frequency, small-fluctuation limit are expressed as (Gold *et al.*, 2000):

$$S_e^P = S_0^P \left[1 + \frac{1}{2} \frac{\lambda_0^2}{(\lambda_0 + 2\mu_0)^2} \sigma_{\lambda\lambda}^2 + \frac{2}{3} \frac{\lambda_0\mu_0}{(\lambda_0 + 2\mu_0)^2} \sigma_{\lambda\mu}^2 + \frac{2}{5} \frac{\mu_0^2}{(\lambda_0 + 2\mu_0)^2} \sigma_{\mu\mu}^2 + \frac{4}{15} \frac{\mu_0}{(\lambda_0 + 2\mu_0)} \sigma_{\mu\mu}^2 \right]$$

$$S_e^S = S_0^S \left[1 + \frac{1}{5} \sigma_{\mu\mu}^2 + \frac{2}{15} \frac{\mu_0}{(\lambda_0 + 2\mu_0)} \sigma_{\mu\mu}^2 \right]$$

For two-dimensional random media Gold *et al.* give the following expressions:

$$S_e^P = S_0^P \left[1 + \frac{1}{2} \frac{\lambda_0^2}{(\lambda_0 + 2\mu_0)^2} \sigma_{\lambda\lambda}^2 + \frac{\lambda_0\mu_0}{(\lambda_0 + 2\mu_0)^2} \sigma_{\lambda\mu}^2 + \frac{3}{4} \frac{\mu_0^2}{(\lambda_0 + 2\mu_0)^2} \sigma_{\mu\mu}^2 + \frac{1}{4} \frac{\mu_0}{(\lambda_0 + 2\mu_0)} \sigma_{\mu\mu}^2 \right]$$

$$S_e^S = S_0^S \left[1 + \frac{1}{4} \sigma_{\mu\mu}^2 + \frac{1}{4} \frac{\mu_0}{(\lambda_0 + 2\mu_0)} \sigma_{\mu\mu}^2 \right]$$

In the above equations, $S_0^P = \sqrt{\rho_0/(\lambda_0 + 2\mu_0)}$ and $S_0^S = \sqrt{\rho_0/\mu_0}$ are the P- and S-wave slownesses in the homogeneous background medium, respectively. The normalized variances and covariances of the fluctuations of parameters x and y are denoted by σ_{xy} . In this small-contrast, low-frequency limit, density heterogeneities do not affect the properties of the effective medium. The derivation assumes isotropic spatial correlation of the heterogeneities.

Uses

The results described in this section can be used for the following purposes:

- to estimate the velocity shift caused by fast path effects in heterogeneous media;
- to relate statistics of observed travel times to the statistics of the heterogeneities; and
- to smooth and upscale heterogeneous media in the low-frequency limit.

Assumptions and limitations

The equations described in this section apply under the following conditions:

- small fluctuations in the material properties of the heterogeneous medium;
- isotropic spatial autocorrelation function of the fluctuations;
- ray-theory results are valid only for wavelengths much smaller than the spatial correlation length of the media; and
- low-frequency, effective-smoothing results are valid only for wavelengths much larger than the spatial correlation length of the medium, and for a smoothing window that is much smaller than the wavelength, but much larger than the spatial correlation length.

3.14 Scattering attenuation

Synopsis

The attenuation coefficient, $\gamma_s = \pi f/QV$ (where Q is the quality factor, V is the seismic velocity, and f is frequency) that results from elastic scattering depends on the ratio of seismic wavelength, λ , to the diameter, d_s , of the scattering heterogeneity. Roughly speaking there are three domains:

- Rayleigh scattering, where $\lambda > d_s$ and $\gamma_s \propto d_s^3 f^4$;
- stochastic/Mie scattering, where $\lambda \approx d_s$ and $\gamma_s \propto d_s f^2$;
- diffusion scattering, where $\lambda < d_s$ and $\gamma_s \propto 1/d_s$.

When $\lambda \gg d_s$, the heterogeneous medium behaves like an effective homogeneous medium, and scattering effects may be negligible. At the other limit, when $\lambda \ll d_s$, the heterogeneous medium may be treated as a piecewise homogeneous medium.

Figure 3.14.1 shows schematically the general scale dependence (or, equivalently, frequency dependence) of wave velocity that is expected owing to scattering in heterogeneous media. At very long wavelengths ($\lambda \gg d_s$) the phase velocity is nondispersive and is close to the static effective medium result. As the wavelength decreases (frequency increases), scattering causes velocity dispersion. In the Rayleigh scattering domain ($\lambda/d_s \approx 2\pi$), the velocity shows a slight decrease with increasing frequency. This is usually followed by a rapid and much larger increase in

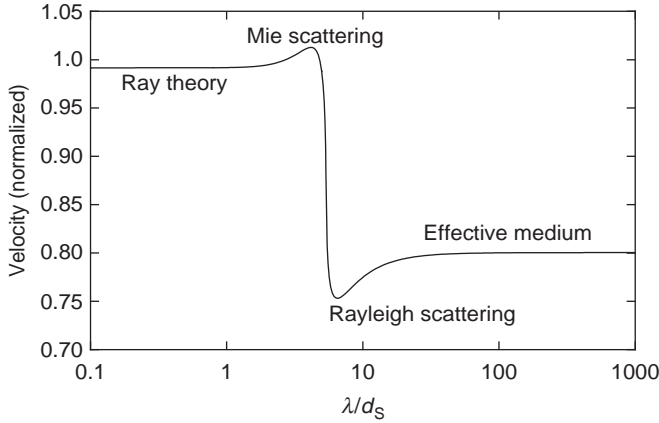


Figure 3.14.1 Scale dependence (or, equivalently, frequency dependence) of the wave velocity due to scattering in heterogeneous media.

phase velocity owing to resonant (or Mie) scattering ($\lambda \approx d_s$). When $\lambda \ll d_s$ (specular scattering or ray theory), the velocity is again nondispersive or weakly dispersive and is usually significantly higher than its long-wavelength limit.

It is usually assumed that the long-wavelength Rayleigh limit is most appropriate for analyzing laboratory rock physics results because the seismic wavelength is often much larger than the grain size. However, Lucet and Zinszner (1992) and Blair (1990), among others, have shown that the scattering heterogeneities can be *clusters* of grains that are comparable to, or larger than, the wavelength. Certainly any of the domains are possible *in situ*.

Blair (1990) suggests a simple (ad hoc) expression that is consistent with both the Rayleigh and diffusion scattering limits:

$$\gamma_s(f) = \frac{C_s}{d_s} \frac{(f/f_d)^4}{(1 + f/f_d)^4}, \quad f_d = \frac{k_s V}{d_s} = \frac{k_s f \lambda}{d_s}$$

where C_s and k_s are constants.

Many theoretical estimates of scattering effects on velocity and attenuation have appeared (see Mehta, 1983, and Berryman, 1992b, for reviews). Most are in the long-wavelength limit, and most assume that the concentration of scatterers is small, and thus only single scattering is considered.

The attenuation of P-waves caused by a low concentration of small spherical inclusions is given by (Yamakawa, 1962; Kuster and Toksöz, 1974)

$$\gamma_{\text{sph}} = c \frac{3\omega}{4V_P} \left(\frac{\omega}{V_P} a \right)^3 \left[2B_0^2 + \frac{2}{3}(1 + 2\zeta^3)B_1^2 + \frac{(2 + 3\zeta^5)}{5}B_2^2 \right]$$

where

$$B_0 = \frac{K - K'}{3K' + 4\mu}$$

$$B_1 = \frac{\rho - \rho'}{3\rho}$$

$$B_2 = \frac{20}{3} \frac{\mu(\mu' - \mu)}{6\mu'(K + 2\mu) + \mu(9K + 8\mu)}$$

$$\zeta = V_P/V_S$$

The terms V_P and V_S are the P- and S-velocities of the host medium, respectively, c is the volume concentration of the spheres, a is their radius, $2\pi f = \omega$ is the frequency, ρ is the density, K is the bulk modulus, and μ is the shear modulus. The unprimed moduli refer to the background host medium and the primed moduli refer to the inclusions.

In the case of elastic spheres in a linear viscous fluid, with viscosity η , the attenuation is given by (Epstein, 1941; Epstein and Carhart, 1953; Kuster and Toksöz, 1974)

$$\gamma_{\text{sph}} = c \frac{\omega}{2V_P} (\rho - \rho') \text{Real} \left[\frac{i + b_0 - ib_0^2/3}{\rho(1 - ib_0) - (\rho + 2\rho')b_0^2/9} \right]$$

where

$$b_0 = (1 + i)a\sqrt{\frac{\pi f \rho}{\eta}}$$

Hudson (1981) gives the attenuation coefficient for elastic waves in cracked media (see Section 4.10 on Hudson). For aligned penny-shaped ellipsoidal cracks with normals along the 3-axis, the attenuation coefficients for P-, SV-, and SH-waves are

$$\gamma_P = \frac{\omega}{V_S} \varepsilon \left(\frac{\omega a}{V_P} \right)^3 \frac{1}{30\pi} \left[AU_1^2 \sin^2 2\theta + BU_3^2 \left(\frac{V_P^2}{V_S^2} - 2 \sin^2 \theta \right)^2 \right]$$

$$\gamma_{SV} = \frac{\omega}{V_S} \varepsilon \left(\frac{\omega a}{V_S} \right)^3 \frac{1}{30\pi} (AU_1^2 \cos^2 2\theta + BU_3^2 \sin^2 2\theta)$$

$$\gamma_{SH} = \frac{\omega}{V_S} \varepsilon \left(\frac{\omega a}{V_S} \right)^3 \frac{1}{30\pi} (AU_1^2 \cos^2 \theta)$$

$$A = \frac{3}{2} + \frac{V_S^5}{V_P^5}$$

$$B = 2 + \frac{15 V_S}{4 V_P} - 10 \frac{V_S^3}{V_P^3} + 8 \frac{V_S^5}{V_P^5}$$

In these expressions, θ is the angle between the direction of propagation and the 3-axis (axis of symmetry), and ε is the crack density parameter:

$$\varepsilon = \frac{N}{V} a^3 = \frac{3\phi}{4\pi\alpha}$$

where N/V is the number of penny-shaped cracks of radius a per unit volume, ϕ is the crack porosity, and α is the crack aspect ratio.

U_1 and U_3 depend on the crack conditions. For dry cracks

$$U_1 = \frac{16(\lambda + 2\mu)}{3(3\lambda + 4\mu)}; \quad U_3 = \frac{4(\lambda + 2\mu)}{3(\lambda + \mu)}$$

For “weak” inclusions (i.e., when $\mu\alpha/(K' + \frac{4}{3}\mu')$ is of the order 1 and is not small enough to be neglected)

$$U_1 = \frac{16(\lambda + 2\mu)}{3(3\lambda + 4\mu)} \frac{1}{(1 + M)}; \quad U_3 = \frac{4(\lambda + 2\mu)}{3(\lambda + \mu)} \frac{1}{(1 + \kappa)}$$

where

$$M = \frac{4\mu'(\lambda + 2\mu)}{\pi\alpha\mu(3\lambda + 4\mu)}; \quad \kappa = \frac{(K' + \frac{4}{3}\mu')(\lambda + 2\mu)}{\pi\alpha\mu(\lambda + \mu)}$$

with K' and μ' equal to the bulk and shear moduli of the inclusion material. The criterion for an inclusion to be “weak” depends on its shape, or aspect ratio α , as well as on the relative moduli of the inclusion and matrix material. Dry cavities can be modeled by setting the inclusion moduli to zero. Fluid-saturated cavities are simulated by setting the inclusion shear modulus to zero. Remember that these give only the scattering losses and do not incorporate other viscous losses caused by the pore fluid.

Hudson also gives expressions for infinitely thin fluid-filled cracks:

$$U_1 = \frac{16(\lambda + 2\mu)}{3(3\lambda + 4\mu)}; \quad U_3 = 0$$

These assume no discontinuity in the normal component of crack displacements and therefore predict no change in the compressional modulus with saturation. There is, however, a shear displacement discontinuity and a resulting effect on shear stiffness. This case should be used with care.

For randomly oriented cracks (isotropic distribution) the P- and S-attenuation coefficients are given as

$$\gamma_P = \frac{\omega}{V_S} \varepsilon \left(\frac{\omega a}{V_P} \right)^3 \frac{4}{15^2 \pi} \left(A U_1^2 + \frac{1}{2} \frac{V_P^5}{V_S^5} B (B - 2) U_3^2 \right)$$

$$\gamma_S = \frac{\omega}{V_S} \varepsilon \left(\frac{\omega a}{V_S} \right)^3 \frac{1}{75 \pi} \left(A U_1^2 + \frac{1}{3} B U_3^2 \right)$$

The fourth-power dependence on ω is characteristic of Rayleigh scattering.

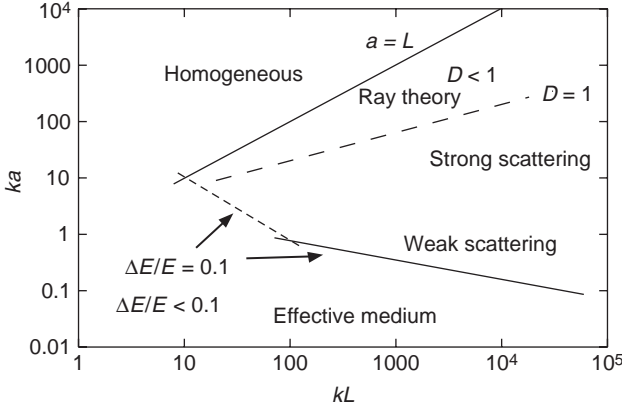


Figure 3.14.2 Domains of applicability for various scattering theories.

Random heterogeneous media with spatially varying velocity $c = c_0 + c'$ may be characterized by the autocorrelation function

$$N(r) = \frac{\langle \xi(r') \xi(r' + r) \rangle}{\langle \xi^2 \rangle}$$

where $\xi = -c'/c_0$ and c_0 denotes the mean background velocity. For small fluctuations, the fractional energy loss caused by scattering is given by (Aki and Richards, 1980)

$$\frac{\Delta E}{E} = \frac{8 \langle \xi^2 \rangle k^4 a^3 L}{1 + 4k^2 a^2}, \quad \text{for } N(r) = e^{-r/a}$$

$$\frac{\Delta E}{E} = \sqrt{\pi} \langle \xi^2 \rangle k^2 a L (1 - e^{-k^2 a^2}), \quad \text{for } N(r) = e^{-r^2/a^2}$$

These expressions are valid for small $\Delta E/E$ values as they are derived under the Born approximation, which assumes that the primary incident waves are unchanged as they propagate through the heterogeneous medium.

Aki and Richards (1980) classify scattering phenomena in terms of two dimensionless numbers ka and kL , where $k = 2\pi/\lambda$ is the wavenumber, a is the characteristic scale of the heterogeneity, and L is the path length of the primary incident wave in the heterogeneous medium. Scattering effects are not very important for very small or very large ka , and they become increasingly important with increasing kL . Scattering problems may be classified on the basis of the fractional energy loss caused by scattering, $\Delta E/E$, and the wave parameter D defined by $D = 4L/ka^2$. The wave parameter is the ratio of the first Fresnel zone to the scale length of the heterogeneity. Ray theory is applicable when $D < 1$. In this case the inhomogeneities are smooth enough to be treated as piecewise homogeneous. Effective medium theories are appropriate when ka and $\Delta E/E$ are small. These domains are summarized in Figure 3.14.2.

Scattering becomes complex when heterogeneity scales are comparable with the wavelength and when the path lengths are long. Energy diffusion models are used for long path lengths and strong scattering.

Uses

The results described in this section can be used to estimate the seismic attenuation caused by scattering.

Assumptions and limitations

The results described in this section have the following limitations:

- formulas for spherical and ellipsoidal inclusions are limited to low pore concentrations and wavelengths much larger than the scatterer diameter;
- formulas for fractional energy loss in random heterogeneous media are limited to weak scattering.

3.15 Waves in cylindrical rods: the resonant bar

Synopsis

Time-harmonic waves propagating in the axial direction along a circular cylindrical rod involve radial, circumferential, and axial components of displacement, u_r , u_θ , and u_z , respectively. Motions that depend on z but are independent of θ may be separated into **torsional** waves involving u_θ only and **longitudinal** waves involving u_r and u_z . **Flexural** waves consist of motions that depend on both z and θ .

Torsional waves

Torsional waves involve purely circumferential displacements that are independent of θ . The dispersion relation (for free-surface boundary conditions) is of the form (Achenbach, 1984)

$$saJ_0(sa) - 2J_1(sa) = 0$$

$$s^2 = \frac{\omega^2}{V_S^2} - k^2$$

where $J_n(\cdot)$ are Bessel functions of the first kind of order n , a is the radius of the cylindrical rod, V_S is the S-wave velocity, and k is the wavenumber for torsional waves.

For practical purposes, the lowest mode of each kind of motion is important. The lowest torsional mode consists of displacement proportional to the radius, and the motion is a rotation of each cross-section of the cylinder about its center. The phase velocity of the lowest torsional mode is nondispersive and is given by

$$V_{\text{torsion}} = V_S = \sqrt{\frac{\mu}{\rho}}$$

where μ and ρ are the shear modulus and density of the rod, respectively.

Longitudinal waves

Longitudinal waves are axially symmetric and have displacement components in the axial and radial directions. The dispersion relation (for free-surface boundary conditions), known as the **Pochhammer** equation, is (Achenbach, 1984)

$$2pa[(sa)^2 + (ka)^2]J_1(pa)J_1(sa) - [(sa)^2 - (ka)^2]^2J_0(pa)J_1(sa) - 4(ka)^2(pa)(sa)J_1(pa)J_0(sa) = 0$$

$$p^2 = \frac{\omega^2}{V_P^2} - k^2$$

where V_P is the P-wave velocity.

The phase velocity of the lowest longitudinal mode for small ka ($ka \ll 1$) can be expressed as

$$V_{\text{long}} = \sqrt{\frac{E}{\rho}} \left[1 - \frac{1}{4}v^2(ka)^2 \right] + O[(Ka)^4]$$

where E is the Young modulus of the cylindrical rod and v is the Poisson ratio of the cylindrical rod.

In the limit as $(ka) \rightarrow 0$, the phase velocity tends to the bar velocity or extensional velocity $V_E = \sqrt{E/\rho}$. For very large ka ($ka \gg 1$), V_{long} approaches the Rayleigh wave velocity.

Flexural waves

Flexural modes have all three displacement components – axial, radial, and circumferential and involve motion that depends on both z and θ . The phase velocity of the lowest flexural mode for small values of ka ($ka \ll 1$) may be written as

$$V_{\text{flex}} = \frac{1}{2} \sqrt{\frac{E}{\rho}} (ka) + O[(ka)^3]$$

The phase velocity of the lowest flexural mode goes to zero as $(ka) \rightarrow 0$ and approaches the Rayleigh wave velocity for large ka values.

Bar resonance

Resonant modes (or standing waves) occur when the bar length is an integer number of half-wavelengths:

$$V = \lambda f = \frac{2Lf}{n}$$

where V is velocity, λ is wavelength, f is the resonant frequency, L is the bar length, and n is a positive integer.

In practice, the shear or extensional velocity is calculated from the observed resonant frequency, most often at the fundamental mode, where $n = 1$.

Porous, fluid-saturated rods

Biot's theory has been used to extend Pochhammer's method of analysis for fluid-saturated porous rods (Gardner, 1962; Berryman, 1983). The dependence of the velocity and attenuation of longitudinal waves on the skeleton and fluid properties is rather complicated. The motions of the solid and the fluid are partly parallel to the axis of the cylinder and partly along the radius. The dispersion relations are obtained from plane-wave solutions of Biot's equations in cylindrical (r, θ, z) coordinates. For an open (unjacketed) surface boundary condition the ω - k_z dispersion relation is given by (in the notation of Berryman, 1983)

$$D_{\text{open}} = \begin{vmatrix} a_{11} & a_{12} & a_{13} \\ a_{21} & a_{22} & 0 \\ a_{31} & a_{32} & a_{33} \end{vmatrix} = 0$$

$$a_{11} = \frac{[(C\Gamma_- - H)k_+^2 + 2\mu_{\text{fr}}k_z^2]J_0(k_+a) + 2\mu_{\text{fr}}k_{r+}J_1(k_+a)/a}{(\Gamma_+ - \Gamma_-)}$$

$$a_{12} = \frac{[(H - C\Gamma_+)k_-^2 - 2\mu_{\text{fr}}k_z^2]J_0(k_-a) - 2\mu_{\text{fr}}k_{r-}J_1(k_-a)/a}{(\Gamma_+ - \Gamma_-)}$$

$$a_{13} = -2\mu_{\text{fr}}k_{\text{sr}}[k_{\text{sr}}J_0(k_{\text{sr}}a) - J_1(k_{\text{sr}}a)/a]$$

$$a_{21} = \frac{(M\Gamma_- - C)k_+^2J_0(k_+a)}{(\Gamma_+ - \Gamma_-)}$$

$$a_{22} = \frac{(C - M\Gamma_+)k_-^2J_0(k_-a)}{(\Gamma_+ - \Gamma_-)}$$

$$a_{23} = 0$$

$$a_{31} = \frac{-2i\mu_{\text{fr}}k_zk_{r+}J_1(k_+a)}{(\Gamma_+ - \Gamma_-)}$$

$$a_{32} = \frac{2i\mu_{\text{fr}}k_zk_{r-}J_1(k_-a)}{(\Gamma_+ - \Gamma_-)}$$

$$a_{33} = -\mu_{\text{fr}}(k_s^2 - 2k_z^2)k_{\text{sr}}J_1(k_{\text{sr}}a)/(ik_z)$$

$$k_{r\pm}^2 = k_{\pm}^2 - k_z^2, \quad k_{\text{sr}}^2 = k_s^2 - k_z^2$$

$$k_s^2 = \omega^2(\rho - \rho_{\text{n}}^2/q)\mu_{\text{fr}}$$

$$k_+^2 = \frac{1}{2} \left[b + f - \sqrt{(b - f)^2 + 4cd} \right]$$

$$k_-^2 = \frac{1}{2} \left[b + f + \sqrt{(b-f)^2 + 4cd} \right]$$

$$b = \omega^2(\rho M - \rho_{\text{fl}} C) / \Delta$$

$$c = \omega^2(\rho_{\text{fl}} M - q C) / \Delta$$

$$d = \omega^2(\rho_{\text{fl}} H - \rho C) / \Delta$$

$$f = \omega^2(q H - \rho_{\text{fl}} C) / \Delta$$

$$\Delta = M H - C^2$$

$$\Gamma_{\pm} = d / (k_{\pm}^2 - b) = (k_{\pm}^2 - f) / c$$

$$H = K_{\text{fr}} + \frac{4}{3} \mu_{\text{fr}} + \frac{(K_0 - K_{\text{fr}})^2}{(D - K_{\text{fr}})}$$

$$C = \frac{(K_0 - K_{\text{fr}}) K_0}{(D - K_{\text{fr}})}$$

$$M = \frac{K_0^2}{(D - K_{\text{fr}})}$$

$$D = K_0 [1 + \phi (K_0 / K_{\text{fl}} - 1)]$$

$$\rho = (1 - \phi) \rho_0 + \phi \rho_{\text{fl}}$$

$$q = \frac{\alpha \rho_{\text{fl}}}{\phi} - \frac{i \eta F(\zeta)}{\omega \kappa}$$

where

$K_{\text{fr}}, \mu_{\text{fr}}$ = effective bulk and shear moduli of rock frame: either the dry frame or the high-frequency unrelaxed “wet frame” moduli predicted by the Mavko–Jizba squirt theory

K_0 = bulk modulus of mineral material making up rock

K_{fl} = effective bulk modulus of pore fluid

ϕ = porosity

ρ_0 = mineral density

ρ_{fl} = fluid density

α = tortuosity parameter (always greater than 1)

η = viscosity of the pore fluid

k = absolute permeability of the rock

ω = angular frequency of the plane wave.

The viscodynamic operator $F(\zeta)$ incorporates the frequency dependence of viscous drag and is defined by

$$F(\zeta) = \frac{1}{4} \frac{\zeta T(\zeta)}{1 + 2i T(\zeta) / \zeta}$$

$$T(\zeta) = \frac{\text{ber}'(\zeta) + i\text{bei}'(\zeta)}{\text{ber}(\zeta) + i\text{bei}(\zeta)} = \frac{e^{i3\pi/4}J_1(\zeta e^{-i\pi/4})}{J_0(\zeta e^{-i\pi/4})}$$

$$\zeta = (\omega/\omega_r)^{1/2} = \left(\frac{\omega h^2 \rho_{\text{fl}}}{\eta} \right)^{1/2}$$

where $\text{ber}(\)$ and $\text{bei}(\)$ are the real and imaginary parts of the Kelvin function, respectively, $J_n(\)$ is a Bessel function of order n , and h is the pore-size parameter.

The pore-size parameter h depends on both the dimensions and shape of the pore space. Stoll (1974) found that values of between $\frac{1}{6}$ and $\frac{1}{7}$ for the mean grain diameter gave good agreement with experimental data from several investigators. For spherical grains, Hovem and Ingram (1979) obtained $h = \phi d/[3(1 - \phi)]$, where d is the grain diameter.

This dispersion relation gives the same results as Gardner (1962). When the surface pores are closed (jacketed) the resulting dispersion relation is

$$D_{\text{closed}} = \begin{vmatrix} a_{11} & a_{12} & a_{13} \\ a_{31} & a_{32} & a_{33} \\ a_{41} & a_{42} & a_{43} \end{vmatrix} = 0$$

$$a_{41} = \frac{k_{r+}\Gamma_- J_1(k_+ a)}{\Gamma_+ - \Gamma_-}; \quad a_{42} = \frac{-k_{r-}\Gamma_+ J_1(k_- a)}{\Gamma_+ - \Gamma_-}; \quad a_{43} = k_{\text{sr}} J_1(k_{\text{sr}} a) \rho_{\text{fl}}/q$$

For open-pore surface conditions the vanishing of the fluid pressure at the surface of the cylinder causes strong radial motion of the fluid relative to the solid. This relative motion absorbs energy, causing greater attenuation than would be present in a plane longitudinal wave in an extended porous saturated medium (White, 1986). Narrow stop bands and sharp peaks in the attenuation can occur if the slow P-wave has wavelength $\lambda < 2.6a$. Such stop bands do not exist in the case of the jacketed, closed-pore surface. A slow extensional wave propagates under jacketed boundary conditions but not under the open-surface condition.

Uses

The results described in this section can be used to model wave propagation and geometric dispersion in resonant bar experiments.

Assumptions and limitations

The results described in this section assume the following:

- an isotropic, linear, homogeneous, and elastic–poroelastic rod of solid circular cross-section;
- for elastic rods the cylindrical surface is taken to be free of tractions; and
- for porous rods, unjacketed and jacketed surface boundary conditions are assumed.

3.16 Waves in boreholes

Synopsis

Elastic wave propagation in the presence of a cylindrical fluid-filled borehole involves different modes caused by internal refraction, constructive interference and trapping of wave energy in the borehole. The theory of borehole wave propagation has been described in the books by White (1983), Paillet and Cheng (1991), and Tang and Cheng (2004), where references to the original literature may be found. The dispersion characteristics of borehole wave modes depend strongly on the shear wave velocity of the elastic medium surrounding the borehole. Two scenarios are usually considered: “fast” formation when the S-wave velocity in the formation is greater than the borehole fluid velocity and “slow” formation when the S-wave velocity in the formation is slower than the borehole fluid velocity. Wave modes are guided by the borehole only when the formation S-wave velocity is greater than the phase velocity of the modes; otherwise the modes become leaky modes, radiating energy into the formation.

In fast formations, pseudo-Rayleigh modes or shear normal modes exist above characteristic cut-off frequencies. The pseudo-Rayleigh mode is strongly dispersive and is a combined effect of reflected waves in the fluid and critical refraction along the borehole walls. The phase velocity of the pseudo-Rayleigh wave at the cut-off frequency drops from the shear wave velocity of the formation and approaches the fluid velocity at high frequencies. In slow formations pseudo-Rayleigh modes do not exist. Stoneley waves in boreholes refer to waves along the borehole interface. At low frequencies the Stoneley waves are referred to as tube waves. Stoneley waves exist at all frequencies and in both fast and slow formations. “Leaky P” modes exist in slow formations and are dominated by critical refraction of P-waves at the borehole wall. They lose energy by conversion to shear waves. Higher-order modes include the dipole or flexural mode and the quadrupole or screw mode (Tang and Cheng, 2004).

Isotropic elastic formation

A low-frequency (static) analysis for a thick-walled elastic tube of inner radius b and outer radius a , with Young’s modulus E , and Poisson ratio ν , containing fluid with bulk modulus B , and density ρ , gives the speed of tube waves as (White, 1983)

$$c_t = \left[\rho \left(\frac{1}{B} + \frac{1}{M} \right) \right]^{-1/2}$$

$$M = \frac{E(a^2 - b^2)}{2[(1 + \nu)(a^2 + b^2) - 2\nu b^2]}$$

For a thin-walled tube with thickness $h = (a - b)$, $a \approx b$, and $M \approx Eh/2b$. For a borehole in an infinite solid $a \gg b$ and the speed of the tube wave in the low-frequency limit is

$$c_t = \left[\rho \left(\frac{1}{B} + \frac{1}{\mu} \right) \right]^{-1/2}$$

where μ is the shear modulus of the formation. For a borehole with a casing of thickness h , inner radius b , and Young's modulus E , the tube wave velocity (in the low-frequency limit) is

$$c_t = \left[\rho \left(\frac{1}{B} + \frac{1}{\mu + Eh/2b} \right) \right]^{-1/2}$$

The ω - k dispersion relation gives a more complete description of the modes. The dispersion relation (or period equation) yields characteristic cut-off frequencies and phase velocities as a function of frequency for the different modes (Paillet and Cheng, 1991; Tang and Cheng, 2004). For a cylindrical borehole of radius R , in an infinite, isotropic, elastic formation with Lamé constants λ and μ , and density ρ , and open-hole boundary conditions at the interface, the dispersion relation is given by (in the notation of Tang and Cheng, 2004)

$$D(\omega, k) = \begin{vmatrix} M_{11} & M_{12} & M_{13} & M_{14} \\ M_{21} & M_{22} & M_{23} & M_{24} \\ M_{31} & M_{32} & M_{33} & M_{34} \\ M_{41} & M_{42} & M_{43} & M_{44} \end{vmatrix} = 0$$

$$M_{11} = -\frac{n}{R}I_n(fR) - fI_{n+1}(fR)$$

$$M_{12} = -pY_1(pR)$$

$$M_{13} = \frac{n}{R}K_n(sR)$$

$$M_{14} = -iksY_1(sR)$$

$$M_{21} = \rho_f \omega^2 I_n(fR)$$

$$M_{22} = \rho(2k^2\beta^2 - \omega^2)K_n(pR) + \frac{2p\rho\beta^2}{R}Y_2(pR)$$

$$M_{23} = -\frac{2n\rho s\beta^2}{R}Y_3(sR)$$

$$M_{24} = 2ik\rho s^2\beta^2 K_n(sR) + \frac{2ik\rho s\beta^2}{R}Y_2(sR)$$

$$M_{31} = 0$$

$$M_{32} = \frac{2n\rho p\beta^2}{R}Y_3(pR)$$

$$M_{33} = -\rho s^2\beta^2 Y_4(sR)$$

$$M_{34} = \frac{2ikns\rho\beta^2}{R}Y_3(sR)$$

$$M_{41} = 0$$

$$M_{42} = -2ikp\rho\beta^2 Y_1(pR)$$

$$M_{43} = \frac{ikn\rho\beta^2}{R} K_n(sR)$$

$$M_{44} = (k^2 + s^2)s\rho\beta^2 Y_1(sR)$$

where I_n and K_n are the modified Bessel functions of the first and second kind, respectively, of order n . The azimuthal order number, n , controls the azimuthal variations, with $n = 0, 1$, and 2 corresponding to monopole, dipole, and quadrupole modes, respectively. In the above expressions Y_i denotes the following combinations of modified Bessel functions:

$$Y_1(x) = -\frac{n}{x}K_n(x) + K_{n+1}(x)$$

$$Y_2(x) = \frac{n(n-1)}{x}K_n(x) + K_{n+1}(x)$$

$$Y_3(x) = \frac{1-n}{x}K_n(x) + K_{n+1}(x)$$

$$Y_4(x) = \left[1 + \frac{2n(n-1)}{x^2}\right]K_n(x) + \frac{2}{x}K_{n+1}(x)$$

Other terms in the expressions are:

ω = angular frequency

k = axial wavenumber

$p = (k^2 - k_\alpha^2)^{1/2}$ = compressional radial wavenumber

$s = (k^2 - k_\beta^2)^{1/2}$ = shear radial wavenumber

$f = (k^2 - k_f^2)^{1/2}$ = radial wavenumber in the borehole fluid

$k_\alpha = \omega/\alpha$ = compressional wavenumber

$k_\beta = \omega/\beta$ = shear wavenumber

$k_f = \omega/\alpha_f$ = acoustic wavenumber in borehole fluid

where α and β are the P- and S-wave velocities in the formation, and α_f is the compressional wave velocity in the borehole fluid. From the roots of the dispersion relation $D(\omega, k) = 0$, the phase and group velocities of the wave modes are obtained as

$$V_{\text{phase}} = \frac{\omega}{k(\omega)}$$

$$V_{\text{group}} = \frac{d\omega}{dk} = -\left(\frac{\partial D}{\partial k}\right) / \left(\frac{\partial D}{\partial \omega}\right)$$

The roots and the partial derivatives have to be calculated numerically.

Transversely isotropic (TI) elastic formation

The elastic properties of the transversely isotropic formation are given by the five independent components of the elastic stiffness tensor (c_{11} , c_{13} , c_{33} , c_{44} , c_{66}), and

ρ denotes the density. The TI symmetry axis is along the z -axis and the borehole axis coincides with the symmetry axis. The borehole radius is R , with borehole fluid density ρ_f , and compressional wave velocity α_f . For open-hole boundary conditions the dispersion relation is given by (Tang and Cheng, 2004)

$$D(\omega, k) = \begin{vmatrix} Q_{11} & Q_{12} & Q_{13} & Q_{14} \\ Q_{21} & Q_{22} & Q_{23} & Q_{24} \\ Q_{31} & Q_{32} & Q_{33} & Q_{34} \\ Q_{41} & Q_{42} & Q_{43} & Q_{44} \end{vmatrix} = 0$$

$$Q_{11} = -\frac{n}{R}I_n(fR) - fI_{n+1}(fR)$$

$$Q_{12} = -(1 + ika')q_p Y_1(q_p R)$$

$$Q_{13} = \frac{n}{R}K_n(q_{sh}R)$$

$$Q_{14} = -(ik + b')q_{sv} Y_1(q_{sv} R)$$

$$Q_{21} = \rho_f \omega^2 I_n(fR)$$

$$Q_{22} = \left[c_{11}q_p^2 - c_{13}k^2 + (c_{11} - c_{13})ika'q_p^2 \right] K_n(q_p R) \\ + \frac{2c_{66}q_p}{R}(1 + ika')Y_2(q_p R)$$

$$Q_{23} = -\frac{2c_{66}nq_{sh}}{R}Y_3(q_{sh}R)$$

$$Q_{24} = \left[(c_{11}q_{sv}^2 - c_{13}k^2)b' + (c_{11} - c_{13})ikq_{sv}^2 \right] K_n(q_{sv} R) \\ + \frac{2c_{66}q_{sv}}{R}(ik + b')Y_2(q_{sv} R)$$

$$Q_{31} = 0$$

$$Q_{32} = \frac{2c_{66}nq_p}{R}(1 + ika')Y_3(q_p R)$$

$$Q_{33} = -c_{66}q_{sh}^2 Y_4(q_{sh} R)$$

$$Q_{34} = \frac{2c_{66}nq_{sv}}{R}(ik + b')Y_3(q_{sv} R)$$

$$Q_{42} = -c_{44}q_p \left[2ik - a'(k^2 + q_p^2) \right] Y_1(q_p R)$$

$$Q_{43} = \frac{iknc_{44}}{R} K_n(q_{sh}R)$$

$$Q_{44} = c_{44}q_{sv}[(k^2 + q_{sv}^2) - 2ikb']Y_1(q_{sv}R)$$

$$a' = -\frac{1}{ik} \frac{(c_{13} + 2c_{44})k^2 - c_{11}q_p^2 - \rho\omega^2}{c_{44}k^2 - (c_{11} - c_{13} - c_{44})q_p^2 - \rho\omega^2}$$

$$b' = -ik \frac{c_{44}k^2 - (c_{11} - c_{13} - c_{44})q_{sv}^2 - \rho\omega^2}{(c_{13} + 2c_{44})k^2 - c_{11}q_{sv}^2 - \rho\omega^2}$$

$$q_{sh} = \sqrt{\frac{c_{44}k^2 - \rho\omega^2}{c_{66}}}$$

$$q_p = \omega \sqrt{\frac{-V + \sqrt{V^2 - 4UW}}{2U}}$$

$$q_{sv} = \omega \sqrt{\frac{-V - \sqrt{V^2 - 4UW}}{2U}}$$

$f = (k^2 - k_f^2)^{1/2}$ = radial wavenumber in the borehole fluid

$k_f = \omega/\alpha_f$ = acoustic wavenumber in the borehole fluid

$$U = c_{11}c_{44}$$

$$V = \rho(c_{11} + c_{44}) - (c_{11}c_{33} - c_{13}^2 - 2c_{13}c_{44})(k^2/\omega^2)$$

$$W = c_{33}c_{44}(\rho/c_{44} - k^2/\omega^2)(\rho/c_{33} - k^2/\omega^2)$$

where I_n and K_n are the modified Bessel functions of the first and second kind, respectively, of order n . The azimuthal order number, n , controls the azimuthal variations, with $n = 0, 1$, and 2 corresponding to monopole, dipole, and quadrupole modes, respectively. In the above expressions Y_i denotes the same combinations of modified Bessel functions as described for the isotropic case.

Isotropic, poroelastic, permeable formation

Borehole wave in permeable formations interacts with the formation permeability through the propagation of Biot slow waves in the pore fluid. The Biot–Rosenbaum theory (Rosenbaum, 1974) was the first to model monopole excitation in an open borehole within an isotropic poroelastic formation. The theory was later extended to transversely isotropic poroelastic formations with multipole excitations (Schmitt, 1989).

The Biot–Rosenbaum model solves the Biot poroelastic equations for a cylindrical borehole geometry and boundary conditions. For the monopole case in an open borehole of radius R , within a permeable formation, the dispersion relation is given by (Tang and Cheng, 2004)

$$D(\omega, k) = \begin{vmatrix} N_{11} & N_{12} & N_{13} & N_{14} \\ N_{21} & N_{22} & N_{23} & N_{24} \\ N_{31} & N_{32} & N_{33} & N_{34} \\ N_{41} & N_{42} & N_{43} & N_{44} \end{vmatrix} = 0$$

$$N_{11} = -fI_1(fR)$$

$$N_{12} = -q_{\text{fast}}(1 + b_{\text{fast}})K_1(q_{\text{fast}}R)$$

$$N_{13} = -q_{\text{slow}}(1 + b_{\text{slow}})K_1(q_{\text{slow}}R)$$

$$N_{14} = -ik(1 + b_s)K_1(q_s R)$$

$$N_{21} = \rho_f \omega^2 I_0(fR)$$

$$N_{22} = -2\mu [q_{\text{fast}}^2 K_0(q_{\text{fast}}R) + q_{\text{fast}} K_1(q_{\text{fast}}R)/R] \\ + k_{\text{fast}}^2 \left[\lambda + \frac{\alpha}{\beta} (\alpha + b_{\text{fast}}) \right] K_0(q_{\text{fast}}R)$$

$$N_{23} = -2\mu [q_{\text{slow}}^2 K_0(q_{\text{slow}}R) + q_{\text{slow}} K_1(q_{\text{slow}}R)/R] \\ + k_{\text{slow}}^2 \left[\lambda + \frac{\alpha}{\beta} (\alpha + b_{\text{slow}}) \right] K_0(q_{\text{slow}}R)$$

$$N_{24} = 2ik\mu [q_s^2 K_0(q_s R) + q_s K_1(q_s R)/R]$$

$$N_{31} = 0$$

$$N_{32} = -2ik\mu q_{\text{fast}} K_1(q_{\text{fast}}R)$$

$$N_{33} = -2ik\mu q_{\text{slow}} K_1(q_{\text{slow}}R)$$

$$N_{34} = \mu (2k^2 - k_{\text{shear}}^2) q_s K_1(q_s R)$$

$$N_{41} = -\rho_f \omega^2 I_0(fR)$$

$$N_{42} = k_{\text{fast}}^2 [(\alpha + b_{\text{fast}})/\beta] K_0(q_{\text{fast}}R)$$

$$N_{43} = k_{\text{slow}}^2 [(\alpha + b_{\text{slow}})/\beta] K_0(q_{\text{slow}}R)$$

$$N_{44} = 0$$

where I_n and K_n are the modified Bessel functions of the first and second kind, respectively, of order n , k is the axial wavenumber along the borehole axis, and ω is the angular frequency. The radial wavenumbers are given by

$$q_{\text{fast}} = \sqrt{k^2 - k_{\text{fast}}^2}$$

$$q_{\text{slow}} = \sqrt{k^2 - k_{\text{slow}}^2}$$

$$q_s = \sqrt{k^2 - k_{\text{shear}}^2}$$

$$f = (k^2 - k_f^2)^{1/2} = \text{the radial wavenumber in the borehole fluid}$$

$$k_f = \omega/\alpha_f = \text{the acoustic wavenumber in the borehole fluid}$$

$$k_{\text{fast}} = k_{p0} \sqrt{\frac{1 + b_{\text{fast}} \rho_{\text{pf}}/\rho}{1 - b_{\text{fast}}/b_0}}$$

$$k_{\text{slow}} = k_{p0} \sqrt{\frac{1 + b_{\text{slow}} \rho_{\text{pf}}/\rho}{1 - b_{\text{slow}}/b_0}}$$

$$k_{p0} = \frac{\omega}{\sqrt{(\lambda + 2\mu + \alpha^2/\beta)/\rho}}$$

$$b_{\text{slow}}^{\text{fast}} = \frac{1}{2} \left[c \mp \sqrt{c^2 - 4\alpha(1 - c)/b_0} \right]$$

$$b_0 = -\frac{\beta(\lambda + 2\mu + \alpha^2/\beta)}{\alpha}$$

$$c = \frac{\alpha - b_s \rho / (\rho_{\text{pf}} b_0)}{\alpha + b_s}$$

$$b_s = \rho_{\text{pf}} \omega^2 \theta$$

$$k_{\text{shear}} = \omega / \sqrt{\mu / (\rho + \rho_{\text{pf}}^2 \omega^2 \theta)}$$

$$\alpha = 1 - K_{\text{dry}}/K_m$$

$$\beta = (\alpha - \phi)/K_m + \phi/K_{\text{pf}}$$

$$\rho = (1 - \phi)\rho_0 + \phi\rho_{\text{pf}}$$

K_{dry} = dry (drained) bulk modulus

λ, μ = Lamé constants of the dry (drained) porous formation

K_m = mineral bulk modulus

ρ_0 = mineral density

K_{pf} = pore fluid bulk modulus

ρ_{pf} = pore fluid density

ϕ = porosity

$\theta = i\kappa(\omega)/\eta\omega$

η = fluid viscosity

$\kappa(\omega)$ = dynamic permeability

The dynamic permeability measures fluid transport in a porous medium under dynamic wave excitation. It is given by (Johnson *et al.*, 1987)

$$\kappa(\omega) = \frac{\kappa_0}{[1 - 4i\tau^2\kappa_0^2\rho_{\text{pf}}\omega/(\eta\Lambda^2\phi^2)]^{1/2} - i\tau\kappa_0\rho_{\text{pf}}\omega/(\eta\phi)}$$

where κ_0 is the static Darcy permeability, τ is tortuosity, Λ is a measure of the pore size given approximately by $\Lambda \approx \sqrt{8\tau\kappa_0/\phi}$.

In the low-frequency limit the dynamic permeability goes to the static Darcy permeability, while in the high-frequency limit

$$\kappa(\omega) \rightarrow i\eta\phi/(\tau\rho_{\text{pf}}\omega)$$

After finding the roots of the dispersion equation numerically, the Stoneley wave phase velocity and attenuation are given by

$$V_{\text{stoneley}} = \omega/\text{Re}(k)$$

$$Q_{\text{stoneley}}^{-1} = 2\text{Im}(k)/\text{Re}(k)$$

Tang *et al.* (1991) present a simplified Biot–Rosenbaum model by decoupling the elastic and flow effects in the full Biot–Rosenbaum model. This reduces the complexity of root finding to an approximate analytical expression for the Stoneley phase wavenumber k :

$$k = \sqrt{k_e^2 + \frac{2i\rho_{\text{pf}}\omega\kappa(\omega)R}{\eta(R^2 - a^2)} \sqrt{-i\omega/D + k_e^2} \frac{K_1(R\sqrt{-i\omega/D + k_e^2})}{K_0(R\sqrt{-i\omega/D + k_e^2})}}$$

$$D = \frac{\kappa(\omega)K_{\text{pf}}/(\phi\eta)}{1 + \frac{K_{\text{pf}}}{\phi(\lambda+2\mu)} \left[1 + \frac{4\alpha\mu/3 - K_{\text{dry}} - \phi(\lambda+2\mu)}{K_{\text{m}}} \right]}$$

a = tool radius

where D is the diffusivity modified to correct for the elasticity of the medium, and K_0 and K_1 are modified Bessel functions of the second kind. The parameter k_e in the above expression is the elastic Stoneley wavenumber, which can be estimated from the density and effective elastic moduli (or P- and S-wave velocities) of the equivalent formation (Tang and Cheng, 2004). The tool radius a can be set to 0 to model a fluid-filled borehole without a tool. A low-frequency approximation to the Stoneley wave slowness (assuming $a = 0$) is given by (Tang and Cheng, 2004)

$$S^2 = \left(\frac{\rho_{\text{pf}}}{K_{\text{pf}}} + \frac{\rho_{\text{pf}}}{\mu} \right) + \left[\frac{2i\rho_{\text{pf}}\kappa_0}{\eta\omega R} \sqrt{-i\omega/D} \frac{K_1(R\sqrt{-i\omega/D})}{K_0(R\sqrt{-i\omega/D})} \right]$$

The first term is the elastic component while the second term represents the effect of formation permeability and fluid flow. The second term is usually small compared with the first term. Therefore it is difficult to estimate formation permeability using this expression for Stoneley wave slowness.

The Stoneley wavenumber k obtained from the simplified theory matches very well the exact wavenumber for fast formations. For slow formations, a better match is obtained by applying an empirical correction to account for borehole compliance. With the empirical correction, the expression for the Stoneley wavenumber is (Tang and Cheng, 2004)

$$k = \sqrt{k_e^2 + \frac{2i\rho_{pf}\omega\kappa(\omega)R}{\eta(R^2 - a^2)} \frac{\sqrt{-i\omega/D + k_e^2}}{1 + B^\gamma} \frac{K_1(R\sqrt{-i\omega/D + k_e^2})}{K_0(R\sqrt{-i\omega/D + k_e^2})}}$$

$$B = f_e R \frac{I_1(f_e R)}{I_0(f_e R)}$$

$f_e = \sqrt{k_e^2 - k_f^2}$ = the radial wavenumber for an equivalent elastic formation

$k_f = \omega/\alpha_f$ = the acoustic wavenumber in the borehole fluid

$\gamma = V_S/\alpha_f$ = the ratio of the formation S-wave velocity to the acoustic velocity in the borehole fluid.

Uses

The results described in this section can be used to model wave propagation and geometric dispersion in boreholes.

Assumptions and limitations

The results described in this section assume the following:

- isotropic or TI, linear, homogeneous, elastic or poroelastic formation;
- a borehole of circular cross-section;
- for the TI dispersion relation, the borehole axis is along the symmetry axis; and
- open-hole boundary conditions at the borehole interface.

Extensions

The Biot–Rosenbaum theory has been extended to anisotropic poroelastic formations with multipole excitations (Schmitt, 1989).

4 Effective elastic media: bounds and mixing laws

4.1 Hashin–Shtrikman–Walpole bounds

Synopsis

If we wish to predict the effective elastic moduli of a mixture of grains and pores theoretically, we generally need to specify: (1) the volume fractions of the various phases, (2) the elastic moduli of the various phases, and (3) the geometric details of how the phases are arranged relative to each other. If we specify only the volume fractions and the constituent moduli, the best we can do is to predict the upper and lower bounds (shown schematically in [Figure 4.1.1](#)).

At any given volume fraction of constituents the effective modulus will fall between the bounds (somewhere along the vertical dashed line in the plot of bulk modulus, [Figure 4.1.1](#)), but its precise value depends on the geometric details. We use, for example, terms like “stiff pore shapes” and “soft pore shapes.” Stiffer shapes cause the value to be higher within the allowable range; softer shapes cause the value to be lower. The best bounds for an isotropic linear elastic composite, defined as giving the narrowest possible range without specifying anything about the geometries of the constituents, are the Hashin–Shtrikman bounds (Hashin and Shtrikman, 1963). When there are only two constituents, the bounds are written as

$$K^{\text{HS}\pm} = K_1 + \frac{f_2}{(K_2 - K_1)^{-1} + f_1(K_1 + \frac{4}{3}\mu_1)^{-1}} \quad (4.1.1)$$

$$\mu^{\text{HS}\pm} = \mu_1 + \frac{f_2}{(\mu_2 - \mu_1)^{-1} + 2f_1(K_1 + 2\mu_1)/[5\mu_1(K_1 + \frac{4}{3}\mu_1)]} \quad (4.1.2)$$

where K_1 and K_2 are the bulk moduli of individual phases; μ_1 and μ_2 are the shear moduli of individual phases; and f_1 and f_2 are the volume fractions of individual phases.

With [equations \(4.1.1\) and \(4.1.2\)](#), upper and lower bounds are computed by interchanging which material is termed 1 and which is termed 2. The expressions yield the upper bound when the stiffest material is termed 1 and the lower bound when the softest material is termed 1. Use of the above equations assumes that the constituent with the larger bulk modulus also has the larger shear modulus and the

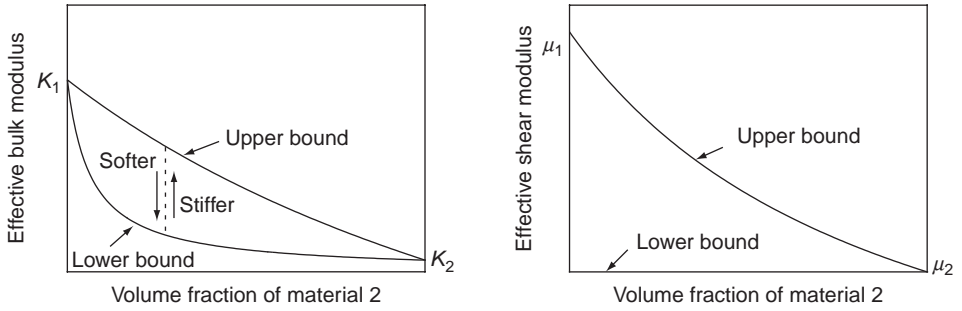


Figure 4.1.1 Schematic representation of the upper and lower bounds on the elastic bulk and shear moduli.

constituent with the smaller bulk modulus also has the smaller shear modulus. Slightly more general forms, sometimes called the Walpole (1966) bounds or the Hashin–Shtrikman–Walpole bounds, can be written as

$$K^{\text{HS}\pm} = K_1 + \frac{f_2}{(K_2 - K_1)^{-1} + f_1(K_1 + \frac{4}{3}\mu_m)^{-1}} \quad (4.1.3)$$

$$\mu^{\text{HS}\pm} = \mu_1 + \frac{f_2}{(\mu_2 - \mu_1)^{-1} + f_1 \left[\mu_1 + \frac{\mu_m}{6} \left(\frac{9K_m + 8\mu_m}{K_m + 2\mu_m} \right) \right]^{-1}} \quad (4.1.4)$$

where the subscripts 1 and 2 again refer to the properties of the two components. Equations (4.1.3) and (4.1.4) yield the upper bound when K_m and μ_m are the maximum bulk and shear moduli of the individual constituents, and the lower bound when K_m and μ_m are the minimum bulk and shear moduli of the constituents. The maximum (minimum) shear modulus might come from a different constituent from the maximum (minimum) bulk modulus. This would be the case, for example, for a mixture of calcite ($K = 71, \mu = 30$ GPa) and quartz ($K = 37, \mu = 45$ GPa). Equation (4.1.4) reduces to equation (4.1.2) when one constituent has both the maximum bulk and shear moduli, while the other constituent has the minimum bulk and shear moduli.

The physical interpretation of the Hashin–Shtrikman bounds for bulk modulus is shown schematically in Figure 4.1.2. The space is filled by an assembly of spheres of material 2, each surrounded by a shell of material 1. Each sphere and its shell have precisely the volume fractions f_1 and f_2 . The upper bound is realized when the stiffer material forms the shell; the lower bound is realized when it is in the core. The physical interpretation implies a very wide distribution of sizes of the coated spheres such that they fill all the space.

A more general form of the Hashin–Shtrikman–Walpole bounds, which can be applied to mixtures of more than two phases (Berryman, 1995), can be written as

$$\begin{aligned} K^{\text{HS}+} &= \Lambda(\mu_{\max}), & K^{\text{HS}-} &= \Lambda(\mu_{\min}) \\ \mu^{\text{HS}+} &= \Gamma(\zeta(K_{\max}, \mu_{\max})), & \mu^{\text{HS}-} &= \Gamma(\zeta(K_{\min}, \mu_{\min})) \end{aligned}$$

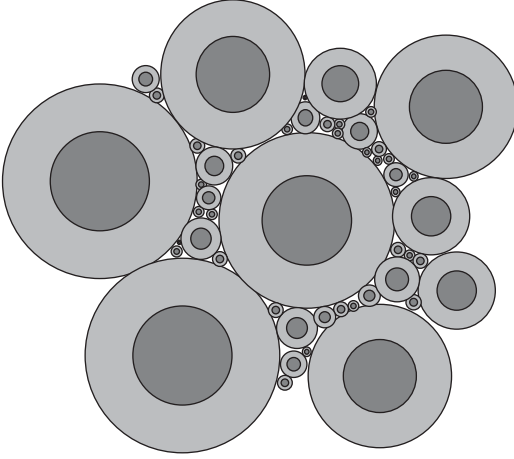


Figure 4.1.2 Physical interpretation of the Hashin–Shtrikman bounds for the bulk modulus of a two-phase material.

where

$$\Lambda(z) = \left\langle \frac{1}{K(r) + \frac{4}{3}z} \right\rangle^{-1} - \frac{4}{3}z$$

$$\Gamma(z) = \left\langle \frac{1}{\mu(r) + z} \right\rangle^{-1} - z$$

$$\zeta(K, \mu) = \frac{\mu}{6} \left(\frac{9K + 8\mu}{K + 2\mu} \right)$$

The brackets $\langle \cdot \rangle$ indicate an average over the medium, which is the same as an average over the constituents weighted by their volume fractions.

Compute the Hashin–Shtrikman upper and lower bounds on the bulk and shear moduli for a mixture of quartz, calcite, and water. The porosity (water fraction) is 27%, quartz is 80% by volume of the solid fraction, and calcite is 20% by volume of the solid fraction. The moduli of the individual constituents are:

$$\begin{aligned} K_{\text{quartz}} &= 36 \text{ GPa} & K_{\text{calcite}} &= 75 \text{ GPa} & K_{\text{water}} &= 2.2 \text{ GPa}, \\ \mu_{\text{quartz}} &= 45 \text{ GPa} & \mu_{\text{calcite}} &= 31 \text{ GPa} & \mu_{\text{water}} &= 0 \text{ GPa} \end{aligned}$$

Hence

$$\begin{aligned} \mu_{\min} &= 0 \text{ GPa}, \quad \mu_{\max} = 45 \text{ GPa}, \quad K_{\min} = 2.2 \text{ GPa}, \text{ and } K_{\max} = 75 \text{ GPa} \\ K^{\text{HS-}} &= \Lambda(\mu_{\min}) \\ &= \left[\frac{\phi}{2.2} + \frac{(1-\phi)(0.8)}{36.0} + \frac{(1-\phi)(0.2)}{75.0} \right]^{-1} \\ &= 7.10 \text{ GPa} \end{aligned}$$

$$\begin{aligned}
K^{\text{HS}+} &= \Lambda(\mu_{\max}) \\
&= \left[\frac{\phi}{2.2 + \left(\frac{4}{3}\right)45} + \frac{(1-\phi)(0.8)}{36.0 + \left(\frac{4}{3}\right)45} + \frac{(1-\phi)(0.2)}{75.0 + \left(\frac{4}{3}\right)45.0} \right]^{-1} - \left(\frac{4}{3}\right)45 \\
&= 26.9 \text{ GPa} \\
\zeta(K_{\max}, \mu_{\max}) &= \frac{45}{6} \left(\frac{9 \times 75 + 8 \times 45}{75 + 2 \times 45} \right) = 47.0 \text{ GPa} \\
\zeta(K_{\min}, \mu_{\min}) &= 0 \text{ GPa} \\
\mu^{\text{HS}+} &= \Gamma(\zeta(K_{\max}, \mu_{\max})) \\
&= \left[\frac{\phi}{47.0} + \frac{(1-\phi)(0.8)}{45.0 + 47.0} + \frac{(1-\phi)(0.2)}{31.0 + 47.0} \right]^{-1} - 47.0 \\
&= 24.6 \text{ GPa} \\
\mu^{\text{HS}-} &= \Gamma(\zeta(K_{\min}, \mu_{\min})) \\
&= 0
\end{aligned}$$

The separation between the upper and lower bounds depends on how different the constituents are. As shown in [Figure 4.1.3](#), the bounds are often quite similar when mixing solids, for the moduli of common minerals are usually within a factor of 2 of each other. Because many effective-medium models (e.g., Biot, Gassmann, Kuster–Toksöz, etc.) assume a homogeneous mineral modulus, it is often useful (and adequate) to represent a mixed mineralogy with an “average mineral” equal to either one of the bounds or to their average $(M^{\text{HS}+} + M^{\text{HS}-})/2$. On the other hand, when the constituents are quite different (such as minerals and pore fluids), the bounds become quite separated, and we lose some of the predictive value.

Note that when $\mu_{\min} = 0$, $K^{\text{HS}-}$ is the same as the Reuss bound. In this case, the Reuss or Hashin–Shtrikman lower bound exactly describes the moduli of a suspension of grains in a pore fluid (see [Section 4.2](#) on Voigt–Reuss bounds and also [Section 4.3](#) on Wood’s relation). These also describe the moduli of a mixture of fluids or gases, or both.

When all phases have the same shear modulus, $\mu = \mu_{\min} = \mu_{\max}$, the upper and lower bounds become identical, and we obtain the expression from Hill (1963) for the effective bulk modulus of a composite with uniform shear modulus (see [Section 4.5](#) on composites with uniform shear modulus).

The Hashin–Shtrikman bounds are computed for the bulk and shear moduli. When bounds on other isotropic elastic constants are needed, the correct procedure is to

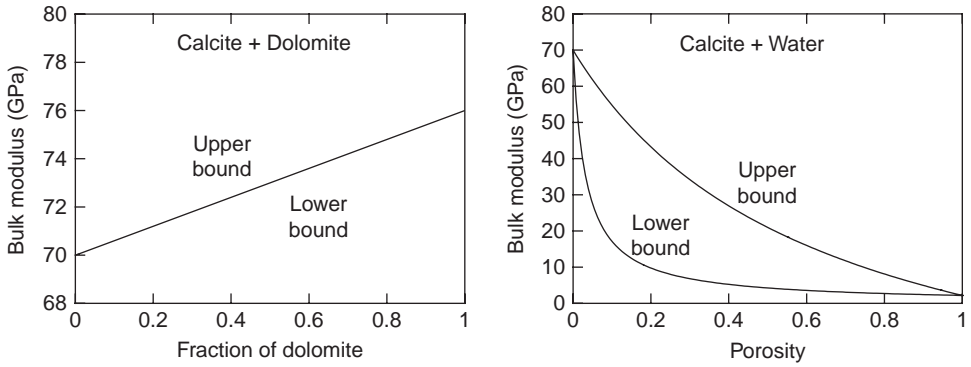


Figure 4.1.3 Hashin–Shtrikman bounds for similar constituents (left) and dissimilar constituents (right).

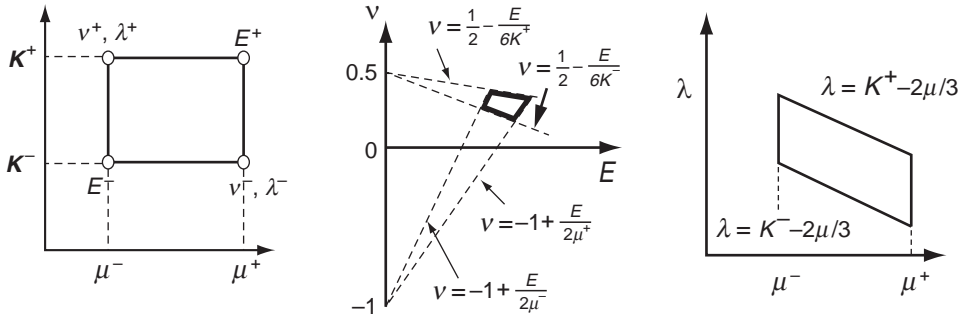


Figure 4.1.4 Schematic representation of the Hashin–Shtrikman bounds in the (K, μ) , (v, E) and (λ, μ) planes.

compute the bounds for bulk and shear moduli and then compute the other elastic constants from these. Figure 4.1.4 shows schematically the bounds in the planes (K, μ) , (v, E) , and (λ, μ) . In each case, the allowed pairs of elastic constants lie within the polygons. Notice how the upper and lower bounds for (K, μ) are uncoupled, i.e., any value $K^- \leq K \leq K^+$ can exist with any value $\mu^- \leq \mu \leq \mu^+$. In contrast, the bounds on (v, E) both depend on (K, μ) – the upper and lower bounds on v depend on the value of E , and vice versa. Similarly, the bounds on λ are coupled to the value of μ . K and μ are more “orthogonal” than λ and μ .

Uses

The bounds described in this section can be used for the following:

- to compute the estimated range of average mineral modulus for a mixture of mineral grains;
- to compute the upper and lower bounds for a mixture of mineral and pore fluid.

Assumptions and limitations

The bounds described in this section apply under the following conditions:

- each constituent is isotropic, linear, and elastic;
- the rock is isotropic, linear, and elastic.

4.2 Voigt and Reuss bounds

Synopsis

If we wish to predict theoretically the effective elastic moduli of a mixture of grains and pores, we generally need to specify: (1) the volume fractions of the various phases, (2) the elastic moduli of the various phases, and (3) the geometric details of how the phases are arranged relative to each other. If we specify only the volume fractions and the constituent moduli, the best we can do is to predict the upper and lower bounds (shown schematically in [Figure 4.2.1](#)).

At any given volume fraction of constituents, the effective modulus will fall between the bounds (somewhere along the vertical dashed line in [Figure 4.2.1](#)), but its precise value depends on the geometric details. We use, for example, terms like “stiff pore shapes” and “soft pore shapes.” Stiffer shapes cause the value to be higher within the allowable range; softer shapes cause the value to be lower. The simplest, but not necessarily the best, bounds are the Voigt and Reuss bounds. (See also [Section 4.1](#) on Hashin–Shtrikman bounds, which are narrower.)

The **Voigt upper bound** of the effective elastic modulus, M_V , of N phases is

$$M_V = \sum_{i=1}^N f_i M_i$$

where f_i is the volume fraction of the i th phase and M_i is the elastic modulus of the i th phase. The Voigt bound is sometimes called the **isostrain average** because it gives the ratio of the average stress to the average strain when all constituents are assumed to have the same strain.

The **Reuss lower bound** of the effective elastic modulus, M_R , is (Reuss, 1929)

$$\frac{1}{M_R} = \sum_{i=1}^N \frac{f_i}{M_i}$$

The Reuss bound is sometimes called the **isostress average** because it gives the ratio of the average stress to the average strain when all constituents are assumed to have the same stress.

When one of the constituents is a liquid or a gas with zero shear modulus, the Reuss average bulk and shear moduli for the composite are exactly the same as given by the Hashin–Shtrikman lower bound.

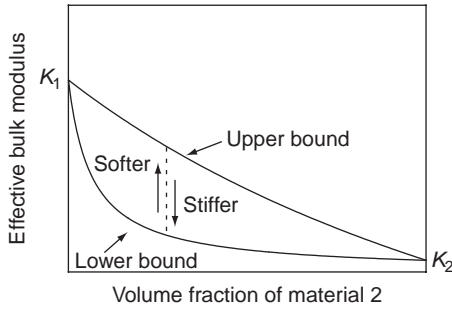


Figure 4.2.1 Effect of changing the volume fraction of constituent materials. The bulk modulus will move along the vertical dotted line between the two bounds.

The Reuss average exactly describes the effective moduli of a suspension of solid grains in a fluid. It also describes the moduli of “shattered” materials in which solid fragments are completely surrounded by the pore fluid.

When all constituents are gases or liquids, or both, with zero shear moduli, the Reuss average gives the effective moduli of the mixture exactly.

In contrast to the Reuss average, which describes a number of real physical systems, real isotropic mixtures can never be as stiff as the Voigt bound (except for the single phase end-members).

Mathematically M in the Reuss average formula can represent any modulus: K , μ , E , and so forth. However, it makes most sense to compute only the Reuss averages of the shear modulus, $M = \mu$, and the bulk modulus, $M = K$, and then compute the other moduli from these.

Uses

The methods described in this section can be used for the following purposes:

- to compute the estimated range of the average mineral modulus for a mixture of mineral grains;
- to compute the upper and lower bounds for a mixture of mineral and pore fluid.

Assumptions and limitations

The methods described in this section presuppose that each constituent is isotropic, linear, and elastic.

4.3 Wood's formula

Synopsis

In a fluid suspension or fluid mixture, where the heterogeneities are small compared with a wavelength, the sound velocity is given exactly by Wood's (1955) relation

$$V = \sqrt{\frac{K_R}{\rho}}$$

where K_R is the Reuss (isostress) average of the composite

$$\frac{1}{K_R} = \sum_{i=1}^N \frac{f_i}{K_i}$$

and ρ is the average density defined by

$$\rho = \sum_{i=1}^N f_i \rho_i$$

f_i , K_i , and ρ_i are the volume fraction, bulk moduli, and densities of the phases, respectively.

Use Wood's relation to estimate the speed of sound in a water-saturated suspension of quartz particles at atmospheric conditions. The quartz properties are $K_{\text{quartz}} = 36$ GPa and $\rho_{\text{quartz}} = 2.65$ g/cm³. The water properties are $K_{\text{water}} = 2.2$ GPa and $\rho_{\text{water}} = 1.0$ g/cm³. The porosity is $\phi = 0.40$.

The Reuss average bulk modulus of the suspension is given by

$$K_{\text{Reuss}} = \left(\frac{\phi}{K_{\text{water}}} + \frac{1-\phi}{K_{\text{quartz}}} \right)^{-1} = \left(\frac{0.4}{2.2} + \frac{0.6}{36} \right)^{-1} = 5.04 \text{ GPa}$$

The density of the suspension is

$$\rho = \phi \rho_{\text{water}} + (1-\phi) \rho_{\text{quartz}} = 0.4 \times 1.0 + 0.6 \times 2.65 = 1.99 \text{ g/cm}^3$$

This gives a sound speed of

$$V = \sqrt{K/\rho} = \sqrt{5.04/1.99} = 1.59 \text{ km/s}$$

Use Wood's relation to estimate the speed of sound in a suspension of quartz particles in water with 50% saturation of air at atmospheric conditions. The quartz properties are $K_{\text{quartz}} = 36$ GPa and $\rho_{\text{quartz}} = 2.65$ g/cm³. The water properties are $K_{\text{water}} = 2.2$ GPa and $\rho_{\text{water}} = 1.0$ g/cm³. The air properties are $K_{\text{air}} = 0.000131$ GPa and $\rho_{\text{air}} = 0.00119$ g/cm³. The porosity is $\phi = 0.40$.

The Reuss average bulk modulus of the suspension is given by

$$\begin{aligned} K_{\text{Reuss}} &= \left(\frac{0.5\phi}{K_{\text{water}}} + \frac{0.5\phi}{K_{\text{air}}} + \frac{1-\phi}{K_{\text{quartz}}} \right)^{-1} \\ &= \left(\frac{0.5 \times 0.4}{2.2} + \frac{0.5 \times 0.4}{0.000131} + \frac{0.6}{36} \right)^{-1} = 0.00065 \text{ GPa} \end{aligned}$$

The density of the suspension is

$$\begin{aligned}\rho &= 0.5\phi\rho_{\text{water}} + 0.5\phi\rho_{\text{air}} + (1 - \phi)\rho_{\text{quartz}} \\ &= 0.5 \times 0.4 \times 1.0 + 0.5 \times 0.4 \times 0.00119 + 0.6 \times 2.65 = 1.79 \text{ g/cm}^3\end{aligned}$$

This gives a sound speed of

$$V = \sqrt{K/\rho} = \sqrt{0.00065/1.79} = 0.019 \text{ km/s}$$

Uses

Wood's formula may be used to estimate the velocity in suspensions.

Assumptions and limitations

Wood's formula presupposes that composite rock and each of its components are isotropic, linear, and elastic.

4.4 Voigt–Reuss–Hill average moduli estimate

Synopsis

The Voigt–Reuss–Hill average is simply the arithmetic average of the Voigt upper bound and the Reuss lower bound. (See the discussion of the Voigt–Reuss bounds in [Section 4.2](#).) This average is expressed as

$$M_{\text{VRH}} = \frac{M_{\text{V}} + M_{\text{R}}}{2}$$

where

$$M_{\text{V}} = \sum_{i=1}^N f_i M_i \quad \frac{1}{M_{\text{R}}} = \sum_{i=1}^N \frac{f_i}{M_i}$$

The terms f_i and M_i are the volume fraction and the modulus of the i th component, respectively. Although M can be any modulus, it makes most sense for it to be the shear modulus or the bulk modulus.

The Voigt–Reuss–Hill average is useful when an *estimate* of the moduli is needed, not just the allowable range of values. An obvious extension would be to average, instead, the Hashin–Shtrikman upper and lower bounds.

This resembles, but is not exactly the same as the average of the algebraic and harmonic means of velocity used by Greenberg and Castagna (1992) in their empirical $V_{\text{P}}\text{--}V_{\text{S}}$ relation (see [Section 7.9](#)).

Uses

The Voigt–Reuss–Hill average is used to estimate the effective elastic moduli of a rock in terms of its constituents and pore space.

Assumptions and limitations

The following limitation and assumption apply to the Voigt–Reuss–Hill average:

- the result is strictly heuristic. Hill (1952) showed that the Voigt and Reuss averages are upper and lower bounds, respectively. Several authors have shown that the average of these bounds can be a useful and sometimes accurate estimate of rock properties;
- the rock is isotropic.

4.5 Composite with uniform shear modulus

Synopsis

Hill (1963) showed that when all of the phases or constituents in a composite have the same shear modulus, μ , the effective P-wave modulus, $M_{\text{eff}} = (K_{\text{eff}} + \frac{4}{3}\mu_{\text{eff}})$, is given exactly by

$$\frac{1}{(K_{\text{eff}} + \frac{4}{3}\mu_{\text{eff}})} = \sum_{i=1}^N \frac{x_i}{(K_i + \frac{4}{3}\mu)} = \left\langle \frac{1}{K + \frac{4}{3}\mu} \right\rangle$$

where x_i is the volume fraction of the i th component, K_i is its bulk modulus, and $\langle \cdot \rangle$ refers to the volume average. Because $\mu_{\text{eff}} = \mu_i = \mu$, any of the effective moduli can then be easily obtained from K_{eff} and μ_{eff} .

This is obviously the same as

$$\frac{1}{(\rho V_P^2)_{\text{eff}}} = \left\langle \frac{1}{\rho V_P^2} \right\rangle$$

This striking result states that the effective moduli of a composite with uniform shear modulus can be found *exactly* if one knows only the volume fractions of the constituents independent of the constituent geometries. There is no dependence, for example, on ellipsoids, spheres, or other idealized shapes.

Hill's equation follows simply from the expressions for Hashin–Shtrikman bounds (see Section 4.1 on Hashin–Shtrikman bounds) on the effective bulk modulus:

$$\frac{1}{K^{\text{HS}\pm} + \frac{4}{3}\mu_{\{\min\}^{\max}}} = \left\langle \frac{1}{K + \frac{4}{3}\mu_{\{\min\}^{\max}}} \right\rangle$$

where μ_{\min} and μ_{\max} are the minimum and maximum shear moduli of the various constituents, yielding, respectively, the lower and upper bounds on the bulk

modulus, $K^{\text{HS}\pm}$. Any composite must have an effective bulk modulus that falls between the bounds. Because here $\mu = \mu_{\min} = \mu_{\max}$, the two bounds on the bulk modulus are equal and reduce to the Hill expression above.

In the case of a mixture of liquids or gases, or both, where $\mu = 0$ for all the constituents, the Hill's equation becomes the well-known isostress equation or Reuss average:

$$\frac{1}{K_{\text{eff}}} = \sum_{i=1}^N \frac{x_i}{K_i} = \left\langle \frac{1}{K} \right\rangle$$

A somewhat surprising result is that a finely layered medium, where each layer is isotropic and has the same shear modulus but a different bulk modulus, is *isotropic* with a bulk modulus given by Hill's equation. (See [Section 4.13](#) on the Backus average.)

Uses

Hill's equation can be used to calculate the effective low-frequency moduli for rocks with spatially nonuniform or *patchy* saturation. At low frequencies, Gassmann's relations predict no change in the shear modulus between dry and saturated patches, allowing this relation to be used to estimate K .

Assumptions and limitations

Hill's equation applies when the composite rock and each of its components are isotropic and have the same shear modulus.

4.6 Rock and pore compressibilities and some pitfalls

Synopsis

This section summarizes useful relations among the compressibilities of porous materials and addresses some commonly made mistakes.

A nonporous elastic solid has a single compressibility

$$\beta = \frac{1}{V} \frac{\partial V}{\partial \sigma}$$

where σ is the hydrostatic stress (defined as being positive in tension) applied on the outer surface and V is the sample bulk volume. In contrast, compressibilities for porous media are more complicated. We have to account for at least two pressures (the

external confining pressure and the internal pore pressure) and two volumes (bulk volume and pore volume). Therefore, we can define at least four compressibilities. Following Zimmerman's (1991a) notation, in which the first subscript indicates the volume change (b for bulk and p for pore) and the second subscript denotes the pressure that is varied (c for confining and p for pore), these compressibilities are

$$\beta_{bc} = \frac{1}{V_b} \left(\frac{\partial V_b}{\partial \sigma_c} \right)_{\sigma_p}$$

$$\beta_{bp} = -\frac{1}{V_b} \left(\frac{\partial V_b}{\partial \sigma_p} \right)_{\sigma_c}$$

$$\beta_{pc} = \frac{1}{v_p} \left(\frac{\partial v_p}{\partial \sigma_c} \right)_{\sigma_p}$$

$$\beta_{pp} = -\frac{1}{v_p} \left(\frac{\partial v_p}{\partial \sigma_p} \right)_{\sigma_c}$$

Note that the signs are chosen to ensure that the compressibilities are positive when *tensional* stress is taken to be positive. Thus, for instance, β_{bp} is to be interpreted as the fractional change in the bulk volume with respect to change in the pore pressure while the confining pressure is held constant. These are the *dry* or *drained* bulk and pore compressibilities. The effective dry bulk modulus is $K_{\text{dry}} = 1/\beta_{bc}$, and the dry-pore-space stiffness is $K_\phi = 1/\beta_{pc}$. In addition, there is the **saturated** or **undrained** bulk compressibility when the mass of the pore fluid is kept constant as the confining pressure changes:

$$\beta_u = \frac{1}{K_{\text{sat low f}}} = \frac{1}{V_b} \left(\frac{\partial V_b}{\partial \sigma_c} \right)_{m\text{-fluid}}$$

This equation assumes that the pore pressure is equilibrated throughout the pore space, and the expression is therefore appropriate for very low frequencies. At high frequencies, with unequilibrated pore pressures, the appropriate bulk modulus is $K_{\text{sat hi f}}$ calculated from some high-frequency theory such as the squirt, Biot, or inclusion models, or some other viscoelastic model. The subscript *m*-fluid indicates constant mass of the pore fluid.

The moduli K_{dry} , $K_{\text{sat low f}}$, $K_{\text{sat hi f}}$, and K_ϕ are the ones most useful in wave-propagation rock physics. The other compressibilities are used in calculations of subsidence caused by fluid withdrawal and reservoir-compressibility analyses. Some of the compressibilities can be related to each other by linear superposition and reciprocity. The well-known Gassmann's equation relates K_{dry} to K_{sat} through the mineral and fluid bulk moduli K_0 and K_{fl} . A few other relations are (for simple derivations, see Zimmerman, 1991a)

$$\beta_{bp} = \beta_{bc} - \frac{1}{K_0}$$

$$\beta_{pc} = \frac{\beta_{bp}}{\phi}$$

$$\beta_{pp} = \left[\beta_{bc} - (1 + \phi) \frac{1}{K_0} \right] / \phi$$

More on dry-rock compressibility

The effective dry-rock compressibility of a homogeneous, linear, porous, elastic solid with any arbitrarily shaped pore space (sometimes called the “drained” or “frame” compressibility) can be written as

$$\frac{1}{K_{dry}} = \frac{1}{K_0} + \frac{1}{V_b} \frac{\partial v_p}{\partial \sigma_c} \Big|_{\sigma_p}$$

or

$$\frac{1}{K_{dry}} = \frac{1}{K_0} + \frac{\phi}{K_\phi} \quad (4.6.1)$$

where

$$\frac{1}{K_\phi} = \frac{1}{v_p} \frac{\partial v_p}{\partial \sigma_c} \Big|_{\sigma_p}$$

is defined as the dry pore-space compressibility (K_ϕ is the dry pore-space stiffness),

$K_{dry} = 1/\beta_{bc}$ = effective bulk modulus of dry porous solid

K_0 = bulk modulus of intrinsic mineral material

V_b = total bulk volume

v_p = pore volume

$\phi = v_p/V_b$ = porosity

σ_c, σ_p = hydrostatic confining stress and pore stress (pore pressure)

We assume that no inelastic effects such as friction or viscosity are present. These equations are strictly true, regardless of pore geometry and pore concentration.

Caution: “Dry rock” is not the same as gas-saturated rock

The dry-frame modulus refers to the incremental bulk deformation resulting from an increment of applied confining pressure while the pore pressure is held constant. This corresponds to a “drained” experiment in which pore fluids can flow freely in or out of the sample to ensure constant pore pressure. Alternatively, it can correspond to an undrained experiment in which the pore fluid has zero bulk

modulus and thus the pore compressions do not induce changes in pore pressure, which is approximately the case for an air-filled sample at standard temperature and pressure. However, at reservoir conditions (high pore pressure), the gas takes on a non-negligible bulk modulus and should be treated as a saturating fluid.

Caution

The harmonic average of the mineral and dry-pore moduli, which resembles [equation \(4.6.1\)](#) above, is incorrect:

$$\frac{1}{K_{\text{dry}}} \stackrel{?}{=} \frac{1-\phi}{K_0} + \frac{\phi}{K_\phi} \quad (\text{incorrect})$$

This equation is sometimes “guessed” because it resembles the Reuss average, but it has no justification from elasticity analysis. It is also *incorrect* to write

$$\frac{1}{K_{\text{dry}}} \stackrel{?}{=} \frac{1}{K_0} + \frac{\partial\phi}{\partial\sigma_c} \quad (\text{incorrect}) \quad (4.6.2)$$

The correct expression is

$$\frac{1}{K_{\text{dry}}} = \frac{1}{(1-\phi)} \left(\frac{1}{K_0} + \frac{\partial\phi}{\partial\sigma_c} \right)$$

The incorrect [equation \(4.6.2\)](#) appears as an intermediate result in some of the classic literature of rock physics. The notable final results are still correct, for the actual derivations are done in terms of the pore volume change, $\partial v_p / \partial\sigma_c$, and not $\partial\phi / \partial\sigma_c$.

Not distinguishing between changes in differential pressure, $\sigma_d = \sigma_c - \sigma_p$, and confining pressure, σ_c , can lead to confusion. Changing σ_c while σ_p is kept constant ($\delta\sigma_p = 0$) is not the same as changing σ_c with $\delta\sigma_p = \delta\sigma_c$ (i.e., the differential stress is kept constant). In the first situation the porous medium deforms with the effective dry modulus K_{dry} . The second situation is one of uniform hydrostatic pressure outside *and* inside the porous rock. For this stress state, the rock deforms with the intrinsic mineral modulus K_0 . Not understanding this can lead to the following erroneous results:

$$\frac{1}{K_0} \stackrel{?}{=} \frac{1}{K_{\text{dry}}} - \frac{1}{(1-\phi)} \frac{\partial\phi}{\partial\sigma_c} \quad (\text{incorrect})$$

or

$$\frac{\partial\phi}{\partial\sigma_c} \stackrel{?}{=} (1-\phi) \left(\frac{1}{K_{\text{dry}}} - \frac{1}{K_0} \right) \quad (\text{incorrect})$$

Table 4.6.1 summarizes some correct and incorrect relations.

Table 4.6.1 *Correct and incorrect versions of the fundamental equations.*

Incorrect	Correct
$\frac{1}{K_{\text{dry}}} \stackrel{?}{=} \frac{1}{K_0} + \frac{\partial \phi}{\partial \sigma_c}$	$\frac{1}{K_{\text{dry}}} = \frac{1}{K_0} + \frac{1}{V_b} \frac{\partial v_p}{\partial \sigma_c}$
$\frac{1}{K_{\text{dry}}} \stackrel{?}{=} \frac{1 - \phi}{K_0} + \frac{\phi}{K_\phi}$	$\frac{1}{K_{\text{dry}}} = \frac{1}{K_0} + \frac{\phi}{K_\phi}$
$\frac{1}{K_{\text{dry}}} \stackrel{?}{=} \frac{1}{K_0} + \frac{1}{(1 - \phi)} \frac{\partial \phi}{\partial \sigma_c}$	$\frac{1}{K_{\text{dry}}} = \frac{1}{(1 - \phi)} \left(\frac{1}{K_0} + \frac{\partial \phi}{\partial \sigma_c} \right)$
$\frac{\partial \phi}{\partial \sigma_c} \stackrel{?}{=} \left(\frac{1}{K_{\text{dry}}} - \frac{1}{K_0} \right) (1 - \phi)$	$\frac{\partial \phi}{\partial \sigma_c} = \frac{1 - \phi}{K_{\text{dry}}} - \frac{1}{K_0}$

Assumptions and limitations

The following presuppositions apply to the equations presented in this section:

- they assume isotropic, linear, porous, and elastic media;
- all derivations here are in the context of linear elasticity with infinitesimal, incremental strains and stresses. Hence Eulerian and Lagrangian formulations are equivalent;
- it is assumed that the temperature is always held constant as the pressure varies; and
- inelastic effects such as friction and viscosity are neglected.

4.7 Kuster and Toksöz formulation for effective moduli

Synopsis

Kuster and Toksöz (1974) derived expressions for P- and S-wave velocities by using a long-wavelength first-order scattering theory. A generalization of their expressions for the effective moduli K_{KT}^* and μ_{KT}^* for a variety of inclusion shapes can be written as (Kuster and Toksöz, 1974; Berryman, 1980b)

$$(K_{\text{KT}}^* - K_m) \frac{(K_m + \frac{4}{3}\mu_m)}{(K_{\text{KT}}^* + \frac{4}{3}\mu_m)} = \sum_{i=1}^N x_i (K_i - K_m) P^{\text{mi}}$$

$$(\mu_{\text{KT}}^* - \mu_m) \frac{(\mu_m + \zeta_m)}{(\mu_{\text{KT}}^* + \zeta_m)} = \sum_{i=1}^N x_i (\mu_i - \mu_m) Q^{\text{mi}}$$

where the summation is over the different inclusion types with volume concentration x_i , and

Table 4.7.1 Coefficients P and Q for some specific shapes. The subscripts m and i refer to the background and inclusion materials (from Berryman, 1995).

Inclusion shape	P^{mi}	Q^{mi}
Spheres	$\frac{K_m + \frac{4}{3}\mu_m}{K_i + \frac{4}{3}\mu_m}$	$\frac{\mu_m + \zeta_m}{\mu_i + \zeta_m}$
Needles	$\frac{K_m + \mu_m + \frac{1}{3}\mu_i}{K_i + \mu_m + \frac{1}{3}\mu_i}$	$\frac{1}{5} \left(\frac{4\mu_m}{\mu_m + \mu_i} + 2 \frac{\mu_m + \gamma_m}{\mu_i + \gamma_m} + \frac{K_i + \frac{4}{3}\mu_m}{K_i + \mu_m + \frac{1}{3}\mu_i} \right)$
Disks	$\frac{K_m + \frac{4}{3}\mu_i}{K_i + \frac{4}{3}\mu_i}$	$\frac{\mu_m + \zeta_i}{\mu_i + \zeta_i}$
Penny cracks	$\frac{K_m + \frac{4}{3}\mu_i}{K_i + \frac{4}{3}\mu_i + \pi\alpha\beta_m}$	$\frac{1}{5} \left(1 + \frac{8\mu_m}{4\mu_i + \pi\alpha(\mu_m + 2\beta_m)} + 2 \frac{K_i + \frac{2}{3}(\mu_i + \mu_m)}{K_i + \frac{4}{3}\mu_i + \pi\alpha\beta_m} \right)$

Notes:

$\beta = \mu \frac{(3K+\mu)}{(3K+4\mu)}$, $\gamma = \mu \frac{(3K+\mu)}{(3K+7\mu)}$, $\zeta = \frac{\mu}{6} \frac{(9K+8\mu)}{(K+2\mu)}$, α = crack aspect ratio, a disk is a crack of zero thickness.

$$\zeta = \frac{\mu (9K + 8\mu)}{6 (K + 2\mu)}$$

The coefficients P^{mi} and Q^{mi} describe the effect of an inclusion of material i in a background medium m . For example, a two-phase material with a single type of inclusion embedded within a background medium has a single term on the right-hand side. Inclusions with different material properties or different shapes require separate terms in the summation. Each set of inclusions must be distributed randomly, and thus its effect is isotropic. These formulas are uncoupled and can be made explicit for easy evaluation. Table 4.7.1 gives expressions for P and Q for some simple inclusion shapes.

Dry cavities can be modeled by setting the inclusion moduli to zero. Fluid-saturated cavities are simulated by setting the inclusion shear modulus to zero.

Caution

Because the cavities are isolated with respect to flow, this approach simulates very high-frequency saturated rock behavior appropriate to ultrasonic laboratory conditions. At low frequencies, when there is time for wave-induced pore-pressure increments to flow and equilibrate, it is better to find the effective moduli for dry cavities and then saturate them with the Gassmann low-frequency relations (see Section 6.3). This should not be confused with the tendency to term this approach a low-frequency theory, for crack dimensions are assumed to be much smaller than a wavelength.

Calculate the effective bulk and shear moduli, K_{KT}^* and μ_{KT}^* , for a quartz matrix with spherical, water-filled inclusions of porosity 0.1:

$$K_m = 37 \text{ GPa} \quad \mu_m = 44 \text{ GPa} \quad K_i = 2.25 \text{ GPa} \quad \mu_i = 0 \text{ GPa}.$$

Volume fraction of spherical inclusions $x_1 = 0.1$ and $N = 1$. The P and Q values for spheres are obtained from the table as follows:

$$P^{m1} = \frac{(37 + \frac{4}{3} \times 44)}{(2.25 + \frac{4}{3} \times 44)} = 1.57$$

$$\zeta_m = \frac{44 (9 \times 37 + 8 \times 44)}{6 (37 + 2 \times 44)} = 40.2$$

$$Q^{m1} = \frac{(44 + 40.2)}{(0 + 40.2)} = 2.095$$

Substituting these in the Kuster–Toksöz equations gives

$$K_{KT}^* = 31.84 \text{ GPa} \quad \mu_{KT}^* = 35.7 \text{ GPa}$$

The P and Q values for ellipsoidal inclusions with arbitrary aspect ratio are the same as given in [Section 4.8](#) on self-consistent methods.

Note that for spherical inclusions, the Kuster–Toksöz expressions for bulk modulus are identical to the Hashin–Shtrikman upper bound, even though the Kuster–Toksöz expressions are formally limited to low porosity.

Assumptions and limitations

The following presuppositions and limitations apply to the Kuster–Toksöz formulations:

- they assume isotropic, linear, and elastic media;
- they are limited to dilute concentrations of the inclusions; and
- they assume idealized ellipsoidal inclusion shapes.

4.8 Self-consistent approximations of effective moduli

Synopsis

Theoretical estimates of the effective moduli of composite or porous elastic materials generally depend on: (1) the properties of the individual components of the composite, (2) the volume fractions of the components, and (3) the geometric details of the shapes and spatial distributions of the components. The bounding methods (see discussions of the Hashin–Shtrikman and Voigt–Reuss bounds, [Sections 4.1](#) and [4.2](#)) establish upper and lower bounds when only (1) and (2) are known, with no geometric details. A second approach improves these estimates by adding statistical information about the phases (e.g., Beran and Molyneux, 1966; McCoy, 1970; Corson,

1974; Watt *et al.*, 1976). A third approach is to assume very specific inclusion shapes. Most methods use the solution for the elastic deformation of a single inclusion of one material in an infinite background medium of the second material and then use one scheme or another to estimate the effective moduli when there is a distribution of these inclusions. These estimates are generally limited to dilute distributions of inclusions, owing to the difficulty of modeling or estimating the elastic interaction of inclusions in close proximity to each other.

A relatively successful, and certainly popular, method to extend these specific geometry methods to slightly higher concentrations of inclusions is the **self-consistent approximation** (Budiansky, 1965; Hill, 1965; Wu, 1966). In this approach one still uses the mathematical solution for the deformation of isolated inclusions, but the interaction of inclusions is approximated by replacing the background medium with the as-yet-unknown effective medium. These methods were made popular following a series of papers by O'Connell and Budiansky (see, for example, O'Connell and Budiansky, 1974). Their equations for effective bulk and shear moduli, K_{SC}^* and μ_{SC}^* , respectively, of a cracked medium with randomly oriented dry penny-shaped cracks (in the limiting case when the aspect ratio α goes to 0) are

$$\frac{K_{SC}^*}{K} = 1 - \frac{16}{9} \left(\frac{1 - v_{SC}^{*2}}{1 - 2v_{SC}^*} \right) \varepsilon$$

$$\frac{\mu_{SC}^*}{\mu} = 1 - \frac{32}{45} \frac{(1 - v_{SC}^*)(5 - v_{SC}^*)}{(2 - v_{SC}^*)} \varepsilon$$

where K and μ are the bulk and shear moduli, respectively, of the uncracked medium, and ε is the crack density parameter, which is defined as the number of cracks per unit volume times the crack radius cubed. The effective Poisson ratio v_{SC}^* is related to ε and the Poisson ratio v of the uncracked solid by

$$\varepsilon = \frac{45}{16} \frac{(v - v_{SC}^*)(2 - v_{SC}^*)}{(1 - v_{SC}^{*2})(10v - 3v_{SC}^* - v_{SC}^*)}$$

This equation must first be solved for v_{SC}^* for a given ε , after which K_{SC}^* and μ_{SC}^* can be evaluated. The nearly linear dependence of v_{SC}^* on ε is well approximated by

$$v_{SC}^* \approx v \left(1 - \frac{16}{9} \varepsilon \right)$$

and this simplifies the calculation of the effective moduli. For fluid-saturated, infinitely thin penny-shaped cracks

$$\frac{K_{SC}^*}{K} = 1$$

$$\frac{\mu_{SC}^*}{\mu} = 1 - \frac{32}{15} \left(\frac{1 - v_{SC}^*}{2 - v_{SC}^*} \right) \varepsilon$$

$$\varepsilon = \frac{45}{32} \frac{(v_{SC}^* - v)(2 - v_{SC}^*)}{(1 - v_{SC}^{*2})(1 - 2v)}$$

Table 4.8.1 Coefficients P and Q for some specific shapes. The subscripts m and i refer to the background and inclusion materials (from Berryman 1995).

Inclusion shape	P^{mi}	Q^{mi}
Spheres	$\frac{K_m + \frac{4}{3}\mu_m}{K_i + \frac{4}{3}\mu_m}$	$\frac{\mu_m + \zeta_m}{\mu_i + \zeta_m}$
Needles	$\frac{K_m + \mu_m + \frac{1}{3}\mu_i}{K_i + \mu_m + \frac{1}{3}\mu_i}$	$\frac{1}{5} \left(\frac{4\mu_m}{\mu_m + \mu_i} + 2 \frac{\mu_m + \gamma_m}{\mu_i + \gamma_m} + \frac{K_i + \frac{4}{3}\mu_m}{K_i + \mu_m + \frac{1}{3}\mu_i} \right)$
Disks	$\frac{K_m + \frac{4}{3}\mu_i}{K_i + \frac{4}{3}\mu_i}$	$\frac{\mu_m + \zeta_i}{\mu_i + \zeta_i}$
Penny cracks	$\frac{K_m + \frac{4}{3}\mu_i}{K_i + \frac{4}{3}\mu_i + \pi\alpha\beta_m}$	$\frac{1}{5} \left[1 + \frac{8\mu_m}{4\mu_i + \pi\alpha(\mu_m + 2\beta_m)} + 2 \frac{K_i + \frac{2}{3}(\mu_i + \mu_m)}{K_i + \frac{4}{3}\mu_i + \pi\alpha\beta_m} \right]$

Notes:

$\beta = \mu \frac{(3K+\mu)}{(3K+4\mu)}$, $\gamma = \mu \frac{(3K+\mu)}{(3K+7\mu)}$, $\zeta = \frac{\mu}{6} \frac{(9K+8\mu)}{(K+2\mu)}$, α = crack aspect ratio, a disk is a crack of zero thickness.

However, this result is inadequate for small aspect ratio cracks with soft-fluid saturation, such as when the parameter $\omega = K_{\text{fluid}}/\alpha K$ is of the order of 1. Then the appropriate equations given by O'Connell and Budiansky are

$$\begin{aligned} \frac{K_{SC}^*}{K} &= 1 - \frac{16}{9} \frac{(1 - v_{SC}^{*2})}{(1 - 2v_{SC}^*)} D \varepsilon \\ \frac{\mu_{SC}^*}{\mu} &= 1 - \frac{32}{45} (1 - v_{SC}^*) \left[D + \frac{3}{(2 - v_{SC}^*)} \right] \varepsilon \\ \varepsilon &= \frac{45}{16} \frac{(v - v_{SC}^*)}{(1 - v_{SC}^{*2})} \frac{(2 - v_{SC}^*)}{[D(1 + 3v)(2 - v_{SC}^*) - 2(1 - 2v)]} \\ D &= \left[1 + \frac{4}{3\pi} \frac{(1 - v_{SC}^{*2})}{(1 - 2v_{SC}^*)} \frac{K}{K_{SC}^*} \omega \right]^{-1} \end{aligned}$$

Wu's self-consistent modulus estimates for two-phase composites may be expressed as (m = matrix, i = inclusion)

$$\begin{aligned} K_{SC}^* &= K_m + x_i(K_i - K_m)P^{*i} \\ \mu_{SC}^* &= \mu_m + x_i(\mu_i - \mu_m)Q^{*i} \end{aligned}$$

Berryman (1980b, 1995) gives a more general form of the self-consistent approximations for N -phase composites:

$$\begin{aligned} \sum_{i=1}^N x_i(K_i - K_{SC}^*)P^{*i} &= 0 \\ \sum_{i=1}^N x_i(\mu_i - \mu_{SC}^*)Q^{*i} &= 0 \end{aligned}$$

where i refers to the i th material, x_i is its volume fraction, P and Q are geometric factors given in Table 4.8.1, and the superscript $*i$ on P and Q indicates that the

factors are for an inclusion of material i in a background medium with self-consistent effective moduli K_{SC}^* and μ_{SC}^* . The summation is over all phases, including minerals and pores. These equations are coupled and must be solved by simultaneous iteration. Although Berryman's self-consistent method does not converge for fluid disks ($\mu_2 = 0$), the formulas for penny-shaped fluid-filled cracks are generally not singular and converge rapidly. However, his estimates for needles, disks, and penny cracks should be used cautiously for fluid-saturated composite materials.

Dry cavities can be modeled by setting the inclusion moduli to zero. Fluid-saturated cavities are simulated by setting the inclusion shear modulus to zero.

Caution

Because the cavities are isolated with respect to flow, this approach simulates very-high-frequency saturated rock behavior appropriate to ultrasonic laboratory conditions. At low frequencies, when there is time for wave-induced pore-pressure increments to flow and equilibrate, it is better to find the effective moduli for dry cavities and then saturate them with the Gassmann low-frequency relations. This should not be confused with the tendency to term this approach a low-frequency theory, for crack dimensions are assumed to be much smaller than a wavelength.

Calculate the self-consistent effective bulk and shear moduli, K_{SC}^* , and μ_{SC}^* , for a water-saturated rock consisting of spherical quartz grains (aspect ratio $\alpha = 1$) and total porosity 0.3. The pore space consists of spherical pores ($\alpha = 1$) and thin, penny-shaped cracks ($\alpha = 10^{-2}$). The thin cracks have a porosity of 0.01, whereas the remaining porosity (0.29) is made up of the spherical pores.

The total number of phases, N , is 3.

$$K_1(\text{quartz}) = 37 \text{ GPa}, \mu_1(\text{quartz}) = 44 \text{ GPa},$$

$$\alpha_1 = 1, x_1 \text{ (volume fraction)} = 0.7$$

$$K_2(\text{water, spherical pores}) = 2.25 \text{ GPa},$$

$$\mu_2(\text{water, spherical pores}) = 0 \text{ GPa},$$

$$\alpha_2(\text{spherical pores}) = 1, x_2 \text{ (volume fraction)} = 0.29$$

$$K_3(\text{water, thin cracks}) = 2.25 \text{ GPa},$$

$$\mu_3(\text{water, thin cracks}) = 0 \text{ GPa},$$

$$\alpha_3(\text{thin cracks}) = 10^{-2}, x_3 \text{ (volume fraction)} = 0.01$$

The coupled equations for K_{SC}^* and μ_{SC}^* are

$$x_1(K_1 - K_{SC}^*)P^{*1} + x_2(K_2 - K_{SC}^*)P^{*2} + x_3(K_3 - K_{SC}^*)P^{*3} = 0$$

$$x_1(\mu_1 - \mu_{SC}^*)Q^{*1} + x_2(\mu_2 - \mu_{SC}^*)Q^{*2} + x_3(\mu_3 - \mu_{SC}^*)Q^{*3} = 0$$

The P 's and Q 's are obtained from [Table 4.8.1](#) or from the more general equation for ellipsoids of arbitrary aspect ratio. In the equations for P and Q , K_m and μ_m are

replaced everywhere by K_{SC}^* and μ_{SC}^* , respectively. The coupled equations are solved iteratively, starting from some initial guess for K_{SC}^* and μ_{SC}^* . The Voigt average may be taken as the starting point. The converged solutions (known as the fixed points of the coupled equations) are $K_{SC}^* = 16.8$ GPa and $\mu_{SC}^* = 11.6$ GPa.

The coefficients P and Q for ellipsoidal inclusions of arbitrary aspect ratio are given by

$$P = \frac{1}{3} T_{ijij}$$

$$Q = \frac{1}{5} (T_{ijij} - \frac{1}{3} T_{iiii})$$

where the tensor T_{ijkl} relates the uniform far-field strain field to the strain within the ellipsoidal inclusion (Wu, 1966). Berryman (1980b) gives the pertinent scalars required for computing P and Q as

$$T_{ijij} = \frac{3F_1}{F_2}$$

$$T_{ijij} - \frac{1}{3} T_{iiii} = \frac{2}{F_3} + \frac{1}{F_4} + \frac{F_4 F_5 + F_6 F_7 - F_8 F_9}{F_2 F_4}$$

where

$$F_1 = 1 + A \left[\frac{3}{2} (f + \theta) - R \left(\frac{3}{2} f + \frac{5}{2} \theta - \frac{4}{3} \right) \right]$$

$$F_2 = 1 + A \left[1 + \frac{3}{2} (f + \theta) - \frac{1}{2} R (3f + 5\theta) \right] + B(3 - 4R) \\ + \frac{1}{2} A(A + 3B)(3 - 4R)[f + \theta - R(f - \theta + 2\theta^2)]$$

$$F_3 = 1 + A \left[1 - (f + \frac{3}{2}\theta) + R(f + \theta) \right]$$

$$F_4 = 1 + \frac{1}{4} A[f + 3\theta - R(f - \theta)]$$

$$F_5 = A \left[-f + R(f + \theta - \frac{4}{3}) \right] + B\theta(3 - 4R)$$

$$F_6 = 1 + A[1 + f - R(f + \theta)] + B(1 - \theta)(3 - 4R)$$

$$F_7 = 2 + \frac{1}{4} A[3f + 9\theta - R(3f + 5\theta)] + B\theta(3 - 4R)$$

$$F_8 = A[1 - 2R + \frac{1}{2} f(R - 1) + \frac{1}{2} \theta(5R - 3)] + B(1 - \theta)(3 - 4R)$$

$$F_9 = A[(R - 1)f - R\theta] + B\theta(3 - 4R)$$

with A , B , and R given by

$$A = \mu_i / \mu_m - 1$$

$$B = \frac{1}{3} \left(\frac{K_i}{K_m} - \frac{\mu_i}{\mu_m} \right)$$

and

$$R = \frac{(1 - 2\nu_m)}{2(1 - \nu_m)}$$

The functions θ and f are given by

$$\theta = \begin{cases} \frac{\alpha}{(\alpha^2 - 1)^{3/2}} [\alpha(\alpha^2 - 1)^{1/2} - \cosh^{-1} \alpha] \\ \frac{\alpha}{(1 - \alpha^2)^{3/2}} [\cos^{-1} \alpha - \alpha(1 - \alpha^2)^{1/2}] \end{cases}$$

for prolate and oblate spheroids, respectively, and

$$f = \frac{\alpha^2}{1 - \alpha^2} (3\theta - 2)$$

Note that $\alpha < 1$ for oblate spheroids and $\alpha > 1$ for prolate spheroids.

Assumptions and limitations

The approach described in this section has the following presuppositions:

- idealized ellipsoidal inclusion shapes;
- isotropic, linear, elastic media; and
- cracks are isolated with respect to fluid flow. Pore pressures are unequilibrated and adiabatic, which is appropriate for high-frequency laboratory conditions. For low-frequency field situations, use dry inclusions and then saturate by using Gassmann relations. This should not be confused with the tendency to term this approach a low-frequency theory, for crack dimensions are assumed to be much smaller than a wavelength.

4.9 Differential effective medium model

Synopsis

The differential effective medium (DEM) theory models two-phase composites by incrementally adding inclusions of one phase (phase 2) to the matrix phase (Cleary *et al.*, 1980; Norris, 1985; Zimmerman, 1991a). The matrix begins as phase 1 (when the concentration of phase 2 is zero) and is changed at each step as a new increment of phase 2 material is added. The process is continued until the desired proportion of

Table 4.9.1 Coefficients P and Q for some specific shapes. The subscripts m and i refer to the background and inclusion materials (from Berryman 1995).

Inclusion shape	P^{mi}	Q^{mi}
Spheres	$\frac{K_m + \frac{4}{3}\mu_m}{K_i + \frac{4}{3}\mu_m}$	$\frac{\mu_m + \zeta_m}{\mu_i + \zeta_m}$
Needles	$\frac{K_m + \mu_m + \frac{1}{3}\mu_i}{K_i + \mu_m + \frac{1}{3}\mu_i}$	$\frac{1}{5} \left(\frac{4\mu_m}{\mu_m + \mu_i} + 2 \frac{\mu_m + \gamma_m}{\mu_i + \gamma_m} + \frac{K_i + \frac{4}{3}\mu_m}{K_i + \mu_m + \frac{1}{3}\mu_i} \right)$
Disks	$\frac{K_m + \frac{4}{3}\mu_i}{K_i + \frac{4}{3}\mu_i}$	$\frac{\mu_m + \zeta_i}{\mu_i + \zeta_i}$
Penny cracks	$\frac{K_m + \frac{4}{3}\mu_i}{K_i + \frac{4}{3}\mu_i + \pi\alpha\beta_m}$	$\frac{1}{5} \left[1 + \frac{8\mu_m}{4\mu_i + \pi\alpha(\mu_m + 2\beta_m)} + 2 \frac{K_i + \frac{2}{3}(\mu_i + \mu_m)}{K_i + \frac{4}{3}\mu_i + \pi\alpha\beta_m} \right]$

Notes:

$\beta = \mu \frac{(3K+\mu)}{(3K+4\mu)}$, $\gamma = \mu \frac{(3K+\mu)}{(3K+7\mu)}$, $\zeta = \frac{\mu}{6} \frac{(9K+8\mu)}{(K+2\mu)}$, α = crack aspect ratio, a disk is a crack of zero thickness.

the constituents is reached. The DEM formulation does not treat each constituent symmetrically. There is a preferred matrix or host material, and the effective moduli depend on the construction path taken to reach the final composite. Starting with material 1 as the host and incrementally adding inclusions of material 2 will not, in general, lead to the same effective properties as starting with phase 2 as the host. For multiple inclusion shapes or multiple constituents, the effective moduli depend not only on the final volume fractions of the constituents but also on the order in which the incremental additions are made. The process of incrementally adding inclusions to the matrix is really a thought experiment and should not be taken to provide an accurate description of the true evolution of rock porosity in nature.

The coupled system of ordinary differential equations for the effective bulk and shear moduli, K^* and μ^* , respectively, are (Berryman, 1992b)

$$(1 - y) \frac{d}{dy} [K^*(y)] = (K_2 - K^*)P^{(*2)}(y)$$

$$(1 - y) \frac{d}{dy} [\mu^*(y)] = (\mu_2 - \mu^*)Q^{(*2)}(y)$$

with initial conditions $K^*(0) = K_1$ and $\mu^*(0) = \mu_1$, where K_1 and μ_1 are the bulk and shear moduli of the initial host material (phase 1), K_2 and μ_2 are the bulk and shear moduli of the incrementally added inclusions (phase 2), and y is the concentration of phase 2.

For fluid inclusions and voids, y equals the porosity, ϕ . The terms P and Q are geometric factors given in Table 4.9.1, and the superscript *2 on P and Q indicates that the factors are for an inclusion of material 2 in a background medium with effective moduli K^* and μ^* . Dry cavities can be modeled by setting the inclusion moduli to zero. Fluid-saturated cavities are simulated by setting the inclusion shear modulus to zero.

Caution

Because the cavities are isolated with respect to flow, this approach simulates very-high-frequency saturated rock behavior appropriate to ultrasonic laboratory conditions. At low frequencies, when there is time for wave-induced pore-pressure increments to flow and equilibrate, it is better to find the effective moduli for dry cavities and then saturate them with the Gassmann low-frequency relations. This should not be confused with the tendency to term this approach a low-frequency theory, for inclusion dimensions are assumed to be much smaller than a wavelength.

The P and Q for ellipsoidal inclusions with arbitrary aspect ratio are the same as given in Section 4.8 for the self-consistent methods, and are repeated in Table 4.9.1.

Norris et al. (1985) have shown that the DEM is realizable and therefore is always consistent with the Hashin–Shtrikman upper and lower bounds.

The DEM equations as given above (Norris, 1985; Zimmerman, 1991b; Berryman et al., 1992) assume that, as each new inclusion (or pore) is introduced, it displaces on average either the host matrix material or the inclusion material, with probabilities $(1 - y)$ and y , respectively. A slightly different derivation by Zimmerman (1984) (superseded by Zimmerman (1991a)) assumed that when a new inclusion is introduced, it always displaces the host material alone. This leads to similar differential equations with $dy/(1 - y)$ replaced by dy . The effective moduli predicted by this version of DEM are always slightly stiffer (for the same inclusion geometry and concentration) than the DEM equations given above. They both predict the same first-order terms in y but begin to diverge at concentrations above 10%. The dependence of effective moduli on concentration goes as $e^{-2y} = (1 - 2y + 2y^2 - \dots)$ for the version without $(1 - y)$, whereas it behaves as $(1 - y)^2 = (1 - 2y + y^2)$ for the version with $(1 - y)$. Including the $(1 - y)$ term makes the results of Zimmerman (1991a) consistent with the Hashin–Shtrikman bounds. In general, for a fixed inclusion geometry and porosity, the Kuster–Toksöz effective moduli are stiffer than the DEM predictions, which in turn are stiffer than the Berryman self-consistent effective moduli.

An important conceptual difference between the DEM and self-consistent schemes for calculating effective moduli of composites is that the DEM scheme identifies one of the constituents as a host or matrix material in which inclusions of the other constituent(s) are embedded, whereas the self-consistent scheme does not identify any specific host material but treats the composite as an aggregate of all the constituents.

Modified DEM with critical porosity constraints

In the usual DEM model, starting from a solid initial host, a porous material stays intact at all porosities and falls apart only at the very end when $y = 1$ (100% porosity). This is because the solid host remains connected, and therefore load bearing.

Although DEM is a good model for materials such as glass foam (Berge et al., 1993) and oceanic basalts (Berge et al., 1992), most reservoir rocks fall apart at

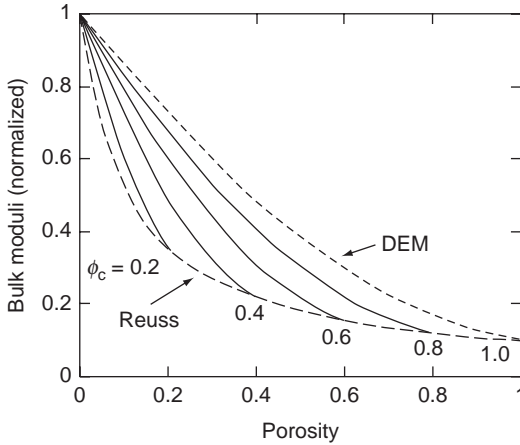


Figure 4.9.1 Normalized bulk-modulus curves for the conventional DEM theory (percolation at $\phi = 1$) and for the modified DEM (percolation at $\phi_c < 1$) for a range of ϕ_c values.

a critical porosity, ϕ_c , significantly less than 1.0 and are not represented very well by the conventional DEM theory. The modified DEM model (Mukerji *et al.*, 1995a) incorporates percolation behavior at any desired ϕ_c by redefining the phase 2 end-member. The inclusions are now no longer made up of pure fluid (the original phase 2 material) but are composite inclusions of the critical phase at ϕ_c with elastic moduli (K_c, μ_c). With this definition, y denotes the concentration of the critical phase in the matrix. The total porosity is given by $\phi = y\phi_c$.

The computations are implemented by replacing (K_2, μ_2) with (K_c, μ_c) everywhere in the equations. Integrating along the reverse path, from $\phi = \phi_c$ to $\phi = 0$ gives lower moduli, for now the softer critical phase is the matrix. The moduli of the critical phase may be taken as the Reuss average value at ϕ_c of the pure end-member moduli. Because the critical phase consists of grains just barely touching each other, better estimates of K_c and μ_c may be obtained from measurements on loose sands, or from models of granular material. For porosities greater than ϕ_c , the material is a suspension and is best characterized by the Reuss average (or Wood's equation).

Figure 4.9.1 shows normalized bulk-modulus curves for the conventional DEM theory (percolation at $\phi = 1$) and for the modified DEM (percolation at $\phi_c < 1$) for a range of ϕ_c values. When $\phi_c = 1$, the modified DEM coincides with the conventional DEM curve. The shapes of the inclusions were taken to be spheres. The path was from 0 to ϕ_c , and (K_c, μ_c) were taken as the Reuss-average values at ϕ_c . For this choice of (K_c, μ_c), estimates along the reversed path coincide with the Reuss curve.

Uses

The purpose of the differential effective-medium model is to estimate the effective elastic moduli of a rock in terms of its constituents and pore space.

Assumptions and limitations

The following assumptions and limitations apply to the differential effective-medium model:

- the rock is isotropic, linear, and elastic;
- the process of incrementally adding inclusions to the matrix is a thought experiment and should not be taken to provide an accurate description of the true evolution of rock porosity in nature;
- idealized ellipsoidal inclusion shapes are assumed; and
- cracks are isolated with respect to fluid flow. Pore pressures are unequilibrated and adiabatic. The model is appropriate for high-frequency laboratory conditions. For low-frequency field situations, use dry inclusions and then saturate using Gassmann relations. This should not be confused with the tendency to term this approach a low-frequency theory, for crack dimensions are assumed to be much smaller than a wavelength.

4.10 Hudson's model for cracked media

Synopsis

Hudson's model is based on a scattering-theory analysis of the mean wavefield in an elastic solid with thin, penny-shaped ellipsoidal cracks or inclusions (Hudson, 1980, 1981). The effective moduli c_{ij}^{eff} are given as

$$c_{ij}^{\text{eff}} = c_{ij}^0 + c_{ij}^1 + c_{ij}^2$$

where c_{ij}^0 are the isotropic background moduli, and c_{ij}^1 , c_{ij}^2 are the first- and second-order corrections, respectively. (See Section 2.2 on anisotropy for the two-index notation of elastic moduli. Note also that Hudson uses a slightly different definition and that there is an extra factor of 2 in his c_{44} , c_{55} , and c_{66} . This makes the equations given in his paper for c_{44}^1 and c_{44}^2 slightly different from those given below, which are consistent with the more standard notation described in Section 2.2 on anisotropy.)

For a single crack set with crack normals aligned along the 3-axis, the cracked media show transverse isotropic symmetry, and the corrections are

$$\begin{aligned} c_{11}^1 &= -\frac{\lambda^2}{\mu} \varepsilon U_3 \\ c_{13}^1 &= -\frac{\lambda(\lambda + 2\mu)}{\mu} \varepsilon U_3 \\ c_{33}^1 &= -\frac{(\lambda + 2\mu)^2}{\mu} \varepsilon U_3 \\ c_{44}^1 &= -\mu \varepsilon U_1 \\ c_{66}^1 &= 0 \end{aligned}$$

and (superscripts on c_{ij} denote second order, not quantities squared)

$$c_{11}^2 = \frac{q}{15} \frac{\lambda^2}{(\lambda + 2\mu)} (\varepsilon U_3)^2$$

$$c_{13}^2 = \frac{q}{15} \lambda (\varepsilon U_3)^2$$

$$c_{33}^2 = \frac{q}{15} (\lambda + 2\mu) (\varepsilon U_3)^2$$

$$c_{44}^2 = \frac{2}{15} \frac{\mu(3\lambda + 8\mu)}{\lambda + 2\mu} (\varepsilon U_1)^2$$

$$c_{66}^2 = 0$$

where

$$q = 15 \frac{\lambda^2}{\mu^2} + 28 \frac{\lambda}{\mu} + 28$$

$$\varepsilon = \frac{N}{V} a^3 = \frac{3\phi}{4\pi\alpha} = \text{crack density}$$

The isotropic background elastic moduli are λ and μ , and a and α are the crack radius and aspect ratio, respectively. The corrections c_{ij}^1 and c_{ij}^2 obey the usual symmetry properties for transverse isotropy or hexagonal symmetry (see [Section 2.2](#) on anisotropy).

Caution

The second-order expansion is not a uniformly converging series and predicts increasing moduli with crack density beyond the formal limit (Cheng, 1993). Better results will be obtained by using just the first-order correction rather than inappropriately using the second-order correction. Cheng gives a new expansion based on the Padé approximation, which avoids this problem.

The terms U_1 and U_3 depend on the crack conditions. For dry cracks

$$U_1 = \frac{16(\lambda + 2\mu)}{3(3\lambda + 4\mu)} \quad U_3 = \frac{4(\lambda + 2\mu)}{3(\lambda + \mu)}$$

For “weak” inclusions (i.e., when $\mu\alpha/(K' + \frac{4}{3}\mu')$ is of the order of 1 and is not small enough to be neglected)

$$U_1 = \frac{16(\lambda + 2\mu)}{3(3\lambda + 4\mu)} \frac{1}{(1 + M)} \quad U_3 = \frac{4(\lambda + 2\mu)}{3(\lambda + \mu)} \frac{1}{(1 + \kappa)}$$

where

$$M = \frac{4\mu'}{\pi\alpha\mu} \frac{(\lambda + 2\mu)}{(3\lambda + 4\mu)} \quad \kappa = \frac{(K' + \frac{4}{3}\mu')(\lambda + 2\mu)}{\pi\alpha\mu(\lambda + \mu)}$$

where K' and μ' are the bulk and shear modulus of the inclusion material. The criteria for an inclusion to be “weak” depend on its shape or aspect ratio α as well as on the relative moduli of the inclusion and matrix material. Dry cavities can be modeled by setting the inclusion moduli to zero. Fluid-saturated cavities are simulated by setting the inclusion shear modulus to zero.

Caution

Because the cavities are isolated with respect to flow, this approach simulates very-high-frequency behavior appropriate to ultrasonic laboratory conditions. At low frequencies, when there is time for wave-induced pore-pressure increments to flow and equilibrate, it is better to find the effective moduli for dry cavities and then saturate them with the Brown and Korrington low-frequency relations (Section 6.5). This should not be confused with the tendency to term this approach a low-frequency theory, for crack dimensions are assumed to be much smaller than a wavelength.

Hudson also gives expressions for infinitely thin, fluid-filled cracks:

$$U_1 = \frac{16(\lambda + 2\mu)}{3(3\lambda + 4\mu)} \quad U_3 = 0$$

These assume no discontinuity in the normal component of crack displacements and therefore predict no change in the compressional modulus with saturation. There is, however, a shear displacement discontinuity and a resulting effect on shear stiffness. This case should be used with care.

The first-order changes λ_1 and μ_1 in the isotropic elastic moduli λ and μ of a material containing randomly oriented inclusions are given by

$$\mu_1 = -\frac{2\mu}{15} \varepsilon(3U_1 + 2U_3)$$

$$3\lambda_1 + 2\mu_1 = -\frac{(3\lambda + 2\mu)^2}{3\mu} \varepsilon U_3$$

These results agree with the self-consistent results of Budiansky and O’Connell (1976).

For two or more crack sets aligned in different directions, corrections for each crack set are calculated separately in a crack-local coordinate system with the 3-axis normal to the crack plane and then rotated or transformed back (see Section 1.4 on coordinate transformations) into the coordinates of c_{ij}^{eff} ; finally the results are added to

obtain the overall correction. Thus, for three crack sets with crack densities ε_1 , ε_2 , and ε_3 with crack normals aligned along the 1-, 2-, and 3-axes, respectively, the overall first-order corrections to c_{ij}^0 , $c_{ij}^{1(3\text{sets})}$ may be given in terms of linear combinations of the corrections for a single set, with the appropriate crack densities as follows (where we have taken into account the symmetry properties of c_{ij}^1):

$$c_{11}^{1(3\text{sets})} = c_{33}^1(\varepsilon_1) + c_{11}^1(\varepsilon_2) + c_{11}^1(\varepsilon_3)$$

$$c_{12}^{1(3\text{sets})} = c_{13}^1(\varepsilon_1) + c_{13}^1(\varepsilon_2) + c_{12}^1(\varepsilon_3)$$

$$c_{13}^{1(3\text{sets})} = c_{13}^1(\varepsilon_1) + c_{12}^1(\varepsilon_2) + c_{13}^1(\varepsilon_3)$$

$$c_{22}^{1(3\text{sets})} = c_{11}^1(\varepsilon_1) + c_{33}^1(\varepsilon_2) + c_{11}^1(\varepsilon_3)$$

$$c_{23}^{1(3\text{sets})} = c_{12}^1(\varepsilon_1) + c_{13}^1(\varepsilon_2) + c_{13}^1(\varepsilon_3)$$

$$c_{33}^{1(3\text{sets})} = c_{11}^1(\varepsilon_1) + c_{11}^1(\varepsilon_2) + c_{33}^1(\varepsilon_3)$$

$$c_{44}^{1(3\text{sets})} = c_{44}^1(\varepsilon_2) + c_{44}^1(\varepsilon_3)$$

$$c_{55}^{1(3\text{sets})} = c_{44}^1(\varepsilon_1) + c_{44}^1(\varepsilon_3)$$

$$c_{66}^{1(3\text{sets})} = c_{44}^1(\varepsilon_1) + c_{44}^1(\varepsilon_2)$$

Note that $c_{66}^1 = 0$ and $c_{12}^1 = c_{11}^1 - 2c_{66}^1 = c_{11}^1$.

Hudson (1981) also gives the attenuation coefficient ($\gamma = \omega Q^{-1}/2V$) for elastic waves in cracked media. For aligned cracks with normals along the 3-axis, the attenuation coefficients for P-, SV-, and SH-waves are

$$\gamma_P = \frac{\omega}{V_S} \varepsilon \left(\frac{\omega a}{V_P} \right)^3 \frac{1}{30\pi} \left[AU_1^2 \sin^2 2\theta + BU_3^2 \left(\frac{V_P^2}{V_S^2} - 2 \sin^2 \theta \right)^2 \right]$$

$$\gamma_{SV} = \frac{\omega}{V_S} \varepsilon \left(\frac{\omega a}{V_S} \right)^3 \frac{1}{30\pi} (AU_1^2 \cos^2 2\theta + BU_3^2 \sin^2 2\theta)$$

$$\gamma_{SH} = \frac{\omega}{V_S} \varepsilon \left(\frac{\omega a}{V_S} \right)^3 \frac{1}{30\pi} (AU_1^2 \cos^2 \theta)$$

$$A = \frac{3}{2} + \frac{V_S^5}{V_P^5}$$

$$B = 2 + \frac{15}{4} \frac{V_S}{V_P} - 10 \frac{V_S^3}{V_P^3} + 8 \frac{V_S^5}{V_P^5}$$

In the preceding expressions, V_P and V_S are the P and S velocities in the uncracked isotropic background matrix, ω is the angular frequency, and θ is the angle between the direction of propagation and the 3-axis (axis of symmetry).

For randomly oriented cracks (isotropic distribution), the P and S attenuation coefficients are given as

$$\gamma_P = \frac{\omega}{V_S} \varepsilon \left(\frac{\omega a}{V_P} \right)^3 \frac{4}{15^2 \pi} \left[A U_1^2 + \frac{1}{2} \frac{V_P^5}{V_S^5} B (B - 2) U_3^2 \right]$$

$$\gamma_S = \frac{\omega}{V_S} \varepsilon \left(\frac{\omega a}{V_S} \right)^3 \frac{1}{75 \pi} \left(A U_1^2 + \frac{1}{3} B U_3^2 \right)$$

The fourth-power dependence on ω is characteristic of Rayleigh scattering.

Hudson (1990) gives results for overall elastic moduli of material with various distributions of penny-shaped cracks. If conditions at the cracks are taken to be uniform, so that U_1 and U_3 do not depend on the polar and azimuthal angles θ and ϕ , the first-order correction is given as

$$c_{ijpq}^1 = -\frac{A}{\mu} U_3 [\lambda^2 \delta_{ij} \delta_{pq} + 2\lambda \mu (\delta_{ij} \tilde{e}_{pq} + \delta_{pq} \tilde{e}_{ij}) + 4\mu^2 \tilde{e}_{ijpq}] \\ - A \mu U_1 (\delta_{jq} \tilde{e}_{ip} + \delta_{jp} \tilde{e}_{iq} + \delta_{iq} \tilde{e}_{jp} + \delta_{ip} \tilde{e}_{jq} - 4\tilde{e}_{ijpq})$$

where

$$A = \int_0^{2\pi} \int_0^{\pi/2} \varepsilon(\theta, \phi) \sin \theta d\theta d\phi$$

$$\tilde{e}_{ij} = \frac{1}{A} \int_0^{2\pi} \int_0^{\pi/2} \varepsilon(\theta, \phi) n_i n_j \sin \theta d\theta d\phi$$

$$\tilde{e}_{ijpq} = \frac{1}{A} \int_0^{2\pi} \int_0^{\pi/2} \varepsilon(\theta, \phi) n_i n_j n_p n_q \sin \theta d\theta d\phi$$

and n_i are the components of the unit vector along the crack normal, $\mathbf{n} = (\sin \theta \cos \phi, \sin \theta \sin \phi, \cos \theta)$, whereas $\varepsilon(\theta, \phi)$ is the crack density distribution function, so that $\varepsilon(\theta, \phi) \sin \theta d\theta d\phi$ is the density of cracks with normals lying in the solid angle between $(\theta, \theta + d\theta)$ and $(\phi, \phi + d\phi)$.

Special cases of crack distributions

- (a) Cracks with total crack density ε_t , which have all their normals aligned along $\theta = \theta_0, \phi = \phi_0$:

$$\varepsilon(\theta, \phi) = \varepsilon_t \frac{\delta(\theta - \theta_0)}{\sin \theta} \delta(\phi - \phi_0)$$

$$A = \varepsilon_t$$

$$\tilde{e}_{ij} = n_i^0 n_j^0$$

$$\tilde{e}_{ijpq} = n_i^0 n_j^0 n_p^0 n_q^0$$

where $n_1^0 = \sin \theta_0 \cos \phi_0, n_2^0 = \sin \theta_0 \sin \phi_0$, and $n_3^0 = \cos \theta_0$.

- (b) Rotationally symmetric crack distributions with normals symmetrically distributed about $\theta = 0$, that is, where ε is a function of θ only:

$$A = 2\pi \int_0^{\pi/2} \varepsilon(\theta) \sin \theta d\theta$$

$$\tilde{\varepsilon}_{12} = \tilde{\varepsilon}_{23} = \tilde{\varepsilon}_{31} = 0$$

$$\tilde{\varepsilon}_{11} = \tilde{\varepsilon}_{22} = \frac{\pi}{A} \int_0^{\pi/2} \varepsilon(\theta) \sin^3 \theta d\theta = \frac{1}{2}(1 - \tilde{\varepsilon}_{33})$$

$$\tilde{\varepsilon}_{1111} = \tilde{\varepsilon}_{2222} = \frac{3\pi}{4A} \int_0^{\pi/2} \varepsilon(\theta) \sin^5 \theta d\theta = 3\tilde{\varepsilon}_{1122} = 3\tilde{\varepsilon}_{1212}, \text{ etc.}$$

$$\tilde{\varepsilon}_{3333} = \frac{8}{3}\tilde{\varepsilon}_{1111} - 4\tilde{\varepsilon}_{11} + 1$$

$$\tilde{\varepsilon}_{1133} = \tilde{\varepsilon}_{11} - \frac{4}{3}\tilde{\varepsilon}_{1111} = \tilde{\varepsilon}_{2233} = \tilde{\varepsilon}_{1313} = \tilde{\varepsilon}_{2323}, \text{ etc.}$$

Elements other than those related to the preceding elements by symmetry are zero. A particular rotationally symmetric distribution is the Fisher distribution, for which $\varepsilon(\theta)$ is

$$\varepsilon(\theta) = \frac{\varepsilon_t}{2\pi \sigma^2} \frac{e^{(\cos \theta)/\sigma^2}}{(e^{1/\sigma^2} - 1)}$$

For small σ^2 , this is approximately a model for a Gaussian distribution on the sphere

$$\varepsilon(\theta) \approx \varepsilon_t \frac{e^{-\theta^2/2\sigma^2}}{2\pi\sigma^2}$$

The proportion of crack normals outside the range $0 \leq \theta \leq 2\sigma$ is approximately $1/e^2$. For this distribution,

$$A = \varepsilon_t$$

$$\tilde{\varepsilon}_{11} = \frac{-1 + 2\sigma^2 e^{1/\sigma^2} - 2\sigma^4 (e^{1/\sigma^2} - 1)}{2(e^{1/\sigma^2} - 1)} \approx \sigma^2$$

$$\tilde{\varepsilon}_{1111} = \frac{3}{8} \left[\frac{-1 + 4\sigma^4 (2e^{1/\sigma^2} + 1) - 24\sigma^6 e^{1/\sigma^2} + 24\sigma^8 (e^{1/\sigma^2} - 1)}{(e^{1/\sigma^2} - 1)} \right] \approx 3\sigma^4$$

This distribution is suitable when crack normals are oriented randomly with a small variance about a mean direction along the 3-axis.

- (c) Cracks with normals randomly distributed at a fixed angle from the 3-axis forming a cone. In this case ε is independent of ϕ and is zero unless $\theta = \theta_0$, $0 \leq \phi \leq 2\pi$.

$$\varepsilon(\theta) = \varepsilon_t \frac{\delta(\theta - \theta_0)}{2\pi \sin \theta}$$

which gives

$$A = \varepsilon_t$$

$$\tilde{\varepsilon}_{11} = \frac{1}{2} \sin^2 \theta_0$$

$$\tilde{\varepsilon}_{1111} = \frac{3}{8} \sin^4 \theta_0$$

and the first-order corrections are

$$c_{1111}^1 = -\frac{\varepsilon_t}{2\mu} [U_3(2\lambda^2 + 4\lambda\mu \sin^2 \theta_0 + 3\mu^2 \sin^4 \theta_0) + U_1\mu^2 \sin^2 \theta_0(4 - 3 \sin^2 \theta_0)]$$

$$= c_{2222}^1$$

$$c_{3333}^1 = -\frac{\varepsilon_t}{\mu} [U_3(\lambda + 2\mu \cos^2 \theta_0)^2 + U_1\mu^2 4 \cos^2 \theta_0 \sin^2 \theta_0]$$

$$c_{1122}^1 = -\frac{\varepsilon_t}{2\mu} [U_3(2\lambda^2 + 4\lambda\mu \sin^2 \theta_0 + \mu^2 \sin^4 \theta_0) - U_1\mu^2 \sin^4 \theta_0]$$

$$c_{1133}^1 = -\frac{\varepsilon_t}{\mu} [U_3(\lambda + \mu \sin^2 \theta_0)(\lambda + 2\mu \cos^2 \theta_0) - U_1\mu^2 2 \sin^2 \theta_0 \cos^2 \theta_0]$$

$$= c_{2233}^1$$

$$c_{1232}^1 = -\frac{\varepsilon_t}{2} \mu [U_3 4 \sin^2 \theta_0 \cos^2 \theta_0 + U_1(\sin^2 \theta_0 + 2 \cos^2 \theta_0 - 4 \sin^2 \theta_0 \cos^2 \theta_0)]$$

$$= c_{1313}^1$$

$$c_{1212}^1 = -\frac{\varepsilon_t}{2} \mu [U_3 \sin^4 \theta_0 + U_1 \sin^2 \theta_0(2 - \sin^2 \theta_0)]$$

Heavily faulted structures

Hudson and Liu (1999) provide a model for the effective elastic properties of rocks with an array of parallel faults based on the averaging process of Schoenberg and Douma (1988). The individual faults themselves are modeled using two different approaches: model 1 as a planar distribution of small circular cracks; model 2 as a planar distribution of small circular welded contacts. Hudson and Liu also give expressions where both models 1 and 2 are replaced by an equivalent layer of constant thickness and appropriate infill material, which can then be averaged using the Backus average. Model 2 (circular contacts) provides expressions for effective elastic properties of heavily cracked media with cracks aligned and confined within the fault planes.

Assuming the fault normals to be aligned along the 3-axis, the elements of the effective stiffness tensor are (Hudson and Liu, 1999)

$$c_{1111} = c_{2222} = \lambda + 2\mu$$

$$c_{3333} = \frac{\lambda + 2\mu}{1 + E_N}$$

$$c_{1122} = \lambda$$

$$c_{1133} = c_{2233} = \frac{\lambda}{1 + E_N}$$

$$c_{2323} = c_{1313} = \frac{\mu}{1 + E_T}$$

$$c_{1212} = \mu$$

The quantities E_N and E_T depend on the fault model. For **model 1**, where the fault plane consists of an array of circular cracks,

$$E_N = \left(\frac{v^s a^3}{H} \right) \left(\frac{\lambda + 2\mu}{\mu} \right) U_3 \left[1 + \pi U_3 (v^s a^2)^{3/2} \left(1 - \frac{\mu}{\lambda + 2\mu} \right) \right]$$

$$E_T = \left(\frac{v^s a^3}{H} \right) U_1 \left[1 + \frac{\pi}{4} U_1 (v^s a^2)^{3/2} \left(3 - 2 \frac{\mu}{\lambda + 2\mu} \right) \right]$$

where a is the crack radius, v^s is the number density of cracks on the fault surface, H is the spacing between parallel faults, and λ and μ are the Lamé parameters of the uncracked background material. The overall number density of cracks, $v = v^s/H$ and the overall crack density $\varepsilon = va^3 = v^s a^3/H$. The relative area of cracking on the fault is given by $r = v^s \pi a^2$.

Alternatively, the faults may be replaced by an elastically equivalent layer with bulk and shear moduli given by

$$K^* = K' - \frac{\pi \alpha \mu}{4} \left(\frac{\mu}{\lambda + 2\mu} \right) \left[1 - \frac{4}{3} \left(\frac{r^3}{\pi} \right)^{1/2} \right]$$

$$\mu^* = \mu' + \frac{3\pi \alpha \mu}{16} \left(\frac{3\lambda + 4\mu}{\lambda + 2\mu} \right) \left[1 - \frac{4}{3} \left(\frac{r^3}{\pi} \right)^{1/2} \right]$$

In the above expressions K' and μ' are, respectively, the bulk and shear moduli of the material filling the cracks, of aspect ratio α , within the faults. Viscous fluid may be modeled by setting μ' to be imaginary. Setting both moduli to zero represents dry cracks. The equivalent layers can be used in Backus averaging to estimate the overall stiffness. These give results very close (but not completely identical, because of the approximations involved) to the results obtained from the equations for c_{ijkl} given above.

For **model 2**, which assumes a planar distribution of small, circular, welded contacts:

$$E_N = \frac{(\lambda + 2\mu)^2}{4\mu(\lambda + \mu)} \frac{1}{(v^w H b)} \left(1 + 2\sqrt{v^w b^2} \right)^{-1}$$

$$E_T = \frac{(3\lambda + 4\mu)}{8(\lambda + \mu)} \frac{1}{(v^w Hb)} \left(1 + 2\sqrt{v^w b^2}\right)^{-1}$$

where b is the radius of the welded contact region and v^w is the number density of welded contacts on the fault surface.

In this case, the relative area of cracking (noncontact) on the fault is given by $r = 1 - v^w \pi b^2$.

Again, as an alternate representation, the faults in model 2 may be replaced by an elastically equivalent layer with bulk and shear moduli given by

$$K^* = K' - \frac{4\mu(d/b)r(1-r)}{3\pi} \frac{(\lambda + \mu)(4\mu - \lambda)}{(3\lambda + 4\mu)(\lambda + 2\mu)} \left[1 + 2\left(\frac{1-r}{\pi}\right)^{1/2}\right]$$

$$\mu^* = \mu' + \frac{8\mu(d/b)r(1-r)}{\pi} \left(\frac{\lambda + \mu}{3\lambda + 4\mu}\right) \left[1 + 2\left(\frac{1-r}{\pi}\right)^{1/2}\right]$$

where d is the aperture of the cracked (noncontact) area. Note that d/b is not the aspect ratio of cracks since b is the radius of the welded regions. The above equations are valid for small d/b . The equivalent layers can be used in Backus averaging to estimate the overall stiffness.

The equations for model 1 are valid for $r \ll 1$ (dilute cracks, predominantly welded) while the equations for model 2 are valid for $(1-r) \ll 1$ (dilute contacts, heavily cracked). Hudson and Liu (1999) show that, to first order, the elastic response of heavily cracked faults (model 2) is the same as that of a cubic packing of identical spheres with the same number density and size of contact areas. To the first order, the actual distribution of contact regions and the shape of cavities between the contact regions do not affect the overall elastic moduli.

Uses

Hudson's model is used to estimate the effective elastic moduli and attenuation of a rock in terms of its constituents and pore space.

Assumptions and limitations

The use of Hudson's model requires the following considerations:

- an idealized crack shape (penny-shaped) with small aspect ratios and either small crack density or small contact density are assumed. The crack radius and the distance between cracks are much smaller than a wavelength. The formal limit quoted by Hudson for both first- and second-order terms is ε less than 0.1;
- the second-order expansion is not a uniformly converging series and predicts increasing moduli with crack density beyond the formal limit (Cheng, 1993). Better results will be obtained by using just the first-order correction rather than inappropriately

using the second-order correction. Cheng gives a new expansion based on the Padé approximation, which avoids this problem;

- cracks are isolated with respect to fluid flow. Pore pressures are unequilibrated and adiabatic. The model is appropriate for high-frequency laboratory conditions. For low-frequency field situations, use Hudson's dry equations and then saturate by using the Brown and Korrington relations (Section 6.5). This should not be confused with the tendency to think of this approach as a low-frequency theory, because crack dimensions are assumed to be much smaller than a wavelength; and
- sometimes a single crack set may not be an adequate representation of crack-induced anisotropy. In this case we need to superpose several crack sets with angular distributions.

4.11 Eshelby–Cheng model for cracked anisotropic media

Synopsis

Cheng (1978, 1993) has given a model for the effective moduli of cracked, transversely isotropic rocks based on Eshelby's (1957) static solution for the strain inside an ellipsoidal inclusion in an isotropic matrix. The effective moduli c_{ij}^{eff} for a rock containing fluid-filled ellipsoidal cracks with their normals aligned along the 3-axis are given as

$$c_{ij}^{\text{eff}} = c_{ij}^0 - \phi c_{ij}^1$$

where ϕ is the porosity and c_{ij}^0 are the moduli of the uncracked isotropic rock. The corrections c_{ij}^1 are

$$c_{11}^1 = \lambda(S_{31} - S_{33} + 1) + \frac{2\mu E}{D(S_{12} - S_{11} + 1)}$$

$$c_{33}^1 = \frac{(\lambda + 2\mu)(-S_{12} - S_{11} + 1) + 2\lambda S_{13} + 4\mu C}{D}$$

$$c_{13}^1 = \frac{(\lambda + 2\mu)(S_{13} + S_{31}) - 4\mu C + \lambda(S_{13} - S_{12} - S_{11} - S_{33} + 2)}{2D}$$

$$c_{44}^1 = \frac{\mu}{1 - 2S_{1313}} \quad c_{66}^1 = \frac{\mu}{1 - 2S_{1212}}$$

with

$$C = \frac{K_{\text{fl}}}{3(K - K_{\text{fl}})}$$

$$D = S_{33}S_{11} + S_{33}S_{12} - 2S_{31}S_{13} - (S_{11} + S_{12} + S_{33} - 1 - 3C) \\ - C[S_{11} + S_{12} + 2(S_{33} - S_{13} - S_{31})]$$

$$E = S_{33}S_{11} - S_{31}S_{13} - (S_{33} + S_{11} - 2C - 1) + C(S_{31} + S_{13} - S_{11} - S_{33})$$

$$S_{11} = QI_{aa} + RI_a \quad S_{33} = Q\left(\frac{4\pi}{3} - 2I_{ac}\alpha^2\right) + I_cR$$

$$S_{12} = QI_{ab} - RI_a \quad S_{13} = QI_{ac}\alpha^2 - RI_a$$

$$S_{31} = QI_{ac} - RI_c \quad S_{1212} = QI_{ab} + RI_a$$

$$S_{1313} = \frac{Q(1 + \alpha^2)I_{ac}}{2} + \frac{R(I_a + I_c)}{2}$$

$$I_a = \frac{2\pi\alpha(\cos^{-1}\alpha - \alpha S_a)}{S_a^3} \quad I_c = 4\pi - 2I_a$$

$$I_{ac} = \frac{I_c - I_a}{3S_a^2} \quad I_{aa} = \pi - \frac{3I_{ac}}{4} \quad I_{ab} = \frac{I_{aa}}{3}$$

$$\sigma = \frac{3K - 2\mu}{6K + 2\mu} \quad S_a = \sqrt{1 - \alpha^2}$$

$$R = \frac{1 - 2\sigma}{8\pi(1 - \sigma)} \quad Q = \frac{3R}{1 - 2\sigma}$$

In the preceding equations, K and μ are the bulk and shear moduli of the isotropic matrix, respectively; K_f is the bulk modulus of the fluid; and α is the crack aspect ratio. Dry cavities can be modeled by setting the inclusion moduli to zero. Do not confuse S with the anisotropic compliance tensor. This model is valid for arbitrary aspect ratios, unlike the Hudson model, which assumes very small aspect ratio cracks (see [Section 4.10](#) on Hudson's model). The results of the two models are essentially the same for small aspect ratios and low crack densities (< 0.1), as long as the "weak inclusion" form of Hudson's theory is used (Cheng, 1993).

Uses

The Eshelby–Cheng model is used to obtain the effective anisotropic stiffness tensor for transversely isotropic, cracked rocks.

Assumptions and limitations

The following presuppositions and limitations apply to the Eshelby–Cheng model:

- the model assumes an isotropic, homogeneous, elastic background matrix and an idealized ellipsoidal crack shape;
- the model assumes low crack concentrations but can handle all aspect ratios; and
- because the cavities are isolated with respect to flow, this approach simulates very-high-frequency behavior appropriate to ultrasonic laboratory conditions.

At low frequencies, when there is time for wave-induced pore-pressure increments to flow and equilibrate, it is better to find the effective moduli for dry cavities and then saturate them with the Brown and Korrington low-frequency relations. This should not be confused with the tendency to term this approach a low-frequency theory, for crack dimensions are assumed to be much smaller than a wavelength.

Extensions

The model has been extended to a transversely isotropic background by Nishizawa (1982).

4.12 *T*-matrix inclusion models for effective moduli

Synopsis

One approach for estimating effective elastic constants for composites is based on the integral equation or *T*-matrix approach of quantum scattering theory. This approach takes into account interactions between inclusions based on multiple-point correlation functions. The integral equation for effective elastic constants of macroscopically homogeneous materials with statistical fluctuation of properties at the microscopic level is very similar to the Lippmann–Schwinger–Dyson equation of multiple scattering in quantum mechanics. The theory in the context of elastic composites was developed by Eimer (1967, 1968), Kröner (1967, 1977, 1986), Zeller and Dederichs (1973), Korrington (1973), and Gubernatis and Krumhansl (1975). Willis (1977) used a *T*-matrix approach to obtain bounds and estimates for anisotropic composites. Middya and Basu (1986) applied the *T*-matrix formalism for polycrystalline aggregates. Jakobsen *et al.* (2003a) synthesized many of the existing effective medium approximations and placed them on a common footing using the *T*-matrix language. They also applied the formalism to model elastic properties of anisotropic shales.

A homogeneous anisotropic matrix with elastic stiffness tensor $\mathbf{C}^{(0)}$ has embedded inclusions, divided into families $r = 1, 2, \dots, N$ having concentrations $v^{(r)}$ and shapes $\alpha^{(r)}$. For ellipsoidal inclusions $\alpha^{(r)}$ denotes the aspect ratio of the r th family of inclusions. While the general theory is not limited to ellipsoidal inclusions, most practical calculations are carried out assuming idealized ellipsoidal shapes. The effective elastic stiffness is given by Jakobsen *et al.* (2003a) as

$$\mathbf{C}_T^* = \mathbf{C}^{(0)} + \langle \mathbf{T}_1 \rangle \left(\mathbf{I} - \langle \mathbf{T}_1 \rangle^{-1} \mathbf{X} \right)^{-1} \quad (4.12.1)$$

where

$$\langle \mathbf{T}_1 \rangle = \sum_r v^{(r)} \mathbf{t}^{(r)}$$

$$\mathbf{X} = - \sum_r \sum_s v^{(r)} \mathbf{t}^{(r)} \mathbf{G}_d^{(rs)} \mathbf{t}^{(s)} v^{(s)}$$

and $\mathbf{I} = I_{ijkl} = \frac{1}{2}(\delta_{ji}\delta_{km} + \delta_{jm}\delta_{kl})$ is the fourth-rank identity tensor. The T -matrix $\mathbf{t}^{(r)}$ for a single inclusion of elastic stiffness $\mathbf{C}^{(r)}$ is given by

$$\mathbf{t}^{(r)} = \delta \mathbf{C}^{(r)} \left(\mathbf{I} - \mathbf{G}^{(r)} \delta \mathbf{C}^{(r)} \right)^{-1}$$

where

$$\delta \mathbf{C}^{(r)} = \mathbf{C}^{(r)} - \mathbf{C}^{(0)}$$

The fourth-rank tensor $\mathbf{G}^{(r)}$ (not the same as the tensor $\mathbf{G}_d^{(rs)}$) is a function of only $\mathbf{C}^{(0)}$ and the inclusion shape. It is computed using the following equations:

$$G_{pqrs}^{(r)} = -\frac{1}{4} \left[E_{pqrs}^{(r)} + E_{pqsr}^{(r)} + E_{qprs}^{(r)} + E_{qpsr}^{(r)} \right]$$

$$E_{pqrs}^{(r)} = \int_0^\pi d\theta \sin \theta \int_0^{2\pi} d\phi D_{qs}^{-1}(k) k_p k_r A^{(r)}(\theta, \phi)$$

$$D_{qs} = C_{qmsn}^{(0)} k_m k_n$$

where k , θ , and ϕ are spherical coordinates in k -space (Fourier space), and the components of the unit k -vector are given as usual by $[\sin \theta \cos \phi, \sin \theta \sin \phi, \cos \theta]$. The term $A^{(r)}(\theta, \phi)$ is a shape factor for the r th inclusion and is independent of elastic constants. For an oblate spheroidal inclusion with short axis b_3 aligned along the x_3 -axis, long axes $b_1 = b_2$, and aspect ratio $\alpha^{(r)} = b_3/b_1$, $A^{(r)}$ is independent of ϕ and is given by

$$A^{(r)}(\theta) = \frac{1}{4\pi} \frac{\alpha^{(r)}}{\left[\sin^2 \theta + (\alpha^{(r)})^2 \cos^2 \theta \right]^{3/2}}$$

For a spherical inclusion $A^{(r)} = 1/(4\pi)$. For the case when $\mathbf{C}^{(0)}$ has hexagonal symmetry and the principal axes of the oblate spheroidal inclusions are aligned along the symmetry axes of $\mathbf{C}^{(0)}$, the nonzero elements of E_{pqrs} are given by definite integrals of polynomial functions (Mura, 1982):

$$E_{1111} = E_{2222} = \frac{\pi}{2} \int_0^1 \Delta(1-x^2) \{ [f(1-x^2) + h\gamma^2 x^2] \\ \times [(3e+d)(1-x^2) + 4f\gamma^2 x^2] - g^2 \gamma^2 x^2 (1-x^2) \} dx$$

$$E_{3333} = 4\pi \int_0^1 \Delta \gamma^2 x^2 [d(1-x^2) + f\gamma^2 x^2] [e(1-x^2) + f\gamma^2 x^2] dx$$

$$E_{1122} = E_{2211} = \frac{\pi}{2} \int_0^1 \Delta(1-x^2) \{ [f(1-x^2) + h\gamma^2 x^2] \\ \times [(e+3d)(1-x^2) + 4f\gamma^2 x^2] - 3g^2 \gamma^2 x^2 (1-x^2) \} dx$$

$$E_{1133} = E_{2233} = 2\pi \int_0^1 \Delta \gamma^2 x^2 \{[(d+e)(1-x^2) + 2f\gamma^2 x^2] \\ \times [f(1-x^2) + h\gamma^2 x^2] - g^2 \gamma^2 x^2 (1-x^2)\} dx$$

$$E_{3311} = E_{3322} = 2\pi \int_0^1 \Delta (1-x^2) [d(1-x^2) + f\gamma^2 x^2] \\ \times [e(1-x^2) + f\gamma^2 x^2] dx$$

$$E_{1212} = \frac{\pi}{2} \int_0^1 \Delta (1-x^2)^2 \{g^2 \gamma^2 x^2 - (d-e)[f(1-x^2) + h\gamma^2 x^2]\} dx$$

$$E_{1313} = E_{2323} = -2\pi \int_0^1 \Delta g \gamma^2 x^2 (1-x^2) [e(1-x^2) + f\gamma^2 x^2] dx$$

where

$$\Delta^{-1} = [e(1-x^2) + f\gamma^2 x^2] \{[d(1-x^2) + f\gamma^2 x^2][f(1-x^2) + h\gamma^2 x^2] - g^2 \gamma^2 x^2 (1-x^2)\}$$

$$d = C_{11}^{(0)} \quad e = [C_{11}^{(0)} - C_{12}^{(0)}]/2$$

$$f = C_{44}^{(0)} \quad g = C_{13}^{(0)} + C_{44}^{(0)} \quad h = C_{33}^{(0)}$$

and x is the integration variable while $\gamma = \alpha$ is the inclusion aspect ratio.

Using these equations, the tensor E_{pqrs} (and hence G_{pqrs}) can be obtained by numerical or symbolic integration. For numerical computations, instead of the more common Voigt notation, the Kelvin notation of fourth-rank tensors in terms of 6×6 matrices is more efficient, since matrix operations can be performed on the Kelvin 6×6 matrices according to the usual matrix rules (see also [Section 2.2](#)).

In the equation for the effective elastic stiffness, the term \mathbf{X} involving the tensor $\mathbf{G}_d^{(rs)}$ represents the two-point interaction between the r th set and the s th set of inclusions. The tensor $\mathbf{G}_d^{(rs)}$ is computed in the same way as the tensor $\mathbf{G}_{ijkl}^{(r)}$ except that the aspect ratio of the associated inclusion is set to be the aspect ratio, α_d , of the ellipsoidal two-point spatial correlation function, representing the symmetry of $p^{(slr)}(\mathbf{x}-\mathbf{x}')$, the conditional probability of finding an inclusion of type s at \mathbf{x}' , given that there is an inclusion of type r at \mathbf{x} . The aspect ratio of the spatial correlation function can be different from the aspect ratio of the inclusions. The effect of spatial distribution is of higher order in the volume concentrations than the effect of inclusion shapes. The effect of spatial distribution becomes important when the inclusion concentration increases beyond the dilute limit. However, even the *T*-matrix approximation given by [equation \(4.12.1\)](#) may be invalid at very high concentration, as it neglects the higher-order interactions beyond two-point interactions (Jakobsen *et al.*, 2003a). According to Jakobsen *et al.* (2003a) it appears to be difficult to determine the range of validity for the various *T*-matrix approximations. For the case

of a matrix phase with just one type of inclusion, Ponte-Castaneda and Willis (1995) found that the T -matrix approximation is consistent only for certain combinations of α_d , (aspect ratio of the correlation function), α (inclusion aspect ratio), and v (inclusion concentration). When $\alpha_d > \alpha$, the minimum possible value for inclusion aspect ratio is $\alpha_{\min} = \alpha_d v$.

Using a series expansion of the reciprocal, the equation for the effective stiffness may be written as

$$\mathbf{C}_T^* = \mathbf{C}^{(0)} + \sum_r v^{(r)} \mathbf{t}^{(r)} - \sum_r \sum_s v^{(r)} \mathbf{t}^{(r)} \mathbf{G}_d^{(rs)} \mathbf{t}^{(s)} v^{(s)} + O\left[\left(v^{(r)}\right)^3\right]$$

which agrees with Eshelby's (1957) dilute estimate to first order in concentration. When the spatial distribution is assumed to be the same for all pairs of interacting inclusions, $\mathbf{G}_d^{(rs)} = \mathbf{G}_d$ for all r and s . Under this assumption the equation for \mathbf{C}_T^* becomes

$$\mathbf{C}_T^* = \mathbf{C}^{(0)} + \left[\sum_r v^{(r)} \mathbf{t}^{(r)} \right] \left\{ \mathbf{I} + \mathbf{G}_d \left[\sum_s \mathbf{t}^{(s)} v^{(s)} \right] \right\}^{-1}$$

or

$$\mathbf{C}_T^* = \mathbf{C}^{(0)} + \left(\sum_r v^{(r)} \mathbf{t}^{(r)} \right) - \left(\sum_r v^{(r)} \mathbf{t}^{(r)} \right) \mathbf{G}_d \left(\sum_s v^{(s)} \mathbf{t}^{(s)} \right) + O\left[\left(v^{(r)}\right)^3\right]$$

These non-self-consistent, second-order T -matrix approximations with a well-defined $\mathbf{C}^{(0)}$ are sometimes termed the generalized **optical potential approximation** (OPA) (Jakobsen *et al.*, 2003a). The generalized OPA equations reduce to Nishizawa's (1982) differential effective medium formulation when the second-order correction terms are dropped, and the calculations are done incrementally, increasing the inclusion concentration in small steps, and taking $\mathbf{C}^{(0)}$ to be the effective stiffness from the previous incremental step. This formulation can be written as a system of ordinary differential equations for the effective stiffness $\mathbf{C}_{\text{DEM}}^*$ (Jakobsen *et al.*, 2000):

$$\left[1 - v^{(r)} \right] \frac{d\mathbf{C}_{\text{DEM}}^*}{dv^{(r)}} = \left[\mathbf{C}^{(r)} - \mathbf{C}_{\text{DEM}}^* \right] \left[\mathbf{I} - \mathbf{G}^{(\text{DEM})} (\mathbf{C}^{(r)} - \mathbf{C}_{\text{DEM}}^*) \right]^{-1}$$

with initial conditions

$$\mathbf{C}_{\text{DEM}}^*(v^{(r)} = 0) = \mathbf{C}^{(0)}$$

The superscript (DEM) on the tensor \mathbf{G} indicates that it is computed for a medium having elastic stiffness $\mathbf{C}_{\text{DEM}}^*$.

When the multiphase aggregate does not have a clearly defined matrix material and each phase is in the form of inclusions embedded in a sea of inclusions, one can set

$\mathbf{C}^{(0)} = \mathbf{C}_T^*$ to give the self-consistent *T*-matrix approximation, also called the generalized **coherent potential approximation** (CPA):

$$\left[\sum_r v^{(r)} \mathbf{t}_*^{(r)} \right] \left\{ \mathbf{I} + \left[\sum_s v^{(s)} \mathbf{t}_*^{(s)} \right]^{-1} \sum_p \sum_q v^{(p)} \mathbf{t}_*^{(p)} \mathbf{G}_{d*}^{(pq)} v^{(q)} \mathbf{t}_*^{(q)} \right\}^{-1} = 0$$

or

$$\left[\sum_r v^{(r)} \mathbf{t}_*^{(r)} \right] - \sum_p \sum_q v^{(p)} \mathbf{t}_*^{(p)} \mathbf{G}_{d*}^{(pq)} v^{(q)} \mathbf{t}_*^{(q)} \approx 0$$

where the subscript $*$ on the tensor quantities \mathbf{t} and \mathbf{G} indicates that they are computed for a reference medium having the (as yet unknown) elastic stiffness \mathbf{C}_T^* . The generalized CPA equations are an implicit set of equations for the effective stiffness, and must be solved iteratively. The generalized CPA reduces to the first-order CPA, ignoring higher-order terms:

$$\sum_r v^{(r)} \mathbf{t}_*^{(r)} \approx 0$$

which is equivalent to Berryman's symmetric self-consistent approximation (see Section 4.8).

When the r th set of inclusions have a spatial distribution described by an orientation distribution function $O^{(r)}(\theta, \psi, \phi)$, the *T*-matrix for the individual inclusion, $\mathbf{t}^{(r)}$, in the above equations for the first- and second-order corrections have to be replaced by the orientation averaged tensor $\bar{\mathbf{t}}^{(r)}$ given by

$$\bar{\mathbf{t}}^{(r)} = \int_0^\pi d\theta \sin \theta \int_0^{2\pi} d\psi \int_0^{2\pi} d\phi O^{(r)}(\theta, \psi, \phi) \mathbf{t}^{(r)}(\theta, \psi, \phi)$$

The three Euler angles (θ, ψ, ϕ) define the orientation of the ellipsoid with principal axes $X_1X_2X_3$ with respect to the fixed global coordinates $x_1x_2x_3$, where θ is the angle between the short axis of the ellipsoid and the x_3 -axis. Computing the orientation average *T*-matrix involves coordinate transformation of the inclusion stiffness tensor $\mathbf{C}^{(r)}$ from the local coordinate system of the inclusion to the global coordinates using the usual transformation laws for the stiffness tensor.

Jakobsen *et al.* (2003b) have extended the *T*-matrix formulation to take into account fluid effects in porous rocks. For a single fully saturated ellipsoidal inclusion of the r th set that is allowed to communicate and exchange fluid mass with other cavities, the *T*-matrix, $\mathbf{t}_{\text{sat}}^{(r)}$ is given as the dry *T*-matrix $\mathbf{t}_{\text{dry}}^{(r)}$ plus an extra term accounting for fluid effects. The *T*-matrix for dry cavities is obtained by setting $\mathbf{C}^{(r)}$ to zero in the above equations. The saturated *T*-matrix is expressed as

$$\mathbf{t}_{\text{sat}}^{(r)} = \mathbf{t}_{\text{dry}}^{(r)} + \frac{\Theta \mathbf{Z}^{(r)} + i\omega\tau\kappa_f \mathbf{X}^{(r)}}{1 + i\omega\tau\gamma^{(r)}}$$

$$\mathbf{X}^{(r)} = \mathbf{t}_{\text{dry}}^{(r)} \mathbf{S}^{(0)} (\mathbf{I}_2 \otimes \mathbf{I}_2) \mathbf{S}^{(0)} \mathbf{t}_{\text{dry}}^{(r)}$$

$$\mathbf{Z}^{(r)} = \mathbf{t}_{\text{dry}}^{(r)} \mathbf{S}^{(0)} (\mathbf{I}_2 \otimes \mathbf{I}_2) \mathbf{S}^{(0)} \left(\sum_r \frac{v^{(r)} \mathbf{t}_{\text{dry}}^{(r)}}{1 + i\omega\tau\gamma^{(r)}} \right)$$

$$\Theta = \kappa_f \left\{ \left(1 - \kappa_f \mathbf{S}_{uvv}^{(0)} \right) \left(\sum_r \frac{v^{(r)}}{1 + i\omega\tau\gamma^{(r)}} \right) + \kappa_f \left(\sum_r \frac{v^{(r)} \left(\mathbf{K}_d^{(r)} \right)_{uvv}}{1 + i\omega\tau\gamma^{(r)}} \right) - \frac{ik_u k_v \Gamma_{uv} \kappa_f}{\omega \eta_f} \right\}^{-1}$$

$$\mathbf{K}_d^{(r)} = \left(\mathbf{I}_4 + \mathbf{G}^{(r)} \mathbf{C}^{(0)} \right)^{-1} \mathbf{S}^{(0)}$$

$$\gamma^{(r)} = 1 + \kappa_f \left(\mathbf{K}_d^{(r)} - \mathbf{S}^{(0)} \right)_{uvv}$$

In the above equations, $\mathbf{S}^{(0)} = [\mathbf{C}^{(0)}]^{-1}$ is the elastic compliance of the background medium, κ_f and η_f are the bulk modulus and viscosity of the fluid, ω is the frequency, τ is a flow-related relaxation-time constant, k_u, k_v are components of the wave vector, and Γ_{uv} is the (possibly anisotropic) permeability tensor of the rock. Repeated subscripts u and v imply summation over $u, v = 1, 2, 3$. The tensors \mathbf{I}_2 and \mathbf{I}_4 are second- and fourth-rank identity tensors, respectively. The dyadic product is denoted by \otimes and $(\mathbf{I}_2 \otimes \mathbf{I}_2)_{ijkl} = \delta_{ij} \delta_{kl}$. Usually the relaxation-time constant τ is poorly defined and has to be calibrated from experimental data. Jakobsen *et al.* (2003b) show that the first-order approximations of these expressions reduce to the Brown and Korrington results (see Section 6.5) in the low-frequency limit.

Uses

The results described in this section can be used to model effective-medium elastic properties of composites made up of anisotropic ellipsoidal inclusions in an anisotropic background. The formulation for saturated, communicating cavities can be used to model fluid-related velocity dispersion and attenuation in porous rocks.

Assumptions and limitations

The results described in this section assume the following:

- idealized ellipsoidal inclusion shape;
- linear elasticity and a Newtonian fluid.

4.13 Elastic constants in finely layered media: Backus average

Synopsis

A transversely isotropic medium with the symmetry axis in the x_3 -direction has an elastic stiffness tensor that can be written in the condensed Voigt matrix form (see Section 2.2 on anisotropy):

$$\begin{bmatrix} a & b & f & 0 & 0 & 0 \\ b & a & f & 0 & 0 & 0 \\ f & f & c & 0 & 0 & 0 \\ 0 & 0 & 0 & d & 0 & 0 \\ 0 & 0 & 0 & 0 & d & 0 \\ 0 & 0 & 0 & 0 & 0 & m \end{bmatrix}, \quad m = \frac{1}{2}(a - b)$$

where a , b , c , d , and f are five independent elastic constants. Backus (1962) showed that in the long-wavelength limit a stratified medium composed of **layers of transversely isotropic materials** (each with its symmetry axis normal to the strata) is also effectively anisotropic, with effective stiffness as follows:

$$\begin{bmatrix} A & B & F & 0 & 0 & 0 \\ B & A & F & 0 & 0 & 0 \\ F & F & C & 0 & 0 & 0 \\ 0 & 0 & 0 & D & 0 & 0 \\ 0 & 0 & 0 & 0 & D & 0 \\ 0 & 0 & 0 & 0 & 0 & M \end{bmatrix}, \quad M = \frac{1}{2}(A - B)$$

where

$$A = \langle a - f^2 c^{-1} \rangle + \langle c^{-1} \rangle^{-1} \langle f c^{-1} \rangle^2$$

$$B = \langle b - f^2 c^{-1} \rangle + \langle c^{-1} \rangle^{-1} \langle f c^{-1} \rangle^2$$

$$C = \langle c^{-1} \rangle^{-1}$$

$$F = \langle c^{-1} \rangle^{-1} \langle f c^{-1} \rangle$$

$$D = \langle d^{-1} \rangle^{-1}$$

$$M = \langle m \rangle$$

The brackets $\langle \cdot \rangle$ indicate averages of the enclosed properties weighted by their volumetric proportions. This is often called the *Backus average*.

If the **individual layers are isotropic**, the effective medium is still transversely isotropic, but the number of independent constants needed to describe each individual layer is reduced to 2:

$$a = c = \lambda + 2\mu, \quad b = f = \lambda, \quad d = m = \mu$$

giving for the effective medium

$$A = \left\langle \frac{4\mu(\lambda + \mu)}{\lambda + 2\mu} \right\rangle + \left\langle \frac{1}{\lambda + 2\mu} \right\rangle^{-1} \left\langle \frac{\lambda}{\lambda + 2\mu} \right\rangle^2$$

$$B = \left\langle \frac{2\mu\lambda}{\lambda + 2\mu} \right\rangle + \left\langle \frac{1}{\lambda + 2\mu} \right\rangle^{-1} \left\langle \frac{\lambda}{\lambda + 2\mu} \right\rangle^2$$

$$\begin{aligned}
 C &= \left\langle \frac{1}{\lambda + 2\mu} \right\rangle^{-1} \\
 F &= \left\langle \frac{1}{\lambda + 2\mu} \right\rangle^{-1} \left\langle \frac{\lambda}{\lambda + 2\mu} \right\rangle \\
 D &= \left\langle \frac{1}{\mu} \right\rangle^{-1} \\
 M &= \langle \mu \rangle
 \end{aligned}$$

In terms of the P- and S-wave velocities and densities in the isotropic layers (Levin, 1979),

$$\begin{aligned}
 a &= \rho V_P^2 \\
 d &= \rho V_S^2 \\
 f &= \rho(V_P^2 - 2V_S^2)
 \end{aligned}$$

the effective parameters can be rewritten as

$$\begin{aligned}
 A &= \left\langle 4\rho V_S^2 \left(1 - \frac{V_S^2}{V_P^2} \right) \right\rangle + \left\langle 1 - 2\frac{V_S^2}{V_P^2} \right\rangle^2 \left\langle (\rho V_P^2)^{-1} \right\rangle^{-1} \\
 B &= \left\langle 2\rho V_S^2 \left(1 - \frac{2V_S^2}{V_P^2} \right) \right\rangle + \left\langle 1 - 2\frac{V_S^2}{V_P^2} \right\rangle^2 \left\langle (\rho V_P^2)^{-1} \right\rangle^{-1} \\
 C &= \left\langle (\rho V_P^2)^{-1} \right\rangle^{-1} \\
 F &= \left\langle 1 - 2\frac{V_S^2}{V_P^2} \right\rangle \left\langle (\rho V_P^2)^{-1} \right\rangle^{-1} \\
 D &= \left\langle (\rho V_S^2)^{-1} \right\rangle^{-1} \\
 M &= \langle \rho V_S^2 \rangle
 \end{aligned}$$

The P- and S-wave velocities in the effective anisotropic medium can be written as

$$\begin{aligned}
 V_{SH,h} &= \sqrt{M/\rho} \\
 V_{SH,v} &= V_{SV,h} = V_{SV,v} = \sqrt{D/\rho} \\
 V_{P,h} &= \sqrt{A/\rho} \\
 V_{P,v} &= \sqrt{C/\rho}
 \end{aligned}$$

where ρ is the average density; $V_{P,v}$ is for the vertically propagating P-wave; $V_{P,h}$ is for the horizontally propagating P-wave; $V_{SH,h}$ is for the horizontally propagating, horizontally polarized S-wave; $V_{SV,h}$ is for the horizontally propagating, vertically polarized S-wave; and $V_{SV,v}$ and $V_{SH,v}$ are for the vertically propagating S-waves of any polarization (vertical is defined as being normal to the layering).

Calculate the effective anisotropic elastic constants and the velocity anisotropy for a thinly layered sequence of dolomite and shale with the following layer properties:

$$V_{P(1)} = 5200 \text{ m/s}, \quad V_{S(1)} = 2700 \text{ m/s}, \quad \rho_1 = 2450 \text{ kg/m}^3, \quad d_1 = 0.75 \text{ m} \\ V_{P(2)} = 2900 \text{ m/s}, \quad V_{S(2)} = 1400 \text{ m/s}, \quad \rho_2 = 2340 \text{ kg/m}^3, \quad d_2 = 0.5 \text{ m}$$

The volumetric fractions are

$$f_1 = d_1/(d_1 + d_2) = 0.6, \quad f_2 = d_2/(d_1 + d_2) = 0.4$$

If one takes the volumetric weighted averages of the appropriate properties,

$$A = f_1 4\rho_1 V_{S(1)}^2 \left(1 - \frac{V_{S(1)}^2}{V_{P(1)}^2} \right) + f_2 4\rho_2 V_{S(2)}^2 \left(1 - \frac{V_{S(2)}^2}{V_{P(2)}^2} \right) \\ + \left[f_1 \left(1 - 2 \frac{V_{S(1)}^2}{V_{P(1)}^2} \right) + f_2 \left(1 - 2 \frac{V_{S(2)}^2}{V_{P(2)}^2} \right) \right]^2 \frac{1}{f_1/(\rho_1 V_{P(1)}^2) + f_2/(\rho_2 V_{P(2)}^2)}$$

$$A = 45.1 \text{ GPa}$$

Similarly, computing the other averages we obtain $C = 34.03 \text{ GPa}$, $D = 8.28 \text{ GPa}$, $M = 12.55 \text{ GPa}$, $F = 16.7 \text{ GPa}$, and $B = A - 2M = 20 \text{ GPa}$.

The average density $\rho = f_1 \rho_1 + f_2 \rho_2 = 2406 \text{ kg/m}^3$. The anisotropic velocities are:

$$V_{SH,h} = \sqrt{M/\rho} = 2284.0 \text{ m/s}$$

$$V_{SH,v} = V_{SV,h} = V_{SV,v} = \sqrt{D/\rho} = 1854.8 \text{ m/s}$$

$$V_{P,h} = \sqrt{A/\rho} = 4329.5 \text{ m/s}$$

$$V_{P,v} = \sqrt{C/\rho} = 3761.0 \text{ m/s}$$

$$\text{P-wave anisotropy} = (4329.5 - 3761.0)/3761.0 \approx 15\%$$

$$\text{S-wave anisotropy} = (2284.0 - 1854.8)/1854.8 \approx 23\%$$

Finally, consider the case in which **each layer is isotropic with the same shear modulus** but with a different bulk modulus. This might be the situation, for example, for a massive, homogeneous rock with fine layers of different fluids or saturations. Then, the elastic constants of the medium become

$$A = C = \left\langle \frac{1}{\rho V_P^2} \right\rangle^{-1} = \left\langle \frac{1}{K + \frac{4}{3}\mu} \right\rangle^{-1}$$

$$B = F = \left\langle \frac{1}{\rho V_P^2} \right\rangle^{-1} - 2\mu = \left\langle \frac{1}{K + \frac{4}{3}\mu} \right\rangle^{-1} - 2\mu = A - 2\mu$$

$$D = M = \mu$$

A finely layered medium of isotropic layers, all having the same shear modulus, is isotropic.

Bakulin and Grechka (2003) show that any effective property, \mathbf{m}^{eff} , of a finely layered medium (in fact, any heterogeneous medium) can be written as

$$\mathbf{F}[\mathbf{m}^{\text{eff}}] = \frac{1}{V} \int_V \mathbf{F}[\mathbf{m}(\mathbf{x})] d\mathbf{x}$$

where \mathbf{F} is the appropriate averaging operator, \mathbf{m} is the parameter (tensor, vector, or scalar) of interest (e.g., the elastic stiffnesses, c_{ij} , or Thomsen parameters, $\varepsilon, \delta, \gamma$), V is the representative volume, and \mathbf{x} denotes the Cartesian coordinates over which \mathbf{m} varies. For example, from the Backus average one can write

$$c_{66}^{\text{eff}} = \frac{1}{V} \int_V c_{66}(\mathbf{x}) d\mathbf{x}$$

where \mathbf{F} is the scalar identity function,

$$c_{44}^{\text{eff}} = \left[\frac{1}{V} \int_V [c_{44}(\mathbf{x})]^{-1} d\mathbf{x} \right]^{-1}$$

where $\mathbf{F}[\mathbf{m}] = \mathbf{m}^{-1}$, and so on. An important consequence is that

$$\mathbf{m}^{\text{eff}} = \bar{\mathbf{m}} + O(\tilde{\mathbf{m}}^2)$$

where

$$\bar{\mathbf{m}} = \frac{1}{V} \int_V \mathbf{m}(\mathbf{x}) d\mathbf{x}$$

$$\tilde{\mathbf{m}} = \mathbf{m} - \bar{\mathbf{m}}$$

In other words, the effective property of a finely layered medium is, to first order, just the arithmetic average of the individual layer properties. The effect of the layer contrasts is second order in the deviations from the mean.

A composite of fine isotropic layers with weak layer contrasts is, to first order, isotropic (Bakulin, 2003). The well-known anisotropy resulting from the Backus average is second order. When the layers are intrinsically anisotropic, as with shales, then the first-order anisotropy is the average of the layer intrinsic anisotropies, and the anisotropy due to the layer contrasts is often less important, especially when the layer contrasts are small.

Uses

The Backus average is used to model a finely stratified medium as a single homogeneous medium.

Assumptions and limitations

The following presuppositions and conditions apply to the Backus average:

- all materials are linearly elastic;
- there are no sources of intrinsic energy dissipation, such as friction or viscosity; and
- the layer thickness must be much smaller than the seismic wavelength. How small is still a subject of disagreement and research, but a rule of thumb is that the wavelength must be at least ten times the layer thickness.

4.14 Elastic constants in finely layered media: general layer anisotropy

Techniques for calculation of the effective elastic moduli of a finely layered one-dimensional medium were first developed by Riznichenko (1949) and Postma (1955). Backus (1962) further developed the method and introduced the well-known Backus average of isotropic or VTI layers (Section 4.13). Helbig and Schoenberg (1987) and Schoenberg and Muir (1989) presented the results for layers with arbitrary anisotropy in convenient matrix form, shown here. Assuming that the x_3 -axis is normal to the layering, one can define the matrices

$$C_{NN}^{(i)} = \begin{bmatrix} c_{33}^{(i)} & c_{34}^{(i)} & c_{35}^{(i)} \\ c_{34}^{(i)} & c_{44}^{(i)} & c_{45}^{(i)} \\ c_{35}^{(i)} & c_{45}^{(i)} & c_{55}^{(i)} \end{bmatrix}$$

$$C_{TN}^{(i)} = \begin{bmatrix} c_{13}^{(i)} & c_{14}^{(i)} & c_{15}^{(i)} \\ c_{23}^{(i)} & c_{24}^{(i)} & c_{25}^{(i)} \\ c_{36}^{(i)} & c_{46}^{(i)} & c_{56}^{(i)} \end{bmatrix}$$

$$C_{TT}^{(i)} = \begin{bmatrix} c_{11}^{(i)} & c_{12}^{(i)} & c_{16}^{(i)} \\ c_{12}^{(i)} & c_{22}^{(i)} & c_{26}^{(i)} \\ c_{16}^{(i)} & c_{26}^{(i)} & c_{66}^{(i)} \end{bmatrix}$$

where the $c_{kl}^{(i)}$ are the Voigt-notation elastic constants of the i th layer. Then the effective medium having the same stress–strain behavior of the composite has the corresponding matrices

$$\bar{C}_{NN} = \begin{bmatrix} \bar{c}_{33} & \bar{c}_{34} & \bar{c}_{35} \\ \bar{c}_{34} & \bar{c}_{44} & \bar{c}_{45} \\ \bar{c}_{35} & \bar{c}_{45} & \bar{c}_{55} \end{bmatrix} = \langle C_{NN}^{-1} \rangle^{-1}$$

$$\bar{C}_{TN} = \begin{bmatrix} \bar{c}_{13} & \bar{c}_{14} & \bar{c}_{15} \\ \bar{c}_{23} & \bar{c}_{24} & \bar{c}_{25} \\ \bar{c}_{36} & \bar{c}_{46} & \bar{c}_{56} \end{bmatrix} = \langle C_{TN} C_{NN}^{-1} \rangle \bar{C}_{NN}$$

$$\bar{C}_{TT} = \begin{bmatrix} \bar{c}_{11} & \bar{c}_{12} & \bar{c}_{16} \\ \bar{c}_{12} & \bar{c}_{22} & \bar{c}_{26} \\ \bar{c}_{16} & \bar{c}_{26} & \bar{c}_{66} \end{bmatrix} = \langle C_{TT} \rangle - \langle C_{TN} C_{NN}^{-1} C_{NT} \rangle + \langle C_{TN} C_{NN}^{-1} \rangle \bar{C}_{NN} \langle C_{NN}^{-1} C_{NT} \rangle$$

where the \bar{c}_{kl} terms are the effective elastic constants. In the above equations the operator $\langle \cdot \rangle$ denotes a thickness-weighted average over the layers.

4.15 Poroelastic Backus average

Synopsis

For a medium consisting of thin poroelastic layers with different saturating fluids, Gelinsky and Shapiro (1997a) give the expressions for the poroelastic constants of the effective homogeneous anisotropic medium. This is equivalent to the Backus average for thin elastic layers (see Section 4.13). At very low frequencies, (quasi-static limit) seismic waves cause interlayer flow across the layer boundaries. At higher frequencies, layers behave as if they are sealed with no flow across the boundaries, and this scenario is equivalent to elastic Backus averaging with saturated rock moduli obtained from Gassmann's relations for individual layers.

When the individual poroelastic layers are themselves transversely anisotropic with a vertical axis of symmetry, x_3 , normal to the layers, each layer is described by five independent stiffness constants, b_d , c_d , f_d , d_d , and m_d , and three additional poroelastic constants, p , q , and r , describing the coupling between fluid flow and elastic deformation. The five stiffness constants correspond to the components of the dry-frame stiffness tensor (see Section 4.13). In the usual two-index Voigt notation they are: $b_d = C_{12}^d$, $c_d = C_{33}^d$, $f_d = C_{13}^d$, $d_d = C_{44}^d = C_{55}^d$, where the sub- and superscript "d" indicates dry frame. The constants p , q , and r for the individual layers can be expressed in terms of the dry anisotropic frame moduli and fluid properties as follows:

$$p = \alpha_1 r \quad q = \alpha_2 r$$

$$r = K_0 \left[\left(1 - \frac{K_d}{K_0} \right) - \phi \left(1 - \frac{K_0}{K_f} \right) \right]^{-1}$$

$$\alpha_1 = 1 - (C_{11}^d + C_{12}^d + C_{13}^d) / (3K_0)$$

$$\alpha_2 = 1 - (2C_{13}^d + C_{33}^d) / (3K_0)$$

$$K_d = \frac{1}{9} C_{ijj} = \text{dry bulk modulus}$$

$$K_0 = \text{mineral bulk modulus}$$

$$K_f = \text{pore fluid bulk modulus}$$

$$\phi = \text{porosity}$$

In the quasi-static limit the effective homogeneous poroelastic medium is itself transversely anisotropic with effective constants given by (Gelinsky and Shapiro, 1997a):

$$\begin{aligned}
 B &= \langle b_d - f_d^2 c_d^{-1} \rangle + \langle f_d^2 c_d^{-1} \rangle^2 \langle c_d^{-1} \rangle^{-1} + \frac{P^2}{R} \\
 C &= \langle c_d^{-1} \rangle^{-1} + \frac{Q^2}{R} \\
 F &= \langle c_d^{-1} \rangle^{-1} \langle f_d c_d^{-1} \rangle + \frac{PQ}{R} \\
 D &= \langle d_d^{-1} \rangle^{-1} \quad M = \langle m_d \rangle \\
 P &= R \left(\left\langle \frac{p}{r} \right\rangle - \left\langle \frac{q}{r} f_d c_d^{-1} \right\rangle + \left\langle \frac{q}{r} c_d^{-1} \right\rangle \langle c_d^{-1} \rangle^{-1} \langle f_d c_d^{-1} \rangle \right) \\
 Q &= R \left\langle \frac{q}{r} c_d^{-1} \right\rangle \langle c_d^{-1} \rangle^{-1} \\
 R &= \left[\langle r^{-1} \rangle + \left\langle \frac{q^2}{r^2} c_d^{-1} \right\rangle - \left\langle \frac{q}{r} c_d^{-1} \right\rangle^2 \langle c_d^{-1} \rangle^{-1} \right]^{-1}
 \end{aligned}$$

The symbol $\langle \cdot \rangle$ indicates volumetric averages of the enclosed properties. When the individual thin layers are transversely isotropic with a horizontal symmetry axis (x_1), the effective medium has orthorhombic symmetry and is described by the stiffness tensor A_{ij} with nine independent constants and four additional Biot parameters, P_1 , P_2 , P_3 , and R . The layers themselves are characterized by the transversely isotropic coefficients, b_d , c_d , f_d , d_d , and m_d , (and $a_d = 2m_d + b_d$), and three additional poroelastic constants, p , q , and r , with x_1 as the symmetry axis instead of x_3 . The effective constants are given by (Gelinsky and Shapiro, 1997a):

$$\begin{aligned}
 A_{11} &= \langle c_d \rangle + \left\langle \frac{f_d}{a_d} \right\rangle^2 \langle a_d^{-1} \rangle^{-1} - \left\langle \frac{f_d^2}{a_d} \right\rangle + \frac{P_1^2}{R} \\
 A_{22} &= \langle a_d \rangle + \left\langle \frac{b_d}{a_d} \right\rangle^2 \langle a_d^{-1} \rangle^{-1} - \left\langle \frac{b_d^2}{a_d} \right\rangle + \frac{P_2^2}{R} \\
 A_{33} &= \langle a_d^{-1} \rangle^{-1} + \frac{P_3^2}{R} \\
 A_{12} &= \langle f_d \rangle + \left\langle \frac{f_d}{a_d} \right\rangle \left\langle \frac{b_d}{a_d} \right\rangle \langle a_d^{-1} \rangle^{-1} - \left\langle \frac{f_d b_d}{a_d} \right\rangle + \frac{P_1 P_2}{R} \\
 A_{13} &= \left\langle \frac{f_d}{a_d} \right\rangle \langle a_d^{-1} \rangle^{-1} + \frac{P_1 P_3}{R} \\
 A_{23} &= \left\langle \frac{b_d}{a_d} \right\rangle \langle a_d^{-1} \rangle^{-1} + \frac{P_2 P_3}{R} \\
 A_{44} &= \left\langle \frac{1}{m_d} \right\rangle^{-1} \\
 A_{55} &= \left\langle \frac{1}{d_d} \right\rangle^{-1}
 \end{aligned}$$

$$\begin{aligned}
A_{66} &= \langle d_d \rangle \\
P_1 &= R \left(\left\langle \frac{q}{r} \right\rangle - \left\langle \frac{p f_d}{r a_d} \right\rangle + \left\langle \frac{p}{r a_d} \right\rangle \left\langle \frac{f_d}{a_d} \right\rangle \langle a_d^{-1} \rangle^{-1} \right) \\
P_2 &= R \left(\left\langle \frac{p}{r} \right\rangle - \left\langle \frac{p b_d}{r a_d} \right\rangle + \left\langle \frac{p}{r a_d} \right\rangle \left\langle \frac{b_d}{a_d} \right\rangle \langle a_d^{-1} \rangle^{-1} \right) \\
P_3 &= R \left(\left\langle \frac{p}{r a_d} \right\rangle \langle a_d^{-1} \rangle^{-1} \right) \\
R &= \left(\left\langle \frac{1}{r} \right\rangle + \left\langle \frac{p^2}{r^2 a_d} \right\rangle - \left\langle \frac{p}{r a_d} \right\rangle^2 \langle a_d^{-1} \rangle^{-1} \right)^{-1}
\end{aligned}$$

When the individual thin layers are isotropic, the effective constants for the equivalent transversely isotropic homogeneous poroelastic medium can be expressed in terms of averages of the Lamé constants λ_d and μ_d of the dry frame of the layers. For isotropic layers, $\alpha_1 = \alpha_2 = \alpha = 1 - K_d/K_0$. In the quasi-static limit the effective poroelastic constants are:

$$\begin{aligned}
B &= 2 \left\langle \frac{\lambda_d \mu_d}{\lambda_d + 2\mu_d} \right\rangle + \left\langle \frac{\lambda_d}{\lambda_d + 2\mu_d} \right\rangle^2 \left\langle \frac{1}{\lambda_d + 2\mu_d} \right\rangle^{-1} + \frac{P^2}{R} \\
C &= \left\langle \frac{1}{\lambda_d + 2\mu_d} \right\rangle^{-1} + \frac{Q^2}{R} \\
F &= \left\langle \frac{1}{\lambda_d + 2\mu_d} \right\rangle^{-1} \left\langle \frac{\lambda_d}{\lambda_d + 2\mu_d} \right\rangle + \frac{PQ}{R} \\
D &= \langle \mu_d^{-1} \rangle^{-1} \quad M = \langle \mu_d \rangle \\
P &= -R \left(2 \left\langle \frac{\alpha \mu_d}{\lambda_d + 2\mu_d} \right\rangle + \left\langle \frac{\alpha}{\lambda_d + 2\mu_d} \right\rangle \left\langle \frac{\lambda_d}{\lambda_d + 2\mu_d} \right\rangle \left\langle \frac{1}{\lambda_d + 2\mu_d} \right\rangle^{-1} \right) \\
Q &= -R \left\langle \frac{\alpha}{\lambda_d + 2\mu_d} \right\rangle \left\langle \frac{1}{\lambda_d + 2\mu_d} \right\rangle^{-1} \\
R &= \left[\langle r^{-1} \rangle + \left\langle \frac{\alpha^2}{\lambda_d + 2\mu_d} \right\rangle - \left\langle \frac{\alpha}{\lambda_d + 2\mu_d} \right\rangle^2 \left\langle \frac{1}{\lambda_d + 2\mu_d} \right\rangle^{-1} \right]^{-1}
\end{aligned}$$

Uses

These equations can be used to model a finely stratified heterogeneous poroelastic medium as an effective homogeneous anisotropic poroelastic medium.

Assumptions and limitations

- All materials are linear and poroelastic.
- Layer thicknesses are much smaller than the seismic wavelength. A rule of thumb is that the wavelength must be at least ten times the layer thickness.

4.16 Seismic response to fractures

Synopsis

One approach to modeling the effects of fractures on the elastic properties of rocks is to represent them as thin layers for which the elastic moduli are smaller (softer) than those of the unfractured background rock. The soft fracture layer modulus represents the extra compliance of the fracture relative to the background rock. When the seismic wavelength is long compared with the layer thickness and fracture spacing, then the overall elastic response of a parallel array of such fracture layers can be estimated using the Backus (1962) average (Section 4.13) (Hudson *et al.*, 1996; Schoenberg, 1980; Schoenberg and Douma, 1988; Hudson and Liu, 1999).

If the thickness of the weak fracture layer is h , and the fracture layer P-wave modulus and shear modulus are M_f and μ_f , respectively, then the total normal and shear displacements across the thin layer under normal and shear stresses, σ_n and σ_τ , are

$$\delta_n = \sigma_n h / M_f \quad \delta_\tau = \sigma_\tau h / (2\mu_f).$$

The *fracture normal and shear compliances*, Z_n and Z_τ , can be defined as

$$\frac{1}{Z_n} = \frac{\partial \sigma_n}{\partial \delta_n} = \frac{M_f}{h}, \quad \frac{1}{Z_\tau} = \frac{\partial \sigma_\tau}{\partial \delta_\tau} = \frac{2\mu_f}{h}$$

where Z_n and Z_τ have units of $(\text{stress}/\text{length})^{-1}$. By defining these fracture compliances, then at long wavelengths the fracture layer can be thought of as a *plane* of weakness, across which displacement discontinuities, δ_n and δ_τ , occur when stress is applied. Hence, these are often referred to as *displacement discontinuity models*.

Quasi-static fracture compliance

Both empirical and model-based methods have been applied to estimating values of fracture compliance (and its reciprocal the *fracture stiffness*). Jaeger *et al.* (2007) give an excellent summary. Myer (2000) represented joint deformation using the solution for the deformation of coplanar two-dimensional elliptical cavities (Figure 4.16.1) from Sneddon and Lowengrub (1969):

$$Z_n = \frac{d\delta_n}{d\sigma_n} = \frac{4(1-\nu)a}{\pi\mu(1-r)} \ln \sec \left[\frac{\pi}{2}(1-r) \right]$$

where μ is the rock shear modulus, ν is the Poisson ratio, r is the fractional area of contact of the crack faces, a is the crack length, and $b = a/(1-r)$ is the center-to-center crack spacing. With this model, crack closure under stress can be modeled using a distribution of crack aspect ratios, α , with a corresponding distribution of closing stresses (Section 2.9)

$$\sigma_{\text{close}} \approx \frac{\pi}{2(1-\nu)} \alpha \mu_0$$

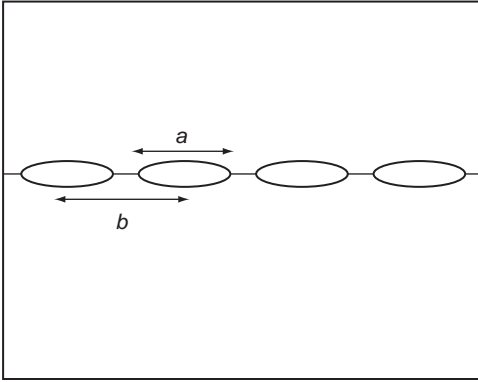


Figure 4.16.1 Representation of a partially open fracture with coplanar two-dimensional elliptical cracks.

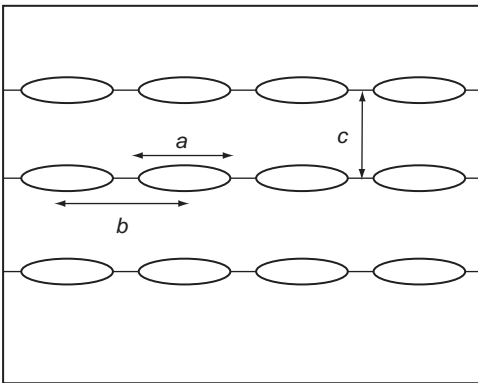


Figure 4.16.2 Representation of parallel partially open fractures with a doubly periodic array of two-dimensional elliptical cracks.

Hence, as normal compressive stress increases, a fraction of the cracks close, the contact area grows, and the fracture stiffens. Delameter *et al.* (1974) solved the related problem of the deformation of a doubly periodic array of cracks (Figure 4.16.2), which represents an extension of the Myer model to a set of parallel fractures. Mavko and Nur (1978) modeled the deformation of two-dimensional nonelliptical cracks (Figure 4.16.3). They showed that the deformation under infinitesimal increments of stress is identical to the deformation of an elliptical crack of the same length; hence, the crack stiffness of the models in Figures 4.16.1 and 4.16.3 will be the same. An important difference of the nonelliptical cracks is that under finite compressive stress, the cracks shorten, leading to increased contact area and fracture stiffening. Mavko and Nur also gave the solution for a nonelliptical crack that makes contact at a midpoint (Figure 4.16.4) before closing.

Another set of theoretical models represents the fracture as a distribution of Hertzian contacts (Section 5.4) of random heights (Greenwood and Williamson, 1966; White, 1983; Brown and Scholz, 1986; Jaeger *et al.*, 2007).

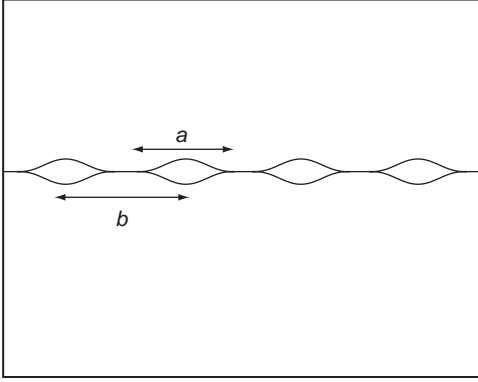


Figure 4.16.3 Representation of a partially open fracture with nonelliptical two-dimensional cracks with tapered ends.

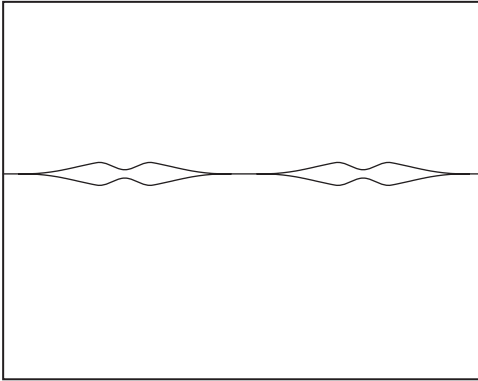


Figure 4.16.4 Representation of a partially open fracture with nonelliptical two-dimensional cracks that make multiple contacts under normal compression.

Based on laboratory measurements of joint closure, Goodman (1976) proposed an empirical stress–displacement function

$$\sigma_n = \sigma_0 \left[1 + \left(\frac{\delta_n}{\delta_m - \delta_n} \right)^t \right]; \quad 0 \leq \delta_n < \delta_m$$

where σ_0 is an initial reference stress at $\delta_n = 0$, δ_m is the maximum possible closure, and t is an empirical exponent. Bandis *et al.* (1983) proposed a simpler form

$$\sigma_n = \frac{1}{Z_0} \frac{\delta_m \delta_n}{\delta_m - \delta_n}$$

leading to the fracture compliance

$$\frac{1}{Z_n} = \frac{d\sigma_n}{d\delta_n} = \frac{1}{Z_0} \left(1 + \frac{Z_0 \sigma_n}{\delta_m} \right)^2$$

where Z_0 is the compliance at zero stress.

As discussed in Section 4.10, Hudson and Liu (1999) estimated the compliance of rough joint faces in contact using two models. In one model they represent the fracture as a planar distribution of small circular cracks with first-order normal and shear compliances equal to

$$\begin{aligned} Z_n &= \frac{\gamma^S a^3}{\mu} U_3 & Z_\tau &= \frac{\gamma^S a^3}{\mu} U_1 \\ &= \frac{ra}{\pi\mu} U_3 & &= \frac{ra}{\pi\mu} U_1 \end{aligned}$$

where γ^S is the number of cracks per unit area of the fracture plane, a is the crack radius, r is the fraction of the fracture plane that is not in contact, and μ is the unfractured rock shear modulus. For dry cracks

$$U_1 = \frac{16(\lambda + 2\mu)}{3(3\lambda + 4\mu)} \quad U_3 = \frac{4(\lambda + 2\mu)}{3(\lambda + \mu)}$$

Hence for dry fractures,

$$\left. \frac{Z_n}{Z_\tau} \right|_{\text{dry}} = 1 - \frac{\nu}{2}$$

where ν is the Poisson ratio of the unfractured rock, or $Z_{n\text{-dry}} \approx Z_{\tau\text{-dry}}$. For “weak” inclusions (i.e., when $\mu\alpha/[K' + \frac{4}{3}\mu']$ is of the order of 1 and is not small enough to be neglected)

$$U_1 = \frac{16(\lambda + 2\mu)}{3(3\lambda + 4\mu)} \frac{1}{(1 + M)}$$

$$U_3 = \frac{4(\lambda + 2\mu)}{3(\lambda + \mu)} \frac{1}{(1 + \kappa)}$$

where

$$M = \frac{4\mu'(\lambda + 2\mu)}{\pi\alpha\mu(3\lambda + 4\mu)}$$

$$\kappa = \frac{[K' + \frac{4}{3}\mu'](\lambda + 2\mu)}{\pi\alpha\mu(\lambda + \mu)}$$

and K' and μ' are the bulk and shear modulus of the inclusion material. Hence, for fluid-filled fractures ($\mu' = 0$)

$$\left. \frac{Z_\tau}{Z_n} \right|_{\text{wet}} = \left. \frac{Z_\tau}{Z_n} \right|_{\text{dry}} \frac{1 + \kappa}{1 + M}$$

In general, shear fracture compliance models depend very much on the amount of shear displacement. Large shear displacement is thought to involve interference of

asperities on opposite fracture faces (Jaeger *et al.*, 2007). At small normal stresses, asperities might slide over one another, causing dilatancy in the fracture zone. At larger normal stresses, asperities need to fail in either brittle or plastic fashion to accommodate slip.

Infinitesimal shear deformation in the fault zone can be modeled analogously to the normal deformation discussed above. Open cracks undergo shear deformation, while welded or frictional contacts have zero slip. The two-dimensional models for normal fracture deformation illustrated in Figures 4.16.1–4.16.4 can be scaled for shear deformation. For example, using dislocation analysis (Section 2.9), both normal and in-plane shear of two-dimensional cracks can be represented using edge dislocations, and hence the normal and shear fracture stiffnesses are equal for dry fractures. In general, a reasonable estimate of the infinitesimal shear compliance can be obtained from the infinitesimal normal compliance using the Hudson and Liu expressions for Z_τ / Z_n .

Dynamic response

The displacement discontinuity model has been applied to derive the dynamic response of waves impinging on the fracture plane (Kendall and Tabor, 1971; Schoenberg, 1980; Angel and Achenbach, 1985; Pyrak-Nolte *et al.*, 1990). Schoenberg (1980) gives expressions for the frequency-dependent P-wave reflection $R(\omega)$ and transmission $T(\omega)$ coefficients for normal incidence:

$$R(\omega) = \frac{-i\varpi}{1 - i\varpi} \quad \varpi = \left(\frac{\omega \rho Z_n V_P}{2} \right)$$

$$T(\omega) = \frac{1}{1 - i\varpi}$$

where ϖ is a dimensionless frequency, ω is the angular frequency, ρ is the density, V_P is the P-wave velocity, and Z_n is the infinitesimal fracture normal compliance. $R(\omega)$ and $T(\omega)$ are frequency-dependent and complex. An excellent review is given by Jaeger *et al.* (2007).

Use

The models presented here can be used to predict the effects of joints and fractures on the static and dynamic elastic properties of rocks.

Assumptions and limitations

The models presented here assume that the unfractured rock mass is isotropic, linear, and elastic. The joints and fractures are assumed to be planar.

4.17 Bound-filling models

Synopsis

The **Voigt–Reuss** (Section 4.2) and **Hashin–Shtrikman–Walpole** (see Section 4.1) bounds yield precise limits on the maximum and minimum possible values for the effective bulk and shear moduli of an isotropic, linear, elastic composite. Specifically, for a mixture of two components, the Hashin–Shtrikman–Walpole bounds can be written as

$$K^{\text{HS}\pm} = K_1 + \frac{f_2}{(K_2 - K_1)^{-1} + f_1(K_1 + \frac{4}{3}\mu_m)^{-1}} \quad (4.17.1)$$

$$\mu^{\text{HS}\pm} = \mu_1 + \frac{f_2}{(\mu_2 - \mu_1)^{-1} + f_1 \left[\mu_1 + \frac{1}{6}\mu_m \left(\frac{9K_m + 8\mu_m}{K_m + 2\mu_m} \right) \right]^{-1}} \quad (4.17.2)$$

where subscripts 1 and 2 refer to properties of the two components, having bulk moduli, K_1, K_2 , shear moduli, μ_1, μ_2 , and volume fractions f_1 and f_2 . Most commonly, these bounds are applied to describe mixtures of mineral and pore fluid, as illustrated in Figure 4.17.1. Equations (4.17.1) and (4.17.2) yield the upper bounds when K_m and μ_m are the maximum bulk and shear moduli of the individual constituents, and the lower bounds when K_m and μ_m are the minimum bulk and shear moduli of the constituents, respectively. The maximum (minimum) shear modulus might come from a different constituent from the maximum (minimum) bulk modulus. For example, this would be the case for a mixture of calcite ($K = 71$ GPa; $\mu = 30$ GPa) and quartz ($K = 37$ GPa; $\mu = 45$ GPa).

Note

Equations (4.17.1) and (4.17.2) simplify to the Hashin–Shtrikman bounds (Section 4.1) when one constituent has both the maximum bulk and shear moduli, while the other constituent has the minimum bulk and shear moduli.

The **modified Hashin–Shtrikman bounds** use exactly the same equations shown above. However, with modified bounds the constituent end members are selected differently, such as a mineral mixed with a fluid–solid suspension (Figure 4.17.1) or a stiffly packed sediment mixed with a fluid–solid suspension. The critical-porosity model (Nur *et al.*, 1991, 1995), described in Section 7.1, identifies a critical porosity, ϕ_c , that separates load-bearing sediments at porosities $\phi < \phi_c$ and suspensions at porosities $\phi > \phi_c$. Modified Hashin–Shtrikman equations (or modified Voigt–Reuss equations) can be constructed to describe mixtures of mineral with the unconsolidated fluid–solid suspension at critical porosity. The modified upper Hashin–Shtrikman curve has been observed empirically to be a useful trend line describing, for example,

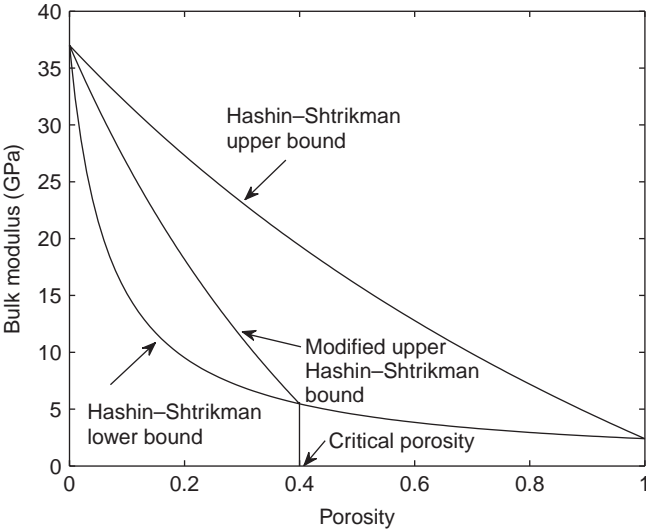


Figure 4.17.1 Hashin–Shtrikman and modified Hashin–Shtrikman bounds for bulk modulus in a quartz–water system.

how the elastic moduli of clean sandstones evolve from deposition through compaction and cementation. The modified upper Hashin–Shtrikman curve, constructed as such, is not a rigorous bound on the elastic properties of clean sand, although sandstone moduli are almost always observed to lie on or below it.

The **Voigt–Reuss–Hill average** (Section 4.4) is an estimate of elastic modulus defined to lie exactly half-way between the Voigt upper and Reuss lower bounds (Figure 4.17.2). A similar estimate can be constructed to lie half-way between the upper and lower Hashin–Shtrikman bounds (Figure 4.17.2). These two estimates have little practical value, except in the case where the constituent end-members are elastically similar, as with a mixture of minerals without pore space. In this latter case, an average of upper and lower bounds yields a useful estimate of the average mineral moduli.

Marion’s (1990) bounding average method (BAM) of fluid substitution (Section 6.9) uses the position of porosity–modulus data between the bounds as an indication of rock stiffness. In Figure 4.17.3, the Hashin–Shtrikman upper and lower bounds are displayed for mixtures of mineral and water. The data point *A* lies a distance *d* above the lower bound, while *D* is the spacing between the bounds at the same porosity. In the bounding average method, it is assumed that the ratio *d*/*D* remains constant if the pore fluid in the rock is changed, without changing the pore geometry or the stiffness of the dry frame. Though not theoretically justified, the BAM method sometimes gives a reasonable estimate of high-frequency fluid-substitution behavior.

Fabricius (2003) introduced the **isoframe model** to describe behavior between the modified upper and lower Hashin–Shtrikman bounds. In this model, the modified upper Hashin–Shtrikman curve is assumed to describe the trend of sediments that

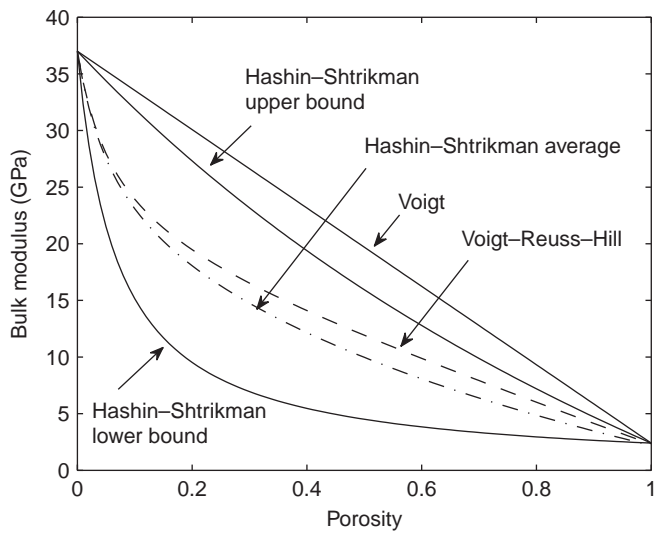


Figure 4.17.2 Hashin-Shtrikman and Voigt-Reuss bounds for bulk modulus in a quartz–water system. The Voigt-Reuss-Hill curve is an average of the Voigt upper and Reuss lower bounds. The Hashin-Shtrikman average curve is an average of the Hashin-Shtrikman upper and lower bounds.

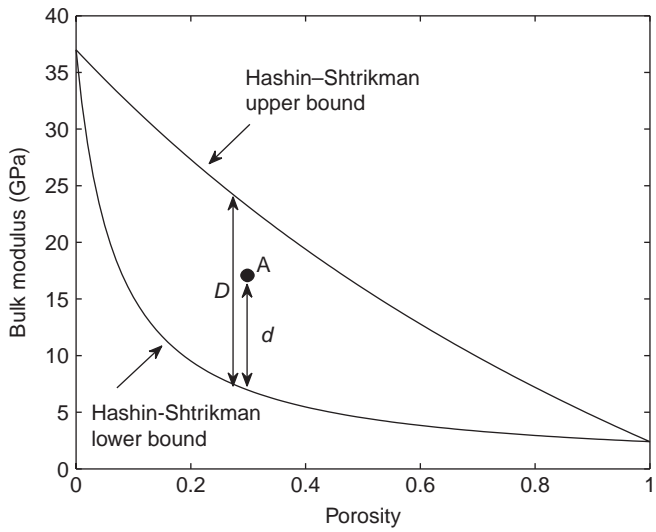


Figure 4.17.3 The bounding average method. It is assumed that the position of a data point A, described as d/D relative to bounds, is a measure of the pore stiffness.

become progressively more compacted and cemented as they trend away from the lower Reuss average (Figure 4.17.4) – an empirical result. It is assumed that these rocks contain only grains that are load-bearing with good grain-to-grain contacts. Sediments that fall below the modified upper bound are assumed to contain inclusions of grain–fluid suspensions, in which the grains are not load-bearing. A family of

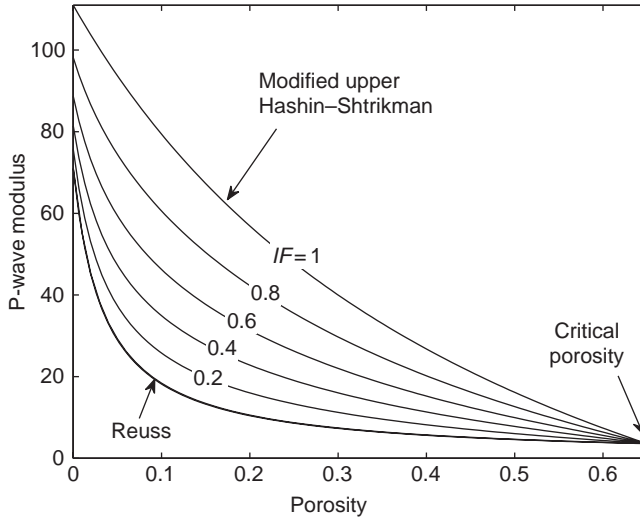


Figure 4.17.4 The isoframe model. The modified upper Hashin–Shtrikman curve is assumed to describe a strong frame of grains in good contact. The Reuss average curve describes a suspension of grains in a fluid. Each isoframe curve is a Hashin–Shtrikman mix of a fraction IF of frame with $(1 - IF)$ of suspension.

curves can be generated (Figure 4.17.4), computed as an upper Hashin–Shtrikman mix of “frame,” taken from the modified upper bound, and suspension, taken from the lower Reuss bound. IF is the volume fraction of load-bearing frame and $1 - IF$ is the fraction of suspension. The isoframe modulus at each porosity is computed from the frame and suspension moduli at the same porosity. The calculation is carried out separately for bulk and shear moduli, from which the P-wave modulus can be calculated.

The bulk modulus K of an elastic porous medium can be expressed as

$$\frac{1}{K} = \frac{1}{K_{\min}} + \frac{\phi}{\tilde{K}_{\phi}}$$

where \tilde{K}_{ϕ} is the saturated pore-space stiffness (Section 2.9) given by

$$\tilde{K}_{\phi} = K_{\phi} + \frac{K_{\min}K_{\text{fluid}}}{K_{\min} + K_{\text{fluid}}}$$

and K_{ϕ} is the dry-rock pore-space stiffness defined in terms of the pore volume v and confining stress σ_c :

$$\frac{1}{K_{\phi}} = \frac{1}{v} \frac{\partial v}{\partial \sigma_c}$$

Figure 4.17.5 shows a plot of bulk modulus versus porosity with contours of constant K_{ϕ} . A large value of K_{ϕ} indicates a stiff pore space, while small K_{ϕ} indicates a soft pore space. $K_{\phi} = 0$ corresponds to a suspension.

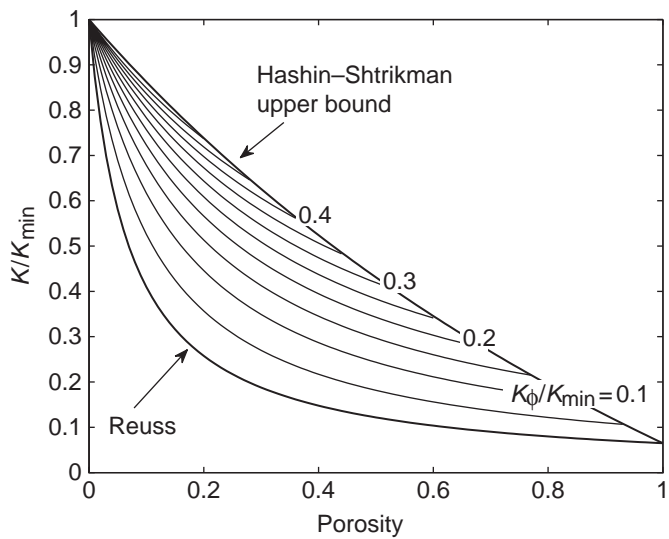


Figure 4.17.5 Normalized bulk modulus versus pressure showing contours of constant K_ϕ .

Uses

The bound-filling models described here provide a means to describe the stiffness of rocks that fall in the range between upper and lower bounds. The modified Hashin–Shtrikman and modified Voigt averages have been found to be useful depth-trend lines for sand and chalk sediments. The BAM model provides a heuristic fluid-substitution strategy that seems to work best at high frequency. The isoframe model allows one to estimate the moduli of rocks composed of a consolidated grain framework with inclusions of nonload-bearing grain suspensions.

Assumptions and limitations

These models are based on isotropic linear elasticity. All of the bound-filling models provided here contain at least some heuristic elements, such as the interpretation of the modified upper bounds.

5 Granular media

5.1 Packing and sorting of spheres

Synopsis

Spheres are often used as idealized representations of grains in unconsolidated and poorly consolidated sands. They provide a means of quantifying geometric relations, such as the porosity and the coordination number, as functions of packing and sorting. Using spheres also allows an analytical treatment of mechanical grain interactions under stress.

Packings of identical spheres

Porosity

Packing of identical spheres has been studied most, and comes closest to representing a very well-sorted sand. [Table 5.1.1](#) lists geometric properties of various packings of identical spheres (summarized from Cumberland and Crawford, 1987, and Bourbié *et al.*, 1987). The first four rows describe perfectly ordered sphere packs. These are directly analogous to the atomic arrangements in crystals having the same symmetries, although natural sands will never achieve such order. The last row in [Table 5.1.1](#) is for a random, close packing of identical spheres. (Note that complementary interpretations are possible, depending on whether the grains or the pores are considered to be spheres.)

Random packing of spheres has been studied both experimentally and theoretically. Denton (1957) performed 116 repeated experiments of moderately dense, random packings of spheres. His results highlight the statistical nature of describing grain packs (hence the use of the term **random packings**). He found a mean porosity of 0.391 with a standard deviation of 0.0016. Cumberland and Crawford (1987) found that Denton's porosity distribution over the many realizations could be described well using a beta distribution, and reasonably well with a normal distribution.

Smith *et al.* (1929) determined the porosity of random sphere packs experimentally using several preparation techniques, summarized in [Table 5.1.2](#). They observed that loose random packings resulting from pouring spheres into a container had a porosity of ~ 0.447 . Shaking systematically decreased porosity, to a minimum of 0.372. Slight tamping reduced the porosity further to a random close-packed value of 0.359.

Table 5.1.1 *Geometric properties of packs of identical spheres.*

Packing type	Porosity (nonspheres)	Solid fraction (spheres)	Void ratio	Specific surface area ^a	Number of contacts per sphere	Radius of maximum inscribable sphere ^{b,c}	Radius of maximum sphere fitting in narrowest channels ^{b,c}
Simple cubic	$1 - \pi/6 = 0.476$	$\pi/6 = 0.524$	0.910	$\pi/2R$	6	0.732	0.414
Simple hexagonal	$1 - 4\pi \cos(\pi/6)/18 = 0.395$	$4\pi \cos(\pi/6)/18 = 0.605$	0.654	$\pi/\sqrt{3}R$	8	0.528	0.414 and 0.155
Tetragonal	$1 - \pi/4.5 = 0.3019$	0.6981	0.432	$2\pi/3R$	10		
Hexagonal close pack	0.259	0.741	0.350	$\pi/\sqrt{2}R$	12	0.225 and 0.414	0.155
Face centered cubic	0.259	0.741	0.350	$\pi/\sqrt{2}R$			
Dense random pack	~ 0.36	~ 0.64	~ 0.56	$\sim 1.92/R$	~ 9		

Notes:

^a Specific surface area, S_v , is defined as the pore surface area in a sample divided by the total volume of the sample. If the grains are spherical, $S_v = 3(1 - \varphi)/R$.

^b Expressed in units of the radius of the packed spheres.

^c Note that if the pore space is modeled as a packing of spherical pores, the inscribable spheres always have radius equal to 1.

Table 5.1.2 *Experimental data from Smith et al. (1929).*

Method of random packing	Total number of spheres counted	Distribution of contacts per sphere											Mean coordination number*	Porosity
		4	5	6	7	8	9	10	11	12				
Poured into beaker	905	6	78	243	328	200	48	2	0	0		6.87 ± 1.05	0.447	
Poured and shaken	906	3	54	173	309	233	118	14	2	0		7.25 ± 1.16	0.440	
Poured and shaken	887	0	14	69	182	316	212	87	7	0		8.05 ± 1.17	0.426	
Shaken to maximum density	1494	0	14	86	192	233	193	161	226	389		9.57 ± 2.02	0.372	
Added in small quantities and intermittently tamped	1562	1	13	77	245	322	310	208	194	192		9.05 ± 1.78	0.359	

Note:

* Column shows mean \pm 1 standard deviation.

More accurate (Cumberland and Crawford, 1987) experimental values for the porosity of random close packs of 0.3634 ± 0.008 and 0.3634 ± 0.004 were found by Scott and Kilgour (1969) and Finney (1970), respectively.

Coordination number

The **coordination** number of a grain pack is the average number of contacts that each grain has with surrounding grains. Table 5.1.1 shows that the coordination numbers for perfect packings of identical spheres range from a low of 6 for a simple cubic packing, to a high of 12 for hexagonal close packing. Coordination numbers in random packings have been determined by tediously counting the contacts in experimentally prepared samples (e.g., Smith *et al.*, 1929; Wadsworth, 1960; Bernal and Mason, 1960). Table 5.1.2 shows results from Smith *et al.* (1929), after counting more than 5000 spheres in five different packings. There are several important conclusions.

- The coordination number increases with decreasing porosity, both being the result of tighter packing.
- Random packs of identical spheres have coordination numbers ranging from ~ 6.9 (loose packings) to ~ 9.1 (tight packings).
- The coordination number varies widely throughout each sample, from 4 to 12; hence, the mean alone does not capture the variability.

Tables 5.1.3–5.1.5 show data illustrating a correlation between coordination number and porosity. Manegold and von Engelhardt (1933) described theoretically the arrangements of identical spheres. They chose a criterion of the most regular packing possible for porosities ranging from 0.2595 to 0.7766. Their results are summarized in Table 5.1.4. Murphy (1982) also compiled coordination number data from the literature, summarized in Table 5.1.5.

Figure 5.1.1 compares coordination number versus porosity from Smith *et al.* (1929), Manegold and von Engelhardt (1933), and Murphy (1982). The data from various sources are consistent with each other and with the exact values for hexagonal close packing, simple hexagonal packing, and simple cubic packing. The thin lines shows the approximate range of \pm one standard deviation of coordination number observed by Smith *et al.* (1929). The standard deviation describes the spatial variation of coordination number throughout the packing, and not the standard deviation of the mean.

One source of uncertainty in the experimental estimation of coordination number is the difficulty of distinguishing between actual grain contacts and near-grain contacts. For the purposes of understanding porosity and transport properties, this distinction might not be important. However, mechanical and elastic properties in granular media are determined entirely by load-bearing grain contacts. For this reason, one might speculate that the equivalent coordination numbers for mechanical applications might be smaller than those shown in Tables 5.1.1–5.1.5. Wadsworth (1960) argued that coordination numbers in random packings may be smaller than those discussed so far, reduced by about 1.

Table 5.1.3 *Data for randomly packed identical spheres from Smith et al. (1929).*

Porosity	Coordination number
0.447	6.87 ± 1.05
0.440	7.25 ± 1.16
0.426	8.05 ± 1.17
0.372	9.57 ± 2.02
0.359	9.05 ± 1.78

Table 5.1.4 *Data for randomly packed identical spheres from Manegold and von Engelhardt (1933).*

Porosity	Coordination number
0.7766	3
0.6599	4
0.5969	5
0.4764	6
0.4388	7
0.3955	8
0.3866	9
0.3019	10
0.2817	11
0.2595	12

Table 5.1.5 *Data compiled by Murphy (1982) – not all identical spheres.*

Porosity	Coordination number
0.20	14.007
0.25	12.336
0.3	10.843
0.35	9.508
0.40	8.315
0.45	7.252
0.50	6.311
0.55	5.488
0.60	4.783

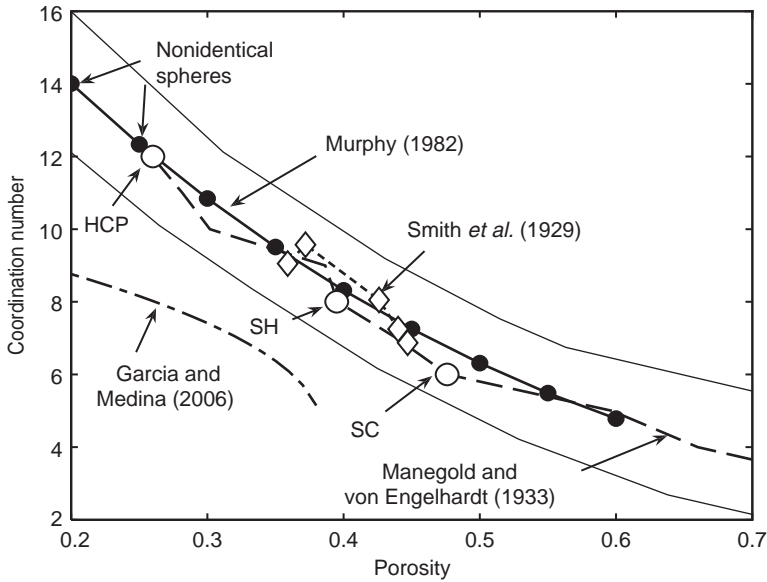


Figure 5.1.1 Coordination number versus porosity in random sphere packs, from Smith *et al.* (1929), Manegold and von Engelhardt (1933), Murphy (1982), and Garcia and Medina (2006). HCP = hexagonal close packed; SH = simple hexagonal; and SC = simple cubic. The thin lines approximately indicate ± 1 standard deviation from the data of Smith *et al.* (1929).

Garcia and Medina (2006) derived a power-law relation between the coordination number and the porosity based on fitting data from numerical simulations of granular media:

$$C = C_0 + 9.7(\phi_0 - \phi)^{0.48}$$

where $C_0 = 4.46$ and $\phi_0 = 0.384$. The relation holds for $\phi \leq \phi_0$. These relations between coordination number and porosity can be used in effective medium models such as those described later in Section 5.4.

Makse *et al.* (2004) derived a similar relation using numerical simulation of frictionless spheres:

$$C = C_0 + 9.1(\phi_0 - \phi)^{0.48}$$

where $C_0 = 6$ and $\phi_0 = 0.37$. The Makse *et al.* relation parallels that of Garcia and Medina, shifted upward by about 1.5.

Binary mixtures of spheres

Binary mixtures of spheres (i.e., two different sphere sizes) add additional complexity to random packings. Cumberland and Crawford (1987) review the specific problem of predicting porosity. Figure 5.1.2 compares theoretical models for porosity

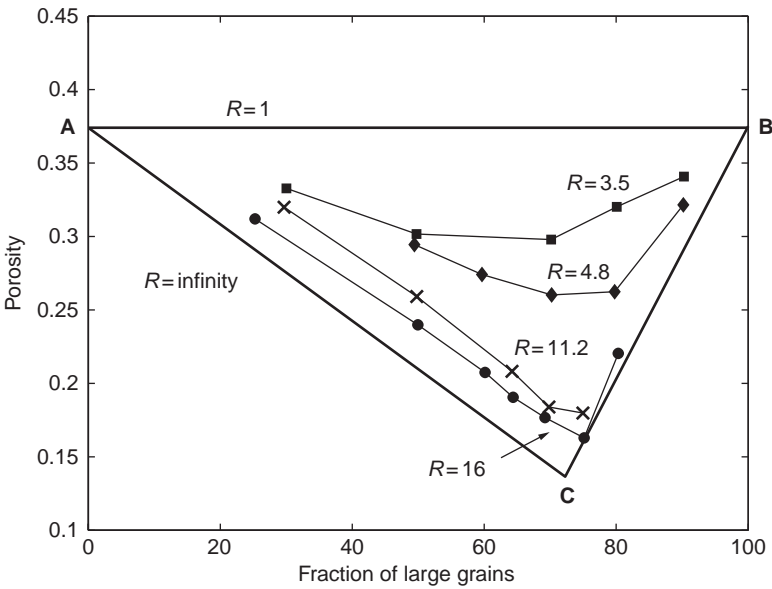


Figure 5.1.2 Porosity in an ideal binary mixture. R is the ratio of the large grain diameter to the small grain diameter. Curves ABC are bounds; highest porosity occurs when $R = 1$, and the lowest occurs when R becomes very large. Data for carefully prepared laboratory binary mixtures are from McGeary (1967).

(Cumberland and Crawford, 1987) in an **ideal binary mixture**. The ideal mixture is composed of two different sphere sizes, where R is the ratio of the large sphere diameter to the small sphere diameter. The horizontal axis is the volume fraction of large grains relative to the total solid volume. Point A represents a random close packing of only small spheres, while point B represents a random packing of only large spheres. Since A and B each correspond to random packings of identical spheres, the porosity in each case should be close to 0.36. The lower curves, ACB, correspond to mixtures where R approaches infinity (practically, $R > 30$). Moving from B toward C corresponds to gradually adding small spheres to the pore space of the large sphere pack, gradually decreasing porosity. The packing of each set of spheres is assumed to be undisturbed by the presence of the other set (*the definition of an ideal binary mixture*). The minimum porosity occurs at point C, where the pore space of the large sphere pack is completely filled by the smaller sphere pack. The total porosity at point C is $\phi = (0.36)^2 = 0.13$ and occurs at a volume fraction of large grains ~ 0.73 . Moving from A toward C corresponds to gradually adding more large grains to the packing of small grains. Each solid large grain replaces a spherical region of the porous small grain packing, hence decreasing porosity. Curve AB corresponds to $R = 1$. In this case, all spheres are identical, so the porosity is always ~ 0.36 . All other ideal binary mixtures should fall within the triangle ABC. Data from McGeary (1967) for ratios $R = 16, 11.2, 4.8$, and 3.5 , are plotted and are observed to lie within the expected bounds. It should be pointed out that McGeary’s experiments

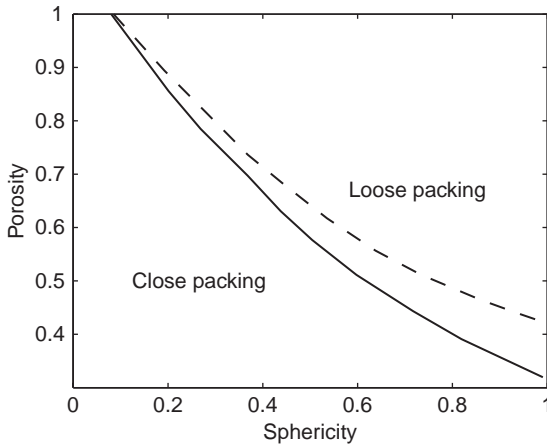


Figure 5.1.3 Trends of porosity versus grain sphericity observed by Waddell (1932).

were designed to approach an ideal mixture. First, a close random packing of large spheres was created, and then small particles were added, while keeping a weight on the packing to minimize disturbing the large grain pack.

The ideal binary mixture model has been used successfully to describe porosities in mixtures of sand and clay (Marion and Nur, 1991; Marion *et al.*, 1992; Yin, 1992).

Other practical parameters affecting packing

Cumberland and Crawford (1987) list a variety of factors affecting the efficiency of packing, and consequently the porosity and coordination number.

Energy of deposition. Experiments with spheres indicate that when spheres are poured (sometimes called *pluviated*), the packing density increases with the height of the drop; for many materials, an optimum drop height exists, above and below which the packing is looser.

Absolute particle size. Experimental evidence suggests that porosity increases with decreasing absolute particle size. This could result from the increased importance of surface forces (e.g., friction and adhesion) as the surface-to-volume ratio grows.

Irregular particle shape. Waddell (1932) defined the sphericity ψ as follows:

$$\psi = \frac{S_{\text{sphere}}}{S_{\text{grain}}}$$

where S_{sphere} is the surface area of a sphere having the same volume as the grain, and S_{grain} is the actual surface area of the grain. Brown *et al.* (1966) found experimentally that deviations from a spherical shape (decreasing sphericity) tend to result in high porosity, as shown in Figure 5.1.3.

Uses

These results can be used to estimate the geometric relations of the packing of granular materials, which is useful for understanding porosity, transport properties, and effective elastic constants.

Assumptions and limitations

The preceding results assume idealized spheres.

5.2 Thomas–Stieber model for sand–shale systems

Synopsis

Thomas and Stieber (1975, 1977) developed a model for the porosity of thinly bedded sands and shales, under the assumption that all rocks in the interval, including dirty sands, can be constructed by mixing clean, high-porosity sand and low-porosity shale (see also Pedersen and Nordal, 1999). Figure 5.2.1 illustrates some of the mixtures

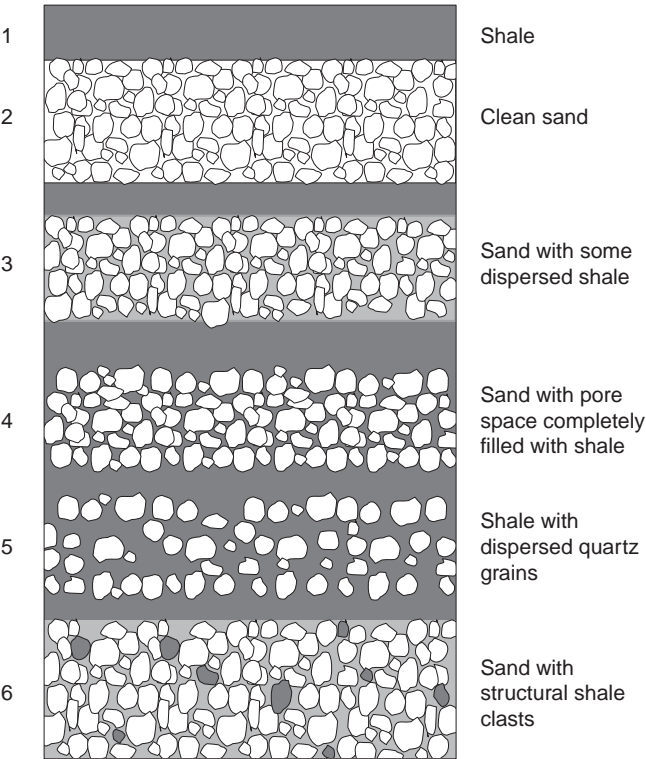


Figure 5.2.1 Laminations of shale, clean sand, sand with dispersed shale, and sand with structural shale clasts.

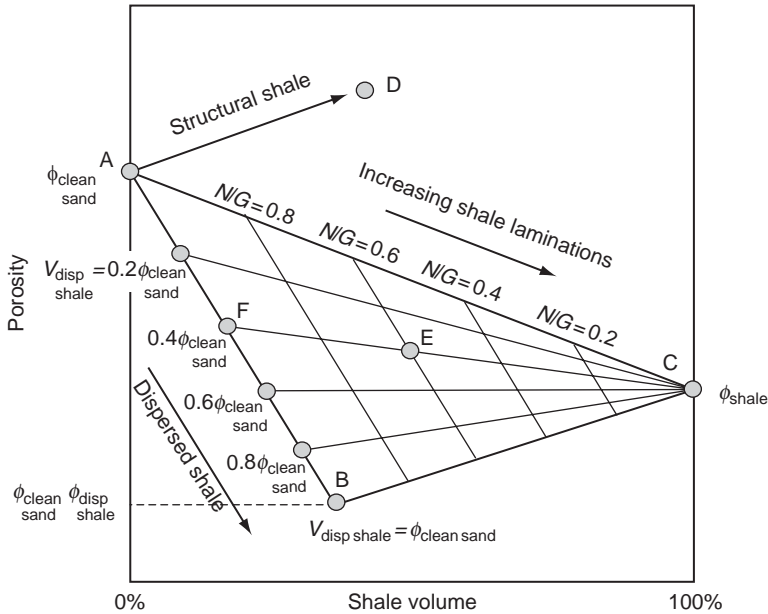


Figure 5.2.2 Porosity versus shale volume in the Thomas–Stieber model. $V_{\text{disp shale}}$ is the volume of dispersed shale in the sand pore space. The minimum porosity occurs when the sand porosity is completely filled with shale, $V_{\text{disp shale}} = \phi_{\text{clean sand}}$. Net-to-gross, N/G , is the thickness fraction of sand in the laminated composite.

considered, and **Figure 5.2.2** shows the associated porosities. The approach to analyzing porosity can be illustrated as a ternary diagram with the following limiting points and boundaries (**Figure 5.2.2**):

1. Shale (layer 1 in **Figure 5.2.1**; point C in **Figure 5.2.2**), with total porosity $\phi_{\text{total}} = \phi_{\text{shale}}$.
2. Clean sand (layer 2 in **Figure 5.2.1**; point A in **Figure 5.2.2**), with total porosity $\phi_{\text{total}} = \phi_{\text{clean sand}}$.
3. Sand with some dispersed shale in the sand pore space (layer 3 in **Figure 5.2.1**; line A–B in **Figure 5.2.2**), with total porosity

$$\phi_{\text{total}} = \phi_{\text{clean sand}} - (1 - \phi_{\text{shale}})V_{\text{disp shale}}$$

where $V_{\text{disp shale}}$ is the volume fraction of microporous dispersed shale (clay) in the sand. It is assumed that the sand packing is undisturbed by the shale in the pore space, as long as $V_{\text{disp shale}} \leq \phi_{\text{clean sand}}$. The total porosity is reduced by the solid fraction of the pore-filling shale, $(1 - \phi_{\text{shale}})V_{\text{disp shale}}$. This is sometimes called an *ideal binary mixture model* (Cumberland and Crawford, 1987; Marion *et al.*, 1992) and corresponds to the limiting case of very large particles (sand) mixed with very small particles (clay).

4. Sand with pore space completely filled with shale (layer 4 in **Figure 5.2.1**; point B in **Figure 5.2.2**), with total porosity

$$\phi_{\text{total}} = \phi_{\text{clean sand}} \phi_{\text{shale}}$$

In this case $V_{\text{disp shale}} = \phi_{\text{clean sand}}$.

5. Shale with dispersed quartz grains (layer 5 in Figure 5.2.1; line B–C in Figure 5.2.2), with total porosity

$$\phi_{\text{total}} = V_{\text{shale}} \phi_{\text{shale}}$$

In this case regions of microporous shale are replaced by solid quartz grains, reducing the total porosity.

6. An additional case falls outside the triangle A–B–C: sand with structural shale clasts (layer 6 in Figure 5.2.1; line A–D in Figure 5.2.2), with porosity

$$\phi_{\text{total}} = \phi_{\text{clean sand}} + \phi_{\text{shale}} V_{\text{shale clast}}$$

In this case, it is assumed that some of the solid quartz grains are replaced by porous shale clasts, resulting in a net increase in total porosity (see also Florez, 2005).

A *laminated* system of rocks has total porosity

$$\phi_{\text{total}} = \sum_i X_i \phi_i$$

where ϕ_i is the total porosity of the i th layer and X_i is the thickness fraction of the i th layer. For a laminated sequence of shale and dirty sand (sand with dispersed shale), the total porosity is

$$\phi = N/G [\phi_{\text{clean sand}} - (1 - \phi_{\text{shale}}) V_{\text{disp shale}}] + (1 - N/G) \phi_{\text{shale}}$$

where net-to-gross, N/G , is the thickness fraction of sand layers. N/G is *not* identical to the shale fraction, since some dispersed shale can be within the sand. The laminated systems fall within the triangle A–B–C in Figure 5.2.2. As mentioned above, the line A–C corresponds to laminations of *clean sand* and shale. Points inside the triangle correspond to laminations of shale with *dirty sand* (sand with dispersed shale).

Figure 5.2.3 is similar to Figure 5.2.2 except that the horizontal axis is the gamma ray response of the thinly laminated system. A practical workflow is to construct the model curves shown in Figure 5.2.3 and then superimpose well-log-derived total porosity and gamma ray data for interpretation to identify laminar, dispersed, and structural shale. For example, point E in Figures 5.2.2 and 5.2.3 can be interpreted as a laminar sequence where the net-to-gross is 60%. Dispersed clay fills 40% of the pore space in the sand layers.

Figure 5.2.4 is similar to Figure 5.2.2, except that the vertical axis now represents bulk density. Table 5.2.1 summarizes total porosity and density at several key locations in the model.

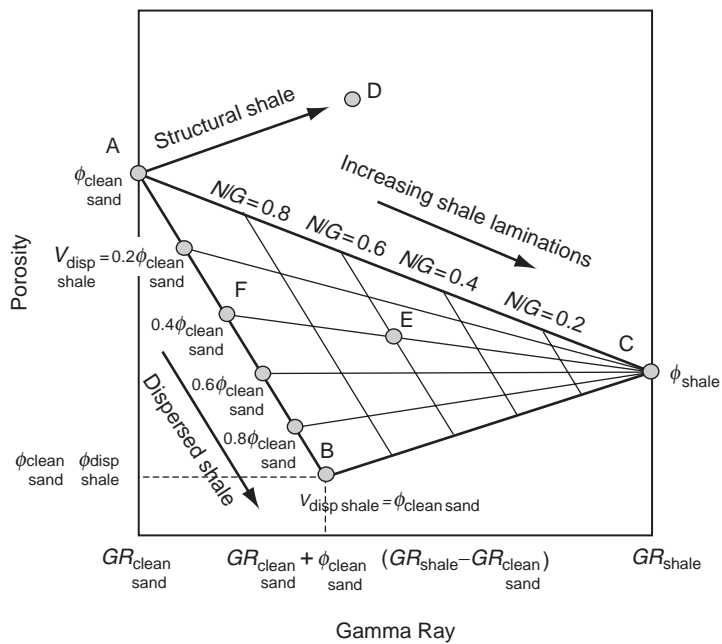


Figure 5.2.3 Porosity versus gamma ray in the Thomas–Stieber model, similar to Figure 5.2.2.

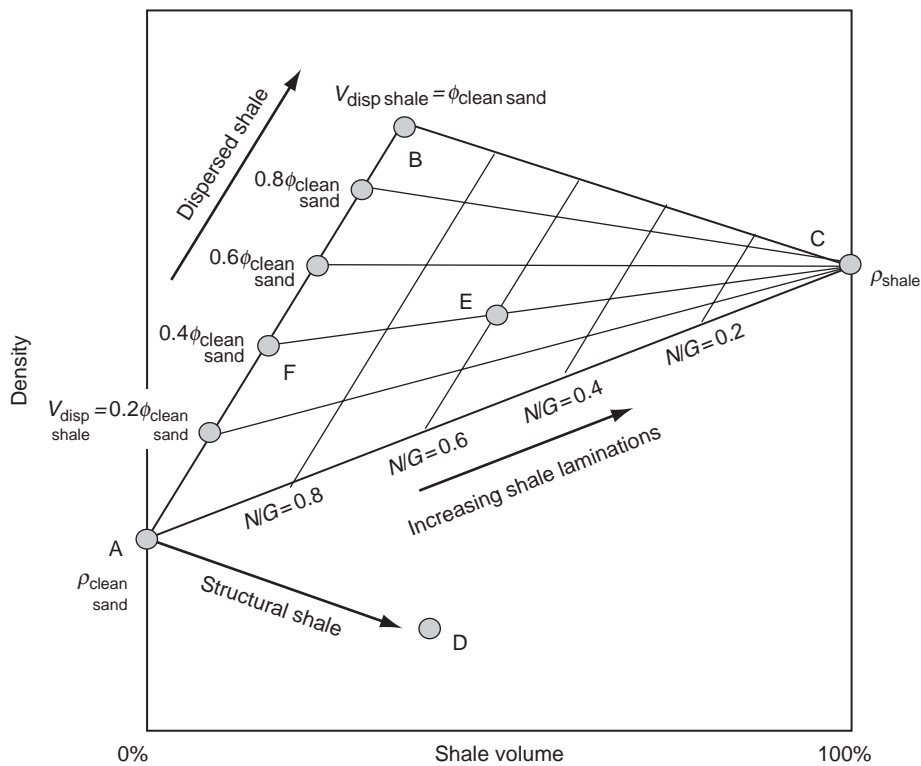


Figure 5.2.4 Bulk density versus V_{shale} in the Thomas–Stieber model, similar to Figure 5.2.2.

Table 5.2.1 *Total porosity and bulk density at key locations in Figures 5.2.2 and 5.2.4, corresponding to the Thomas–Stieber model.*

	Total porosity	Bulk density
Point A	$\phi_{\text{clean sand}}$	$\rho_{\text{clean sand}}$
Point C	ϕ_{shale}	ρ_{shale}
Line A–C	$\phi = N/G\phi_{\text{clean sand}} + (1 - N/G)\phi_{\text{shale}}$	$N/G\rho_{\text{clean sand}} + (1 - N/G)\rho_{\text{shale}}$
Point B	$\phi_{\text{clean}}\phi_{\text{shale}}$	$\rho_{\text{clean sand}} + \phi_{\text{clean sand}}(\rho_{\text{shale}} - \rho_{\text{water}}) = \phi_{\text{clean sand}}\rho_{\text{shale}} + (1 - \phi_{\text{clean sand}})\rho_{\text{quartz sand}}$
Line A–B	$\phi_{\text{total}} = \phi_{\text{clean sand}} - (1 - \phi_{\text{shale}})V_{\text{disp shale}}$	$\rho_{\text{clean sand}} + V_{\text{shale}}(\rho_{\text{shale}} - \rho_{\text{water}})$
Line B–C	$\phi_{\text{total}} = V_{\text{shale}}\phi_{\text{shale}}$	$V_{\text{shale}}\rho_{\text{shale}} + (1 - V_{\text{shale}})\rho_{\text{quartz}}$

Notes:

$\phi_{\text{clean sand}}$, ϕ_{shale} = porosities of clean sand and shale; N/G = fractional thickness of sand layers; $V_{\text{disp shale}}$ = volume fraction of dispersed shale in sand;
 V_{shale} = total volume fraction of shale in the laminated stack; and, $\rho_{\text{clean sand}}$, ρ_{shale} , ρ_{water} , ρ_{quartz} = densities of clean sand, water-saturated shale, water, and quartz.

Assumptions and limitations

There are several important assumptions made in the Thomas–Stieber model:

- clean sand is homogeneous with constant porosity;
- shale is the only destroyer of porosity; i.e., reduction of porosity by cementation and/or sorting is ignored; and
- the shale content in sands is primarily detrital, having essentially the same properties as the shale laminae.

Extensions

The Thomas–Stieber model focuses on volumetrics. Yin (1992) and Marion *et al.* (1992) developed a model for predicting seismic velocities in the same dispersed clay systems. The Backus average allows an exact prediction of elastic properties of a thinly laminated composite in terms of the individual layer properties.

5.3 Particle size and sorting

Synopsis

Particle size

Particle size is one of the most fundamental parameters of clastic rocks. The Udden–Wentworth scale uses a geometric progression of grain diameters in millimeters, $d = 1, 2, 4, 8, 16, \dots$, and divides sediments into seven grain-size grades: clay, silt, sand, granules, pebbles, cobbles, and boulders. The Udden–Wentworth scale is summarized in Table 5.3.1. The third column in the table is a subclassification: vc = very coarse, c = coarse, m = medium, f = fine, and vf = very fine. Krumbein introduced a logarithmic transformation of the Udden–Wentworth scale, known as the **phi-scale**, which is the most used measure of grain size:

$$\phi = -\log_2 d$$

A lesser-known description is the **psi-scale**, $\psi = -\phi$.

Sorting

Sorting is the term that geologists use to describe the size distributions that are a fundamental property of all naturally occurring packings of particles or grains. Sorting is no more than a measure of the spread of the grain sizes, and there are standard statistical methods to describe the spread of any population. Two of the main parameters to measure the spread of a population are the standard deviation and the coefficient of variation (the standard deviation normalized by the mean).

Table 5.3.1 Grain sizes and classes, according to the Udden–Wentworth scale.

Diameter (mm)	ϕ		Class
4096	−12		Block
2048	−11	vc	Boulder
1024	−10	c	
512	−9	m	
256	−8	f	
128	−7	c	Cobble
64	−6	f	
32	−5	vc	Pebble
16	−4	c	
8	−3	m	
4	−2	f	
2	−1		Granule
1	0	vc	Sand
0.50	1	c	
0.25	2	m	
0.125	3	f	
0.063	4	vf	
0.031	5	c	Silt
0.015	6	m	
0.008	7	f	
0.004	8	vf	
			Clay

In the **phi-scale**, sorting is usually expressed as being equal to the **standard deviation** (Boggs, 2001). Sorting is often estimated graphically by plotting a frequency histogram of grain sizes (measured by weight) expressed in the phi-scale, and normalized by the total weight of grains (see Figure 5.3.1). The cumulative distribution function (CDF) of grain sizes, ranging from 0% to 100%, is derived by successively adding and smoothing the frequencies in the histogram (from small to large sizes). The CDF makes it easy to identify the percentiles of the distribution. For example, the 25th percentile, ϕ_{25} , is the value of ϕ such that 25% of the grains by weight are smaller.

Folk and Ward (1957) suggested various measures of the grain size distribution that can be computed from the graphically determined percentiles (after Tucker, 2001):

Median $MD = \phi_{50}$

Mean $M = \frac{\phi_{16} + \phi_{50} + \phi_{84}}{3}$

Standard deviation $\sigma\phi = \frac{\phi_{84} - \phi_{16}}{4} + \frac{\phi_{95} - \phi_5}{6.6}$

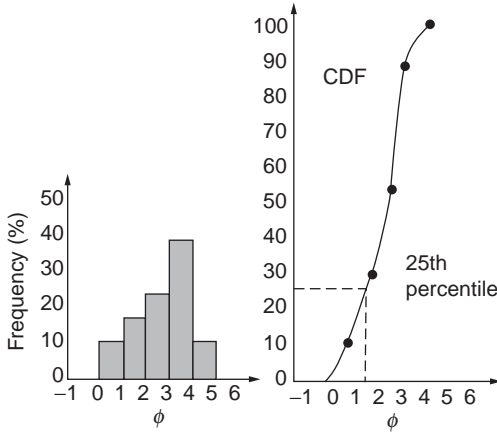


Figure 5.3.1 Frequency histogram of grain sizes (left) and the corresponding cumulative distribution function (after Tucker, 2001).

$$\text{Skewness} \quad SK = \frac{\phi_{16} + \phi_{84} - 2\phi_{50}}{2(\phi_{84} - \phi_{16})} + \frac{\phi_5 + \phi_{95} - 2\phi_{50}}{2(\phi_{95} - \phi_5)}$$

Statistics such as these, measured in phi units, should have ϕ attached to them. The Folk and Ward formula for **phi standard deviation**, $\sigma\phi$, follows from assuming a log-normal distribution of grain diameters in millimeters, which corresponds to a normal distribution of sizes in ϕ . If grain sizes have a normal distribution, then 68% of the grains fall between ± 1 standard deviation, or between ϕ_{16} and ϕ_{84} . Then we can write $\sigma\phi_{68} = (\phi_{84} - \phi_{16})/2$. Similarly, in a normal distribution, 90% of the grains fall between ± 1.65 standard deviations, or between ϕ_{05} and ϕ_{95} . Hence, $\sigma\phi_{90} = (\phi_{95} - \phi_{05})/3.30$. The Folk and Ward phi standard deviation is the average of these two estimates: $\sigma\phi = [(\phi_{84} - \phi_{16})/2 + (\phi_{95} - \phi_{05})/3.30]/2$. The sorting constant S_0 is equal to the phi standard deviation:

$$S_0 = \frac{\phi_{84} - \phi_{16}}{4} + \frac{\phi_{95} - \phi_5}{6.6} \approx \frac{\phi_{84} - \phi_{16}}{2}$$

It is interesting to convert this expression back to the millimeter scale:

$$S_0 \approx \frac{\phi_{84} - \phi_{16}}{2} \Rightarrow 2^{S_0} = \sqrt{\frac{d_{16}}{d_{84}}}$$

Another popular way to express the variation of the population in millimeters is using the **coefficient of variation**, which is the standard deviation divided by the mean.

It is worth pointing out that many serious sedimentologists have studied distributions of grain sizes using standard statistical methods, without attempting to define or redefine the term sorting.

5.4 Random spherical grain packings: contact models and effective moduli

Synopsis

Contact stiffnesses and effective moduli

The effective elastic properties of packings of spherical particles depend on *normal and tangential contact stiffnesses of a two-particle combination*, shown schematically in Figure 5.4.1. The normal stiffness of two identical spheres is defined as the ratio of a confining force increment to the shortening of a sphere radius. The tangential stiffness of two identical spheres is the ratio of a tangential force increment to the increment of the tangential displacement of the center relative to the contact region:

$$S_n = \frac{\partial F}{\partial \delta} \quad S_\tau = \frac{\partial T}{\partial \tau}$$

where S_n and S_τ are the normal and tangential stiffnesses, respectively, F is the normal force, T is the tangential force, δ is the normal displacement, and τ is the tangential displacement.

For a random sphere packing, effective bulk and shear moduli can be expressed through porosity ϕ , coordination number C (the average number of contacts per sphere), sphere radius R , and the normal and tangential stiffnesses, S_n and S_τ , respectively, of a two-sphere combination:

$$K_{\text{eff}} = \frac{C(1 - \phi)}{12\pi R} S_n$$

$$\mu_{\text{eff}} = \frac{C(1 - \phi)}{20\pi R} (S_n + 1.5S_\tau)$$

The effective P- and S-wave velocities are (Winkler, 1983)

$$V_P^2 = \frac{3C}{20\pi R\rho} (S_n + \frac{2}{3}S_\tau)$$

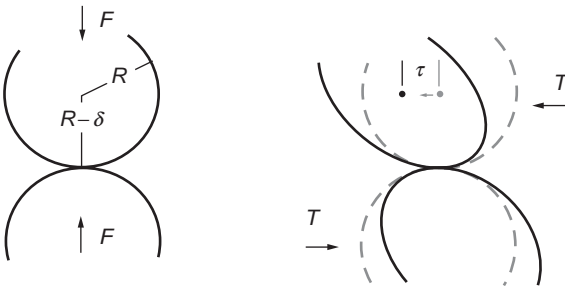


Figure 5.4.1 Normal and tangential displacement in a two-particle system.

$$V_S^2 = \frac{C}{20\pi R\rho} (S_n + \frac{3}{2}S_\tau)$$

$$\frac{V_P^2}{V_S^2} = 2 \frac{3S_n/S_\tau + 2}{2S_n/S_\tau + 3}$$

where ρ is the grain-material density. Wang and Nur (1992) summarize some of the existing granular media models.

Observed values of the coordination number relative to the porosity are discussed in Section 5.1.

The Hertz–Mindlin Model

In the **Hertz model** of normal compression of two identical spheres, the radius of the contact area, a , and the normal displacement, δ , are

$$a = \left[\frac{3FR}{8\mu} (1 - \nu) \right]^{1/3}, \quad \delta = \frac{a^2}{R}$$

where μ and ν are the shear modulus and the Poisson ratio of the grain material, respectively.

If a hydrostatic confining pressure P is applied to a random, identical-sphere packing, the confining force acting between two particles is

$$F = \frac{4\pi R^2 P}{C(1 - \phi)}$$

Then

$$a = R \left[\frac{3\pi(1 - \nu)}{2C(1 - \phi)\mu} P \right]^{1/3}$$

The normal stiffness is

$$S_n = \frac{4\mu a}{1 - \nu}$$

The effective bulk modulus of a dry, random, identical-sphere packing is then

$$K_{\text{eff}} = \left[\frac{C^2(1 - \phi)^2 \mu^2}{18\pi^2(1 - \nu)^2} P \right]^{1/3}$$

Mindlin (1949) shows that if the spheres are first pressed together, and a tangential force is applied *afterward*, slip may occur at the edges of the contact (Figure 5.4.1). The extent of the slip depends on the coefficient of friction η between the contacting

bodies. The normal stiffness of the two-grain system remains the same as that given by the Hertz solution. The shear stiffness is

$$S_\tau = \frac{8a\mu(1 - F_t/\eta F_n)^{1/3}}{2 - \nu}, \quad F_t \leq \eta F_n$$

where ν and μ are the Poisson ratio and shear modulus of the solid grains, respectively, and F_n and F_t are the normal and tangential forces applied to the spheres, respectively. Typically, if we are only concerned with acoustic wave propagation, the normal force, which is due to the confining (overburden) stress imposed on the granular system, is much larger than the tangential force, which is imposed by the very small oscillatory stress due to the propagating wave: $F_t \ll F_n$. As a result, the shear and normal stiffnesses are as follows (the latter being the same as in the Hertz solution):

$$S_\tau = \frac{8a\mu}{2 - \nu}, \quad S_n = \frac{4a\mu}{1 - \nu}$$

The effective shear modulus of a dry, random, identical-sphere packing is then

$$\mu_{\text{eff}} = \frac{5 - 4\nu}{5(2 - \nu)} \left[\frac{3C^2(1 - \phi)^2\mu^2}{2\pi^2(1 - \nu)^2} P \right]^{1/3}$$

The ratio of the bulk modulus to the shear modulus and the effective Poisson ratio of the dry frame of this system are

$$\frac{K_{\text{eff}}}{\mu_{\text{eff}}} = \frac{5(2 - \nu)}{3(5 - 4\nu)}, \quad \nu_{\text{eff}} = \frac{\nu}{2(5 - 3\nu)}$$

The Hertz–Mindlin model can be used to describe the properties of precompacted granular rocks.

One may also consider the case of **absolutely frictionless spheres**, where $\eta = 0$ ($\eta \rightarrow 0$, as $(F_t/\eta F_n) \rightarrow 1$) and therefore $S_\tau = 0$. In this case, the effective bulk and shear moduli of the pack become

$$K_{\text{eff}} = \frac{C(1 - \phi)}{12\pi R} S_n, \quad \mu_{\text{eff}} = \frac{C(1 - \phi)}{20\pi R} S_n, \quad \frac{K_{\text{eff}}}{\mu_{\text{eff}}} = \frac{5}{3}$$

and the effective Poisson ratio becomes exactly 0.25.

Figure 5.4.2 demonstrates that there is a large difference between the effective Poisson ratio of a dry frictionless pack and that of a dry pack with perfect adhesion between the particles. In the latter case, the effective Poisson ratio does not exceed 0.1 regardless of the grain material.

The absence of friction between particles may conceivably occur in an unconsolidated system because of the presence of a lubricant at some contacts. It is virtually impossible to predict in advance which fraction of the individual contacts is

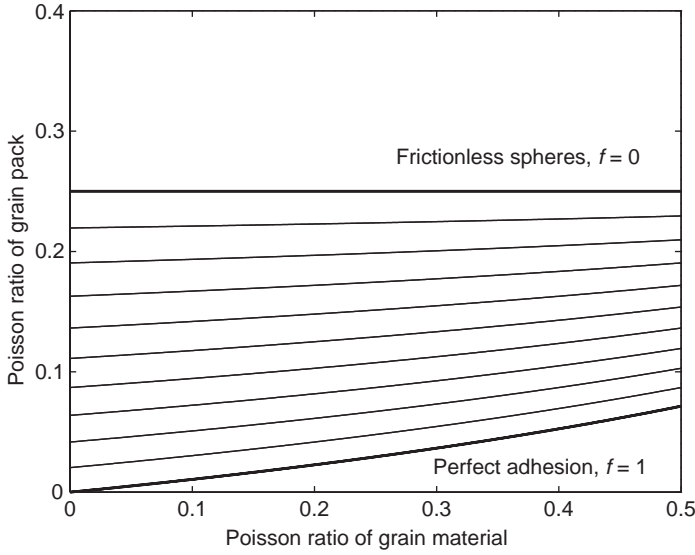


Figure 5.4.2 Poisson ratio of a grain pack versus that of the grain material. The upper bold curve is for frictionless spheres while the lower bold curve is for spheres with perfect adhesion. The thin curves in between are for values of f varying between 0 and 1, with a step size of 0.1.

frictionless ($S_\tau = 0$), and which has perfect adhesion ($S_\tau = 8a\mu/(2 - \nu)$). To account for all possibilities, an ad hoc coefficient f ($0 \leq f \leq 1$) can be introduced such that

$$S_n = \frac{4a\mu}{1 - \nu}, \quad S_\tau = f \frac{8a\mu}{2 - \nu}$$

and the grains have perfect adhesion for $f = 1$ and no friction for $f = 0$. As a result, the effective bulk modulus of the pack remains the same, but the expression for the effective shear modulus becomes

$$\mu_{\text{eff}} = \frac{2 + 3f - \nu(1 + 3f)}{5(2 - \nu)} \left[\frac{3C^2(1 - \phi)^2 \mu^2}{2\pi^2(1 - \nu)^2} P \right]^{1/3}$$

and

$$\frac{K_{\text{eff}}}{\mu_{\text{eff}}} = \frac{5(2 - \nu)}{3[2 + 3f - \nu(1 + 3f)]}, \quad \nu_{\text{eff}} = \frac{2 - 2f + \nu(2f - 1)}{2[4 + f - \nu(2 + f)]}$$

Figure 5.4.2 demonstrates how the Poisson ratio of the dry pack gradually moves from the frictionless line down to the perfect-adhesion curve.

The Walton model

It is assumed in the Walton model (Walton, 1987) that *normal and shear deformation of a two-grain combination occur simultaneously*. This assumption leads to results

somewhat different from those given by the Hertz–Mindlin model. Specifically, there is no partial slip in the contact area. The slip occurs across the whole area once applied tractions exceed the friction resistance. The results discussed in the following paragraphs are given for two special cases: infinitely rough spheres (where the friction coefficient is very large) and ideally smooth spheres (where the friction coefficient is zero).

Under *hydrostatic pressure* P , an identical-sphere random packing is isotropic. Its effective bulk and shear moduli for the rough-spheres case (dry pack) are described by

$$K_{\text{eff}} = \frac{1}{6} \left[\frac{3(1-\phi)^2 C^2 P}{\pi^4 B^2} \right]^{1/3}, \quad \mu_{\text{eff}} = \frac{3}{5} K_{\text{eff}} \frac{5B+A}{2B+A}$$

$$A = \frac{1}{4\pi} \left(\frac{1}{\mu} - \frac{1}{\mu + \lambda} \right), \quad B = \frac{1}{4\pi} \left(\frac{1}{\mu} + \frac{1}{\mu + \lambda} \right)$$

where λ is Lamé's coefficient of the grain material. For the smooth-spheres case (dry pack),

$$\mu_{\text{eff}} = \frac{1}{10} \left[\frac{3(1-\phi)^2 C^2 P}{\pi^4 B^2} \right]^{1/3}, \quad K_{\text{eff}} = \frac{5}{3} \mu_{\text{eff}}$$

It is clear that the effective density of the aggregate is

$$\rho_{\text{eff}} = (1 - \phi)\rho$$

Under *uniaxial pressure* σ_1 , a dry, identical-sphere packing is transversely isotropic, and if the spheres are infinitely rough, it can be described by the following five constants:

$$C_{11} = 3(\alpha + 2\beta), \quad C_{12} = \alpha - 2\beta, \quad C_{13} = 2C_{12}$$

$$C_{33} = 8(\alpha + \beta), \quad C_{44} = \alpha + 7\beta$$

where

$$\alpha = \frac{(1-\phi)Ce}{32\pi^2 B}, \quad \beta = \frac{(1-\phi)Ce}{32\pi^2(2B+A)}$$

$$e = \left[\frac{24\pi^2 B(2B+A)\sigma_1}{(1-\phi)AC} \right]^{1/3}$$

The Digby model

The Digby model gives effective moduli for a dry, random packing of identical elastic spherical particles. Neighboring particles are initially firmly bonded across small, flat, circular regions of radius a . Outside these adhesion surfaces, the shape of

each particle is assumed to be ideally smooth (with a continuous first derivative). Notice that this condition differs from that of Hertz, where the shape of a particle is not smooth at the intersection of the spherical surface and the plane of contact. Digby's normal and shear stiffnesses under hydrostatic pressure P are (Digby, 1981)

$$S_n = \frac{4\mu b}{1-\nu}, \quad S_\tau = \frac{8\mu a}{2-\nu}$$

where ν and μ are the Poisson ratio and shear modulus of the grain material, respectively. Parameter b can be found from the relation

$$\frac{b}{R} = \left[d^2 + \left(\frac{a}{R} \right)^2 \right]^{1/2}$$

where d satisfies the cubic equation

$$d^3 + \frac{3}{2} \left(\frac{a}{R} \right)^2 d - \frac{3\pi(1-\nu)P}{2C(1-\phi)\mu} = 0$$

Use the Digby model to estimate the effective bulk and shear moduli for a dry random pack of spherical grains under a confining pressure of 10 MPa. The ratio of the radius of the initially bonded area to the grain radius a/R is 0.01. The bulk and shear moduli of the grain material are $K = 37$ GPa and $\mu = 44$ GPa, respectively. The porosity of the grain pack is 0.36.

The Poisson ratio ν for the grain material is calculated from K and μ :

$$\nu = \frac{3K - 2\mu}{2(3K + \mu)} = 0.07$$

The coordination number $C = 9$. Solving the cubic equation for d

$$d^3 + \frac{3}{2} \left(\frac{a}{R} \right)^2 d - \frac{3\pi(1-\nu)P}{2C(1-\phi)\mu} = 0$$

and taking the real root, neglecting the pair of complex conjugate roots, we obtain $d = 0.0547$. Next, we calculate b/R as

$$\frac{b}{R} = \sqrt{d^2 + \left(\frac{a}{R} \right)^2} = 0.0556$$

The values of a/R and b/R are used to compute S_n/R and S_τ/R :

$$\frac{S_n}{R} = \frac{4\mu(b/R)}{1-\nu} = 10.5 \quad \frac{S_\tau}{R} = \frac{8\mu(a/R)}{2-\nu} = 1.8$$

which then finally give us

$$K_{\text{eff}} = \frac{C(1 - \phi)}{12\pi} (S_n/R) = 1.6 \text{ GPa}$$

and

$$\mu_{\text{eff}} = \frac{C(1 - \phi)}{20\pi} [(S_n/R) + 1.5(S_\tau/R)] = 1.2 \text{ GPa}$$

The Jenkins *et al.* model

Jenkins *et al.* (2005) derive expressions for the effective moduli of a random packing of identical frictionless spheres. Their approach differs from that of Digby (1981), Walton (1987), and Hertz–Mindlin in that under applied deviatoric strain, the particle motion of each sphere relative to its neighbors is allowed to deviate from the mean homogeneous strain field of a corresponding homogeneous effective medium. Under hydrostatic compression, the grain motion is consistent with homogeneous strain. The additional degrees of freedom of particle motion result in calculated shear moduli that are smaller than predicted by the above-mentioned models.

The expressions for dry effective shear modulus, μ_E , and effective Lamé constant, λ_E , in terms of the coordination number, C , grain diameter, d , and porosity, ϕ , are

$$\begin{aligned} \mu_E &= \frac{C(1 - \phi)}{5\pi d} K_N \{ 1 - 2[\psi^{-1}(\omega_1 + 2\omega_2) - \psi^{-2}(\kappa_1 + 2\kappa_2) \\ &\quad + \psi^{-3}(\xi_1 + 2\xi_2)] \} \\ \lambda_E &= \frac{C(1 - \phi)}{5\pi d} K_N \{ 1 - 2\psi^{-1}(\omega_1 + 7\omega_2) + 2\psi^{-2}(\kappa_1 + 2\kappa_2 + 5\kappa_3) \\ &\quad - 2\psi^{-3}(\xi_1 + 2\xi_2 + 5\xi_3) \} \end{aligned}$$

where

$$\begin{aligned} \psi &= C/3 \\ \omega_1 &= (166 - 11C)/128 \\ \tilde{\omega}_1 &= (38 - 11C)/128 \\ \omega_2 &= -(C + 14)/128 \\ \alpha_1 &= (19C - 22)/48 \\ \alpha_2 &= (22 - 3C)/16 \\ \tilde{\alpha}_2 &= (18 - 9C)/48 \end{aligned}$$

$$\begin{aligned}
\kappa_1 &= -(\alpha_1 \tilde{\omega}_1 + \tilde{\alpha}_2 \tilde{\omega}_1 + 2\tilde{\alpha}_2 \omega_2) + \tilde{\omega}_1 - [0.52(C-2)(C-4) \\
&\quad + 0.10C(C-2) - 0.13C(C-4) - 0.01C^2]/16\pi \\
\kappa_2 &= -\alpha_1 \omega_2 + \omega_2 + [0.44(C-2)(C-4) - 0.24C(C-2) \\
&\quad - 0.11C(C-4) - 0.14C^2]/16\pi \\
\kappa_3 &= -(\alpha_1 \omega_2 + \tilde{\alpha}_2 \omega_2) + \omega_2 - [0.44(C-2)(C-4) - 0.42C(C-2) \\
&\quad - 0.11C(C-4) + 0.04C^2]/16\pi \\
\eta_1 &= -\alpha_1^2 + \alpha_1 + [1.96(C-2)(C-4) + 3.30C(C-2) \\
&\quad + 0.49C(C-4) + 0.32C^2]/16\pi \\
\eta_2 &= -(2\alpha_1 \tilde{\alpha}_2 + \tilde{\alpha}_2^2) + \tilde{\alpha}_2 - [2.16(C-2)(C-4) + 2.30C(C-2) \\
&\quad + 0.54C(C-4) - 0.06C^2]/16\pi \\
\xi_1 &= (\eta_1 \omega_1 + \eta_2 \omega_1 + 2\eta_2 \omega_2) \\
\xi_2 &= \eta_1 \omega_2 \\
\xi_3 &= (\eta_1 \omega_2 + \eta_2 \omega_2)
\end{aligned}$$

In the above expressions, K_N is the contact normal stiffness determined from Hertz–Mindlin theory:

$$K_N = \frac{\mu d}{(1-\nu)} \left[\frac{3\pi(1-\nu)P}{2C(1-\phi)\mu} \right]^{1/3}$$

where μ and ν are the shear modulus and Poisson ratio of the solid material making up the grains, and P is the pressure. Note that the normal stiffness K_N defined above is related to the S_N , defined earlier, as $K_N = S_N/2$. The difference occurs because S_N is defined in terms of the incremental change in grain *radius*, R , under compression, while K_N is defined in terms of the incremental change in grain *diameter*, d , under compression.

The Brandt model

The Brandt model allows one to calculate the bulk modulus of randomly packed elastic spheres of identical mechanical properties but different sizes. This packing is subject to external and internal hydrostatic pressures. The effective pressure P is the difference between these two pressures. The effective bulk modulus is (Brandt, 1955)

$$\begin{aligned}
K_{\text{eff}} &= \frac{2P^{1/3}}{9\phi} \left[\frac{E}{1.75(1-\nu^2)} \right]^{2/3} Z - 1.5PZ \\
Z &= \frac{(1+30.75z)^{5/3}}{1+46.13z}, \quad z = \frac{K^{3/2}(1-\nu^2)}{E\sqrt{P}}
\end{aligned}$$

In this case E is the mineral Young's modulus and K is the fluid bulk modulus.

The Johnson *et al.* model

Norris and Johnson (1997) and Johnson *et al.* (1998) have developed an effective medium theory for the nonlinear elasticity of granular sphere packs, generalizing the earlier results of Walton, based on the underlying Hertz–Mindlin theory of grain-to-grain contacts. Johnson *et al.* (1998) show that for this model, the second-order elastic constants, C_{ijkl} , are unique path-independent functions of an arbitrary strain environment ε_{ij} . However, the stress tensor σ_{ij} depends on the strain path, and consequently C_{ijkl} (considered as a function of applied stresses) are path dependent. For a pack of identical spheres of radius R with no-slip Hertz–Mindlin contacts, the elastic constants in the effective medium approximation are given by Johnson *et al.* (1997) as

$$C_{ijkl} = \frac{3n(1 - \phi)}{4\pi^2 R^{1/2} B_W (2B_W + C_W)} \times \left\langle \xi^{1/2} [2C_W N_i N_j N_k N_l + B_W (\delta_{ik} N_j N_l + \delta_{il} N_j N_k + \delta_{jl} N_i N_k + \delta_{jk} N_i N_l)] \right\rangle$$

where $\langle \dots \rangle$ denotes an average over all solid angles. ϕ is porosity, n is the coordination number or average number of contacts per grain, N_i is the unit vector along sphere centers, and $\xi \equiv -N_i \varepsilon_{ij} N_j R$ is the normal component of displacement at the contacts:

$$B_W = \frac{2}{\pi C_n}$$

$$C_W = \frac{4}{\pi} \left[\frac{1}{C_t} - \frac{1}{C_n} \right]$$

$$C_n = \frac{4\mu_S}{1 - \nu_S}$$

$$C_t = \frac{8\mu_S}{2 - \nu_S}$$

where μ_S and ν_S are the shear modulus and the Poisson ratio of individual grains, respectively.

When the strain is a combination of hydrostatic compression and uniaxial compression (along the 3-axis),

$$\varepsilon_{ij} = \varepsilon \delta_{ij} + \varepsilon_3 \delta_{i3} \delta_{j3},$$

the sphere pack exhibits transversely isotropic symmetry. Assuming the angular distribution of contacts to be isotropic, explicit expressions for the five independent elements of the stiffness tensor are given as (Johnson *et al.*, 1998):

$$C_{11} \equiv C_{1111} = \frac{\gamma}{\alpha} \left\{ 2B_W [I_0(\alpha) - I_2(\alpha)] + \frac{3}{4} C_W [I_0(\alpha) - 2I_2(\alpha) + I_4(\alpha)] \right\}$$

$$\begin{aligned}
C_{13} &\equiv C_{1133} = \frac{\gamma}{\alpha} \{C_W[I_2(\alpha) - I_4(\alpha)]\} \\
C_{33} &\equiv C_{3333} = \frac{\gamma}{\alpha} [4B_W I_2(\alpha) + 2C_W I_4(\alpha)] \\
C_{44} &\equiv C_{2323} = \frac{\gamma}{\alpha} \left\{ \frac{1}{2} B_W [I_0(\alpha) + I_2(\alpha)] + C_W [I_2(\alpha) - I_4(\alpha)] \right\} \\
C_{66} &\equiv C_{1212} = \frac{\gamma}{\alpha} \left\{ B_W [I_0(\alpha) - I_2(\alpha)] + \frac{1}{4} C_W [I_0(\alpha) - 2I_2(\alpha) + I_4(\alpha)] \right\}
\end{aligned}$$

where

$$\begin{aligned}
\alpha &= \sqrt{\varepsilon/\varepsilon_3} \\
\gamma &= \frac{3n(1-\phi)(-\varepsilon)^{1/2}}{4\pi^2 B_W(2B_W + C_W)} = \frac{3}{32} n C_n C_t (1-\phi)(-\varepsilon)^{1/2}
\end{aligned}$$

The integral $I_n(\alpha) \equiv \int_0^1 x^n \sqrt{\alpha^2 + x^2} dx$ can be evaluated analytically as

$$\begin{aligned}
I_0(\alpha) &= \frac{1}{2} \left[\sqrt{1 + \alpha^2} + \alpha^2 \ln \left(\frac{1 + \sqrt{1 + \alpha^2}}{\alpha} \right) \right] \\
I_2(\alpha) &= \frac{1}{4} \left[(1 + \alpha^2)^{3/2} - \alpha^2 I_0(\alpha) \right] \\
I_4(\alpha) &= \frac{1}{6} \left[(1 + \alpha^2)^{3/2} - 3\alpha^2 I_2(\alpha) \right]
\end{aligned}$$

The results of the Johnson *et al.* model are consistent with the Walton model in the limiting cases of pure hydrostatic strain ($\varepsilon_3 \rightarrow 0$) and pure uniaxial strain ($\varepsilon \rightarrow 0$). When a small uniaxial strain is superimposed on a large isotropic strain, the equations can be expanded and simplified to the first order in $\varepsilon_3/\varepsilon$ (Johnson *et al.*, 1998), giving

$$\begin{aligned}
C_{11} &= \gamma \left[\frac{4B_W}{3} + \frac{2C_W}{5} + \frac{\varepsilon_3}{\varepsilon} \left(\frac{2B_W}{15} + \frac{C_W}{35} \right) \right] \\
C_{13} &= \gamma \left[\frac{2C_W}{15} + \frac{\varepsilon_3}{\varepsilon} \left(\frac{C_W}{35} \right) \right] \\
C_{33} &= \gamma \left[\frac{4B_W}{3} + \frac{2C_W}{5} + \frac{\varepsilon_3}{\varepsilon} \left(\frac{2B_W}{5} + \frac{C_W}{7} \right) \right] \\
C_{44} &= \gamma \left[\frac{2B_W}{3} + \frac{2C_W}{15} + \frac{\varepsilon_3}{\varepsilon} \left(\frac{2B_W}{15} + \frac{C_W}{35} \right) \right] \\
C_{66} &= \gamma \left[\frac{2B_W}{3} + \frac{2C_W}{15} + \frac{\varepsilon_3}{\varepsilon} \left(\frac{B_W}{15} + \frac{C_W}{105} \right) \right]
\end{aligned}$$

The components of the stress tensor σ_{ij} depend on the strain path. When the system first undergoes hydrostatic strain followed by a uniaxial strain, the nonzero components of the stress tensor, σ_{33} and $\sigma_{11} = \sigma_{22}$ are given by

$$\begin{aligned}\sigma_{33} &= -\frac{2(-\varepsilon)^{3/2}(1-\phi)n}{4\pi\alpha^3} \\ &\quad \times \{C_t[\alpha^2 I_0(\alpha) + (1-\alpha^2)I_2(\alpha) - I_4(\alpha) - \frac{2}{3}\alpha^3] + C_n[\alpha^2 I_2(\alpha) + I_4(\alpha)]\} \\ \sigma_{11} &= -\frac{(-\varepsilon)^{3/2}(1-\phi)n}{4\pi\alpha^3} \left\{ -C_t[\alpha^2 I_0(\alpha) + (1-\alpha^2)I_2(\alpha) - I_4(\alpha) - \frac{2}{3}\alpha^3] \right. \\ &\quad \left. + C_n[\alpha^2 I_0(\alpha) + (1-\alpha^2)I_2(\alpha) - I_4(\alpha)] \right\}\end{aligned}$$

When a uniaxial compression is followed by an isotropic compression, the stresses are

$$\begin{aligned}\sigma_{33} &= -\frac{2(-\varepsilon)^{3/2}(1-\phi)n}{4\pi\alpha^3} \left\{ \frac{1}{12}C_t + C_n[\alpha^2 I_2(\alpha) + I_4(\alpha)] \right\} \\ \sigma_{11} &= -\frac{(-\varepsilon)^{3/2}(1-\phi)n}{4\pi\alpha^3} \left\{ -\frac{1}{12}C_t + C_n[\alpha^2 I_0(\alpha) + (1-\alpha^2)I_2(\alpha) - I_4(\alpha)] \right\}\end{aligned}$$

and finally when the two strain components are applied simultaneously the stress components are

$$\begin{aligned}\sigma_{33} &= -\frac{2(-\varepsilon)^{3/2}(1-\phi)n}{4\pi\alpha^3} \{C_t[I_2(\alpha) - I_4(\alpha)] + C_n[\alpha^2 I_2(\alpha) + I_4(\alpha)]\} \\ \sigma_{11} &= -\frac{(-\varepsilon)^{3/2}(1-\phi)n}{4\pi\alpha^3} \{-C_t[I_2(\alpha) - I_4(\alpha)] \\ &\quad + C_n[\alpha^2 I_0(\alpha) + (1-\alpha^2)I_2(\alpha) - I_4(\alpha)]\}\end{aligned}$$

The differences in the stresses for the three different strain paths are quite small (Johnson *et al.*, 1998).

The concept of third-order elastic constants described by nonlinear hyperelasticity with three third-order constants breaks down for unconsolidated granular media with uniaxial strain superposed on a large hydrostatic strain. The changes in second-order elastic constants due to an imposed strain are governed (to the first order) by four “third-order” moduli and not just the usual three third-order moduli (Norris and Johnson, 1997). In granular media, the contact forces are path dependent and are not derivable from a potential energy function. As a result, the system cannot be described by an equivalent nonlinear hyperelastic medium.

The cemented-sand model

The cemented-sand model allows one to calculate the bulk and shear moduli of dry sand in which cement is deposited *at grain contacts*. The cement is elastic and its properties may differ from those of the spheres.

It is assumed that the starting framework of cemented sand is a dense, random pack of identical spherical grains with porosity $\phi_0 \approx 0.36$ and an average number of

contacts per grain $C = 9$. Adding cement to the grains reduces porosity and increases the effective elastic moduli of the aggregate. Then, these effective dry-rock bulk and shear moduli are (Dvorkin and Nur, 1996)

$$\begin{aligned} K_{\text{eff}} &= \frac{1}{6} C (1 - \phi_0) M_c \hat{S}_n \\ \mu_{\text{eff}} &= \frac{3}{5} K_{\text{eff}} + \frac{3}{20} C (1 - \phi_0) \mu_c \hat{S}_\tau \\ M_c &= \rho_c V_{\text{Pc}}^2 \\ \mu_c &= \rho_c V_{\text{Sc}}^2 \end{aligned}$$

where ρ_c is the density of the cement and V_{Pc} and V_{Sc} are its P- and S-wave velocities, respectively. Parameters \hat{S}_n and \hat{S}_τ are proportional to the normal and shear stiffnesses, respectively, of a cemented two-grain combination. They depend on the amount of contact cement and on the properties of the cement and the grains as defined in the following relations:

$$\begin{aligned} \hat{S}_n &= A_n \alpha^2 + B_n \alpha + C_n \\ A_n &= -0.024153 \Lambda_n^{-1.3646} \\ B_n &= 0.20405 \Lambda_n^{-0.89008} \\ C_n &= 0.00024649 \Lambda_n^{-1.9864} \\ \hat{S}_\tau &= A_\tau \alpha^2 + B_\tau \alpha + C_\tau \\ A_\tau &= -10^{-2} (2.26v^2 + 2.07v + 2.3) \Lambda_\tau^{0.079v^2 + 0.1754v - 1.342} \\ B_\tau &= (0.0573v^2 + 0.0937v + 0.202) \Lambda_\tau^{0.0274v^2 + 0.0529v - 0.8765} \\ C_\tau &= 10^{-4} (9.654v^2 + 4.945v + 3.1) \Lambda_\tau^{0.01867v^2 + 0.4011v - 1.8186} \\ \Lambda_n &= \frac{2\mu_c (1 - v)(1 - v_c)}{\pi\mu (1 - 2v_c)} \\ \Lambda_\tau &= \frac{\mu_c}{\pi\mu} \\ \alpha &= \frac{a}{R} \end{aligned}$$

where μ and v are the shear modulus and the Poisson ratio of the grains, respectively; μ_c and v_c are the shear modulus and the Poisson ratio of the cement, respectively; a is the radius of the contact cement layer; and R is the grain radius.

The amount of contact cement can be expressed through the ratio α of the radius of the cement layer a to the grain radius R :

$$\alpha = \frac{a}{R}$$

The radius a of the contact cement layer is not necessarily directly related to the total amount of cement; part of the cement may be deposited away from the intergranular contacts. However, by assuming that porosity reduction in sands is due to

cementation only and by adopting certain schemes of cement deposition, we can relate the parameter α to the current porosity of cemented sand ϕ . For example, we can use Scheme 1 (see Figure 5.4.3 below), in which all cement is deposited at grain contacts, to obtain the formula

$$\alpha = 2 \left[\frac{\phi_0 - \phi}{3C(1 - \phi_0)} \right]^{1/4} = 2 \left[\frac{S\phi_0}{3C(1 - \phi_0)} \right]^{1/4}$$

or we can use Scheme 2, in which cement is evenly deposited on the grain surface:

$$\alpha = \left[\frac{2(\phi_0 - \phi)}{3(1 - \phi_0)} \right]^{1/2} = \left[\frac{2S\phi_0}{3(1 - \phi_0)} \right]^{1/2}$$

In these formulas, S is the cement saturation of the pore space. It is the fraction of the pore space (of the uncemented sand) occupied by cement (in the cemented sand).

If the properties of the cement are identical to those of the grains, the cementation theory gives results that are very close to those of the Digby model. The cementation theory allows one to **diagnose** a rock by determining what type of cement prevails. For example, the theory helps to distinguish between quartz and clay cement (Figure 5.4.4). Generally, the model predicts V_P much more reliably than V_S .

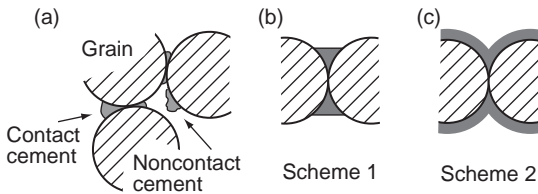


Figure 5.4.3 (a) Schematic representation of types of cement deposition. (b) All cement deposited at grain contacts. (c) Cement deposited in uniform layer around grains.

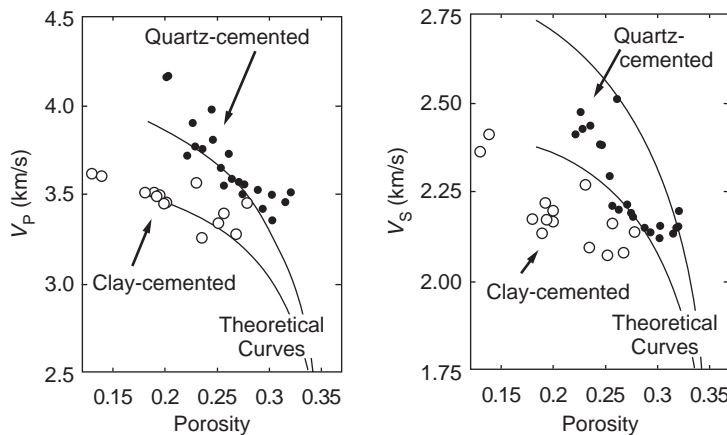


Figure 5.4.4 Predictions of V_P and V_S using the Scheme 2 model for quartz and clay cement, compared with data from quartz- and clay-cemented rocks from the North Sea.

The uncemented (soft) sand model

The uncemented-sand (or “soft-sand”) model allows one to calculate the bulk and shear moduli of dry sand in which cement is deposited *away from grain contacts*. It is assumed that the starting framework of uncemented sand is a dense random pack of identical spherical grains with porosity ϕ_0 about 0.36 and average number of contacts per grain $C=5$ to 9. At this porosity, the contact Hertz–Mindlin theory gives the following expressions for the effective bulk (K_{HM}) and shear (μ_{HM}) moduli of a dry, dense, random pack of identical spherical grains subject to a hydrostatic pressure P :

$$K_{\text{HM}} = \left[\frac{C^2(1 - \phi_0)^2 \mu^2}{18\pi^2(1 - \nu)^2} P \right]^{1/3}$$

$$\mu_{\text{HM}} = \frac{5 - 4\nu}{5(2 - \nu)} \left[\frac{3C^2(1 - \phi_0)^2 \mu^2}{2\pi^2(1 - \nu)^2} P \right]^{1/3}$$

where ν is the grain Poisson ratio and μ is the grain shear modulus. A version of the same model allows a fraction f of grain contacts to have perfect adhesion and the rest to be frictionless; it uses

$$\mu_{\text{HM}} = \frac{2 + 3f - \nu(1 + 3f)}{5(2 - \nu)} \left[\frac{3C^2(1 - \phi)^2 \mu^2}{2\pi^2(1 - \nu)^2} P \right]^{1/3}$$

To find the effective moduli (K_{eff} and μ_{eff}) at a different porosity ϕ , a heuristic modified Hashin–Shtrikman lower bound is used:

$$K_{\text{eff}} = \left[\frac{\phi/\phi_0}{K_{\text{HM}} + \frac{4}{3}\mu_{\text{HM}}} + \frac{1 - \phi/\phi_0}{K + \frac{4}{3}\mu_{\text{HM}}} \right]^{-1} - \frac{4}{3}\mu_{\text{HM}}$$

$$\mu_{\text{eff}} = \left[\frac{\phi/\phi_0}{\mu_{\text{HM}} + \frac{\mu_{\text{HM}}}{6} \left(\frac{9K_{\text{HM}} + 8\mu_{\text{HM}}}{K_{\text{HM}} + 2\mu_{\text{HM}}} \right)} + \frac{1 - \phi/\phi_0}{\mu + \frac{\mu_{\text{HM}}}{6} \left(\frac{9K_{\text{HM}} + 8\mu_{\text{HM}}}{K_{\text{HM}} + 2\mu_{\text{HM}}} \right)} \right]^{-1}$$

$$- \frac{\mu_{\text{HM}}}{6} \left(\frac{9K_{\text{HM}} + 8\mu_{\text{HM}}}{K_{\text{HM}} + 2\mu_{\text{HM}}} \right)$$

where K is the grain bulk modulus. Figure 5.4.5 shows the curves from this model in terms of the P-wave modulus, $M = K + \frac{4}{3}\mu$. Figure 5.4.6 illustrates the effect of the parameter f (the fraction of the perfect-adhesion contacts) on the elastic moduli and velocity in a dry pack of identical quartz grains.

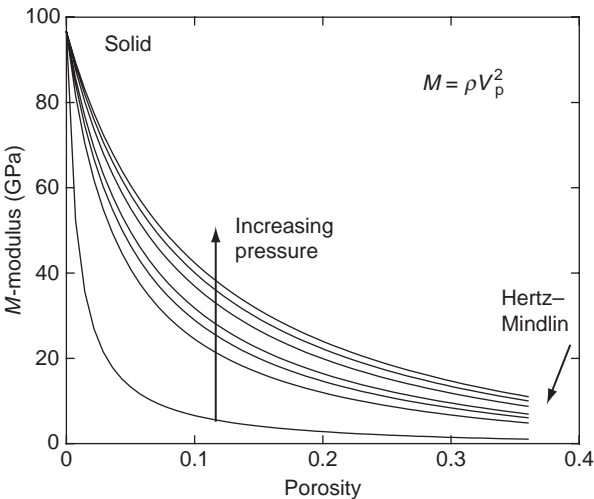


Figure 5.4.5 Illustration of the modified lower Hashin–Shtrikman bound for various effective pressures. The pressure dependence follows from the Hertz–Mindlin theory incorporated into the right end-member. All grain contacts have perfect adhesion. The grains are pure quartz.

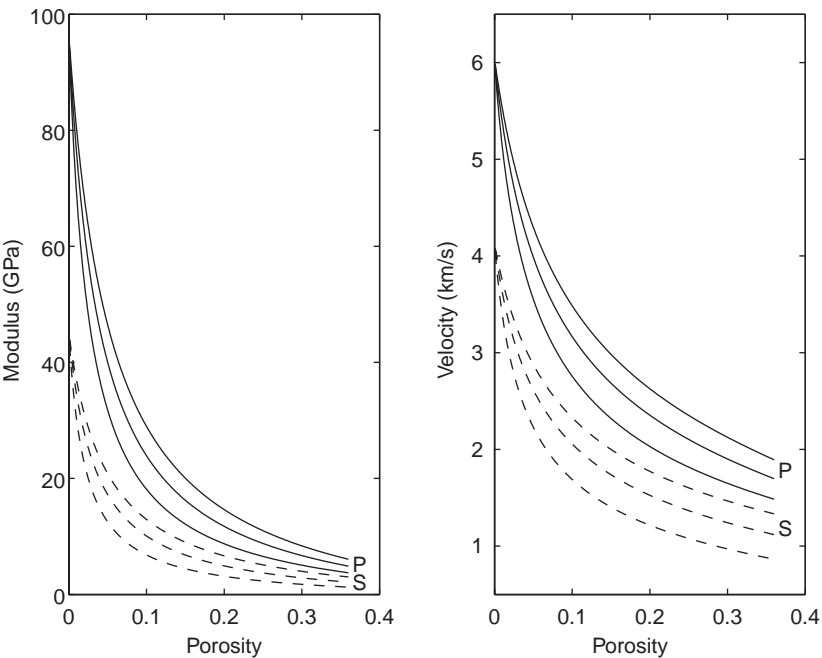


Figure 5.4.6 Illustration of the modified lower Hashin–Shtrikman bound for a varying fractions of contact with perfect adhesion. The grains are pure quartz and the pack is dry. The effective pressure is 20 MPa and the critical porosity is 0.36. Left: shear and compressional modulus versus porosity. Right: V_P and V_S versus porosity. Solid curves are for the P-wave velocity and modulus, while dashed lines are for the S-wave velocity and modulus. For each computed parameter (modulus and velocity) the upper curves are for perfect adhesion while the lower curves are for perfect slip. The curve in between is for $f = 0.5$.

Calculate V_P and V_S in uncemented dry quartz sand of porosity 0.3, at 40 MPa overburden and 20 MPa pore pressure. Use the uncemented sand model. For pure quartz, $\mu = 45$ GPa, $K = 36.6$ GPa, and $\nu = 0.06$. Then, for effective pressure 20 MPa = 0.02 GPa,

$$K_{\text{HM}} = \left[\frac{9^2(1 - 0.36)^2 45^2}{18 \cdot 3.14^2(1 - 0.06)^2} 0.02 \right]^{1/3} = 2 \text{ GPa}$$

$$\mu_{\text{HM}} = \frac{5 - 4 \cdot 0.06}{5(2 - 0.06)} \left[\frac{3 \cdot 9^2(1 - 0.36)^2 45^2}{2 \cdot 3.14^2(1 - 0.06)^2} 0.02 \right]^{1/3} = 3 \text{ GPa}$$

Next,

$$K_{\text{eff}} = \left(\frac{0.3/0.36}{2 + \frac{4}{3} \cdot 3} + \frac{1 - 0.3/0.36}{36.6 + \frac{4}{3} \cdot 3} \right)^{-1} - \frac{4}{3} \cdot 3 = 3 \text{ GPa}$$

$$\mu_{\text{eff}} = \left(\frac{0.3/0.36}{3 + 2.625} + \frac{1 - 0.3/0.36}{45 + 2.625} \right)^{-1} - 2.625 = 3.97 \text{ GPa}$$

Pure quartz density is 2.65 g/cm^3 ; then, the density of the sandstone is

$$2.65 \cdot (1 - 0.3) = 1.855 \text{ g/cm}^3$$

The P-wave velocity is

$$V_P = \sqrt{\frac{3 + \frac{4}{3} \cdot 3.6}{1.855}} = 2.05 \text{ km/s}$$

and the S-wave velocity is

$$V_S = \sqrt{\frac{3.6}{1.855}} = 1.39 \text{ km/s}$$

The stiff-sand and intermediate stiff-sand models

A counterpart to the soft-sand model is the “stiff-sand” model, which uses precisely the same end-members in the porosity–elastic-modulus plane but connects them with a heuristic modified Hashin–Shtrikman *upper* bound:

$$K_{\text{eff}} = \left[\frac{\phi/\phi_0}{K_{\text{HM}} + \frac{4}{3}\mu} + \frac{1 - \phi/\phi_0}{K + \frac{4}{3}\mu} \right]^{-1} - \frac{4}{3}\mu$$

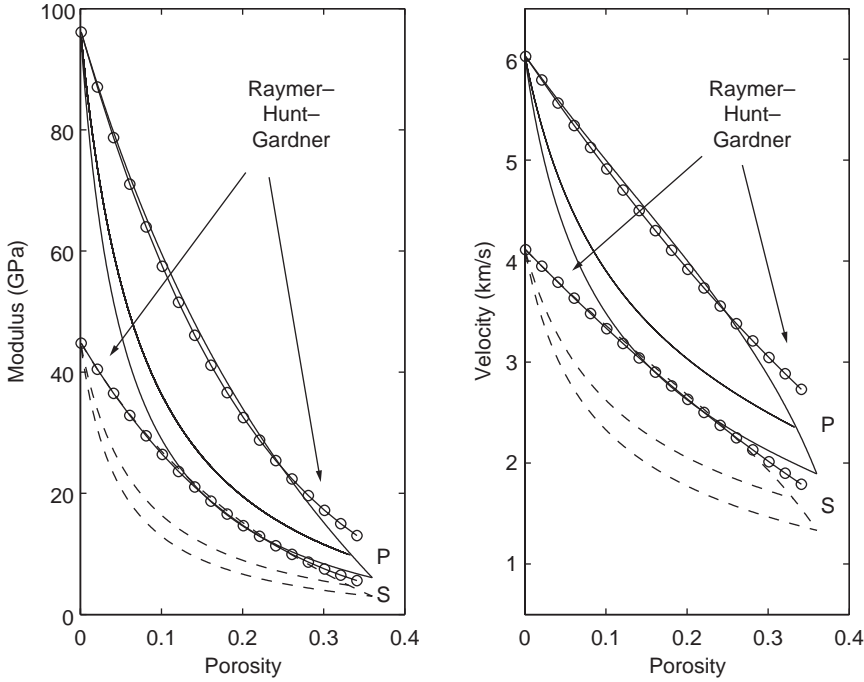


Figure 5.4.7 Illustration of the modified lower and upper Hashin–Shtrikman bounds (soft- and stiff-sand models, respectively). The grains are pure quartz and the pack is dry. The effective pressure is 20 MPa, the coordination number is 9, and the critical porosity is 0.36. Left: shear and compressional moduli versus porosity. Right: V_P and V_S versus porosity. Solid curves are for the P-wave velocity and modulus while dashed lines are for the S-wave velocity and modulus. The curves between the two bounds are for the intermediate stiff-sand model that uses the soft-sand equation with an artificial coordination number of 15.

$$\mu_{\text{eff}} = \left[\frac{\phi/\phi_0}{\mu_{\text{HM}} + \frac{\mu}{6} \left(\frac{9K+8\mu}{K+2\mu} \right)} + \frac{1-\phi/\phi_0}{\mu + \frac{\mu}{6} \left(\frac{9K+8\mu}{K+2\mu} \right)} \right]^{-1} - \frac{\mu}{6} \left(\frac{9K+8\mu}{K+2\mu} \right)$$

where K_{HM} and μ_{HM} are precisely the same as in the soft-sand model. [Figure 5.4.7](#) compares the elastic moduli and velocity in a dry pack of identical quartz grains as calculated by the soft- and stiff-sand models. Notice that the stiff-sand model produces velocity–porosity curves that are essentially identical to those from the Raymer–Hunt–Gardner empirical model.

The intermediate stiff-sand model uses the functional form of the soft-sand model (the modified Hashin–Shtrikman lower bound) but with the high-porosity end-point situated on the stiff-sand model curve. The easiest way to generate such curves is by simply increasing the coordination number in the soft-sand model ([Figure 5.4.7](#)). This artificially increased coordination number may not be representative of the actual coordination number of the grain pack at the high-porosity end-point.

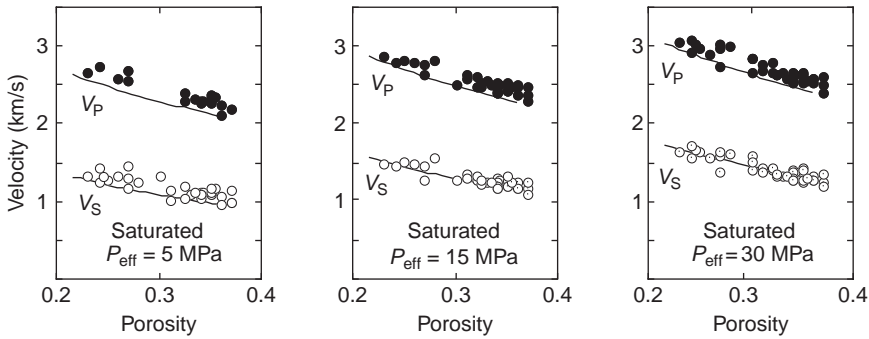


Figure 5.4.8 Prediction of V_P and V_S using the modified lower Hashin–Shtrikman bound, compared with measured velocities from unconsolidated North Sea samples.

These models connect two end-members; one has zero porosity and the modulus of the solid phase, and the other has high porosity and a pressure-dependent modulus, as given by the Hertz–Mindlin theory. This contact theory allows one to describe the noticeable pressure dependence normally observed in sands. Notice that in many experiments on natural sands and artificial granular packs, the observed dependence of the elastic moduli on pressure is different from that given by the Hertz–Mindlin theory. This is because the grains are not perfect spheres, and the contacts have configurations different from those between perfectly spherical particles.

The high-porosity end-member does not necessarily have to be calculated from the Hertz–Mindlin theory. The end-member can be measured experimentally on high-porosity sands from a given reservoir. Then, to estimate the moduli of sands of different porosities, the modified Hashin–Shtrikman lower bound formulas can be used, where K_{HM} and μ_{HM} are set at the measured values.

This method provides estimates for velocities in uncemented sands. In [Figures 5.4.8](#) and [5.4.9](#), the curves are from the theory.

This method can also be used for estimating velocities in sands of porosities exceeding 0.36.

Caveat on the use of effective medium models for granular media

Granular media have properties lying somewhat between solids and liquids and are sometimes considered to be a distinct form of matter. Complex behavior arises from the ability of grains to move relative to each other, modify their packing and coordination numbers, and rotate. Observed behavior, depending on the stress and strain conditions, is sometimes approximately nonlinearly elastic, sometimes viscoelastic, and sometimes somewhat fluid-like. A number of authors (Goddard, [1990](#); Makse *et al.*, [1999](#), [2000](#), [2004](#)) have shown that this complex behavior causes effective medium theory to fail in cohesionless granular assemblies. Closed-form effective

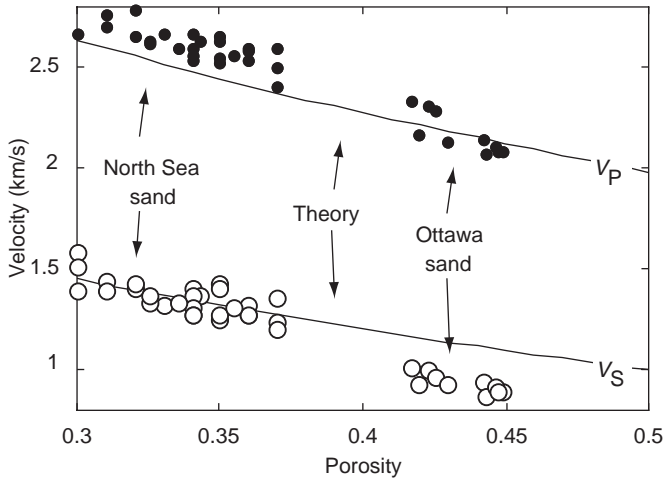


Figure 5.4.9 Prediction of V_P and V_S using the modified lower Hashin–Shtrikman bound, compared with measured velocities from North Sea and Ottawa sand samples.

medium theories tend to predict the incorrect (relative to laboratory observations) dependence of effective moduli on pressure, and poor estimates of the bulk to shear moduli ratio. Numerical methods, referred to as “molecular dynamics” or “discrete element modeling,” which simulate the motions and interactions of thousands of grains, appear to come closer to predicting observed behavior (e.g., Makse *et al.*, 2004; Garcia and Medina, 2006). Closed-form effective medium models can be useful, because it is not always practical to run a numerical simulation; however, model predictions of the types presented in this section must be used with care.

Uses

The methods can be used to model granular high-porosity rocks, as well as rocks in the entire porosity range, depending on what type of diagenetic transformation reduced the original high porosity.

Assumptions and limitations

The grain contact models presuppose the following:

- the strains are small;
- grains are identical, homogeneous, isotropic, elastic spheres;
- except for the models for regular packings, packings are assumed to be random and statistically isotropic; and
- the effective elastic constants are relevant for long-wavelength propagation, where wavelengths are much longer (more than 10 times) compared with the grain radius.

Extensions

To calculate the effective elastic moduli of saturated rocks (and their low-frequency acoustic velocities), Gassmann's formula should be applied.

5.5 Ordered spherical grain packings: effective moduli

Synopsis

Ordered packings of identical spherical particles are generally anisotropic; thus their effective elastic properties can be described through stiffness matrices.

Simple cubic packing

The coordination number is 6, and the porosity is 47%. The stiffness matrix is

$$\begin{pmatrix} C_{11} & C_{12} & C_{12} & 0 & 0 & 0 \\ C_{12} & C_{11} & C_{12} & 0 & 0 & 0 \\ C_{12} & C_{12} & C_{11} & 0 & 0 & 0 \\ 0 & 0 & 0 & \frac{1}{2}(C_{11} - C_{12}) & 0 & 0 \\ 0 & 0 & 0 & 0 & \frac{1}{2}(C_{11} - C_{12}) & 0 \\ 0 & 0 & 0 & 0 & 0 & \frac{1}{2}(C_{11} - C_{12}) \end{pmatrix}$$

where

$$c_{11} = c_0 \quad c_{12} = \frac{\nu}{2(2 - \nu)} c_0 \quad c_0 = \left[\frac{3\mu^2 P}{2(1 - \nu)^2} \right]^{1/3}$$

P is the hydrostatic pressure, and μ and ν are the shear modulus and Poisson ratio of the grain material, respectively.

Hexagonal close packing

The coordination number is 12, and the porosity is about 26%. The stiffness matrix is

$$\begin{pmatrix} C_{11} & C_{12} & C_{13} & 0 & 0 & 0 \\ C_{12} & C_{11} & C_{13} & 0 & 0 & 0 \\ C_{13} & C_{13} & C_{33} & 0 & 0 & 0 \\ 0 & 0 & 0 & C_{44} & 0 & 0 \\ 0 & 0 & 0 & 0 & C_{44} & 0 \\ 0 & 0 & 0 & 0 & 0 & C_{66} \end{pmatrix}$$

where

$$c_{11} = \frac{1152 - 1848v + 725v^2}{24(2 - v)(12 - 11v)} c_0$$

$$c_{12} = \frac{v(120 - 109v)}{24(2 - v)(12 - 11v)} c_0$$

$$c_{13} = \frac{v}{3(2 - v)} c_0$$

$$c_{33} = \frac{4(3 - 2v)}{3(2 - v)} c_0$$

$$c_{44} = c_{55} = \frac{6 - 5v}{3(2 - v)} c_0$$

$$c_{66} = \frac{576 - 948v + 417v^2}{24(2 - v)(12 - 11v)} c_0$$

Face-centered cubic packing

The coordination number is 12, and the porosity is about 26%. The stiffness matrix is

$$\begin{pmatrix} C_{11} & C_{12} & C_{12} & 0 & 0 & 0 \\ C_{12} & C_{11} & C_{12} & 0 & 0 & 0 \\ C_{12} & C_{12} & C_{11} & 0 & 0 & 0 \\ 0 & 0 & 0 & C_{44} & 0 & 0 \\ 0 & 0 & 0 & 0 & C_{44} & 0 \\ 0 & 0 & 0 & 0 & 0 & C_{44} \end{pmatrix}$$

where

$$c_{11} = 2c_{44} = \frac{4 - 3v}{2 - v} c_0$$

$$c_{12} = \frac{v}{2(2 - v)} c_0$$

Uses

The results of this section are sometimes used to estimate the elastic properties of granular materials.

Assumptions and limitations

These models assume identical, elastic, spherical grains under small-strain conditions.

6 Fluid effects on wave propagation

6.1 Biot's velocity relations

Synopsis

Biot (1956) derived theoretical formulas for predicting the frequency-dependent velocities of saturated rocks in terms of the dry-rock properties. His formulation incorporates some, but not all, of the mechanisms of viscous and inertial interaction between the pore fluid and the mineral matrix of the rock. The low-frequency limiting velocities, V_{P0} and V_{S0} , are the same as those predicted by Gassmann's relations (see the discussion of Gassmann in Section 6.3). The high-frequency limiting velocities, $V_{P\infty}$ and $V_{S\infty}$ (cast in the notation of Johnson and Plona, 1982), are given by

$$V_{P\infty}(\text{fast, slow}) = \left\{ \frac{\Delta \pm [\Delta^2 - 4(\rho_{11}\rho_{22} - \rho_{12}^2)(PR - Q^2)]^{1/2}}{2(\rho_{11}\rho_{22} - \rho_{12}^2)} \right\}^{1/2}$$

$$V_{S\infty} = \left(\frac{\mu_{\text{fr}}}{\rho - \phi\rho_{\text{fl}}\alpha^{-1}} \right)^{1/2}$$

$$\Delta = P\rho_{22} + R\rho_{11} - 2Q\rho_{12}$$

$$P = \frac{(1 - \phi)(1 - \phi - K_{\text{fr}}/K_0)K_0 + \phi K_0 K_{\text{fr}}/K_{\text{fl}}}{1 - \phi - K_{\text{fr}}/K_0 + \phi K_0/K_{\text{fl}}} + \frac{4}{3}\mu_{\text{fr}}$$

$$Q = \frac{(1 - \phi - K_{\text{fr}}/K_0)\phi K_0}{1 - \phi - K_{\text{fr}}/K_0 + \phi K_0/K_{\text{fl}}}$$

$$R = \frac{\phi^2 K_0}{1 - \phi - K_{\text{fr}}/K_0 + \phi K_0/K_{\text{fl}}}$$

$$\rho_{11} = (1 - \phi)\rho_0 - (1 - \alpha)\phi\rho_{\text{fl}}$$

$$\rho_{22} = \alpha\phi\rho_{\text{fl}}$$

$$\rho_{12} = (1 - \alpha)\phi\rho_{\text{fl}}$$

$$\rho = \rho_0(1 - \phi) + \rho_{\text{fl}}\phi$$

where K_{fr} and μ_{fr} are the effective bulk and shear moduli of the rock frame, respectively – either the dry-frame moduli or the high-frequency, unrelaxed, “wet-frame” moduli predicted by the Mavko–Jizba squirt theory (Section 6.10); K_0 is the bulk modulus of the mineral material making up the rock; K_{fl} is the effective bulk modulus of the pore fluid; ϕ is the porosity; ρ_0 is the mineral density; ρ_{fl} is the fluid density; and α is the tortuosity parameter, which is always greater than or equal to 1.

The term ρ_{12} describes the induced mass resulting from inertial drag caused by the relative acceleration of the solid frame and the pore fluid. The tortuosity, α (sometimes called the structure factor), is a purely geometrical factor independent of the solid or fluid densities. Berryman (1981) obtained the relation

$$\alpha = 1 - r \left(1 - \frac{1}{\phi} \right)$$

where $r = \frac{1}{2}$ for spheres, and lies between 0 and 1 for other ellipsoids. For uniform cylindrical pores with axes parallel to the pore pressure gradient, α equals 1 (the minimum possible value), whereas for a random system of pores with all possible orientations, $\alpha = 3$ (Stoll, 1977). The high-frequency limiting velocities depend quite strongly on α , with higher fast P-wave velocities for lower α values.

The two solutions given above for the high-frequency limiting P-wave velocity, designated by \pm , correspond to the “fast” and “slow” waves. The fast wave is the compressional body-wave most easily observed in the laboratory and the field, and it corresponds to overall fluid and solid motions that are in phase. The slow wave is a highly dissipative wave in which the overall solid and fluid motions are out of phase.

Another approximate expression for the high-frequency limit of the fast P-wave velocity is (Geertsma and Smit, 1961)

$$V_{\text{P}\infty} = \left\{ \frac{1}{\rho_0(1 - \phi) + \phi\rho_{\text{fl}}(1 - \alpha^{-1})} \left[(K_{\text{fr}} + \frac{4}{3}\mu_{\text{fr}}) + \frac{\phi \frac{\rho}{\rho_{\text{fl}}} \alpha^{-1} + \left(1 - \frac{K_{\text{fr}}}{K_0} \right) \left(1 - \frac{K_{\text{fr}}}{K_0} - 2\phi\alpha^{-1} \right)}{\left(1 - \frac{K_{\text{fr}}}{K_0} - \phi \right) \frac{1}{K_0} + \frac{\phi}{K_{\text{fl}}}} \right] \right\}^{1/2}$$

Caution

This form predicts velocities that are too high (by about 3–6%) compared with the actual high-frequency limit.

The complete frequency dependence can be obtained from the roots of the dispersion relations (Biot, 1956; Stoll, 1977; Berryman, 1980a):

$$\begin{vmatrix} H/V_P^2 - \rho & \rho_{fl} - C/V_P^2 \\ C/V_P^2 - \rho_{fl} & q - M/V_P^2 \end{vmatrix} = 0$$

$$\begin{vmatrix} \rho - \mu_{fr}/V_S^2 & \rho_{fl} \\ \rho_{fl} & q \end{vmatrix} = 0$$

The complex roots are

$$\frac{1}{V_P^2} = \frac{-(Hq + M\rho - 2C\rho_{fl}) \pm \sqrt{(Hq + M\rho - 2C\rho_{fl})^2 - 4(C^2 - MH)(\rho_{fl}^2 - \rho q)}}{2(C^2 - MH)}$$

$$\frac{1}{V_S^2} = \frac{q\rho - \rho_{fl}^2}{q\mu_{fr}}$$

The real and imaginary parts of the roots give the velocity and the attenuation, respectively. Again, the two solutions correspond to the fast and slow P-waves. The various terms are

$$H = K_{fr} + \frac{4}{3}\mu_{fr} + \frac{(K_0 - K_{fr})^2}{(D - K_{fr})}$$

$$C = \frac{(K_0 - K_{fr})K_0}{(D - K_{fr})}$$

$$M = \frac{K_0^2}{(D - K_{fr})}$$

$$D = K_0 \left[1 + \phi \left(\frac{K_0}{K_{fl}} - 1 \right) \right]$$

$$\rho = (1 - \phi)\rho_0 + \phi\rho_{fl}$$

$$q = \frac{\alpha\rho_{fl}}{\phi} - \frac{i\eta F(\zeta)}{\omega\kappa}$$

where η is the viscosity of the pore fluid, κ is the absolute permeability of the rock, and ω is the angular frequency of the plane wave.

The viscodynamic operator $F(\zeta)$ incorporates the frequency dependence of viscous drag and is defined by

$$F(\zeta) = \frac{1}{4} \left(\frac{\zeta T(\zeta)}{1 + 2iT(\zeta)/\zeta} \right)$$

$$T(\zeta) = \frac{\text{ber}'(\zeta) + i\text{bei}'(\zeta)}{\text{ber}(\zeta) + i\text{bei}(\zeta)} = \frac{e^{i3\pi/4} J_1(\zeta e^{-i\pi/4})}{J_0(\zeta e^{-i\pi/4})}$$

$$\zeta = (\omega/\omega_r)^{1/2} = \left(\frac{\omega a^2 \rho_{\text{fl}}}{\eta} \right)^{1/2}$$

where $\text{ber}(\cdot)$ and $\text{bei}(\cdot)$ are real and imaginary parts of the Kelvin function, respectively, $J_n(\cdot)$ is a Bessel function of order n , and a is the pore-size parameter.

The pore-size parameter a depends on both the dimensions and the shape of the pore space. Stoll (1974) found that values between $\frac{1}{6}$ and $\frac{1}{7}$ of the mean grain diameter gave good agreement with experimental data from several investigators. For spherical grains, Hovem and Ingram (1979) obtained $a = \phi d/[3(1 - \phi)]$, where d is the grain diameter. The velocity dispersion curve for fast P-waves can be closely approximated by a standard linear solid viscoelastic model when $\kappa/a^2 \geq 1$ (see Sections 3.8 and 6.12). However, for most consolidated crustal rocks, κ/a^2 is usually less than 1.

At very low frequencies, $F(\zeta) \rightarrow 1$ and at very high frequencies (large ζ), the asymptotic values are $T(\zeta) \rightarrow (1 + i)/\sqrt{2}$ and $F(\zeta) \rightarrow (\kappa/4)(1 + i)/\sqrt{2}$.

The reference frequency, f_c , which determines the low-frequency range, $f \ll f_c$, and the high-frequency range, $f \gg f_c$, is given by

$$f_c = \frac{\phi \eta}{2\pi \rho_{\text{fl}} \kappa}$$

One interpretation of this relation is that it is the frequency where viscous forces acting on the pore fluid approximately equal the inertial forces acting on it. In the high-frequency limit, the fluid motion is dominated by inertial effects, and in the low-frequency limit, the fluid motion is dominated by viscous effects.

As mentioned above, Biot's theory predicts the existence of a slow, highly attenuated P-wave in addition to the usual fast P- and S-waves. The slow P-wave has been observed in the laboratory, and it is sometimes invoked to explain diffusional loss mechanisms.

Slow S-wave

In the Biot theory the only loss mechanism is the average motion of the fluid with respect to the solid frame, ignoring viscous losses within the pore fluid. The fluid strain-rate term is not incorporated into the constitutive equations. As a result, the Biot relaxation term includes only a part of the drag force involving permeability, but does not account for the dissipation due to shear drag within the fluid. Incorporation of the viscous term is achieved by volume averaging of the pore-scale constitutive relations of the solid and fluid constituents (de al Cruz and Spanos, 1985; Sahay *et al.*, 2001; Spanos, 2002). This gives rise to two propagating shear processes, corresponding to in-phase and out-of-phase shear motion of the phases, with fast and slow S-wave velocities V_{SI} and V_{SII} , respectively. The slow S-wave has the characteristics of a rapidly decaying viscous wave in a Newtonian fluid. The slow S-wave

may play a role in attenuation of fast P- and S-waves by drawing energy from fast waves due to mode conversion at interfaces and discontinuities. Incorporation of the fluid strain-rate term introduces an additional relaxation frequency, the saturated shear frame relaxation frequency (Sahay, 2008), given by $\omega_\beta = \mu_{fr}/\eta$, which is typically above Biot's peak relaxation frequency. Expressions for the complex fast and slow S-wave velocities derived from the extended theory are given by Sahay (2008) as

$$V_{SI,SI} = \left(\frac{T \pm \sqrt{T^2 - 4\Delta}}{2} \right)^{1/2}$$

$$T = \left(\frac{\mu_{fr}}{\rho} \right) \left\{ 1 + \frac{1}{1 + i(\omega_i/\omega)} d_f m_f - i \frac{\omega}{\omega_\beta} \left[\gamma + \frac{1}{1 + i(\omega_i/\omega)} d_f m_s \left(\frac{\phi}{m_f} - \gamma \right) \right] \right\}$$

$$\Delta = -i\omega \frac{1}{1 + i(\omega_i/\omega)} \left(\frac{\mu_{fr}}{\rho} \right) d_f v$$

$v = \eta/\rho_{fl}$ = kinematic shear viscosity of pore fluid

$$\gamma = 1 - \mu_{fr}/\mu_0$$

μ_{fr}, μ_0 = shear moduli of dry rock frame and solid mineral, respectively

$m_s = (1 - \phi)\rho_0/\rho$ = solid mass fraction

$m_f = \phi\rho_{fl}/\rho$ = fluid mass fraction

$$d_f = \frac{1}{\alpha - m_f}$$

$$\omega_i = d_f \omega_c = d_f 2\pi f_c = \frac{1}{\alpha - m_f} \frac{\phi\eta}{\rho_{fl}K}$$

The frequency ω_i interpreted as the Biot critical frequency scaled by tortuosity, is the peak frequency associated with Biot relaxation. Asymptotic approximations for $\omega \ll \omega_i$ and $\omega_i \ll \omega < \omega_\beta$ are derived by Sahay (2008):

$$V_{SI} \approx \begin{cases} \sqrt{\frac{\mu_{fr}}{\rho}} \left(1 - \frac{i}{2} \frac{\omega}{\omega_i} d_f m_f \right) & \omega \ll \omega_i \\ \sqrt{\frac{\mu_{fr}}{\rho(1 - m_f/\alpha)}} \left\{ 1 - \frac{i}{2} \left[\frac{\omega_i m_f}{\omega \alpha} + \frac{\omega}{\omega_\beta} \left(\gamma(1 - \alpha^{-1}) + \frac{m_s \phi}{m_f \alpha} \right) \right] \right\} & \omega_i \ll \omega < \omega_\beta \end{cases}$$

$$V_{SI} \approx \begin{cases} \omega \sqrt{\frac{v}{\omega_i}} \left(\frac{\omega \alpha}{\omega_i 2} - i \right) & \omega \ll \omega_i \\ \omega^{1/2} \sqrt{\frac{v}{2\alpha}} (1 - i) & \omega_i \ll \omega < \omega_\beta \end{cases}$$

The slow S-wave mode in the regime above the Biot relaxation frequency is a diffusive viscous wave with a phase velocity that has a square-root frequency dependence, and a diffusion constant given by the kinematic shear viscosity scaled by the tortuosity. Below the Biot relaxation frequency the viscous drag of the fluid on the solid frame dominates over inertial effects. The slow S-wave is highly attenuating with a linear and a quadratic frequency dependence of its attenuation and phase velocity, respectively (Sahay, 2008).

Uses

Biot's theory can be used for the following purposes:

- estimating saturated-rock velocities from dry-rock velocities;
- estimating frequency dependence of velocities; and
- estimating reservoir compaction caused by pumping using the quasi-static limit of Biot's poroelasticity theory.

Assumptions and limitations

The use of Biot's equations presented in this section requires the following considerations:

- the rock is isotropic;
- all minerals making up the rock have the same bulk and shear moduli;
- the fluid-bearing rock is completely saturated; and
- the pore fluid is Newtonian.

Caution

For most crustal rocks the amount of squirt dispersion (which is not included in Biot's formulation) is comparable to or greater than Biot's dispersion, and thus using Biot's theory alone will lead to poor predictions of high-frequency saturated velocities. Exceptions include very-high-permeability materials such as ocean sediments and glass beads, materials at very high effective pressure, or near open boundaries, such as at a borehole or at the surfaces of a laboratory sample. The recommended procedure is to use the Mavko–Jizba squirt theory (Section 6.10) first to estimate the high-frequency wet-frame moduli and then to substitute them into Biot's equations.

- The wavelength, even in the high-frequency limit, is much larger than the grain or pore scale.

Extensions

Biot's theory has been extended to anisotropic media (Biot, 1962).

6.2 Geertsma–Smit approximations of Biot's relations

Synopsis

Biot's theoretical formulas predict the frequency-dependent velocities of saturated rocks in terms of the dry-rock properties (see also Biot's relations, [Section 6.1](#)). Low- and middle-frequency approximations (Geertsma and Smit, 1961) of his relations may be expressed as

$$V_P^2 = \frac{V_{P\infty}^4 + V_{P0}^4 (f_c/f)^2}{V_{P\infty}^2 + V_{P0}^2 (f_c/f)^2}$$

where V_P is the frequency-dependent P-wave velocity of saturated rock, V_{P0} is the Biot–Gassmann low-frequency limiting P-wave velocity, $V_{P\infty}$ is the Biot high-frequency limiting P-wave velocity, f is the frequency, and f_c is Biot's reference frequency, which determines the low-frequency range, $f \ll f_c$, and the high-frequency range, $f \gg f_c$, given by

$$f_c = \frac{\phi\eta}{2\pi\rho_f\kappa}$$

where ϕ is porosity, ρ_f is fluid density, η is the viscosity of the pore fluid, and κ is the absolute permeability of the rock.

Uses

The Geertsma–Smit approximations can be used for the following:

- estimating saturated-rock velocities from dry-rock velocities; and
- estimating the frequency dependence of velocities.

Assumptions and limitations

The use of the Geertsma–Smit approximations presented in this section requires the following considerations:

- mathematical approximations are valid at moderate-to-low seismic frequencies, so that $f < f_c$. This generally means moderate-to-low permeabilities, but it is in this range of permeabilities that squirt dispersion may dominate the Biot effect;
- the rock is isotropic;
- all minerals making up the rock have the same bulk and shear moduli; and
- fluid-bearing rock is completely saturated.

Caution

For most crustal rocks the amount of squirt dispersion (not included in Biot's theory) is comparable to or greater than Biot's dispersion, and thus using Biot's

theory alone will lead to poor predictions of high-frequency saturated velocities. Exceptions include very high-permeability materials such as ocean sediments and glass beads, or materials at very high effective pressure. The recommended procedure is to use the Mavko–Jizba squirt theory (Section 6.10), first to estimate the high-frequency wet-frame moduli and then to substitute them into the Biot or Geertsma–Smit equations.

6.3 Gassmann's relations: isotropic form

Synopsis

One of the most important problems in the rock physics analysis of logs, cores, and seismic data is using seismic velocities in rocks saturated with one fluid to predict those of rocks saturated with a second fluid, or equivalently, predicting saturated-rock velocities from dry-rock velocities, and vice versa. This is the *fluid substitution problem*.

Generally, when a rock is loaded under an increment of compression, such as from a passing seismic wave, an increment of pore-pressure change is induced, which resists the compression and therefore stiffens the rock. The low-frequency Gassmann–Biot (Gassmann, 1951; Biot, 1956) theory predicts the resulting increase in effective bulk modulus, K_{sat} , of the saturated rock using the following equation:

$$\frac{K_{\text{sat}}}{K_0 - K_{\text{sat}}} = \frac{K_{\text{dry}}}{K_0 - K_{\text{dry}}} + \frac{K_{\text{fl}}}{\phi(K_0 - K_{\text{fl}})}, \quad \mu_{\text{sat}} = \mu_{\text{dry}}$$

where K_{dry} is the effective bulk modulus of dry rock, K_{sat} is the effective bulk modulus of the rock with pore fluid, K_0 is the bulk modulus of mineral material making up rock, K_{fl} is the effective bulk modulus of pore fluid, ϕ is the porosity, μ_{dry} is the effective shear modulus of dry rock, and μ_{sat} is the effective shear modulus of rock with pore fluid.

Gassmann's equation assumes a homogeneous mineral modulus and statistical isotropy of the pore space but is free of assumptions about the pore geometry. Most importantly, it is valid only at sufficiently **low frequencies** such that the induced pore pressures are equilibrated throughout the pore space (i.e., there is sufficient time for the pore fluid to flow and eliminate wave-induced pore-pressure gradients). This limitation to low frequencies explains why Gassmann's relation works best for very low-frequency *in-situ* seismic data (<100 Hz) and may perform less well as frequencies increase toward sonic logging ($\approx 10^4$ Hz) and laboratory ultrasonic measurements ($\approx 10^6$ Hz).

Caution: “dry rock” is not the same as gas-saturated rock

The “dry-rock” or “dry-frame” modulus refers to the incremental bulk deformation resulting from an increment of applied confining pressure with the pore pressure held constant. This corresponds to a “drained” experiment, in which pore fluids can flow freely in or out of the sample to ensure constant pore pressure. Alternatively, the “dry-frame” modulus can correspond to an undrained experiment in which the pore fluid has zero bulk modulus, and in which pore compression therefore does not induce changes in pore pressure. This is approximately the case for an air-filled sample at standard temperature and pressure. However, at reservoir conditions (high pore pressure), gas takes on a non-negligible bulk modulus and should be treated as a saturating fluid.

Caution

Laboratory measurements on very dry rocks, such as those prepared in a vacuum oven, are sometimes *too dry*. Several investigators have found that the first few percent of fluid saturation added to an extremely dry rock will lower the frame moduli, probably as a result of disrupting surface forces acting on the pore surfaces. It is this slightly wet or moist rock modulus that should be used as the “dry-rock” modulus in Gassmann’s relations. A more thorough discussion is given in [Section 6.17](#).

Although we often describe Gassmann’s relations as allowing us to predict saturated-rock moduli from dry-rock moduli, and vice versa, the most common *in-situ* problem is to predict the changes that result when one fluid is replaced with another. One procedure is simply to apply the equation twice: transform the moduli from the initial fluid saturation to the dry state, and then immediately transform from the dry moduli to the new fluid-saturated state. Equivalently, we can algebraically eliminate the dry-rock moduli from the equation and relate the saturated-rock moduli $K_{\text{sat } 1}$ and $K_{\text{sat } 2}$ in terms of the two fluid bulk moduli $K_{\text{fl } 1}$ and $K_{\text{fl } 2}$ as follows:

$$\frac{K_{\text{sat } 1}}{K_0 - K_{\text{sat } 1}} - \frac{K_{\text{fl } 1}}{\phi(K_0 - K_{\text{fl } 1})} = \frac{K_{\text{sat } 2}}{K_0 - K_{\text{sat } 2}} - \frac{K_{\text{fl } 2}}{\phi(K_0 - K_{\text{fl } 2})}$$

Caution

It is *not correct* simply to replace K_{dry} in Gassmann’s equation by $K_{\text{sat } 2}$.

A few more explicit, but entirely equivalent, forms of the equations are

$$K_{\text{sat}} = K_{\text{dry}} + \frac{(1 - K_{\text{dry}}/K_0)^2}{\phi/K_{\text{fl}} + (1 - \phi)/K_0 - K_{\text{dry}}/K_0^2}$$

$$K_{\text{sat}} = \frac{\phi(1/K_0 - 1/K_{\text{fl}}) + 1/K_0 - 1/K_{\text{dry}}}{(\phi/K_{\text{dry}})(1/K_0 - 1/K_{\text{fl}}) + (1/K_0)(1/K_0 - 1/K_{\text{dry}})}$$

$$\frac{1}{K_{\text{sat}}} = \frac{1}{K_0} + \frac{\phi}{K_{\phi} + K_0 K_{\text{fl}}/(K_0 - K_{\text{fl}})}$$

$$K_{\text{dry}} = \frac{K_{\text{sat}}(\phi K_0/K_{\text{fl}} + 1 - \phi) - K_0}{\phi K_0/K_{\text{fl}} + K_{\text{sat}}/K_0 - 1 - \phi}$$

Note that the dry pore-space compressibility is

$$\frac{1}{K_{\phi}} = \frac{1}{v_p} \left. \frac{\partial v_p}{\partial \sigma} \right|_P$$

where v_p is the pore volume, σ is the confining pressure, and P is the pore pressure.

Use Gassmann's relation to compare the bulk modulus of a dry quartz sandstone having the properties $\phi = 0.20$, $K_{\text{dry}} = 12$ GPa, and $K_0 = 36$ GPa with the bulk moduli when the rock is saturated with gas and with water at $T = 80^\circ\text{C}$ and pore pressure $P_p = 300$ bar.

Calculate the bulk moduli and density for gas and for water using the Batzle–Wang formulas discussed in [Section 6.21](#). A gas with gravity 1 will have the properties $K_{\text{gas}} = 0.133$ GPa and $\rho_{\text{gas}} = 0.336$ g/cm³, and water with salinity 50 000 ppm will have properties $K_{\text{water}} = 3.013$ GPa and $\rho_{\text{water}} = 1.055$ g/cm³.

Next, substitute these into Gassmann's relations

$$\frac{K_{\text{sat-gas}}}{36 - K_{\text{sat-gas}}} = \frac{12}{36 - 12} + \frac{0.133}{0.20(36 - 0.133)}$$

to yield a value of $K_{\text{sat-gas}} = 12.29$ GPa for the gas-saturated rock. Similarly,

$$\frac{K_{\text{sat-water}}}{36 - K_{\text{sat-water}}} = \frac{12}{36 - 12} + \frac{3.013}{0.20(36 - 3.013)}$$

which yields a value of $K_{\text{sat-water}} = 17.6$ GPa for the water-saturated rock.

Compressibility form

An equivalent form of Gassmann's isotropic relation can be written compactly in terms of compressibilities:

$$(C_{\text{sat}} - C_0)^{-1} = (C_{\text{dry}} - C_0)^{-1} + [\phi(C_{\text{fl}} - C_0)]^{-1}$$

where

$$C_{\text{sat}} = \frac{1}{K_{\text{sat}}} \quad C_{\text{dry}} = \frac{1}{K_{\text{dry}}} \quad C_{\text{fl}} = \frac{1}{K_{\text{fl}}} \quad C_0 = \frac{1}{K_0}$$

Reuss average form

An equivalent form can be written as

$$\frac{K_{\text{sat}}}{K_0 - K_{\text{sat}}} = \frac{K_{\text{dry}}}{K_0 - K_{\text{dry}}} + \frac{K_{\text{R}}}{K_0 - K_{\text{R}}}$$

where

$$K_{\text{R}} = \left(\frac{\phi}{K_{\text{fl}}} + \frac{1 - \phi}{K_0} \right)^{-1}$$

is the Reuss average modulus of the fluid and mineral at porosity ϕ . This is consistent with the obvious result that when the dry-frame modulus of the rock goes to zero, the fluid-saturated sample will behave as a suspension and lie on the Reuss bound.

Linear form

A particularly useful exact *linear* form of Gassmann's relation follows from the simple graphical construction shown in Figure 6.3.1 (Mavko and Mukerji, 1995). Draw a straight line from the mineral modulus on the left-hand axis (at $\phi = 0$) through the data point (A) corresponding to the rock modulus with the initial pore fluid (in this case, air). The line intersects the Reuss average for that pore fluid at some porosity, ϕ_{R} , which is a measure of the pore-space stiffness. Then the rock modulus (point A') for a new pore fluid (in this case, water) falls along a second straight line from the mineral modulus, intersecting the Reuss average for the new pore fluid at ϕ_{R} . Then we can write, *exactly*,

$$\Delta K_{\text{Gass}}(\phi) = \frac{\phi}{\phi_{\text{R}}} \Delta K_{\text{R}}(\phi_{\text{R}})$$

where $\Delta K_{\text{Gass}} = K_{\text{sat } 2} - K_{\text{sat } 1}$ is the Gassmann-predicted change of saturated-rock bulk modulus between any two pore fluids (including gas), and $\Delta K_{\text{R}}(\phi_{\text{R}})$ is the difference in the Reuss average for the two fluids *evaluated at the intercept porosity* ϕ_{R} .

Because pore-fluid moduli are usually much smaller than mineral moduli, we can approximate the Reuss average as

$$K_{\text{R}}(\phi_{\text{R}}) = \frac{K_{\text{fl}} K_0}{\phi_{\text{R}} K_0 + (1 - \phi_{\text{R}}) K_{\text{fl}}} \approx \frac{K_{\text{fl}}}{\phi_{\text{R}}}$$

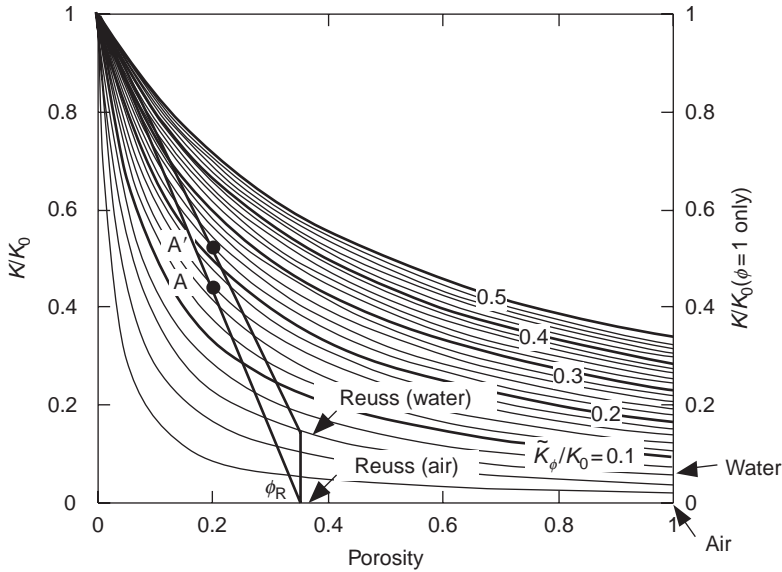


Figure 6.3.1 ϕ_R is the porosity where a straight line drawn from the mineral modulus on the left-hand axis, through the data point (A or A'), intersects the Reuss average for that corresponding pore fluid. The change in rock bulk modulus between any two pore fluids ($A-A'$) is proportional to the change in Reuss average for the same two fluids evaluated at the intercept porosity ϕ_R .

Then, the linear form of Gassmann's relations can be approximated as

$$\Delta K_{\text{Gass}}(\phi) \approx \frac{\phi}{\phi_{\text{R}}^2} \Delta K_{\text{fl}}$$

P-wave modulus form

Because Gassmann's relations predict no change in the shear modulus, we can also write the linear form of Gassmann's relation as

$$\Delta M_{\text{Gass}}(\phi) = \Delta K_{\text{Gass}}(\phi) \approx \frac{\phi}{\phi_{\text{R}}^2} \Delta K_{\text{fl}}$$

where $\Delta M_{\text{Gass}}(\phi)$ is the predicted change in the P-wave modulus $M = K + \frac{4}{3}\mu$. Similarly, we can write

$$\Delta K_{\text{Gass}} = \Delta M_{\text{Gass}} = \Delta \lambda_{\text{Gass}}$$

where λ is Lamé's parameter.

Velocity form

Murphy *et al.* (1991) suggested a velocity form of Gassmann's relation

$$\rho_{\text{sat}} V_{\text{Psat}}^2 = K_{\text{p}} + K_{\text{dry}} + \frac{4}{3} \mu$$

$$\rho_{\text{sat}} V_{\text{Ssat}}^2 = \mu$$

which is easily written as

$$\frac{V_{\text{Psat}}^2}{V_{\text{Ssat}}^2} = \frac{K_{\text{p}}}{\mu} + \frac{K_{\text{dry}}}{\mu} + \frac{4}{3}$$

where ρ_{sat} is the density of the saturated rock, V_{Psat} is the P-wave saturated rock velocity, V_{Ssat} is the S-wave saturated rock velocity, K_{dry} is the dry-rock bulk modulus, $\mu = \mu_{\text{dry}} = \mu_{\text{sat}}$ is the rock shear modulus, and

$$K_{\text{p}} = \frac{(1 - K_{\text{dry}}/K_0)^2}{\phi/K_{\text{fl}} + (1 - \phi)/K_0 - K_{\text{dry}}/K_0^2}$$

Pore stiffness interpretation

One can write the dry-rock compressibility at constant pore pressure, K_{dry}^{-1} , as (Walsh, 1965; Zimmerman, 1991a)

$$\frac{1}{K_{\text{dry}}} = \frac{1}{K_0} + \frac{\phi}{K_{\phi}}$$

where

$$\frac{1}{K_{\phi}} = \frac{1}{v_{\text{p}}} \left. \frac{\partial v_{\text{p}}}{\partial \sigma} \right|_P$$

is the effective dry-rock pore-space compressibility, defined as the ratio of the fractional change in pore volume, v_{p} , to an increment of applied external hydrostatic stress, σ , at *constant pore pressure* (see Section 2.9). This is related to another pore compressibility, $K_{\phi\text{P}}^{-1}$, which is more familiar to reservoir engineers and hydrogeologists:

$$\frac{1}{K_{\phi\text{P}}} = - \frac{1}{v_{\text{p}}} \left. \frac{\partial v_{\text{p}}}{\partial P} \right|_{\sigma}$$

which is the ratio of the fractional change in pore volume to an increment of applied pore pressure, at *constant confining pressure*, also expressed by (Zimmerman, 1991a)

$$\frac{1}{K_{\phi\text{P}}} = \frac{1}{K_{\phi}} - \frac{1}{K_0}$$

Figure 6.3.2 shows a plot of normalized dry bulk modulus, K_{dry}/K_0 , versus porosity, computed for various values of normalized pore-space stiffness, K_{ϕ}/K_0 .

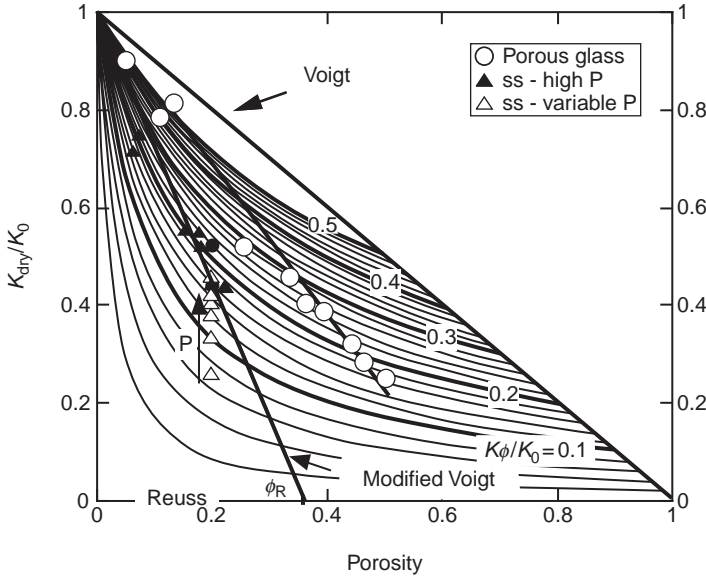


Figure 6.3.2 Normalized dry bulk modulus, K_{dry}/K_0 , versus porosity, computed for various values of normalized pore-space stiffness, K_ϕ/K_0 .

The data points plotted in Figure 6.3.2 are dynamic bulk moduli (calculated from ultrasonic velocities) for: (1) ten clean sandstones, all at a pressure of 40 MPa (Han, 1986); (2) a single clean sandstone at pressures ranging from 5 to 40 MPa (Han, 1986); and (3) porous glass (Walsh *et al.*, 1965). Effective pore-space compressibilities for each point can be read directly from the contours.

Similarly, the low-frequency *saturated* rock compressibility, K_{sat}^{-1} , can be written as

$$\frac{1}{K_{\text{sat}}} = \frac{1}{K_0} + \frac{\phi}{\tilde{K}_\phi}$$

where

$$\tilde{K}_\phi = K_\phi + \frac{K_0 K_{\text{fl}}}{K_0 - K_{\text{fl}}} \approx K_\phi + K_{\text{fl}}$$

Here K_{fl} is the pore-fluid bulk modulus and K_ϕ is the same *dry* pore-space stiffness defined above. The functional form for K_{sat} is exactly the same as for K_{dry} . The difference is only in the term \tilde{K}_ϕ , which is equal to the dry-pore stiffness, K_ϕ , incremented by a fluid term $F = (K_0 K_{\text{fl}})/(K_0 - K_{\text{fl}}) \approx K_{\text{fl}}$. Hence, the only effect of a change in fluid is a change in the modified pore stiffness \tilde{K}_ϕ .

Therefore, fluid substitution, as predicted by Gassmann's equation, can be applied by computing this change, $\Delta\tilde{K}_\phi$, and then jumping the appropriate number of contours, as illustrated in Figure 6.3.3.

For the example shown, the starting point A was one of Han's (1986) data points for an effective dry-rock bulk modulus, $K_{\text{dry}}/K_0 = 0.44$, and porosity, $\phi = 0.20$. Because the rock is dry, $F^{(1)}/K_0 \approx 0$. To saturate with water ($K_{\text{fl}}/K_0 \approx 0.056$), we

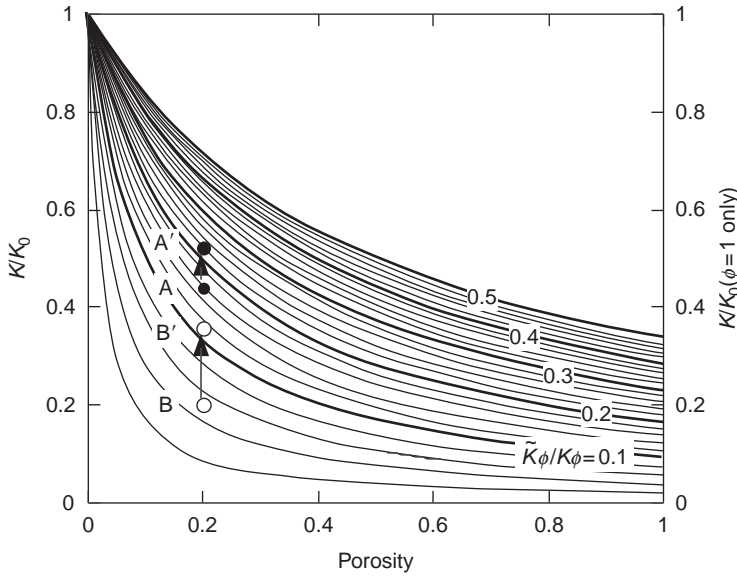


Figure 6.3.3 Normalized low-frequency saturated bulk modulus, K/K_0 , versus porosity, computed for various values of the normalized modified pore-space stiffness, \tilde{K}_ϕ/K_0 .

move up the amount $(F^{(2)} - F^{(1)})/K_0 = 0.06$, or three contours. The water-saturated modulus can be read off directly as $K_{\text{sat}}/K_0 = 0.52$, point A' . Obviously, the technique works equally well for going from dry to saturated, saturated to dry, or from one fluid to another. All we do is compute $\Delta F/K_0$ and count the contours.

The second example shown (points $B-B'$) is for the same two pore fluids and the same porosity. However, the change in rock stiffness during fluid substitution is much larger.

This illustrates the important point that a softer rock will have a larger sensitivity to fluid substitution than a stiffer rock at the same porosity. In fact, anything that causes the velocity input to Gassmann's equation to be higher (such as a stiffer rock, a measurement error, or velocities contaminated by velocity dispersion) will result in a smaller predicted sensitivity to changes in pore fluids. Similarly, lower input velocities will lead to a larger predicted sensitivity.

Biot coefficient

The dry-rock modulus can be written as

$$K_{\text{dry}} = K_0(1 - \beta)$$

where K_{dry} and K_0 are the bulk moduli of the dry rock and the mineral, and β is sometimes called the **Biot coefficient**, defined as the ratio of pore-volume change Δv_p to bulk-volume change, ΔV , at constant pore pressure:

$$\beta = \frac{\Delta v_p}{\Delta V} \Big|_{\text{dry}} = \frac{\phi K_{\text{dry}}}{K_\phi} = 1 - \frac{K_{\text{dry}}}{K_0}$$

Then, Gassmann's equation can be expressed as

$$K_{\text{sat}} = K_{\text{dry}} + \beta^2 M$$

where

$$\frac{1}{M} = \frac{\beta - \phi}{K_0} + \frac{\phi}{K_{\text{fl}}}$$

V_P but no V_S

In practice, fluid substitution is performed by starting with compressional- and shear-wave velocities measured on rocks saturated with the *initial* pore fluid (or gas) and then extracting the bulk and shear moduli. Then the bulk modulus of the rock saturated with the *new* pore fluid is calculated by using Gassmann's relation, and the velocities are reconstructed.

A practical problem arises when we wish to estimate the change of V_P during fluid substitution, but the shear velocity is unknown, which is often the case *in situ*. Then, strictly speaking, K cannot be extracted from V_P , and Gassmann's relations cannot be applied. To get around this problem, a common approach is to estimate V_S from an empirical V_S – V_P relation or to assume a dry-rock Poisson ratio (Castagna *et al.*, 1985; Greenberg and Castagna, 1992; see Section 7.9).

Mavko *et al.* (1995) have suggested an approximate method that operates directly on the P-wave modulus, $M = \rho V_P^2$. The method is equivalent to replacing the bulk moduli of the rock and mineral in Gassmann's relation with the corresponding P-wave moduli. For example,

$$\frac{M_{\text{sat}}}{M_0 - M_{\text{sat}}} \approx \frac{M_{\text{dry}}}{M_0 - M_{\text{dry}}} + \frac{M_{\text{fl}}}{\phi(M_0 - M_{\text{fl}})}$$

where M_{sat} , M_{dry} , M_0 , and M_{fl} are the P-wave moduli of the saturated rock, the dry rock, the mineral, and the pore fluid, respectively. The approximate method performs the same operation with the P-wave modulus, M , as is performed with the bulk modulus, K , in any of the various exact forms of Gassmann's relations listed above.

Uses

Gassmann's relations are used to estimate the change of low-frequency elastic moduli of porous media caused by a change of pore fluids.

Assumptions and limitations

The following considerations apply to the use of Gassmann's relations.

- **low seismic frequencies** are assumed, so that pore pressures are equilibrated throughout the pore space. *In-situ* seismic conditions should generally be acceptable.

Ultrasonic laboratory conditions will generally **not** be described well with Gassmann's equation. Sonic-logging frequencies may or may not be within the range of validity, depending on the rock type and the fluid viscosity;

- the rock is isotropic;
- all minerals making up the rock have the same bulk and shear moduli; and
- fluid-bearing rock is completely saturated.

Extensions

Gassmann's relations can be extended in the following ways:

- for mixed mineralogy, one can usually use an effective average modulus for K_0 ;
- for clay-filled rocks, it sometimes works best to consider the "soft" clay to be part of the pore-filling phase rather than part of the mineral matrix. Then the pore fluid is "mud," and its modulus can be estimated with an isostress calculation, as in the next item; and
- for partially saturated rocks at sufficiently low frequencies, one can usually use an effective modulus for the pore fluid that is an isostress average of the moduli of the liquid and gaseous phases (see [Section 6.17](#)):

$$\frac{1}{K_{fl}} = \frac{S}{K_L} + \frac{1-S}{K_G}$$

where K_L is the bulk modulus of the liquid phase, K_G is the bulk modulus of the gas phase, and S is the saturation of the liquid phase.

- For rocks with mixed mineralogy, use Brown and Korrington's extension of Gassmann's relations (see [Section 6.4](#)).
- For anisotropic rocks, use the anisotropic form of Gassmann's relations (see [Section 6.5](#)).
- Berryman and Milton (1991) have extended Gassmann's relation to include multiple porous constituents (see [Section 6.6](#)).

6.4 Brown and Korrington's generalized Gassmann equations for mixed mineralogy

Synopsis

Brown and Korrington (1975) generalized Gassmann's (1951) isotropic fluid substitution equations to the case where the solid phase of the rock is heterogeneous (i.e., mixed mineralogy).

$$\frac{K_{sat}}{K_S - K_{sat}} = \frac{K_{dry}}{K_S - K_{dry}} + \frac{K_{\phi S}}{K_S} \frac{K_{fl}}{\phi(K_{\phi S} - K_{fl})}, \quad \mu_{sat} = \mu_{dry}$$

where K_{dry} is the dry-rock bulk modulus, K_{sat} is the bulk modulus of the rock saturated with a pore fluid, K_{fl} is the fluid bulk modulus, μ_{dry} is the dry-rock shear modulus, μ_{sat} is the saturated-rock shear modulus, and ϕ is porosity.

Two additional moduli K_S and $K_{\phi S}$ are defined as

$$\frac{1}{K_S} = -\frac{1}{V} \left(\frac{\partial V}{\partial P_C} \right) \Big|_{P_D = \text{constant}}$$

$$\frac{1}{K_{\phi S}} = -\frac{1}{V_{\phi}} \left(\frac{\partial V_{\phi}}{\partial P_C} \right) \Big|_{P_D = \text{constant}}$$

where V is the total volume of a sample of rock, V_{ϕ} is the volume of pore space within the sample, P_C is the confining pressure, $P_D = P_C - P_P$ is the differential pressure, and P_P is the pore pressure. These special moduli (see also Zimmerman, 1991a) describe the effect on sample volume and pore volume of equally incrementing confining pressure and pore pressure – sometimes called the “unjacketed” case.

Caution

The notation here is different from that in Brown and Korrington (1975) and Zimmerman (1991a).

The Brown and Korrington fluid substitution equation can also be written in terms of compressibilities

$$(C_{\text{sat}} - C_S)^{-1} = (C_{\text{dry}} - C_S)^{-1} + [\phi(C_{\text{fl}} - C_{\phi S})]^{-1}$$

where $C_{\text{sat}} = 1/K_{\text{sat}}$, $C_{\text{dry}} = 1/K_{\text{dry}}$, $C_S = 1/K_S$, and $C_{\phi S} = 1/K_{\phi S}$.

When the mineral phase is homogeneous, then $K_S = K_{\phi S} = K_{\text{mineral}}$, and $C_S = C_{\phi S} = C_{\text{mineral}}$, where $C_{\text{mineral}} = 1/K_{\text{mineral}}$, and K_{mineral} is the mineral bulk modulus. Thus, if there is only a single mineral, both the modulus and compressibility forms of fluid substitution presented here reduce exactly to the isotropic Gassmann equations.

A practical problem with using the Brown and Korrington equations for fluid substitution is that we seldom have knowledge of C_S and $C_{\phi S}$ (or K_S and $K_{\phi S}$). One useful constraint comes from the relation

$$C_{\phi S} = \frac{1}{\phi} C_S - \frac{1 - \phi}{\phi} \bar{C}_{\text{mineral}}$$

where $\bar{C}_{\text{mineral}} = 1/\bar{K}_{\text{mineral}}$ is the true effective compressibility of the mineral mix. \bar{K}_{mineral} must satisfy the Hashin–Shtrikman bounds, $K_{\text{mineral}}^{\text{HS}\pm}$, and might be estimated, for example, using a Voigt–Reuss–Hill average of the individual mineral bulk moduli. Insights into the value of K_S come from knowledge of the grain

microstructure. K_S might lie close to the upper bound of the mineral bulk modulus, if the softest phases, such as clay, are pore-filling. On the other hand, if the softest minerals are load-bearing, then K_S might be closer to the lower bound. Once an estimate of K_S is made, a consistent estimate of $K\phi_S$ can be found from the above relation.

Uses

The Gassmann and Brown–Korrington relations are used to estimate the change of low-frequency elastic moduli of porous media caused by a change of pore fluids.

Assumptions and limitations

The following considerations apply to the use of Gassmann and Brown–Korrington relations.

- **Low seismic frequencies** are assumed, so that pore pressures are equilibrated throughout the pore space. *In-situ* seismic conditions should generally be acceptable. Ultrasonic laboratory conditions will generally **not** be described well with Gassmann or Brown–Korrington equations. Sonic-logging frequencies may or may not be within the range of validity, depending on the rock type and fluid viscosity.
- The rock is isotropic.
- Fluid-bearing rock is completely saturated.

6.5 Fluid substitution in anisotropic rocks

Synopsis

In addition to his famous isotropic equations, Gassmann (1951) published fluid-substitution equations for *anisotropic* porous rocks. In terms of the anisotropic linear elastic stiffness components, c_{ijkl} , his result is written as

$$c_{ijkl}^{\text{sat}} = c_{ijkl}^{\text{dry}} + \frac{\left(K_0\delta_{ij} - c_{ijaa}^{\text{dry}}/3\right)\left(K_0\delta_{kl} - c_{bbkl}^{\text{dry}}/3\right)}{(K_0/K_{\text{fl}})\phi(K_0 - K_{\text{fl}}) + \left(K_0 - c_{ccdd}^{\text{dry}}/9\right)}$$

where c_{ijkl}^{dry} is the effective elastic stiffness element of dry rock, c_{ijkl}^{sat} is the effective elastic stiffness element of rock saturated with pore fluid, K_0 is the mineral bulk modulus, K_{fl} is the fluid bulk modulus, and ϕ is porosity:

$$\delta_{ij} = \begin{cases} 1 & \text{for } i = j \\ 0 & \text{for } i \neq j \end{cases}$$

The inverse of Gassmann's anisotropic equation (not given in Gassmann's paper) can be written as

$$c_{ijkl}^{\text{dry}} = c_{ijkl}^{\text{sat}} - \frac{(K_0 \delta_{ij} - c_{ijaa}^{\text{sat}}/3)(K_0 \delta_{kl} - c_{bbkl}^{\text{sat}}/3)}{(K_0/K_{\text{fl}})\phi(K_0 - K_{\text{fl}}) - (K_0 - c_{ccdd}^{\text{sat}}/9)}$$

Successive application of the second equation followed by the first one allows us to apply fluid substitution from any initial fluid to any final fluid.

Similarly, Gassmann (1951) gave anisotropic fluid-substitution expressions in terms of the elastic compliances:

$$s_{ijkl}^{\text{sat}} = s_{ijkl}^{\text{dry}} - \frac{(s_{ijaa}^{\text{dry}} - \delta_{ij}/3K_0)(s_{bbkl}^{\text{dry}} - \delta_{kl}/3K_0)}{(s_{ccdd}^{\text{dry}} - 1/K_0) + \phi(1/K_{\text{fl}} - 1/K_0)}$$

where s_{ijkl}^{dry} is the effective elastic compliance element of dry rock, s_{ijkl}^{sat} is the effective elastic compliance element of rock saturated with pore fluid, K_0 is the bulk modulus of the solid mineral, K_{fl} is the bulk modulus of the fluid, and ϕ is porosity.

The inverse expression (not in Gassmann's original paper) is written as

$$s_{ijkl}^{\text{dry}} = s_{ijkl}^{\text{sat}} + \frac{(s_{ijaa}^{\text{sat}} - \delta_{ij}/3K_0)(s_{bbkl}^{\text{sat}} - \delta_{kl}/3K_0)}{(s_{ccdd}^{\text{sat}} - 1/K_0) - \phi(1/K_{\text{fl}} - 1/K_0)}$$

Gassmann's equations assume that the mineral is homogeneous and isotropic, although the dry and saturated rocks can have arbitrary anisotropy. In all of the equations of this section, a repeated index within a term implies a sum over 1–3 (e.g., $c_{ij\alpha\alpha} = c_{ij11} + c_{ij22} + c_{ij33}$).

Brown and Korrington (1975) also gave expressions for fluid substitution in anisotropic rocks, expressed in the compliance domain. Their result is very similar to Gassmann's, except that they allow for an **anisotropic mineral**. (Brown and Korrington also made a generalization to allow for mixed mineralogy. That generalization is shown in Section 6.4 for isotropic rocks.)

$$s_{ijkl}^{\text{sat}} = s_{ijkl}^{\text{dry}} - \frac{(s_{ijaa}^{\text{dry}} - s_{ijaa}^0)(s_{bbkl}^{\text{dry}} - s_{bbkl}^0)}{(s_{ccdd}^{\text{dry}} - s_{ccdd}^0) + \phi(\beta_{\text{fl}} - \beta_0)}$$

where s_{ijkl}^{dry} is the effective elastic compliance tensor element of dry rock, s_{ijkl}^{sat} is the effective elastic compliance element of rock saturated with pore fluid, s_{ijkl}^0 is the effective elastic compliance element of the solid mineral, β_{fl} is the fluid compressibility $= 1/K_{\text{fl}}$, β_0 is the mineral compressibility $= s_{\alpha\alpha\gamma\gamma}^0 = 1/K_0$, and ϕ is porosity.

The inverse is given by

$$s_{ijkl}^{\text{dry}} = s_{ijkl}^{\text{sat}} + \frac{(s_{ijaa}^{\text{sat}} - s_{ijaa}^0)(s_{bbkl}^{\text{sat}} - s_{bbkl}^0)}{(s_{ccdd}^{\text{sat}} - s_{ccdd}^0) - \phi(1/K_{\text{fl}} - 1/K_0)}$$

The practical differences between the Gassmann and Brown–Korringa equations presented here appear to be inconsequential. Even though mineral grains are usually highly anisotropic, Brown and Korringa’s equations imply that all grains in the rock are crystallographically aligned, which will not be the case in real rocks. Furthermore, complete elastic tensors for rock-forming minerals are generally not well known. In most cases, our only practical choice will be to assume an average isotropic mineral modulus.

One of the major disadvantages in the application of the anisotropic Gassmann equation is that in the field we seldom measure enough parameters to completely characterize the stiffness tensor of a rock. Mavko and Bandyopadhyay (2008) find an approximate form of fluid substitution, for vertically propagating seismic waves in a transversely isotropic medium with a vertical axis of symmetry (VTI). The anisotropic correction for the fluid effect depends only on Thomsen’s parameter δ :

$$c_{3333}^{\text{sat}} \approx c_{3333}^{\text{dry}} + \left[\frac{(K_{\text{fl}}/K_0)(K_0 - K_{\text{iso}}^{\text{dry}})^2}{\phi(K_0 - K_{\text{fl}}) + (K_{\text{fl}}/K_0)(K_0 - K_{\text{iso}}^{\text{dry}})} \right] \left(1 - \delta \frac{\frac{4}{3}c_{3333}^{\text{dry}}}{K_0 - K_{\text{iso}}^{\text{dry}}} \right)$$

$$c_{3333}^{\text{dry}} \approx c_{3333}^{\text{sat}} - \left[\frac{(K_{\text{fl}}/K_0)(K_0 - K_{\text{iso}}^{\text{sat}})^2}{\phi(K_0 - K_{\text{fl}}) - (K_{\text{fl}}/K_0)(K_0 - K_{\text{iso}}^{\text{sat}})} \right] \left(1 - \delta \frac{\frac{4}{3}c_{3333}^{\text{sat}}}{K_0 - K_{\text{iso}}^{\text{sat}}} \right)$$

where $K_{\text{iso}}^{\text{dry}}$ and $K_{\text{iso}}^{\text{sat}}$ are the apparent isotropic bulk moduli of the dry and saturated rock, respectively, computed from the vertical P- and S-wave velocities: $K_{\text{iso}} = \rho(V_P^2 - \frac{4}{3}V_S^2)$. In these equations, the term within the square brackets is just the difference between the dry and saturated apparent bulk moduli as predicted by the isotropic Gassmann equation. The approximation is good for porosities larger than the magnitude of the Thomsen parameters (ϵ, γ, δ).

Uses

The equations of Gassmann and Brown and Korringa are applicable to the fluid substitution problem in anisotropic rocks.

Assumptions and limitations

The following considerations apply to the use of Brown and Korringa’s relations:

- **low seismic frequencies** (equilibrated pore pressures). *In-situ* seismic frequencies generally should be acceptable. Ultrasonic laboratory conditions will generally **not** be described well with Brown and Korringa’s equations. Sonic-logging frequencies may or may not be within the range of validity, depending on the rock type and fluid viscosity;
- all minerals making up the rock have the same moduli; and
- fluid-bearing rock is completely saturated.

Extensions

The following extensions of the anisotropic fluid substitution relations can be made:

- for mixed mineralogy, one can usually use an effective average set of mineral compliances for S_{ijkl}^0 ;
- for clay-filled rocks, it often works best to consider the “soft” clay to be part of the pore-filling phase rather than part of the mineral matrix. Then, the pore fluid is “mud,” and its modulus can be estimated using an isostress calculation, as in the next item; and
- for partially saturated rocks at sufficiently low frequencies, one can usually use an effective modulus for the pore fluid that is an isostress average of the moduli of the liquid and gaseous phases:

$$\beta_{\text{fl}} = S\beta_L + (1 - S)\beta_G$$

where β_L is the compressibility of the liquid phase, β_G is the compressibility of the gas phase, and S is the liquid saturation.

6.6 Generalized Gassmann's equations for composite porous media

Synopsis

The generalized Gassmann's equation (Berryman and Milton, 1991) describes the static or low-frequency effective bulk modulus of a fluid-filled porous medium when the porous medium is a composite of two porous phases, each of which could be separately described by the more conventional Gassmann relations (Figure 6.6.1). This is an improvement over the usual Gassmann equation, which assumes that the porous medium is composed of a single, statistically homogeneous porous constituent with a single pore-space stiffness and a single solid mineral. Like Gassmann's equation, the generalized Gassmann formulation is completely independent of the pore geometry. The generalized formulation assumes that the two porous constituents are bonded at points of contact and fill all the space of the composite porous medium. Furthermore, like the Gassmann formulation, it is assumed that the frequency is low enough that viscous and inertial effects are negligible, and that any stress-induced increments of pore pressure are uniform within each constituent, although they could be different from one constituent to another (Berryman and Milton extend this to include dynamic poroelasticity, which is not presented here).

The pore microstructure within each phase is statistically homogeneous and much smaller than the size of the inclusions of each phase, which in turn are smaller than the size of the macroscopic sample. The inclusions of each porous phase are large enough to have effective dry-frame bulk moduli, $K_{\text{dry}}^{(1)}$ and $K_{\text{dry}}^{(2)}$; porosities, $\phi^{(1)}$ and $\phi^{(2)}$; and solid mineral moduli, $K_0^{(1)}$ and $K_0^{(2)}$, respectively. The volume fractions of the two porous phases are $f^{(1)}$ and $f^{(2)}$, where $f^{(1)} + f^{(2)} = 1$. The generalized Gassmann

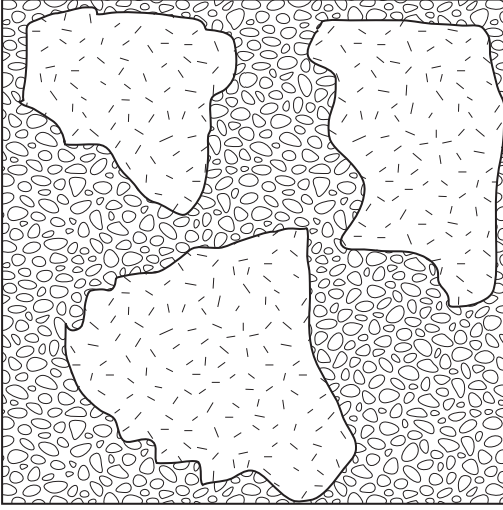


Figure 6.6.1 Composite porous medium with two porous phases.

equation relates the effective saturated bulk modulus of the macroscopic sample, K_{sat}^* , to its dry-frame bulk modulus, K_{dry}^* , through two other elastic constants defined by

$$\frac{1}{K_s^*} = -\frac{1}{V} \left(\frac{\partial V}{\partial p_f} \right)_{p_d=\text{const}}$$

and

$$\frac{1}{K_\phi^*} = -\frac{1}{V_\phi} \left(\frac{\partial V_\phi}{\partial p_f} \right)_{p_d=\text{const}}$$

where V is the total sample volume, V_ϕ is the total pore volume, p_f is the pore pressure, and $p_d = p - p_f$ is the differential pressure, with p as the confining pressure. For a single-phase porous medium made up of a single solid-mineral constituent with modulus K_0 , the two moduli are equal to the mineral modulus: $K_s = K_\phi = K_0$. The relation between K_{sat}^* and K_{dry}^* for a composite porous medium is

$$K_{\text{sat}}^* = K_{\text{dry}}^* + \alpha^* C$$

$$C = \frac{\alpha^*}{\alpha^*/K_s^* + \phi \left(1/K_f - 1/K_\phi^* \right)}$$

$$\alpha^* = 1 - \frac{K_{\text{dry}}^*}{K_s^*}$$

where K_f is the fluid bulk modulus. The constants K_s^* and K_ϕ^* can be expressed in terms of the moduli of the two porous constituents making up the composite medium. The key idea leading to the results is that whenever two scalar fields, such as p_d

and p_f , can be varied independently in a linear composite with only two constituents, there exists a special value of the increment ratio $\delta p_d/\delta p$ that corresponds to an overall expansion or contraction of the medium without any relative shape change. This guarantees the existence of a set of consistency relations, allowing K_s^* and K_ϕ^* to be written in terms of the dry-frame modulus and the constituent moduli. By linearity, the coefficients for the special value of $\delta p_d/\delta p$ are also the coefficients for any other arbitrary ratio. The relation for K_s^* is

$$\frac{1/K_0^{(1)} - 1/K_0^{(2)}}{1/K_{\text{dry}}^{(2)} - 1/K_{\text{dry}}^{(1)}} = \frac{1/K_0^{(1)} - 1/K_s^*}{1/K_{\text{dry}}^* - 1/K_{\text{dry}}^{(1)}} = \frac{1/K_s^* - 1/K_0^{(2)}}{1/K_{\text{dry}}^{(2)} - 1/K_{\text{dry}}^*}$$

or, equivalently, in terms of α^*

$$\frac{\alpha^* - \alpha^{(1)}}{\alpha^{(2)} - \alpha^{(1)}} = \frac{K_{\text{dry}}^* - K_{\text{dry}}^{(1)}}{K_{\text{dry}}^{(2)} - K_{\text{dry}}^{(1)}}$$

where $\alpha^{(1)} = 1 - K_{\text{dry}}^{(1)}/K_0^{(1)}$ and $\alpha^{(2)} = 1 - K_{\text{dry}}^{(2)}/K_0^{(2)}$. Other equivalent expressions are

$$\frac{1}{K_s^*} = \frac{1}{K_0^{(1)}} - \frac{1/K_0^{(1)} - 1/K_0^{(2)}}{1/K_{\text{dry}}^{(2)} - 1/K_{\text{dry}}^{(1)}} [1/K_{\text{dry}}^* - 1/K_{\text{dry}}^{(1)}]$$

and

$$\frac{1}{K_s^*} = \frac{1}{K_0^{(2)}} - \frac{1/K_0^{(1)} - 1/K_0^{(2)}}{1/K_{\text{dry}}^{(2)} - 1/K_{\text{dry}}^{(1)}} [1/K_{\text{dry}}^* - 1/K_{\text{dry}}^{(2)}]$$

The relation for K_ϕ^* is given by

$$\frac{\langle \phi \rangle}{K_\phi^*} = \frac{\alpha^*}{K_s^*} - \left\langle \frac{\alpha(x) - \phi(x)}{K_0(x)} \right\rangle - (\langle \alpha(x) \rangle - \alpha^*) \left(\frac{\alpha^{(1)} - \alpha^{(2)}}{K_{\text{dry}}^{(1)} - K_{\text{dry}}^{(2)}} \right)$$

where $\langle q(x) \rangle = f^{(1)}q^{(1)} + f^{(2)}q^{(2)}$ denotes the volume average of any quantity q . Gassmann's equation for a single porous medium is recovered correctly from the generalized equations when $K_0^{(1)} = K_0^{(2)} = K_0 = K_s^* = K_\phi^*$ and $K_{\text{dry}}^{(1)} = K_{\text{dry}}^{(2)} = K_{\text{dry}}^*$.

Uses

The generalized Gassmann equations can be used to calculate low-frequency saturated velocities from dry velocities for composite porous media made of two porous constituents. Examples include shaley patches embedded within a sand, microporous grains within a rock with macroporosity, or large nonporous inclusions within an otherwise porous rock.

Assumptions and limitations

The preceding equations imply the following assumptions:

- the rock is isotropic and made of up to two porous constituents;
- all minerals making up the rock are linearly elastic;
- fluid-bearing rock is completely saturated;
- the porosity in each phase is uniform, and the pore structure in each phase is smaller than the size of inclusions of each porous phase; and
- the size of the porous inclusions is big enough to have a well-defined dry-frame modulus but is much smaller than the wavelength and the macroscopic sample.

Extensions

For more than two porous constituents, the composite may be modeled by dividing it into separate regions, each containing only two phases. This approach is restrictive and not always possible.

6.7 Generalized Gassmann equations for solid pore-filling material

Synopsis

The traditional Gassmann and Brown–Korringa models for fluid substitution in a porous rock (see [Sections 6.3–6.6](#)) apply only when the pore-filling material is a fluid with zero shear modulus. Ciz and Shapiro (2007) have generalized the equations to account for a solid that fills the pore space. The effective compliance of the solid-saturated porous material is given as (Ciz and Shapiro, 2007):

$$S_{ijkl}^{\text{sat}} = S_{ijkl}^{\text{dry}} - \left(S_{ijkl}^{\text{dry}} - S_{ijkl}^0 \right) \left[\phi (S^{if} - S^\phi) + S^{\text{dry}} - S^0 \right]_{mnpq}^{-1} \left(S_{mnpq}^{\text{dry}} - S_{mnpq}^0 \right)$$

where S_{ijkl}^{dry} is the effective drained elastic compliance tensor of dry rock with empty pores, S_{ijkl}^{sat} is the effective elastic compliance tensor of rock with saturated pores, S_{ijkl}^0 is the effective elastic compliance tensor of mineral material making up the dry-rock frame, and ϕ is porosity.

In the above equations, two compliances are introduced, related to the strain averaged over the pore volume V_ϕ :

$$S_{ijkl}^\phi = -\frac{1}{V_\phi} \left(\frac{\partial \zeta_{ij}}{\partial \sigma_{kl}^f} \right)_{\text{const-}\sigma^d}$$

$$S_{ijkl}^{if} = -\frac{1}{V_\phi} \left(\frac{\partial \zeta_{ij}}{\partial \sigma_{kl}^f} \right)_{\text{const-}m^{if}}$$

$$\varsigma_{ij} = \int_{V_\phi} \frac{1}{2} (u_{i,j} + u_{j,i}) d^3x = \text{strain integrated over the pore volume}$$

u_i = displacement field

$\sigma_{ij}^d = \sigma_{ij}^c - \sigma_{ij}^f$ = differential stress

σ_{ij}^c = confining stress

σ_{ij}^f = pore stress (reduces to pore pressure for pore-filling fluid)

m^{if} = mass of pore-filling material

The pore compliance S_{ijkl}^ϕ was introduced earlier by Brown and Korringa (1975), and for a homogeneous mineral frame $S_{ijkl}^\phi = S_{ijkl}^0$. The generalized compliance tensor S_{ijkl}^{if} introduced by Ciz and Shapiro is related to the volume average strain of the filled pore space at constant mass. In general, this compliance differs from the compliance tensor of the pore-filling solid. For a fluid, the compliance tensor reduces to the fluid compressibility.

For isotropic materials, the results can be expressed in terms of bulk and shear moduli as

$$K_{\text{sat}}^{-1} = K_{\text{dry}}^{-1} - \frac{(K_{\text{dry}}^{-1} - K_0^{-1})^2}{\phi(K_{\text{if}}^{-1} - K_\phi^{-1}) + (K_{\text{dry}}^{-1} - K_0^{-1})}$$

$$\mu_{\text{sat}}^{-1} = \mu_{\text{dry}}^{-1} - \frac{(\mu_{\text{dry}}^{-1} - \mu_0^{-1})^2}{\phi(\mu_{\text{if}}^{-1} - \mu_\phi^{-1}) + (\mu_{\text{dry}}^{-1} - \mu_0^{-1})}$$

where the subscript 0 refers to the mineral material of the porous frame, *dry* refers to the drained frame, and *sat* refers to bulk and shear moduli of the solid- (or liquid-) saturated porous material. These equations reduce to the classical Gassmann and Brown–Korringa results for a pore-filling liquid with zero shear modulus. For a homogeneous mineral frame, $K_\phi = K_0$. According to Ciz and Shapiro, the unknown parameters K_{if} and μ_{if} can be approximated by the bulk and shear moduli of the pore-filling solid. The approximation is good for contrasts in elastic moduli between the pore solid and the mineral frame of up to 20% and can still be applied for contrasts up to 40%. This approximation greatly simplifies the application of the equations. Ciz and Shapiro heuristically extend the equations to viscoelastic pore-filling material by introducing complex bulk and shear moduli K_{if} and μ_{if} in the equations.

Uses

These equations can be used to estimate the change in the elastic moduli of porous rock with a change in pore-filling material when the pore-filling material has a finite shear modulus; such is the case with heavy oils, which behave like quasi-solids at low temperatures.

Assumptions and limitations

- The derivation assumes all materials are linear and elastic.
- The pore-filling material completely saturates the pore space.

6.8 Fluid substitution in thinly laminated reservoirs

Synopsis

In laminated sand–shale sequences, fluid changes, if any, are likely to occur only in the sandy layers, while fluid changes in the shale are prevented by the capillary-held water and extremely low permeability (Katahara, 2004; Skelt, 2004). When the laminations are subresolution, measurements (seismic, sonic, or ultrasonic) yield average properties of the *composite*, rather than of the individual layers. If the subresolution heterogeneity is ignored when computing fluid substitution, the velocity changes are likely to be overpredicted (Skelt, 2004). A better approach for fluid substitution is first to down scale the measured composite values to individual sand and shale properties, and then to apply fluid substitution only to the sand.

For P- and S-waves propagating normal to the layering, the composite (upscaled) wave velocity is related to the individual layer properties via the Backus (1962) average:

$$\frac{1}{\rho V^2} = \frac{(1 - f_{\text{shale}})}{\rho_{\text{sand}} V_{\text{sand}}^2} + \frac{f_{\text{shale}}}{\rho_{\text{shale}} V_{\text{shale}}^2}$$

where V is the measured composite velocity, $\rho = (1 - f_{\text{shale}})\rho_{\text{sand}} + f_{\text{shale}}\rho_{\text{shale}}$ is the measured composite density, $M = \rho V^2$ is the wave modulus of the composite (P- or S-wave), ρ_{sand} is the sand bulk density, V_{sand} is the sand velocity (V_P or V_S), f_{shale} is the shale *thickness* fraction (1 – net/gross), ρ_{shale} is the shale bulk density, and V_{shale} is the shale velocity (V_P or V_S).

The Backus average assumes that layers are very thin relative to the wavelength. If expressed in terms of *wave compliance*, $C = 1/M = 1/\rho V^2$, the Backus average becomes linear for both P- and S-waves:

$$C_P = (1 - f_{\text{shale}})C_{P\text{-sand}} + f_{\text{shale}}C_{P\text{-shale}}$$

$$C_S = (1 - f_{\text{shale}})C_{S\text{-sand}} + f_{\text{shale}}C_{S\text{-shale}}$$

Solving the above equations for sand properties yields

$$\rho_{\text{sand}} = \frac{\rho - f_{\text{shale}} \rho_{\text{shale}}}{(1 - f_{\text{shale}})}$$

$$C_{P\text{-sand}} = \frac{C_P - f_{\text{shale}} C_{P\text{-shale}}}{(1 - f_{\text{shale}})}$$

$$C_{S\text{-sand}} = \frac{C_S - f_{\text{shale}} C_{S\text{-shale}}}{(1 - f_{\text{shale}})}$$

where $C_{P\text{-sand}}$ and $C_{S\text{-sand}}$ are the wave compliances measured from P- and S-wave velocities, respectively. Hence, sand properties can be estimated if the shale thickness fraction can be estimated (e.g., from a Thomas–Stieber analysis), and if the shale compliance and density can be estimated from shaley log intervals or regional trends.

The sand P-wave modulus, $M_{P\text{-sand}}$, shear modulus, μ_{sand} , and bulk modulus, K_{sand} , are given by

$$M_{P\text{-sand}} = \frac{1}{C_{P\text{-sand}}}$$

$$\mu_{\text{sand}} = \frac{1}{C_{S\text{-sand}}}$$

$$K_{\text{sand}} = M_{P\text{-sand}} - \frac{4}{3} \mu_{\text{sand}}$$

Finally, Gassmann fluid substitution can be applied to the sand bulk modulus, and the sand–shale composite can be upscaled again using the Backus average. If shear data are not available, the approximate form of Gassmann’s equation (Section 6.3) can be applied to the sand P-wave modulus, $M_{P\text{-sand}}$.

Caution

When the fraction of sand becomes very small, the inversion for sand properties, as outlined above, becomes unreliable (Skelt, 2004). Small errors in the shale properties become magnified, and predicted sand properties can be incorrect.

Katahara (2004) presented a more stable approach for downscaling, illustrated in Figure 6.8.1. Regional shale and sand trends are plotted in the plane of ρ versus C_P . Multiple sand trends can be plotted, representing water, gas, and oil sands. The observed trend of laminated sands is also plotted, extending between the sand and shale trends. Because both the density and compliance of the composite are linear functions of the sand and shale densities and compliances, any measured point, B, should fall along a straight line between a shale point, A, and a sand point, C. The shale fraction is related to the distances $|BC|$ and $|AC|$ by

$$f_{\text{shale}} = \frac{|BC|}{|AC|}$$

Plausible sand and shale end-member properties corresponding to any composite point, B, are found by drawing a line through B, parallel to the laminated-sand trend (Katahara, 2004). The intersections of the line with the shale trend (point A) and sand trend (point C) are the end-members. Fluid substitution can be applied to the sand point, C. The method guarantees that the downscaled end-members are always consistent with the established trends.

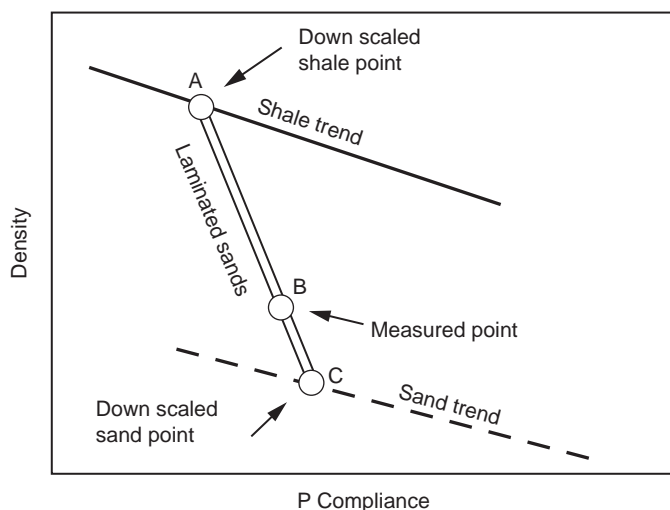


Figure 6.8.1 Katahara's graphical method for down scaling laminated sand data into estimates of the constituent sand and shale end-members.

Caution

Before applying Gassmann fluid substitution to the sand point, remember to estimate the downscaled sand porosity (e.g., from the sand density), and the sand fluid saturation.

Subresolution shale laminations within a reservoir can cause several effects:

- fluid changes will only occur within the permeable layers, not within the shales;
- because fluid changes only occur within the permeable fraction of the interval, the observed fluid-related changes in density and velocity are less than if the entire interval were permeable – approximately $(1 - f_{\text{shale}})$ of the effect; and
- shale laminations tend to increase the V_P/V_S ratio – both because the shale fractions have higher V_P/V_S and also because the effects of hydrocarbons on V_P/V_S are diminished.

Uses

This approach can be used for fluid substitution when subresolution impermeable layers lie within the interval.

Assumptions and limitations

- As with any Gassman-related fluid substitution method, the seismic frequency must be low enough that wave-induced increments of pore pressure can equilibrate throughout the pore space during a seismic period.
- In the case discussed here, the equilibration only needs to take place within each sand layer.

- Downscaling to sand properties requires that reasonable estimates of shale properties and the shale fraction can be made.
- Describing the laminated composite using the Backus average implies that the layer thicknesses are very much smaller than the wavelength.

Extensions

Fluid substitution within the sand can be done using either the Gassmann or Brown–Korrington equations, depending on the sand mineralogy. If the sand itself is anisotropic, then the corresponding anisotropic fluid substitution algorithms can be applied. The anisotropy resulting from the lamination of shales with sands is not relevant to choosing the fluid substitution algorithm; the choice depends only on the properties of the permeable intervals where fluids are changing.

6.9 BAM: Marion's bounding average method

Synopsis

Marion (1990) developed a heuristic method based on theoretical bounds for estimating how elastic moduli and velocities change when one pore-filling phase is substituted for another. The Hashin–Shtrikman (1963) bounds define the range of elastic moduli (velocities) possible for a given volume mix of two phases, either liquid or solid (see Figure 6.9.1). At any given volume fraction of constituents, the effective modulus will fall between the bounds (somewhere along the vertical dashed line in the top figure), but its precise value depends on the geometric details of the grains and pores. We use, for example, terms such as “stiff pore shapes” and “soft pore shapes.” Stiffer shapes cause the value to be higher within the allowable range; softer shapes cause the value to be lower.

Marion reasoned that the fractional vertical position within the bounds, $w = d/D$, where $0 \leq w \leq 1$, is therefore a measure of the pore geometry and is independent of the pore-filling properties – a reasonable assumption, but one that has not been proved. Because changing the pore-filling material does not change the geometry, w should remain constant, $w = d/D = d'/D'$, with any change in pore fluids. His method is as follows:

1. Begin with measurements of the modulus with the first pore-filling material (liquid, gas, or solid). Calculate the theoretical upper bound, M_1^+ , and lower bound, M_1^- , corresponding to this state. (The subscript 1 refers to this first state with the first pore-filling material.) Plot the measured data value, M_1 , and measure w relative to these bounds.

$$w = \frac{M_1 - M_1^-}{M_1^+ - M_1^-}$$

2. Recalculate the theoretical upper and lower bounds, M_2^+ and M_2^- , corresponding to the second pore-filling material of interest. Plot a point at the same position w relative to the new bounds. This is the new estimated modulus, M_2 ,

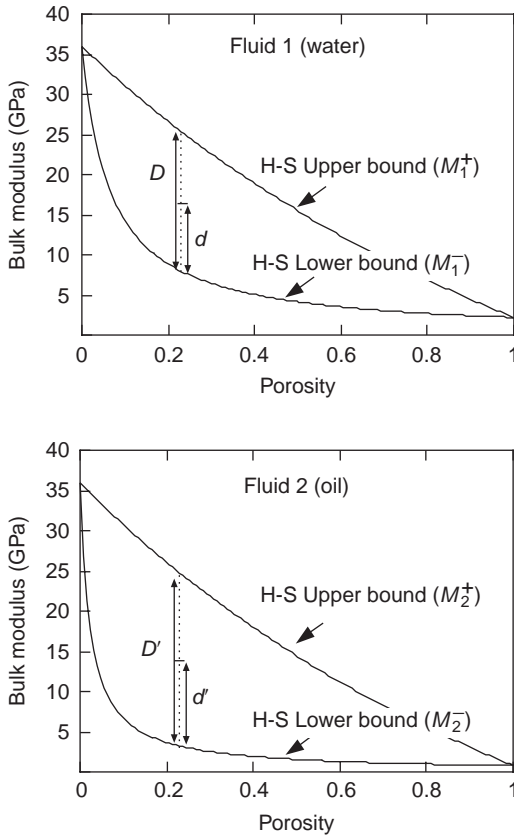


Figure 6.9.1 Hashin–Shtrikman bounds. The fractional vertical position within the bounds is $w = d/D$.

$$M_2 = M_2^- + w(M_2^+ - M_2^-)$$

Marion and others (Marion and Nur, 1991; Marion *et al.*, 1992) showed that this method works quite well for several examples: predicting water-saturated rock velocities from dry-rock velocities and predicting frozen-rock (ice-filled) velocities from water-saturated velocities.

Uses

Marion’s bounding average method is applicable to the fluid substitution problem.

Assumptions and limitations

Marion’s bounding average method is primarily heuristic. Therefore, it needs to be tested empirically. A stronger theoretical basis would also be desirable. Nevertheless, it looks quite promising and extremely flexible.

Extensions

The simplicity of the method suggests that it be tried for comparing the effects of water-filled pores with clay-filled pores, altered clay grains versus the original crystalline grain, and so forth.

6.10 Mavko–Jizba squirt relations

Synopsis

The *squirt* or *local flow* model suggests that the fluctuating stresses in a rock caused by a passing seismic wave induce pore-pressure gradients at virtually all scales of pore-space heterogeneity – particularly on the scale of individual grains and pores. These gradients impact the viscoelastic behavior of the rock; at high frequencies, when the gradients are unrelaxed, all elastic moduli (including the shear modulus) will be stiffer than at low frequencies, when the gradients are relaxed (the latter case being modeled by Gassmann). Mavko and Jizba (1991) derived simple theoretical formulas for predicting the very high-frequency moduli of saturated rocks in terms of the pressure dependence of dry rocks. The prediction is made in two steps: first, the squirt effect is incorporated as high-frequency “wet-frame moduli” K_{uf} and μ_{uf} , which are derived from the normal dry moduli as

$$\frac{1}{K_{uf}} \approx \frac{1}{K_{dry-hiP}} + \left(\frac{1}{K_{fl}} - \frac{1}{K_0} \right) \phi_{soft}$$

$$\left(\frac{1}{\mu_{uf}} - \frac{1}{\mu_{dry}} \right) = \frac{4}{15} \left(\frac{1}{K_{uf}} - \frac{1}{K_{dry}} \right)$$

where K_{uf} is the effective high-frequency, unrelaxed, wet-frame bulk modulus, K_{dry} is the effective bulk modulus of dry rock, $K_{dry-hiP}$ is the effective bulk modulus of dry rock at very high pressure, K_0 is the bulk modulus of the mineral material making up the rock, K_{fl} is the effective bulk modulus of the pore fluid, ϕ_{soft} is the soft porosity – the amount of porosity that closes at high pressure. This is often small enough to ignore. μ_{uf} is the effective high-frequency, unrelaxed, wet-frame shear modulus, and μ_{dry} is the effective shear modulus of dry rock.

These frame moduli are then substituted into Gassmann’s or Biot’s relations to incorporate the remaining fluid-saturation effects. For most crustal rocks the amount of squirt dispersion is comparable to or greater than Biot’s dispersion, and thus using Biot’s theory alone will lead to poor predictions of high-frequency saturated velocities. (Exceptions include very high-permeability materials such as ocean sediments and glass beads; rocks at very high effective pressure when most of the soft, crack-like porosity is closed; or rocks near free boundaries such as borehole walls.)

A more detailed analysis of the frequency dependence of the squirt mechanism is presented in [Section 6.11](#).

Although the formulation presented here is independent of any idealized crack shape, the squirt behavior is also implicit in virtually all published formulations for effective moduli based on elliptical cracks (see [Sections 4.7–4.11](#)). In most of those models, the cavities are treated as being isolated with respect to flow, thus simulating the high-frequency limit of the squirt model.

Uses

The Mavko–Jizba squirt relations can be used to calculate high-frequency saturated rock velocities from dry-rock velocities.

Assumptions and limitations

The use of the Mavko–Jizba squirt relations requires the following considerations:

- high seismic frequencies that are ideally suited for ultrasonic laboratory measurements are assumed. *In-situ* seismic velocities generally will have neither squirt nor Biot dispersion and should be described using Gassmann's equations. Sonic-logging frequencies may or may not be within the range of validity, depending on the rock type and fluid viscosity;
- the rock is isotropic;
- all minerals making up the rock have the same bulk and shear moduli; and
- fluid-bearing rock is completely saturated.

Extensions

The Mavko–Jizba squirt relations can be extended in the following ways:

- for mixed mineralogy, one can usually use an effective average modulus for K_0 ;
- for clay-filled rocks, it often works best to consider the “soft” clay to be part of the pore-filling phase rather than part of the mineral matrix. Then the pore fluid is “mud,” and its modulus can be estimated with an isostress calculation; and
- the anisotropic form of these squirt relations has been found by Mukerji and Mavko (1994) and is discussed in [Section 6.14](#).

6.11 Extension of Mavko–Jizba squirt relations for all frequencies

Synopsis

The Mavko and Jizba (1991) squirt relations (see [Section 6.10](#)) predict the very high-frequency moduli of saturated rocks. At a low frequency, these moduli can be calculated from Gassmann's (1951) equations. Dvorkin *et al.* (1995) introduced

a model for calculating these moduli, velocities, and attenuations at any intermediate frequency. As input, the model uses such experimentally measurable parameters as the dry-rock elastic properties at a given effective pressure, the dry-rock bulk modulus at very high effective pressure, the bulk moduli of the solid and fluid phases, and the rock density and porosity. One additional parameter (Z), which determines the frequency scale of the dispersion, is proportional to the **characteristic squirt-flow length**. This parameter can be found by matching the theoretical velocity to that measured experimentally at a given frequency. Then the theory can be used to calculate velocities and attenuation at any frequency and with any pore fluid. The algorithm for calculating velocities and attenuation at a given frequency follows.

Step 1: Calculate the bulk modulus of the dry modified solid (K_{msd}) from

$$\frac{1}{K_{\text{msd}}} = \frac{1}{K_0} - \frac{1}{K_{\text{dry-hiP}}} + \frac{1}{K_{\text{dry}}}$$

Step 2: Calculate the ratio of the induced pore-pressure increment to the confining-stress increment ($dP/d\sigma$) from

$$\frac{dP}{d\sigma} = - \left[\alpha_0 \left(1 + \frac{\phi K_{\text{dry}}}{\alpha_0^2 F_0} \right) \right]^{-1}$$

where

$$\frac{1}{F_0} = \frac{1}{K_{\text{fl}}} + \frac{1}{\phi Q_0}$$

$$\alpha_0 = 1 - \frac{K_{\text{dry}}}{K_0}$$

$$Q_0 = \frac{K_0}{\alpha_0 - \phi}$$

Step 3: Assume a certain value for the frequency-dispersion parameter Z (start with $Z = 0.001$) and calculate the bulk modulus of the saturated modified solid (K_{ms}) from

$$K_{\text{ms}} = \frac{K_{\text{msd}} + \alpha K_0 [1 - f(\xi)]}{1 + \alpha f(\xi) dP/d\sigma}$$

where

$$\alpha = 1 - \frac{K_{\text{msd}}}{K_0}, \quad f(\xi) = \frac{2J_1(\xi)}{\xi J_0(\xi)}, \quad \xi = Z\sqrt{i\omega}$$

and where ω is angular frequency, and J_0 and J_1 are Bessel functions of zero and first order, respectively.

Step 4: Calculate the bulk modulus of the modified frame (K_m) from

$$\frac{1}{K_m} = \frac{1}{K_{ms}} + \frac{1}{K_{\text{dry-hiP}}} - \frac{1}{K_0}$$

Step 5: Calculate the bulk modulus of the saturated rock (K_r) from

$$K_r = \frac{K_m}{1 + \alpha_m dP/d\sigma}$$

where

$$\alpha_m = 1 - \frac{K_m}{K_{ms}}$$

Step 6: Calculate the shear modulus of the modified frame (μ_m) from

$$\frac{1}{\mu_{\text{dry}}} - \frac{1}{\mu_m} = \frac{4}{15} \left(\frac{1}{K_{\text{dry}}} - \frac{1}{K_{\text{md}}} \right)$$

where

$$\frac{1}{K_{\text{md}}} = \frac{1}{\tilde{K}_{ms}} + \frac{1}{K_{\text{dry-hiP}}} - \frac{1}{K_0}$$

$$\tilde{K}_{ms} = K_{\text{msd}} + \alpha K_0 [1 - f(\xi)]$$

Step 7: Finally, calculate velocities V_P and V_S and inverse quality factors Q_P^{-1} and Q_S^{-1} from

$$V_P = \sqrt{\frac{\text{Re}(K_r + \frac{4}{3}\mu_m)}{\rho}}, \quad V_S = \sqrt{\frac{\text{Re}(\mu_m)}{\rho}}$$

$$Q_P^{-1} = \left| \frac{\text{Im}(K_r + \frac{4}{3}\mu_m)}{\text{Re}(K_r + \frac{4}{3}\mu_m)} \right|, \quad Q_S^{-1} = \left| \frac{\text{Im}(\mu_m)}{\text{Re}(\mu_m)} \right|$$

Step 8: The velocities and inverse quality factors have been found for an assumed Z value (Figure 6.11.1). To find the true Z value, one has to change it until the theoretical value of one of the four parameters (V_P , V_S , Q_P^{-1} , or Q_S^{-1}) matches the experimentally measured value at a given frequency. It is preferred that V_P be used for this purpose. The Z value thus obtained should be used for calculating the velocities and quality factors at varying frequencies. The Z value can also be used for a different pore fluid. In the latter case, use the following value for Z :

$$Z_{\text{new}} = Z \sqrt{\frac{\eta_{\text{new}}}{\eta}}$$

where the subscript *new* indicates the new pore fluid.

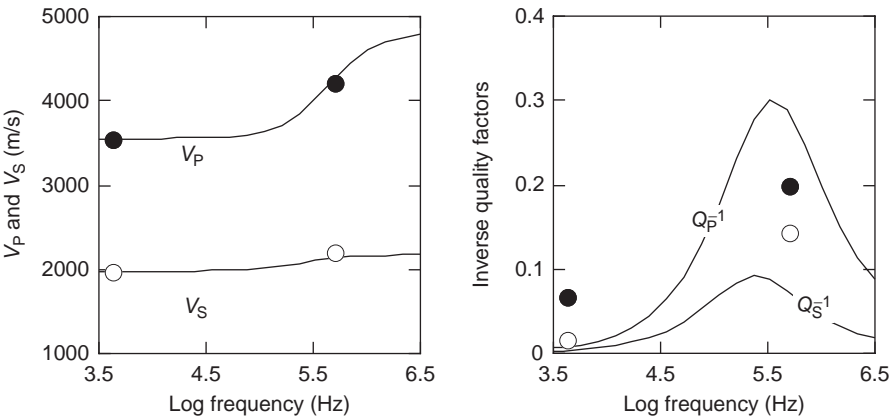


Figure 6.11.1 The V_S and inverse quality factors have been predicted by determining Z from V_P measurements (0.18 porosity limestone). Closed symbols are for P-waves; open symbols are for S-waves.

The notation used is: K_{dry} is the effective bulk modulus of dry rock, $K_{\text{dry-hiP}}$ is the effective bulk modulus of dry rock at very high pressure, K_0 is the bulk modulus of the mineral material making up the rock, K_{fl} is the effective bulk modulus of the pore fluid, η is the viscosity of the pore fluid, ϕ is porosity, μ_{dry} is the effective shear modulus of dry rock, ρ is rock density, and ω is angular frequency.

Uses

The extension of the Mavko–Jizba squirt relations can be used to calculate saturated-rock velocities and attenuation at any frequency.

Assumptions and limitations

The following assumptions underlie the extension of the Mavko–Jizba squirt relations:

- the rock is isotropic;
- all minerals making up the rock have the same bulk and shear moduli; and
- fluid-bearing rock is completely saturated.

Extensions

Additional extensions of the Mavko–Jizba squirt relations include the following:

- for mixed mineralogy, one can usually use an effective average modulus for K_0 ;
- Murphy *et al.* (1984) introduced a micromechanical model to describe the squirt-flow mechanism. They considered a composite grain-contact stiffness, which is the parallel combination of the solid–solid contact stiffness and the stiffness of a fluid-filled gap, shown in Figure 6.11.2.

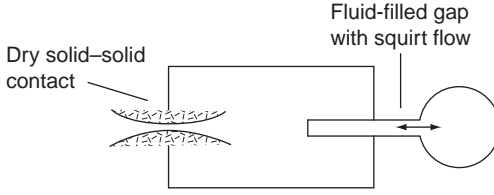


Figure 6.11.2 Schematic of a micromechanical model to describe the squirt-flow mechanism.

When modeling the solid–solid contact, surface energy is taken into account. The hydrodynamic contact model takes into account the squirt flow of pore fluid between a thin crack and a stiff, large pore. The results qualitatively match the observed velocity dispersion and attenuation in sandstones.

6.12 Biot–squirt model

Synopsis

Dvorkin and Nur (1993) and Dvorkin *et al.* (1994) introduced a unified Biot–squirt (BISQ) model. The model is applicable to rocks at high pressure with compliant cracks closed. The rock is partially saturated or apparently fully saturated (meaning that there are small, undetectable amounts of free gas left in pores). The zero-frequency velocity limit, as given by BISQ, is

$$V_{P0} = \sqrt{\frac{M_{\text{dry}}}{\rho}}$$

The M_{dry} term is the dry-rock uniaxial-strain modulus ($M_{\text{dry}} = \rho_{\text{dry}} V_{P-\text{dry}}^2$), ρ is rock density (at saturation), and $V_{P-\text{dry}}$ and ρ_{dry} are the dry-rock P-wave velocity and density, respectively. The BISQ high-frequency velocity limit is the same as in the Biot theory.

BISQ gives the following expressions for P-wave velocity (V_P), the attenuation coefficient (a_P), and the inverse quality factor (Q_P^{-1}) at **apparently full saturation**:

$$V_P = \frac{1}{\text{Re}(\sqrt{Y})}, \quad a_P = \omega \text{Im}(\sqrt{Y}), \quad Q_P^{-1} = \frac{2a_P V_P}{\omega}$$

$$Y = -\frac{B}{2A} - \sqrt{\left(\frac{B}{2A}\right)^2 - \frac{C}{A}}, \quad A = \frac{\phi F_{\text{sq}} M_{\text{dry}}}{\rho_2^2}$$

$$B = \left[F_{\text{sq}} \left(2\gamma - \phi - \phi \frac{\rho_1}{\rho_2} \right) - \left(M_{\text{dry}} + F_{\text{sq}} \frac{\gamma^2}{\phi} \right) \left(1 + \frac{\rho_a}{\rho_2} + i \frac{\omega_c}{\omega} \right) \right] / \rho_2$$

$$C = \frac{\rho_1}{\rho_2} + \left(1 + \frac{\rho_1}{\rho_2} \right) \left(\frac{\rho_a}{\rho_2} + i \frac{\omega_c}{\omega} \right), \quad F_{\text{sq}} = F \left[1 - \frac{2J_1(\lambda R)}{\lambda R J_0(\lambda R)} \right]$$

$$\lambda^2 = \frac{\rho_{\text{fl}} \omega^2}{F} \left(\frac{\phi + \rho_{\text{a}}/\rho_{\text{fl}}}{\phi} + i \frac{\omega_{\text{c}}}{\omega} \right), \quad \rho_1 = (1 - \phi)\rho_{\text{s}}, \quad \rho_2 = \phi\rho_{\text{fl}}$$

$$\omega_{\text{c}} = \frac{\eta\phi}{k\rho_{\text{fl}}}, \quad \gamma = 1 - \frac{K_{\text{dry}}}{K_0}, \quad \frac{1}{F} = \frac{1}{K_{\text{fl}}} + \frac{1}{\phi K_0} \left(1 - \phi - \frac{K_{\text{dry}}}{K_0} \right)$$

where R is the **characteristic squirt-flow length**, ϕ is porosity, ρ_{s} and ρ_{fl} are the solid-phase and fluid-phase densities, respectively; $\rho_{\text{a}} = (1 - \alpha)\phi\rho_{\text{fl}}$ is the Biot inertial-coupling density; η is the pore-fluid viscosity; k is rock permeability; K_{dry} is the dry-rock bulk modulus; K_0 and K_{fl} are the solid-phase and the fluid-phase bulk moduli, respectively; ω is the angular frequency; and J_0 and J_1 are Bessel functions of zero and first order, respectively. The tortuosity α (sometimes called the structure factor) is a purely geometrical factor independent of the solid or fluid densities and is always greater than 1 (see Section 6.1).

All input parameters, except for the **characteristic squirt-flow length**, are experimentally measurable. The latter has to be either guessed (it should have the same order of magnitude as the average grain size or the average crack length) or adjusted by using an experimental measurement of velocity versus frequency (see Section 6.11).

For **partially saturated** rock at saturation S ,

$$R_{\text{s}} = R\sqrt{S}$$

has to be used instead of R in the preceding formulas. To avoid numerical problems (caused by resonance) at high frequencies,

$$\lambda^2 = i \frac{\rho_{\text{fl}} \omega \omega_{\text{c}}}{F}$$

can be used instead of

$$\lambda^2 = \frac{\rho_{\text{fl}} \omega^2}{F} \left(\frac{\phi + \rho_{\text{a}}/\rho_{\text{fl}}}{\phi} + i \frac{\omega_{\text{c}}}{\omega} \right)$$

At lower frequencies, $\omega_{\text{c}}/\omega \gg 1$, the following simplified formulas can be used:

$$Y = \frac{(1 - \phi)\rho_{\text{s}} + \phi\rho_{\text{fl}}}{M_{\text{dry}} + F_{\text{sq}}\gamma^2/\phi}, \quad F_{\text{sq}} = F \left[1 - \frac{2J_1(\xi)}{\xi J_0(\xi)} \right]$$

$$\xi = \sqrt{i \frac{R^2 \omega}{\kappa}}, \quad \kappa = \frac{kF}{\eta\phi}$$

The BISQ formulas give the Biot theory expressions for the velocity and attenuation if $F_{\text{sq}} = F$.

Uses

The BISQ formulas can be used to calculate partially saturated rock velocities and attenuation (at high pressure) at any frequency.

Assumptions and limitations

The BISQ formulas are based on the following assumptions:

- the rock is isotropic;
- all minerals making up the rock have the same bulk and shear moduli.

In the low-frequency limit, the BISQ formulas are not consistent with the Gassmann predictions.

Extensions

- For mixed mineralogy, one can usually use an effective average modulus for K_0 .

6.13 Chapman *et al.* squirt model

Synopsis

Chapman *et al.* (2002) presented a *squirt* or *local flow* model that considers frequency-dependent, wave-induced exchange of fluids between pores and cracks, as well as between cracks of different orientations. The cracks are idealized as oblate spheroids with small aspect ratio r , uniform crack radius a , and crack density ε . The pores are considered to be spherical. The bulk and shear moduli and Lamé parameter of the solid mineral matrix (rock without cracks or pores) are denoted by K , μ , and λ , respectively, while the fluid bulk modulus is K_f . The total porosity is ϕ .

The frequency-dependent effective bulk and shear moduli, K_{eff} and μ_{eff} , are expressed as follows (Chapman *et al.*, 2006):

$$K_{\text{eff}} = K - \varepsilon \left\{ \frac{4(3\lambda + 2\mu)(\lambda + 2\mu)}{\mu(\lambda + \mu)} [1 - 3A(\omega)] - 4\pi r A(\omega) \right\} \\ - \phi \left\{ \frac{3\lambda + 2\mu}{4\mu} \left[\frac{\lambda + 2\mu}{3\lambda + 2\mu} + B(\omega) \right] - 3B(\omega) \right\}$$

and

$$\mu_{\text{eff}} = \mu - \frac{16}{45} \varepsilon \frac{1}{1 + K_c} \frac{\mu(\lambda + 2\mu)}{3\lambda + 4\mu} \left(K_c + \frac{1}{1 + i\omega\tau} \right) - \frac{32}{45} \varepsilon \frac{\mu(\lambda + 2\mu)}{3\lambda + 4\mu} \\ - \phi \frac{15\mu(\lambda + 2\mu)}{9\lambda + 14\mu}$$

where ω is the angular frequency, and the other parameters are

$$A(\omega) = \frac{(1 + i\omega\gamma\tau) \frac{\lambda+2\mu}{\lambda+\mu} \left[\frac{16\varepsilon}{27\phi(1+K_p)} + \frac{\lambda+\mu}{3\lambda+2\mu} \right] + i\omega\tau \left[\frac{1}{3(1+K_c)} - \gamma' \right]}{1 + i\omega\tau + (1 + i\omega\gamma\tau) \frac{16\varepsilon(1+K_c)}{9\phi(1+K_p)} \frac{\lambda+2\mu}{\lambda+\mu}}$$

$$B(\omega) = \frac{\frac{1}{3(1+K_c)} + \frac{9(1+K_p)}{16(1+K_c)} \frac{(\lambda+\mu)}{(3\lambda+2\mu)} + \frac{i\omega\tau}{1+i\omega\tau} \left[\gamma' - \frac{1}{3(1+K_c)} \right]}{\frac{9(1+K_p)}{16(1+K_c)} \frac{(\lambda+\mu)}{(3\lambda+2\mu)} + \frac{1+i\omega\tau}{1+i\omega\tau}}$$

$$\gamma' = \gamma \frac{\lambda + 2\mu}{(3\lambda + 2\mu)(1 + K_p)}$$

$$\gamma = \frac{3\pi(\lambda + \mu)(1 + K_p)}{4(\lambda + 2\mu)(1 + K_c)}$$

$$K_p = \frac{4\mu}{3K_f}$$

and

$$K_c = \frac{\pi\mu r(\lambda + \mu)}{K_f(\lambda + 2\mu)}$$

The timescale parameter τ controls the frequency regime over which the dispersion occurs. It is proportional to the fluid viscosity η and inversely proportional to the permeability k , and depends on the crack radius a . For small aspect ratios ($r < 10^{-3}$), τ is approximately given by

$$\tau \approx \frac{4\eta a^3(1 - \nu)}{9k\zeta\mu}$$

where ζ is a characteristic grain size, and ν is the Poisson ratio of the solid mineral.

One of the requirements for any model of fluid-related dispersion is that in the low-frequency limit the predictions should be consistent with the Gassmann equations. The Chapman *et al.* (2002) formulas are consistent with the Gassmann predictions in the low-frequency limit, whereas the BISQ model (Dvorkin and Nur, 1993) and the equant porosity model (Hudson *et al.*, 1996) are not.

Uses

The formulas can be used to calculate squirt-related velocity dispersion and attenuation at any frequency.

Assumptions and limitations

The formulas assume idealized spherical pores and penny-shaped crack geometry, with all cracks having the same radius:

- the rock is isotropic;
- all minerals making up the rock have the same bulk and shear moduli.

Extensions

- The formulation has been extended to meso-scale aligned fractures with coupled fluid motion at two scales (Chapman, 2003).

6.14 Anisotropic squirt

Synopsis

The *squirt* or *local flow* model suggests that the fluctuating stresses in a rock caused by a passing seismic wave induce pore-pressure gradients at virtually all scales of pore-space heterogeneity – particularly on the scale of individual grains and pores. These gradients impact the viscoelastic behavior of the rock; at high frequencies, when the gradients are unrelaxed, all elastic moduli will be stiffer than at low frequencies, when the gradients are relaxed. (The latter case is modeled by the anisotropic Gassmann and Brown and Korrington (1975) formalisms.) Mukerji and Mavko (1994) derived simple theoretical formulas for predicting the very high-frequency compliances of saturated anisotropic rocks in terms of the pressure dependence of dry rocks. The prediction is made in two steps: first, the squirt effect is incorporated as high-frequency “wet-frame compliances” $S_{ijkl}^{(\text{wet})}$, which are derived from the dry compliances $S_{ijkl}^{(\text{dry})}$. Then these wet-frame compliances are substituted into the Gassmann (Section 6.3), Brown and Korrington (see Section 6.4) or Biot relations (see Section 6.1) (in place of the dry compliances) to incorporate the remaining fluid saturation effects. For most crustal rocks, the amount of squirt dispersion is comparable to or greater than Biot’s dispersion, and thus using Biot’s theory alone will lead to poor predictions of high-frequency saturated velocities. Exceptions include very high permeability materials such as ocean sediments and glass beads, rocks at very high effective pressure, when most of the soft, crack-like porosity is closed, and rocks near free boundaries such as borehole walls.

The wet-frame compliance is given by (repeated indices imply summation)

$$S_{ijkl}^{(\text{wet})} \approx S_{ijkl}^{(\text{dry})} - \frac{\Delta S_{\alpha\alpha\beta\beta}^{(\text{dry})}}{1 + \phi_{\text{soft}}(\beta_f - \beta_0)/\Delta S_{\gamma\gamma\delta\delta}^{(\text{dry})}} G_{ijkl}$$

where $\Delta S_{ijkl}^{(\text{dry})} = S_{ijkl}^{(\text{dry})} - S_{ijkl}^{(\text{dry high P})}$ is the change in dry compliance between the pressure of interest and very high confining pressure, ϕ_{soft} is the soft porosity that closes under high confining pressure, and β_f and β_0 are the fluid and mineral compressibilities, respectively. The soft porosity is often small enough that the second term in the denominator can be ignored. The tensor G_{ijkl} represents the fraction of the total compliance that is caused by volumetric deformation of crack-like pore space with different orientations for a given externally applied load. The tensor depends on the symmetry of the crack distribution function and is expressed as an integral over all orientations:

$$G_{ijkl} = \int f(\Omega) n_i n_j n_k n_l d\Omega$$

where $f(\Omega)$ is the crack-orientation distribution function normalized so that its integral over all angles equals unity, and n_i is the unit normal to the crack faces. Elements of

Table 6.14.1 Elements of the tensor G_{ijkl} for isotropic symmetry.

ij	11	22	33	23	13	12
kl						
11	1/5	1/15	1/15	0	0	0
22	1/15	1/5	1/15	0	0	0
33	1/15	1/15	1/5	0	0	0
23	0	0	0	1/15	0	0
13	0	0	0	0	1/15	0
12	0	0	0	0	0	1/15

G_{ijkl} with any permutation of a given set $ijkl$ are equal. Note that G_{ijkl} has more symmetries than the elastic compliance tensor. For **isotropic** symmetry, the elements of G_{ijkl} are given by the Table 6.14.1.

Table 6.14.1 gives exactly the same result as the isotropic equations of Mavko and Jizba (1991) presented in Section 6.10.

When the rock is **transversely isotropic** with the 3-axis as the axis of rotational symmetry, the five independent components of G_{ijkl} are

$$G_{1111} = \Delta\tilde{S}_{1111}^{(\text{dry})} - \frac{4\alpha}{1-4\alpha} [\Delta\tilde{S}_{1122}^{(\text{dry})} + \Delta\tilde{S}_{1133}^{(\text{dry})}]$$

$$G_{1122} = \frac{\Delta\tilde{S}_{1122}^{(\text{dry})}}{1-4\alpha}$$

$$G_{1133} = \frac{\Delta\tilde{S}_{1133}^{(\text{dry})}}{1-4\alpha}$$

$$G_{3333} = \Delta\tilde{S}_{3333}^{(\text{dry})} - \frac{8\alpha\Delta\tilde{S}_{1133}^{(\text{dry})}}{1-4\alpha}$$

$$G_{2323} = \frac{\Delta\tilde{S}_{2323}^{(\text{dry})}}{1-4\alpha} - \frac{\Delta\tilde{S}_{1111}^{(\text{dry})} + \Delta\tilde{S}_{3333}^{(\text{dry})}}{4(1-4\alpha)} + \frac{G_{1111} + G_{3333}}{4}$$

The nine independent components of G_{ijkl} for **orthorhombic** symmetry are

$$G_{1111} = \Delta\tilde{S}_{1111}^{(\text{dry})} - \frac{4\alpha}{1-4\alpha} [\Delta\tilde{S}_{1122}^{(\text{dry})} + \Delta\tilde{S}_{1133}^{(\text{dry})}]$$

$$G_{2222} = \Delta\tilde{S}_{2222}^{(\text{dry})} - \frac{4\alpha}{1-4\alpha} [\Delta\tilde{S}_{1122}^{(\text{dry})} + \Delta\tilde{S}_{2233}^{(\text{dry})}]$$

$$G_{3333} = \Delta\tilde{S}_{3333}^{(\text{dry})} - \frac{4\alpha}{1-4\alpha} [\Delta\tilde{S}_{1133}^{(\text{dry})} + \Delta\tilde{S}_{2233}^{(\text{dry})}]$$

$$G_{1122} = \frac{\Delta\tilde{S}_{1122}^{(\text{dry})}}{1-4\alpha}$$

$$G_{1133} = \frac{\Delta \tilde{S}_{1133}^{(\text{dry})}}{1 - 4\alpha}$$

$$G_{2233} = \frac{\Delta \tilde{S}_{2233}^{(\text{dry})}}{1 - 4\alpha}$$

$$G_{2323} = \frac{\Delta \tilde{S}_{2323}^{(\text{dry})}}{1 - 4\alpha} - \frac{\Delta \tilde{S}_{2222}^{(\text{dry})} + \Delta \tilde{S}_{3333}^{(\text{dry})}}{4(1 - 4\alpha)} + \frac{G_{2222} + G_{3333}}{4}$$

$$G_{1313} = \frac{\Delta \tilde{S}_{1313}^{(\text{dry})}}{1 - 4\alpha} - \frac{\Delta \tilde{S}_{1111}^{(\text{dry})} + \Delta \tilde{S}_{3333}^{(\text{dry})}}{4(1 - 4\alpha)} + \frac{G_{1111} + G_{3333}}{4}$$

$$G_{1212} = \frac{\Delta \tilde{S}_{1212}^{(\text{dry})}}{1 - 4\alpha} - \frac{\Delta \tilde{S}_{1111}^{(\text{dry})} + \Delta \tilde{S}_{2222}^{(\text{dry})}}{4(1 - 4\alpha)} + \frac{G_{1111} + G_{2222}}{4}$$

where

$$\Delta \tilde{S}_{ijkl}^{(\text{dry})} = \frac{\Delta S_{ijkl}^{(\text{dry})}}{\Delta S_{\gamma\gamma\beta\beta}^{(\text{dry})}}$$

$$\alpha = \frac{1}{4}(\Delta \tilde{S}_{\gamma\beta\gamma\beta}^{(\text{dry})} - 1)$$

Computed from the dry data, α is the ratio of the representative shear-to-normal compliance of a crack set, including all elastic interactions with other cracks. When the orthorhombic anisotropy is due to three mutually perpendicular crack sets, superposed on a general orthorhombic background, with the crack normals along the three symmetry axes, the wet-frame compliances are obtained from

$$\begin{aligned} S_{ijkl}^{(\text{dry})} - S_{ijkl}^{(\text{wet})} \approx & \frac{\Delta S_{1111}^{(\text{dry})}}{1 + \phi_{\text{soft}}^{(1)}(\beta_f - \beta_0)/\Delta S_{1111}^{(\text{dry})}} \delta_{i1} \delta_{j1} \delta_{k1} \delta_{l1} \\ & + \frac{\Delta S_{2222}^{(\text{dry})}}{1 + \phi_{\text{soft}}^{(2)}(\beta_f - \beta_0)/\Delta S_{2222}^{(\text{dry})}} \delta_{i2} \delta_{j2} \delta_{k2} \delta_{l2} \\ & + \frac{\Delta S_{3333}^{(\text{dry})}}{1 + \phi_{\text{soft}}^{(3)}(\beta_f - \beta_0)/\Delta S_{3333}^{(\text{dry})}} \delta_{i3} \delta_{j3} \delta_{k3} \delta_{l3} \end{aligned}$$

where δ_{ij} is the Kronecker delta, and $\phi_{\text{soft}}^{(i)}$ refers to the soft porosity caused by the i th crack set. The above expressions assume that the intrinsic compliance tensor of planar crack-like features is sparse, the largest components being the normal and shear compliances, whereas the other components are approximately zero. This general property of planar crack formulations reflects an approximate decoupling of normal and shear deformation of the crack and decoupling of the in-plane and out-of-plane compressive deformation. In the case of a *single crack set* (with crack normals along

the 3-axis) the wet-frame compliances can be calculated from the dry compliances for a completely general, nonsparse crack compliance as

$$S_{ijkl}^{(\text{wet})} = S_{ijkl}^{(\text{dry})} - \frac{\Delta S_{\lambda\lambda ij}^{(\text{dry})} \Delta S_{\eta\eta kl}^{(\text{dry})}}{\Delta S_{\gamma\gamma\delta\delta}^{(\text{dry})} + \phi_{\text{soft}}(\beta_f - \beta_0)}$$

Little or no change of the $\Delta S_{1111}^{(\text{dry})}$ and $\Delta S_{2222}^{(\text{dry})}$ dry compliances with stress would indicate that all the soft, crack-like porosity is aligned normal to the 3-axis. However, a rotationally symmetric distribution of cracks may often be a better model of crack-induced transversely isotropic rocks than just a single set of aligned cracks. In this case the equations in terms of G_{ijkl} should be used.

The anisotropic squirt formulation presented here does not assume any idealized crack geometries. Because the high-frequency saturated compliances are predicted entirely in terms of the measured dry compliances, the formulation automatically incorporates all elastic pore interactions, and there is no limitation to low crack density.

Although the formulation presented here is independent of any idealized crack shape, the squirt behavior is also implicit in virtually all published formulations for effective moduli based on elliptical cracks (see [Sections 4.7–4.11](#)). In most of those models, the cavities are treated as isolated with respect to flow, thus simulating the high-frequency limit of the squirt model.

Uses

The anisotropic squirt formulation can be used to calculate high-frequency, saturated-rock velocities from dry-rock velocities.

Assumptions and limitations

The use of the anisotropic squirt formulation requires the following considerations:

- high seismic frequencies ideally suited for ultrasonic laboratory measurements are assumed. *In-situ* seismic velocities will generally have neither squirt nor Biot dispersion and should be described by using Brown and Korrington equations. Sonic-logging frequencies may or may not be within the range of validity, depending on the rock type and fluid viscosity;
- all minerals making up rock have the same compliances; and
- fluid-bearing rock is completely saturated.

Extensions

The following extensions of the anisotropic squirt formulation can be made:

- for mixed mineralogy, one can usually use an effective average modulus for β_0 ;
- for clay-filled rocks, it often works best to consider the “soft” clay to be part of the pore-filling phase rather than part of the mineral matrix. The pore fluid is then “mud,” and its modulus can be estimated with an isostress calculation.

6.15 Common features of fluid-related velocity dispersion mechanisms

Synopsis

Many physical mechanisms have been proposed and modeled to explain velocity dispersion and attenuation in rocks: scattering (see Section 3.14), viscous and inertial fluid effects (see Sections 6.1, 6.2, and 6.10–6.19), hysteresis related to surface forces, thermoelastic effects, phase changes, and so forth. Scattering and surface forces appear to dominate in dry or nearly dry conditions (Tutuncu, 1992; Sharma and Tutuncu, 1994). Viscous fluid mechanisms dominate when there is more than a trace of pore fluids, such as in the case of the poroelasticity described by Biot (1956) and the local flow or squirt mechanism (Stoll and Bryan, 1970; Mavko and Nur, 1975; O’Connell and Budiansky, 1977; Stoll, 1989; Dvorkin and Nur, 1993). Extensive reviews of these were given by Knopoff (1964), Mavko, Kjartansson, and Winkler (1979), and Bourbié *et al.* (1987), among others. Extensive reviews of these were given by Winkler (1985, 1986).

This section highlights some features that attenuation–dispersion models have in common. These suggest a simple approach to analyzing dispersion, bypassing some of the complexity of the individual theories, complexity that is often not warranted by available data.

Although the various dispersion mechanisms and their mathematical descriptions are distinct, most can be described by the following three key parameters (see Figure 6.15.1):

1. a **low-frequency** limiting velocity V_0 (or modulus, M_0) often referred to as the “relaxed” state;
2. a **high-frequency** limiting velocity V_∞ (or modulus, M_∞) referred to as the “unrelaxed” state;
3. a **characteristic frequency**, f_c , that separates high-frequency behavior from low-frequency behavior and specifies the range in which velocity changes most rapidly.

High- and low-frequency limits

Of the three key parameters, usually the low- and high-frequency limits can be estimated most easily. These require the fewest assumptions about the rock micro-geometry and are, therefore, the most robust. In rocks, the velocity (or modulus) generally increases with frequency (though not necessarily monotonically in the case of scattering), and thus $M_\infty > M_0$. The total amount of dispersion between very low-frequency and very high-frequency $(M_\infty - M_0)/M = \Delta M/M$ is referred to as the **modulus defect** (Zener, 1948), where $M = \sqrt{M_0 M_\infty}$.

One of the first steps in analyzing any dispersion mechanism should be to estimate the modulus defect to see whether the effect is large enough to warrant any additional modeling. In most situations all but one or two mechanisms can be eliminated based on the size of the modulus defect alone.

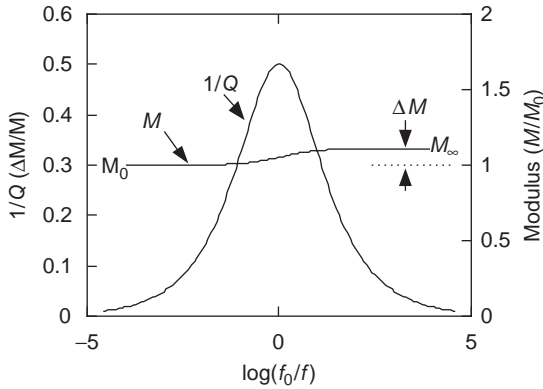


Figure 6.15.1 Key parameters in various dispersion mechanisms: M_0 , the low-frequency limiting modulus, M_∞ , the high-frequency limiting modulus, and f_c , the characteristic frequency separating high- and low-frequency behavior.

As an example, consider the local flow or squirt mechanism, which is discussed in Sections 6.10–6.14 and 6.17. The squirt model recognizes that natural heterogeneities in pore stiffness, pore orientation, fluid compressibility, and saturation can cause spatial variations in wave-induced pore pressures at the pore scale. At sufficiently low frequencies, there is time for the fluid to flow and eliminate these variations; hence, the very low-frequency limiting bulk and shear moduli can be predicted by Gassmann's theory (Section 6.3), or by Brown and Korringa's theory (Section 6.5) if the rock is anisotropic. At high frequencies, the pore-pressure variations persist, causing the rock to be stiffer. The high-frequency limiting moduli may be estimated from dry-rock data using the Mavko and Jizba method (Section 6.10). These low- and high-frequency limits are relatively easy to estimate and require minimum assumptions about pore microgeometry. In contrast, calculating the detailed frequency variation between the low- and high-frequency regimes requires estimates of the pore aspect-ratio or throat-size distributions.

Other simple estimates of the high- and low-frequency limits associated with the squirt mechanism can be made by using ellipsoidal crack models such as the Kuster and Toksöz model (Section 4.7), the self-consistent model (Section 4.8), the DEM model (Section 4.9), or Hudson's model (Section 4.10). In each case, the *dry rock* is modeled by setting the inclusion moduli to zero. The *high-frequency saturated* rock conditions are simulated by assigning fluid moduli to the inclusions. Because each model treats the cavities as isolated with respect to flow, this yields the unrelaxed moduli for squirt. The *low-frequency saturated* moduli are found by taking the model-predicted effective moduli for dry cavities and saturating them with the Gassmann low-frequency relations (see Section 6.3).

The characteristic frequency is also simple to estimate for most models but usually depends more on poorly determined details of grain and pore microgeometry. Hence, the estimated critical frequency is usually less robust. Table 6.15.1 summarizes

Table 6.15.1 *High- and low-frequency limits and characteristic frequency of dispersion mechanisms.*

Mechanism ^a	Low-frequency limit ^a	High-frequency limit ^a	Characteristic frequency (f_c)
Biot [6.1] Squirt [6.10–6.14]	Gassmann's relations [6.3]	Biot's high-frequency formula [6.1]	$f_{\text{Biot}} \approx \phi\eta/2\pi\rho\eta\kappa$
^b	Gassmann's relations [6.3]	Mavko–Jizba relations [6.10]	$f_{\text{squirt}} \approx K_0\alpha^3/\eta$
^c	Kuster–Toksöz dry relations [4.7] → Gassmann	Kuster–Toksöz saturated relations	“
^c	DEM dry relations [4.9] → Gassmann	DEM saturated relations	“
^c	Self-consistent dry relations [4.8] → Gassmann	Self-consistent saturated relations	“
^d	Hudson's dry relations [4.10] → Brown and Korrington [6.5]	Hudson's saturated relations	“
Patchy saturation [6.17, 6.18]			
^e	Gassmann's relations [6.3]	Hill equation [4.5]	$f_{\text{patchy}} \approx \kappa/L^2\eta(\beta_p + \beta_n)$
^f	Gassmann's relations [6.3]	White high-frequency formula [6.18]	$f_{\text{patchy}} \approx \kappa K_s/\pi L^2\eta$
^g	Generalized Gassmann's relations [6.6]	Dutta–Odé high-frequency formula [6.18]	“
Viscous shear	^h	^h	$f_{\text{visc.crack}} \approx \eta\mu/2\pi\eta$
Scattering [3.10–3.14]			
ⁱ	Effective medium theory [4.1–4.15]	Ray theory [3.11–3.13]	$f_{\text{scatter}} \approx V/2\pi\alpha$
^j	Backus average [4.13]	Time average [3.11–3.13]	“

^a Numbers in brackets [] refer to sections in this book.

^b Inputs are measured dry-rock moduli; no idealized pore geometry.

^c Pore space is modeled as idealized ellipsoidal cracks.

^d Anisotropic rock modeled as idealized penny-shaped cracks with preferred orientations.

^e Dry rock is homogeneous; saturation has arbitrarily shaped patches.

^f Dry rock is homogeneous; saturation is in spherical patches. Same limits as ^e.

^g Dry rock can be heterogeneous; saturation is in spherical patches.

^h The mechanism modeled by Walsh (1969) is related to shearing of penny-shaped cracks with viscous fluids. Interesting only for extremely high viscosity or extremely high frequency.

ⁱ General heterogeneous three-dimensional medium.

^j Normal-incidence propagation through a layered medium.

ϕ = porosity, L = characteristic size (or correlation length), K_0 , μ = bulk and shear moduli of mineral of saturation heterogeneity, K_s = saturated rock modulus, ρ_n = density of the pore fluid, β_n = compressibility of the pore fluid, η = viscosity of the pore space, α = pore aspect ratio, a = characteristic size (or correlation length) of scatterers, κ = rock permeability, V = wave velocity at f_c .

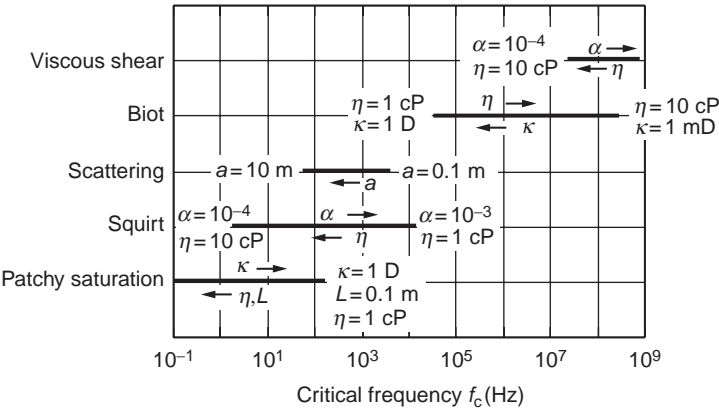


Figure 6.15.2 Comparison of characteristic frequencies for typical rock and fluid parameters. Arrows show the direction of change as the labeled parameter increases.

approaches to estimating the low-frequency moduli, high-frequency moduli, and characteristic frequencies for five important categories of velocity dispersion and attenuation.

Each mechanism shown in the table has an f_c value that depends on poorly determined parameters. The Biot (see Section 6.1) and patchy (see Section 6.17) models depend on the permeability. The squirt (see Sections 6.10–6.14) and viscous shear (Walsh, 1969) models require the crack aspect ratio. Furthermore, the formula for f_c -squirt is only a rough approximation, for the dependence on α^3 is of unknown reliability. The patchy-saturation (see Section 6.17) and scattering (see Sections 3.10–3.14) models depend on the scale of saturation and scattering heterogeneities. Unlike the other parameters, which are determined by grain and pore size, saturation and scattering can involve all scales, ranging from the pore scale to the basin scale.

Figure 6.15.2 compares some values for f_c predicted by the various expressions in the table. The following parameters (or ranges of parameters) were used:

- $\phi = 0.2$ = porosity
- $\rho_f = 1.0 \text{ g/cm}^3$ = fluid density
- $\eta = 1\text{--}10 \text{ cP}$ = fluid viscosity
- $\kappa = 1\text{--}1000 \text{ mD}$ = permeability
- $\alpha = 10^{-3}\text{--}10^{-4}$ = crack aspect ratio
- $V = 3500 \text{ m/s}$ = wave velocity
- $a, L = 0.1\text{--}10 \text{ m}$ = characteristic scale of heterogeneity
- $\mu = 17 \text{ GPa}$ = rock shear modulus
- $K = 18 \text{ GPa}$ = rock bulk modulus

Caution

Other values for rock and fluid parameters can change f_c considerably.

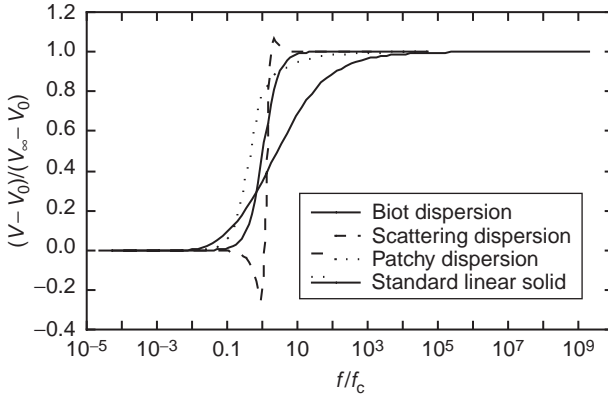


Figure 6.15.3 Comparison of the complete *normalized* velocity-versus-frequency dependence predicted by the Biot, patchy-saturation, and scattering models.

Complete frequency dependence

Figure 6.15.3 compares the complete *normalized* velocity-versus-frequency dependence predicted by the Biot, patchy-saturation, and scattering models. Although there are differences, each follows roughly the same trend from the low-frequency limits to the high-frequency limits, and the most rapid transition is in the range $f \approx f_c$. This is not always strictly true for the Biot mechanism, where certain combinations of parameters can cause the transition to occur at frequencies far from f_{Biot} . All are qualitatively similar to the dispersion predicted by the standard linear solid (see Section 3.8):

$$\text{Re}(M(\omega)) = \frac{M_0 M_\infty [1 + (f/f_c)^2]}{M_\infty + (f/f_c)^2 M_0}$$

Because the value of f_c and the resulting curves depend on poorly determined parameters, we suggest that a simple and practical way to estimate dispersion curves is to use the standard linear solid. The uncertainty in the rock microgeometry, permeability, and heterogeneous scales – as well as the approximations in the theories themselves – often makes a more detailed analysis unwarranted.

Attenuation

The Kramers–Kronig relations (see Section 3.9) completely specify the relation between velocity dispersion and attenuation. If velocity is known for all frequencies, then attenuation is determined for all frequencies. The attenuation versus frequency for the standard linear solid is given by

$$\frac{1}{Q} = \frac{M_\infty - M_0}{\sqrt{M_\infty M_0}} \frac{f/f_c}{1 + (f/f_c)^2}$$

Similarly, it can be argued (see [Section 3.8](#)) that, in general, the order of magnitude of attenuation can be determined from the modulus defect:

$$\frac{1}{Q} \approx \frac{M_\infty - M_0}{\sqrt{M_\infty M_0}}$$

Uses

The preceding simplified relations can be used to estimate velocity dispersion and attenuation in rocks.

Assumptions and limitations

This discussion is based on the premise that difficulties in measuring attenuation and velocity dispersion, and in estimating aspect ratios, permeability, and heterogeneous scales, often make detailed analysis of dispersion unwarranted. Fortunately, much about attenuation–dispersion behavior can be estimated robustly from the high- and low-frequency limits and the characteristic frequency of each physical mechanism.

6.16 Dvorkin–Mavko attenuation model

Synopsis

Dvorkin and Mavko (2006) present a theory for calculating the P- and S-wave inverse quality factors (Q_P^{-1} and Q_S^{-1} , respectively) at partial and full saturation. The basis for the quality factor estimation is the standard linear solid (SLS) model ([Section 3.8](#)) that links the inverse quality factor Q^{-1} to the corresponding elastic modulus M versus frequency f dispersion as

$$Q^{-1}(f) = \frac{(M_\infty - M_0)(f/f_c)}{\sqrt{M_0 M_\infty}[1 + (f/f_c)^2]}$$

where M_0 and M_∞ are the low- and high-frequency limits of the modulus M , respectively; and f_c is the critical frequency at which the inverse quality factor is maximum.

Partial water saturation

Consider rock in which K_{dry} is the bulk modulus of the dry frame of the rock; K_{mineral} is the bulk modulus of the mineral phase; and ϕ is the total porosity. Its bulk modulus at partial water saturation S_w is (according to Gassmann's equation)

$$K_0 = K_{\text{mineral}} \frac{\phi K_{\text{dry}} - (1 + \phi) K_{\text{fl}} K_{\text{dry}} / K_{\text{mineral}} + K_{\text{fl}}}{(1 - \phi) K_{\text{fl}} + \phi K_{\text{mineral}} - K_{\text{fl}} K_{\text{dry}} / K_{\text{mineral}}}$$

where K_{fl} is the bulk modulus of the pore fluid which is a *uniform* mixture of water with the bulk modulus K_W and hydrocarbon (e.g., gas) with the bulk modulus K_G :

$$\frac{1}{K_{fl}} = \frac{S_W}{K_W} + \frac{1 - S_W}{K_G}$$

Then the compressional modulus M_0 is obtained from K_0 and the shear modulus of the dry frame μ_{dry} as

$$M_0 = K_0 + \frac{4}{3}\mu_{dry}$$

Alternatively, to obtain M_0 , one may use the approximate V_P -only fluid-substitution equation with the dry-frame compressional modulus M_{dry} and the mineral-phase compressional modulus $M_{mineral}$:

$$M_0 = M_{mineral} \frac{\phi M_{dry} - (1 + \phi)K_{fl}M_{dry}/M_{mineral} + K_{fl}}{(1 - \phi)K_{fl} + \phi M_{mineral} - K_{fl}M_{dry}/M_{mineral}}$$

The compressional modulus M_0 thus obtained (either by Gassmann's equation or V_P -only fluid-substitution) is considered the low-frequency limit of the compressional modulus M .

The high-frequency limit of the compressional modulus M_∞ is calculated using the patchy-saturation equations (Section 6.17). It is assumed that the difference between M_0 and M_∞ is nonzero only at water saturation larger than the irreducible water saturation S_{irr} . For $S_W \leq S_{irr}$, $M_\infty = M_0$, i.e., $Q_P^{-1} = 0$.

For $S_W > S_{irr}$

$$\frac{1}{K_\infty + \frac{4}{3}\mu_{dry}} = \frac{(S_W - S_{irr})/(1 - S_{irr})}{K_P + \frac{4}{3}\mu_{dry}} + \frac{(1 - S_W)/(1 - S_{irr})}{K_{mineral-irr} + \frac{4}{3}\mu_{dry}}$$

where

$$K_P = K_{mineral} \frac{\phi K_{dry} - (1 + \phi)K_W K_{dry}/K_{mineral} + K_W}{(1 - \phi)K_W + \phi K_{mineral} - K_W K_{dry}/K_{mineral}}$$

$$K_{mineral-irr} = K_{mineral} \frac{\phi K_{dry} - (1 + \phi)K_{fl-irr} K_{dry}/K_{mineral} + K_{fl-irr}}{(1 - \phi)K_{fl-irr} + \phi K_{mineral} - K_{fl-irr} K_{dry}/K_{mineral}}$$

$$\frac{1}{K_{fl-irr}} = \frac{S_{irr}}{K_W} + \frac{1 - S_{irr}}{K_G}$$

Then the high-frequency limit of the compressional modulus M_∞ is

$$M_\infty = K_\infty + \frac{4}{3}\mu_{dry}$$

and the inverse P-wave quality factor Q_P^{-1} is calculated from the SLS dispersion equation as presented at the beginning of this section.

The alternative V_P -only fluid-substitution equations are

$$\frac{1}{M_\infty} = \frac{(S_W - S_{\text{irr}})/(1 - S_{\text{irr}})}{M_P} + \frac{(1 - S_W)/(1 - S_{\text{irr}})}{M_{\text{mineral-irr}}}$$

where

$$M_P = M_{\text{mineral}} \frac{\phi M_{\text{dry}} - (1 + \phi) K_W M_{\text{dry}}/M_{\text{mineral}} + K_W}{(1 - \phi) K_W + \phi M_{\text{mineral}} - K_W M_{\text{dry}}/M_{\text{mineral}}}$$

$$M_{\text{mineral-irr}} = M_{\text{mineral}} \frac{\phi M_{\text{dry}} - (1 + \phi) K_{\text{fl-irr}} M_{\text{dry}}/M_{\text{mineral}} + K_{\text{fl-irr}}}{(1 - \phi) K_{\text{fl-irr}} + \phi M_{\text{mineral}} - K_{\text{fl-irr}} M_{\text{dry}}/M_{\text{mineral}}}$$

Full water saturation (wet rock)

Attenuation is calculated not at a point but in an interval. The necessary condition for attenuation is elastic heterogeneity in rock. The low-frequency limit of the compressional modulus is calculated by theoretically substituting the pore fluid into the dry-frame modulus of the spatially averaged rock while the high-frequency modulus is the spatial average of the saturated-rock modulus. The difference between these two estimates may give rise to noticeable P-wave attenuation if elastic heterogeneity in rock is substantial.

Specifically, in an interval of a layered medium, the average porosity is the arithmetic average of the porosity: $\bar{\phi} = \langle \phi \rangle$; the average dry-frame compressional modulus is the harmonic average of these moduli: $\bar{M}_{\text{dry}} = \langle M_{\text{dry}}^{-1} \rangle^{-1}$; the average low-frequency compressional modulus limit is obtained from the V_P -only (or, more rigorously, Gassmann's) equation applied to these averaged values:

$$M_0 = \bar{M}_{\text{mineral}} \frac{\bar{\phi} \bar{M}_{\text{dry}} - (1 + \bar{\phi}) K_W \bar{M}_{\text{dry}}/\bar{M}_{\text{mineral}} + K_W}{(1 - \bar{\phi}) K_W + \bar{\phi} \bar{M}_{\text{mineral}} - K_W \bar{M}_{\text{dry}}/\bar{M}_{\text{mineral}}}$$

where \bar{M}_{mineral} can be estimated by averaging the mineral-component moduli in the interval by, for example, Hill's equation or harmonically.

The high-frequency limit is the harmonic average of the wet moduli in the interval:

$$M_\infty = \left\langle \left(M_{\text{mineral}} \frac{\phi M_{\text{dry}} - (1 + \phi) K_{\text{fl}} M_{\text{dry}}/M_{\text{mineral}} + K_{\text{fl}}}{(1 - \phi) K_{\text{fl}} + \phi M_{\text{mineral}} - K_{\text{fl}} M_{\text{dry}}/M_{\text{mineral}}} \right)^{-1} \right\rangle^{-1}$$

Finally, the inverse P-wave quality factor Q_P^{-1} is calculated from the SLS dispersion equation as presented at the beginning of this section.

Example for wet rock. Consider a model rock that is fully water-saturated (wet) and has two parts. One part (80% of the rock volume) is shale with porosity 0.4; the clay content is 0.8 (the rest is quartz); and the P-wave velocity 1.9 km/s. The other part (the remaining 20%) is clean, high-porosity, slightly-cemented sand with porosity 0.3 and P-wave velocity 3.4 km/s. The compressional modulus is 7 GPa in the shale and

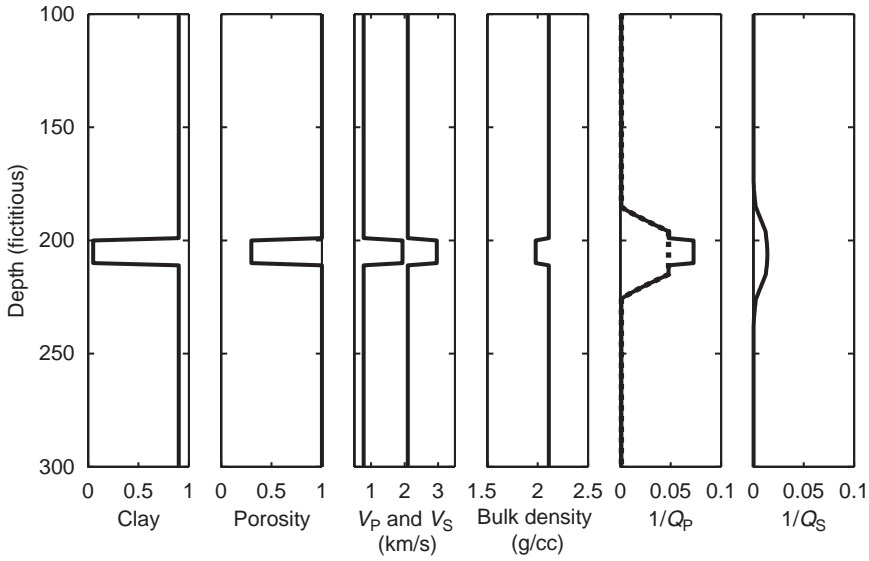


Figure 6.16.1 A pseudo-Earth model with a relatively fast gas-sand interval embedded in soft shale. From left to right: clay content; total porosity; velocity; bulk density; the inverse P-wave quality factor for wet background (dotted curve) and at the actual gas saturation (solid curve); and the inverse S-wave quality factor.

25 GPa in the sand. Because of the difference between the compliance of the sand and shale parts, their deformation due to a passing wave is different, which leads to macroscopic “squirt-flow.”

At high frequency, there is essentially no cross-flow between sand and shale, simply because the flow cannot fully develop during the short cycle of oscillation. The effective elastic modulus of the system is the harmonic (Backus) average of the moduli of the two parts: $M_{\infty} = 16$ GPa.

At low frequency, the cross-flow can easily develop. In this case, the fluid reacts to the combined deformation of the dry frames of the sand and shale. The dry-frame compressional modulus in the shale is 2 GPa, while that in the sand is 20 GPa. The dry-frame modulus of the combined dry frames can be estimated as the harmonic average of the two: 7 GPa. The arithmetically averaged porosity of the model rock is 0.32. To estimate the effective compressional modulus of the combined dry frame with water, we theoretically substitute water into this combined frame. The result is $M_0 = 13$ GPa. The maximum inverse quality factor $Q_{P_{\max}}^{-1}$ is about 0.1 ($Q = 10$), which translates into a noticeable attenuation coefficient 0.05 dB/m at 50 Hz.

At partial saturation, the background inverse quality factor $Q_{P_{\text{back}}}^{-1}$ is calculated as if the entire interval were wet. This value is added to $Q_{P-S_w}^{-1}$ which is calculated at partial saturation (as shown above) to (approximately) arrive at the total inverse quality factor:

$$Q_{P_{\text{total}}}^{-1} = Q_{P_{\text{back}}}^{-1} + Q_{P-S_w}^{-1}$$

An example of applying this model to a pseudo-Earth model is shown in [Figure 6.16.1](#).

S-wave attenuation

To model the S-wave inverse quality factor, Dvorkin and Mavko (2006) assume that the reduction in the compressional modulus between the high-frequency and low-frequency limits in *wet rock* is due to the introduction of a hypothetical set of aligned defects or flaws (e.g., cracks). The *same set of defects* is responsible for the reduction in the shear modulus between the high- and low-frequency limits. Finally, Hudson's theory for cracked media is used to link the shear-modulus-versus-frequency dispersion to the compressional-modulus-versus-frequency dispersion and show that the proportionality coefficient between the two is a function of the P-to-S-wave velocity ratio (or Poisson's ratio). This coefficient falls between 0.5 and 3 for Poisson's ratio contained in the interval 0.25 to 0.35, typical for saturated Earth materials.

The three proposed versions for Q_S^{-1} calculation from Q_P^{-1} (as calculated using the above theory) are:

$$\frac{Q_P^{-1}}{Q_S^{-1}} = \frac{1}{4} \frac{(M/\mu - 2)^2 (3M/\mu - 2)}{(M/\mu - 1)(M/\mu)}$$

$$\frac{Q_P^{-1}}{Q_S^{-1}} = \frac{5}{4} \frac{(M/\mu - 2)^2}{(M/\mu - 1)} \bigg/ \left[\frac{2M/\mu}{(3M/\mu - 2)} + \frac{M/\mu}{3(M/\mu - 1)} \right]$$

$$\frac{Q_P^{-1}}{Q_S^{-1}} = \frac{1}{M/\mu} \left[\frac{4}{3} + \frac{5}{4} \frac{(M/\mu - \frac{2}{3})(M/\mu - \frac{4}{3})^2}{M/\mu - \frac{8}{9}} \right]$$

where M is the compressional modulus at full water saturation. All three equations provide results of the same order of magnitude. The result according to the third equation is displayed in Figure 6.16.1.

Assumptions and limitations

This model estimates fluid-related dispersion and attenuation. The magnitude of attenuation is estimated as being proportional to the difference between the relaxed and unrelaxed moduli, using the dispersion–attenuation relation predicted by the standard linear solid (SLS) model. Choice of the SLS model ignores uncertainty associated with unknown distributions of fluid relaxation times. For partial saturation, the unrelaxed modulus is estimated using the patchy saturation model, while the relaxed modulus is estimated using the fine-scale saturation model. For full water saturation, the unrelaxed modulus is estimated as the spatial average of point-by-point Gassmann predictions of saturated moduli, while the relaxed modulus is estimated from the Gassmann prediction of saturated moduli applied to the spatial average of dry-rock moduli.

6.17 Partial and multiphase saturations

Synopsis

One of the most fundamental observations of rock physics is that seismic velocities are sensitive to pore fluids. The first-order low-frequency effects for *single fluid phases* are often described quite well with Gassmann's (1951) relations, which are discussed in Section 6.3. We summarize here variations on those fluid effects that result from *partial or mixed saturations*.

Caveat on very dry rocks

Figure 6.17.1 illustrates some key features of the saturation problem. The data are for limestones measured by Cadoret (1993) using the resonant bar technique at 1 kHz. The very-dry-rock velocity is approximately 2.84 km/s. Upon initial introduction of moisture (water), the velocity drops by about 4%. This apparent softening of the rock occurs at tiny volumes of pore fluid equivalent to a few monolayers of liquid if distributed uniformly over the internal surfaces of the pore space. These amounts are hardly sufficient for a fluid dynamic description, as in the Biot–Gassmann theories. Similar behavior has been reported in sandstones by Murphy (1982), Knight and Dvorkin (1992), and Tutuncu (1992).

This velocity drop has been attributed to softening of cements (sometimes called “chemical weakening”), to clay swelling, and to surface effects. In the latter model, very dry surfaces attract each other via cohesive forces, giving a mechanical effect resembling an increase in effective stress. Water or other pore fluids disrupt these forces. A fairly thorough treatment of the subject is found in the articles of Sharma and Tutuncu (Tutuncu, 1992; Tutuncu and Sharma, 1992; Sharma and Tutuncu, 1994; Sharma *et al.*, 1994).

After the first few percent of water saturation, additional fluid effects are primarily elastic and fluid dynamic and are amenable to analysis, for example, by the Biot–Gassmann (Sections 6.1–6.3) and squirt (Sections 6.10–6.14) models.

Figures 6.17.2 and 6.17.3 (Clark *et al.*, 1980; Winkler and Murphy, 1995) illustrate further the sensitivity of mechanical properties to very small amounts of water. Figure 6.17.2 shows normalized ultrasonic shear-wave velocity in sandstones and carbonates, plotted versus water vapor partial pressure. In all cases, increased exposure to water molecules systematically decreases the shear stiffness of the rocks, even though the amount of water is equivalent to only a few monolayers of molecules coating the pore surfaces. Figure 6.17.3 shows shear-wave attenuation versus water vapor partial pressure. Attenuation is very small in dry rocks, but increases rapidly upon exposure to moisture.

Several authors (Murphy *et al.*, 1991; Cadoret, 1993) have pointed out that classical fluid-mechanical models such as the Biot–Gassmann theories perform

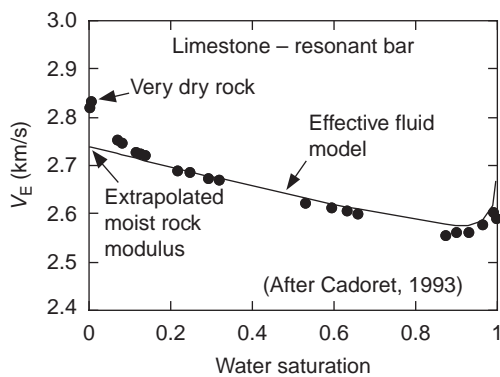


Figure 6.17.1 Extensional-wave velocity versus saturation.

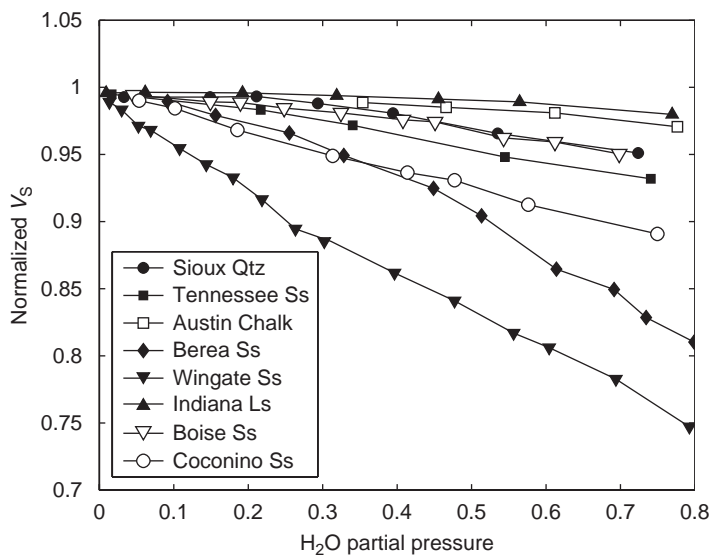


Figure 6.17.2 Normalized ultrasonic shear-wave velocity versus water partial pressure (Clark *et al.*, 1980).

poorly when the measured very-dry-rock values are used for the “dry rock” or “dry frame.” The models can be fairly accurate if the extrapolated “moist” rock modulus (see Figure 6.17.1) is used instead. For this reason, and to avoid the artifacts of ultra-dry rocks, it is often recommended to use samples that are at room conditions or that have been prepared in a constant-humidity environment for measuring “dry-rock” data. For the rest of this section, it is assumed that the ultra-dry artifacts have been avoided.

Caveat on frequency

It is well known that the Gassmann theory (see Section 6.3) is valid only at sufficiently **low frequencies** that the induced pore pressures are equilibrated throughout the pore space (i.e., that there is sufficient time for the pore fluid to flow and

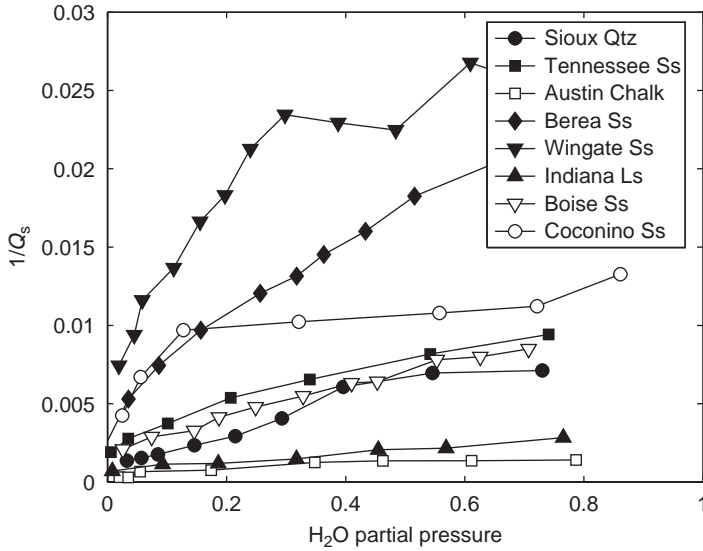


Figure 6.17.3 Normalized ultrasonic shear-wave attenuation versus water partial pressure (Clark *et al.*, 1980).

eliminate wave-induced pore-pressure gradients). This limitation to low frequencies explains why Gassmann's relation works best for very-low-frequency, *in-situ* seismic data (< 100 Hz) and may perform less well as frequencies increase toward sonic-logging ($\approx 10^4$ Hz) and laboratory ultrasonic measurements ($\approx 10^6$ Hz). Knight and Nolen-Hoeksema (1990) studied the effects of pore-scale fluid distributions on ultrasonic measurements.

Effective fluid model

The most common approach to modeling partial saturation (air/water or gas/water) or mixed fluid saturations (gas/water/oil) is to replace the collection of phases with a single "effective fluid."

When a rock is stressed by a passing wave, pores are always elastically compressed more than the solid grains. This pore compression tends to induce increments of pore fluid pressure, which resist the compression; hence, pore phases with the largest bulk modulus K_{fl} stiffen the rock most. For single fluid phases, the effect is described quite elegantly by Gassmann's (1951) relation (see Section 6.3):

$$\frac{K_{sat}}{K_0 - K_{sat}} = \frac{K_{dry}}{K_0 - K_{dry}} + \frac{K_{fl}}{\phi(K_0 - K_{fl})}, \quad \mu_{sat} = \mu_{dry}$$

where K_{dry} is the effective bulk modulus of the dry rock, K_{sat} is the effective bulk modulus of the rock with pore fluid, K_0 is the bulk modulus of the mineral material making up the rock, K_{fl} is the effective bulk modulus of the pore fluid, ϕ is porosity,

μ_{dry} is the effective shear modulus of the dry rock, and μ_{sat} is the effective shear modulus of the rock with the pore fluid.

Implicit in Gassmann's relation is the stress-induced pore pressure

$$\begin{aligned}\frac{dP}{d\sigma} &= \frac{1}{1 + K_{\phi}(1/K_{\text{fl}} - 1/K_0)} \\ &= \frac{1}{1 + \phi(1/K_{\text{fl}} - 1/K_0)(1/K_{\text{dry}} - 1/K_0)^{-1}}\end{aligned}$$

where P is the increment of pore pressure and σ is the applied hydrostatic stress. If there are multiple pore-fluid phases with different fluid bulk moduli, then there is a tendency for each to have a different induced pore pressure. However, when the phases are intimately mixed at the finest scales, these pore-pressure increments can equilibrate with each other to a single average value. This is an *isostress* situation, and therefore the effective bulk modulus of the mixture of fluids is described well by the Reuss average (see Section 4.2) as follows:

$$\frac{1}{K_{\text{fl}}} = \sum \frac{S_i}{K_i}$$

where K_{fl} is the effective bulk modulus of the fluid mixture, K_i denotes the bulk moduli of the individual gas and fluid phases, and S_i represents their saturations. The rock moduli can often be predicted quite accurately by inserting this effective-fluid modulus into Gassmann's relation. The effective-fluid (air + water) prediction is superimposed on the data in Figure 6.17.1 and reproduces the overall trend quite well. This approach has been discussed, for example, by Domenico (1976), Murphy (1984), Cadoret (1993), Mavko and Nolen-Hoeksema (1994), and many others.

Caution

It is thought that the effective-fluid model is valid only when all of the fluid phases are mixed at the finest scale.

Critical relaxation scale

A critical assumption in the effective-fluid model represented by the Reuss average is that differences in wave-induced pore pressure have time to flow and equilibrate among the various phases. As discussed in Section 8.1, the characteristic relaxation time or diffusion time for heterogeneous pore pressures of scale L is

$$\tau \approx \frac{L^2}{D}$$

where $D = kK_{\text{fl}}/\eta$ is the diffusivity, k is the permeability, K_{fl} is the fluid bulk modulus, and η is the viscosity. Therefore, at a seismic frequency $f = 1/\tau$, pore pressure heterogeneities caused by saturation heterogeneities will have time to relax and reach a local isostress state over scales smaller than

$$L_c \approx \sqrt{\tau D} = \sqrt{D/f}$$

and will be described *locally* by the effective-fluid model mentioned in the previous discussion. Spatial fluctuations on scales larger than L_c will tend to persist and will not be described well by the effective-fluid model.

Patchy saturation

Consider the situation of a homogeneous rock type with spatially variable saturation $S_i(x, y, z)$. Each “patch” or pixel at scale $\approx L_c$ will have fluid phases equilibrated within the patch at scales smaller than L_c , but neighboring patches at scales $> L_c$ will not be equilibrated with each other. Each patch will have a different effective fluid described approximately by the Reuss average. Consequently, the rock in each patch will have a different bulk modulus describable locally with Gassmann’s relations. Yet, the shear modulus will remain unchanged and spatially uniform.

The effective moduli of the rock with spatially varying bulk modulus but uniform shear modulus is described exactly by the equation of Hill (1963) discussed in [Section 4.5](#):

$$K_{\text{eff}} = \left\langle \frac{1}{K + \frac{4}{3}\mu} \right\rangle^{-1} - \frac{4}{3}\mu$$

This striking result states that the effective moduli of a composite with uniform shear modulus can be found *exactly* by knowing only the volume fractions of the constituents independent of the constituent geometries. There is no dependence, for example, on ellipsoids, spheres, or other idealized shapes.

[Figure 6.17.4](#) shows the P-wave velocity versus water saturation for another limestone (data from Cadoret, 1993). Unlike the effective-fluid behavior, which shows a small decrease in velocity with increasing saturation and then an abrupt increase as S_w approaches unity, the patchy model predicts a monotonic, almost linear increase in velocity from the dry to saturated values. The deviation of the data from the effective-fluid curve at saturations greater than 0.8 is an indication of patchy saturation (Cadoret, 1993).

The velocity-versus-saturation curves shown in [Figure 6.17.4](#) for the effective-fluid model and patchy-saturation model represent approximate lower and upper bounds, respectively, at low frequencies. The lower effective-fluid curve is achieved when the fluid phases are mixed at the finest scales. The upper patchy-saturation curve is achieved when there is the greatest separation of phases: when each patch of size $> L_c$

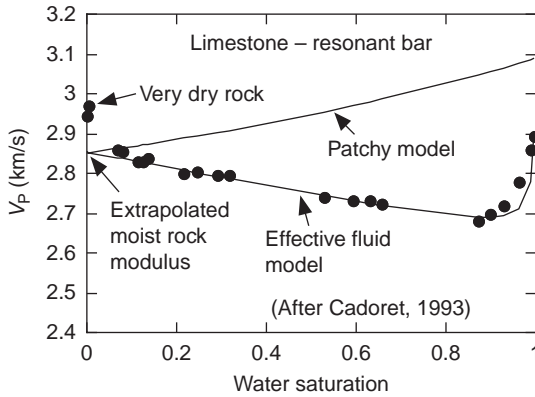


Figure 6.17.4 P-wave velocity versus saturation.

has only a single phase. Any velocity between these “bounds” can occur when there is a range of saturation scales.

Saturation-related velocity dispersion

The difference between effective-fluid behavior and patchy-saturation behavior is largely a matter of the scales at which the various phases are mixed. The critical-relaxation scale L_c , which separates the two domains, is related to the seismic frequency. Hence, spatially varying saturations can be a source of velocity dispersion. Attempts to quantify this velocity dispersion have been made by White (1975) and by Dutta and Odé (1979) (see Sections 6.15 and 6.18).

Voigt average approximation

It can be shown that an approximation to the patchy-saturation “upper bound” can be found by first computing the Voigt average (see Section 4.2) of the fluid modulus:

$$K_{fl} = \sum S_i K_i$$

where K_{fl} is the effective bulk modulus of the fluid mixture, K_i denotes the bulk moduli of the individual gas and fluid phases, and S_i represents their saturations. Next, this average fluid is put into Gassmann’s equations to predict the overall rock moduli. This is in contrast to the effective-fluid model discussed earlier, in which the Reuss average of the fluid moduli was put into the Gassmann equations.

Brie’s fluid mixing equation

Brie *et al.* (1995) suggest an empirical fluid mixing law, given by

$$K_{Brie} = (K_{liquid} - K_{gas})(1 - S_{gas})^e + K_{gas}$$

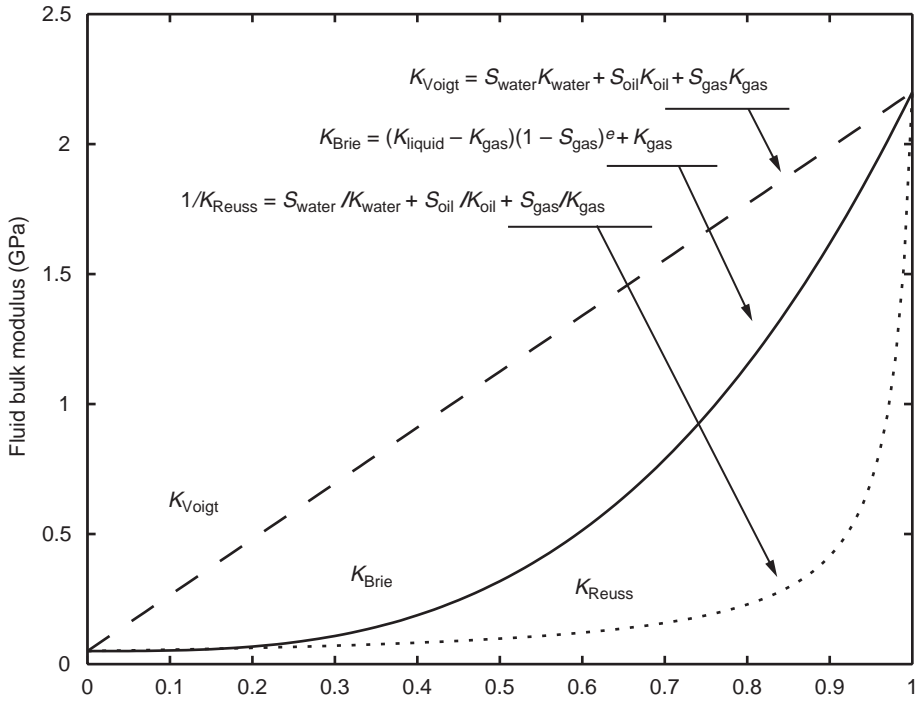


Figure 6.17.5 Comparison of effective fluid moduli, governed by the following equations: Brie's patchy mixer (solid line), $K_{\text{Brie}} = (K_{\text{liquid}} - K_{\text{gas}})(1 - S_{\text{gas}})^e + K_{\text{gas}}$; patchy mix Voigt average (dashed line), $K_{\text{Voigt}} = S_{\text{water}}K_{\text{water}} + S_{\text{oil}}K_{\text{oil}} + S_{\text{gas}}K_{\text{gas}}$; and fine-scale mix Reuss average (dotted line), $1/K_{\text{Reuss}} = S_{\text{water}}/K_{\text{water}} + S_{\text{oil}}/K_{\text{oil}} + S_{\text{gas}}/K_{\text{gas}}$.

where K_{gas} is the gas bulk modulus, $K_{\text{liquid}} = (S_{\text{water}}/K_{\text{water}} + S_{\text{oil}}/K_{\text{oil}})^{-1}$ is the liquid bulk modulus given by the Reuss average of the water and oil moduli, K_{water} and K_{oil} , and e is an empirical constant, typically equal to about 3.

Figure 6.17.5 compares the effective fluid moduli predicted by the Reuss, Voigt, and Brie averages. While the Voigt and Reuss are bounds for the effective fluid, data rarely fall near the Voigt average. A more useful range is to assume that the effective fluid modulus will fall roughly between the Reuss and Brie averages.

6.18 Partial saturation: White and Dutta–Odé model for velocity dispersion and attenuation

Synopsis

Consider the situation of a reservoir rock with spatially variable saturation $S_i(x, y, z)$. Each “patch” at scale $\approx L_c$ (where $L_c \approx \sqrt{\tau D} = \sqrt{D/f}$ is the critical fluid-diffusion relaxation scale, $D = kK_{\text{fl}}/\eta$ is the diffusivity, k is the permeability, K_{fl} is the fluid bulk modulus, and η is the viscosity) will have fluid phases equilibrated within the

patch at scales smaller than L_c , but neighboring patches at scales $>L_c$ will not be equilibrated with each other. Fluid flow resulting from unequilibrated pore pressures between patches of different fluids will cause attenuation and dispersion of seismic waves traveling through the rock. White (1975) modeled the seismic effects of patchy saturation by considering porous rocks saturated with brine but containing spherical gas-filled regions. Dutta and Odé (1979) gave a more rigorous solution for White's model by using Biot's equations for poroelasticity. The patches (spheres) of heterogeneous saturation are much larger than the grain scale but are much smaller than the wavelength. The idealized geometry of a unit cell consists of a gas-filled sphere of radius a placed at the center of a brine-saturated spherical shell of outer radius b ($b > a$). Adjacent unit cells do not interact with each other. The gas saturation is $S_g = a^3/b^3$. The inner region will be denoted by subscript 1 and the outer shell by subscript 2. In the more rigorous Dutta and Odé formulation, the dry-frame properties (denoted by subscript "dry" in the following equations) in the two regions may be different. However, in White's approximate formulation, the dry-frame properties are assumed to be the same in regions 1 and 2. White's equations as given below (incorporating a correction pointed out by Dutta and Seriff, 1979) yield results that agree very well with the Dutta–Odé results. The complex bulk modulus, K^* , for the partially saturated porous rock as a function of angular frequency ω is given by

$$K^* = \frac{K_\infty}{1 - K_\infty W} = K_r^* + iK_i^*$$

where

$$W = \frac{3a^2(R_1 - R_2)(-Q_1 + Q_2)}{b^3 i\omega(Z_1 + Z_2)}$$

$$R_1 = \frac{K_1 - K_{\text{dry}_1}}{1 - K_{\text{dry}_1}/K_{0_1}} \frac{3K_2 + 4\mu_2}{K_2(3K_1 + 4\mu_2) + 4\mu_2(K_1 - K_2)S_g}$$

$$R_2 = \frac{K_2 - K_{\text{dry}_2}}{1 - K_{\text{dry}_2}/K_{0_2}} \frac{3K_1 + 4\mu_1}{K_2(3K_1 + 4\mu_2) + 4\mu_2(K_1 - K_2)S_g}$$

$$Z_1 = \frac{\eta_1 a}{\kappa_1} \left[\frac{1 - e^{-2\alpha_1 a}}{(\alpha_1 a - 1) + (\alpha_1 a + 1)e^{-2\alpha_1 a}} \right]$$

$$Z_2 = -\frac{\eta_2 a}{\kappa_2} \left[\frac{(\alpha_2 b + 1) + (\alpha_2 b - 1)e^{2\alpha_2(b-a)}}{(\alpha_2 b + 1)(\alpha_2 a - 1) - (\alpha_2 b - 1)(\alpha_2 a + 1)e^{2\alpha_2(b-a)}} \right]$$

$$\alpha_j = (i\omega\eta_j/\kappa_j K_{Ej})^{1/2}$$

$$K_{Ej} = \left[1 - \frac{K_{fj}(1 - K_j/K_{0j})(1 - K_{\text{dry}j}/K_{0j})}{\phi K_j(1 - K_{fj}/K_{0j})} \right] K_{Aj}$$

$$K_{Aj} = \left(\frac{\phi}{K_{fj}} + \frac{1-\phi}{K_{0j}} - \frac{K_{dryj}}{K_{0j}^2} \right)^{-1}$$

$$Q_j = \frac{(1 - K_{dryj}/K_{0j})K_{Aj}}{K_j}$$

Here, $j=1$ or 2 denotes quantities corresponding to the two different regions; η and K_f are the fluid viscosity and bulk modulus, respectively; ϕ is the porosity; κ is the permeability; and K_0 is the bulk modulus of the solid mineral grains. The saturated bulk and shear moduli, K_j and μ_j , respectively, of region j are obtained from Gassmann's equation using K_{dryj} , μ_{dryj} , and K_{fj} . When the dry-frame moduli are the same in both regions, $\mu_1 = \mu_2 = \mu_{dry}$ because Gassmann predicts no change in the shear modulus upon fluid substitution. At the high-frequency limit, when there is no fluid flow across the fluid interface between regions 1 and 2, the bulk modulus is given by

$$K_{\infty}(\text{no-flow}) = \frac{K_2(3K_1 + 4\mu_2) + 4\mu_2(K_1 - K_2)S_g}{(3K_1 + 4\mu_2) - 3(K_1 - K_2)S_g}$$

This assumes that the dry-frame properties are the same in the two regions. The low-frequency limiting bulk modulus is given by Gassmann's relation with an effective fluid modulus equal to the Reuss average of the fluid moduli. In this limit the fluid pressure is constant and uniform throughout the medium:

$$K(\text{low-frequency}) = \frac{K_2(K_1 - K_{dry}) + S_g K_{dry}(K_2 - K_1)}{(K_1 - K_{dry}) + S_g(K_2 - K_1)}$$

Note that in White (1975) the expressions for K_E and Q had the P-wave modulus $M_j = K_j + 4\mu_j/3$ in the denominator instead of K_j . As pointed out by Dutta and Seriff (1979), this form does not give the right low-frequency limit. An estimate of the transition frequency separating the relaxed and unrelaxed (no-flow) states is given by

$$f_c \approx \frac{\kappa_2 K_{E2}}{\pi \eta_2 b^2}$$

which has the length-squared dependence characteristic of diffusive phenomena. When the central sphere is saturated with a very compressible gas (caution: this may not hold at reservoir pressures) $R_1, Q_1, Z_1 \approx 0$. The expression for the effective complex bulk modulus then reduces to

$$K^* = \frac{K_{\infty}}{1 + 3a^2 R_2 Q_2 K_{\infty} / (b^3 i \omega Z_2)}$$

Dutta and Odé obtained more rigorous solutions for the same spherical geometry by solving a boundary-value problem involving Biot's poroelastic field equations. They considered steady-state, time-harmonic solutions for \mathbf{u} and \mathbf{w} , the displacement

of the porous frame and the displacement of the pore fluid relative to the frame, respectively. The solutions in the two regions are given in terms of spherical Bessel and Neumann functions, j_1 and n_1 , of order 1. The general solution for \mathbf{w} in region 1 for purely radial motion is

$$\mathbf{w}(r) = \mathbf{w}_c(r) + \mathbf{w}_d(r)$$

$$\mathbf{w}_c(r) = C_1 j_1(k_c r) + C_2 n_1(k_c r)$$

$$\mathbf{w}_d(r) = C_3 j_1(k_d r) + C_4 n_1(k_d r)$$

where C_1 , C_2 , C_3 , and C_4 are integration constants to be determined from the boundary conditions at $r=0$, $r=a$, and $r=b$. A similar solution holds for region 2, but with integration constants C_5 , C_6 , C_7 , and C_8 . The wavenumbers k_c and k_d in each region are given in terms of the moduli and density corresponding to that region:

$$\frac{k_c^2}{\omega^2} = \frac{\rho_f(M\sigma_c + 2\gamma D) - \rho(2\gamma D\sigma_c + 2D)}{(4\gamma^2 D^2 - 2DM)}$$

$$\frac{k_d^2}{\omega^2} = \frac{\rho_f(M\sigma_d + 2\gamma D) - \rho(2\gamma D\sigma_d + 2D)}{(4\gamma^2 D^2 - 2DM)}$$

where

$$\rho = (1 - \phi)\rho_0 + \phi\rho_f$$

$$\gamma = 1 - \frac{K_{\text{dry}}}{K_0}$$

$$M = K + \frac{4}{3}\mu$$

$$D = \frac{K_0}{2} \left[\gamma + \frac{\phi}{K_f} (K_0 - K_f) \right]^{-1}$$

and σ_c and σ_d are the two complex roots of the quadratic equation

$$\begin{aligned} &(\rho_f M - 2\rho\gamma D)\sigma^2 + \left(Mm - 2\rho D - \frac{i\eta M}{\kappa\omega} \right)\sigma \\ &+ \left(2m\gamma D - 2\rho_f D - 2i\frac{\eta\gamma D}{\kappa\omega} \right) = 0 \end{aligned}$$

where $m = s\rho_f/\phi$. The tortuosity parameter s (sometimes called the structure factor) is a purely geometrical factor independent of the solid or fluid densities and is never less than 1 (see [Section 6.1](#) on Biot theory). For idealized geometries and uniform flow, s usually lies between 1 and 5. Berryman (1981) obtained the relation

$$s = 1 - \xi \left(1 - \frac{1}{\phi} \right)$$

where $\zeta = \frac{1}{2}$ for spheres and lies between 0 and 1 for other ellipsoids. For uniform cylindrical pores with axes parallel to the pore pressure gradient, s equals 1 (the minimum possible value), whereas for a random system of pores with all possible orientations, $s = 3$ (Stoll, 1977). The solutions for \mathbf{u} are given as

$$\mathbf{u}(r) = \mathbf{u}_c(r) + \mathbf{u}_d(r)$$

$$\mathbf{u}_c(r) = \sigma_d \mathbf{w}_c(r), \quad \mathbf{u}_d(r) = \sigma_c \mathbf{w}_d(r)$$

The integration constants are obtained from the following boundary conditions:

$$(1) \quad r \rightarrow 0, w_1(r) \rightarrow 0$$

$$(2) \quad r \rightarrow 0, u_1(r) \rightarrow 0$$

$$(3) \quad r = a, u_1(r) = u_2(r)$$

$$(4) \quad r = a, w_1(r) = w_2(r)$$

$$(5) \quad r = a, \tau_1(r) = \tau_2(r)$$

$$(6) \quad r = a, p_1(r) = p_2(r)$$

$$(7) \quad r = b, \tau_2(r) = -\tau_0$$

$$(8) \quad r = b, w_2(r) = 0$$

The first two conditions imply no displacements at the center of the sphere because of purely radial flow and finite fluid pressure at the origin. These require $C_2 = C_4 = 0$. Conditions (3)–(6) come from continuity of displacements and stresses at the interface. The bulk radial stress is denoted by τ , and p denotes the fluid pressure. These parameters are obtained from \mathbf{u} and \mathbf{w} by

$$\tau = M \frac{\partial \mathbf{u}}{\partial r} + 2(M - 2\mu) \frac{\mathbf{u}}{r} + 2\gamma D \left(\frac{\partial \mathbf{w}}{\partial r} + \frac{2}{r} \mathbf{w} \right)$$

$$p = -2\gamma D \left(\frac{\partial \mathbf{u}}{\partial r} + \frac{2}{r} \mathbf{u} \right) - 2D \left(\frac{\partial \mathbf{w}}{\partial r} + \frac{2}{r} \mathbf{w} \right)$$

Condition (7) gives the amplitude τ_0 of the applied stress at the outer boundary, and condition (8) implies that the outer boundary is jacketed. These boundary conditions are not unique and could be replaced by others that may be appropriate for the situation under consideration. The jacketed outer boundary is consistent with non-interacting unit cells. The remaining six integration constants are obtained by solving the linear system of equations given by the boundary conditions. Solving the linear system requires considerable care (Dutta and Odé, 1979). The equations may become ill-conditioned because of the wide range of the arguments of the spherical Bessel and Neumann functions. Once the complete solution for $\mathbf{u}(r)$ is obtained, the effective complex bulk modulus for the partially saturated medium is given by

$$K^*(\omega) = -\frac{\tau_0}{\Delta V/V} = -\frac{\tau_0 b}{3\mathbf{u}(b)}$$

The P-wave velocity V_p^* and attenuation coefficient α_p^* are given in terms of the complex P-wave modulus M^* and the effective density ρ^*

$$\rho^* = S_g[(1 - \phi)\rho_0 + \phi\rho_{f1}] + (1 - S_g)[(1 - \phi)\rho_0 + \phi\rho_{f2}]$$

$$M^* = (M_r^* + iM_i^*) = (K_r^* + 4\mu^*/3 + iK_i)$$

$$\mu^* = \mu_1 = \mu_2 = \mu_{\text{dry}}$$

$$V_p^* = (|M^*|/\rho^*)^{1/2} / \cos(\theta_p^*/2)$$

$$\alpha_p^* = \omega \tan(\theta_p^*/2) / V_p^*$$

$$\theta_p^* = \tan^{-1}(M_i^*/M_r^*)$$

Uses

The White and Dutta–Odé models can be used to calculate velocity dispersion and attenuation in porous media with patchy partial saturation.

Assumptions and limitations

The White and Dutta–Odé models are based on the following assumptions:

- the rock is isotropic;
- all minerals making up the rock are isotropic and linearly elastic;
- the patchy saturation has an idealized geometry consisting of a sphere saturated with one fluid within a spherical shell saturated with another fluid;
- the porosity in each saturated region is uniform, and the pore structure is smaller than the size of the spheres; and
- the patches (spheres) of heterogeneous saturation are much larger than the grain scale but are much smaller than the wavelength.

6.19 Velocity dispersion, attenuation, and dynamic permeability in heterogeneous poroelastic media

Synopsis

Wave-induced fluid flow in heterogeneous porous media can cause velocity dispersion and attenuation. The scale of the heterogeneities is considered to be much larger than the pore scale but much smaller than the wavelength of the seismic wave. An example would be heterogeneities caused by patchy saturation discussed in [Section 6.17](#). Muller and Gurevich (2005a, 2005b, 2006) applied the method of statistical smoothing for Biot's poroelasticity equations in a random, heterogeneous, porous medium and derived the effective wavenumbers for the fast and slow P-waves. The parameters of the poroelastic random medium consist of a smooth background

component and a zero-mean fluctuating component. The statistical properties of the relative fluctuations of any two parameters X and Y are described by variances and covariances denoted by σ_{XX}^2 and σ_{XY}^2 , respectively. The spatial distribution of the random heterogeneities is described by a normalized spatial correlation function $B(\mathbf{r})$. In the following equations, all poroelastic parameters are assumed to have the same normalized spatial correlation function and correlation length, though the general results of Muller and Gurevich (2005a) allow for different correlation lengths associated with each random property.

The effective P-wavenumber \bar{k}_P in three-dimensional random poroelastic media with small fluctuations can be written as (Muller and Gurevich, 2005b)

$$\bar{k}_P = k_P \left(1 + \Delta_2 + \Delta_1 k_{Ps}^2 \int_0^\infty r B(r) \exp(irk_{Ps}) dr \right)$$

where k_P is the wavenumber in the homogeneous background and the dimensionless coefficients Δ_1 and Δ_2 are given by

$$\Delta_1 = \frac{\alpha^2 M}{2P_d} \left(\sigma_{HH}^2 - 2\sigma_{HC}^2 + \sigma_{CC}^2 + \frac{32}{15} \frac{G^2}{H^2} \sigma_{GG}^2 - \frac{8}{3} \frac{G}{H} \sigma_{HG}^2 + \frac{8}{3} \frac{G}{H} \sigma_{GC}^2 \right)$$

$$\Delta_2 = \Delta_1 + \frac{1}{2} \sigma_{HH}^2 - \frac{4}{3} \frac{G}{H} \sigma_{HG}^2 + \left(\frac{4G}{H} + 1 \right) \frac{4}{15} \frac{G}{H} \sigma_{GG}^2$$

and the other parameters are: $k_{Ps} = \sqrt{i\omega\eta/(\kappa_0 N)}$ is the wavenumber of the Biot slow wave in the homogeneous background, ω is the angular frequency, η is the fluid viscosity, κ_0 is the background permeability, G is the background shear modulus, P_d is the dry (drained) P-wave modulus of the background, H is the saturated P-wave modulus of the background, related to P_d by Gassmann's equation as $H = P_d + \alpha^2 M$, $M = [(\alpha - \phi)/K_0 + \phi/K_f]^{-1}$, ϕ is the background porosity, $\alpha = 1 - K_d/K_0$ is the Biot–Willis coefficient, K_d is the dry bulk modulus, K_0 is the mineral (solid-phase) bulk modulus, K_f is the fluid bulk modulus, $N = MP_d/H$, and $C = \alpha M$.

Expressions for velocity dispersion $V(\omega)$ and attenuation or inverse quality factor Q^{-1} are obtained from the real and imaginary parts of the effective wavenumber:

$$V(\omega) = \frac{\omega}{\text{Re}\{\bar{k}_P\}} = V_0 \left[1 - \Delta_2 + 2\Delta_1 k_{Ps}^2 \int_0^\infty r B(r) \exp(-rk_{Ps}) \sin(rk_{Ps}) dr \right]$$

$V_0 = \sqrt{H/\rho}$ = constant background P-wave velocity in the saturated porous medium and ρ is the saturated bulk density.

$k_{Ps} = \sqrt{\eta\omega/(2\kappa_0 N)}$ = real part of the slow P-wavenumber k_{Ps} .

For low-loss media, Q^{-1} can be written as

$$Q^{-1}(\omega) = \frac{2 \text{Im}\{\bar{k}_P\}}{\text{Re}\{\bar{k}_P\}} = 4\Delta_1 k_{Ps}^2 \int_0^\infty r B(r) \exp(-rk_{Ps}) \cos(rk_{Ps}) dr$$

The term Δ_1 is a measure of the magnitude of attenuation and frequency-dependent velocity dispersion, while Δ_2 produces a frequency-independent velocity shift.

The validity of the approximations for the effective P-wavenumber are expressed mathematically as

$$\max\{\Delta_1(|k_{\text{Ps}}|a)^2, \Delta_2\} \ll 1$$

$$a^2 \gg \frac{\kappa_0 N}{\eta \omega_B}$$

where a is the correlation length and $\omega_B = \phi\eta/(\kappa_0\rho_f)$ is the Biot characteristic frequency with ρ_f being the fluid density. These conditions arise from the weak-contrast assumption and the low-frequency approximation necessary for the derivation (Muller and Gurevich, 2005b).

The spatial correlation function $B(r)$ and the power spectrum of the fluctuations $\Phi(k)$ are related by a Fourier transform. If the medium is statistically isotropic the relation can be expressed as a three-dimensional Hankel transform:

$$B(r) = \frac{4\pi}{r} \int_0^\infty k \Phi(k) \sin(kr) dk$$

where k is the spatial wavenumber of the fluctuations. In terms of the power spectrum, the expressions for velocity and inverse quality factor are (Muller and Gurevich, 2005b):

$$V(\omega) = V_0 \left[1 - \Delta_2 + 16\pi\Delta_1 \int_0^\infty \frac{k_{\text{Ps}}^4 k^2}{4k_{\text{Ps}}^4 + k^4} \Phi(k) dk \right]$$

$$Q^{-1}(\omega) = 16\pi\Delta_1 \int_0^\infty \frac{k_{\text{Ps}}^2 k^4}{4k_{\text{Ps}}^4 + k^4} \Phi(k) dk$$

The factor

$$\Theta(k, k_{\text{Ps}}) = \frac{k_{\text{Ps}}^2 k^4}{4k_{\text{Ps}}^4 + k^4}$$

acts as a filter and controls which part of the fluctuation spectrum gives contributions to the velocity dispersion and attenuation.

Results for specific correlation functions

Muller and Gurevich (2005b) give explicit analytic results for specific correlation functions. For an exponential correlation function $B(r) = \exp[-|r|/a]$ and

$$V(\omega) = V_0 \left[1 - \Delta_2 + \Delta_1 \frac{4(ak_{\text{Ps}})^3(1 + k_{\text{Ps}}a)}{(1 + 2k_{\text{Ps}}a + 2k_{\text{Ps}}^2a^2)^2} \right]$$

$$Q^{-1}(\omega) = \Delta_1 \frac{4(ak_{\text{PsR}})^2(1 + 2k_{\text{PsR}}a)}{(1 + 2k_{\text{PsR}}a + 2k_{\text{PsR}}^2a^2)^2}$$

For a Gaussian correlation function $B(r) = \exp(-r^2/a^2)$, and Muller and Gurevich obtain

$$V(\omega) = V_0 \left\{ 1 - \Delta_2 + \Delta_1 (ak_{\text{PsR}})^2 \frac{\sqrt{\pi}}{4} \sum_{z=z_-}^{z=z_+} ak_{\text{PsR}} z^* \exp[(ak_{\text{PsR}}z)^2/4] \operatorname{erfc}[ak_{\text{PsR}}z/2] \right\}$$

$$Q^{-1}(\omega) = 2\Delta_1 (ak_{\text{PsR}})^2 \left\{ 1 - \frac{\sqrt{\pi}}{4} \sum_{z=z_-}^{z=z_+} ak_{\text{PsR}} z \exp[(ak_{\text{PsR}}z)^2/4] \operatorname{erfc}[ak_{\text{PsR}}z/2] \right\}$$

where $z_+ = 1 + i$, $z_- = 1 - i$, and z^* denotes the complex conjugate.

The von Karman correlation function with two parameters, the correlation length a , and the Hurst coefficient ν ($0 < \nu \leq 1$), is expressed as

$$B(r) = 2^{1-\nu} \Gamma^{-1}(\nu) \left(\frac{r}{a}\right)^\nu K_\nu(r/a)$$

where Γ is the Gamma function and K_ν is the modified Bessel function of the third kind. When $\nu = \frac{1}{2}$, the von Karman function becomes identical to the exponential correlation function. The equivalent spectral representation for general ν is

$$\Phi(k) = \frac{a^3 \Gamma(\nu + \frac{3}{2})}{\pi^{3/2} \Gamma(\nu) (1 + k^2 a^2)^{\nu+3/2}}$$

Using the spectral representation, Muller and Gurevich (2005b) derive expressions for fast P-wave velocity dispersion and inverse quality factor as described below:

$$V(\omega) = V_0 [1 - \Delta_2 - \frac{1}{2} c_1 \Delta_1 (\Psi_1 + \Psi_2 + \Psi_3)]$$

$$Q^{-1}(\omega) = c_1 \Delta_1 [\Omega_1 + \Omega_2 + \Omega_3]$$

with

$$\Psi_1 = -4c_2(1 + \nu)(ak_{\text{PsR}})^2 {}_3F_2 \left(1, 1 + \frac{\nu}{2}, \frac{3}{2} + \frac{\nu}{2}; \frac{3}{4}, \frac{5}{4}; -4(ak_{\text{PsR}})^4 \right)$$

$$\Psi_2 = \frac{1}{2} \Gamma \left(\nu + \frac{1}{2} \right) (2\nu + 3) c_3 B^{-3/4-\nu/2} \cos \left[\left(\frac{3}{4} + \frac{\nu}{2} \right) A \right]$$

$$\Psi_3 = \Gamma \left(\nu + \frac{3}{2} \right) \left(\frac{3}{2} + \nu \right) B^{-5/4-\nu/2} \left[2(ak_{\text{PsR}})^2 \cos(c_3 A) + \sin(c_3 A) \right]$$

$$\Omega_1 = c_2 {}_3F_2 \left(1, \frac{1}{2} + \frac{\nu}{2}, 1 + \frac{\nu}{2}; \frac{1}{4}, \frac{3}{4}; -4(ak_{\text{PsR}})^4 \right)$$

$$\Omega_2 = -\frac{1}{2}\Gamma\left(v + \frac{3}{2}\right)(2v + 3)B^{-3/4-v/2} \cos\left[\left(\frac{3}{4} + \frac{v}{2}\right)A\right]$$

$$\Omega_3 = \Gamma\left(v + \frac{5}{2}\right)B^{-5/4-v/2} \left[2(ak_{\text{Psr}})^2 \cos(c_3 A) + \sin(c_3 A)\right]$$

$$c_1 = \frac{16\sqrt{\pi}(ak_{\text{Psr}})^3}{\Gamma(v)(2v + 3)}$$

$$c_2 = \frac{\Gamma(v + 1)(2v + 3)}{2\sqrt{\pi}ak_{\text{Psr}}}$$

$$c_3 = \frac{1}{4} + \frac{v}{2}$$

$$A = 2 \arctan\left[2(ak_{\text{Psr}})^2\right]$$

$$B = 1 + 4(ak_{\text{Psr}})^4$$

$${}_pF_q(\xi_1, \dots, \xi_p; \varsigma_1, \dots, \varsigma_q; x) = \text{generalized hypergeometric function}$$

Low- and high-frequency limits

The low-frequency limit when there is enough time for the wave-induced pore pressures to equilibrate is referred to as the “relaxed” or “quasi-static” limit with P-wave phase velocity V_{qs} . The other limiting situation is when frequencies are high enough that there is no time for flow-induced equilibration of pore pressures. This limit is the “unrelaxed” or “no-flow” limit, with phase velocity $V_{\text{nf}} \geq V_{\text{qs}}$. Though the no-flow limit might be called the “high-frequency” limit, the wavelengths are still much longer than the scale of the heterogeneities. The limiting velocities for the P-wave are given by (Muller and Gurevich, 2005b)

$$V_{\text{qs}} = V_0(1 - \Delta_2)$$

$$V_{\text{nf}} = V_0(1 + \Delta_1 - \Delta_2)$$

and the relative magnitude of the velocity dispersion effect is

$$\frac{V_{\text{nf}} - V_{\text{qs}}}{V_0} = \Delta_1$$

The limiting velocities do not depend on the spatial correlation functions and are independent of geometry of the heterogeneities. For a porous medium, such that all poroelastic moduli are homogeneous and the only fluctuations are in the bulk modulus of the fluid, the quasi-static limit corresponds to a Reuss average (Wood’s average) of the pore-fluid bulk moduli, followed by Gassmann’s fluid substitution

(see Section 6.3); the no-flow limit corresponds to a Hill's average (Section 4.5) of the saturated P-wave moduli.

In the low-frequency limit, $Q^{-1} \propto \omega$, while for correlation functions that can be expanded in a power series as

$$B(r/a) = 1 - (r/a) + O(r^2/a^2) + \dots$$

the high-frequency asymptotic behavior of Q^{-1} is given by $Q^{-1} \propto 1/\sqrt{\omega}$. For a Gaussian correlation function, there is a much faster decrease of attenuation with frequency given by $Q^{-1} \propto 1/\omega$. For all correlation functions, maximum attenuation occurs at the resonance condition when the diffusion wavelength equals the correlation length or $k_{ps}a \approx 1$. The corresponding frequency is given as $\omega_{\max} \approx 2\kappa_0 N/a^2\eta$.

Permeability fluctuations

The equations in the above sections for the effective P-wavenumber \bar{k}_p in three-dimensional random poroelastic media were derived for a medium with a homogeneous permeability. Muller and Gurevich (2006) extended the theory to take into account spatial fluctuations of permeability, and derive expressions for the effective slow P-wavenumber \bar{k}_{ps} . They also identify a dynamic permeability for the heterogeneous poroelastic medium. The dynamic permeability of Muller and Gurevich is different from the dynamic permeability of Johnson *et al.* (1987), which is frequency-dependent permeability arising from inertial effects at frequencies of the order of Biot's characteristic frequency. The dynamic permeability of Muller and Gurevich is related to wave-induced flow at frequencies much lower than the Biot characteristic frequency.

The relative fluctuation in the property X is denoted by ε_X with zero mean and variance σ_{XX}^2 . The fluctuation of permeability, κ , is parameterized in terms of the variance σ_{pp}^2 of the reciprocal permeability $p = 1/\kappa$. The slow P-wave effective wavenumber is given as (Muller *et al.*, 2007):

$$\bar{k}_{ps}^2 = k_{ps}^2 [1 + \Delta_S \xi(\omega)]$$

$$\xi(\omega) = 1 + k_{ps}^2 \int_0^\infty r B(r) \exp(ik_{ps}r) dr$$

$$\Delta_S = \left\langle \left(\frac{\alpha^2 M}{P_d} \varepsilon_\alpha - \varepsilon_{K_f} + \varepsilon_\phi \right)^2 \right\rangle + \frac{\sigma_{pp}^2}{3}$$

where $\langle \cdot \rangle$ denotes ensemble averages. For a one-dimensional random medium

$$\xi^{(1D)}(\omega) = 1 + ik_{ps} \int_0^\infty B(r) \exp(ik_{ps}r) dr$$

$$\Delta^{(1D)}_S = \left\langle \left(\frac{\alpha^2 M}{P_d} \varepsilon_\alpha - \varepsilon_{K_f} + \varepsilon_\phi \right)^2 \right\rangle + \sigma_{pp}^2$$

An effective dynamic permeability κ^* can be derived from the relation $\bar{k}_{\text{Ps}} = \sqrt{i\omega\eta/(\kappa^*N)}$ as (Muller *et al.*, 2007):

$$\frac{\kappa^{*(3\text{D})}}{\kappa_0} = 1 - \frac{\sigma_{pp}^2}{3} + \frac{2}{3}\sigma_{pp}^2 k_{\text{PsF}}^2 \int_0^\infty r B(r) \exp(-rk_{\text{PsF}}) \sin(rk_{\text{PsF}}) dr$$

$$\frac{\kappa^{*(1\text{D})}}{\kappa_0} = 1 - \sigma_{pp}^2 + \sqrt{2}\sigma_{pp}^2 k_{\text{PsF}} \int_0^\infty B(r) \exp(-rk_{\text{PsF}}) \sin(rk_{\text{PsF}} + \pi/4) dr$$

In the low-frequency limit,

$$\kappa^{*(3\text{D})}(\omega \rightarrow 0) \approx \kappa_0(1 - \sigma_{\kappa\kappa}^2/3)$$

$$\kappa^{*(1\text{D})}(\omega \rightarrow 0) \approx \kappa_0(1 - \sigma_{\kappa\kappa}^2)$$

The one-dimensional low-frequency limit corresponds to a harmonic average of the permeability for small fluctuations. The high-frequency limit, for both one and three dimensions, is just the arithmetic average of the permeability values. The effective permeability is bounded by the harmonic and arithmetic average:

$$\left\langle \frac{1}{\kappa} \right\rangle^{-1} = \kappa^{*(1\text{D})}(\omega \rightarrow 0) < \kappa^{*(3\text{D})}(\omega \rightarrow 0) < \kappa^{*(1\text{D},3\text{D})}(\omega \rightarrow \infty) = \langle \kappa \rangle$$

The one-dimensional result for the frequency-dependent effective permeability can be expressed in a rescaled form as (Muller *et al.*, 2007):

$$\frac{\kappa^{*(1\text{D})}}{\kappa_0} = \left\langle \frac{1}{\kappa} \right\rangle^{-1} \langle \kappa \rangle^{-1} + \sigma_R^2 \sqrt{2} k_{\text{PsF}} \int_0^\infty B(r) \exp(-rk_{\text{PsF}}) \sin(rk_{\text{PsF}} + \pi/4) dr$$

$$\sigma_R^2 = 1 - \left[\left\langle \frac{1}{\kappa} \right\rangle \langle \kappa \rangle \right]^{-1} = \text{normalized difference of the harmonic and arithmetic averages.}$$

An extended first-order approximation for the effective fast P-wavenumber \bar{k}_{P} can be obtained by using \bar{k}_{Ps} in place of the background slow P-wavenumber k_{Ps} in the expressions for \bar{k}_{P} . Numerical results by Muller *et al.* (2007) show that including the permeability fluctuations (with correlation lengths of elastic moduli and permeability fluctuations equal) has the following effects compared with the homogeneous permeability case: the maximum attenuation peak shifts to slightly lower frequencies; the magnitude of maximum attenuation is slightly reduced; there is a broadening of the attenuation peak; and phase velocities are slightly faster.

Uses

The results described in this section can be used to estimate velocity dispersion and attenuation caused by fluid-flow effects in heterogeneous porous media.

Assumptions and limitations

The equations described in this section apply under the following conditions:

- linear poroelastic media;
- small fluctuations in the material properties of the heterogeneous medium. Numerical tests in one dimension indicate that the model works for relative contrasts of at least 30%;
- isotropic spatial autocorrelation function of the fluctuations; and
- low-frequency approximation. The scale of the heterogeneities is smaller than the wavelength, but larger than the pore scale.

6.20 Waves in a pure viscous fluid

Synopsis

Acoustic waves in a pure viscous fluid are dispersive and attenuate because of the shear component in the wave-induced deformation of an elementary fluid volume. The linearized wave equation in a viscous fluid can be derived from the Navier–Stokes equation (Schlichting, 1951) as

$$\rho \frac{\partial^2 u}{\partial t^2} = c_0^2 \frac{\partial^2 u}{\partial x^2} + \frac{4}{3} \eta \frac{\partial^3 u}{\partial x^2 \partial t} \quad c_0^2 = \frac{K_f}{\rho}$$

Then the wavenumber-to-angular-frequency ratio is

$$\begin{aligned} \frac{k}{\omega} &= \sqrt{\frac{c_0^2 + i\gamma\omega}{c_0^4 + \gamma^2\omega^2}} = \frac{e^{i \arctan z/2}}{c_0 \sqrt[4]{1+z^2}} \\ &= \frac{1}{c_0 \sqrt[4]{1+z^2}} \left(\sqrt{\frac{\sqrt{1+z^2}+1}{2\sqrt{1+z^2}}} + i \sqrt{\frac{\sqrt{1+z^2}-1}{2\sqrt{1+z^2}}} \right) \end{aligned}$$

$$\gamma = \frac{4\eta}{3\rho}, \quad z = \frac{\gamma\omega}{c_0^2}$$

and the phase velocity, attenuation coefficient, and inverse quality factor are

$$V = c_0 \sqrt{\frac{2(1+z^2)}{\sqrt{1+z^2}+1}}$$

$$a = \frac{\omega}{c_0} \sqrt{\frac{\sqrt{1+z^2}-1}{2(1+z^2)}}$$

$$Q^{-1} = 2 \sqrt{\frac{\sqrt{1+z^2}-1}{\sqrt{1+z^2}+1}}$$

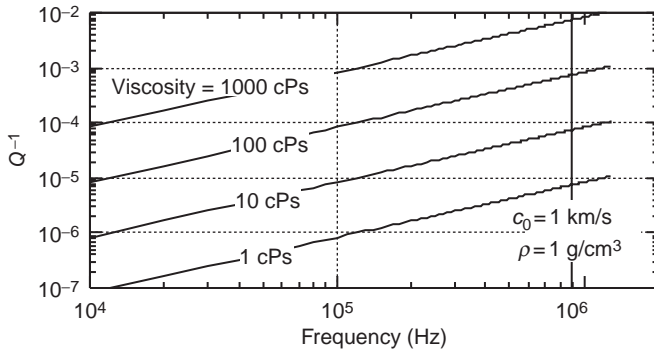


Figure 6.20.1 Inverse quality factor for acoustic waves in viscous fluid.

If $z \ll 1$ these expressions can be simplified to

$$V = c_0 \left[1 + 2 \left(\frac{4\pi\eta f}{3\rho c_0^2} \right)^2 \right] \quad a = \frac{8\pi^2\eta f^2}{3\rho c_0^3} \quad Q^{-1} = \frac{8\pi\eta f}{3\rho c_0^2}$$

where u is displacement, ρ is density, η is viscosity, K_f is the bulk modulus of the fluid, x is a coordinate, t is time, k is the wavenumber, ω is angular frequency, V is the phase velocity, a is an attenuation coefficient, Q is the quality factor, and f is frequency.

Attenuation is very small at low frequency and for a low-viscosity fluid; however, it may become noticeable in high-viscosity fluids (Figure 6.20.1).

Uses

The equations presented in this section can be used for estimating the frequency dependence of the acoustic velocity in viscous fluids.

Assumptions and limitations

The preceding equations assume that the fluid is Newtonian. Many high-viscosity oils are non-Newtonian (i.e., their flow cannot be accurately described by the Navier–Stokes equation).

6.21 Physical properties of gases and fluids

Synopsis

The **bulk modulus** (K) of a fluid or a gas is defined as

$$K = \frac{1}{\beta} = -\frac{dP}{dV/V} = \rho \frac{dP}{d\rho}$$

where β is compressibility, P is pressure, and V is volume. For small pressure variations (typical for wave propagation), the pressure variation is related to the density variation through the acoustic velocity c_0 (which is 1500 m/s for water at room conditions) as follows:

$$dP = c_0^2 d\rho.$$

Therefore,

$$K = \rho c_0^2.$$

Batzle and Wang (1992) have summarized some important properties of reservoir fluids.

Brine

The **density of brine** ρ_B of salinity S of sodium chloride is

$$\rho_B = \rho_w + S\{0.668 + 0.44S + 10^{-6}[300P - 2400P S \\ + T(80 + 3T - 3300S - 13P + 47P S)]\}$$

where the **density of pure water** (ρ_w) is

$$\rho_w = 1 + 10^{-6}(-80T - 3.3T^2 + 0.00175T^3 \\ + 489P - 2TP + 0.016T^2P - 1.3 \times 10^{-5}T^3P \\ - 0.333P^2 - 0.002TP^2)$$

In these formulas pressure P is in MPa, temperature T is in degrees Celsius, salinity S is in fractions of one (parts per million divided by 10^6), and density (ρ_B and ρ_w) is in g/cm³.

The **acoustic velocity in brine** V_B in m/s is

$$V_B = V_w + S(1170 - 9.6T + 0.055T^2 - 8.5 \times 10^{-5}T^3 \\ + 2.6P - 0.0029TP - 0.0476P^2) \\ + S^{3/2}(780 - 10P + 0.16P^2) - 1820S^2$$

where the **acoustic velocity in pure water** V_w in m/s is

$$V_w = \sum_{i=0}^4 \sum_{j=0}^3 \omega_{ij} T^i P^j$$

and coefficients ω_{ij} are

$$\begin{aligned}
\omega_{00} &= 1402.85 & \omega_{02} &= 3.437 \times 10^{-3} \\
\omega_{10} &= 4.871 & \omega_{12} &= 1.739 \times 10^{-4} \\
\omega_{20} &= -0.04783 & \omega_{22} &= -2.135 \times 10^{-6} \\
\omega_{30} &= 1.487 \times 10^{-4} & \omega_{32} &= -1.455 \times 10^{-8} \\
\omega_{40} &= -2.197 \times 10^{-7} & \omega_{42} &= 5.230 \times 10^{-11} \\
\omega_{01} &= 1.524 & \omega_{03} &= -1.197 \times 10^{-5} \\
\omega_{11} &= -0.0111 & \omega_{13} &= -1.628 \times 10^{-6} \\
\omega_{21} &= 2.747 \times 10^{-4} & \omega_{23} &= 1.237 \times 10^{-8} \\
\omega_{31} &= -6.503 \times 10^{-7} & \omega_{33} &= 1.327 \times 10^{-10} \\
\omega_{41} &= 7.987 \times 10^{-10} & \omega_{43} &= -4.614 \times 10^{-13}
\end{aligned}$$

We define the **gas–water ratio** R_G as the ratio of the volume of dissolved gas at standard conditions to the volume of brine. Then, for temperatures below 250 °C, the maximum amount of methane that can go into solution in brine is

$$\begin{aligned}
\log_{10}(R_G) &= \log_{10}(0.712P|T - 76.71|^{1.5} + 3676P^{0.64}) \\
&\quad - 4 - 7.786S(T + 17.78)^{-0.306}
\end{aligned}$$

If K_B is the bulk modulus of the gas-free brine, and K_G is that of brine with gas–water ratio R_G , then

$$\frac{K_B}{K_G} = 1 + 0.0494R_G$$

(i.e., the bulk modulus decreases linearly with increasing gas content). Experimental data are sparse for the density of brine, but the consensus is that the density is almost independent of the amount of dissolved gas.

The **viscosity of brine** η in cPs for temperatures below 250 °C is

$$\eta = 0.1 + 0.333S + (1.65 + 91.9S^3) \exp\{-[0.42(S^{0.8} - 0.17)^2 + 0.045]T^{0.8}\}$$

Gas

Natural gas is characterized by its gravity G , which is the ratio of gas density to air density at 15.6 °C and atmospheric pressure. The gravity of methane is 0.56. The gravity of heavier gases may be as large as 1.8. Algorithms for calculating the **gas density** and the **bulk modulus** follow.

Step 1: Calculate absolute temperature T_a as

$$T_a = T + 273.15$$

where T is in degrees Celsius.

Step 2: Calculate the pseudo-pressure P_r and the pseudo-temperature T_r as

$$P_r = \frac{P}{4.892 - 0.4048G} \quad T_r = \frac{T_a}{94.72 + 170.75G}$$

where pressure is in MPa.

Step 3: Calculate **density** ρ_G in g/cm^3 as

$$\rho_G \approx \frac{28.8GP}{ZRT_a}$$

$$Z = aP_r + b + E \quad E = cd$$

$$d = \exp \left\{ - \left[0.45 + 8 \left(0.56 - \frac{1}{T_r} \right)^2 \right] \frac{P_r^{1.2}}{T_r} \right\}$$

$$c = 0.109(3.85 - T_r)^2 \quad b = 0.642T_r - 0.007T_r^4 - 0.52$$

$$a = 0.03 + 0.00527(3.5 - T_r)^3$$

$$R = 8.31441 \text{ J/(g mol deg) (gas constant)}$$

Step 4: Calculate the adiabatic **bulk modulus** K_G in MPa as

$$K_G \approx \frac{P\gamma}{1 - P_r/(Zf)}, \quad \gamma = 0.85 + \frac{5.6}{P_r + 2} + \frac{27.1}{(P_r + 3.5)^2} - 8.7e^{-0.65(P_r+1)}$$

$$f = cdm + a, \quad m = 1.2 \left\{ - \left[0.45 + 8 \left(0.56 - \frac{1}{T_r} \right)^2 \right] \frac{P_r^{0.2}}{T_r} \right\}$$

The preceding approximate expressions for ρ_G and K_G are valid as long as P_r and T_r are not both within 0.1 of unity.

Oil

Oil density under room conditions may vary from under 0.5 to 1 g/cm^3 , and most produced oils are in the 0.7–0.8 g/cm^3 range. A reference (standard) density that can be used to characterize an oil ρ_0 is measured at 15.6 °C and atmospheric pressure. A widely used classification of crude oil is the American Petroleum Institute's oil gravity (API gravity). It is defined as

$$\text{API} = \frac{141.5}{\rho_0} - 131.5$$

where density is in g/cm^3 . API gravity may be about 5 for very heavy oils and about 100 for light condensates.

Acoustic velocity V_P in oil may generally vary with temperature T and **molecular weight** M :

$$V_P(T, M) = V_0 - b\Delta T - a_m \left(\frac{1}{M} - \frac{1}{M_0} \right)$$

$$\frac{1}{b} = 0.306 - \frac{7.6}{M}$$

In this formula, V_0 is the velocity of oil of molecular weight M_0 at temperature T_0 ; a_m is a positive function of temperature, and thus oil velocity increases with molecular weight. When components are mixed, velocity can be approximately calculated as a fractional average of the end components.

For **dead oil** (oil with no dissolved gas), the effects of pressure and temperature on density are largely independent. The pressure dependence is

$$\rho_P = \rho_0 + (0.00277P - 1.71 \times 10^{-7} P^3)(\rho_0 - 1.15)^2 + 3.49 \times 10^{-4} P$$

where ρ_P is the density in g/cm^3 at pressure P in MPa. Temperature dependence of density at a given pressure P is

$$\rho = \rho_P / [0.972 + 3.81 \times 10^{-4} (T + 17.78)^{1.175}]$$

where temperature is in degrees Celsius.

The **acoustic velocity** in **dead oil** depends on pressure and temperature as

$$V_P(\text{m/s}) = 2096 \left(\frac{\rho_0}{2.6 - \rho_0} \right)^{1/2} - 3.7T + 4.64P$$

$$+ 0.0115[4.12(1.08\rho_0^{-1} - 1)^{1.2} - 1]TP$$

or, in terms of API gravity as

$$V_P(\text{ft/s}) = 15450(77.1 + \text{API})^{-1/2} - 3.7T + 4.64P$$

$$+ 0.0115[0.36\text{API}^{1/2} - 1]TP$$

Live oil

Large amounts of **gas can be dissolved in an oil**. The original fluid *in situ* is usually characterized by R_G , the volume ratio of liberated gas to remaining oil at atmospheric pressure and 15.6°C . The maximum amount of gas that can be dissolved in an oil is a function of pressure, temperature, and the composition of both the gas and the oil:

$$R_G^{(\max)} = 0.02123 G \left[P \exp \left(\frac{4.072}{\rho_0} - 0.00377T \right) \right]^{1.205}$$

or, in terms of API gravity:

$$R_G^{(\max)} = 2.03G[P \exp(0.02878 \text{ API} - 0.00377 T)]^{1.205}$$

where R_G is in liters/liter (1 L/L = 5.615 ft³/bbl) and G is the gas gravity. Temperature is in degrees Celsius, and pressure is in MPa.

Velocities in oils with dissolved gas can still be calculated versus pressure and temperature as follows, by using the preceding formulas with a pseudo-density ρ' used instead of ρ_0 :

$$\rho' = \frac{\rho_0}{B_0} (1 + 0.001 R_G)^{-1}$$

$$B_0 = 0.972 + 0.00038 \left[2.4 R_G \left(\frac{G}{\rho_0} \right)^{1/2} + T + 17.8 \right]^{1.175}$$

The true **density of oil with gas** (in g/cm³) at saturation can be calculated as

$$\rho_G = (\rho_0 + 0.0012 G R_G) / B_0$$

For temperatures and pressures that differ from those at saturation, ρ_G must be adjusted using the temperature and pressure corrections described in the section above on dead oil.

Calculate the density and acoustic velocity of live oil of 30 API gravity at 80 °C and 20 MPa. The gas–oil ratio R_G is 100, and the gas gravity is 0.6.

Calculate ρ_0 from API as

$$\rho_0 = \frac{141.5}{\text{API} + 131.5} = \frac{141.5}{30 + 131.5} = 0.876 \text{ g/cm}^3$$

Calculate B_0 as

$$B_0 = 0.972 + 0.00038 \left[2.4 R_G \left(\frac{G}{\rho_0} \right)^{1/2} + T + 17.8 \right]^{1.175}$$

$$B_0 = 0.972 + 0.00038 \left[2.4 \times 100 \times \left(\frac{0.6}{0.876} \right)^{1/2} + 80 + 17.8 \right]^{1.175}$$

$$= 1.2770$$

Calculate the pseudo-density ρ' as

$$\rho' = \frac{\rho_0}{B_0} (1 + 0.001 R_G)^{-1} = 0.623 \text{ g/cm}^3$$

Calculate the density of oil with gas ρ_G as

$$\rho_G = (\rho_0 + 0.0012GR_G)/B_0 = 0.7424 \text{ g/cm}^3$$

Correct this density for pressure and find the density ρ_P as

$$\begin{aligned}\rho_P &= \rho_G + (0.00277P - 1.71 \times 10^{-7}P^3)(\rho_G - 1.15)^2 + 3.49 \times 10^{-4}P \\ &= 0.742 + (0.00277 \times 20 - 1.71 \times 10^{-7} \times 20^3)(0.742 - 1.15)^2 \\ &\quad + 3.49 \times 10^{-4} \times 20 = 0.758 \text{ g/cm}^3\end{aligned}$$

Finally, apply the temperature correction to obtain the actual density as

$$\begin{aligned}\rho &= \rho_P / [0.972 + 3.81 \times 10^{-4}(T + 17.78)^{1.175}] \\ &= 0.758 / [0.972 + 3.81 \times 10^{-4}(80 + 17.78)^{1.175}] = 0.718 \text{ g/cm}^3\end{aligned}$$

Calculate the velocity in oil with gas V_P as

$$\begin{aligned}V_P &= 2096 \left(\frac{\rho'}{2.6 - \rho'} \right)^{1/2} - 3.7T + 4.64P \\ &\quad + 0.0115 \left[4.12(1.08/\rho' - 1)^{1/2} - 1 \right] TP \\ &= 2096 \left(\frac{0.623}{2.6 - 0.623} \right)^{1/2} - 3.7 \times 80 + 4.64 \times 20 \\ &\quad + 0.0115 \left[4.12(1.08/0.623 - 1)^{1/2} - 1 \right] \times 80 \times 20 \\ &= 1020 \text{ m/s}\end{aligned}$$

The **viscosity of dead oil** (η) decreases rapidly with increasing temperature. At room pressure for a gas-free oil we have

$$\log_{10}(\eta + 1) = 0.505y(17.8 + T)^{-1.163}$$

$$\log_{10}(y) = 5.693 - 2.863/\rho_0$$

Pressure has a smaller influence on viscosity and can be estimated independently of the temperature influence. If oil viscosity is η_0 at a given temperature and room pressure, its viscosity at pressure P and the same temperature is

$$\eta = \eta_0 + 0.145PI$$

$$\log_{10}(I) = 18.6[0.1 \log_{10}(\eta_0) + (\log_{10}(\eta_0) + 2)^{-0.1} - 0.985]$$

Viscosity in these formulas is in centipoise, temperature is in degrees Celsius, and pressure is in MPa.

Uses

The equations presented in this section are used to estimate acoustic velocities and densities of pore fluids.

Assumptions and limitations

The formulas are mostly based on empirical measurements summarized by Batzle and Wang (1992).

7 Empirical relations

7.1 Velocity–porosity models: critical porosity and Nur’s modified Voigt average

Synopsis

Nur *et al.* (1991, 1995) and other workers have championed the simple, if not obvious, idea that the P and S velocities of rocks should trend between the velocities of the mineral grains in the limit of low porosity and the values for a mineral–pore–fluid suspension in the limit of high porosity. This idea is based on the observation that for most porous materials there is a **critical porosity**, ϕ_c , that separates their mechanical and acoustic behavior into two distinct domains. For porosities lower than ϕ_c , the mineral grains are load-bearing, whereas for porosities greater than ϕ_c , the rock simply “falls apart” and becomes a suspension, in which the fluid phase is load-bearing. The transition from solid to suspension is implicit in the well-known empirical velocity–porosity relations of Raymer *et al.* (1980) discussed in Section 7.4.

In the **suspension domain**, $\phi > \phi_c$, the effective bulk and shear moduli can be estimated quite accurately using the Reuss (isostress) average:

$$K_R^{-1} = (1 - \phi)K_0^{-1} + \phi K_f^{-1}, \quad \mu_R = 0$$

where K_0 and K_f are the bulk moduli of the mineral material and the fluid, respectively. The effective shear modulus of the suspension is zero because the shear modulus of the fluid is zero.

In the **load-bearing domain**, $\phi < \phi_c$, the moduli decrease rapidly from the mineral values at zero porosity to the suspension values at the critical porosity. Nur found that this dependence can often be approximated with a straight line when expressed as ρV^2 versus porosity. Figure 7.1.1 illustrates this behavior with laboratory ultrasonic sandstone data from Han (1986) for samples at 40 MPa effective pressure with clay content <10% by volume. In the figure, ρV_P^2 is the P-wave modulus ($K + \frac{4}{3}\mu$) and ρV_S^2 is the shear modulus.

A geometric interpretation of the mineral-to-critical-porosity trend is simply that if we make the porosity large enough, the grains must lose contact and the rock must lose its rigidity. The geologic interpretation is that, at least for clastics, the weak suspension state at critical porosity, ϕ_c , describes the sediment when it is first deposited before compaction and diagenesis. The value of ϕ_c is determined by the

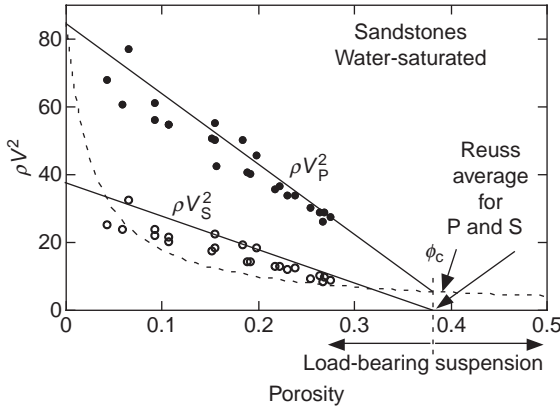


Figure 7.1.1 Critical porosity behavior: ρV_P^2 (P-wave modulus) versus porosity and ρV_S^2 (shear modulus) versus porosity, both trending between the mineral value at zero porosity and the Reuss average at critical porosity.

grain sorting and angularity at deposition. Subsequent compaction and diagenesis move the sample along an upward trajectory as the porosity is reduced and the elastic stiffness is increased.

Although there is nothing special about a linear trend of ρV^2 versus ϕ , it does describe sandstones fairly well, and it leads to convenient mathematical properties. For dry rocks, the bulk and shear moduli can be expressed as the linear functions

$$K_{\text{dry}} = K_0 \left(1 - \frac{\phi}{\phi_c} \right)$$

$$\mu_{\text{dry}} = \mu_0 \left(1 - \frac{\phi}{\phi_c} \right)$$

where K_0 and μ_0 are the mineral bulk and shear moduli, respectively. Thus, the dry-rock bulk and shear moduli trend linearly between K_0, μ_0 at $\phi = 0$ and $K_{\text{dry}} = \mu_{\text{dry}} = 0$ at $\phi = \phi_c$.

This linear dependence can be thought of as a **modified Voigt average** (see [Section 4.2](#)), where one end-member is the mineral and the other end-member is the suspension at the critical porosity, which can be measured or estimated using the Reuss average. Then we can write

$$M_{\text{MV}} = (1 - \phi')M_0 + \phi'M_c$$

where M_0 and M_c are the moduli (bulk or shear) of the mineral material at zero porosity and of the suspension at the critical porosity. The porosity is scaled by the critical porosity, $\phi' = \phi/\phi_c$, and thus ϕ' ranges from 0 to 1 as ϕ ranges from 0 to ϕ_c . Note that using the suspension modulus M_c in this form automatically incorporates the effect of pore fluids on the modified Voigt average, which is equivalent to applying Gassmann's relations to the dry-rock-modulus–porosity relations (see [Section 6.3](#) on Gassmann's relations).

Table 7.1.1. Typical values of critical porosity.

Material	Critical porosity
Natural rocks	
Sandstones	40%
Limestones	60%
Dolomites	40%
Pumice	80%
Chalks	65%
Rock salt	40%
Cracked igneous rocks	5%
Oceanic basalts	20%
Artificial rocks	
Sintered glass beads	40%
Glass foam	90%

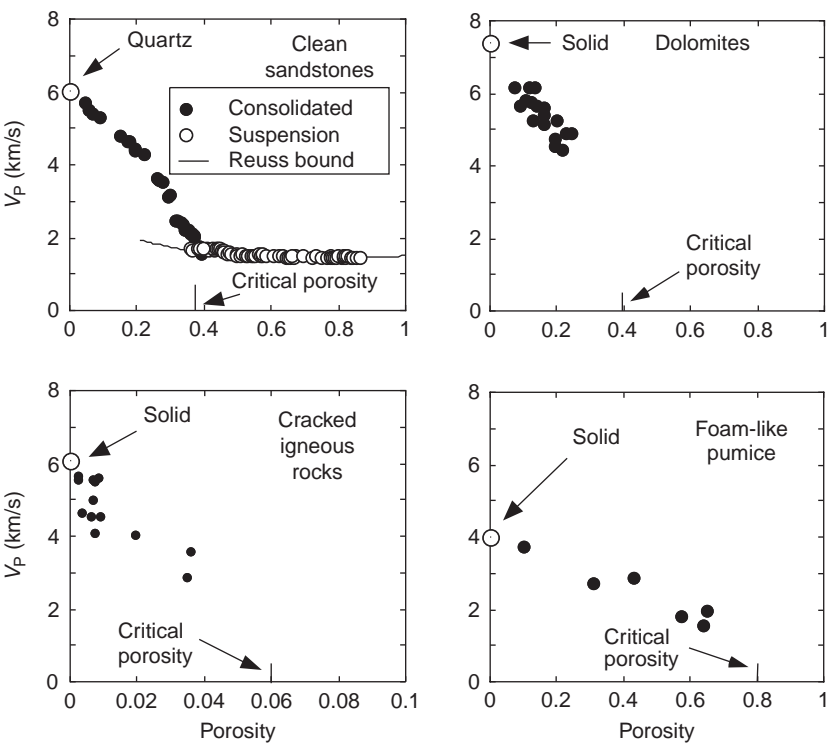


Figure 7.1.2 Examples of critical-porosity behavior in various rock types.

The critical porosity value depends on the internal structure of the rock. It may be very small for cracked rocks, large for foam-like rocks, and intermediate for granular rocks. Examples of critical porosity behavior in sandstones, dolomites, pumice, and cracked igneous rocks are shown in [Figure 7.1.2](#) and [Table 7.1.1](#).

Uses

The equations presented in this section can be used for relating velocity and porosity.

Assumptions and limitations

The model discussed in this section has the following limitations:

- the critical porosity result is empirical;
- because only the variation with porosity is described, one must apply other corrections to account for parameters such as clay content.

Extensions

Similar descriptions of the failure strength of porous media can be quantified in terms of the critical porosity.

7.2 Velocity–porosity models: Geertsma’s empirical relations for compressibility

Synopsis

Geertsma (1961) suggested the following empirical estimate of bulk modulus in dry rocks with porosities $0 < \phi < 0.3$:

$$\frac{1}{K_{\text{dry}}} = \frac{1}{K_0}(1 + 50\phi)$$

where K_{dry} is the dry-rock bulk modulus and K_0 is the mineral bulk modulus.

Uses

This equation can be used to relate bulk modulus to porosity in rocks empirically.

Assumptions and limitations

This relation is empirical.

7.3 Velocity–porosity models: Wyllie’s time-average equation

Synopsis

Measurements by Wyllie *et al.* (1956, 1958, 1963) revealed that a relatively simple monotonic relation often can be found between velocity and porosity in sedimentary rocks when: (1) they have relatively uniform mineralogy, (2) they are fluid-saturated,

Table 7.3.1 *Typical mineral P-wave velocities.*

	V_{P-0} (m/s)
Sandstones	5480–5950
Limestones	6400–7000
Dolomites	7000–7925

and (3) they are at high effective pressure. Wyllie *et al.* approximated these relations with the expression

$$\frac{1}{V_P} = \frac{\phi}{V_{P-fl}} + \frac{1 - \phi}{V_{P-0}}$$

where V_P , V_{P-0} , and V_{P-fl} are the P-wave velocities of the saturated rocks, of the mineral material making up the rocks, and of the pore fluid, respectively. Some useful values for V_{P-0} are shown in [Table 7.3.1](#).

The interpretation of this expression is that the total transit time is the sum of the transit time in the mineral plus the transit time in the pore fluid. Hence, it is often called the **time-average equation**.

Caution

The time-average equation is heuristic and cannot be justified theoretically. The argument that the total transit time can be written as the sum of the transit time in each of the phases is a seismic ray theory assumption and can be correct only if: (1) the wavelength is small compared with the typical pore size and grain size and (2) the pores and grains are arranged as homogeneous layers perpendicular to the ray path. Because neither of these assumptions is even remotely true, the agreement with observations is only fortuitous. Attempts to overinterpret observations in terms of the mineralogy and fluid properties can lead to errors. An illustration of this point is that a form of the time-average equation is sometimes used to interpret shear velocities. To do this, a finite value of shear velocity in the fluid is used, which is clearly nonsense.

Uses

Wyllie’s time-average equation can be used for the following purposes:

- to estimate the expected seismic velocities of rocks with a given mineralogy and pore fluid;
- to estimate the porosity from measurements of seismic velocity and knowledge of the rock type and pore-fluid content.

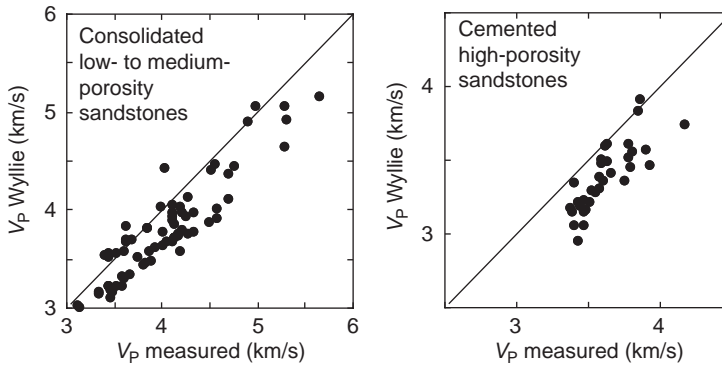


Figure 7.3.1 Comparison of predicted and measured velocity in water-saturated medium-to-low-porosity shaley sandstones (40 MPa effective pressure). The velocity in pure quartz is taken at 6.038 km/s, which follows from the bulk modulus, shear modulus, and density being 38 GPa, 44 GPa, and 2.65 g/cm³, respectively. The velocity in clay is 3.41 km/s, which follows from the bulk modulus, shear modulus, and density being 21 GPa, 7 GPa, and 2.58 g/cm³, respectively.

Assumptions and limitations

The use of the time-average equation requires the following serious considerations:

- the rock is isotropic;
- the rock must be fluid saturated;
- the time-average equation works best if rocks are at high enough effective pressure to be at the “terminal velocity,” which is usually of the order of 30 MPa. Most rocks show an increase of velocity with pressure owing to the progressive closing of compliant crack-like parts of the pore space, including microcracks, compliant grain boundaries, and narrow tips of otherwise equant-shaped pores. Usually the velocity appears to level off at high pressure, approaching a limiting “terminal” velocity when, presumably, all the crack-like pore space is closed. Because the compliant fraction of the pore space can have a very small porosity and yet have a very large effect on velocity, its presence, at low pressures, can cause a very poor correlation between porosity and velocity; hence, the requirement for high effective pressure. At low pressures or in uncompacted situations, the time-average equation tends to overpredict the velocity and porosity. Log analysts sometimes use a compaction correction, which is an empirical attempt to correct for the effect of compliant porosity. The time-average equation underpredicts velocities in consolidated low-to-medium-porosity rocks and in high-porosity cemented rocks, as shown in [Figure 7.3.1](#);
- the time-average relation should not be used to relate velocity to porosity in unconsolidated uncemented rocks;
- the time-average relation works best with primary porosity. Secondary or vuggy porosity tends to be “stiffer” than primary porosity and therefore lowers the velocity less. In these situations, the time-average equations tend to underpredict the velocity and the porosity. Empirical corrections can be attempted to adjust for this;

- the time-average relation assumes a single homogeneous mineralogy. Empirical corrections for mixed mineralogy, such as shaliness, can be attempted to adjust for this; and
- the time-average equation usually works best for intermediate porosities (see the Raymer equations in [Section 7.4](#)).

Extension

The time-average equation can be extended in the following ways:

- for mixed mineralogy one can often use an effective average velocity for the mineral material;
- empirical corrections can sometimes be found for shaliness, compaction, and secondary porosity, but they should be calibrated when possible.

7.4 Velocity–porosity models: Raymer–Hunt–Gardner relations

Synopsis

Raymer *et al.* (1980) suggested improvements to Wyllie’s empirical velocity-to-travel time relations as follows:

$$V = (1 - \phi)^2 V_0 + \phi V_{fl}, \quad \phi < 37\%$$

$$\frac{1}{\rho V^2} = \frac{\phi}{\rho_{fl} V_{fl}^2} + \frac{1 - \phi}{\rho_0 V_0^2}, \quad \phi > 47\%$$

where V , V_{fl} , and V_0 are the velocities in the rock, the pore fluid, and the minerals, respectively. The terms ρ , ρ_{fl} , and ρ_0 are the densities of the rock, the pore fluid, and the minerals, respectively. Note that the second relation is the same as the isostress or Reuss average (see [Section 4.2](#)) of the P-wave moduli. A third expression for intermediate porosities is derived as a simple interpolation of these two:

$$\frac{1}{V} = \frac{0.47 - \phi}{0.10} \frac{1}{V_{37}} + \frac{\phi - 0.37}{0.10} \frac{1}{V_{47}}$$

where V_{37} is calculated from the low-porosity formula at $\phi = 0.37$, and V_{47} is calculated from the high-porosity formula at $\phi = 0.47$.

[Figure 7.4.1](#) shows a comparison of predicted and measured velocities in water-saturated shaley sandstones at 40 MPa effective pressure. [Figure 7.4.2](#) compares the predictions of Raymer *et al.* (1980), Wyllie *et al.* (1956), and Gardner *et al.* (1974) for velocity versus porosity to data for water-saturated clay-free sandstones. None of the equations adequately models the uncemented sands.

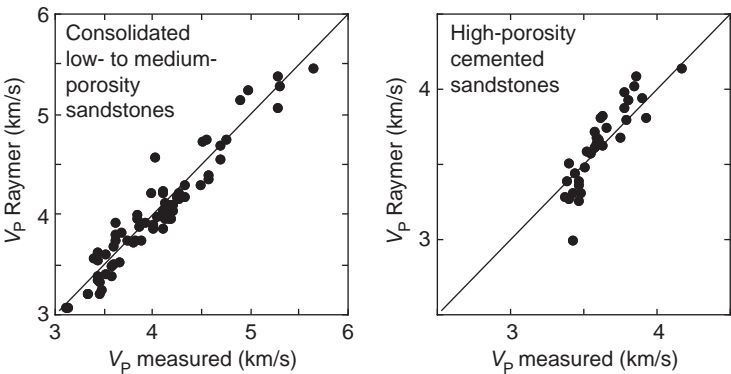


Figure 7.4.1 Comparison of predicted and measured velocities in water-saturated shaley sandstones (40 MPa effective pressure). The velocity in pure quartz is taken at 6.038 km/s, which follows from the bulk modulus, shear modulus, and density being 38 GPa, 44 GPa, and 2.65 g/cm³, respectively. The velocity in clay is 3.41 km/s, which follows from the bulk modulus, shear modulus, and density being 21 GPa, 7 GPa, and 2.58 g/cm³, respectively.

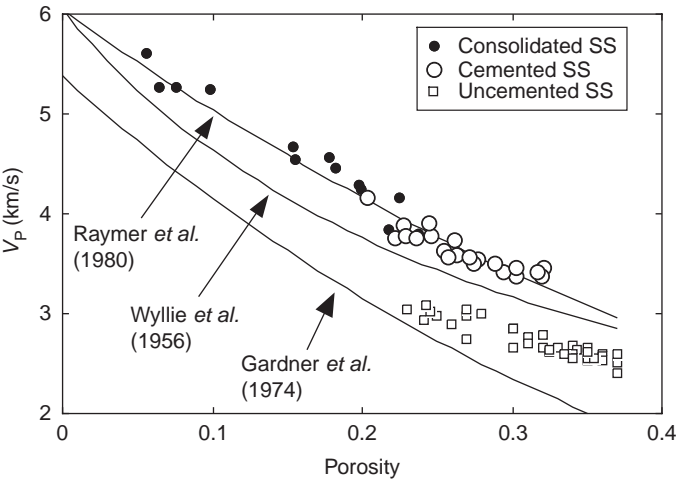


Figure 7.4.2 Velocity versus porosity in water-saturated clay-free sandstones. The Wyllie *et al.* (1956) equation underestimates the consolidated rock values. The Gardner *et al.* (1974) equation underpredicts all of the measured values. None of the equations adequately models the uncemented sands. For the predictions, the mineral is taken as quartz.

Uses

The Raymer–Hunt–Gardner relations have the following uses:

- to estimate the seismic velocities of rocks with a given mineralogy and pore fluid;
- to estimate the porosity from measurements of seismic velocity and knowledge of the rock type and pore-fluid content.

Assumptions and limitations

The use of the Raymer–Hunt–Gardner relations requires the following considerations:

- the rock is isotropic;
- all minerals making up the rock have the same velocities;
- the rock is fluid-saturated;
- the method is empirical. See also the discussion and limitations of Wyllie's time-average equation (Section 7.3);
- these relations should work best at high enough effective pressure to be at the “terminal velocity,” usually of the order of 30 MPa. Most rocks show an increase of velocity with pressure owing to the progressive closing of compliant crack-like parts of the pore space, including microcracks, compliant grain boundaries, and narrow tips of otherwise equant-shaped pores. Usually the velocity appears to level off at high pressure, approaching a limiting “terminal” velocity, when, presumably, all the crack-like pore space is closed. Because the compliant fraction of the pore space can have very small porosity and yet have a very large effect on velocity, its presence, at low pressures, can cause a very poor correlation between porosity and velocity; hence, the requirement for high effective pressure. These relations work well for consolidated low-to-medium porosity and high-porosity cemented sandstones; and
- these relations should not be used for unconsolidated uncemented rocks.

7.5 Velocity–porosity–clay models: Han's empirical relations for shaley sandstones

Synopsis

Han (1986) found empirical regressions relating ultrasonic (laboratory) velocities to porosity and clay content. These were determined from a set of 80 *well-consolidated* Gulf Coast sandstones with porosities, ϕ , ranging from 3% to 30% and clay volume fractions, C , ranging from 0% to 55%. The study found that clean sandstone velocities can be related empirically to porosity alone with very high accuracy. When clay is present, the correlation with porosity is relatively poor but becomes very accurate if clay volume is also included in the regression. The regressions are shown in Figure 7.5.1 and Table 7.5.1.

Eberhart-Phillips (1989) used a multivariate analysis to investigate the combined influences of effective pressure, porosity, and clay content on Han's measurements of velocities in water-saturated shaley sandstones. She found that the water-saturated P- and S-wave ultrasonic velocities (in km/s) could be described empirically by

$$V_P = 5.77 - 6.94\phi - 1.73\sqrt{C} + 0.446(P_e - 1.0e^{-16.7P_e})$$

$$V_S = 3.70 - 4.94\phi - 1.57\sqrt{C} + 0.361(P_e - 1.0e^{-16.7P_e})$$

Table 7.5.1 Han's empirical relations between ultrasonic V_P and V_S in km/s with porosity and clay volume fractions.

Clean sandstones (determined from ten samples)		
Water-saturated		
40 MPa	$V_P = 6.08 - 8.06\phi$	$V_S = 4.06 - 6.28\phi$
Shaley sandstones (determined from 70 samples)		
Water-saturated		
40 MPa	$V_P = 5.59 - 6.93\phi - 2.18C$	$V_S = 3.52 - 4.91\phi - 1.89C$
30 MPa	$V_P = 5.55 - 6.96\phi - 2.18C$	$V_S = 3.47 - 4.84\phi - 1.87C$
20 MPa	$V_P = 5.49 - 6.94\phi - 2.17C$	$V_S = 3.39 - 4.73\phi - 1.81C$
10 MPa	$V_P = 5.39 - 7.08\phi - 2.13C$	$V_S = 3.29 - 4.73\phi - 1.74C$
5 MPa	$V_P = 5.26 - 7.08\phi - 2.02C$	$V_S = 3.16 - 4.77\phi - 1.64C$
Dry		
40 MPa	$V_P = 5.41 - 6.35\phi - 2.87C$	$V_S = 3.57 - 4.57\phi - 1.83C$

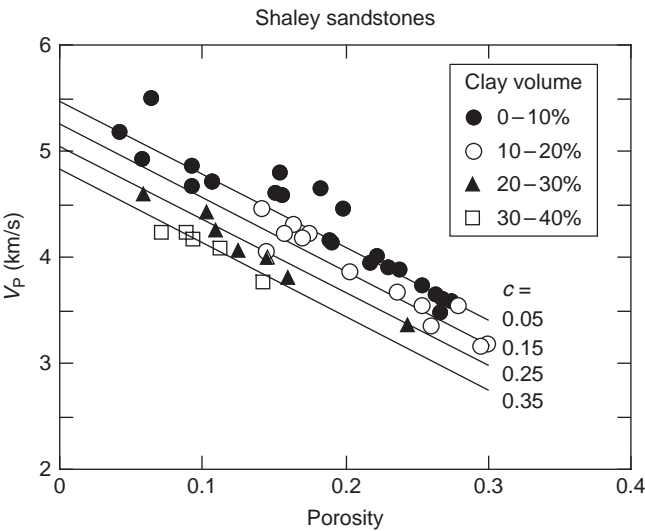


Figure 7.5.1 Han's water-saturated ultrasonic velocity data at 40 MPa compared with his empirical relations evaluated at four different clay fractions.

where P_e is the effective pressure in kilobars. The model accounts for 95% of the variance and has a root mean squared (rms) error of 0.1 km/s.

Uses

These relations can be used to relate velocity, porosity, and clay content empirically in shaley sandstones.

Assumptions and limitations

The preceding relations have the following limitations:

- these relations are empirical and thus, strictly speaking, they apply only to the set of rocks studied. However, the result should extend in general to many consolidated sandstones. In any case, the key result is that clay content is an important parameter for quantifying velocity; if possible, the regression coefficients should be recalibrated from cores or logs at the site being studied, but be sure to include clay;
- Han's linear regression coefficients change slightly with confining pressure. They are fairly stable above about 10 MPa; below this, they vary more, and the correlation coefficients degrade;
- a common mistake is to try to overinterpret the empirical coefficients by comparing the equations, for example, to Wyllie's time-average equation (see [Section 7.3](#)). This can lead to nonsensical interpreted values for the velocities of water and clay. This is not surprising, for Wyllie's equations are only heuristic and;
- it is dangerous to extrapolate the results to values of porosity or clay content outside the range of the experiments. Note, for example, that the intercepts of the various equations corresponding to no porosity and no clay do not agree with each other and generally do not agree with the velocities in pure quartz.

7.6 Velocity–porosity–clay models: Tosaya's empirical relations for shaley sandstones

Synopsis

On the basis of their measurements, Tosaya and Nur (1982) determined empirical regressions relating ultrasonic (laboratory) P- and S-wave velocities to porosity and clay content. For water-saturated rocks at an effective pressure of 40 MPa, they found

$$V_P(\text{km/s}) = 5.8 - 8.6\phi - 2.4C$$

$$V_S(\text{km/s}) = 3.7 - 6.3\phi - 2.1C$$

where ϕ is the porosity and C is the clay content by volume. See also Han's relation in [Section 7.5](#).

Uses

Tosaya's relations can be used to relate velocity, porosity, and clay content empirically in shaley sandstones.

Assumptions and limitations

Tosaya's relations have the following limitations:

- these relations are empirical, and thus strictly speaking they apply only to the set of rocks studied. However, the result should extend in general to many consolidated sandstones. In any case, the key result is that clay content is an important parameter for quantifying velocity; if possible, the regression coefficients should be recalibrated from cores or logs at the site being studied, but be sure to include clay;
- the relation given above holds only for the high effective pressure value of 40 MPa.
- a common mistake is to try to overinterpret the empirical coefficients by comparing the equations, for example, to Wyllie's time-average equation (see [Section 7.3](#)). This can lead to nonsensical interpreted values for the velocities of water and clay. This is not surprising, because Wyllie's equations are heuristic only; and
- it is dangerous to extrapolate the results to values of porosity or clay content outside the range of the experiments.

7.7 Velocity–porosity–clay models: Castagna's empirical relations for velocities

Synopsis

On the basis of log measurements, Castagna *et al.* (1985) determined empirical regressions relating velocities with porosity and clay content under water-saturated conditions. See also [Section 7.9](#) on V_P – V_S relations.

For mudrock (clastic silicate rock composed primarily of clay and silt-sized particles), they found the relation between V_P and V_S (in km/s) to be

$$V_P(\text{km/s}) = 1.36 + 1.16V_S$$

where V_P and V_S are the P- and S-wave velocities, respectively.

For shaley sands of the Frio formation they found

$$V_P(\text{km/s}) = 5.81 - 9.42\phi - 2.21C$$

$$V_S(\text{km/s}) = 3.89 - 7.07\phi - 2.04C$$

where ϕ is porosity and C is the clay volume fraction.

Uses

Castagna's relations for velocities can be used to relate velocity, porosity, and clay content empirically in shaley sandstones.

Assumptions and limitations

Castagna's empirical relations have the following limitations:

- these relations are empirical, and thus strictly speaking they apply only to the set of rocks studied;
- a common mistake is to try to overinterpret the empirical coefficients by comparing the equations, for example, to Wyllie's time-average equation (see [Section 7.3](#)). This can lead to nonsensical interpreted values for the velocities of water and clay. This is not surprising because Wyllie's equations are heuristic only; there is no theoretical justification for them, and they do not represent an empirical best fit to any data.

7.8 V_P – V_S –density models: Brocher's compilation

Synopsis

Brocher (2005) compiled data on crustal rocks from the laboratory, wireline logs, VSP (vertical seismic profiling), and field tomography, from which he found empirical relations among V_P , V_S , bulk density (ρ), and Poisson's ratio (ν) for crustal rocks. The data represented a broad range of lithologies, including sandstones, shales, mafics, gabbros, calcium-rich rocks (dolomites and anorthosite), and other crystalline rocks. The resulting empirical relations are intended to represent the average behavior of crustal rocks over a large depth range. Brocher compared his results with an excellent compilation of other published empirical relations, which are summarized in this section.

V_P –density

Brocher (2005) computed the following polynomial fit to the Nafe–Drake curve (Ludwig *et al.*, 1970) relating P-wave velocity and bulk density, previously presented only graphically:

$$\begin{aligned} \rho(\text{g/cm}^3) = & 1.6612V_P(\text{km/s}) - 0.4721V_P^2 + 0.0671V_P^3 \\ & - 0.0043V_P^4 + 0.000106V_P^5 \end{aligned} \quad (7.8.1)$$

Equation (7.8.1) is intended for velocities in the range $1.5 < V_P < 8.5$ km/s and all crustal rocks, except crustal mafic and calcium-rich rocks. Brocher also presented an inverse relation

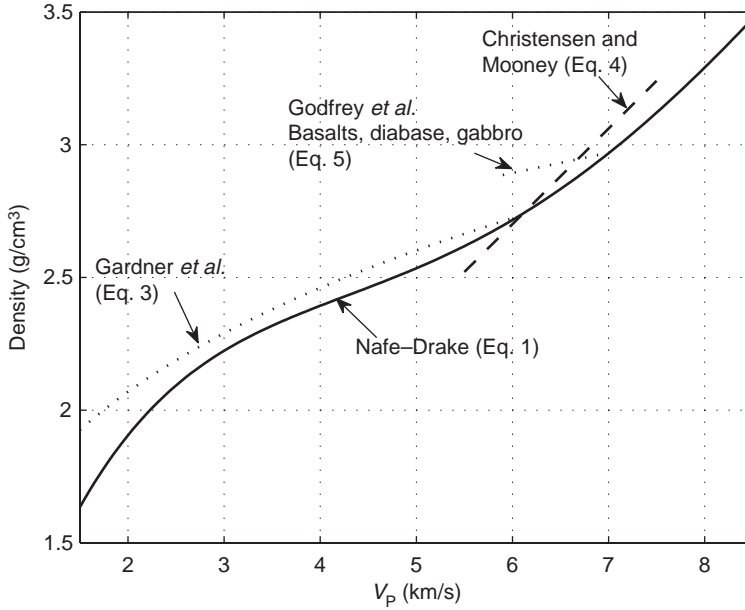


Figure 7.8.1 Brocher's comparison of empirical V_P -bulk density trends for crustal rocks, equations (7.8.1), (7.8.3)–(7.8.5).

$$V_P(\text{km/s}) = 39.128\rho(\text{g/cm}^3) - 63.064\rho^2 + 37.083\rho^3 - 9.1819\rho^4 + 0.8228\rho^5 \quad (7.8.2)$$

which is accurate in the density range $2.0 < \rho < 3.5 \text{ g/cm}^3$. Equations (7.8.1) and (7.8.2) can be compared with an equation from Gardner *et al.* (1974) for sedimentary rocks:

$$\rho(\text{g/cm}^3) = 1.74V_P^{0.25} \quad (7.8.3)$$

which is valid for velocities in the range $1.5 < V_P < 6.1$.

Christensen and Mooney (1995) published a relation between P-wave velocity and bulk density in crystalline rocks at 10 km depth (except for volcanic and monomineralic rocks) and in the range $5.5 < V_P < 7.5$:

$$\rho(\text{g/cm}^3) = 0.541 + 0.360V_P \quad (7.8.4)$$

Godfrey *et al.* (1997) proposed a linear relation for basalt, diabase, and gabbro, based on data reported by Christensen and Mooney (1995):

$$\rho(\text{g/cm}^3) = 2.4372 + 0.0761V_P \quad (7.8.5)$$

Equation (7.8.5) is also intended for crustal rocks at 10 km depth in the velocity range $5.9 < V_P < 7.1$.

Equations (7.8.1) and (7.8.3)–(7.8.5) are compared in Figure 7.8.1.

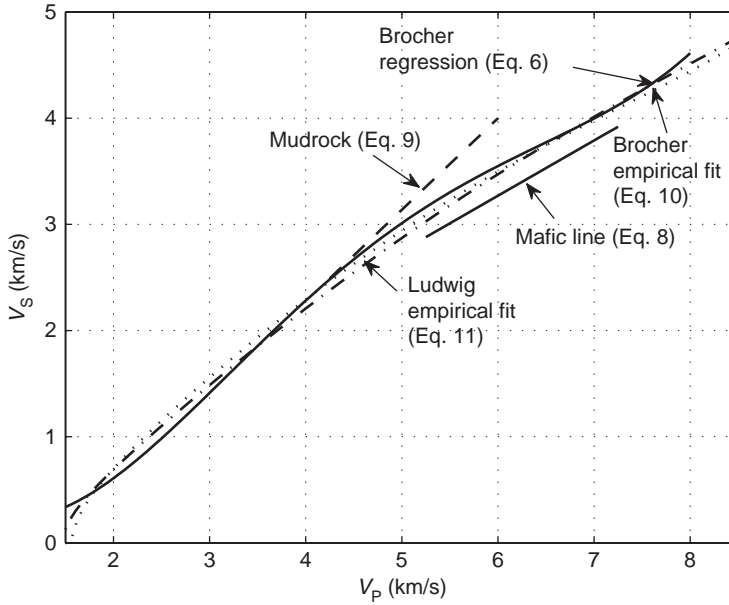


Figure 7.8.2 Brocher's comparison of empirical V_P - V_S trends for crustal rocks, equations (7.8.6), (7.8.8)–(7.8.11).

V_P - V_S

Brocher (2005) derived the following expression relating V_P and V_S in a broad range of lithologies (excluding calcium-rich and mafic rocks, gabbros, and serpentinites), using data from Ludwig *et al.* (1970):

$$V_S(\text{km/s}) = 0.7858 - 1.2344V_P + 0.7949V_P^2 - 0.1238V_P^3 + 0.0064V_P^4 \quad (7.8.6)$$

Equation (7.8.6) is accurate for velocities in the range $1.5 < V_P < 8.0$ km/s. The inverse is given as

$$V_P(\text{km/s}) = 0.9409 + 2.0947V_S - 0.8206V_S^2 + 0.2683V_S^3 - 0.0251V_S^4 \quad (7.8.7)$$

Brocher's relation, intended more specifically for calcium-rich (dolomites and anorthosites), mafic rocks, and gabbros, labeled the "mafic line" in Figure 7.8.2, is given by

$$V_S(\text{km/s}) = 2.88 + 0.52(V_P - 5.25), \quad 5.25 < V_P < 7.25 \quad (7.8.8)$$

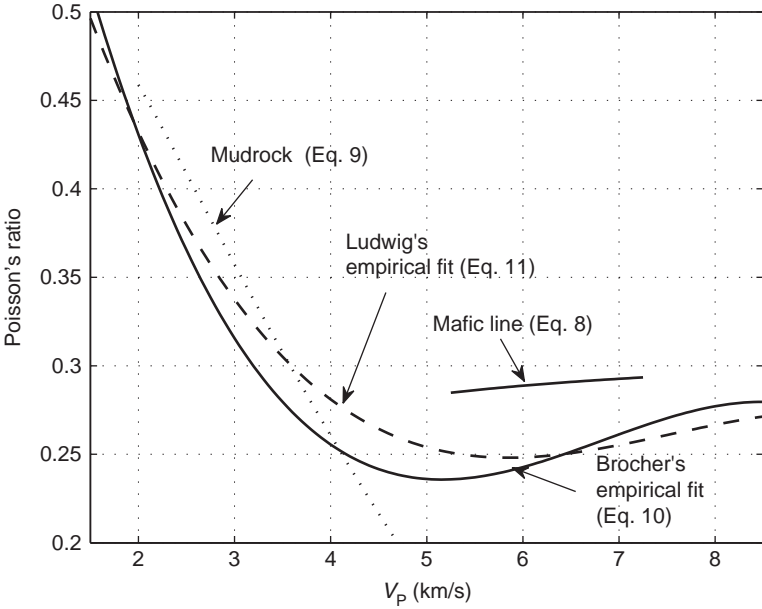


Figure 7.8.3 Brocher’s comparison of empirical V_P –Poisson’s ratio trends for crustal rocks, equations (7.8.8)–(7.8.11).

Equations (7.8.7) and (7.8.8) can be compared with the well-known mudrock line of Castagna *et al.* (1985):

$$V_S(\text{km/s}) = (V_P - 1.36)/1.16 \quad (7.8.9)$$

Figure 7.8.2 compares equations (7.8.6) and (7.8.8)–(7.8.11).

V_P –Poisson’s ratio

Brocher (2005) computed the following equation, labeled “Brocher’s empirical fit,” relating P-wave velocity and Poisson’s ratio, valid in the range, $1.5 < V_P < 8.5$:

$$\nu = 0.8835 - 0.315V_P + 0.0491V_P^2 - 0.0024V_P^3 \quad (7.8.10)$$

A similar relation, derived by Brocher from data by Ludwig *et al.* (1970), labeled “Ludwig’s empirical fit,” is

$$\nu = 0.769 - 0.226V_P + 0.0316V_P^2 - 0.0014V_P^3 \quad (7.8.11)$$

Equations (7.8.8)–(7.8.11) are compared in Figure 7.8.3.

Uses

These equations can be used to link V_P , V_S , and density in crustal rocks.

Assumptions and limitations

The equations in this section are empirical. Many of them, particularly those of Brocher, are intended to represent a broad range of crustal lithologies and depths. Dependence of the relations on pore fluids is not shown; it can be assumed that these represent water-saturated rocks.

7.9 V_P – V_S relations

Synopsis

V_P – V_S relations are key to the determination of lithology from seismic or sonic log data as well as for direct seismic identification of pore fluids using, for example, AVO analysis. Castagna *et al.* (1993) give an excellent review of the subject.

There is a wide and sometimes confusing variety of published V_P – V_S relations and V_S prediction techniques, which at first appear to be quite distinct. However, most reduce to the same two simple steps.

1. Establish empirical relations among V_P , V_S , and porosity, ϕ , for one reference pore fluid – most often water-saturated or dry.
2. Use Gassmann's (1951) relations to map these empirical relations to other pore-fluid states (see Section 6.3).

Although some of the effective-medium models summarized in Chapter 4 predict both P- and S-velocities on the basis of idealized pore geometries, the fact remains that the most reliable and most often used V_P – V_S relations are empirical fits to laboratory or log data, or both. The most useful role of theoretical methods is extending these empirical relations to different pore fluids or measurement frequencies, which accounts for the two steps listed above.

We summarize here a few of the popular V_P – V_S relations compared with laboratory and log data sets and illustrate some of the variations that can result from lithology, pore fluids, and measurement frequency.

Some empirical relations

Limestones

Figure 7.9.1 shows laboratory ultrasonic V_P – V_S data for water-saturated limestones from Pickett (1963), Milholland *et al.* (1980), and Castagna *et al.* (1993), as compiled by Castagna *et al.* (1993). Superimposed, for comparison, are Pickett's (1963) empirical limestone relation derived from laboratory core data:

$$V_S = V_P/1.9 \text{ (km/s)}$$

and a least-squares polynomial fit to the data derived by Castagna *et al.* (1993):

$$V_S = -0.055V_P^2 + 1.017V_P - 1.031 \text{ (km/s)}$$

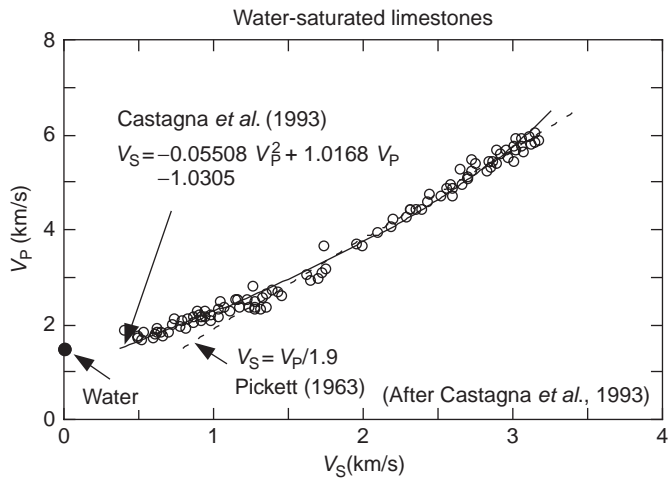


Figure 7.9.1 Laboratory ultrasonic V_P – V_S data for water-saturated limestones.

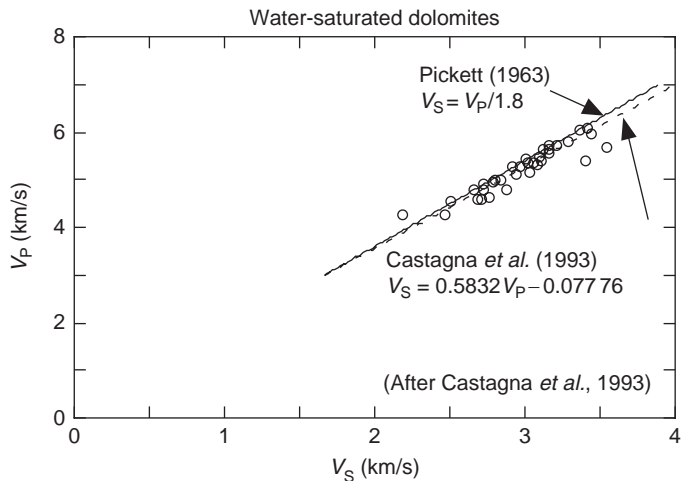


Figure 7.9.2 Laboratory V_P – V_S data for water-saturated dolomites.

At higher velocities, Pickett’s straight line fits the data better, although at lower velocities (higher porosities), the data deviate from a straight line and trend toward the water point, $V_P = 1.5$ km/s, $V_S = 0$. In fact, this limit is more accurately described as a suspension of grains in water at the critical porosity (see the discussion below), at which the grains lose contact and the shear velocity vanishes.

Dolomite

Figure 7.9.2 shows laboratory V_P – V_S data for water-saturated dolomites from Castagna *et al.* (1993). Superimposed, for comparison, are Pickett’s (1963) dolomite (laboratory) relation

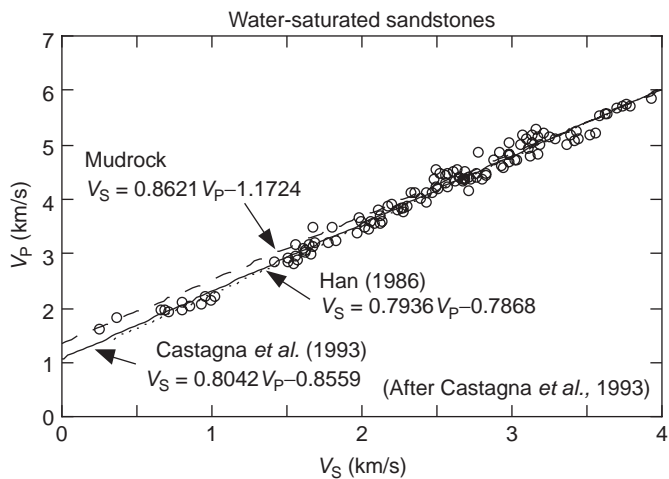


Figure 7.9.3 Laboratory V_P – V_S data for water-saturated sandstones.

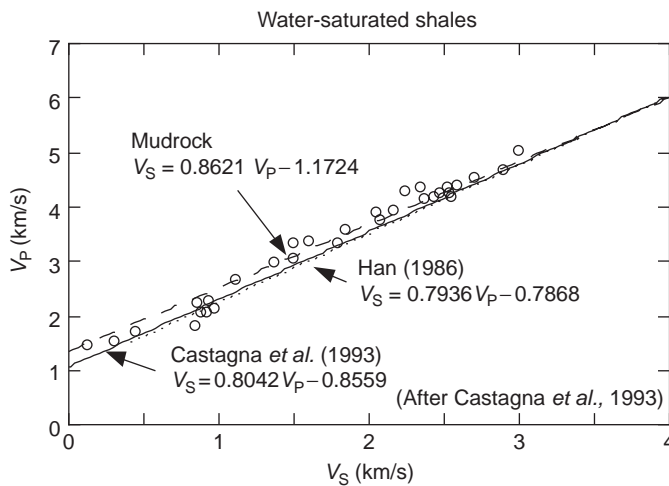


Figure 7.9.4 Laboratory V_P – V_S data for water-saturated shales.

$$V_S = V_P/1.8 \text{ (km/s)}$$

and a least-squares linear fit (Castagna *et al.*, 1993)

$$V_S = 0.583V_P - 0.078 \text{ (km/s)}$$

For the data shown, the two relations are essentially equivalent. The data range is too limited to speculate about behavior at much lower velocity (higher porosity).

Sandstones and shales

Figures 7.9.3 and 7.9.4 show laboratory V_P – V_S data for water-saturated sandstones and shales from Castagna *et al.* (1985, 1993) and Thomsen (1986), as compiled by

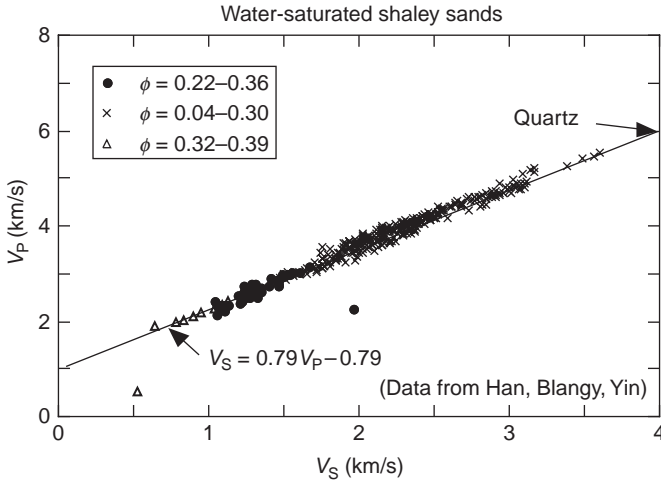


Figure 7.9.5 Laboratory ultrasonic V_P – V_S data for water-saturated shaley sands.

Castagna *et al.* (1993). Superimposed, for comparison, are a least-squares linear fit to these data offered by Castagna *et al.* (1993),

$$V_S = 0.804V_P - 0.856 \text{ (km/s)}$$

the famous “mudrock line” of Castagna *et al.* (1985), which was derived from *in-situ* data,

$$V_S = 0.862V_P - 1.172 \text{ (km/s)}$$

and the following empirical relation of Han (1986), which is based on laboratory ultrasonic data:

$$V_S = 0.794V_P - 0.787 \text{ (km/s)}$$

Of these three relations, those by Han (1986) and Castagna *et al.* (1985) are essentially the same and give the best overall fit to the sandstones. The mudrock line predicts systematically lower V_S because it is best suited to the most shaley samples, as seen in Figure 7.9.4. Castagna *et al.* (1993) suggest that if the lithology is well known, one can fine tune these relations to slightly lower V_S/V_P for high shale content and higher V_S/V_P in cleaner sands. When the lithology is not well constrained, the Han and the Castagna *et al.* lines give a reasonable average.

Figure 7.9.5 compares laboratory ultrasonic data for a larger set of water-saturated sands. The lowest porosity samples ($\phi = 0.04$ – 0.30) are from a set of consolidated shaley Gulf Coast sandstones studied by Han (1986). The medium porosities ($\phi = 0.22$ – 0.36) are poorly consolidated North Sea samples studied by Blangy (1992). The very-high-porosity samples ($\phi = 0.32$ – 0.39) are unconsolidated clean Ottawa sand studied by Yin (1992). The samples span clay volume fractions from 0% to 55%,

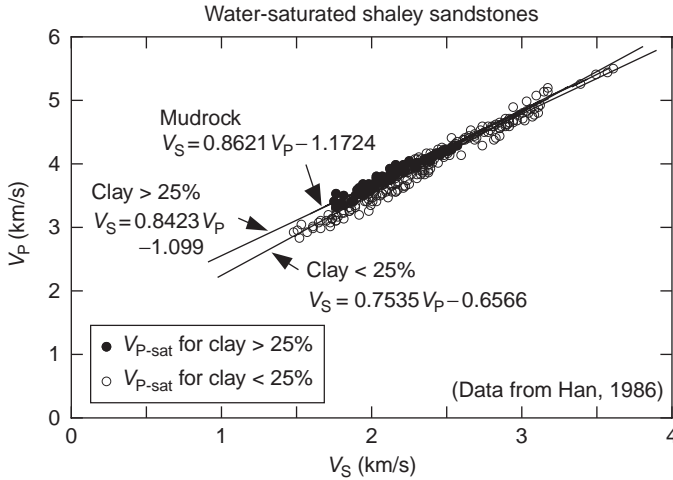


Figure 7.9.6 Laboratory ultrasonic V_P - V_S data for water-saturated shaly sands, differentiated by clay content.

porosities from 0.04 to 0.39, and confining pressures from 0 to 40 MPa. In spite of this, there is a remarkably systematic trend well represented by Han's relation as follows:

$$V_S = 0.79V_P - 0.79 \text{ (km/s)}$$

Sandstones: more on the effects of clay

Figure 7.9.6 shows again the ultrasonic laboratory data for 70 water-saturated shaly sandstone samples from Han (1986). The data are separated by clay volume fractions greater than 25% and less than 25%. Regressions to each part of the data set are shown as follows:

$$V_S = 0.842V_P - 1.099, \quad \text{clay} > 25\%$$

$$V_S = 0.754V_P - 0.657, \quad \text{clay} < 25\%$$

The mudrock line (upper line) is a reasonable fit to the trend but is skewed toward higher clay and lies almost on top of the regression for clay >25%.

Sandstones: effects of porosity

Figure 7.9.7 shows the laboratory ultrasonic data for water-saturated shaly sandstones from Han (1986) separated into porosity greater than 15% and less than 15%. Regressions to each part of the data set are shown as follows:

$$V_S = 0.756V_P - 0.662, \quad \text{porosity} > 15\%$$

$$V_S = 0.853V_P - 1.137, \quad \text{porosity} < 15\%$$

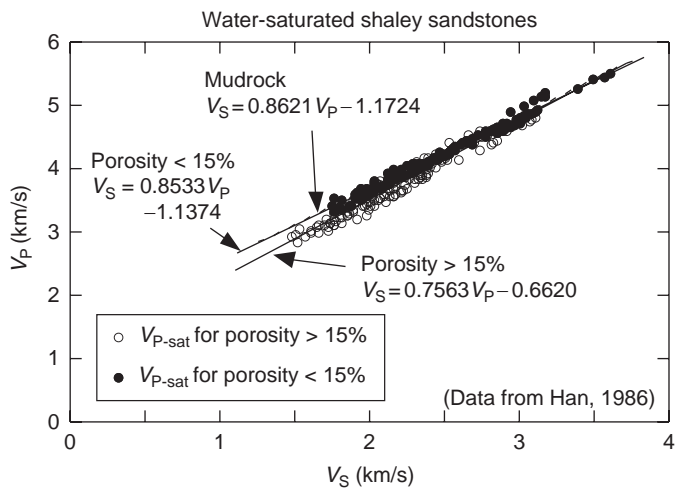


Figure 7.9.7 Laboratory ultrasonic V_P – V_S data for water-saturated shaley sands, differentiated by porosity.

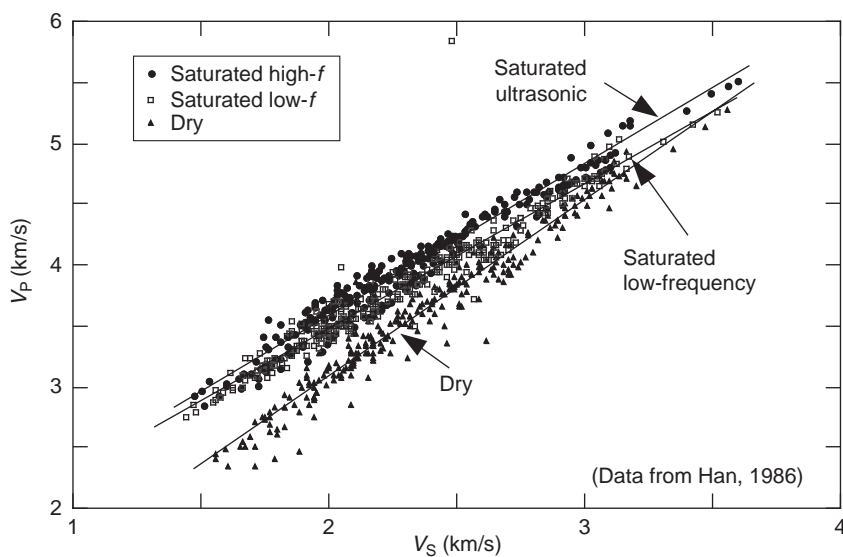


Figure 7.9.8 V_P – V_S for shaley sandstone under several different conditions described in the text.

Note that the low-porosity line is very close to the mudrock line, which as we saw above, fits the high clay values, whereas the high-porosity line is similar to the clean sand (low-clay) regression in [Figure 7.9.6](#).

Sandstones: effects of fluids and frequency

[Figure 7.9.8](#) compares V_P – V_S at several conditions based on the shaley sandstone data of Han (1986). The “dry” and “saturated ultrasonic” points are the measured ultrasonic

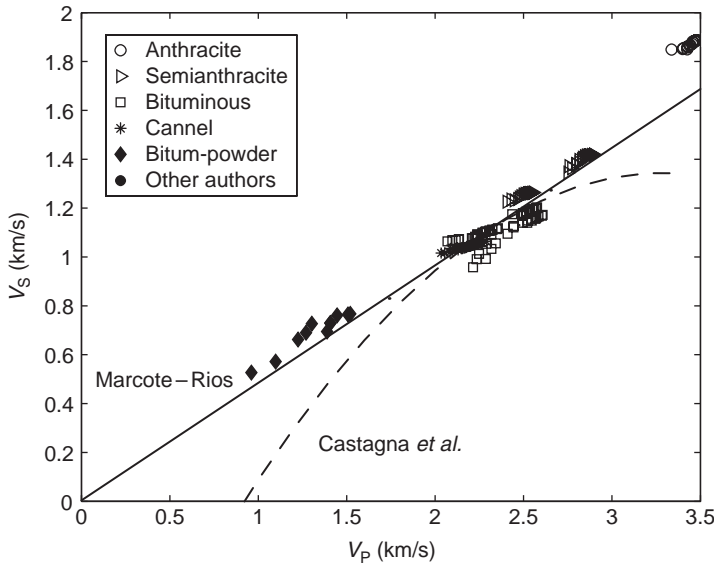


Figure 7.9.9 V_P versus V_S for different coals. The solid line is the best fit through all data. The dashed line is for some bituminous coals.

data. The “saturated low-frequency” points are estimates of low-frequency saturated data computed from the dry measurements using the low-frequency Gassmann’s relations (see Section 6.3). It is no surprise that the water-saturated samples have higher V_P/V_S because of the well-known larger effects of pore fluids on P-velocities than on S-velocities. Less often recognized is that the velocity dispersion that almost always occurs in ultrasonic measurements appears to increase V_P/V_S systematically.

Coal

Figure 7.9.9 shows laboratory ultrasonic data for coal (anthracite, semianthracite, bituminous, cannel, and bituminous powder), measured by Marcote–Rios (personal communication, 2007), plus data reported by Greenhalgh and Emerson (1986), Yu *et al.* (1993), and Castagna *et al.* (1993) on bituminous coals. The Marcote–Rios regression

$$V_S = 0.4811V_P + 0.00382 \text{ (km/s)}$$

is for all data in the plot. In addition, a quadratic fit is shown for the data published by Greenhalgh and Emerson (1986) and Castagna *et al.* (1993), given by

$$V_S = -0.232V_P^2 + 1.5421V_P - 1.214 \text{ (km/s)}$$

Critical porosity model

The P- and S-velocities of rocks (as well as their V_P/V_S ratio) generally trend between the velocities of the mineral grains in the limit of low porosity and the values for a

mineral–pore–fluid suspension in the limit of high porosity. For most porous materials there is a **critical porosity**, ϕ_c , that separates their mechanical and acoustic behavior into two distinct domains. For porosities lower than ϕ_c the mineral grains are load-bearing, whereas for porosities greater than ϕ_c the rock simply “falls apart” and becomes a suspension in which the fluid phase is load-bearing (see [Section 7.1](#) on critical porosity). The transition from solid to suspension is implicit in the Raymer *et al.* (1980) empirical velocity–porosity relation (see [Section 7.4](#)) and the work of Krief *et al.* (1990), which is discussed below.

A geometric interpretation of the mineral-to-critical-porosity trend is simply that if we make the porosity large enough, the grains must lose contact and their rigidity. The geologic interpretation is that, at least for clastics, the weak suspension state at critical porosity, ϕ_c , describes the sediment when it is first deposited before compaction and diagenesis. The value of ϕ_c is determined by the grain sorting and angularity at deposition. Subsequent compaction and diagenesis move the sample along an upward trajectory as the porosity is reduced and the elastic stiffness is increased.

The value of ϕ_c depends on the rock type. For example $\phi_c \approx 0.4$ for sandstones; $\phi_c \approx 0.7$ for chalks; $\phi_c \approx 0.9$ for pumice and porous glass; and $\phi_c \approx 0.02$ – 0.03 for granites.

In the **suspension domain**, the effective bulk and shear moduli of the rock K and μ can be estimated quite accurately by using the Reuss (isostress) average (see [Section 4.2](#) on the Voigt–Reuss average and [Section 7.1](#) on critical porosity) as follows:

$$\frac{1}{K} = \frac{\phi}{K_f} + \frac{1 - \phi}{K_0}, \quad \mu = 0$$

where K_f and K_0 are the bulk moduli of the fluid and mineral and ϕ is the porosity.

In the **load-bearing domain**, $\phi < \phi_c$, the moduli decrease rapidly from the mineral values at zero porosity to the suspension values at the critical porosity. Nur *et al.* (1995) found that this dependence can often be approximated with a straight line when expressed as modulus versus porosity. Although there is nothing special about a linear trend of modulus versus ϕ , it does describe sandstones fairly well, and it leads to convenient mathematical properties. For dry rocks, the bulk and shear moduli can be expressed as the linear functions

$$K_{\text{dry}} = K_0 \left(1 - \frac{\phi}{\phi_c} \right)$$

$$\mu_{\text{dry}} = \mu_0 \left(1 - \frac{\phi}{\phi_c} \right)$$

where K_0 and μ_0 are the mineral bulk and shear moduli, respectively. Thus, the dry-rock bulk and shear moduli trend linearly between K_0, μ_0 at $\phi = 0$, and $K_{\text{dry}} = \mu_{\text{dry}} = 0$

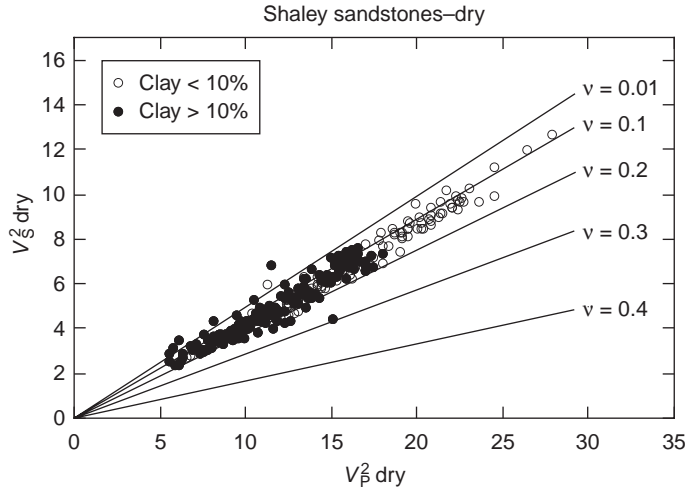


Figure 7.9.10 Velocity data from Han (1986) illustrating that Poisson’s ratio is approximately constant for dry sandstones.

at $\phi = \phi_c$. At low frequency, changes of pore fluids have little or no effect on the shear modulus. However, it can be shown (see Section 6.3 on Gassmann) that with a change of pore fluids the straight line in the K – ϕ plane remains a straight line, trending between K_0 at $\phi = 0$ and the Reuss average bulk modulus at $\phi = \phi_c$. Thus, the effect of pore fluids on K or $\rho V^2 = K + \frac{4}{3}\mu$ is automatically incorporated by the change of the Reuss average at $\phi = \phi_c$.

The relevance of the critical porosity model to V_P – V_S relations is simply that V_S/V_P should generally trend toward the value for the solid mineral material in the limit of low porosity and toward the value for a fluid suspension as the porosity approaches ϕ_c (Castagna *et al.*, 1993). Furthermore, if the modulus–porosity relations are linear (or nearly so), then it follows that V_S/V_P for a dry rock at any porosity ($0 < \phi < \phi_c$) will equal the V_S/V_P of the mineral. The same is true if K_{dry} and μ_{dry} are any other functions of porosity but are proportional to each other [$K_{\text{dry}}(\phi) \propto \mu_{\text{dry}}(\phi)$]. Equivalently, the Poisson ratio ν for the dry rock will equal the Poisson ratio of the mineral grains, as is often observed (Pickett, 1963; Krief *et al.*, 1990).

$$\left(\frac{V_S}{V_P}\right)_{\text{dry rock}} \approx \left(\frac{V_S}{V_P}\right)_{\text{mineral}}$$

$$\nu_{\text{dry rock}} \approx \nu_{\text{mineral}}$$

Figure 7.9.10 illustrates the approximately constant dry-rock Poisson ratio observed for a large set of ultrasonic sandstone velocities (from Han, 1986) over a large range of effective pressures ($5 < P_{\text{eff}} < 40$ MPa) and clay contents ($0 < C < 55\%$ by volume).

To summarize, the critical porosity model suggests that P- and S-wave velocities trend systematically between their mineral values at zero porosity to fluid-suspension values ($V_S = 0$, $V_P = V_{\text{suspension}} \approx V_{\text{fluid}}$) at the critical porosity ϕ_c , which is a characteristic of each class of rocks. Expressed in the modulus versus porosity domain, if dry rock ρV_P^2 versus ϕ is proportional to ρV_S^2 versus ϕ (for example, both ρV_P^2 and ρV_S^2 are linear in ϕ), then V_S/V_P of the dry rock will be equal to V_S/V_P of the mineral.

The V_P – V_S relation for different pore fluids is found using Gassmann's relation, which is applied automatically if the trend terminates on the Reuss average at ϕ_c (see a discussion of this in [Section 6.3](#) on Gassmann's relation).

Krief's relations

Krief *et al.* (1990) suggested a V_P – V_S prediction technique that very much resembles the critical porosity model. The model again combines the same two elements.

1. An empirical V_P – V_S – ϕ relation for water-saturated rocks, which we will show is approximately the same as that predicted by the simple critical porosity model.
2. Gassmann's relation to extend the empirical relation to other pore fluids.

If we model the dry rock as a porous elastic solid, then with great generality we can write the dry-rock bulk modulus as

$$K_{\text{dry}} = K_0(1 - \beta)$$

where K_{dry} and K_0 are the bulk moduli of the dry rock and mineral and β is Biot's coefficient (see [Section 4.6](#) on compressibilities and [Section 2.9](#) on the deformation of cavities). An equivalent expression is

$$\frac{1}{K_{\text{dry}}} = \frac{1}{K_0} + \frac{\phi}{K_\phi}$$

where K_ϕ is the pore-space stiffness (see [Section 2.9](#)) and ϕ is the porosity, so that

$$\frac{1}{K_\phi} = \frac{1}{\nu_p} \frac{d\nu_p}{d\sigma} \bigg|_{P_p=\text{constant}}, \quad \beta = \frac{d\nu_p}{dV} \bigg|_{P_p=\text{constant}} = \frac{\phi K_{\text{dry}}}{K_\phi}$$

where ν_p is the pore volume, V is the bulk volume, σ is confining pressure, and P_p is pore pressure. The parameters β and K_ϕ are two equivalent descriptions of the pore-space stiffness. Ascertaining β versus ϕ or K_ϕ versus ϕ determines the rock bulk modulus K_{dry} versus ϕ .

Krief *et al.* (1990) used the data of Raymer *et al.* (1980) to find a relation for β versus ϕ empirically as follows:

$$(1 - \beta) = (1 - \phi)^{m(\phi)}, \quad \text{where} \quad m(\phi) = 3/(1 - \phi)$$

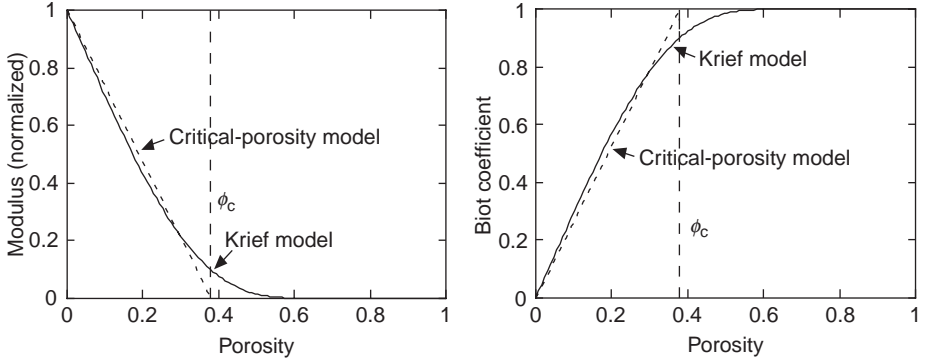


Figure 7.9.11 Left: bulk and shear moduli (same curves when normalized by their mineral values) as predicted by Krief's model and a linear critical porosity model. Right: Biot coefficient predicted by both models.

Next, they used the empirical result shown by Pickett (1963) and others that the dry-rock Poisson ratio is often approximately equal to the mineral Poisson ratio, or $\mu_{\text{dry}}/K_{\text{dry}} = \mu_0/K_0$. Combining these two empirical results gives

$$K_{\text{dry}} = K_0(1 - \phi)^{m(\phi)}$$

$$\mu_{\text{dry}} = \mu_0(1 - \phi)^{m(\phi)}, \quad \text{where } m(\phi) = 3/(1 - \phi)$$

Plots of K_{dry} versus ϕ , μ_{dry} versus ϕ , and β versus ϕ are shown in Figure 7.9.11.

It is clear from these plots that the effective moduli K_{dry} and μ_{dry} display the critical porosity behavior, for they approach zero at $\phi \approx 0.4$ – 0.5 (see the previous discussion). This is no surprise because $\beta(\phi)$ is an empirical fit to shaley sand data, which always exhibit this behavior.

Compare these with the linear moduli–porosity relations for dry rocks suggested by Nur *et al.* (1995) for the critical porosity model

$$K_{\text{dry}} = K_0 \left(1 - \frac{\phi}{\phi_c} \right) \quad 0 \leq \phi \leq \phi_c$$

$$\mu_{\text{dry}} = \mu_0 \left(1 - \frac{\phi}{\phi_c} \right)$$

where K_0 and μ_0 are the mineral moduli and ϕ_c is the critical porosity. These imply a Biot coefficient of

$$\beta = \begin{cases} \phi/\phi_c, & 0 \leq \phi \leq \phi_c \\ 1, & \phi > \phi_c \end{cases}$$

As shown in [Figure 7.9.11](#), these linear forms of K_{dry} , μ_{dry} , and β are essentially the same as Krief's expressions in the range $0 \leq \phi \leq \phi_c$.

The Reuss average values for the moduli of a suspension, $K_{\text{dry}} = \mu_{\text{dry}} = 0$; $\beta = 1$ are essentially the same as Krief's expressions for $\phi > \phi_c$. Krief's nonlinear form results from trying to fit a single function $\beta(\phi)$ to the two mechanically distinct domains, $\phi < \phi_c$ and $\phi > \phi_c$. The critical porosity model expresses the result with simpler piecewise functions.

Expressions for any other pore fluid are obtained by combining the expression $K_{\text{dry}} = K_0(1 - \beta)$ of Krief *et al.* with Gassmann's equations. Although these are also nonlinear, Krief *et al.* suggest a simple approximation

$$\frac{V_{\text{P-sat}}^2 - V_{\text{fl}}^2}{V_{\text{S-sat}}^2} = \frac{V_{\text{P0}}^2 - V_{\text{fl}}^2}{V_{\text{S0}}^2}$$

where $V_{\text{P-sat}}$, V_{P0} , and V_{fl} are the P-wave velocities of the saturated rock, the mineral, and the pore fluid, respectively, and $V_{\text{S-sat}}$ and V_{S0} are the S-wave velocities in the saturated rock and mineral. Rewriting this slightly gives

$$V_{\text{P-sat}}^2 = V_{\text{fl}}^2 + V_{\text{S-sat}}^2 \left(\frac{V_{\text{P0}}^2 - V_{\text{fl}}^2}{V_{\text{S0}}^2} \right)$$

which is a straight line (in velocity-squared) connecting the mineral point (V_{P0}^2 , V_{S0}^2) and the fluid point (V_{fl}^2 , 0). We suggest that a more accurate (and nearly identical) model is to recognize that velocities tend toward those of a suspension at high porosity rather than toward a fluid, which yields the modified form

$$\frac{V_{\text{P-sat}}^2 - V_{\text{R}}^2}{V_{\text{S-sat}}^2} = \frac{V_{\text{P0}}^2 - V_{\text{R}}^2}{V_{\text{S0}}^2}$$

where V_{R} is the velocity of a suspension of minerals in a fluid given by the Reuss average ([Section 4.2](#)) or Wood's relation ([Section 4.3](#)) at the critical porosity.

It is easy to show that this modified form of Krief's expression is exactly equivalent to the linear (modified Voigt) K versus ϕ and μ versus ϕ relations in the critical porosity model with the fluid effects given by Gassmann.

Greenberg and Castagna's relations

Greenberg and Castagna (1992) have given empirical relations for estimating V_{S} from V_{P} in multiminerale, brine-saturated rocks based on empirical, polynomial $V_{\text{P}}-V_{\text{S}}$ relations in pure monomineralic lithologies (Castagna *et al.*, 1993). The shear-wave velocity in brine-saturated composite lithologies is approximated by a simple average of the arithmetic and harmonic means of the constituent pure lithology shear velocities:

Table 7.9.1 Regression coefficients for pure lithologies.^a

Lithology	a_{i2}	a_{i1}	a_{i0}	R^2
Sandstone	0	0.804 16	–0.855 88	0.983 52
Limestone	–0.055 08	1.016 77	–1.030 49	0.990 96
Dolomite	0	0.583 21	–0.077 75	0.874 44
Shale	0	0.769 69	–0.867 35	0.979 39

Note:

^a V_P and V_S in km/s: $V_S = a_{i2}V_P^2 + a_{i1}V_P + a_{i0}$ (Castagna *et al.*, 1993).

$$V_S = \frac{1}{2} \left\{ \left[\sum_{i=1}^L X_i \sum_{j=0}^{N_i} a_{ij} V_P^j \right] + \left[\sum_{i=1}^L X_i \left(\sum_{j=0}^{N_i} a_{ij} V_P^j \right)^{-1} \right]^{-1} \right\}$$
$$\sum_{i=1}^L X_i = 1$$

where L is the number of pure monomineralic lithologic constituents, X_i are the volume fractions of lithological constituents, a_{ij} are the empirical regression coefficients, N_i is the order of polynomial for constituent i , and V_P and V_S are the P- and S-wave velocities (km/s), respectively, in composite brine-saturated, multimineralic rock.

Castagna *et al.* (1993) gave representative polynomial regression coefficients for pure monomineralic lithologies as detailed in Table 7.9.1. Note that the preceding relation is for 100% brine-saturated rocks. To estimate V_S from measured V_P for other fluid saturations, Gassmann’s equation has to be used in an iterative manner. In the following, the subscript b denotes velocities at 100% brine saturation, and the subscript f denotes velocities at any other fluid saturation (e.g., oil or a mixture of oil, brine, and gas). The method consists of iteratively finding a (V_P , V_S) point on the brine relation that transforms, with Gassmann’s relation, to the measured V_P and the unknown V_S for the new fluid saturation. The resulting curves are shown in Figure 7.9.12. The steps are as follows.

1. Start with an initial guess for V_{Pb} .
2. Calculate V_{Sb} corresponding to V_{Pb} from the empirical regression.
3. Perform fluid substitution using V_{Pb} and V_{Sb} in the Gassmann equation to obtain V_{Sf} .
4. With the calculated V_{Sf} and the measured V_{Pf} , use the Gassmann relation to obtain a new estimate of V_{Pb} . Check the result against the previous value of V_{Pb} for convergence. If convergence criterion is met, stop; if not, go back to step 2 and continue.

When the measured P-velocity and desired S-velocity are for 100% brine saturation, then of course iterations are not required. The desired V_S is obtained from a single application of the empirical regression. This method requires prior knowledge

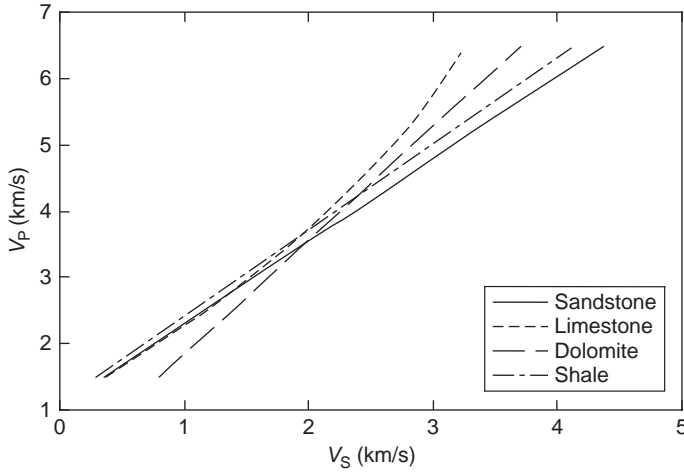


Figure 7.9.12 Typical V_P – V_S curves corresponding to the regression coefficients in Table 7.9.1.

of the lithology, porosity, saturation, and elastic moduli and densities of the constituent minerals and pore fluids.

Estimate, using the Greenberg–Castagna empirical relations, the shear-wave velocity in a brine-saturated shaley sandstone (60% sandstone, 40% shale) with $V_P = 3.0$ km/s.

Here $L = 2$ with X_1 (sandstone) = 0.6 and X_2 (shale) = 0.4.

The regressions for pure lithologic constituents give us

$$V_{S\text{-sand}} = 0.80416 V_P - 0.85588 = 1.5566 \text{ km/s}$$

$$V_{S\text{-shale}} = 0.76969 V_P - 0.86735 = 1.4417 \text{ km/s}$$

The weighted arithmetic and harmonic means are

$$V_{S\text{-arith}} = 0.6V_{S\text{-sand}} + 0.4V_{S\text{-shale}} = 1.5106 \text{ km/s}$$

$$V_{S\text{-harm}} = (0.6/V_{S\text{-sand}} + 0.4/V_{S\text{-shale}})^{-1} = 1.5085 \text{ km/s}$$

and finally the estimated V_S is given by

$$V_S = \frac{1}{2}(V_{S\text{-arith}} + V_{S\text{-harm}}) = 1.51 \text{ km/s}$$

Vernik's relations

The Greenberg–Castagna (1992) empirical relations discussed previously are appropriate for consolidated rocks with P-wave velocities greater than about 2.6 km/s. However, when extrapolated to low velocities, these relations yield unphysical

results – specifically $V_S = 0$ at $V_P = 1.06$ km/s, which is slower than the V_P for water. Vernik *et al.* (2002) developed a nonlinear regression for brine-saturated sandstones that honors the observed high-velocity limit for arenites ($V_P \approx 5.48$ km/s, $V_S \approx 3.53$ km/s) and the velocity of a quartz–water suspension ($V_P \approx 1.7$ km/s at $V_S = 0$) at a critical porosity $\phi \approx 0.4$:

$$V_S = (-1.267 + 0.372V_P^2 + 0.00284V_P^4)^{1/2} \text{ (km/s)}$$

Their corresponding expression for shale is

$$V_S = (-0.79 + 0.287V_P^2 + 0.00284V_P^4)^{1/2} \text{ (km/s)}$$

Williams's relation

Williams (1990) used empirical V_P – V_S relations from acoustic logs to differentiate hydrocarbon-bearing sandstones from water-bearing sandstones and shales statistically. His least-squares regressions are:

$$V_P/V_S = 1.182 + 0.00422 \Delta t_S \quad (\text{water-bearing sands})$$

$$V_P/V_S = 1.276 + 0.00374 \Delta t_S \quad (\text{shales})$$

where Δt_S is the shear-wave slowness in $\mu\text{s}/\text{ft}$. The effect of replacing water with more compressible hydrocarbons is a large decrease in P-wave velocity with little change (slight increase) in S-wave velocity. This causes a large reduction in the V_P/V_S ratio in hydrocarbon sands compared with water-saturated sands having a similar Δt_S . A measured V_P/V_S and Δt_S is classified as either water-bearing or hydrocarbon-bearing by comparing it with the regression and using a statistically determined threshold to make the decision. Williams chose the threshold so that the probability of correctly identifying a water-saturated sandstone is 95%. For this threshold a measured V_P/V_S is classified as water-bearing if

$$V_P/V_S \text{ (measured)} \geq \min[V_P/V_S(\text{sand}), V_P/V_S(\text{shale})] - 0.09$$

and as potentially hydrocarbon-bearing otherwise. Williams found that when $\Delta t_S < 130 \mu\text{s}/\text{ft}$ (or $\Delta t_P < 75 \mu\text{s}/\text{ft}$), the rock is too stiff to give any statistically significant V_P/V_S anomaly upon fluid substitution.

Xu and White's relation

Xu and White (1995) developed a theoretical model for velocities in shaley sandstones. The formulation uses the Kuster–Toksöz and differential effective-medium theories to estimate the dry rock P- and S-velocities, and the low-frequency

saturated velocities are obtained from Gassmann's equation. The sand–clay mixture is modeled with ellipsoidal inclusions of two different aspect ratios. The sand fraction has stiffer pores with aspect ratio $\alpha \approx 0.1$ – 0.15 , whereas the clay-related pores are more compliant with $\alpha \approx 0.02$ – 0.05 . The velocity model simulates the “V”-shaped velocity–porosity relation of Marion *et al.* (1992) for sand–clay mixtures. The total porosity $\phi = \phi_{\text{sand}} + \phi_{\text{clay}}$, where ϕ_{sand} and ϕ_{clay} are the porosities associated with the sand and clay fractions, respectively. These are approximated by

$$\phi_{\text{sand}} = (1 - \phi - V_{\text{clay}}) \frac{\phi}{1 - \phi} = V_{\text{sand}} \frac{\phi}{1 - \phi}$$

$$\phi_{\text{clay}} = V_{\text{clay}} \frac{\phi}{1 - \phi}$$

where V_{sand} and V_{clay} denote the volumetric sand and clay content, respectively. The shale volume from logs may be used as an estimate of V_{clay} . Though the log-derived shale volume includes silts and overestimates clay content, results obtained by Xu and White justify its use. The properties of the solid mineral mixture are estimated by a Wyllie time average of the quartz and clay mineral velocities and arithmetic average of their densities by

$$\frac{1}{V_{P_0}} = \left(\frac{1 - \phi - V_{\text{clay}}}{1 - \phi} \right) \frac{1}{V_{P_{\text{quartz}}}} + \frac{V_{\text{clay}}}{1 - \phi} \frac{1}{V_{P_{\text{clay}}}}$$

$$\frac{1}{V_{S_0}} = \left(\frac{1 - \phi - V_{\text{clay}}}{1 - \phi} \right) \frac{1}{V_{S_{\text{quartz}}}} + \frac{V_{\text{clay}}}{1 - \phi} \frac{1}{V_{S_{\text{clay}}}}$$

$$\rho_0 = \left(\frac{1 - \phi - V_{\text{clay}}}{1 - \phi} \right) \rho_{\text{quartz}} + \frac{V_{\text{clay}}}{1 - \phi} \rho_{\text{clay}}$$

where the subscript 0 denotes the mineral properties. These mineral properties are then used in the Kuster–Toksöz formulation along with the porosity and clay content to calculate dry-rock moduli and velocities. The limitation of small-pore concentration of the Kuster–Toksöz model is handled by incrementally adding the pores in small steps so that the noninteraction criterion is satisfied in each step. Gassmann's equations are used to obtain low-frequency saturated velocities. High-frequency saturated velocities are calculated by using fluid-filled ellipsoidal inclusions in the Kuster–Toksöz model.

The model can be used to predict shear-wave velocities (Xu and White, 1994). Estimates of V_S may be obtained from known mineral matrix properties and measured porosity and clay content or from measured V_P and either porosity or clay content.

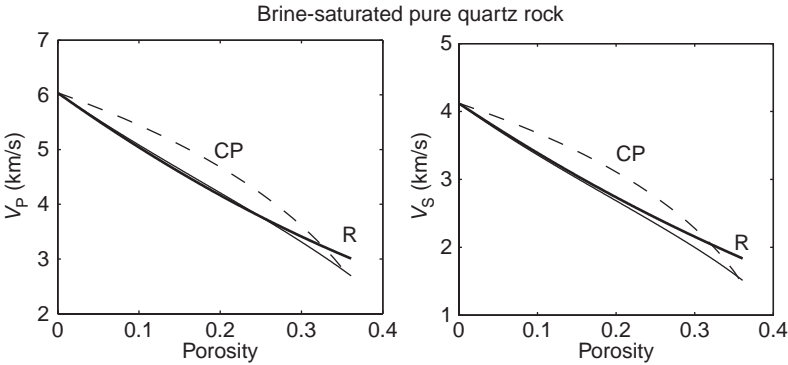


Figure 7.9.13 The stiff-sand (slender curves), critical porosity (dashed curves labeled “CP”), and RHG velocity predictions (heavy curves, labeled “R”) for P- (left) and S-wave (right) velocity in pure-quartz, brine-saturated rock.

Xu and White recommend using measurements of P-wave sonic log because it is more reliable than estimates of shale volume and porosity.

Raymer-form V_S prediction

Dvorkin (2007, personal communication) uses the Raymer–Hunt–Gardner functional form $V_P = (1 - \phi)^2 V_{Ps} + \phi V_{Pf}$, where V_{Ps} and V_{Pf} denote the P-wave velocity in the solid and in the pore-fluid phases, respectively, and ϕ is the total porosity, to relate the S-wave velocity in dry rock to porosity and mineralogy as $V_{Sdry} = (1 - \phi)^2 V_{Ss}$, where V_{Ss} is the S-wave velocity in the solid phase. Assuming that the shear modulus of rock does not depend on the pore fluid, V_S in wet rock is $V_{Swet} = V_{Sdry} \sqrt{\rho_{bdry} / \rho_{bwet}}$, where ρ_{bdry} and ρ_{bwet} denote the bulk density of the dry and wet rock, respectively. This equation for V_S prediction reiterates the critical porosity concept of Nur *et al.* (1995): the V_P/V_S ratio in dry rock equals that in the solid phase. However, the velocity–porosity trend that follows from this equation differs somewhat from the traditional critical porosity trend. This V_S predictor exhibits a velocity–porosity trend essentially identical to that from the stiff-sand (the modified lower Hashin–Shtrikman) model (Figure 7.9.13).

Uses

The relations discussed in this section can be used to relate P- and S-velocity and porosity empirically for use in lithology detection and direct fluid identification.

Assumptions and limitations

Strictly speaking, the empirical relations discussed in this section apply only to the set of rocks studied.

7.10 Velocity–density relations

Synopsis

Many seismic modeling and interpretation schemes require, as a minimum, P-wave velocity V_P , S-wave velocity, V_S , and bulk density ρ_b . Laboratory and log measurements can often yield all three together. But there are many applications where only V_P is known, and density or V_S must be estimated empirically from V_P . Section 7.9 summarizes some V_P – V_S relations. Here we summarize some popular and useful V_P –density relations. Castagna *et al.* (1993) give a very good summary of the topic. See also Section 7.8 on Brocher’s relations.

Density is a simple volumetric average of the rock constituent densities and is closely related to porosity by

$$\rho_b = (1 - \phi)\rho_0 + \phi\rho_f$$

where ρ_0 is the density of mineral grains, ρ_f is the density of pore fluids, and ϕ is porosity.

The problem is that velocity is often not very well related to porosity (and therefore to density). Cracks and crack-like flaws and grain boundaries can substantially decrease V_P and V_S , even though the cracks may have near-zero porosity.

Table 7.10.1 Polynomial and power-law forms of the Gardner *et al.* (1974) velocity–density relationships presented by Castagna *et al.* (1993). Units are km/s and g/cm³ for velocity and density, respectively.

Coefficients for the equation $\rho_b = aV_P^2 + bV_P + c$				
Lithology	a	b	c	V_P range (km/s)
Shale	−0.0261	0.373	1.458	1.5–5.0
Sandstone	−0.0115	0.261	1.515	1.5–6.0
Limestone	−0.0296	0.461	0.963	3.5–6.4
Dolomite	−0.0235	0.390	1.242	4.5–7.1
Anhydrite	−0.0203	0.321	1.732	4.6–7.4
Coefficients for the equation $\rho_b = dV_P^f$				
Lithology	d	f		V_P range (km/s)
Shale	1.75	0.265		1.5–5.0
Sandstone	1.66	0.261		1.5–6.0
Limestone ^a	1.36	0.386		3.5–6.4
Dolomite	1.74	0.252		4.5–7.1
Anhydrite	2.19	0.160		4.6–7.4

Note:
^a Coefficients for limestone have been revised here to better reflect observed trends.

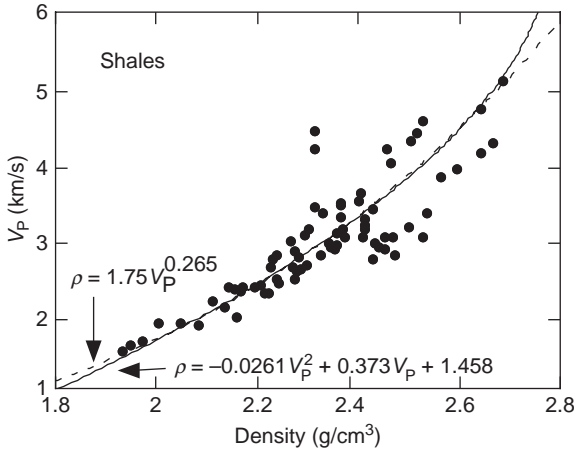


Figure 7.10.1 Both forms of Gardner’s relations applied to log and laboratory shale data, as presented by Castagna *et al.* (1993).

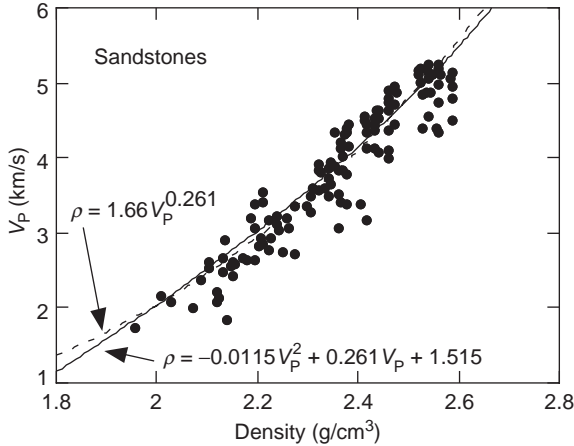


Figure 7.10.2 Both forms of Gardner’s relations applied to log and laboratory sandstone data, as presented by Castagna *et al.* (1993).

Velocity–porosity relations can be improved by fluid saturation and high effective pressures, both of which minimize the effect of these cracks. Consequently, we also expect velocity–density relations to be more reliable under high effective pressures and fluid saturation.

Gardner *et al.* (1974) suggested a useful empirical relation between P-wave velocity and density that represents an average over many rock types:

$$\rho_b \approx 1.741 V_P^{0.25}$$

where V_P is in km/s and ρ_b is in g/cm^3 , or

$$\rho_b \approx 0.23 V_P^{0.25}$$

where V_P is in ft/s.

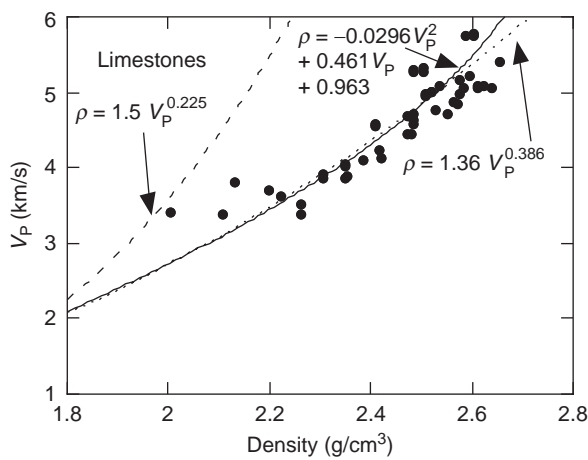


Figure 7.10.3 Both forms of Gardner’s relations applied to laboratory limestone data. Note that the published power-law form does not fit as well as the polynomial. We also show a revised power-law form fit to these data, which agrees very well with the polynomial.

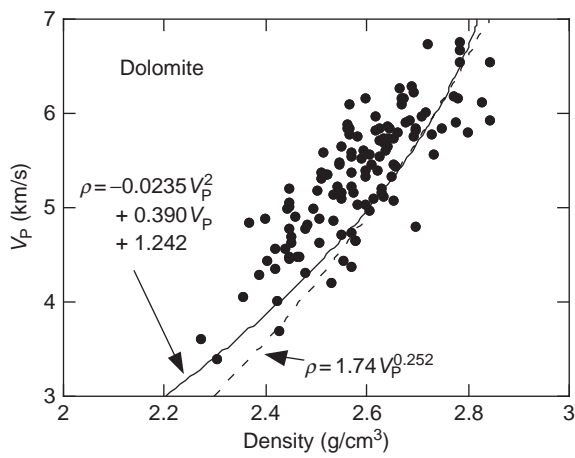


Figure 7.10.4 Both forms of Gardner’s relations applied to laboratory dolomite data.

More useful predictions can be obtained by using the lithology-specific forms given by Gardner *et al.* (1974). Castagna *et al.* (1993) suggested slight improvements to Gardner’s relations and summarized these, as shown in Table 7.10.1, in both polynomial and power-law form. Figures 7.10.1–7.10.4 show Gardner’s relations applied to laboratory data.

Assumption and limitations

Gardner’s relations are empirical.

7.11 Eaton and Bowers pore-pressure relations

Synopsis

Following Eaton (1975), Gutierrez *et al.* (2006) present the following equation for pore-pressure prediction from measured P-wave velocity:

$$P_{\text{over}} - P_p = (P_{\text{over}} - P_{\text{hyd}})(V_p/V_{\text{pn}})^3$$

where P_p is the actual pore pressure, P_{over} is the vertical overburden stress, P_{hyd} is the normal hydrostatic pressure, V_p is the measured velocity, and V_{pn} is the normal-compaction velocity. This equation implies that if $V_p = V_{\text{pn}}$, i.e., the rock is normally compacted, $P_p = P_{\text{hyd}}$. Conversely, if $V_p < V_{\text{pn}}$, i.e., the measured velocity is smaller than the normal velocity, $P_p > P_{\text{hyd}}$, which means that the rock is overpressured. The Eaton equation is applicable to overpressure due to undercompaction of shale which occurs during monotonic overburden stress increase due to burial.

Bowers (1995) considers overpressure generation not only due to undercompaction but also due to tectonic unloading, such as occurs during uplift of rock. Gutierrez *et al.* (2006) present Bowers's equation as

$$P_{\text{over}} - P_p = [(V_p - 5000)/a]^{1/b}$$

where pressure is in psi and velocity is in ft/s. The coefficients calibrated to the monotonic-compaction data from the Gulf of Mexico are $a = 9.18448$ and $b = 0.764984$. These coefficients may be different in environments where abnormal pore pressure is generated by unloading, kerogen maturation, or clay mineral transformations.

Assumption and limitations

The constants and trends used in these equations are highly site-specific and require thorough calibration using real pore-pressure measurements. As a result, we caution against using the constants appropriate for one basin at another location. Moreover, these constants may vary even within the same basin between different fault blocks. The normal compaction trends for the P-wave velocity are sometimes simply not present in basins where all drilled wells encounter overpressure, i.e., the measured velocity is always abnormally slow. In this case, an assumed normal velocity trend has to be adopted.

7.12 Kan and Swan pore-pressure relations

Synopsis

Hottman and Johnson (1965) established an empirical relation between the pore-pressure gradient, $P(z)/z$, and Δt , the departure of sonic interval transit time from a

Table 7.12.1 *Kan and Swan’s (2001) empirical coefficients.*

Basin and age	c_1 (Pa/ μ s)	c_2 (Pa · m/ μ s ²)
Gulf of Mexico Miocene	143	−0.42
Gulf of Mexico Pliocene	67.6	−0.10
Gulf of Mexico Pleistocene	42.7	−0.028
North Sea	13.1	0.168
Alaska	36.5	0.48
Northwest Australia	42.4	0.22
South China Sea	32.8	1.54

background trend of transit time with depth. The background trend is for normally pressured shale undergoing normal compaction. The relation is given by

$$P(z)/z = R_w + c_1 \Delta t + c_2 (\Delta t)^2$$

where R_w is the hydrostatic pore-pressure gradient (in Pa/m), z is the depth in meters, and $\Delta t = t(z) - t_0 \exp(-z/k)$ is the interval transit time departure in μ s/m.

The normal compaction shale trend is given by $t_0 \exp(-z/k)$, where t_0 is the transit time of the shale at $z = 0$ and k is determined from log data in normally pressured shale. Kan and Swan (2001) give a compilation of coefficients c_1 and c_2 for specific basins and ages, determined by empirical regression (Table 7.12.1). With the appropriate coefficients, Kan and Swan expect the empirical equation to be reasonably accurate for pressure gradients up to 20 kPa/m as long as the overpressure is caused only by undercompaction.

Assumption and limitations

- The relation is empirical.
- The relation applies strictly only to overpressure caused by undercompaction and not to other mechanisms such as aquathermal pressure, kerogen maturation, and other late-stage mechanisms.

7.13 Attenuation and quality factor relations

Klimentos and McCann (1990) present a statistical relation between the compressional-wave attenuation coefficient α (measured in dB/cm), porosity ϕ , and clay content C (both measured in volume fraction) obtained in water-saturated sandstone samples. The porosity of the samples ranges from 0.05 to 0.30, and the clay content ranges from zero to 0.25. The differential pressure is 40 MPa and the frequency is 1 MHz. The relation is

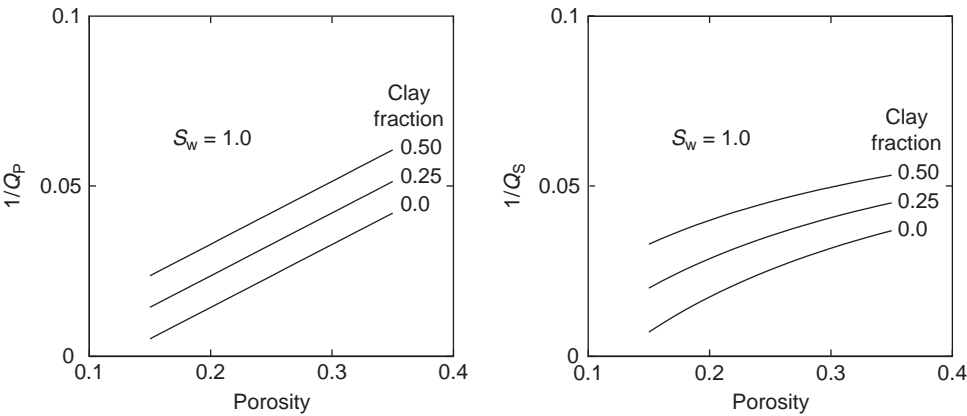


Figure 7.13.1 The P- and S-wave inverse quality factors in fully water-saturated sandstone versus porosity for a clay content of zero, 0.25, and 0.5 (from bottom to top). The effective pressure is 30 MPa, the frequency is 1 MHz, and the permeability is 100 mD. The inverse quality factors increase with increasing clay content.

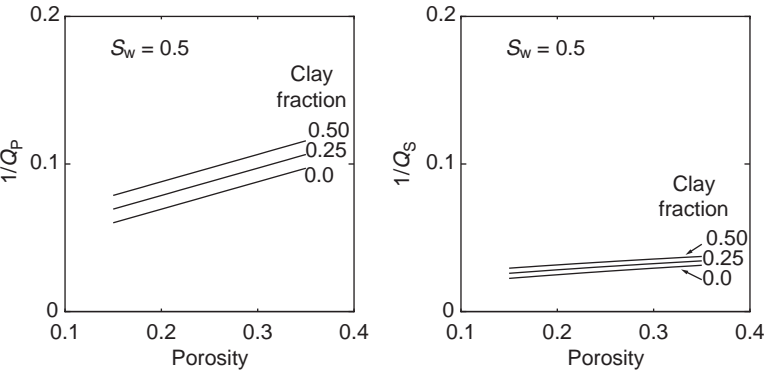


Figure 7.13.2 Same as Figure 7.13.1 but with a water saturation of 0.5. Again, the clay content is zero, 0.25, and 0.5 (from bottom to top). The effective pressure is 30 MPa, frequency is 1 MHz, and permeability is 100 mD. The inverse quality factors increase with increasing clay content.

$$\alpha = 3.15\phi + 24.1C - 0.132$$

with a correlation coefficient of 0.88.

Koesoemadinata and McMechan (2001) use a large number of experimental results in sandstones to obtain statistical relations between the P- and S-wave inverse quality factors and the effective pressure, porosity, clay content, water saturation, permeability, and frequency. Figures 7.13.1 and 7.13.2 display selected results from these relations.

Uses

These relations can be used to estimate attenuation versus porosity, clay content, saturation, frequency, pressure, and permeability.

Assumptions and limitations

These relations are strictly empirical and mostly valid at laboratory ultrasonic frequencies. They may not be applicable in the well-log, VSP, and/or seismic frequency ranges.

7.14 Velocity–porosity–strength relations

Synopsis

Chang *et al.* (2004) and Zoback (2007), summarize 30 empirical equations relating physical properties (such as velocity, Young’s modulus, and porosity) to unconfined compressive strength (UCS) in sandstone, shale, and limestone and dolomite; see Tables 7.14.1–7.14.3. While some equations work reasonably well (for example, some strength–porosity relationships for sandstone and shale), data on rock strength show considerable scatter around the empirical regressions, emphasizing the importance of local calibration before utilizing any of the relationships presented. Nonetheless, some reasonable correlations can be found between velocity, porosity, and rock strength that can be used for applications related to well-bore stability, where having a lower-bound estimate of rock strength is especially useful.

Table 7.14.1 Empirical relations for sandstones (Chang *et al.*, 2004; Zoback, 2007).

UCS =		Equation number
$0.035 V_P - 31.5$	Thuringia, Germany; Freyburg (1972)	(1)
$1200 \exp(-0.036 \Delta t)$	Bowen Basin, Australia. Fine-grained consolidated and unconsolidated sandstone; McNally (1987)	(2)
$1.4138 \times 10^7 \Delta t^{-3}$	Gulf Coast, weak unconsolidated sandstone	(3)
$3.3 \times 10^{-20} \rho^2 V_P^4 \times [(1+\nu)/(1-\nu)]^2 \times (1-2\nu)[1+0.78V_{\text{clay}}]$	Gulf Coast sandstones with UCS > 30 MPa; Fjaer <i>et al.</i> (2008)	(4)
$1.745 \times 10^{-9} \rho V_P^2 - 21$	Cook Inlet, Alaska; coarse-grained sandstone and conglomerates; Moos <i>et al.</i> (1999)	(5)
$42.1 \exp(1.9 \times 10^{-11} \rho V_P^2)$	Australia; consolidated sandstones with UCS > 80 MPa, porosity between 0.05 and 0.12; Chang <i>et al.</i> (2004)	(6)
$3.87 \exp(1.14 \times 10^{-10} \rho V_P^2)$	Gulf of Mexico; Chang <i>et al.</i> (2004)	(7)
$46.2 \exp(0.027E)$	Chang <i>et al.</i> (2004)	(8)
$2.28 + 4.1089E$	Worldwide; Bradford <i>et al.</i> (1998)	(9)
$254(1 - 2.7\phi)^2$	Worldwide; very clean, well-consolidated sandstones with porosity < 0.3; Vernik <i>et al.</i> (1993)	(10)
$277 \exp(-10\phi)$	Sandstones with $2 < \text{UCS} < 360$ MPa, and $0.002 < \phi < 0.3$; Chang <i>et al.</i> (2004)	(11)

Table 7.14.2 Empirical relations for shales (Chang et al., 2004; Zoback, 2007).

UCS =		Equation number
$0.77(304.8/\Delta t)^{2.93}$	North Sea, high-porosity Tertiary shales; Horsrud (2001)	(12)
$0.43(304.8/\Delta t)^{3.2}$	Gulf of Mexico, Pliocene and younger shales; Chang et al. (2004)	(13)
$1.35(304.8/\Delta t)^{2.6}$	Worldwide; Chang et al. (2004)	(14)
$0.5(304.8/\Delta t)^3$	Gulf of Mexico; Chang et al. (2004)	(15)
$10(304.8/\Delta t - 1)$	North Sea, high-porosity Tertiary shales; Lal (1999)	(16)
$7.97E^{0.91}$	North Sea, high-porosity Tertiary shales; Horsrud (2001)	(17)
$7.22E^{0.712}$	Strong, compacted shales; Chang et al. (2004)	(18)
$1.001\phi^{-1.143}$	Low-porosity (<0.1), high-strength (~79 MPa) shales; Lashkaripour and Dusseault (1993)	(19)
$2.922\phi^{-0.96}$	North Sea, high-porosity Tertiary shales; Horsrud (2001)	(20)
$0.286\phi^{-1.762}$	High-porosity (>0.27) shales; Chang et al. (2004)	(21)

Table 7.14.3 Empirical relations for limestone and dolomite (Chang et al., 2004; Zoback, 2007).

UCS =		Equation number
$(7682/\Delta t)^{1.82}/145$	Militzer and Stoll (1973)	(22)
$10^{(2.44 + 109.14/\Delta t)}/145$	Golubev and Rabinovich (1976)	(23)
$13.8E^{0.51}$	Limestone with $10 < \text{UCS} < 300$ MPa; Chang et al. (2004)	(24)
$25.1E^{0.34}$	Dolomite with $60 < \text{UCS} < 100$ MPa; Chang et al. (2004)	(25)
$276(1-3\phi)^2$	Korobcheyev deposit, Russia; Rzhnevsky and Novik (1971)	(26)
$143.8 \exp(-6.95\phi)$	Middle East, low- to moderate-porosity (0.05–0.2), high UCS (30–150 MPa); Chang et al. (2004)	(27)
$135.9 \exp(-4.8\phi)$	low- to moderate-porosity (0.0–0.2), high UCS (10–300 MPa); Chang et al. (2004)	(28)

Units and symbols in the tables are:

UCS (MPa):	unconfined compressive strength
Δt (μs/ft):	P-wave sonic transit time
V_p (m/s):	P-wave velocity
ρ (kg/m ³):	bulk density
E (GPa):	Young’s modulus
ϕ (fraction):	porosity
V_{clay} (fraction):	clay fraction
GR (API):	gamma-ray log value

In addition to UCS, another material parameter of interest in estimating rock strength is the angle of internal friction, $\theta = \tan^{-1}\mu$, where μ is the coefficient of internal

Table 7.14.4 *Angles of internal friction.*

θ (deg) =		Equation number
$\sin^{-1}[(V_P - 1000)/(V_P + 1000)]$	Shales; Lal (1999)	(29)
$57.8 - 105\phi$ Sandstone	Weingarten and Perkins (1995)	(30)
$\tan^{-1} \left[\frac{(GR - GR_{\text{sand}})\mu_{\text{shale}} + (GR_{\text{shale}} - GR)\mu_{\text{sand}}}{GR_{\text{shale}} - GR_{\text{sand}}} \right]$	Shaley sandstones; Chang <i>et al.</i> (2004)	(31)

friction. Chang *et al.* (2004) give the relations for θ , summarized in Table 7.14.4. These relations are of doubtful reliability, but show trends that are approximately in agreement with observations (Wong *et al.*, 1993; Horsrud, 2001).

Use of equation (30) in Table 7.14.4 requires the reference values of GR and μ (coefficient of internal friction) for pure shale and pure sand end-members. These have to be assumed or calibrated from well logs.

Uses

These equations can be used to estimate rock strength from properties measurable with geophysical well logs.

Assumptions and limitations

- The relations described in this section are obtained from empirical fits that show considerable scatter, especially for carbonates. Relations should be locally calibrated when possible.
- Relations for well-consolidated rocks (e.g., equations (10), (18), and (19) in the tables) should not be used for estimating strength of poorly consolidated, weak rocks. Equations (3) and (5) provide reasonable estimates for weak sands.
- Equation (11) for sandstones gives a reasonable fit to UCS for porosities >0.1, with 80% of the data within ± 30 MPa.
- Equations (15), and (19)–(21) for shales predict shale strength fairly well. For porosities > 0.1, equations (19)–(21) fit 90% of the data to within ± 10 MPa.

8 Flow and diffusion

8.1 Darcy's law

Synopsis

It was established experimentally by Darcy (1856) that the fluid flow rate is linearly related to the pressure gradient in a fluid-saturated porous medium by the following equation:

$$Q_x = -A \frac{\kappa}{\eta} \frac{\partial P}{\partial x}$$

where Q_x is the volumetric fluid flow rate in the x direction, κ is the permeability of the medium, η is the dynamic viscosity of the fluid, P is the fluid pressure, and A is the cross-sectional area normal to the pressure gradient.

This can be expressed more generally as

$$\mathbf{Q} = -\frac{\boldsymbol{\kappa}}{\eta} A \text{ grad } P$$

where \mathbf{Q} is the vector fluid volumetric velocity field and $\boldsymbol{\kappa}$ is the permeability tensor.

Permeability, $\boldsymbol{\kappa}$, has units of area (m^2 in SI units), but the more convenient and traditional unit is the **Darcy**:

$$1 \text{ Darcy} = 0.986923 \times 10^{-12} \text{ m}^2$$

In a water-saturated rock with a permeability of 1 Darcy, a pressure gradient of 1 bar/cm gives a flow velocity of 1 cm/s.

The hydraulic conductivity K is related to permeability k as

$$K = \frac{k \rho g}{\eta}$$

where $g = 9.81 \text{ m/s}^2$ is the acceleration due to gravity. Hence, the units of hydraulic conductivity are m/s.

For water with density $1 \text{ g/cm}^3 = 1000 \text{ kg/m}^3$ and dynamic viscosity $1 \text{ cP} = 0.001 \text{ Pa s}$, the permeability of $1 \text{ mD} = 10^{-15} \text{ m}^2$ translates into a hydraulic conductivity of $9.81 \times 10^{-9} \text{ m/s} = 9.81 \times 10^{-7} \text{ cm/s} \approx 10^{-6} \text{ cm/s}$. Hydraulic conductivity is often used in ground water flow applications.

If the linear (not volumetric) velocity field V is considered,

$$\mathbf{V} = -\frac{\mathbf{\kappa}}{\eta} \text{grad } P$$

Using this latter notation, Darcy's law for **multiphase flow** of immiscible fluids in porous media (with porosity ϕ) is often stated as

$$\mathbf{V}_i = -\frac{\kappa_{ri}\mathbf{\kappa}}{\eta_i} \text{grad } P_i$$

where the subscript i refers to each phase and κ_{ri} is the relative permeability of phase i . Simultaneous flow of multiphase immiscible fluids is possible only when the saturation of each phase is greater than the irreducible saturation, and each phase is continuous within the porous medium. The relative permeabilities depend on the saturations S_i and show hysteresis, for they depend on the path taken to reach a particular saturation. The pressures P_i in any two phases are related by the capillary pressure P_c , which itself is a function of the saturations. For a two-phase system with fluid 1 as the wetting fluid and fluid 2 as the nonwetting fluid, $P_c = P_2 - P_1$. The presence of a residual nonwetting fluid can interfere considerably with the flow of the wetting phase. Hence the maximum value of κ_{r1} may be substantially less than 1. There are extensions of Darcy's law for multiphase flow (Dullien, 1992) that take into account cross-coupling between the fluid velocity in phase i and the pressure gradient in phase j . The cross-coupling becomes important only at very high viscosity ratios ($\eta_i/\eta_j \gg 1$) because of an apparent lubricating effect.

In a one-dimensional, immiscible displacement of fluid 2 by fluid 1 (e.g., water displacing oil in a water flood), the time history of the saturation $S_1(x, t)$ is governed by the following equation (Marle, 1981):

$$\frac{V}{\phi} \left[\frac{d\xi_1}{dS_1} \frac{\partial S_1}{\partial x} + \frac{\partial}{\partial x} \left(\Psi_1 \frac{\partial S_1}{\partial x} \right) \right] + \frac{\partial S_1}{\partial t} = 0$$

where

$$V = V_1 + V_2$$

$$\xi_1 = \frac{\eta_2/\kappa_{r2} + \kappa(\rho_1 - \rho_2)g/V}{\eta_1/\kappa_{r1} + \eta_2/\kappa_{r2}}$$

$$\Psi_1 = \frac{\kappa}{V} \frac{1}{\eta_1/\kappa_{r1} + \eta_2/\kappa_{r2} \frac{dP_c}{dS_1}}$$

where V_1 and V_2 are the Darcy fluid velocities in phases 1 and 2, respectively, and g is the acceleration due to gravity. The requirement that the two phases completely fill the pore space implies $S_1 + S_2 = 1$. Neglecting the effects of capillary pressure gives the **Buckley–Leverett** equation for immiscible displacement:

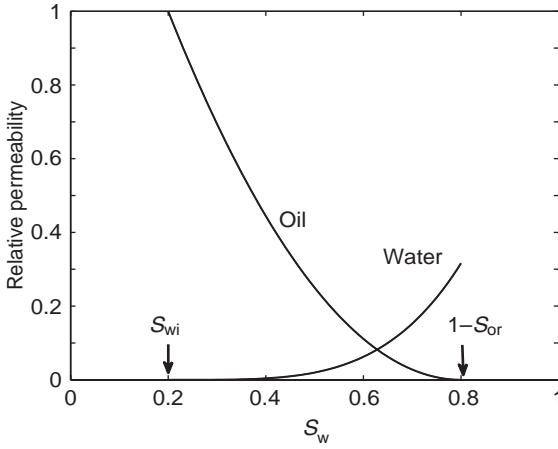


Figure 8.1.1 Relative permeability for water (the rising curve) and oil (falling curve) according to equations of Desbrandes (1985) for an irreducible water saturation of 0.2 and a residual oil saturation of 0.2.

$$\left(\frac{V}{\phi} \frac{d\xi_1}{dS_1} \right) \frac{\partial S_1}{\partial x} + \frac{\partial S_1}{\partial t} = 0$$

This represents a saturation wavefront traveling with velocity $(V/\phi) (d\xi_1/dS_1)$.

Desbrandes (1985) presented the following empirical equations that link the relative permeability for water (k_{rw}) and oil (k_{ro}) to water saturation (S_w), irreducible water saturation (S_{wi}), and residual oil saturation (S_{or}):

$$k_{rw} = \left(\frac{S_w - S_{wi}}{1 - S_{wi}} \right)^4$$

$$k_{ro} = \left(\frac{1 - S_{or} - S_w}{1 - S_{or} - S_{wi}} \right)^2$$

where saturation can vary from 0 to 1. These relative permeability curves are plotted in Figure 8.1.1.

Diffusivity

If the fluid and the matrix containing it are compressible and elastic, the saturated system can take on the behavior of the diffusion equation. If we combine Darcy's law with the equation of mass conservation given by

$$\nabla \cdot (\rho \mathbf{V}) + \frac{\partial(\rho \phi)}{\partial t} = 0$$

plus Hooke's law expressing the compressibility of the fluid, β_f , and of the pore volume, β_{pv} , and drop nonlinear terms in pressure, we obtain the classical diffusion equation:

$$\nabla^2 P = \frac{1}{D} \frac{\partial P}{\partial t}$$

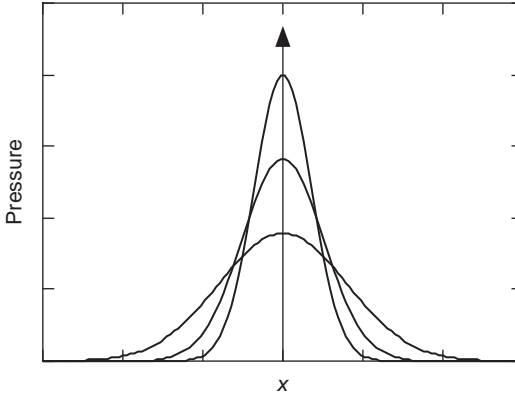


Figure 8.1.2 Pressure curves for one-dimensional diffusion.

where D is the diffusivity:

$$D = \frac{\kappa}{\eta\phi(\beta_{fl} + \beta_{pv})}$$

One-dimensional diffusion

Consider the one-dimensional diffusion that follows an initial pressure pulse:

$$P = P_0 \delta(x)$$

We obtain the standard result, illustrated in [Figure 8.1.2](#), that

$$P(x, t) = \frac{P_0}{\sqrt{4\pi Dt}} e^{-x^2/4Dt} = \frac{P_0}{\sqrt{4\pi Dt}} e^{-\tau/t}$$

where the characteristic time depends on the length scale x and the diffusivity:

$$\tau = \frac{x^2}{4D}$$

Sinusoidal pressure disturbance

Consider an instantaneous sinusoidal pore-pressure disturbance in the saturated system, as shown in [Figure 8.1.3](#).

The disturbance will decay approximately as $e^{-t/\tau}$, where the diffusion time is again related to the length and diffusivity by

$$\tau_d = \frac{\lambda^2}{4D}$$

It is interesting to ask, when is the diffusion time equal to the period of the seismic wave causing such a disturbance? The seismic period is

$$\tau_s = \frac{\lambda}{V_p}$$

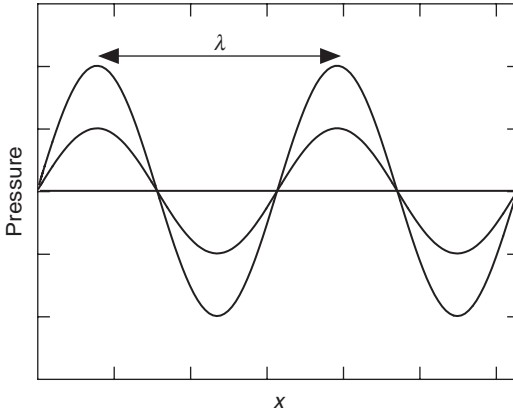


Figure 8.1.3 Decay of an instantaneous sinusoidal pore-pressure disturbance in a saturated system.

Equating τ_d to τ_s gives

$$\tau_d = \tau_s \quad \Rightarrow \quad \frac{\lambda^2}{4D} = \frac{\lambda}{V_p}$$

which finally gives

$$\tau = \frac{4D}{V_p}$$

For a rock with a permeability of 1 milliDarcy (1 mD), the critical frequency ($1/\tau$) is 10 MHz.

Assumptions and limitations

The following considerations apply to the use of Darcy's law:

- Darcy's law applies to a representative elementary volume much larger than the grain or pore scale;
- Darcy's law is applicable when inertial forces are negligible in comparison to pressure gradient and viscous forces, and the Reynolds number Re is small ($Re \approx 1-10$). The Reynolds number for porous media is given by $Re = \rho v l / \eta$, where ρ is the fluid density, η is the fluid viscosity, v is the fluid velocity, and l is a characteristic length of fluid flow determined by pore dimensions. At high Re , inertial forces can no longer be neglected in comparison with viscous forces, and Darcy's law breaks down;
- some authors mention a minimum threshold pressure gradient below which there is very little flow (Bear, 1972). Non-Darcy behavior below the threshold pressure gradient has been attributed to streaming potentials in fine-grained soils, immobile adsorbed water layers, and clay–water interaction, giving rise to non-Newtonian fluid viscosity; and
- when the mean free path of gas molecules is comparable to or larger than the dimensions of the pore space, the continuum description of gas flow becomes invalid. In these cases, measured permeability to gas is larger than the permeability to liquid. This is sometimes thought of as the increase in apparent gas permeability

caused by slip at the gas–mineral interface. This is known as the Klinkenberg effect (Bear, 1972). The Klinkenberg correction is given by

$$\kappa_g = \kappa_l \left(1 + \frac{4c\lambda}{r} \right) = \kappa_l \left(1 + \frac{b}{P} \right)$$

where κ_g is the gas permeability, κ_l is the liquid permeability, λ is the mean free path of gas molecules at the pressure P at which κ_g is measured, $c \approx 1$ is a proportionality factor, b is an empirical parameter that is best determined by measuring κ_g at several pressures, and r is the radius of the capillary.

Extensions

When inertial forces are not negligible (large Reynolds number), Forchheimer suggested a nonlinear relation between the fluid flux and the pressure gradient (Bear, 1972) as follows:

$$\frac{dP}{dx} = aV + bV^2$$

where a and b are constants.

Another extension to Darcy's law was proposed by Brinkman by adding a Laplacian term to account for solid–fluid interface interactions (Sahimi, 1995). The modified equation, sometimes termed the Darcy–Brinkman equation is:

$$\nabla P = -\frac{\eta'}{K}V + \eta'\nabla^2 V$$

where the viscosity η' can, in principle, be different from the pure fluid viscosity, η , though in Brinkman's original paper and in many applications they are taken to be the same (Sahimi, 1995). The Darcy–Brinkman equation is useful for modeling flow in very high-porosity media, and also in transition zones between porous media flow and open-channel flow.

8.2 Viscous flow

Synopsis

In a Newtonian, viscous, incompressible fluid, stresses and velocities are related by Stokes' law (Segel, 1987):

$$\sigma_{ij} = -P\delta_{ij} + 2\eta D_{ij}$$

$$D_{ij} = \frac{1}{2} \left(\frac{\partial v_i}{\partial x_j} + \frac{\partial v_j}{\partial x_i} \right)$$

where σ_{ij} denotes the elements of the stress tensor, v_i represents the components of the velocity vector, P is pressure, and η is dynamic viscosity.

For a simple shear flow between two walls, this law is called the Newton friction law and is expressed as

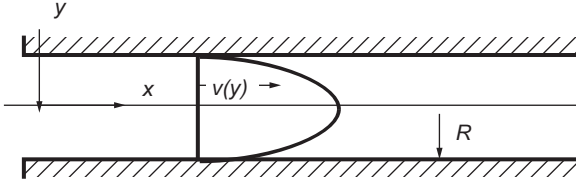


Figure 8.2.1 Steady laminar flow in a two-dimensional slot, or in a pipe of circular cross-section.

$$\tau = \eta \frac{dv}{dy},$$

where τ is the shear stress along the flow, v is velocity along the flow, and y is the coordinate perpendicular to the flow.

The Navier–Stokes equation for a Newtonian viscous incompressible flow is (e.g., Segel, 1987)

$$\rho \left(\frac{\partial \mathbf{v}}{\partial t} + \mathbf{v} \cdot \text{grad } \mathbf{v} \right) = - \text{grad } P + \eta \Delta \mathbf{v}$$

where ρ is density, t is time, \mathbf{v} is vector velocity, and Δ is the Laplace operator.

Useful examples of viscous flow

- (a) Steady two-dimensional laminar flow between two walls (Lamb, 1945):

$$v(y) = -\frac{1}{2\eta} \frac{dP}{dx} (R^2 - y^2), \quad Q = -\frac{2}{3\eta} \frac{dP}{dx} R^3$$

where $2R$ is the distance between the walls and Q is the volumetric flow rate per unit width of the slit (Figure 8.2.1).

- (b) Steady two-dimensional laminar flow in a circular pipe:

$$v(y) = -\frac{1}{4\eta} \frac{dp}{dx} (R^2 - y^2), \quad Q = -\frac{\pi}{8\eta} \frac{dP}{dx} R^4$$

where R is the radius of the pipe (see Figure 8.2.1).

- (c) Steady laminar flow in a pipe of elliptical cross-section (Lamb, 1945):

$$Q = -\frac{\pi}{4\eta} \frac{dP}{dx} \frac{a^3 b^3}{a^2 + b^2}$$

where a and b are the semiaxes of the cross-section.

- (d) Steady laminar flow in a pipe of rectangular cross-section:

$$Q = -\frac{1}{24\eta} \frac{dP}{dx} ab(a^2 + b^2) + \frac{8}{\pi^5 \eta} \frac{dP}{dx} \sum_{n=1}^{\infty} \frac{1}{(2n-1)^5} \\ \times \left[a^4 \tanh\left(\pi b \frac{2n-1}{2a}\right) + b^4 \tanh\left(\pi a \frac{2n-1}{2b}\right) \right]$$

where a and b are the sides of the rectangle. For a square this equation yields

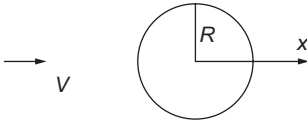


Figure 8.2.2 Steady laminar flow past a sphere.

$$Q = -0.035144 \frac{a^4}{\eta} \frac{dP}{dx}$$

- (e) Steady laminar flow in a pipe of equilateral triangular cross-section with the length of a side b :

$$Q = -\frac{\sqrt{3}b^4}{320\eta} \frac{dP}{dx}$$

- (f) Steady laminar flow past a sphere (pressure on the surface of the sphere depends on the x coordinate only):

$$P = -\frac{3}{2}\eta \frac{x}{R^2} v$$

where v is the undisturbed velocity of the viscous flow (velocity at infinity), and the origin of the x -axis is in the center of the sphere of radius R (Figure 8.2.2). The total resistance force is $6\pi\eta v R$.

The combination

$$Re = \frac{\rho v R}{\eta}$$

where R is the characteristic length of a flow (e.g., the pipe radius) and Re is the **Reynolds number**. Flows where $Re < 1$ are called **creeping flows**. (Viscous forces are the dominant factors in such flows.) A flow becomes turbulent (i.e., nonlaminar) if $Re > 2000$.

Uses

The equations presented in this section are used to describe viscous flow in pores.

Assumptions and limitations

The equations presented in this section assume that the fluid is incompressible and Newtonian.

8.3 Capillary forces

Synopsis

A **surface tension**, γ , exists at the interface between two immiscible fluids or between a fluid and a solid (Figure 8.3.1). The surface tension acts tangentially to

Table 8.3.1 Typical values for surface tension (at 20 °C, unless otherwise noted).

Interface	γ in mN/m
Water–air	72.80
Octane–air	21.62
Heptane–air	20.14
Mercury–air	486.5
Water–mercury	415
Ethylene glycol–air (25 °C)	47.3
Benzene–air	28.88
Toluene–air	28.52
Ethanol–air	22.39

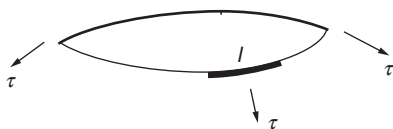


Figure 8.3.1 Surface tensional forces at a liquid–solid or liquid–liquid interface.

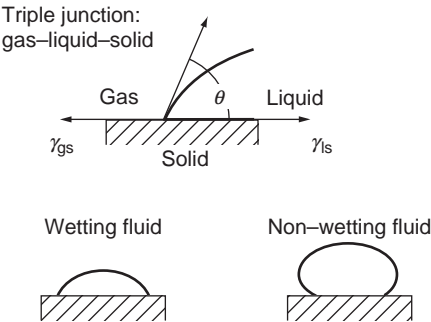


Figure 8.3.2 Triple junction at the interface between a solid, a liquid, and a gas. Top: the contact angle at the triple junction. Bottom: schematic of wetting and nonwetting fluids.

the interface surface. If τ is a force acting on length l of the surface, then the surface tension is defined as $\gamma = \tau/l$; hence, the unit of surface tension is force per unit length (N/m). A surface tension may be different at interfaces between different materials. For example, γ_{ow} (oil–water) differs from γ_{og} (oil–gas) and from γ_{wg} (water–gas). Some typical values of fluid–fluid surface tensions are shown in [Table 8.3.1](#).

The force equilibrium condition at a triple point of contact between a solid, a liquid, and a gas is given by ([Figure 8.3.2](#)) Young’s relation:

$$\gamma_{lg} \cos(\theta) + \gamma_{ls} = \gamma_{gs}, \quad \cos(\theta) = \frac{\gamma_{gs} - \gamma_{ls}}{\gamma_{lg}}$$

where γ_{lg} , γ_{ls} , and γ_{gs} are the liquid–gas, liquid–solid, and gas–solid interfacial tensions, respectively. The angle θ is the **contact angle**. The liquid within the droplet is **wetting** if $\theta < 90^\circ$ and **nonwetting** if $\theta > 90^\circ$. The equilibrium will not exist if

$$|(\gamma_{gs} - \gamma_{ls})/\gamma_{lg}| > 1$$

A similar situation can occur at the triple interface of a solid and two immiscible liquids.

The surface tension between a solid and liquid is difficult to measure. Some techniques are based on directly measuring the contact angle of a drop (goniometry), while others are based on measurements of the force of interaction between the solid and a test liquid (tensiometry). The observed contact angle can be affected by the liquid and solid compositions, the surface roughness, temperature, pressure, heterogeneity along the surface, and the amount of time elapsed since the liquid and solid came into contact. The contact angle for a fluid contact advancing (or recently advanced) along the solid surface is usually larger than the contact angle on a receding (or recently receded) contact.

If a sphere of oil (radius R) is floating inside water, the oil–water surface tension, γ , has the effect of contracting the sphere, causing the pressure inside the sphere, P_o , to be greater than pressure in the surrounding water P_w . The difference between these two pressures is called **capillary pressure**: $P_c = P_o - P_w$ and is given by the Laplace equation:

$$P_c = 2\gamma/R$$

In general, capillary pressure inside a surface of two principal radii of curvature R_1 and R_2 is

$$P_c = \gamma \left(\frac{1}{R_1} \pm \frac{1}{R_2} \right)$$

where the plus sign corresponds to the case in which the centers of curvature are located on the same side of the interface (e.g., a sphere), and the minus sign corresponds to the case in which the centers of the curvature are located on opposite sides (e.g., a torus).

If the pore fluid is wetting, a pendular ring may exist at the point of contact of two grains (see Figure 8.3.3). The capillary pressure at any point P on the surface of the ring depends on the contact angle θ of the liquid with the grains and on the radii of curvature, R_1 and R_2 , at that point, as follows:

$$P_c = \gamma \left(\frac{1}{R_1} - \frac{1}{R_2} \right) \cos(\theta)$$

If $\theta = 0$, we have the following expression at the contact point of two identical spherical grains of radius R (Gvirtzman and Roberts, 1991):

$$R_1 = R \frac{\sin(\phi) + \cos(\phi) - 1}{\cos(\phi)}, \quad R_2 = R \frac{1 - \cos(\phi)}{\cos(\phi)}$$

where ϕ is the angle between the line connecting the centers of the spheres and the line from the center of the sphere to the edge of the pendular ring. The ring will exist as long

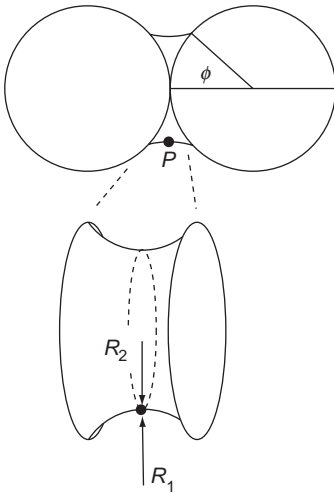


Figure 8.3.3 A pendular ring of fluid between two grains, showing the two radii of curvature at point P .

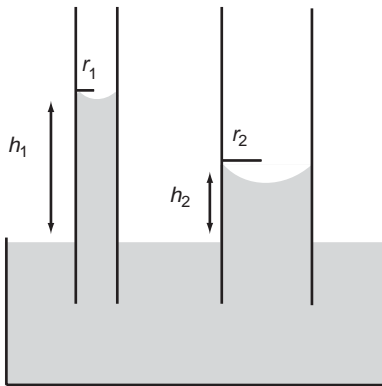


Figure 8.3.4 Capillary rise of a wetting fluid inside tubes of different radii.

as its capillary pressure is smaller than the external pressure. The preceding formulas show that this condition is valid for $\phi < 53^\circ$. The maximum volume of this ring is about 0.09 times the volume of an individual grain. This maximum volume tends to decrease with increasing angle θ (e.g., it is 0.04 times the grain volume for $\theta = 32^\circ$).

When a narrow tube is brought into contact with a wetting liquid, the liquid rises inside the tube (see Figure 8.3.4). The weight of the fluid column is supported by the capillary forces. The height of this rise (h) is

$$h = \frac{2\gamma \cos \theta}{\Delta \rho g r}$$

where γ is the surface tension between the two fluids in the tube; θ is the contact angle of the wetting liquid on the tube surface; $\Delta \rho$ is the density contrast of the fluids

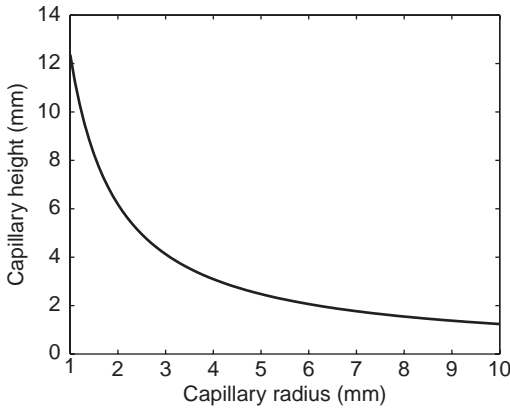


Figure 8.3.5 Capillary rise of a wetting fluid as a function of tube radius, for an air–water system with a contact angle of 30° .

(approximately 1000 kg/m^3 for a water–air system); g is the acceleration due to gravity (9.8 m/s^2); and r is the radius of the tube. For a tube containing water and air with surface tension at room conditions of about 0.07 N/m , and assuming a contact angle of 30° , we plot the capillary equilibrium height versus the tube radius in [Figure 8.3.5](#).

Imbibition refers to the increase of the wetting-fluid saturation in a rock, while **drainage** refers to the decrease of the wetting-fluid saturation. Imagine a rock fully saturated with water, the wetting phase. If the rock is put in contact with oil (the nonwetting phase), the oil will not enter the pore space because of the capillary forces holding the water in place. If the oil is pressurized to the capillary pressure of the largest pore throats, oil will begin to enter (drainage). Further increases in oil pressure will allow the oil to be forced into successively smaller and smaller throats, until eventually a limit is reached, corresponding to the **irreducible water saturation** (see [Figure 8.3.6](#)). Dropping the oil pressure causes the water to re-enter the rock, displacing oil. The saturation–pressure curve for imbibition will generally be different than the curve for drainage (see [Figure 8.3.6](#)). At zero oil pressure, some **residual oil** will remain in the rock, trapped in bypassed pores.

Uses

The formulas presented in this section can be used to calculate wetting pore-fluid geometry in granular rocks.

Assumptions and limitations

Some of the formulas in this section are based on idealized geometries. For example, the description of pendular rings is for spherical grains. The equation for capillary rise is for tubes of circular cross-section.

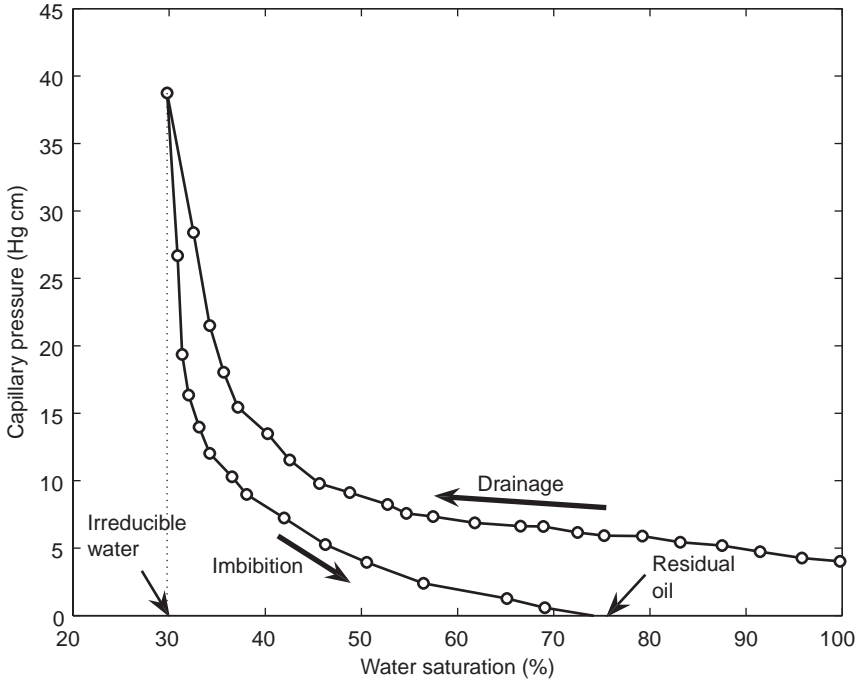


Figure 8.3.6 Typical imbibition–drainage curves for a water-wet rock.

8.4 Kozeny–Carman relation for flow

Synopsis

The Kozeny–Carman (Carman, 1961) relation provides a way to estimate the permeability of a porous medium in terms of generalized parameters such as porosity, surface area, and particle size. The derivation is based on flow through a pipe having a circular cross-section with radius R . The flux in the pipe of length l can be written as

$$Q = -\frac{\pi R^4}{8\eta} \frac{\Delta P}{l}$$

where P is the pressure and η is the dynamic viscosity. Assume that the direction of this pipe is at an angle to the pressure gradient, which is applied to a permeable block of length L ($L \leq l$) and cross-sectional area A (Figure 8.4.1). Comparison with Darcy's law,

$$Q = -\kappa \frac{A \Delta P}{\eta L}$$

where κ is the permeability, gives an effective permeability for the block expressed as

$$\kappa = \frac{\pi R^4 L}{8A} \frac{1}{l} = \frac{\pi R^4}{8A\tau}$$

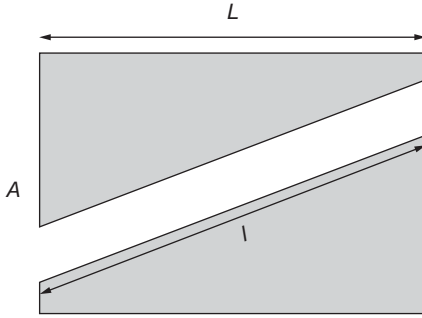


Figure 8.4.1 Solid block with a pipe used for Kozeny–Carman derivations. The notation is explained in the text.

where τ is the tortuosity (defined as the ratio of total flow-path length to length of the sample).

The porosity, ϕ , and the specific surface area, S (defined as the pore surface area divided by the sample volume), can be expressed in terms of the properties of the pipe by the following relations:

$$\phi = \frac{\pi R^2 l}{AL} = \frac{\pi R^2}{A} \tau$$

$$S = \frac{2\pi R l}{AL} = \frac{2\pi R \tau}{A} = \frac{\pi R^2 \tau}{A} \frac{2}{R} = \frac{2\phi}{R}$$

Finally, we can express the permeability of the block with the pipe in terms of the more general properties, ϕ and S , to obtain the Kozeny–Carman relation:

$$\kappa = \frac{1}{2} \frac{\phi^3}{S^2 \tau^2} = \frac{\phi}{8\tau^2} R^2$$

This relation, which is exact for an ideal circular pipe geometry, is often presented in general terms as

$$\kappa = B \frac{\phi^3}{S^2 \tau^2}$$

where B is a geometric factor that accounts for the irregularities of pore shapes.

The exact expressions for viscous flow through pipes of elliptical, square, and triangular cross-sections allows us to derive the Kozeny–Carman relations for these shapes. Specifically, for the elliptical cross-section with semiaxes a and b ,

$$\kappa = \frac{\pi}{4} \frac{a^3 b^3}{a^2 + b^2} \frac{1}{A \tau}$$

$$\phi = \frac{\pi ab}{A} \tau$$

$$S = \frac{\pi \sqrt{2(a^2 + b^2)} l}{AL}$$

Then,

$$\kappa = \frac{1}{4} \frac{b^2}{1 + (b/a)^2} \frac{\phi}{\tau} = \frac{1}{2} \frac{\phi^3}{S^2 \tau^2}$$

which implies the universality of the latter expression for pores of elliptical cross-section.

Similarly, for a square pipe whose side is a ,

$$\kappa = 0.035144 a^2 \frac{\phi}{\tau^2} = 0.562 \frac{\phi^3}{S^2 \tau^2}$$

and for a pipe of equilateral triangular cross-section,

$$\kappa = \frac{\phi a^2}{80 \tau^2} = 0.6 \frac{\phi^3}{S^2 \tau^2}$$

Notice that the factors of similar magnitude (0.5, 0.562, and 0.6) relate permeability to $\phi^3/S^2\tau^2$ in these three pipe geometries.

A common extension of the Kozeny–Carman relation for a circular pipe is to consider a packing of identical spheres of diameter d . Although this granular pore-space geometry is not consistent with the pipe-like geometry, it is common to use the original Kozeny–Carman functional form. This allows a direct estimate of the specific surface area in terms of the porosity, $S = 6(1-\phi)/d$, which leads to the permeability expression

$$\kappa = \frac{1}{72} \frac{\phi^3}{(1-\phi)^2 \tau^2} d^2$$

or

$$\kappa = B \frac{\phi^3}{(1-\phi)^2} d^2$$

where the factor of $1/72$ and the tortuosity have been absorbed into the constant B .

Bourbié *et al.* (1987) discuss a more general form,

$$\frac{\kappa}{d^2} \propto \phi^n$$

in which n has been observed experimentally to vary with porosity from $n \geq 7$ ($\phi < 5\%$) to $n \leq 2$ ($\phi > 30\%$). The Kozeny–Carman value of $n = 3$ appears to be appropriate for very clean materials such as Fontainebleau sandstone and sintered glass, whereas $n = 4$ or 5 is probably more appropriate for more general natural materials (Bourbié *et al.*, 1987).

Mavko and Nur (1997) suggest that one explanation for the apparent dependence of the coefficient, n , on porosity is the existence of a percolation porosity, ϕ_c , below which the remaining porosity is disconnected and does not contribute to flow.

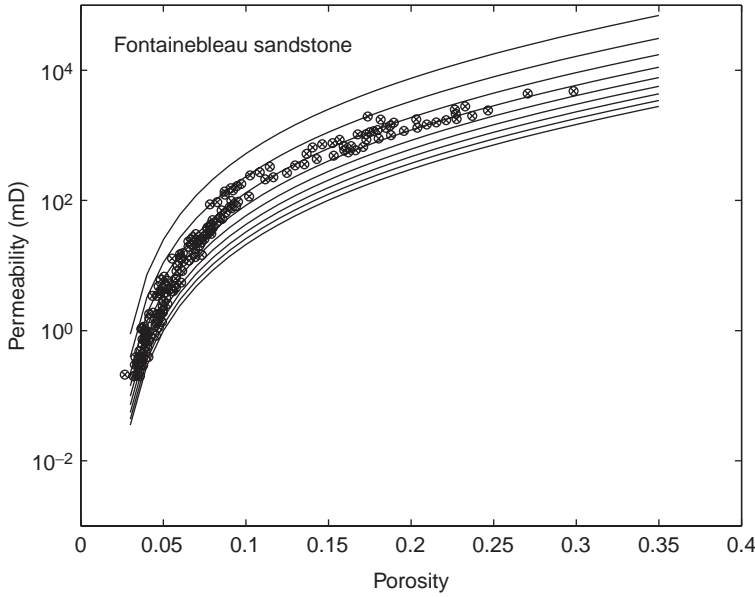


Figure 8.4.2 Permeability versus porosity for the Fontainebleau dataset with theoretical curves superimposed according to the Kozeny–Carman equation. The threshold porosity is 0.02, and the tortuosity varies from 1 (upper curve) to 5 (lower curve) with a constant increment of 0.5.

Experiments suggest that this percolation porosity is of the order of 1–3%, although it depends on the mechanism of porosity reduction. The percolation effect can be incorporated into the Kozeny–Carman relations simply by replacing ϕ by $(\phi - \phi_c)$. The idea is that it is only the porosity *in excess* of the threshold porosity that determines the permeability. Substituting this into the Kozeny–Carman equation gives

$$\frac{\kappa}{d^2} = \frac{1}{72} \frac{(\phi - \phi_c)^3}{[1 - (\phi - \phi_c)]^2 \tau^2}$$

or

$$\begin{aligned} \kappa &= B \frac{(\phi - \phi_c)^3}{(1 + \phi_c - \phi)^2} d^2 \\ &\approx B(\phi - \phi_c)^3 d^2 \end{aligned}$$

The result is that the derived $n=3$ behavior can be retained while fitting the permeability behavior over a large range in porosity.

Remember that in all of the above formulations of the Kozeny–Carman relation, the unit of permeability is length squared (e.g., m^2), where the length unit is that used for the pipe radius or particle size (e.g., m). The porosity is expressed as a unitless volume fraction, and the unit of the specific surface area is the inverse length (e.g., m^{-1}).

The same equation for permeability in milliDarcy, particle size in mm, and porosity in fraction of unity reads as

$$\frac{\kappa}{d^2} = \frac{10^9}{72} \frac{(\phi - \phi_c)^3}{[1 - (\phi - \phi_c)]^2 \tau^2}$$

Figure 8.4.2 compares laboratory permeability data of Fontainebleau sandstone with permeability calculations according to the above Kozeny–Carman equation. The threshold porosity is 0.02, and tortuosity varies from 1 (upper curve) to 5 (lower curve) with constant increment 0.5. The grain size is 0.25 mm. The apparent tortuosity values appropriate for this dataset are between 1.5 and 3.

Calculate the permeability of a sandstone sample which has porosity 0.32 and an average grain size of 100 μm . Use the Kozeny–Carman relation modified for a percolation porosity:

$$\kappa = B \frac{(\phi - \phi_c)^3}{(1 + \phi_c - \phi)^2} d^2$$

Assume that $B = 15$ and $\phi_c = 0.035$. The units of B in this equation are such that expressing d in microns gives permeability in milliDarcy. Then

$$\begin{aligned} \kappa &= B \frac{(\phi - \phi_c)^3}{(1 + \phi_c - \phi)^2} d^2 = 15 \frac{(0.32 - 0.035)^3}{(1 + 0.035 - 0.32)^2} 100^2 \\ &= 6792.3 \text{ milliDarcy} = 6.79 \text{ Darcy} \end{aligned}$$

Compare the permeabilities κ_1 and κ_2 of two sandstones that have the same porosity and pore microstructure, but different average grain sizes, $d_1 = 80 \mu\text{m}$ and $d_2 = 240 \mu\text{m}$.

Assuming that B and ϕ_c are the same for both sandstones since they have the same pore microstructure, we can express the ratio of their permeabilities as

$$\frac{\kappa_1}{\kappa_2} = \frac{d_1^2}{d_2^2} = \frac{80^2}{240^2} = \frac{1}{9}$$

The sandstone with larger average grain size has a higher permeability (by a factor of 9), even though both have the same total porosity.

Mixed particle sizes

Extensive tests (Rumpf and Gupte, 1971; Dullien, 1991) on laboratory data for granular media with mixed particle sizes (poor sorting) suggest that the Kozeny–Carman relation can still be applied using an effective or average particle size \bar{D} , defined by

$$\frac{1}{\bar{D}} = \frac{\int D^2 n(D) dD}{\int D^3 n(D) dD}$$

where $n(D)$ is the number distribution of each size particle. This can be written in terms of a discrete size distribution as follows:

$$\frac{1}{\bar{D}} = \frac{\sum_i D_i^2 n_i}{\sum_i D_i^3 n_i}$$

This can be converted to a mass distribution by noting that

$$m_i = n_i \frac{4}{3} \pi r_i^3 \rho_i = n_i \left(\frac{1}{6} \pi \rho_i \right) D_i^3$$

where m_i , r_i , and ρ_i are the mass, radius, and density of the i th particle size. Then, one can write

$$\frac{1}{\bar{D}} = \frac{\sum_i (m_i / \rho_i D_i)}{\sum_i (m_i / \rho_i)}$$

If the densities of all particles are the same, then

$$\frac{1}{\bar{D}} = \frac{\sum_i (m_i / D_i)}{\sum_i m_i} = \sum_i \frac{f_i}{D_i}$$

where f_i is either the mass fraction or the volume fraction of each particle size.

An equivalent description of the particle mixture is in terms of specific surface areas. The specific surface area (pore surface area divided by bulk sample volume) for a mixture of spherical particles is

$$\bar{S} = 3(1 - \phi) \sum_i \frac{f_i}{r_i}$$

Uses

The Kozeny–Carman relation can be used to estimate the permeability from geometric properties of a rock.

Assumptions and limitations

The following assumptions and limitations apply to the Kozeny–Carman relation:

- the derivation is heuristic. Strictly speaking, it should hold only for rocks with porosity in the form of circular pipes. Nevertheless, in practice it often gives reasonable results. When possible it should be tested and calibrated for the rocks of interest;
- the rock is isotropic; and
- fluid-bearing rock is completely saturated.

8.5 Permeability relations with S_{wi}

Synopsis

The following family of empirical equations relate permeability to porosity and irreducible water saturation (Schlumberger, 1991):

the Tixier equation

$$k = 62500 \phi^6 / S_{wi}^2$$

the Timur equation

$$k = 10000 \phi^{4.5} / S_{wi}^2 \quad \text{or} \quad k = 8581 \phi^{4.4} / S_{wi}^2$$

the Coates–Dumanoir equation

$$k = (90000 / m^4) \phi^{2m} / S_{wi}^2$$

where m is the cementation exponent (see Archie's law, Section 9.4); and the Coates equation

$$k = 4900 \phi^4 (1 - S_{wi})^2 / S_{wi}^2$$

where the permeability is in milliDarcy and porosity and irreducible water saturation are unitless volume fractions.

The irreducible water saturation is by definition the lowest water saturation that can be achieved in a core plug by displacing the water by oil or gas. The state is usually achieved by flowing oil or gas through a water-saturated sample, or by spinning the sample in a centrifuge to displace the water with oil or gas. The term is somewhat imprecise, because the irreducible water saturation is dependent on the final drive pressure (when flowing oil or gas) or the maximum speed of rotation (in a centrifuge). The related term, connate water saturation, is the lowest water saturation found *in situ*. The smaller the grain size, the larger the irreducible water saturation, because the capillary forces that retain water are stronger in thinner capillaries.

Figure 8.5.1 compares laboratory permeability data for Fontainebleau sandstone with permeability calculations according to the above equations. Fontainebleau is an extremely clean and well-sorted sandstone with large grain size (about 0.25 mm). As a result, we expect very low irreducible water saturation. This is consistent with Figure 8.5.1, where these data are matched by the curves with S_{wi} between 0.05 and 0.10.

Figure 8.5.2 compares permeability calculations according to these equations with the Kozeny–Carman formula. All equations provide essentially identical results, except for the Tixier equation, which gives smaller permeability in the low-to-medium porosity range.

Combining the Kozeny–Carman equation for permeability (κ_{KC}):

$$\frac{\kappa_{KC}}{d^2} = \frac{10^9}{72} \frac{(\phi - \phi_c)^3}{[1 - (\phi - \phi_c)]^2 \tau^2}$$

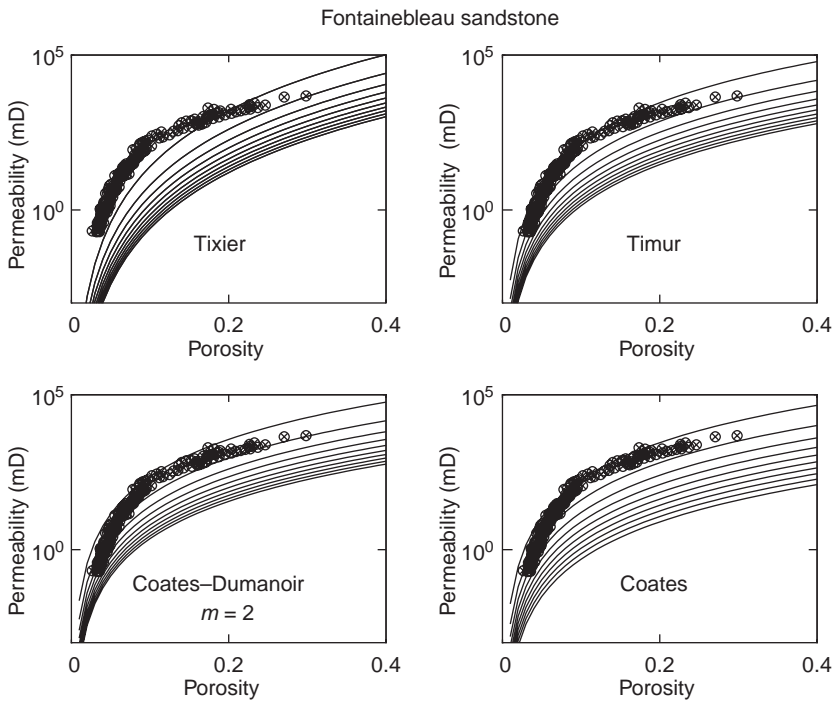


Figure 8.5.1 Permeability versus porosity for the Fontainebleau dataset, with theoretical curves superimposed according to the above equations. The irreducible water saturation varies from 0.05 for the upper curve to 0.50 for the lower curve, with a constant increment of 0.05. The cementation exponent in the Coates–Dumanoir equation is 2 in this example.

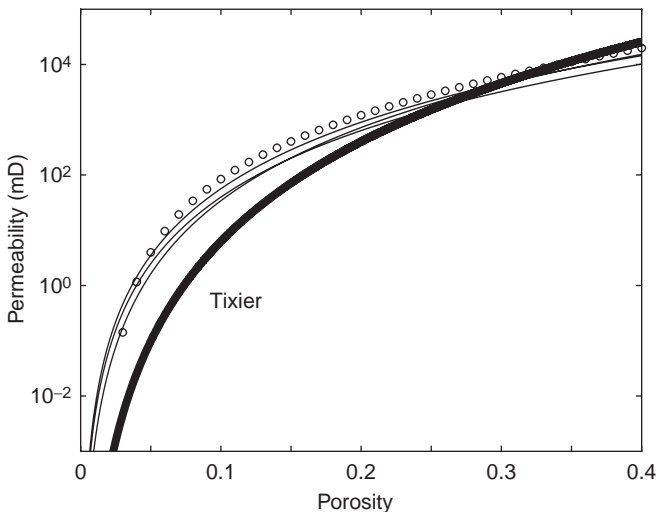


Figure 8.5.2 Permeability versus porosity according to the Tixier equation (bold curve), Timur, Coates–Dumanoir, and Coates equations (fine curves); and the Kozeny–Carman equation (open symbols). In these calculations we used a tortuosity of 2.5; an irreducible water saturation of 0.1; a threshold porosity of 0.02; and a grain size of 0.25 mm.

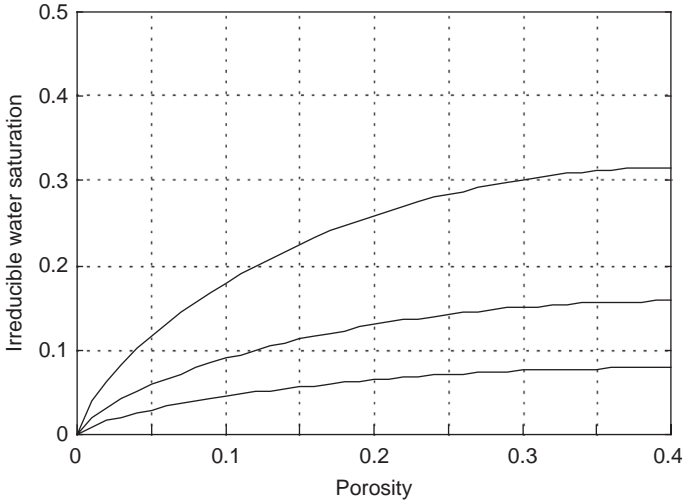


Figure 8.5.3 Irreducible water saturation versus porosity according to the last equation in the text below. The curves from top to bottom are for grain sizes of 0.05, 0.1, and 0.2 mm, respectively.

where κ_{KC} is in mD, d is in mm, and porosity (ϕ and ϕ_c) varies from 0 to 1, with the Timur equation:

$$\kappa_{TIM} = 8581 \phi^{4.4} / S_{wi}^2$$

yields the following relation between S_{wi} and d :

$$S_{wi} = \frac{0.025 \phi^{2.2} [1 - (\phi - \phi_c)] \tau}{d (\phi - \phi_c)^{1.5}}$$

where d is in mm. For $\phi_c = 0$ this equation becomes

$$S_{wi} = \frac{0.025 \phi^{0.7} (1 - \phi) \tau}{d}$$

Assume $\tau = 2$. Then the curves of S_{wi} versus ϕ according to the last equation are plotted in Figure 8.5.3.

The result shown in Figure 8.5.3 is somewhat counterintuitive: the irreducible water saturation increases with increasing porosity. This is due to the fact that in Timur's equation, and at fixed permeability, S_{wi} increases with increasing ϕ . An explanation may be that to maintain fixed permeability at increasing porosity, the pore size needs to reduce, thus resulting in increasing S_{wi} .

Caution

This S_{wi} equation is obtained by the ad hoc equating of two different permeability equations, one of which is based on a crude idealization of the pore-space geometry, while the other is purely empirical. Therefore, the resulting S_{wi} may deviate from factual experimental values.

Uses

The permeability relations with irreducible water saturation can be used to estimate the permeability from this parameter often available from laboratory experiments.

Assumptions and limitations

The following assumptions and limitations apply to the permeability relations with irreducible water saturation:

- these equations are strictly empirical, although they implicitly use the physics-based relation between the grain size and irreducible water saturation. The functional forms used in these equations have to be calibrated, whenever possible, to site-specific data;
- the rock is isotropic; and
- fluid-bearing rock is completely saturated.

8.6 Permeability of fractured formations

Synopsis

Many models for the permeability of fractured formations are based on the expression for viscous flow rate between two parallel walls:

$$Q = -\frac{h^3}{12\eta} \frac{\Delta P}{l}$$

where h is the aperture of the fracture, Q is the volume flow rate per unit length of fracture (normal to the direction of flow), η is the fluid viscosity, and ΔP is the pressure drop over length l .

For a set of parallel fractures with spacing D the fracture porosity is

$$\phi = h/D$$

A tortuosity can be defined in the similar way as in the Kozeny–Carman formalism (Figure 8.4.1) or, through the angle α of the fracture plane to the pressure gradient vector:

$$\tau = 1/\cos \alpha$$

Then, using Darcy's definition of permeability, the permeability of a formation with parallel fracture planes at angle α relative to the pressure gradient is

$$k = \frac{\phi h^2}{12\tau^2} = \frac{\phi h^2}{12} \cos^2 \alpha$$

If the matrix of the rock (the material between the fractures) has permeability k_m then the combined total permeability k_t will simply be the sum of the two, the matrix permeability and the permeability of the fractures:

$$k_t = k_m + k = k_m + \frac{\phi h^2}{12} \cos^2 \alpha$$

Since real fracture surfaces are irregular, the simple model for parallel plates must be modified (see Jaeger *et al.*, 2007, for an excellent summary). A common approach is to approximate the irregular channel with a smooth parallel channel having an effective **hydraulic aperture** h_H . It was shown (Beran, 1968) that the hydraulic aperture is bounded as

$$\langle h^{-3} \rangle^{-1} \leq h_H^3 \leq \langle h^3 \rangle$$

where the operator $\langle \cdot \rangle$ is the average over the plane of the fracture. The lower bound $\langle h^{-3} \rangle^{-1/3}$ corresponds to the case where the aperture fluctuates only in the direction of flow, while the upper bound $\langle h^3 \rangle^{1/3}$ corresponds to the case where the aperture varies only in the direction normal to flow.

Renshaw (1995) gave an expression for hydraulic aperture

$$h_H^3 = \langle h \rangle^3 \left[1 + \sigma_h^2 / \langle h \rangle^2 \right]^{-3/2}$$

where σ_h^2 is the variance of h . Other analyses have been presented by Elrod (1979), Dagan (1993), and Jaeger *et al.* (2007).

Uses

The permeability relations for a fractured formation can be used in reservoirs, such as chalks, carbonates, and shales, where fluid transport is dominated by natural or artificial fractures.

Assumptions and limitations

The following assumptions and limitations apply to the permeability relations in fractured formations:

- these equations are derived for an idealized pore geometry and thus may fail in an environment without adequate hydraulic communication between fractures and/or complex fracture geometry;
- fluid-bearing rock is completely saturated.

8.7 Diffusion and filtration: special cases

Synopsis

Nonlinear diffusion

Some rocks, such as coals, exhibit strong sensitivity of permeability (κ) and porosity (ϕ) to net pressure changes. During an injection test in a well, apparent permeability may be 10–20 times larger than that registered during a production test in the same well. In this situation, the assumption of constant permeability, which leads to the

linear diffusion equation, is not valid. The following nonlinear diffusion equation must be used (Walls *et al.*, 1991):

$$\frac{\eta\phi(\beta_{\text{fl}} + \beta_{\text{pv}})}{\kappa} \frac{\partial P}{\partial t} = \Delta P + (\beta_{\text{fl}} + \gamma)(\nabla P)^2$$

where fluid compressibility β_{fl} and pore-volume compressibility β_{pv} are defined as

$$\beta_{\text{fl}} = \frac{1}{\rho} \frac{\partial \rho}{\partial P}, \quad \beta_{\text{pv}} = \frac{1}{v_p} \frac{\partial v_p}{\partial P}$$

where v_p is the pore volume and ρ is the fluid density. The permeability–pressure parameter γ is defined as

$$\gamma = \frac{1}{\kappa} \frac{\partial \kappa}{\partial P}$$

For one-dimensional plane filtration, the diffusion equation given above is

$$\frac{\eta\phi(\beta_{\text{fl}} + \beta_{\text{pv}})}{\kappa} \frac{\partial P}{\partial t} = \frac{\partial^2 P}{\partial x^2} + (\beta_{\text{fl}} + \gamma) \left(\frac{\partial P}{\partial x} \right)^2$$

For one-dimensional radial filtration it is

$$\frac{\eta\phi(\beta_{\text{fl}} + \beta_{\text{pv}})}{\kappa} \frac{\partial P}{\partial t} = \frac{\partial^2 P}{\partial r^2} + \frac{1}{r} \frac{\partial P}{\partial r} + (\beta_{\text{fl}} + \gamma) \left(\frac{\partial P}{\partial r} \right)^2$$

Hyperbolic equation of filtration (diffusion)

The diffusion equations presented above imply that changes in pore pressure propagate through a reservoir with infinitely high velocity. This artifact results from using the original Darcy's law, which states that volumetric fluid flow rate and pressure gradient are linearly related. In fact, according to Newton's second law, pressure gradient (or acting force) should also be proportional to acceleration (time derivative of the fluid flow rate). This modified Darcy's law was first used by Biot (1956) in his theory of dynamic poroelasticity:

$$-\frac{\partial P}{\partial x} = \frac{\eta}{\kappa} V_x + \frac{\tau \rho}{\phi} \frac{\partial V_x}{\partial t}$$

where τ is tortuosity. The latter equation, if used instead of the traditional Darcy's law,

$$-\frac{\partial P}{\partial x} = \frac{\eta}{\kappa} V_x$$

yields the following hyperbolic equation that governs plane one-dimensional filtration:

$$\frac{\partial^2 P}{\partial x^2} = \tau \rho (\beta_{\text{fl}} + \beta_{\text{pv}}) \frac{\partial^2 P}{\partial t^2} + \frac{\eta\phi(\beta_{\text{fl}} + \beta_{\text{pv}})}{\kappa} \frac{\partial P}{\partial t}$$

This equation differs from the classical diffusion equation because of the inertia term,

$$\tau\rho(\beta_{\text{fl}} + \beta_{\text{pv}})\frac{\partial^2 P}{\partial t^2}$$

Changes in pore pressure propagate through a reservoir with a finite velocity, c :

$$c = \sqrt{\frac{1}{\tau\rho(\beta_{\text{fl}} + \beta_{\text{pv}})}}$$

This is the velocity of the slow Biot wave in a very rigid rock.

Uses

The equations presented in this section can be used to calculate fluid filtration and pore-pressure pulse propagation in rocks.

Assumptions and limitations

The equations presented in this section assume that the fluid is Newtonian and the flow is isothermal.

9 Electrical properties

9.1 Bounds and effective medium models

Synopsis

If we wish to predict the effective dielectric permittivity ε of a mixture of phases theoretically, we generally need to specify: (1) the volume fractions of the various phases, (2) the dielectric permittivity of the various phases, and (3) the geometric details of how the phases are arranged relative to each other. If we specify only the volume fractions and the constituent dielectric permittivities, then the best we can do is to predict the upper and lower bounds.

Bounds: The best bounds, defined as giving the narrowest possible range without specifying anything about the geometries of the constituents, are the Hashin–Shtrikman (Hashin and Shtrikman, 1962) bounds. For a two-phase composite, the Hashin–Shtrikman bounds for dielectric permittivity are given by

$$\varepsilon^{\pm} = \varepsilon_1 + \frac{f_2}{(\varepsilon_2 - \varepsilon_1)^{-1} + f_1/(3\varepsilon_1)}$$

where ε_1 and ε_2 are the dielectric permittivity of individual phases, and f_1 and f_2 are volume fractions of individual phases.

Upper and lower bounds are computed by interchanging which material is termed 1 and which is termed 2. The expressions give the upper bound when the material with higher permittivity is termed 1 and the lower bound when the lower permittivity material is termed 1.

A more general form of the bounds, which can be applied to more than two phases (Berryman, 1995), can be written as

$$\varepsilon^{\text{HS}+} = \sum(\varepsilon_{\text{max}}) \quad \varepsilon^{\text{HS}-} = \sum(\varepsilon_{\text{min}})$$

$$\sum(z) = \left\langle \frac{1}{\varepsilon(r) + 2z} \right\rangle^{-1} - 2z$$

where z is just the argument of the function $\sum(\cdot)$, and r is the spatial position. The brackets $\langle \cdot \rangle$ indicate an average over the medium, which is the same as an average over the constituents weighted by their volume fractions.

Spherical inclusions: Estimates of the effective dielectric permittivity, ε^* , of a composite may be obtained by using various approximations, both self-consistent and non-self-consistent. The Clausius–Mossotti formula for a two-component material with spherical inclusions of material 2 in a host of material 1 is given by

$$\frac{\varepsilon_{\text{CM}}^* - \varepsilon_2}{\varepsilon_{\text{CM}}^* + 2\varepsilon_2} = f_1 \frac{\varepsilon_1 - \varepsilon_2}{\varepsilon_1 + 2\varepsilon_2}$$

or equivalently

$$\varepsilon_{\text{CM}}^* = \sum (\varepsilon_2)$$

This non-self-consistent estimate, also known as the Lorentz–Lorenz or Maxwell–Garnett equation, actually coincides with the Hashin–Shtrikman bounds. The two bounds are obtained by interchanging the role of spherical inclusions and host material.

The self-consistent (SC) or **coherent potential approximation** (Bruggeman, 1935; Landauer, 1952; Berryman, 1995) for the effective dielectric permittivity $\varepsilon_{\text{SC}}^*$ of a composite made up of spherical inclusions of N phases may be written as

$$\sum_{i=1}^N f_i \frac{\varepsilon_i - \varepsilon_{\text{SC}}^*}{\varepsilon_i + 2\varepsilon_{\text{SC}}^*} = 0$$

or

$$\varepsilon_{\text{SC}}^* = \sum (\varepsilon_{\text{SC}}^*)$$

The solution, which is a fixed point of the function $\sum(\varepsilon)$, is obtained by iteration. In this approximation, all N components are treated symmetrically with no preferred host material.

In the differential effective medium (DEM) approach (Bruggeman, 1935; Sen *et al.*, 1981), infinitesimal increments of inclusions are added to the host material until the desired volume fractions are reached. For a two-component composite with material 1 as the host containing spherical inclusions of material 2, the effective dielectric permittivity $\varepsilon_{\text{DEM}}^*$ is obtained by solving the differential equation

$$(1 - y) \frac{d}{dy} [\varepsilon_{\text{DEM}}^*(y)] = \frac{\varepsilon_2 - \varepsilon_{\text{DEM}}^*(y)}{\varepsilon_2 + 2\varepsilon_{\text{DEM}}^*(y)} [3\varepsilon_{\text{DEM}}^*(y)]$$

where $y = f_2$ is the volume fraction of spherical inclusions. The analytic solution with the initial condition $\varepsilon_{\text{DEM}}^*(y = 0) = \varepsilon_1$ is (Berryman, 1995)

$$\left[\frac{\varepsilon_2 - \varepsilon_{\text{DEM}}^*(y)}{\varepsilon_2 - \varepsilon_1} \right] \left[\frac{\varepsilon_1}{\varepsilon_{\text{DEM}}^*(y)} \right]^{1/3} = 1 - y$$

The DEM results are path dependent and depend on which material is chosen as the host. The Hanai–Bruggeman approach (Bruggeman, 1935; Hanai, 1968) starts with

the rock as the host into which infinitesimal amounts of spherical inclusions of water are added. This results in a rock with zero direct current (DC) conductivity because at each stage the fluid inclusions are isolated and there is no conducting path (usually the rock mineral itself does not contribute to the DC electrical conductivity). Sen *et al.* (1981) in their self-similar model of coated spheres start with water as the initial host and incrementally add spherical inclusions of mineral material. This leads to a composite rock with a finite DC conductivity because a conducting path always exists through the fluid. Both the Hanai–Bruggeman and the Sen *et al.* formulas are obtained from the DEM result with the appropriate choice of host and inclusion.

Bounds and estimates for electrical conductivity, σ , can be obtained from the preceding equations by replacing ϵ everywhere with σ . This is because the governing relations for dielectric permittivity and electrical conductivity (and other properties such as magnetic permeability and thermal conductivity) are mathematically equivalent (Berryman, 1995). The relationship between the dielectric constant, the electrical field, \mathbf{E} , and the displacement field, \mathbf{D} , is $\mathbf{D} = \epsilon\mathbf{E}$. In the absence of charges $\nabla \cdot \mathbf{D} = 0$, and $\nabla \times \mathbf{E} = 0$ because the electric field is the gradient of a potential. Similarly, for:

- *electrical conductivity, σ , $\mathbf{J} = \sigma \mathbf{E}$ from Ohm's law, where \mathbf{J} is the current density, $\nabla \cdot \mathbf{J} = 0$ in the absence of current source and sinks, and $\nabla \times \mathbf{E} = 0$;*
- *magnetic permeability, μ , $\mathbf{B} = \mu\mathbf{H}$, where \mathbf{B} is the magnetic induction, \mathbf{H} is the magnetic field, $\nabla \cdot \mathbf{B} = 0$, and in the absence of currents $\nabla \times \mathbf{H} = 0$; and*
- *thermal conductivity, κ , $\mathbf{q} = -\kappa\nabla\theta$ from Fourier's law for heat flux \mathbf{q} and temperature θ , $\nabla \cdot \mathbf{q} = 0$ when heat is conserved, and $\nabla \times \nabla\theta = 0$.*

Ellipsoidal inclusions: Estimates for the effective dielectric permittivity of composites with nonspherical, ellipsoidal inclusions require the use of depolarizing factors L_a, L_b, L_c along the principal directions a, b, c of the ellipsoid. The generalization of the Clausius–Mossotti relation for randomly arranged ellipsoidal inclusions in an isotropic composite is (Berryman, 1995)

$$\frac{\epsilon_{\text{CM}}^* - \epsilon_m}{\epsilon_{\text{CM}}^* + 2\epsilon_m} = \sum_{i=1}^N f_i(\epsilon_i - \epsilon_m) R^{mi}$$

and the self-consistent estimate for ellipsoidal inclusions in an isotropic composite is (Berryman, 1995)

$$\sum_{i=1}^N f_i(\epsilon_i - \epsilon_{\text{SC}}^*) R^{*i} = 0$$

where R is a function of the depolarizing factors L_a, L_b, L_c :

$$R^{mi} = \frac{1}{9} \sum_{j=a,b,c} \frac{1}{L_j \epsilon_i + (1 - L_j) \epsilon_m}$$

The superscripts m and i refer to the host matrix phase and the inclusion phase. In the self-consistent formula, the superscript $*$ on R indicates that ϵ_m should be replaced by ϵ_{SC}^* in the expression for R . Depolarizing factors and the coefficient R for some

Table 9.1.1 Coefficient R and depolarizing factors L_j for some specific shapes. The subscripts m and i refer to the background and inclusion materials (from Berryman, 1995).

Inclusion shape	L_a, L_b, L_c	R^{mi}
Spheres	$\frac{1}{3}, \frac{1}{3}, \frac{1}{3}$	$\frac{1}{\epsilon_i + 2\epsilon_m}$
Needles	$0, \frac{1}{2}, \frac{1}{2}$	$\frac{1}{9} \left(\frac{1}{\epsilon_m} + \frac{4}{\epsilon_i + \epsilon_m} \right)$
Disks	$1, 0, 0$	$\frac{1}{9} \left(\frac{1}{\epsilon_i} + \frac{2}{\epsilon_m} \right)$

specific shapes are given in the Table 9.1.1. Depolarizing factors for more general ellipsoidal shapes are tabulated by Osborn (1945) and Stoner (1945).

Ellipsoidal inclusion models have been used to model the effects of pore-scale fluid distributions on the effective dielectric properties of partially saturated rocks theoretically (Knight and Nur, 1987; Endres and Knight, 1992).

Layered media: Exact results for the long-wavelength effective dielectric permittivity of a layered medium (layer thicknesses much smaller than the wavelength) are given by (Sen *et al.*, 1981)

$$\epsilon_{\parallel}^* = \langle \epsilon_i \rangle$$

and

$$\frac{1}{\epsilon_{\perp}^*} = \left\langle \frac{1}{\epsilon_i} \right\rangle$$

for fields parallel to the layer interfaces and perpendicular to the interfaces, respectively, where ϵ_i is the dielectric permittivity of each constituent layer. The direction of wave propagation is perpendicular to the field direction.

Uses

- The equations presented in this section can be used for the following purposes:
- to estimate the range of the average mineral dielectric constant for a mixture of mineral grains;
 - to compute the upper and lower bounds for a mixture of mineral and pore fluid.

Assumptions and limitations

- The following assumption and limitation apply to the equations in this section:
- most inclusion models assume the rock is isotropic;
 - effective medium theories are valid when wavelengths are much longer than the scale of the heterogeneities.

9.2 Velocity dispersion and attenuation

Synopsis

The complex wavenumber associated with propagation of electromagnetic waves of angular frequency ω is given by $k = \omega\sqrt{\varepsilon\mu}$, where both ε , the dielectric permittivity, and μ , the magnetic permeability, are in general frequency-dependent, complex quantities denoted by

$$\varepsilon = \varepsilon' - i\left(\frac{\sigma}{\omega} + \varepsilon''\right)$$

$$\mu = \mu' - i\mu''$$

where σ is the electrical conductivity. For most nonmagnetic earth materials, the magnetic permeability equals μ_0 , the magnetic permeability of free space. The dielectric permittivity normalized by ε_0 , the dielectric permittivity of free space, is often termed the relative dielectric permittivity or **dielectric constant** κ , which is a dimensionless measure of the dielectric behavior. The dielectric susceptibility $\chi = \kappa - 1$.

The real part, k_R , of the complex wavenumber describes the propagation of an electromagnetic wavefield, whereas the imaginary part, k_I , governs the decay in field amplitude with propagation distance. A plane wave of amplitude E_0 propagating along the z direction and polarized along the x direction may be described by

$$E_x = E_0 e^{i(\omega t - kz)} = E_0 e^{-k_I z} e^{i(\omega t - k_R z)}$$

The **skin depth**, the distance over which the field amplitude falls to $1/e$ of its initial value, is equal to $1/k_I$. The dissipation may also be characterized by the loss tangent, the ratio of the imaginary part of the dielectric permittivity to the real part:

$$\tan \delta = \frac{\sigma}{\omega \varepsilon'} + \frac{\varepsilon''}{\varepsilon'}$$

Relations between the various parameters may be easily derived (e.g., Guéguen and Palciauskas, 1994). With $\mu = \mu_0$:

$$k_R = \omega \sqrt{\mu_0 \varepsilon'} \sqrt{\frac{1 + \cos \delta}{2 \cos \delta}}$$

$$k_I = \omega \sqrt{\mu_0 \varepsilon'} \sqrt{\frac{1 - \cos \delta}{2 \cos \delta}}$$

$$\varepsilon' = \frac{k_R^2 - k_I^2}{\mu_0 \omega^2}, \quad \frac{\sigma}{\omega} + \varepsilon'' = \frac{2k_R k_I}{\mu_0 \omega^2}$$

$$\tan \delta = \frac{2k_R k_I}{k_R^2 - k_I^2}$$

$$V = \frac{\omega}{k_R} = \frac{1}{\sqrt{\mu_0 \varepsilon'}} \sqrt{\frac{2 \cos \delta}{1 + \cos \delta}}$$

where V is the phase velocity. When there is no attenuation $\delta = 0$ and

$$V = \frac{1}{\sqrt{\mu_0 \varepsilon'}} = \frac{c}{\sqrt{\kappa'}}$$

where $c = 1/\sqrt{\mu_0 \varepsilon_0}$ is the speed of light in a vacuum and κ' is the real part of the dielectric constant.

In the high-frequency *propagation* regime ($\omega \gg \sigma/\varepsilon'$), displacement currents dominate, whereas conduction currents are negligible. Electromagnetic waves propagate with little attenuation and dispersion. In this high-frequency limit the wave-number is

$$k_{\text{hif}} = \omega \sqrt{\mu_0 \varepsilon'} \sqrt{1 - i \frac{\varepsilon''}{\varepsilon'}}$$

In the low-frequency *diffusion* regime ($\omega \ll \sigma/\varepsilon'$), conduction currents dominate, and an electromagnetic pulse tends to spread out with a \sqrt{t} time dependence characteristic of diffusive processes. The wavenumber in this low-frequency limit is

$$k_{\text{lowf}} = (1 - i) \sqrt{\frac{\omega \sigma \mu_0}{2}}$$

For typical crustal rocks the diffusion region falls below about 100 kHz.

The Debye (1945) and the Cole–Cole (1941) models are two common phenomenological models that describe the frequency dependence of the complex dielectric constant. In the **Debye** model, which is identical to the standard linear solid model for viscoelasticity (see Section 3.8), the dielectric constant as a function of frequency is given by

$$\kappa(\omega) = \kappa' - i\kappa'' = \kappa_\infty + \frac{\kappa_0 - \kappa_\infty}{1 + i\omega\tau}$$

$$\kappa' = \kappa_\infty + \frac{\kappa_0 - \kappa_\infty}{1 + (\omega\tau)^2}$$

$$\kappa'' = (\kappa_0 - \kappa_\infty) \frac{\omega\tau}{1 + (\omega\tau)^2}$$

where τ is the characteristic relaxation time, κ_0 is the low-frequency limit, and κ_∞ is the high-frequency limit.

The **Cole–Cole** model is given by

$$\kappa(\omega) = \kappa_\infty + \frac{\kappa_0 - \kappa_\infty}{1 + (i\omega\tau)^{1-\alpha}}, \quad 0 \leq \alpha \leq 1$$

When the parameter α equals 0, the Cole–Cole model reduces to the Debye model. Sherman (1988) described the frequency-dependent dielectric constant of brine-saturated rocks as a sum of two Debye models – one for interfacial polarization (below 1 GHz) and another for dipole polarization in brine (above 1 GHz).

The amplitude reflection and transmission coefficients for uniform, linearly polarized, homogeneous plane waves are given by **Fresnel's equations** (e.g., Jackson, 1975). For a plane wave incident from medium 1 onto an interface between two isotropic, homogeneous half-spaces, medium 1 and 2, the equations are as follows.

- Electric field transverse to the plane of incidence (TE mode):

$$\frac{E_r^\perp}{E_i^\perp} = \frac{\sqrt{\mu_1 \varepsilon_1} \cos \theta_i - (\mu_1 / \mu_2) \sqrt{\mu_2 \varepsilon_2 - \mu_1 \varepsilon_1 \sin^2 \theta_i}}{\sqrt{\mu_1 \varepsilon_1} \cos \theta_i + (\mu_1 / \mu_2) \sqrt{\mu_2 \varepsilon_2 - \mu_1 \varepsilon_1 \sin^2 \theta_i}}$$

$$\frac{E_t^\perp}{E_i^\perp} = \frac{2\sqrt{\mu_1 \varepsilon_1} \cos \theta_i}{\sqrt{\mu_1 \varepsilon_1} \cos \theta_i + (\mu_1 / \mu_2) \sqrt{\mu_2 \varepsilon_2 - \mu_1 \varepsilon_1 \sin^2 \theta_i}}$$

- Electric field in the plane of incidence (TM mode):

$$\frac{E_r^\parallel}{E_i^\parallel} = \frac{\sqrt{\mu_1 \varepsilon_1} \sqrt{\mu_2 \varepsilon_2 - \mu_1 \varepsilon_1 \sin^2 \theta_i} - \mu_1 \varepsilon_2 \cos \theta_i}{\sqrt{\mu_1 \varepsilon_1} \sqrt{\mu_2 \varepsilon_2 - \mu_1 \varepsilon_1 \sin^2 \theta_i} + \mu_1 \varepsilon_2 \cos \theta_i}$$

$$\frac{E_t^\parallel}{E_i^\parallel} = \frac{2\sqrt{\mu_1 \varepsilon_1 \mu_2 \varepsilon_2} \cos \theta_i}{\sqrt{\mu_1 \varepsilon_1} \sqrt{\mu_2 \varepsilon_2 - \mu_1 \varepsilon_1 \sin^2 \theta_i} + \mu_1 \varepsilon_2 \cos \theta_i}$$

where θ_i is the angle of incidence; E_i^\perp , E_r^\perp , E_t^\perp are the incident, reflected, and transmitted transverse electric field amplitudes, respectively; E_i^\parallel , E_r^\parallel , E_t^\parallel are the incident, reflected, and transmitted parallel electric field amplitudes, respectively; μ_1 , μ_2 are the magnetic permeability of medium 1 and 2; and ε_1 , ε_2 are the dielectric permittivity of medium 1 and 2.

The positive direction of polarization is taken to be the same for incident, reflected, and transmitted electric fields. In terms of the electromagnetic plane-wave impedance $Z = \sqrt{\mu/\varepsilon} = \omega\mu/k$, the amplitude reflection coefficients may be expressed as

$$R_{TE}^\perp = \frac{E_r^\perp}{E_i^\perp} = \frac{Z_2 \cos \theta_i - Z_1 \sqrt{1 - (Z_1 \varepsilon_1 / Z_2 \varepsilon_2)^2 \sin^2 \theta_i}}{Z_2 \cos \theta_i + Z_1 \sqrt{1 - (Z_1 \varepsilon_1 / Z_2 \varepsilon_2)^2 \sin^2 \theta_i}}$$

$$R_{TM}^\parallel = \frac{E_r^\parallel}{E_i^\parallel} = \frac{Z_2 \sqrt{1 - (Z_1 \varepsilon_1 / Z_2 \varepsilon_2)^2 \sin^2 \theta_i} - Z_1 \cos \theta_i}{Z_2 \sqrt{1 - (Z_1 \varepsilon_1 / Z_2 \varepsilon_2)^2 \sin^2 \theta_i} + Z_1 \cos \theta_i}$$

For normal incidence, the incident plane is no longer uniquely defined, and the difference between transverse and parallel modes disappears. The reflection coefficient is then

$$R_{TE}^\perp = \frac{Z_2 - Z_1}{Z_2 + Z_1} = R_{TM}^\parallel$$

Electromagnetic wave propagation in layered media can be calculated using propagator matrices (Ward and Hohmann, 1987). The electric and magnetic fields at the top and bottom of the stack of layers are related by a product of propagator matrices, one for each layer. The calculations are done in the frequency domain and include the effects of all multiples. For waves traveling perpendicularly to the layers with layer impedances and thicknesses Z_j and d_j , respectively,

$$\begin{bmatrix} E_y \\ H_x \end{bmatrix}_{j-1} = \mathbf{A}_j \begin{bmatrix} E_y \\ H_x \end{bmatrix}_j$$

Each layer matrix \mathbf{A}_j has the form

$$\mathbf{A}_j = \begin{bmatrix} \cosh(ik_j d_j) & -Z_j \sinh(ik_j d_j) \\ -\frac{1}{Z_j} \sinh(ik_j d_j) & \cosh(ik_j d_j) \end{bmatrix}$$

Uses

The results described in this section can be used for computing electromagnetic wave propagation, velocity dispersion, and attenuation.

Assumptions and limitations

The results described in this section are based on the following assumptions:

- isotropic homogeneous media, except for layered media;
- plane-wave propagation.

9.3 Empirical relations

Synopsis

The **Lichtnecker–Rother** empirical formula for the effective dielectric constant κ^* of a mixture of N constituents is given by a simple volumetric power-law average of the dielectric constants of the constituents (Sherman, 1986; Guéguen and Palciauskas, 1994):

$$\kappa^* = \left[\sum_{i=1}^N f_i (\kappa_i)^\gamma \right]^{1/\gamma}, \quad -1 \leq \gamma \leq 1$$

where κ_i is the dielectric constant of individual phases and f_i are the volume fractions of individual phases.

For $\gamma = \frac{1}{2}$ this is equivalent to the complex refractive index method (CRIM) formula:

$$\sqrt{\kappa^*} = \sum_{i=1}^N f_i \sqrt{\kappa_i}$$

The CRIM equation (Meador and Cox, 1975; Endres and Knight, 1992) is analogous to the time-average equation of Wyllie (see Section 7.3) because the velocity of electromagnetic wave propagation is inversely proportional to $\sqrt{\kappa}$. The CRIM empirical relation has been found to give reasonable results at high frequencies (above ~ 0.5 GHz). The **Odelevskii** formula for two phases is (Shen, 1985)

$$\varepsilon^* = B + \left(B^2 + \frac{1}{2}\varepsilon_1\varepsilon_2\right)^{1/2}$$

$$B = \frac{1}{4}[(3f_1 - 1)\varepsilon_1 + (3f_2 - 1)\varepsilon_2]$$

Typically, only the real part of the dielectric permittivity is used in this empirical formula.

Topp's relation (Topp *et al.*, 1980), based on measurements on a variety of soil samples at frequencies of 20 MHz to 1 GHz, is used widely in interpretation of time domain reflectometry (TDR) measurements for volumetric soil water content. The empirical relations are

$$\theta_v = -5.3 \times 10^{-2} + 2.92 \times 10^{-2}\kappa_a - 5.5 \times 10^{-4}\kappa_a^2 + 4.3 \times 10^{-6}\kappa_a^3$$

$$\kappa_a = 3.03 + 9.3\theta_v + 146.0\theta_v^2 - 76.7\theta_v^3$$

where κ_a is the apparent dielectric constant as measured by pulse transmission (such as in TDR or coaxial transmission lines) with dielectric losses excluded, and θ_v is the volumetric soil water content, the ratio of volume of water to the total volume of the sample. The estimation error for the data of Topp *et al.* (1980) was about 1.3%. The relations do not violate the Hashin–Shtrikman bounds for most materials. They do not give good estimates for soils with high clay content or organic matter and should be recalibrated for such material. Brisco *et al.* (1992) published empirical relations between volumetric soil water content and the real part of the dielectric constant measured by portable dielectric probes (PDP) utilizing frequencies from 0.45 to 9.3 GHz. The PDP measure both the real and imaginary components of the dielectric constant. In general TDR can sample soil layers 0–5 cm or deeper, whereas the PDP sample layers of about 1 cm thickness. Empirical relations in different frequency bands from Brisco *et al.* are summarized in Table 9.3.1.

Olhoeft (1979) obtained the following empirical relation between the measured effective dielectric constant and density for dry rocks:

$$\kappa' = \left(\kappa_0'^{1/\rho_0}\right)^\rho = 1.91^\rho$$

where κ_0' , ρ_0 are the mineral dielectric constant and the mineral density (g/cm^3), and κ' , ρ are the dry-rock dielectric constant and dry bulk density (g/cm^3).

The coefficient 1.91 was obtained from a best fit to data on a variety of terrestrial and lunar rock samples. The relation becomes poor for rocks with water-containing clays and conducting minerals such as sulfides and magnetite.

Table 9.3.1 Regression coefficients and coefficient of determination R^2 for empirical relations between volumetric water content and dielectric constant (real part) at different portable dielectric probe frequencies (Brisco et al., 1992).

$\theta_v = a + b\kappa' + c\kappa'^2 + d\kappa'^3$					
Frequency (GHz)	a	b	c	d	R^2
9.3 (X-band)	-3.58×10^{-2}	4.23×10^{-2}	-0.153×10^{-4}	17.7×10^{-6}	0.86
5.3 (C-band)	-1.01×10^{-2}	2.62×10^{-2}	-4.71×10^{-4}	4.12×10^{-6}	0.91
1.25 (L-band)	-2.78×10^{-2}	2.80×10^{-2}	-5.86×10^{-4}	5.03×10^{-6}	0.95
0.45 (P-band)	-1.88×10^{-2}	2.46×10^{-2}	-4.34×10^{-4}	3.61×10^{-6}	0.95

Knight and Nur (1987) measured the complex dielectric constant of eight different sandstones at different saturations and frequencies. They obtained a power-law dependence of κ' (the real part of the complex dielectric constant) on frequency ω expressed by

$$\kappa' = A\omega^{-\alpha}$$

where A and α are empirical parameters determined by fitting to the data and depend on saturation and rock type. For the different samples measured by Knight and Nur, α ranged from 0.08 to 0.266 at a saturation of 0.36 by deionized water. At the same saturation $\log A$ ranged from about 1.1 to 1.8.

Mazáč *et al.* (1990) correlated aquifer hydraulic conductivity K determined from pumping tests with electrical resistivities ρ interpreted from vertical electrical sounding. Their relation is

$$K(10^{-5} \text{ m/s}) = \frac{\rho^{1.195}(\text{ohm m})}{97.5}$$

The correlation coefficient was 0.871.

Koesoemadinata and McMechan (2003) have given empirical relations between the dielectric constant (κ), and porosity (ϕ), clay content (C), density (ρ), and permeability (k). The regressions are based on data from about 30 samples of Ferron sandstone, a fine- to medium-grained sandstone with porosity ranging from 10% to 24% and clay content ranging from 10% to 22%. The κ data were measured on dry (<1% water saturation by volume) samples at 50 MHz.

$$\kappa = -2.90299 \ln \phi + 12.8161 \qquad R^2 = 0.66$$

$$\kappa = -0.35978 \ln k + 5.35307 \qquad R^2 = 0.78$$

$$\kappa = -0.2572 \ln k - 0.07298 \phi + 6.41999 \qquad R^2 = 0.82$$

$$\kappa = 7.1806\rho - 11.0397 \qquad R^2 = 0.65$$

$$\kappa = 6.6611\rho + 0.0818C - 11.1742 \qquad R^2 = 0.79$$

In the above empirical regressions, permeability is in mD, density is in g/cm^3 , and porosity and clay content are given as a percentage, while κ is dimensionless.

Uses

The equations presented in this section can be used to relate rock and soil properties such as porosity, saturation, soil moisture content, and hydraulic conductivity to electrical measurements.

Assumptions and limitations

The relations are empirical and therefore strictly valid only for the data set from which they were derived. The relations may need to be recalibrated to specific locations or rock and soil types.

9.4 Electrical conductivity in porous rocks

Synopsis

Most crustal rocks are made up of minerals that are semiconductors or insulators (silicates and oxides). Conducting currents in fluid-saturated rocks caused by an applied DC voltage arise primarily from the flow of ions within the pore fluids. The ratio of the conductivity of the pore fluid to the bulk conductivity of the fully saturated rock is known as the **formation factor**, F (Archie, 1942):

$$F = \frac{\sigma_w}{\sigma} = \frac{R_0}{R_w}$$

where σ_w , R_w are the conductivity and the resistivity of the pore fluid, and σ , R_0 are the conductivity and the resistivity of rock fully saturated with formation water.

The Hashin–Shtrikman lower bound on F for a rock with porosity ϕ is (Berryman, 1995)

$$F^{\text{HS-}} = 1 + \frac{3}{2} \frac{1 - \phi}{\phi}$$

The differential effective medium (DEM) theory of Sen *et al.* (1981) predicts (as $\omega \rightarrow 0$ where ω is the frequency)

$$\sigma = \sigma_w \phi^{3/2}$$

or

$$F_{\text{DEM}} = \phi^{-3/2}$$

In this version of the DEM model, spheres of nonconducting mineral grains are embedded in the conducting fluid host so that a conducting path always exists

through the fluid for all porosities (see Section 9.1). The exponent depends on the shape of the inclusions and is greater than 1.5 for plate- or needle-like inclusions.

Archie's law (1942), which forms the basis for resistivity log interpretation, is an empirical relation relating the formation factor to the porosity in *brine-saturated clean* (no shale) reservoir rocks:

$$F = \phi^{-m}$$

The exponent m (sometimes termed the cementation exponent) varies between approximately 1.3 and 2.5 for most sedimentary rocks and is close to 2 for sandstones. For natural and artificial unconsolidated sands and glass beads, m is close to 1.3 for spherical grains and increases to 1.9 for thin disk-like grains (Wyllie and Gregory, 1953; Jackson *et al.*, 1978). Carbonates show a much wider range of variation and have m values as high as 5 (Focke and Munn, 1987). The minimum value of m is 1 when porosity is 100% and the rock is fully saturated with brine. This corresponds to an open fracture.

Archie's law is sometimes written as

$$F = (\phi - \phi_0)^{-m}$$

or

$$F = a\phi^{-m}$$

where ϕ_0 is a percolation porosity below which there are no conducting pathways and the rock conductivity is zero and a is an empirical constant close to 1. A value different from 1 (usually greater than 1) results from trying to fit an Archie-like model to rocks that do not follow Archie behavior. Clean, well-sorted sands with electrical conduction occurring only by diffusion of ions in the pore fluid are best described by Archie's law. Shaley sands, rocks with moldic secondary porosity, and rocks with isolated microporous grains are examples of non-Archie rocks (Herrick, 1988).

Archie's second law for saturation relates the DC resistivity, R_t , of a partially saturated rock to the brine saturation, S_w , and the porosity by

$$S_w^{-n} = \frac{R_t}{R_0} = \phi^m \frac{R_t}{R_w}$$

where R_0 is the DC resistivity of the same rock at $S_w = 1$, and the saturation exponent, n , derived empirically, is around 2. The value of n depends on the type of the pore fluid and is different for gas-brine saturation versus oil-brine saturation. Experimentally, saturation exponents for oil-wet porous media have been found to be substantially higher ($n \approx 2.5$ – 9.5) than for water-wet media (Sharma *et al.*, 1991). In terms of conductivity Archie's second law may be expressed as

$$\sigma_t = (S_w^n \phi^m) \sigma_w$$

where $\sigma_t = 1/R_t$ is the conductivity of the partially saturated rock. Archie's empirical relations have been found to be applicable to a remarkably wide range of rocks (Ransom, 1984).

Shaley sands: Electrical conductivity in shaley sands is complicated by the presence of clays. Excess ions in a diffuse double layer around clay particles provide current conduction pathways along the clay surface in addition to the current flow by ions diffusing through the bulk pore fluid. The conductivity of this surface layer depends on the brine conductivity, and hence the overall bulk conductivity of the saturated rock is a nonlinear function of the brine conductivity. A wide variety of formulations have been used to model conductivity in shaley sands, and Worthington (1985) describes over 30 shaley sand models used in well log interpretation. Almost all of the models try to modify Archie's relation and account for the excess conductivity by introducing a shale conductivity term X :

$$\sigma = \frac{1}{F} \sigma_w, \quad \text{clean sands, Archie}$$

$$\sigma = \frac{1}{F} \sigma_w + X, \quad \text{shaley sands}$$

The various models differ in their choice of X . Some of the earlier models described X in terms of the volume of shale V_{sh} , as determined from logs:

$$\sigma = \frac{1}{F} \sigma_w + V_{sh} \sigma_{sh}, \quad \text{Simandoux (1963)}$$

$$\sqrt{\sigma} = \sqrt{\frac{1}{F} \sigma_w + V_{sh}^\alpha \sqrt{\sigma_{sh}}}, \quad \alpha = 1 - \frac{V_{sh}}{2}, \quad \text{Poupon and Leveaux (1971)}$$

"Indonesia formula"

where σ_{sh} is the conductivity of fully brine-saturated shale. Although these equations are applicable to log interpretation and may be used without calibration with core data, they do not have much physical basis and do not allow a complete representation of conductivity behavior for all ranges of σ_w . More recent models attempt to capture the physics of the diffuse ion double layer surrounding clay particles. Of these, the Waxman–Smits model (Waxman and Smits, 1968) and its various modifications such as the dual-water model (Clavier *et al.*, 1984) and the Waxman–Smits–Juhász model (Juhász, 1981) are the most widely accepted. The Waxman–Smits formula is

$$\sigma = \frac{1}{F} (\sigma_w + B Q_v)$$

$$B = 4.6(1 - 0.6e^{-\sigma_w/1.3})$$

$$Q_v = \frac{\text{CEC}(1 - \phi)\rho_0}{\phi}$$

where CEC is the cation exchange capacity and ρ_0 is the mineral grain density.

Note that here and in the following we use shaley sand equations $F = a\phi^{-m}$ and not σ_w/σ . The cation exchange capacity is a measure of the excess charges and Q_v is the charge per unit pore volume. Clays often have an excess negative electrical charge within the sheet-like particles. This is compensated by positive counterions clinging to the outside surface of the dry clay sheets. The resulting positive surface charge is a property of the dry clay mineral and is called the cation exchange capacity (Clavier *et al.*, 1984). In the presence of an electrolytic solution such as brine, the electrical forces holding the positive counterions at the clay surface are reduced. The counterions can move along the surface contributing to the electrical conductivity. The average mobility of the ions is described by B . The parameter B is a source of uncertainty, and several expressions for it have been developed since the original paper. Juhász (1981) gives the following expressions for B :

$$B = \frac{-5.41 + 0.133T - 1.253 \times 10^{-4}T^{-2}}{1 + R_w^{1.23}(0.025T - 1.07)}$$

where T is the temperature in degrees Fahrenheit or

$$B = \frac{-1.28 + 0.225T - 4.059 \times 10^{-4}T^{-2}}{1 + R_w^{1.23}(0.045T - 0.27)}$$

for temperature in degrees Celsius. Application of the Waxman–Smits equation requires calibration with core CEC measurements, which are not always available.

The normalized Waxman–Smits or Waxman–Smits–Juhász model (Juhász, 1981) does not require CEC data because it uses V_{sh} derived from logs to estimate Q_v by normalizing it to the shale response. In this model

$$BQ_v = Q_{vn}(\sigma_{wsh} - \sigma_w)$$

$$Q_{vn} = \frac{Q_v}{Q_{vsh}} = \frac{V_{sh}\phi_{sh}}{\phi}$$

where ϕ is the total porosity (density porosity), ϕ_{sh} is the total shale porosity, and σ_{wsh} is the shale water conductivity obtained from $\sigma_{wsh} = F\sigma_{sh}$, where σ_{sh} is the conductivity of 100% brine-saturated shale. The normalized Q_v ranges from 0 in clean sands to 1 in shales. Brine saturation S_w can be obtained from these models by solving (Bilodeaux, 1997)

$$S_w = \left[\frac{FR_w}{R_t(1 + R_wBQ_v/S_w)} \right]^{1/n}$$

For $n = 2$ the explicit solution (ignoring the negative root) is

$$S_w = \sqrt{\frac{FR_w}{R_t} + \left(\frac{BQ_v R_w}{2}\right)^2} - \frac{BQ_v R_w}{2}$$

The dual-water model divides the total water content into the bound clay water, for which the conductivity depends only on the clay counterions, and the far water, away from the clay, for which the conductivity corresponds to the ions in the bulk formation water (Clavier *et al.*, 1984). The bound water reduces the water conductivity σ_w by a factor of $(1 - \alpha v_Q Q_v)$. The dual-water model formula is (Clavier *et al.*, 1984; Sen and Goode, 1988)

$$\sigma = \phi^m [\sigma_w (1 - \alpha v_Q Q_v) + \beta Q_v]$$

where v_Q is the amount of clay water associated with 1 milliequivalent of clay counterions, β is the counterion mobility in the clay double layer, and α is the ratio of the diffuse double-layer thickness to the bound water layer thickness. At high salinities (salt concentration exceeding 0.35 mol/ml) $\alpha = 1$. At low salinities it is a function of σ_w , and is given by

$$\alpha = \sqrt{\frac{\gamma_1 \langle n_1 \rangle}{\gamma \langle n \rangle}}$$

where $\langle n \rangle$ is the salt concentration in bulk water at 25 °C in mol/ml, γ is the NaCl activity coefficient at that concentration, $\langle n_1 \rangle = 0.35$ mol/ml, and $\gamma_1 = 0.71$, i.e., the corresponding NaCl activity coefficient.

Although v_Q and β have a temperature and salinity dependence, Clavier *et al.* (1984) recommend the following values for v_Q and β :

$$v_Q = 0.28 \text{ ml/meq}$$

$$\beta = 2.05 \text{ (S/m)/(meq/cm}^3\text{)}$$

These values are based on analysis of CEC data for clays and conductivity data on core samples. At low salinities, v_Q varies with \sqrt{T} and increases by about 26% from 25 to 200 °C.

Generalizing from theoretical solutions for electrolytic conduction past charged spheres in the presence of double layers, Sen and Goode (1988) proposed the following shaley-sand equation:

$$\sigma = \frac{1}{F} \left(\sigma_w + \frac{AQ_v}{1 + CQ_v/\sigma_w} \right) + EQ_v$$

The constants A and C depend on pore geometry and ion mobility, and the term EQ_v accounts for conductivity by surface counterions even when water conductivity is zero. Sen and Goode were able to express the relation in terms of Archie's exponent m by fitting to core data (about 140 cores)

$$\sigma = \phi^m \left(\sigma_w + \frac{m1.93Q_v}{1 + 0.7/\sigma_w} \right) + 1.3\phi^m Q_v$$

where conductivities are in mho/m and Q_v is in meq/ml.

In the limit of no clay ($Q_v = 0$) or no counterion mobility ($A = C = 0$) the expression reduces to Archie's equation. In the limits of high and low brine conductivity, with nonzero Q_v , the expression becomes

$$\sigma = \frac{1}{F} (\sigma_w + AQ_v) + EQ_v, \quad \text{high-}\sigma_w \text{ limit}$$

$$\sigma = \frac{1}{F} \left(1 + \frac{A}{C} \right) \sigma_w + EQ_v, \quad \text{low-}\sigma_w \text{ limit}$$

At low σ_w the σ versus σ_w curve has a higher slope than at the high- σ_w limit. At high σ_w the electric current is more concentrated in the pore-space bulk fluid than in the clay double layer, whereas for low σ_w the currents are mostly concentrated within the double layer. This gives rise to the curvature in the σ versus σ_w behavior.

Uses

The equations presented in this section can be used to interpret resistivity logs.

Assumptions and limitations

Models for log interpretation involve much empiricism, and empirical relations should be calibrated to specific locations and formations.

9.5 Cross-property bounds and relations between elastic and electrical parameters

Faust (1953) presents an empirical relation between the measured resistivity R_0 of a water-saturated formation and V_P :

$$V_P = 2.2888 \left(Z \frac{R_0}{R_w} \right)^{1/6}$$

where R_w is the resistivity of formation water, Z is depth in km, and V_P is in km/s.

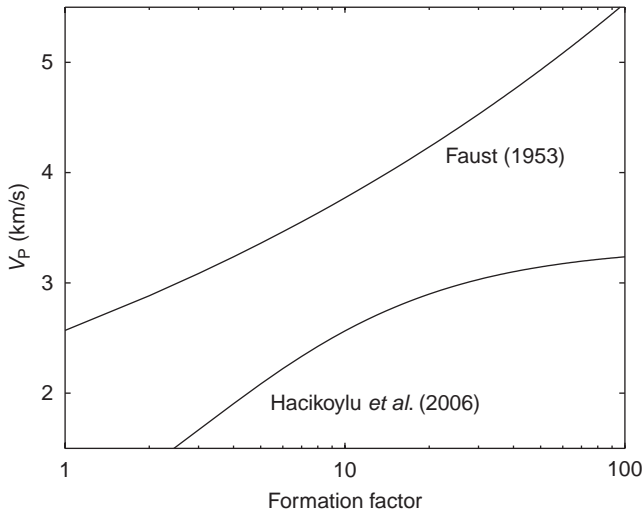


Figure 9.5.1 P-wave velocity versus formation factor according to the Faust (1953) and Hacikoylu *et al.* (2006) equations.

Faust's original form of the empirical relation is

$$V(\text{ft/s}) = \gamma(Z[R_t])^{1/6}$$

$$\gamma = 1948$$

where depth is in feet and $[R_t]$ is a dimensionless ratio of the average formation resistivity to the average formation water resistivity.

Hacikoylu *et al.* (2006) show that this equation is only applicable for consolidated sandstone with small clay content. Hacikoylu *et al.* (2006) use theoretical velocity–porosity relations for soft sediment in combination with equations for the formation factor to obtain a velocity–resistivity relation appropriate for soft sediment. They show that this theoretical dependence can be approximated by the following equation:

$$V_P = \frac{R_0/R_w}{0.9 + c(R_0/R_w)}$$

where V_P is in km/s and the coefficient c varies between 0.27 and 0.32 for Gulf of Mexico shale data.

Figure 9.5.1 displays V_P versus the formation factor $F = R_0/R_w$ for both equations, using $Z = 2$ km and $c = 0.3$.

Koesoemadinata and McMechan (2003) have given empirical relations between the ultrasonic P-wave velocity (V_P), dielectric constant (κ), porosity (ϕ), density (ρ), and permeability (k). The regressions are based on data from about 30 samples of Ferron sandstone, a fine- to medium-grained sandstone with porosity ranging from

10% to 24% and clay content ranging from 10% to 22%. The V_P and κ data were measured on dry ($< 1\%$ water saturation by volume) samples at 125 kHz and 50 MHz, respectively.

$$\kappa = 0.00119 V_P + 1.41383 \quad R^2 = 0.55$$

$$\kappa = 0.00058 V_P - 0.16294 \ln k + 3.3758 \quad R^2 = 0.64$$

$$\kappa = 0.00072 V_P - 0.06851 \phi + 3.8133 \quad R^2 = 0.65$$

$$\kappa = 0.00072 V_P + 2.3032\rho - 2.4137 \quad R^2 = 0.68$$

$$V_P = 479.6734\kappa + 380.980 \quad R^2 = 0.55$$

$$V_P = 229.35033 \kappa - 104.8169 \ln k + 1756.658 \quad R^2 = 0.64$$

In the above empirical regressions V_P is in m/s, permeability is in mD, density is in g/cm^3 , porosity is given as a percentage, and κ is dimensionless. R^2 is the coefficient of determination for the regression.

Carcione *et al.* (2007) have compiled and derived cross-property relations and bounds relating electrical conductivity to elastic moduli and velocities of rocks. The cross-property relations are based on existing empirical and theoretical relations between electrical conductivity and porosity and between elastic moduli and porosity. The basic approach is as follows. If the relation between porosity, ϕ , and conductivity, σ , is described by $\sigma = f(\phi)$, while the relation between elastic velocity v and porosity is given by $v = g(\phi)$, then the cross-property relation can be obtained by eliminating ϕ to give $\sigma = f(g^{-1}(v))$.

Dry rocks

For a dry rock with randomly oriented penny-shaped cracks of zero conductivity in an isotropic elastic medium, Bristow (1960) gave the following relations between dry-rock elastic moduli and electrical conductivity:

Bristow

$$\frac{K_s - K_m}{K_m} = \frac{2(1 - \nu_s^2)}{1 - 2\nu_s} \frac{\sigma_s - \sigma_m}{\sigma_m}$$

$$\frac{\mu_s - \mu_m}{\mu_m} = \frac{4}{5} (1 - \nu_s)(5 - \nu_s) \left(\frac{\sigma_s - \sigma_m}{\sigma_m} \right)$$

where K_m , μ_m are the dry-rock bulk and shear moduli, σ_m is the dry-rock electrical conductivity, K_s , μ_s , ν_s are bulk modulus, shear modulus, and Poisson ratio for the solid mineral, and σ_s is the electrical conductivity of the solid mineral.

For the case of a porous, “dry” rock (drained, pore-fluid bulk modulus = 0) consisting of an insulating solid mineral ($\sigma_s = 0$) with porosity ϕ , filled with an electrically conductive pore fluid of conductivity $\sigma_f \neq 0$, Berryman and Milton (1988) obtained the following bounds relating the bulk and shear moduli (K, μ) to the electrical conductivity, σ , of the rock:

Berryman–Milton bounds

$$\frac{1}{2} \frac{(1 - \phi)\sigma}{(\phi\sigma_f - \sigma)} \leq 1 - \frac{3\phi K}{4\mu_s(1 - \phi - K/K_s)}$$

$$\frac{1}{2} \frac{(1 - \phi)\sigma}{(\phi\sigma_f - \sigma)} \leq \frac{21}{5 - 21B} \left[1 + B - \frac{6A\phi\mu}{(1 - \phi)\mu_s - \mu} \right]$$

$$A = \frac{6(K_s + 2\mu_s)^2}{(3K_s + \mu_s)^2}$$

$$B = \frac{5\mu_s(4K_s + 3\mu_s)}{(3K_s + \mu_s)^2}$$

Gibiansky and Torquato (1996) obtained the following cross-property bound for a dry, cracked rock with a finitely conducting solid mineral:

Gibiansky–Torquato bound

$$\frac{1}{K_m} - \frac{1}{K_s} \geq \frac{3\sigma_s}{2\mu_s} \frac{1 - \nu_s}{1 + \nu_s} \left(\frac{1}{\sigma_m} - \frac{1}{\sigma_s} \right)$$

Wet rocks

For fluid-saturated rocks with pore-fluid bulk modulus K_f and pore-fluid conductivity σ_f , such that $K_f/K_s \leq \sigma_f/\sigma_s$, Milton (1981) obtained the following inequalities for the effective elastic moduli (K, μ) and the effective electrical conductivity, σ :

Milton bounds

$$\frac{K}{K_s} \leq \frac{\sigma}{\sigma_s}, \quad \frac{\mu}{K_s} \leq \frac{3\sigma}{2\sigma_s}$$

These inequalities remain valid when both $K_f = 0$ and $\sigma_f = 0$.

Combining Archie’s relation (see [Section 9.4](#))

$$\sigma = \sigma_f \phi^m$$

where m is Archie’s cementation factor, with the Wyllie time-average relation (see [Section 7.3](#))

$$\phi = \frac{1/V_P - 1/V_0}{1/V_f - 1/V_0}$$

where V_P is the P-wave velocity in the porous rock, V_0 is the P-wave velocity in the solid mineral grain, and V_f is the wave velocity in the pore fluid gives the following relation between bulk rock conductivity and elastic-wave velocity:

Archie/time-average

$$\sigma = \sigma_f \left(\frac{V_0/V_P - 1}{V_0/V_f - 1} \right)^m$$

Substituting porosity from Archie's equation into the Raymer–Hunt–Gardner velocity–porosity relation (see [Section 7.4](#)) gives:

Archie/Raymer

$$V_P = \left[1 - \left(\frac{\sigma}{\sigma_f} \right)^{1/m} \right]^2 V_0 + \left(\frac{\sigma}{\sigma_f} \right)^{1/m} V_f$$

Similarly, solving for porosity from the Wyllie time-average equation and substituting into various conductivity–porosity relations gives the following cross-property expressions (Carcione *et al.*, 2007):

Glover et al. (2000)/time-average

$$\sigma = (1 - \phi)^p \sigma_s + \sigma_f \phi^m, \quad \phi = \frac{1/V_P - 1/V_0}{1/V_f - 1/V_0}$$

Hermance (1979)/time-average

$$\sigma = (\sigma_f - \sigma_s) \phi^m + \sigma_s, \quad \phi = \frac{1/V_P - 1/V_0}{1/V_f - 1/V_0}$$

Self-similar (Sen et al., 1981)/time-average

$$V_P = \left[\left(\frac{1}{V_f} - \frac{1}{V_0} \right) \left(\frac{\sigma_s - \sigma}{\sigma_s - \sigma_f} \right) \left(\frac{\sigma_f}{\sigma} \right)^{1-1/m} + \frac{1}{V_0} \right]^{-1}$$

Brito Dos Santos *et al.* (1988) obtained the above relation combining the self-similar conductivity model and the Wyllie time-average relation for elastic velocity, for a porous medium with a conducting matrix. It should be noted that the results from the Hermance (1979) and Glover *et al.* (2000) conductivity–porosity relations lie outside the Hashin–Shtrikman bounds.

Raymer–Hunt–Gardner's velocity–porosity relation combined with the Hashin–Shtrikman lower bound on conductivity gives the following relation (Hacikoylu *et al.*, 2006):

HS/Raymer

$$V_P = (1 - \phi + \phi_p)^2 V_0 + (\phi - \phi_p) V_f, \quad \phi = \frac{3\sigma}{\sigma + 2\sigma_f}$$

where ϕ_p is the critical porosity (see Section 7.1), taken to be 0.4 in Hacikoylu *et al.* (2006).

HS models

The Hashin–Shtrikman upper and lower bounds for electrical conductivity (see Section 9.1) can be solved for porosity, which can then be inserted in the corresponding Hashin–Shtrikman bounds for elastic moduli to obtain relations between elastic and electrical properties. The porosity of a two-constituent composite, in terms of the upper and lower Hashin–Shtrikman bounds on the electrical conductivity, is given as follows (Carcione *et al.*, 2007):

$$\phi = \left(\frac{\sigma_s - \sigma_{HS}^-}{\sigma_s - \sigma_f} \right) \left(\frac{\sigma_f + 2\sigma_s}{\sigma_{HS}^- + 2\sigma_s} \right) = \left(\frac{\sigma_s - \sigma_{HS}^+}{\sigma_s - \sigma_f} \right) \left(\frac{3\sigma_f}{\sigma_{HS}^+ + 2\sigma_f} \right)$$

where σ_{HS}^+ and σ_{HS}^- are the upper and lower Hashin–Shtrikman bounds for electrical conductivity, respectively.

Carcione *et al.* substitute this porosity expression into the expression for the Hashin–Shtrikman lower bound for the elastic bulk modulus, K_{HS}^- , giving:

$$K_{HS}^- = \left[\left(\frac{\sigma_s - \sigma_{HS}^-}{\sigma_s - \sigma_f} \right) \left(\frac{\sigma_f + 2\sigma_s}{\sigma_{HS}^- + 2\sigma_s} \right) \left(\frac{1}{K_f} - \frac{1}{K_s} \right) + \frac{1}{K_s} \right]^{-1}$$

Similar expressions can be obtained using the upper bound.

Gassmann-based relations

Carcione *et al.* (2007) suggest using Gassmann's relation to derive relations between elastic and electrical properties. Gassmann's relation (see Section 6.3) relates the elastic bulk modulus K_m of a dry rock to the bulk modulus K_{sat} of the same rock fully saturated with a fluid of bulk modulus K_f . One form of Gassmann's relation is

$$K_{sat} = \frac{K_s - K_m(\phi) + \phi K_m(\phi)(K_s/K_f - 1)}{1 - \phi - K_m(\phi)/K_s + \phi K_s/K_f}$$

For the dry bulk modulus, Carcione *et al.* suggest using a dry modulus–porosity relation based on Krief's equation (see Section 7.8):

$$K_m = K_s(1 - \phi)^{(1-\phi+A)/(1-\phi)}$$

$$\mu_m = \left(\frac{\mu_s}{K_s} \right) K_m$$

Other K_m - ϕ models, such as the soft-sand or cemented-sand models described in [Section 5.4](#), can also be used. The porosity is then replaced by a porosity derived from one of the many σ - ϕ relations such as the following:

$$\phi = \left(\frac{\sigma}{\sigma_f} \right)^{1/m} \quad \text{Archie}$$

$$\phi = \left(\frac{\sigma - \sigma_s}{\sigma_f - \sigma_s} \right)^{1/m} \quad \text{Hermance}$$

$$\phi = \left(\frac{\sigma^{1/\gamma} - \sigma_s^{1/\gamma}}{\sigma_f^{1/\gamma} - \sigma_s^{1/\gamma}} \right) \quad \gamma = 2 \quad \text{CRIM (see Section 9.3)}$$

$$\phi = \left(\frac{\sigma - \sigma_s}{\sigma_f - \sigma_s} \right) \left(\frac{\sigma_f}{\sigma} \right)^{1-1/m} \quad \text{self-similar}$$

$$\phi = \left(\frac{\sigma_s - \sigma}{\sigma_s - \sigma_f} \right) \left(\frac{\sigma_f + 2\sigma_s}{\sigma + 2\sigma_s} \right) \quad \text{HS lower bound}$$

$$\phi = \left(\frac{\sigma_s - \sigma}{\sigma_s - \sigma_f} \right) \left(\frac{3\sigma_f}{\sigma + 2\sigma_f} \right) \quad \text{HS upper bound}$$

Layered media

By combining the Backus-averaged elastic modulus (see [Section 4.13](#)) and electrical conductivity for a two-constituent layered medium with layering perpendicular to the 3-axis, Carcione *et al.* (2007) give the following relations:

$$\frac{\sigma_{11} - \sigma_2}{\sigma_1 - \sigma_2} = \frac{c_{66} - \mu_2}{\mu_1 - \mu_2}$$

$$\frac{\sigma_{33}^{-1} - \sigma_2^{-1}}{\sigma_1^{-1} - \sigma_2^{-1}} = \frac{c_{44}^{-1} - \mu_2^{-1}}{\mu_1^{-1} - \mu_2^{-1}}$$

Subscripts 1 and 2 denote the properties of the constituent layers, and the anisotropic effective averaged quantities are denoted by the usual two-index notation.

Uses

These relations can be used to estimate seismic velocity from measured electrical properties.

Assumptions and limitations

The empirical equations may not be valid for rock types and environments that are different from the ones used to establish the relations. The Faust (1953) equation may not be valid in soft, shaley sediment. The coefficient c in the Hacikoylu *et al.* (2006) equation may have to be adjusted for environments other than the Gulf of Mexico. When combining two relations for elastic and electric properties to obtain a cross-property relation, the resulting equation will be a good description of the cross-relation only if the original equations for elastic and electrical properties themselves are good descriptors. These cross-relations have not been tested widely with controlled data. Two of the empirical relations (Glover *et al.* and Hermance) violate the theoretical Hashin–Shtrikman bounds.

Appendices

A.1 Typical rock properties

Chalks

Chalk data are plotted in [Figures A.1.1](#) and [A.1.2](#) and summarized in [Table A.1.1](#).

- Low-porosity samples (Brevik, 1995) are from a Cretaceous gas-condensate reservoir. Each data point represents average values (averaged over an interval of porosity). Saturation (gas–brine) in these samples is highly correlated with porosity: $S_w \approx 0.70$ at $\phi \approx 0.1$ and $S_w \approx 0.15$ at $\phi \approx 0.35$. High-porosity samples (Urmos and Wilkens, 1993), water-saturated.
- **Measurement type:** sonic logs, log porosity.
- **Data source:** Urmos and Wilkens (1993); Brevik (1995).

Table A.1.1 *Properties of chalk shown in [Figures A.1.1](#) and [A.1.2](#).*

	Minimum	Maximum	Mean	Standard deviation
V_P (km/s)	1.53	4.30	2.16	0.32
V_S (km/s)	1.59	2.51	2.03	0.30
V_P/V_S	1.62	1.79	1.67	0.06
Porosity	0.10	0.75	0.50	0.08
Density (g/cm ³)	1.43	2.57	1.85	0.13
Impedance 10 ⁶ (kg/m ³)(m/s)	2.30	10.99	4.02	0.89

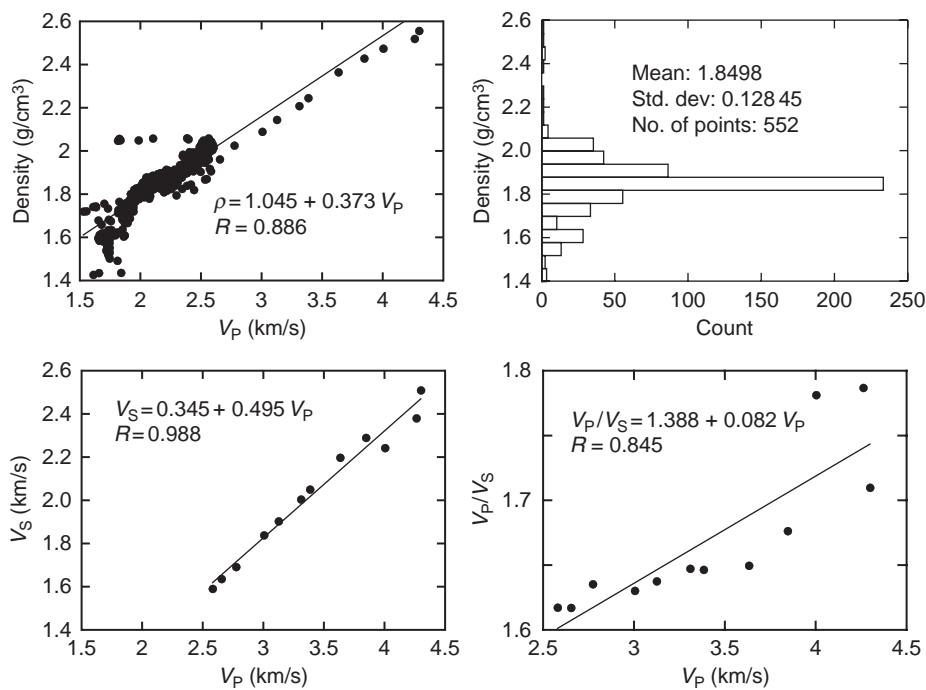


Figure A.1.1 Properties of chalk.

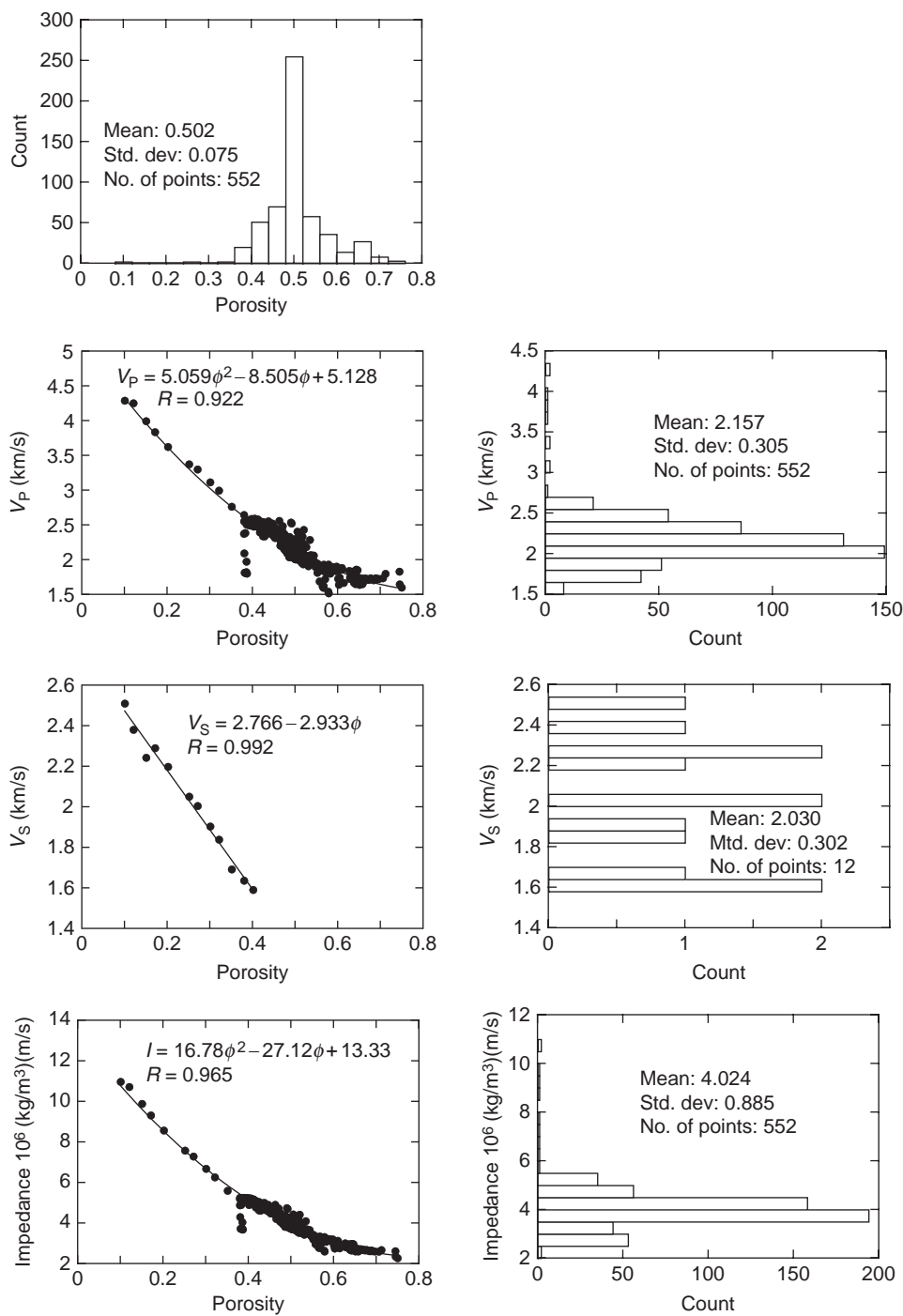


Figure A.1.2 Properties of chalk.

Dolomite

Dolomite data are plotted in [Figures A.1.3 and A.1.4](#) and summarized in [Table A.1.2](#).

- **Saturation:** Water-saturated, calculated from dry data using Gassmann’s equations.
- **Measurement type:** Ultrasonic.
- **Effective pressure:** 10, 15, 35 MPa.
- **Data source:** Geertsma (1961); Yale and Jamieson (1994).

Table A.1.2 Properties of dolomite shown in [Figures A.1.3 and A.1.4](#).

	Minimum	Maximum	Mean	Standard deviation
V_P (km/s)	3.41	7.02	5.39	0.69
V_S (km/s)	2.01	3.64	2.97	0.37
V_P/V_S	1.59	2.09	1.82	0.07
Porosity	0.00	0.32	0.13	0.06
Density (g/cm^3)	2.27	2.84	2.59	0.12
Impedance 10^7 (kg/m^3)(m/s)	0.78	1.93	1.40	0.23

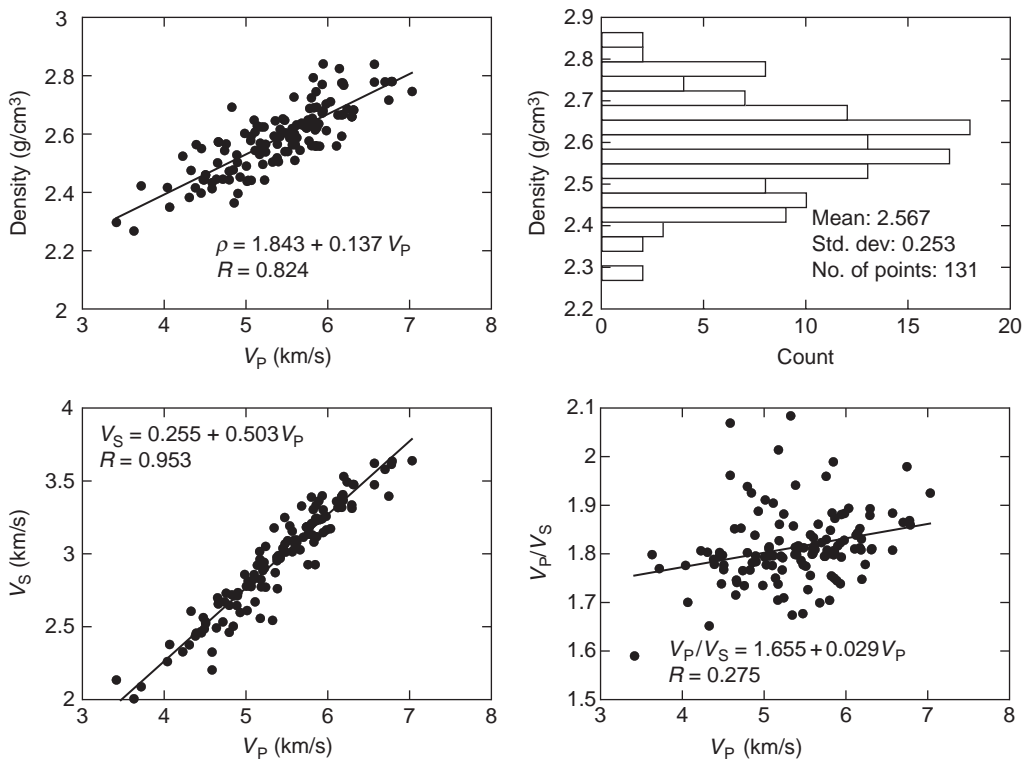


Figure A.1.3 Properties of dolomite.

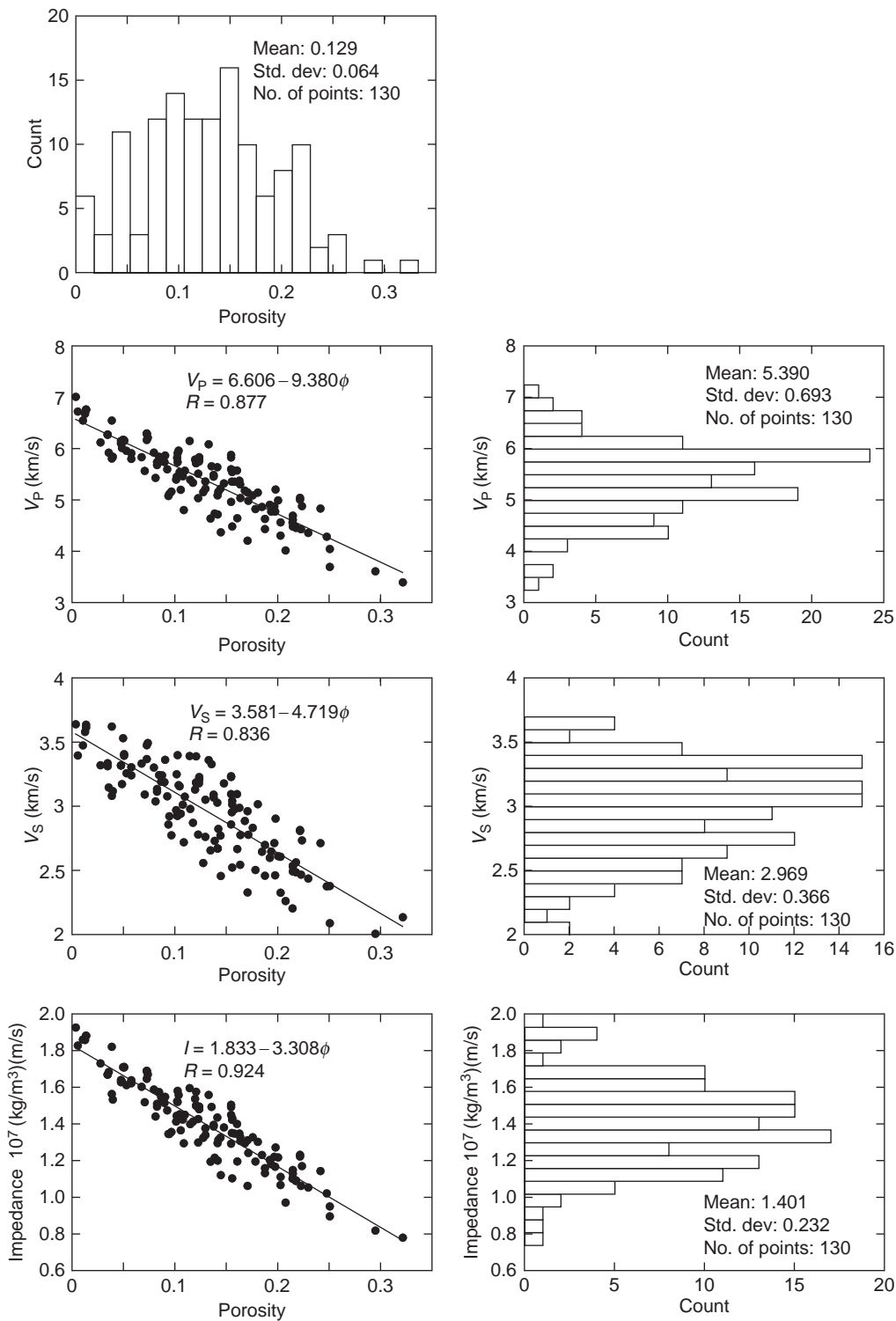


Figure A.1.4 Properties of dolomite.

Sandstones

Sandstone data are plotted in Figures A.1.5 and A.1.6 and summarized in Table A.1.3.

- **Saturation:** Water-saturated.
- **Measurement type:** Ultrasonic.
- **Effective pressure:** 30, 40 MPa.
- **Data source:** Han (1986).

Table A.1.3 Properties of sandstone shown in Figures A.1.5 and A.1.6.

	Minimum	Maximum	Mean	Standard deviation
V_P (km/s)	3.13	5.52	4.09	0.51
V_S (km/s)	1.73	3.60	2.41	0.40
V_P/V_S	1.53	1.89	1.71	0.08
Porosity	0.04	0.30	0.16	0.07
Density (g/cm ³)	2.09	2.64	2.37	0.13
Impedance 10 ⁶ (kg/m ³)(m/s)	6.60	13.97	9.73	1.64

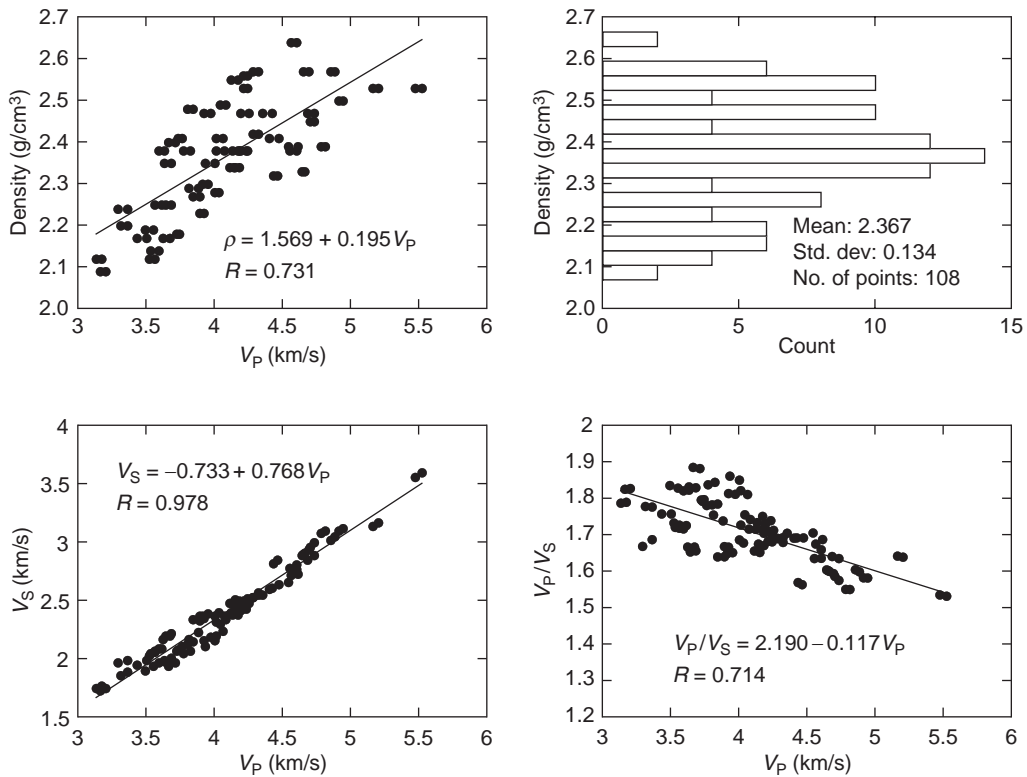


Figure A.1.5 Properties of sandstone.

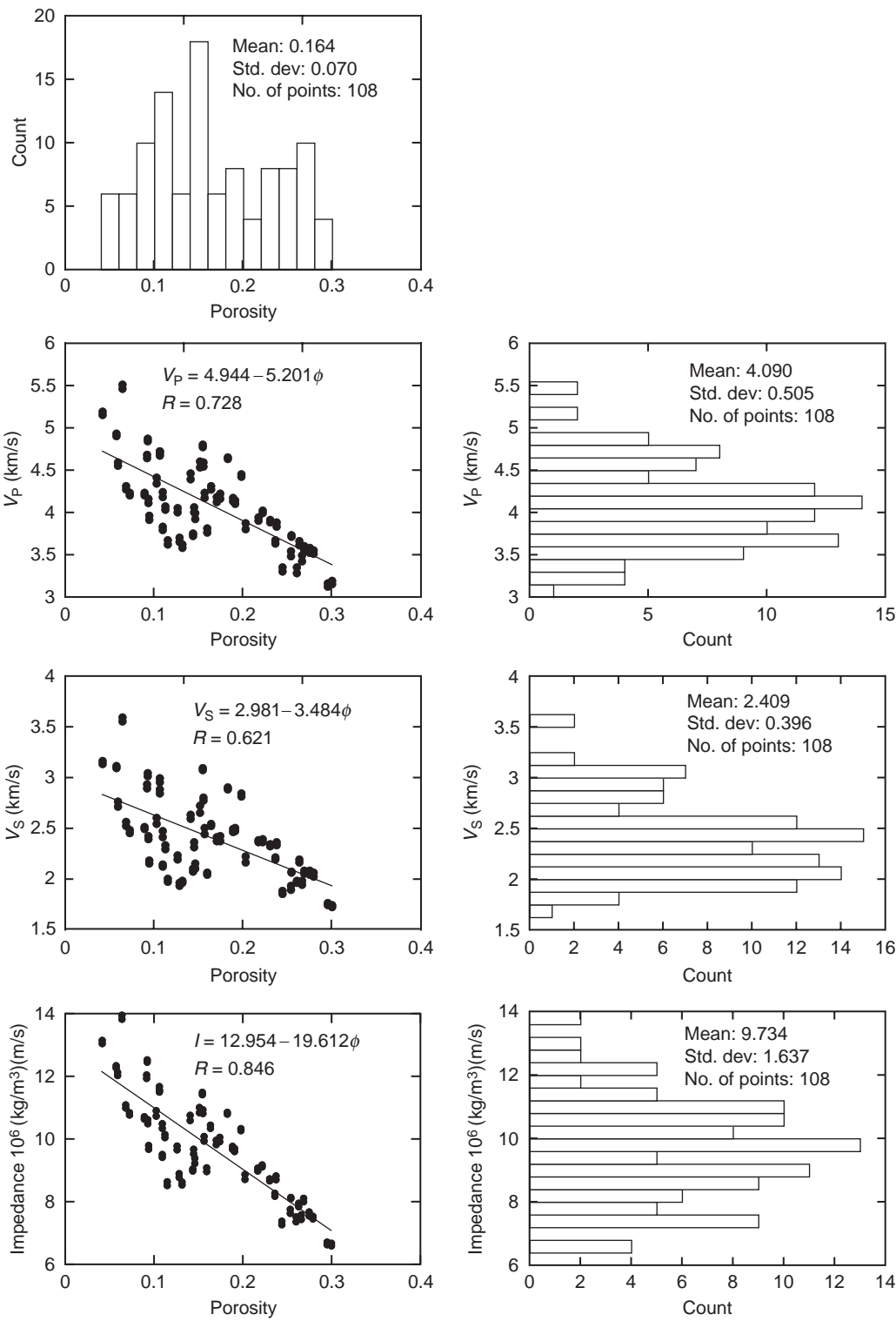


Figure A.1.6 Properties of sandstone.

Tight-gas sandstones

Tight-gas sandstone data are plotted in Figures A.1.7 and A.1.8 and summarized in Table A.1.4.

- **Saturation:** Dry.
- **Measurement type:** Ultrasonic.
- **Effective pressure:** 40 MPa.
- **Data source:** Jizba (1991).

Table A.1.4 Properties of tight-gas sandstone shown in Figures A.1.7 and A.1.8.

	Minimum	Maximum	Mean	Standard deviation
V_P (km/s)	3.81	5.57	4.67	0.38
V_S (km/s)	2.59	3.50	3.06	0.23
V_P/V_S	1.42	1.68	1.53	0.05
Porosity	0.01	0.14	0.05	0.04
Density (g/cm^3)	2.26	2.67	2.51	0.11
Impedance 10^7 (kg/m^3)(m/s)	0.89	1.49	1.17	0.13

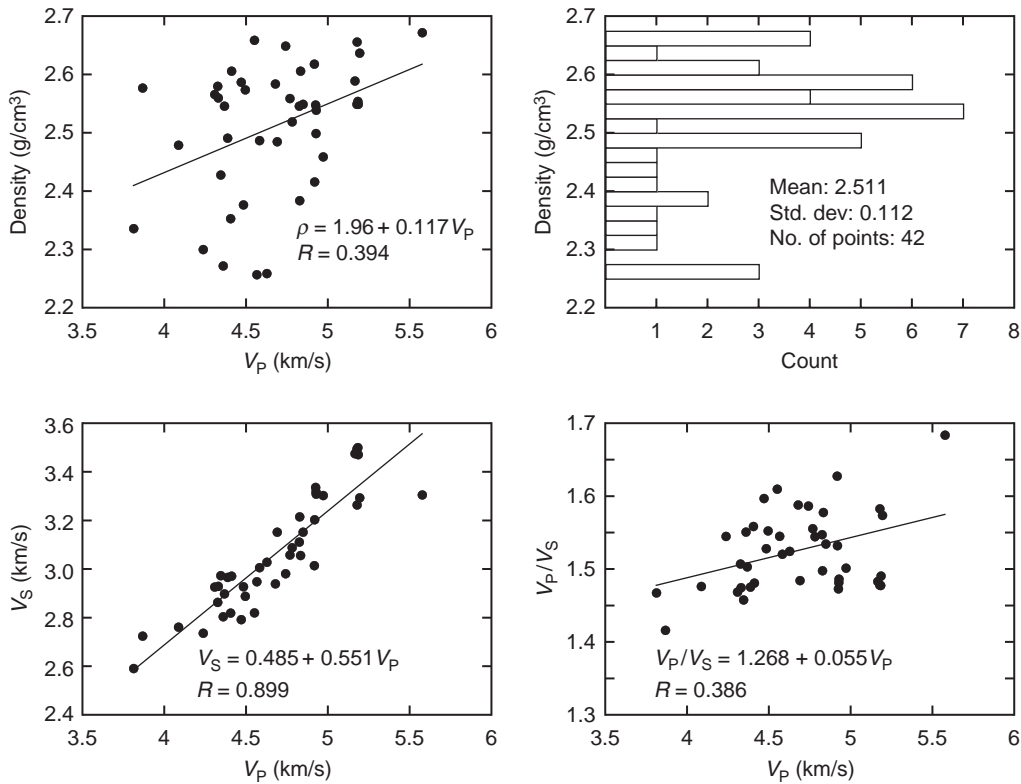


Figure A.1.7 Properties of tight-gas sandstone.

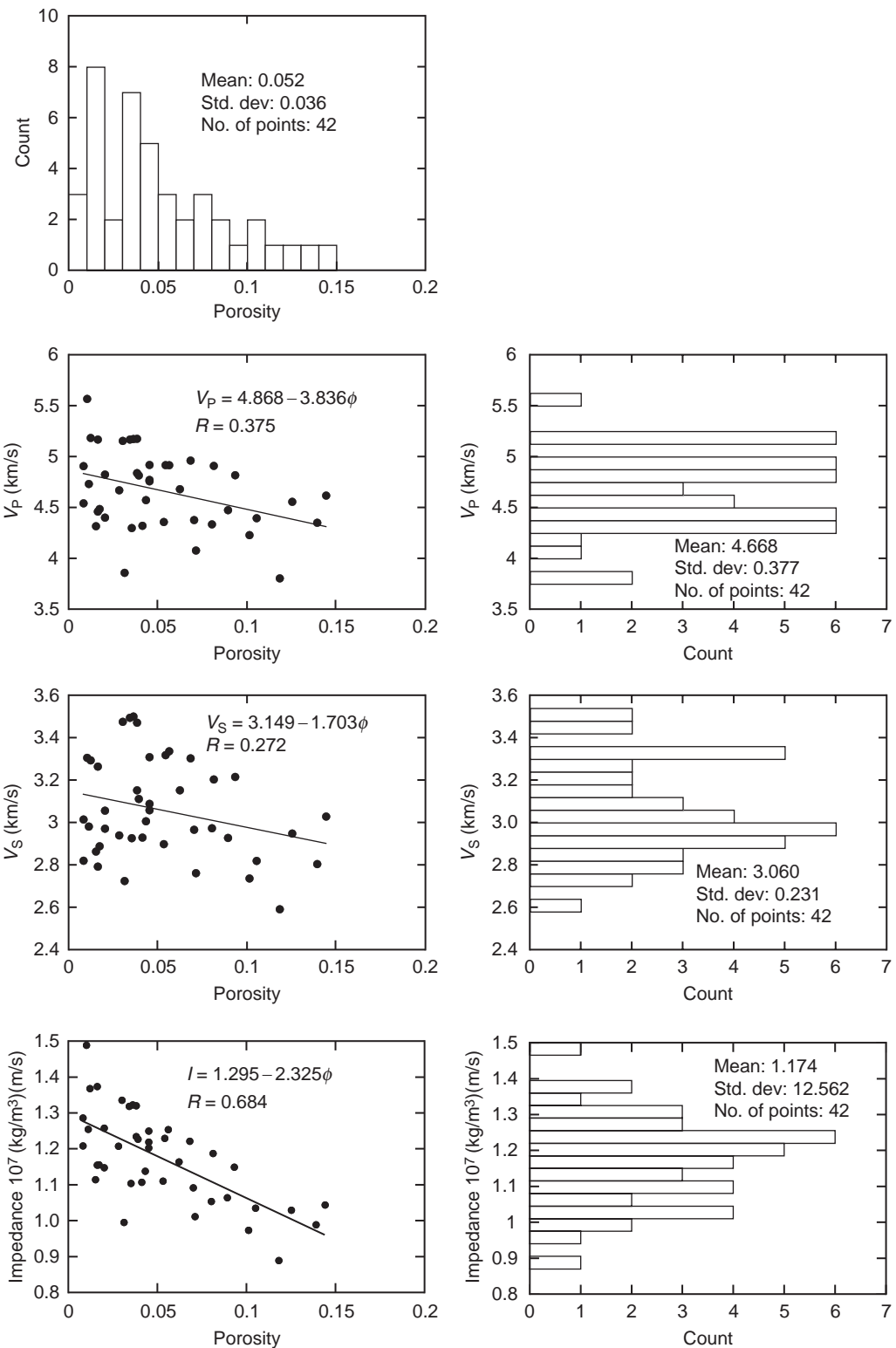


Figure A.1.8 Properties of tight-gas sandstone.

Limestone

Limestone data are plotted in [Figures A.1.9](#) and [A.1.10](#) and summarized in [Table A.1.5](#).

- **Saturation:** Some water-saturated; others water-saturated as calculated from dry data using Gassmann’s equations.
- **Measurement type:** Ultrasonic, resonant bar.
- **Effective pressure:** 10, 30, 40, 50 MPa.
- **Data source:** Lucet (1989); Cadoret (1993); Yale and Jamieson (1994).

Table A.1.5 Properties of limestone shown in [Figures A.1.9](#) and [A.1.10](#).

	Minimum	Maximum	Mean	Standard deviation
V_P (km/s)	3.39	5.79	4.63	0.66
V_S (km/s)	1.67	3.04	2.44	0.37
V_P/V_S	1.72	2.04	1.88	0.08
Porosity	0.03	0.41	0.15	0.09
Density (g/cm ³)	2.00	2.65	2.43	0.16
Impedance 10 ⁷ (kg/m ³)(m/s)	0.69	1.51	1.43	0.22

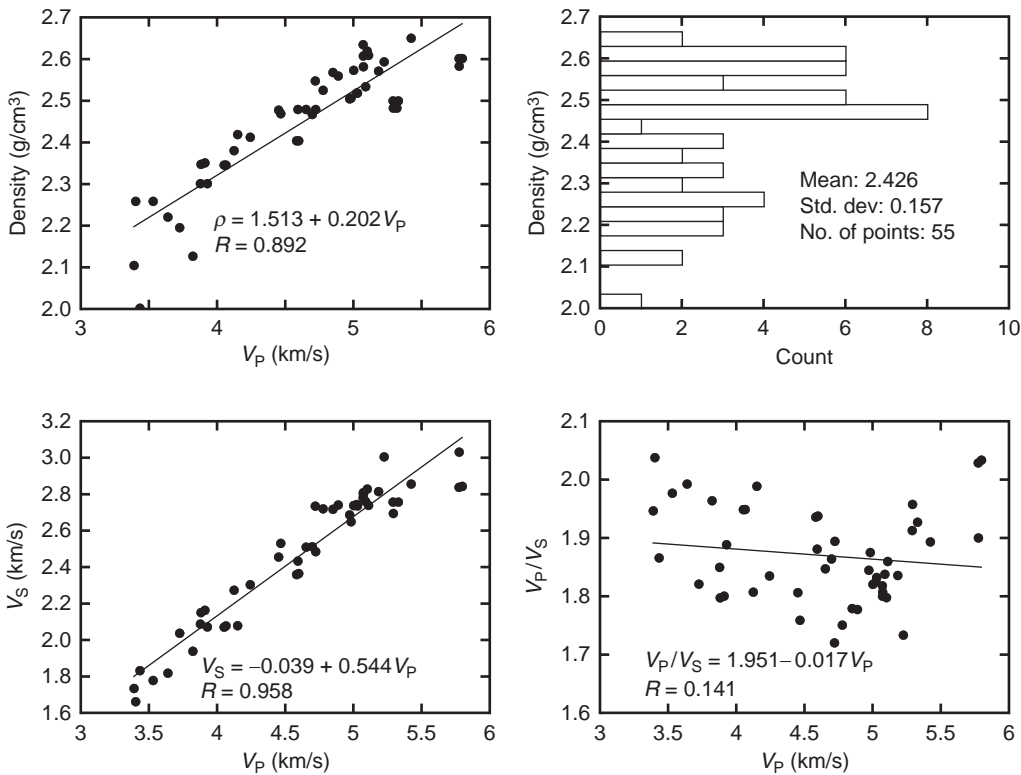


Figure A.1.9 Properties of limestone.

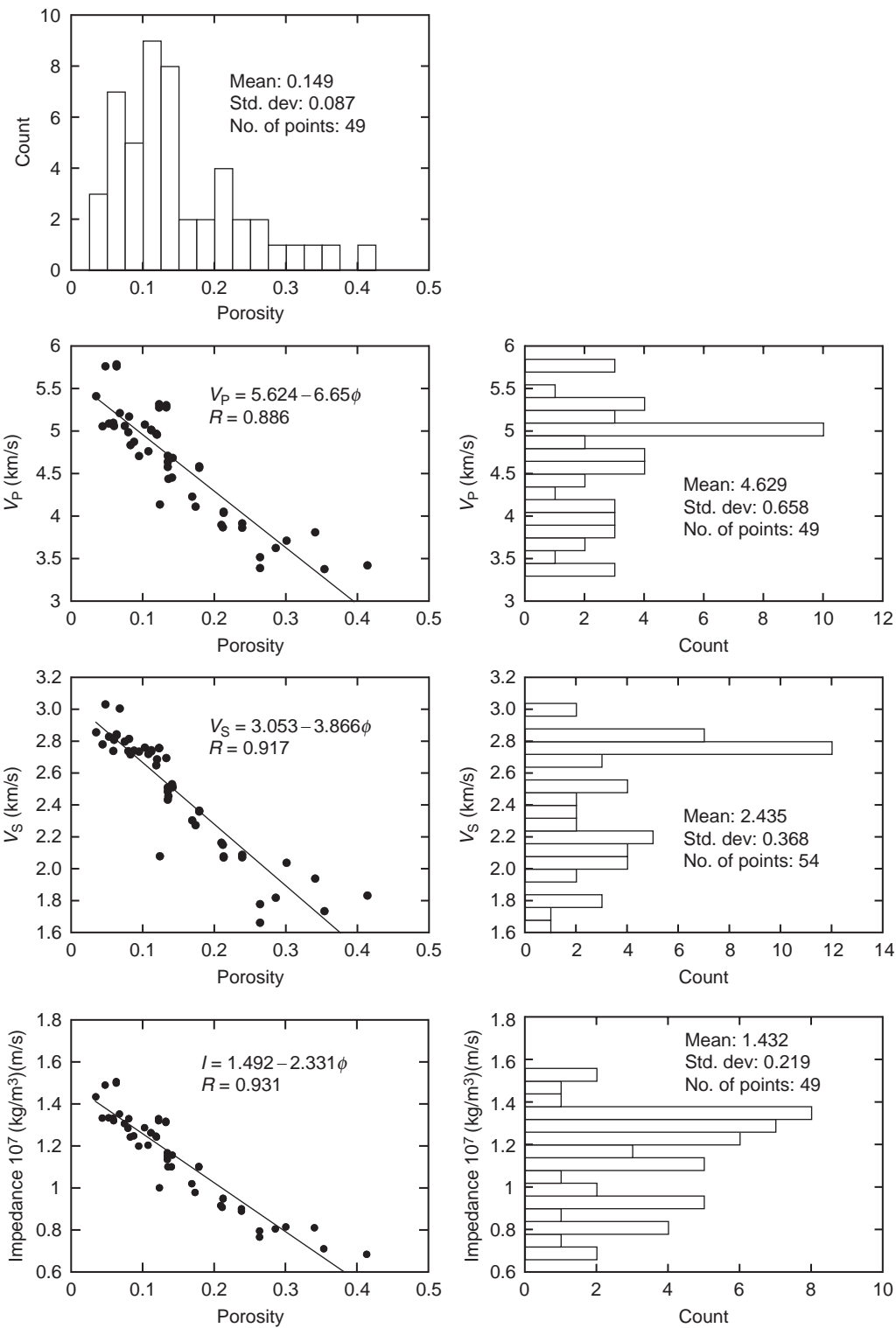


Figure A.1.10 Properties of limestone.

High-porosity sandstones

High-porosity sandstone data are plotted in Figures A.1.11 and A.1.12 and summarized in Table A.1.6.

- **Saturation:** Water-saturated.
- **Measurement type:** Ultrasonic.
- **Effective pressure:** 35, 40 MPa.
- **Data source:** Strandenes (1991).

Table A.1.6 Properties of high-porosity sandstone shown in Figures A.1.11 and A.1.12.

	Minimum	Maximum	Mean	Standard deviation
V_P (km/s)	3.46	4.79	3.80	0.24
V_S (km/s)	1.95	2.66	2.16	0.15
V_P/V_S	1.68	1.88	1.75	0.13
Porosity	0.02	0.32	0.18	0.08
Density (g/cm^3)	2.12	2.69	2.33	0.13
Impedance 10^6 (kg/m^3)(m/s)	7.57	9.98	8.57	0.67

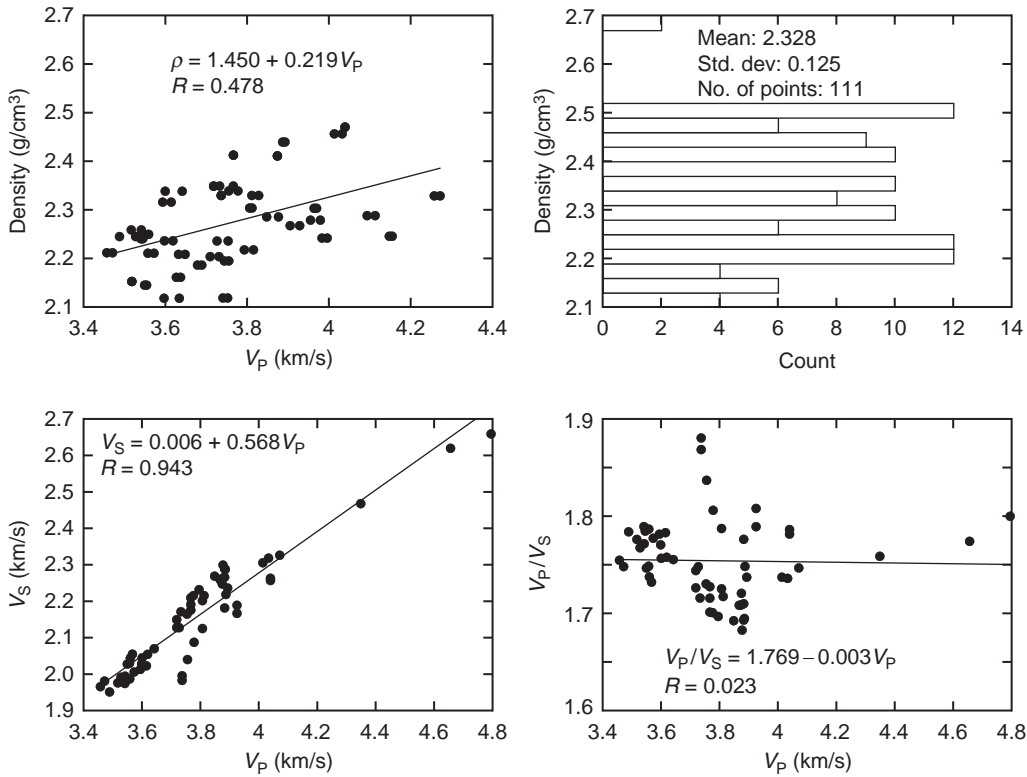


Figure A.1.11 Properties of high-porosity sandstone.

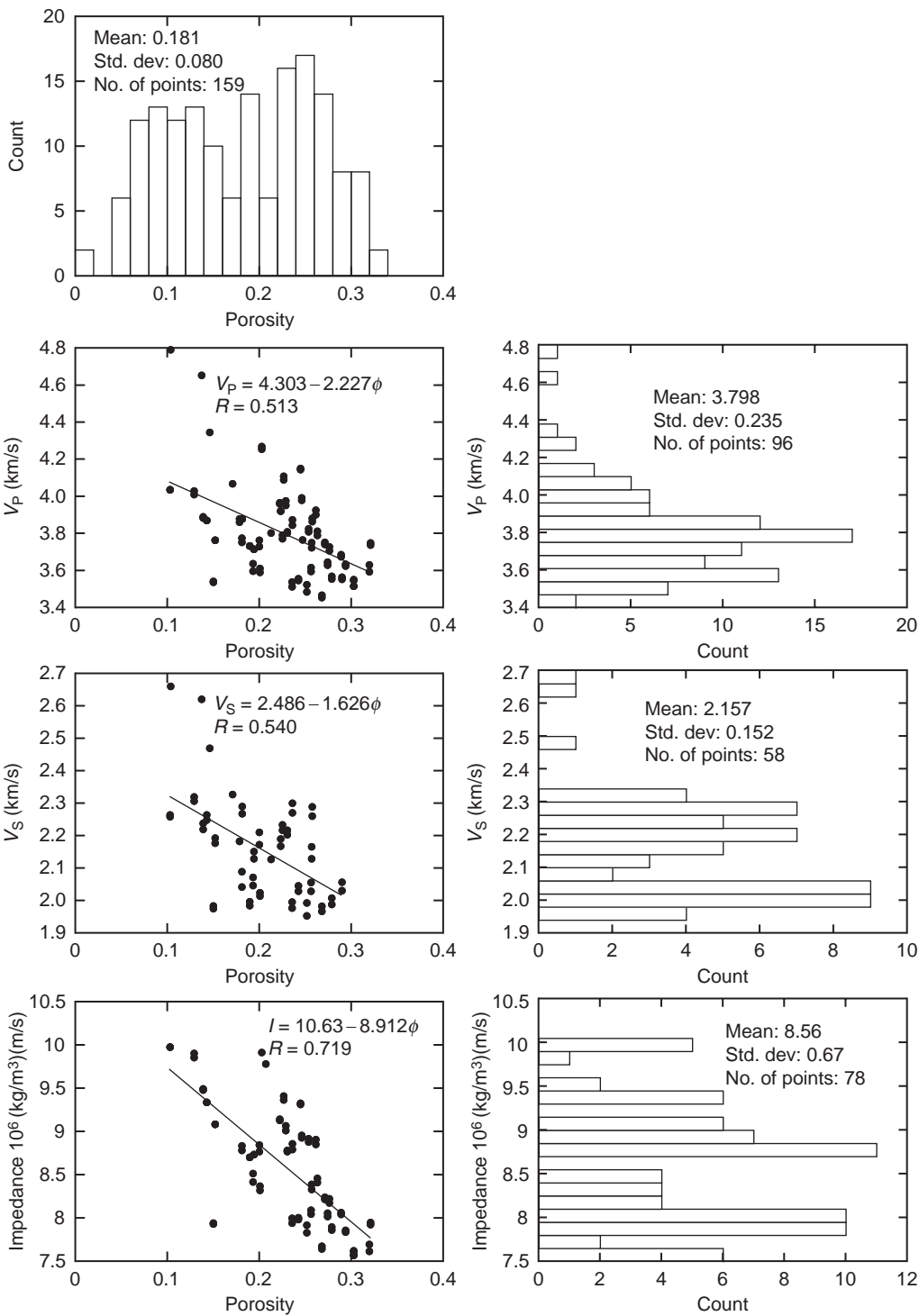


Figure A.1.12 Properties of high-porosity sandstone.

Poorly consolidated sandstones

Poorly consolidated sandstone data are plotted in Figures A.1.13 and A.1.14 and summarized in Table A.1.7.

- **Saturation:** Water-saturated.
- **Measurement type:** Ultrasonic.
- **Effective pressure:** 30 MPa.
- **Data source:** Blangy (1992).

Table A.1.7 Properties of poorly consolidated sandstone shown in Figures A.1.13 and A.1.14.

	Minimum	Maximum	Mean	Standard deviation
V_P (km/s)	2.43	3.14	2.73	0.18
V_S (km/s)	1.21	1.66	1.37	0.12
V_P/V_S	1.88	2.24	2.02	0.09
Porosity	0.22	0.36	0.31	0.04
Density (g/cm^3)	2.01	2.23	2.11	0.05
Impedance 10^6 (kg/m^3)(m/s)	4.89	7.02	5.77	0.51

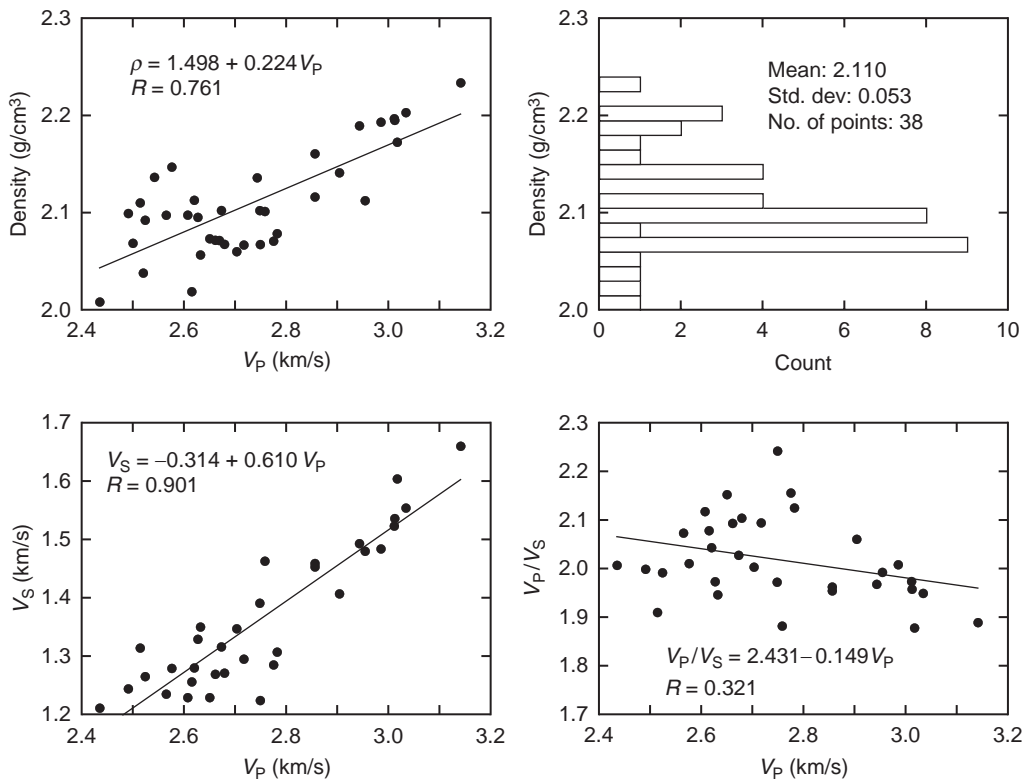


Figure A.1.13 Properties of poorly consolidated sandstone.

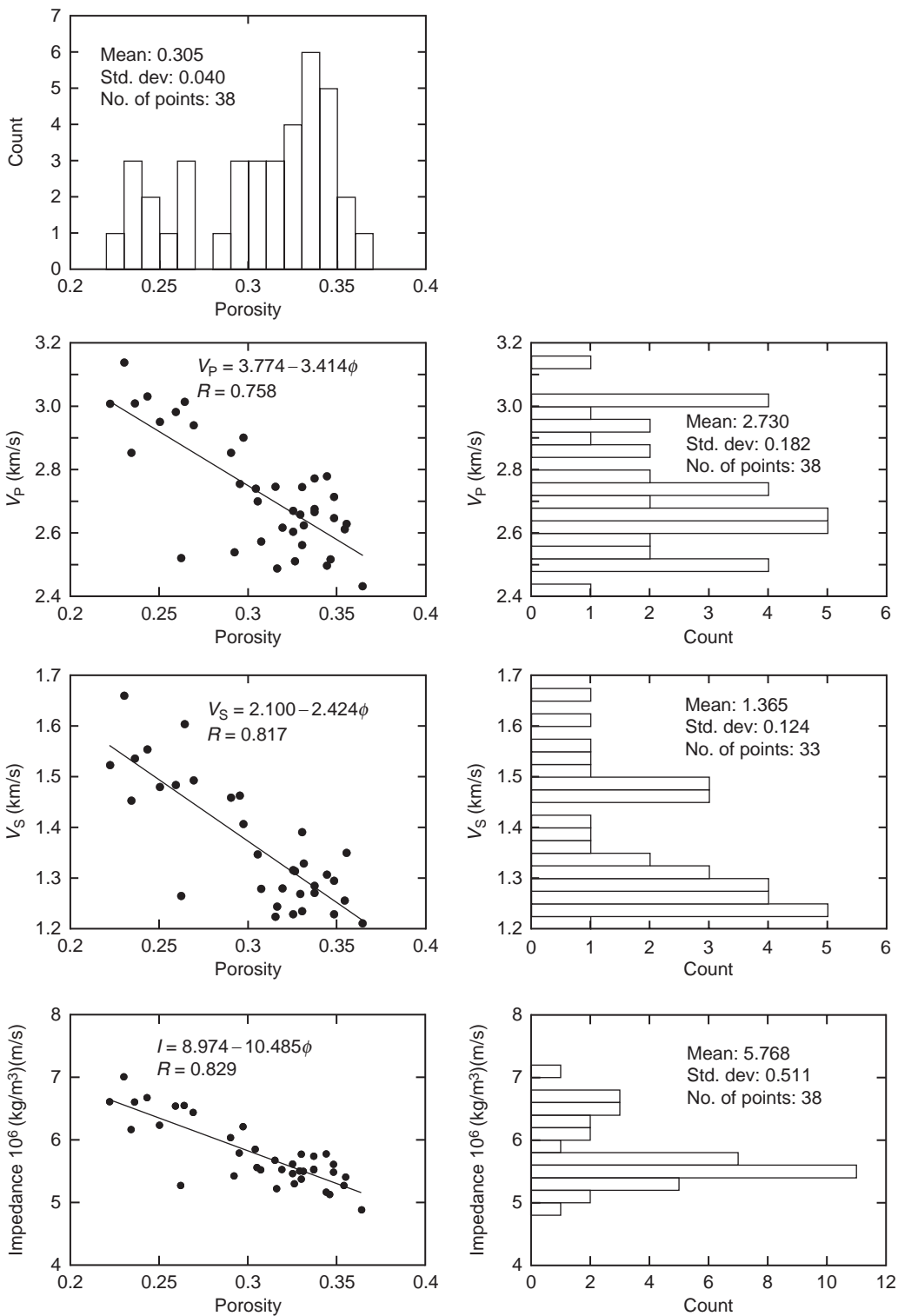


Figure A.1.14 Properties of poorly consolidated sandstone.

A.2

Conversions

Mass/weight

1 g	= 10 ⁻³ kg
1 kg	= 2.204623 lb
1 lb	= 0.4535924 kg
1 ton (USA)	= 2000 lb
	= 907.2 kg
1 ton (imperial)	= 2240 lb
	= 1016 kg
1 ton (metric)	= 1000 kg
	= 2204.622 lb
1 oz (avdp.)	= 28.3495 g
1 oz (troy)	= 31.103 48 g

Length

1 m	= 39.37 in
	= 3.2808399 ft
1 cm	= 0.3937 in
	= 0.032808399 ft
	= 0.01 m
1 in	= 2.540 005 cm
	= 0.025400 05 m
1 ft	= 30.480 06 cm
	= 0.3048006 m
1 km	= 0.62137 mile
1 mile	= 1.60935 km
1 nautical mile	= 1.15077 miles
	= 1.852 km

1 μm	$= 10^{-6} \text{ m}$
	$= 10^{-4} \text{ cm}$
	$= 3.937 \times 10^{-5} \text{ in}$
1 \AA	$= 10^{-10} \text{ m}$
	$= 10^{-8} \text{ cm}$
	$= 3.937 \times 10^{-9} \text{ in}$
1 light year	$= 9.4543 \times 10^{25} \text{ \AA}$
	$= 9.454 \times 10^{12} \text{ km}$
1 astronomical unit	$= 1.4960 \times 10^8 \text{ km}$
1 hair's breadth	$= 0.01 \text{ cm}$
1 arm's length	$= 70 \text{ cm}$
1 cubit (Roman)	$= 44.4 \text{ cm}$
1 fathom	$= 182.88 \text{ cm}$
1 gnat's eye	$= 0.0125 \text{ cm}$
1 klick	$= 1 \text{ km}$

Velocity/slowness/transit time

1 m/s	$= 3.2808 \text{ ft/s}$
	$= 0.3048 \times 10^6 / (1 \mu\text{s/ft})$
1 ft/s	$= 0.3048 \text{ m/s}$
1 mile/h	$= 1.609 \text{ km/h}$
	$= 0.447 \text{ m/s}$
	$= 1.47 \text{ ft/s}$

Area

1 m^2	$= 10^4 \text{ cm}^2$
	$= 10.764 \text{ ft}^2$
	$= 1550.0 \text{ in}^2$
	$= 2.47104 \times 10^{-4} \text{ acres}$
	$= 10^{-4} \text{ hectares}$
1 ft^2	$= 929.030 \text{ cm}^2$
	$= 0.092\,903 \text{ m}^2$
	$= 144 \text{ in}^2$
	$= 2.2957 \times 10^{-5} \text{ acres}$
	$= 9.29 \times 10^{-6} \text{ hectares}$
1 acre	$= 4.0469 \times 10^7 \text{ cm}^2$
	$= 4.0469 \times 10^3 \text{ m}^2$
	$= 43\,560 \text{ ft}^2$
	$= 0.0015625 \text{ mile}^2$
	$= 0.40469 \text{ hectares}$
1 hectare	$= 10^8 \text{ cm}^2$
	$= 10^4 \text{ m}^2$
	$= 1.0764 \times 10^5 \text{ ft}^2$
	$= 3.8610 \times 10^{-3} \text{ mile}^2$
	$= 2.4711 \text{ acre}$

$$\begin{aligned}1 \text{ km}^2 &= 10^{10} \text{ cm}^2 \\&= 10^6 \text{ m}^2 \\&= 100 \text{ hectare} \\&= 247.105 \text{ acre} \\&= 0.386 \text{ 10 mile}^2\end{aligned}$$

Density

$$\begin{aligned}1 \text{ g/cm}^3 &= 0.036127 \text{ lb/in}^3 \\&= 62.42797 \text{ lb/ft}^3 \\&= 1000 \text{ kg/m}^3 \\1 \text{ lb/in}^3 &= 27.6799 \text{ g/cm}^3 \\&= 27679.9 \text{ kg/m}^3 \\1 \text{ lb/ft}^3 &= 0.016018 \text{ g/cm}^3\end{aligned}$$

Volume

$$\begin{aligned}1 \text{ cm}^3 &= 0.0610238 \text{ in}^3 \\1 \text{ in}^3 &= 16.38706 \text{ cm}^3 \\1 \text{ liter} &= 0.264172 \text{ gallons} \\&= 0.035315 \text{ ft}^3 \\&= 1.056688 \text{ qt} \\&= 1000 \text{ cm}^3 \\1 \text{ bbl} &= 0.158987 \text{ m}^3 \\&= 42 \text{ gallons} \\&= 5.6146 \text{ ft}^3 \\1 \text{ m}^3 &= 6.2898106 \text{ bbl} \\1 \text{ ft}^3 &= 7.481 \text{ gallon (US)} \\&= 0.1781 \text{ bbl} \\1 \text{ gallon (US)} &= 0.1337 \text{ ft}^3\end{aligned}$$

Force

$$\begin{aligned}1 \text{ N} &= 1 \text{ kg m/s}^2 \\1 \text{ lb} &= 4.4482 \text{ N} \\1 \text{ dyn} &= 10^{-5} \text{ N} \\1 \text{ kg force} &= 9.80665 \text{ N} \\&= 9.80665 \times 10^5 \text{ dyne}\end{aligned}$$

Pressure

$$\begin{aligned}1 \text{ atm (76 cm Hg)} &= 1.01325 \text{ bar} \\&= 1.033227 \text{ kg force/cm}^2 \\&= 14.695949 \text{ psi} \\1 \text{ bar} &= 10^6 \text{ dyne/cm}^2 \\&= 10^5 \text{ N/m}^2 \\&= 0.1 \text{ MPa}\end{aligned}$$

1 kg force/cm ²	= 9.80665 × 10 ⁵ dyne/cm ²
	= 0.96784 atm
1 psi	= 0.070307 kg-force/cm ²
	= 0.006895 MPa
	= 0.06895 bar
1 kpsi	= 70.307 kg-force/cm ²
	= 6.895 MPa
	= 68.95 bar
1 Pa	= 1 N/m ²
	= 1.4504 × 10 ⁻⁴ psi
1 MPa	= 10 ⁶ Pa
	= 145.0378 psi
	= 10 bar
1 kbar	= 100 MPa

Pressure gradients (or mud weight to pressure gradient)

1 psi/ft	= 144 lb/ft ³
	= 19.24 lb/gallons
	≈ 0.0225 MPa/m
	= 22.5 kPa/m
lb/gallon	= 0.052 psi/ft

Mud density to pressure gradient

1 psi/ft	⇔ 2.31 g/cm ³
----------	--------------------------

Viscosity

1 Poise	= 1 dyne s/cm ²
1 cP	= 0.01 Poise

Permeability

1 Darcy	= 0.986923 × 10 ⁻¹² m ²
	= 0.986923 μm ²
	= 0.986923 × 10 ⁻⁸ cm ²
	= 1.06 × 10 ⁻¹¹ ft ²

Gas-oil ratio

1 liter/liter	= 5.615 ft ³ /bbl
---------------	------------------------------

Other conversions

1 year	= 3.1536 × 10 ⁷ s
1 erg	= 10 ⁻⁷ m ² kg/s ²

1 joule (J)	$= 10^7 \text{ erg}$
	$= 1 \text{ m}^2 \text{ kg/s}^2$
1 calorie (cal)	$= 4.186 \text{ J}$
	$= 4.186 \times 10^7 \text{ erg}$
1 watt	$= 1 \text{ m}^2 \text{ kg/s}^3$
1 kilocalorie	$= 4186.8 \text{ m}^2 \text{ kg/s}^2$
1 BTU	$= 252 \text{ cal}$
	$= 1054 \text{ J}$
1 eV	$= 1.60 \times 10^{-19} \text{ J}$
1 weber/m ²	$= 1 \text{ tesla}$
	$= 10^4 \text{ gauss}$
1 radian (rad)	$= 57.30^\circ$
1 second of arc	$= 4.848 \times 10^{-6} \text{ rad}$

A.3 Physical constants

Astronomical constants

Mass of the Sun	$1.989 \times 10^{33} \text{ g}$
Mass of the Earth	$5.976 \times 10^{27} \text{ g}$
Equatorial radius of the Earth	$6.378 \, 16 \times 10^8 \text{ cm}$
Polar radius of the Earth	$6.356 \, 78 \times 10^8 \text{ cm}$
Gravitational acceleration at equator	978.03 cm s^{-2}
Gravitational acceleration at pole	983.20 cm s^{-2}

Fundamental constants

Gravitational constant, G	$6.670 \times 10^{-8} \text{ dyne cm}^2 \text{ g}^{-2}$
Speed of light, c (in vacuum)	$2.998 \times 10^{10} \text{ cm s}^{-1}$
Gas constant, R	$8.314 \times 10^7 \text{ erg K}^{-1} \text{ mol}^{-1}$
	$0.082057 \text{ L atm K}^{-1} \text{ mol}^{-1}$
Avogadro's number, N	$6.022 \times 10^{23} \text{ mol}^{-1}$
Planck's constant, h	$6.625 \times 10^{-27} \text{ erg s}$
Boltzmann's constant	$1.3805 \times 10^{-16} \text{ erg K}^{-1}$
Mass of an electron	$9.110 \times 10^{-28} \text{ g}$
Mass of a proton	$1.673 \times 10^{-24} \text{ g}$
Charge of an electron	$1.602 \times 10^{-19} \text{ C}$
Electron gyromagnetic ratio, γ_e	$1.760859770 \times 10^{11} \text{ s}^{-1} \text{ T}^{-1}$
Nucleus gyromagnetic ratio, γ	
^1H	$2\pi \times 42.576 \times 10^6 \text{ s}^{-1} \text{ T}^{-1}$
^3He	$-2\pi \times 32.434 \times 10^6 \text{ s}^{-1} \text{ T}^{-1}$
^{14}N	$2\pi \times 3.0766 \times 10^6 \text{ s}^{-1} \text{ T}^{-1}$
^{17}O	$-2\pi \times 5.7716 \times 10^6 \text{ s}^{-1} \text{ T}^{-1}$

A.4

Moduli and density of common minerals

Table A.4.1 summarizes moduli, densities, and velocities for many common minerals. The data have been taken from a variety of sources, but we drew heavily from extensive compilations by Ellis *et al.* (1988), Blangy (1992), Castagna *et al.* (1993), and Carmichael (1989).

Tables A.4.2a–g summarize densities and anisotropic elastic constants for many common minerals. The data have been taken from an extensive compilation by Bass (1995).

A.5

Velocities and moduli of ice and methane hydrate

Tables A.5.1 and A.5.2, from Helgerud (2001) summarize ultrasonic velocities, Poisson’s ratio, and dynamic elastic moduli for compacted polycrystalline ice and methane hydrate, as a function of temperature (in degrees Celsius) and pressure (in psi).

Table A.4.1 *Moduli, densities, and velocities of common minerals.*

Mineral	Bulk modulus (GPa)	Shear modulus (GPa)	Density (g/cm ³)	V _P (km/s)	V _S (km/s)	Poisson ratio	References
Olivines							
Forsterite	129.8	84.4	3.32	8.54	5.04	0.23	[1–3]
“Olivine”	130	80	3.32	8.45	4.91	0.24	[54]
Garnets							
Almandine	176.3	95.2	4.18	8.51	4.77	0.27	[1]
Zircon	19.8	19.7	4.56	3.18	2.08	0.13	[4, 7]
Epidotes							
Epidote	106.5	61.1	3.40	7.43	4.24	0.26	[9]
Dravite	102.1	78.7	3.05	8.24	5.08	0.19	[4–6]
Pyroxenes							
Diopside	111.2	63.7	3.31	7.70	4.39	0.26	[8, 9]
Augite	94.1	57.0	3.26	7.22	4.18	0.25	[9]
	13.5	24.1	3.26	3.74	2.72	0.06	[10]
Sheet silicates							
Muscovite	61.5	41.1	2.79	6.46	3.84	0.23	[11]
	42.9	22.2	2.79	5.10	2.82	0.28	[55]
	52.0	30.9	2.79	5.78	3.33	0.25	[24]
Phlogopite	58.5	40.1	2.80	6.33	3.79	0.22	[11]
	40.4	13.4	2.80	4.56	2.19	0.35	[55]
Biotite	59.7	42.3	3.05	6.17	3.73	0.21	[11]
	41.1	12.4	3.05	4.35	2.02	0.36	[55]
Clays							
Kaolinite	1.5	1.4	1.58	1.44	0.93	0.14	[10]

“Gulf clays” (Han) ^a	25	9	2.55	3.81	1.88	0.34	[50, 53]
“Gulf clays” (Tosaya) ^a	21	7	2.6	3.41	1.64	0.35	[49, 53]
Mixed clays ^a				3.40	1.60		[49]
				3.41	1.63		[50]
				3.60	1.85		[51]
Montmorillonite– illite mixture ^a				4.32	2.54		[52]
Illite ^a							
Framework silicates							
Perthite	46.7	23.63	2.54	5.55	3.05	0.28	[54]
Plagioclase feldspar	75.6	25.6	2.63	6.46	3.12	0.35	[10]
(Albite)							
“Average”	37.5	15.0	2.62	4.68	2.39	0.32	
feldspar							
Quartz	37	44.0	2.65	6.05	4.09	0.08	[54]
	36.6	45.0	2.65	6.04	4.12	0.06	[14–16]
	36.5	45.6	2.65	6.06	4.15	0.06	[44]
	37.9	44.3	2.65	6.05	4.09	0.08	[47]
Quartz with clay (Han)	39	33.0	2.65	5.59	3.52	0.17	[50, 53]
Oxides							
Corundum	252.9	162.1	3.99	10.84	6.37	0.24	[17, 18]
Hematite	100.2	95.2	5.24	6.58	3.51	0.14	[19, 20]
	154.1	77.4	5.24	7.01	3.84	0.28	[10, 12]
Rutile	217.1	108.1	4.26	9.21	5.04	0.29	[21, 22]
Spinel	203.1	116.1	3.63	9.93	5.65	0.26	[1]

Table A.4.1 (cont.)

Mineral	Bulk modulus (GPa)	Shear modulus (GPa)	Density (g/cm ³)	V _P (km/s)	V _S (km/s)	Poisson ratio	References
Magnetite	161.4 59.2	91.4 18.7	5.20 4.81	7.38 4.18	4.19 1.97	0.26 0.36	[4, 23, 24] [10]
Hydroxides							
Limonite	60.1	31.3	3.55	5.36	2.97	0.28	[10]
Sulfides							
Pyrite	147.4 138.6	132.5 109.8	4.93 4.81	8.10 7.70	5.18 4.78	0.15 0.19	[25] [10]
Pyrrhotite	53.8	34.7	4.55	4.69	2.76	0.23	[10]
Sphalerite	75.2	32.3	4.08	5.38	2.81	0.31	[26, 27]
Sulfates							
Barite	54.5 58.9 53.0	23.8 22.8 22.3	4.51 4.43 4.50	4.37 4.49 4.29	2.30 2.27 2.22	0.31 0.33 0.32	[14] [28] [7]
Celestite	81.9 82.5	21.4 12.9	3.96 3.95	5.28 5.02	2.33 1.81	0.38 0.43	[4] [28]
Anhydrite	56.1 62.1 42.5	29.1 33.6 15.7	2.98 2.96 2.35	5.64 6.01 5.80	3.13 3.37	0.28 0.27	[30] [48] [29, 56, 57]
Gypsum			2.35	5.80			
Polyhalite			2.78	5.30			[31]
Carbonates							
Calcite	76.8 63.7 70.2 74.8 68.3 123.7	32.0 31.7 29.0 30.6 28.4 51.0	2.71 2.70 2.71 2.71 2.71 3.96	6.64 6.26 6.34 6.53 6.26 6.96	3.44 3.42 3.27 3.36 3.24 3.59	0.32 0.29 0.32 0.32 0.32 0.32	[14] [32] [33] [43] [44] [34]
Siderite							

Dolomite	94.9	45.0	2.87	7.34	3.96	0.30	[35]
	69.4	51.6	2.88	6.93	4.23	0.20	[13]
	76.4	49.7	2.87	7.05	4.16	0.23	[45]
Aragonite	44.8	38.8	2.92	5.75	3.64	0.16	[19, 20, 36]
Natronite	52.6	31.6	2.54	6.11	3.53	0.26	[53, 54]
Phosphates							
Hydroxyapatite	83.9	60.7	3.22	7.15	4.34	0.21	[4]
Fluorapatite	86.5	46.6	3.21	6.80	3.81	0.27	[37]
Fluorite	86.4	41.8	3.18	6.68	3.62	0.29	[38, 39]
Halite	24.8	14.9	2.16	4.55	2.63	0.25	[14, 40–42]
			2.16	4.50	2.59		[46]
Sylvite	17.4	9.4	1.99	3.88	2.18	0.27	[40]
Organic							
Kerogen	2.9	2.7	1.3	2.25	1.45	0.14	[53, 54]
Zeolites							
Narolite	46.6	28.0	2.25	6.11	3.53	0.25	[53, 54]

Note:

^a Clay velocities were interpreted by extrapolating empirical relations for mixed lithologies to 100% clay (Castagna *et al.*, 1993).

References: [1] Verma (1960); [2] Graham and Barsch (1969); [3] Kumazawa and Anderson (1969); [4] Hearmon (1956); [5] Mason (1950); [6] Voigt (1890); [7] Huntington (1958); [8] Ryzhova *et al.* (1966); [9] Alexandrov *et al.* (1964); [10] Woerber *et al.* (1963); [11] Alexandrov and Ryzhova (1961a); [12] Wyllie *et al.* (1956); [13] *Log Interpretation Charts* (1984); [14] Simmons (1965); [15] Mason (1943); [16] Koga *et al.* (1958); [17] Wachtman *et al.* (1960); [18] Bernstein (1963); [19] Hearmon (1946); [20] Voigt (1907); [21] Birch (1960a); [22] Joshi and Mitra (1960); [23] Doraiswami (1947); [24] Alexandrov and Ryzhova (1961b); [25] Simmons and Birch (1963); [26] Einspruch and Manning (1963); [27] Berlincourt *et al.* (1963); [28] Seshagiri Rao (1951); [29] Tixier and Alger (1967); [30] Schwerdtner *et al.* (1965); [31] *Formation Evaluation Data Handbook* (1982); [32] Bhimasenacher (1945); [33] Peselnick and Robie (1963); [34] Christensen (1972); [35] Humbert and Plicque (1972); [36] Birch (1960b); [37] Yoon and Newnham (1969); [38] Bergmann (1954); [39] Huffman and Norwood (1960); [40] Spangenburg and Haussuhl (1957); [41] Lazarus (1949); [42] Papadakis (1963); [43] Dandekar (1968); [44] Anderson and Liebermann (1966); [45] Nur and Simmonds (1969b); [46] Birch (1966); [47] McSkimin *et al.* (1965); [48] Rafavich *et al.* (1984); [49] Tosaya (1982); [50] Han *et al.* (1986); [51] Castagna *et al.* (1985); [52] Eastwood and Castagna (1986); [53] Blangy (1992); [54] Carmichael (1989); [55] Ellis *et al.* (1988); [56] Choy *et al.* (1979); [57] Bhalla *et al.* (1984).

Table A.4.2 *Moduli, densities and velocities of common minerals (compiled by Bass, 1995).*
Table A.4.2a *Elastic moduli of cubic crystals at room pressure and temperature.*

Material	ρ (Mg/m ³)	Subscript on c_{ij} (GPa)			K_S (GPa)	G (GPa)	Source
		11	44	12			
Elements, metallic compounds							
Au, gold	19.283	191	42.4	162	171.7	27.6	e
Ag, silver	10.500	122	45.4	92	102.0	29.2	e
C, diamond	3.512	1079	578	124	443.0	535.7	h
Cu, copper	8.932	169	75.3	122	137.3	46.9	d
Fe, α -iron	7.874	230	117	135	166.7	81.5	e
Binary oxides							
CaO, lime	3.346	224	80.6	60	114.7	81.2	d, l
Fe _{0.92} O, wustite	5.681	245.7	44.7	149.3	181.4	46.1	m
MgO, periclase	3.584	294	155	93	160.0	130.3	d
Spinel-structured oxides							
Fe ₃ O ₄ , magnetite	5.206	270	98.7	108	162.0	91.2	e
MgAl ₂ O ₄ , spinel	3.578	282.9	154.8	155.4	197.9	108.5	u
Sulfides							
FeS ₂ , pyrite	5.016	361	105.2	33.6	142.7	125.7	k
PbS, galena	7.597	127	23	24.4	58.6	31.9	e
ZnS, spalerite	4.088	102	44.6	64.6	77.1	31.5	e
Binary Halides							
CaF ₂ , fluorite	3.181	165	33.9	47	86.3	42.4	d
NaCl, halite	2.163	49.1	12.8	12.8	24.9	14.7	d
KCl, sylvite	1.987	40.5	6.27	6.9	18.1	9.4	d

Table A.4.2b Elastic moduli of hexagonal crystals at room pressure and temperature (Bass, 1995).

Material	ρ (Mg/m ³)	Subscript on c_{ij} (GPa)				K_S (GPa)	G (GPa)	Source
		11	33	44	12	13		
Be ₃ Al ₂ Si ₆ O ₁₈ , beryl	2.698	308.5	283.4	66.1	128.9	118.5	79.2	v
C, graphite	2.26	1060	36.5	0.3	180	15	109.3	b
Ice (257 K)	–	13.5	14.9	3.09	6.5	5.9	8.72	d
Ice (270 K)	0.9175	13.7	14.7	2.96	6.97	5.63	8.73	c

Table A.4.2c Elastic moduli of trigonal crystals (six moduli) at room pressure and temperature (Bass, 1995).

Material	ρ (Mg/m ³)	Subscript on c_{ij} (GPa)						K_S (GPa)	G (GPa)	Source
		11	33	44	12	13	14			
Al ₂ O ₃ , corundum	3.982	497	501	146.8	162	116	–21.9	253.5	163.2	i
CaCO ₃ , calcite	2.712	144	84.0	33.5	53.9	51.1	–20.5	73.3	32.0	d
Fe ₂ O ₃ , hematite	5.254							206.6	91.0	g
SiO ₂ , α -quartz	2.648	86.6	106.1	57.8	6.7	12.6	–17.8	37.8	44.3	d
Tourmaline	3.100	305.0	176.4	64.8	108	51	–6	127.2	81.5	j

Table A.4.2d Elastic moduli of trigonal crystals (seven moduli) at room pressure and temperature (Bass, 1995).

Material	ρ (Mg/m ³)	Subscript on c_{ij} (GPa)					K_S (GPa)	G (GPa)	Source
		11	33	44	12	13	14	15	
Dolomite, CaMg(CO ₃) ₂	3.795	205	113	39.8	71.0	57.4	-19.5	13.7	d, f

Table A.4.2e Elastic moduli of tetragonal crystals (six moduli) at room pressure and temperature (Bass, 1995).

Material	ρ (Mg/m ³)	Subscript on c_{ij} (GPa)						K_S (GPa)	G (GPa)	Source
		11	33	44	66	12	13			
SiO ₂ , stishovite	4.290	453	776	252	302	211	203	316	220	r
SiO ₂ , α -cristobalite	2.335	59.4	42.4	67.2	25.7	3.8	-4.4	16.4	39.1	t

Table A.4.2f Elastic moduli of orthorhombic crystals (nine moduli) at room pressure and temperature (Bass, 1995).

Material	ρ (Mg/m ³)	Subscript on c_{ij} (GPa)								K_s (GPa)	G (GPa)	Source	
		11	22	33	44	55	66	12	13				23
MgSiO ₃	4.108	515	525	435	179	202	175	117	117	139	246.4	184.2	s
NaMgF ₃	3.058	126	147	143	47	45	50	50	45	43	75.7	46.7	w
Enstatite, MgSiO ₃	3.198	225	178	214	78	76	82	72	54	53	107.8	75.7	q
Ferrosilite, FeSiO ₃	4.002	198	136	175	59	58	49	84	72	55	101	52	a
Al ₂ SiO ₅ , andalusite	3.145	233	289	380	100	88	112	98	116	81	162	99.1	o
Al ₂ SiO ₅ , sillimanite	3.241	287	232	388	122	81	89	159	83	95	170.8	91.5	o
Sulfur	2.065	24	21	48	4.3	8.7	7.6	13.3	17.1	15.9	19.1	6.7	d
BaSO ₄ , barite	4.473	89	81	107	12	28	27	48	32	30	55.0	22.8	d
CaSO ₄ , anhydrite	2.963	93.8	185	112	33	27	9.3	17	15	32	54.9	29.3	d
CaCO ₃ , aragonite	2.930	160	87	85	41	26	43	37	1.7	16	46.9	38.5	d

Table A.4.2g Elastic moduli of monoclinic crystals at room pressure and temperature (Bass, 1995).

Material	ρ (Mg/m ³)	Subscript on c_{ij} (GPa)												K_S (GPa)	G (GPa)	Source	
		11	22	33	44	55	66	12	13	23	15	25	35				46
Feldspars																	
NaAlSi ₃ O ₈ , albite		74	131	128	17	30	32	36	39	31	-6.6	-13	-20	-2.5	56.9	28.6	d
CaAl ₂ Si ₂ O ₈ , anorthite		124	205	156	24	40	42	66	50	42	-19	-7	-18	-1	84.2	39.9	e
labradorite		99	158	150	22	35	37	63	49	27	-2.5	-11	-12	-5.4	74.5	33.7	e
KAlSi ₃ O ₈ , microcline		67	169	118	14	24	36	45	27	20	-0.2	-12	-15	-1.9	55.4	28.1	e
KAlSi ₃ O ₈ , oligoclase		81	163	124	19	27	36	38	53	33	-16	-24	-6	-0.9	62.0	29.3	e
Silicates																	
SiO ₂ , coesite	2.911	161	230	232	68	73	59	82	103	36	-36	2.6	-39	9.9	113.7	61.6	p
KAl ₃ Si ₃ O ₁₀ (OH) ₂ , muscovite	2.844	184	178	59	16	18	72	48	24	22	-2	3.9	1.2	0.5	58.2	35.3	n
Sulfides, sulfates																	
CaSO ₄ , gypsum	2.317	94.5	65.2	50.2	8.6	32	11	38	28	32	-11	6.9	-7.5	-1.1	42.5	15.7	d

References: a, Bass (1984); b, Blaklee *et al.* (1970); c, Gammon *et al.* (1980); d, Hearmon (1979); e, Hearmon (1984); f, Humbert and Plique (1972); g, Liebermann and Schreiber (1968); h, McSkimin and Bond (1972); i, Ohno *et al.* (1986); j, Ozkan and Jamieson (1978); k, Simmons and Birch (1963); l, Soga (1967); m, Sumino *et al.* (1980); n, Vaughan and Guggenheim (1986); o, Verma (1960); p, Weidner and Carleton (1977); q, Weidner and Hamaya (1983); r, Weidner *et al.* (1982); s, Yeganeh-Haeri *et al.* (1989); t, Yeganeh-Haeri *et al.* (1992); u, Yoneda (1990); v, Yoon and Newham (1973); w, Zhao and Weidner (1993).

Table A.5.1 *Regressions of velocities, Poisson’s ratio and dynamic elastic moduli versus temperature (–20 to –5 °C) and piston pressure (3250–4750 psi) in compacted, polycrystalline ice. $F(T, P) = aT + bP + c$.*

$F(T, P)$	a	b	c	std
V_P (m/s)	-2.80 ± 0.01	$(1.98 \pm 0.11) \times 10^{-3}$	3870.1 ± 0.5	0.9
V_S (m/s)	-1.31 ± 0.01	$-(1.83 \pm 0.07) \times 10^{-3}$	1949.3 ± 0.3	0.6
ν	$-(2.0 \pm 0.2) \times 10^{-5}$	$(6.4 \pm 0.2) \times 10^{-7}$	0.3301 ± 0.0001	0.0002
M (GPa)	$-(2.01 \pm 0.01) \times 10^{-2}$	$(1.41 \pm 0.08) \times 10^{-5}$	13.748 ± 0.003	0.007
G (GPa)	$-(4.72 \pm 0.02) \times 10^{-3}$	$-(6.6 \pm 0.3) \times 10^{-6}$	3.488 ± 0.001	0.002
K (GPa)	$-(1.38 \pm 0.01) \times 10^{-2}$	$(2.30 \pm 0.09) \times 10^{-5}$	9.097 ± 0.004	0.008

Table A.5.2 *Regressions of velocities, Poisson’s ratio and dynamic elastic moduli versus temperature (–15 to 15 °C) and piston pressure (4000–9000 psi) in compacted, polycrystalline methane hydrate. $F(T, P) = aT + bP + c$.*

$F(T, P)$	a	b	c	std
V_P (m/s)	-2.27 ± 0.01	$(2.52 \pm 0.07) \times 10^{-3}$	3778.0 ± 0.6	2
V_S (m/s)	-1.04 ± 0.01	$-(1.08 \pm 0.03) \times 10^{-3}$	1963.6 ± 0.3	1
ν	0	$(6.83 \pm 0.06) \times 10^{-7}$	$0.314\,03 \pm 0.000\,05$	0.0003
M (GPa)	$-(1.47 \pm 0.01) \times 10^{-2}$	$(1.99 \pm 0.05) \times 10^{-5}$	13.527 ± 0.004	0.02
G (GPa)	$-(3.77 \pm 0.03) \times 10^{-3}$	$-(3.9 \pm 0.1) \times 10^{-6}$	3.574 ± 0.001	0.004
K (GPa)	$-(9.71 \pm 0.06) \times 10^{-3}$	$(2.51 \pm 0.03) \times 10^{-5}$	8.762 ± 0.003	0.01

A.6 Physical properties of common gases

Compiled from American Air Liquid, on-line gas data, <http://www.airliquide.com>.

Air

Normal composition of dry air

- 78.09% N₂, 20.94% O₂, 0.93% Ar.

Molecular weight

- Molecular weight: 28.95 g/mol.

Density

- Density of air at 1 atm of pressure is 1.291 kg/m³ at 0 °C or 1.222 kg/m³ at 15.6 °C.

Bulk modulus

- Bulk modulus of air at 1 atm of pressure is 1.01 bar = 0.101 MPa.

Critical point

- Critical temperature: -140.5 °C.
- Critical pressure: 37.71 bar.

Gaseous phase

- Gas density (1.013 bar at boiling point): 3.2 kg/m³.
- Gas density (1.013 bar and 15 °C): 1.202 kg/m³.
- Compressibility factor (*Z*) (1.013 bar and 15 °C): 0.9992.
- Specific gravity (air = 1) (1.013 bar and 21 °C): 1.
- Specific volume (1.013 bar and 21 °C): 0.833 m³/kg.
- Heat capacity at constant pressure (*C_p*) (1.013 bar and 21 °C): 0.029 kJ/(mol K).
- Heat capacity at constant volume (*C_v*) (1.013 bar and 21 °C): 0.02 kJ/(mol K).
- Ratio of specific heats (*Gamma*: *C_p*/*C_v*) (1.013 bar and 21 °C): 1.4028.
- Viscosity (1 bar and 0 °C): 0.0001695 Poise.
- Thermal conductivity (1.013 bar and 0 °C): 23.94 mW/(m K).

Miscellaneous

- Solubility in water (1.013 bar and 0 °C): 0.0292 vol/vol.

Carbon dioxide (CO₂)**Molecular weight**

- Molecular weight: 44.01 g/mol.

Solid phase

- Latent heat of fusion (1013 bar, at triple point): 196.104 kJ/kg.
- Solid density: 1562 kg/m³.

Liquid phase

- Liquid density (at -20 °C and 19.7 bar): 1032 kg/m³.
- Liquid/gas equivalent (1.013 bar and 15 °C (per kg of solid)): 845 vol/vol.
- Boiling point (sublimation): -78.5 °C.
- Latent heat of vaporization (1.013 bar at boiling point): 571.08 kJ/kg.
- Vapor pressure (at 20 °C): 58.5 bar.

Critical point

- Critical temperature: 31 °C.
- Critical pressure: 73.825 bar.
- Critical density: 464 kg/m³.

Triple point

- Triple point temperature: -56.6 °C.
- Triple point pressure: 5.185 bar.

Gaseous phase

- Gas density (1.013 bar at sublimation point): 2.814 kg/m³.
- Gas density (1.013 bar and 15 °C): 1.87 kg/m³.
- Compressibility factor (Z) (1.013 bar and 15 °C): 0.9942.
- Specific gravity (air = 1) (1.013 bar and 21 °C): 1.521.
- Specific volume (1.013 bar and 21 °C): 0.547 m³/kg.
- Heat capacity at constant pressure (C_p) (1.013 bar and 25 °C): 0.037 kJ/(mol K).
- Heat capacity at constant volume (C_v) (1.013 bar and 25 °C): 0.028 kJ/(mol K).
- Ratio of specific heats (Gamma: C_p/C_v) (1.013 bar and 25 °C): 1.293759.
- Viscosity (1.013 bar and 0 °C): 0.0001372 Poise.
- Thermal conductivity (1.013 bar and 0 °C): 14.65 mW/(m K).

Miscellaneous

- Solubility in water (1.013 bar and 0 °C): 1.7163 vol/vol.
- Concentration in air: 0.03 vol %.

Ethane (C₂H₆)**Molecular weight**

- Molecular weight: 30.069 g/mol.

Critical point

- Critical temperature: 32.2 °C.
- Critical pressure: 48.839 bar.

Gaseous phase

- Gas density (1.013 bar at boiling point): 2.054 kg/m³.
- Gas density (1.013 bar and 15 °C): 1.282 kg/m³.
- Compressibility factor (Z) (1.013 bar and 15 °C): 0.9912.
- Specific gravity (air = 1) (1.013 bar and 15 °C): 1.047.
- Specific volume (1.013 bar and 21 °C): 0.799 m³/kg.
- Heat capacity at constant pressure (C_p) (1 bar and 25 °C): 0.053 kJ/(mol K).
- Heat capacity at constant volume (C_v) (1 bar and 25 °C): 0.044 kJ/(mol K).
- Ratio of specific heats (Gamma: C_p/C_v) (1 bar and 25 °C): 1.193 258.
- Viscosity (1.013 bar and 0 °C (32 °F)): 0.0000855 Poise.
- Thermal conductivity (1.013 bar and 0 °C): 18 mW/(m K).

Miscellaneous

- Solubility in water (1.013 bar and 20 °C): 0.052 vol/vol.
- Autoignition temperature: 515 °C.

Methane (CH₄)**Molecular weight**

- Molecular weight: 16.043 g/mol.

Critical point

- Critical temperature: −82.7 °C.
- Critical pressure: 45.96 bar.

Gaseous phase

- Gas density (1.013 bar at boiling point): 1.819 kg/m³.
- Gas density (1.013 bar and 15 °C): 0.68 kg/m³.
- Compressibility factor (Z) (1.013 bar and 15 °C): 0.998.
- Specific gravity (air = 1) (1.013 bar and 21 °C): 0.55.
- Specific volume (1.013 bar and 21 °C): 1.48 m³/kg.
- Heat capacity at constant pressure (C_p) (1 bar and 25 °C): 0.035 kJ/(mol K).
- Heat capacity at constant volume (C_v) (1 bar and 25 °C): 0.027 kJ/(mol K).
- Ratio of specific heats (Gamma: C_p/C_v) (1 bar and 25 °C): 1.305 454.
- Viscosity (1.013 bar and 0 °C): 0.0001027 Poise.
- Thermal conductivity (1.013 bar and 0 °C): 32.81 mW/(m K).

Miscellaneous

- Solubility in water (1.013 bar and 2 °C): 0.054 vol/vol.
- Autoignition temperature: 595 °C.

Helium (He)

Molecular weight

- Molecular weight: 4.0026 g/mol.

Critical point

- Critical temperature: $-268\text{ }^{\circ}\text{C}$.
- Critical pressure: 2.275 bar.
- Critical density: 69.64 kg/m^3 .

Gaseous phase

- Gas density (1.013 bar at boiling point): 16.891 kg/m^3 .
- Gas density (1.013 bar and $15\text{ }^{\circ}\text{C}$): 0.169 kg/m^3 .
- Compressibility factor (Z) (1.013 bar and $15\text{ }^{\circ}\text{C}$): 1.0005.
- Specific gravity (air = 1) (1.013 bar and $21\text{ }^{\circ}\text{C}$): 0.138.
- Specific volume (1.013 bar and $21\text{ }^{\circ}\text{C}$): $6.037\text{ m}^3/\text{kg}$.
- Heat capacity at constant pressure (C_p) (1 bar and $25\text{ }^{\circ}\text{C}$): $0.02\text{ kJ}/(\text{mol K})$.
- Heat capacity at constant volume (C_v) (1 bar and $25\text{ }^{\circ}\text{C}$): $0.012\text{ kJ}/(\text{mol K})$.
- Ratio of specific heats (γ : C_p/C_v) (1 bar and $25\text{ }^{\circ}\text{C}$): 1.664.
- Viscosity (1.013 bar and $0\text{ }^{\circ}\text{C}$): 0.0001863 Poise .
- Thermal conductivity (1.013 bar and $0\text{ }^{\circ}\text{C}$): $142.64\text{ mW}/(\text{m K})$.

Miscellaneous

- Solubility in water ($20\text{ }^{\circ}\text{C}$ and 1 bar): 0.0089 vol/vol .

Hydrogen (H_2)

Molecular weight

- Molecular weight: 2.016 g/mol.

Critical point

- Critical temperature: $-240\text{ }^{\circ}\text{C}$.
- Critical pressure: 12.98 bar.
- Critical density: 30.09 kg/m^3 .

Triple point

- Triple point temperature: $-259.3\text{ }^{\circ}\text{C}$.
- Triple point pressure: 0.072 bar.

Gaseous phase

- Gas density (1.013 bar at boiling point): 1.312 kg/m^3 .
- Gas density (1.013 bar and $15\text{ }^{\circ}\text{C}$): 0.085 kg/m^3 .
- Compressibility factor (Z) (1.013 bar and $15\text{ }^{\circ}\text{C}$): 1.001.
- Specific gravity (air = 1) (1.013 bar and $21\text{ }^{\circ}\text{C}$): 0.0696.
- Specific volume (1.013 bar and $21\text{ }^{\circ}\text{C}$): $11.986\text{ m}^3/\text{kg}$.

- Heat capacity at constant pressure (C_p) (1 bar and 25 °C): 0.029 kJ/(mol K).
- Heat capacity at constant volume (C_v) (1 bar and 25 °C): 0.021 kJ/(mol K).
- Ratio of specific heats (Gamma: C_p/C_v) (1 bar and 25 °C): 1.384 259.
- Viscosity (1.013 bar and 15 °C): 0.000 0865 Poise.
- Thermal conductivity (1.013 bar and 0 °C): 168.35 mW/(m K).

Miscellaneous

- Solubility in water (1.013 bar and 0 °C): 0.0214 vol/vol.
- Concentration in air: 0.0000005 vol/vol.
- Autoignition temperature: 560 °C.

Nitrogen (N₂)

Molecular weight

- Molecular weight: 28.0134 g/mol.

Critical point

- Critical temperature: −147 °C.
- Critical pressure: 33.999 bar.
- Critical density: 314.03 kg/m³.

Triple point

- Triple point temperature: −210.1 °C.
- Triple point pressure: 0.1253 bar.

Gaseous phase

- Gas density (1.013 bar at boiling point): 4.614 kg/m³.
- Gas density (1.013 bar and 15 °C): 1.185 kg/m³.
- Compressibility factor (Z) (1.013 bar and 15 °C): 0.9997.
- Specific gravity (air = 1) (1.013 bar and 21 °C): 0.967.
- Specific volume (1.013 bar and 21 °C): 0.862 m³/kg.
- Heat capacity at constant pressure (C_p) (1.013 bar and 25 °C): 0.029 kJ/(mol K).
- Heat capacity at constant volume (C_v) (1.013 bar and 25 °C): 0.02 kJ/(mol K).
- Ratio of specific heats (Gamma: C_p/C_v) (1.013 bar and 25 °C): 1.403 846.
- Viscosity (1.013 bar and 0 °C): 0.0001657 Poise.
- Thermal conductivity (1.013 bar and 0 °C): 24 mW/(m K).

Miscellaneous

- Solubility in water (1.013 bar and 0 °C): 0.0234 vol/vol.
- Concentration in air: 0.7808 vol/vol.

Oxygen (O₂)

Molecular weight

- Molecular weight: 31.9988 g/mol.

Critical point

- Critical temperature: -118.6°C .
- Critical pressure: 50.43 bar.
- Critical density: 436.1 kg/m^3 .

Triple point

- Triple point temperature: -218.8°C .
- Triple point pressure: 0.001 52 bar.

Gaseous phase

- Gas density (1.013 bar at boiling point): 4.475 kg/m^3 .
- Gas density (1.013 bar and 15°C): 1.354 kg/m^3 .
- Compressibility factor (Z) (1.013 bar and 15°C): 0.9994.
- Specific gravity (air = 1) (1.013 bar and 21°C): 1.105.
- Specific volume (1.013 bar and 21°C): $0.755\text{ m}^3/\text{kg}$.
- Heat capacity at constant pressure (C_p) (1 bar and 25°C): $0.029\text{ kJ}/(\text{mol K})$.
- Heat capacity at constant volume (C_v) (1 bar and 25°C): $0.021\text{ kJ}/(\text{mol K})$.
- Ratio of specific heats (Gamma: C_p/C_v) (1 bar and 25°C): 1.393 365.
- Viscosity (1.013 bar and 0°C): 0.0001909 Poise.
- Thermal conductivity (1.013 bar and 0°C): $24.24\text{ mW}/(\text{m K})$.

Miscellaneous

- Solubility in water (1.013 bar and 0°C): 0.0489 vol/vol.
- Concentration in air: 0.2094 vol/vol.

A.7 Velocity, moduli, and density of carbon dioxide

Tables A.7.1–A.7.3 summarize velocities, densities, and moduli for CO₂ as functions of temperature and pressure. Z. Wang (Wang, 2000a) provided the data. Bold numerals are actual measurements, while others are interpolations.

A.8 Standard temperature and pressure

There is a wide variation in definition of standard temperature and pressure (STP). Table A.8.1 lists some in current use (compiled from Wikipedia:http://en.wikipedia.org/wiki/Standard_conditions_for_temperature_and_pressure).

Table A.7.1 *Velocity for CO₂ as a function of temperature and pressure.*

Velocities (m/s)		T (°C)											P (MPa)
P (psi)		17	27	37	47	57	67	77	87	97	107	117	127
14.5	264	268	272	276	280	284	288	291	295	299	302	306	0.10
145	256	261	266	270	275	279	284	288	292	296	300	304	1.00
580	220	231	241	251	259	264	271	276	281	287	292	296	4.00
1015	379	185	209	219	237	252	263	270	276	282	285	290	7.00
1450	483	411	142	183	212	238	249	257	265	272	278	286	10.01
2030	554	496	366	269	247	248	255	260	269	278	285	291	14.01
2900	637	586	502	441	382	358	353	345	337	328	320	314	20.01
3625	688	640	591	538	488	460	431	413	397	382	366	352	25.01
4350	737	687	641	596	552	521	494	470	450	429	412	397	30.02
5800	814	766	714	676	639	615	592	564	545	526	504	487	40.02

Table A.7.2 *Density for CO₂ as a function of temperature and pressure.*

Densities (kg/m ³)		T (°C)										P (MPa)	
P (psi)		17	27	37	47	57	67	77	87	97	107	117	127
14.5	1.86	1.80	1.74	1.68	1.63	1.58	1.54	1.49	1.45	1.41	1.38	1.34	0.10
145	19.63	18.84	18.13	17.48	16.88	16.32	15.80	15.31	14.86	14.44	14.04	13.66	1.00
580	129.00	93.95	87.09	81.69	77.24	73.45	70.13	67.19	64.54	62.15	60.00	57.97	4.00
1015	830.00	680.00	200.72	182.83	163.62	149.60	139.28	130.94	123.91	117.86	112.75	107.94	7.00
1450	917.00	805.00	683.00	449.73	327.61	267.15	235.50	213.81	197.32	184.22	174.09	164.43	10.01
2030	930.00	860.00	780.00	690.00	570.00	480.00	390.00	335.00	300.00	275.00	252.00	235.00	14.01
2900	960.00	910.00	860.00	800.00	740.00	680.00	620.00	560.00	510.00	470.00	420.00	390.00	20.01
3625	990.00	950.00	900.00	850.00	790.00	750.00	700.00	640.00	590.00	550.00	510.00	480.00	25.01
4350	1008.00	970.00	930.00	890.00	850.00	810.00	770.00	720.00	680.00	630.00	600.00	570.00	30.02
5800	1040.00	1000.00	970.00	940.00	900.00	870.00	840.00	800.00	770.00	730.00	700.00	670.00	40.02

Table A.7.3 Bulk modulus for CO₂ as a function of temperature and pressure.

Bulk moduli (GPa)		T (°C)										P (MPa)		
P (psi)		17	27	37	47	57	67	77	87	97	107	117	127	
14.5	0.000 13	0.000 13	0.000 13	0.000 13	0.000 13	0.000 13	0.000 13	0.000 13	0.000 13	0.000 13	0.000 13	0.000 13	0.000 13	0.10
145	0.001 29	0.001 28	0.001 28	0.001 28	0.001 28	0.001 28	0.001 27	0.001 27	0.001 27	0.001 27	0.001 26	0.001 26	0.001 26	1.00
580	0.006 24	0.005 01	0.005 04	0.005 13	0.005 18	0.005 18	0.005 14	0.005 17	0.005 17	0.005 10	0.005 10	0.005 11	0.005 07	4.00
1015	0.119 22	0.023 27	0.008 73	0.008 79	0.009 23	0.009 51	0.009 51	0.009 65	0.009 65	0.009 55	0.009 41	0.009 37	0.009 16	7.00
1450	0.213 93	0.135 98	0.015 99	0.012 82	0.014 69	0.015 20	0.014 60	0.014 60	0.014 12	0.013 86	0.013 63	0.013 46	0.013 41	10.01
2030	0.285 43	0.211 57	0.104 49	0.049 93	0.034 78	0.029 52	0.025 36	0.022 65	0.022 65	0.021 71	0.021 25	0.020 47	0.019 90	14.01
2900	0.389 54	0.312 49	0.216 72	0.155 58	0.107 98	0.087 15	0.077 26	0.066 65	0.066 65	0.057 92	0.050 56	0.043 01	0.038 45	20.01
3625	0.468 61	0.389 12	0.314 35	0.246 03	0.188 13	0.158 70	0.130 03	0.109 16	0.109 16	0.092 99	0.080 26	0.068 32	0.059 47	25.01
4350	0.547 51	0.457 81	0.382 12	0.316 14	0.259 00	0.219 87	0.187 91	0.187 91	0.159 05	0.137 70	0.115 95	0.101 85	0.089 84	30.02
5800	0.689 10	0.586 76	0.494 50	0.429 56	0.367 49	0.329 06	0.294 39	0.254 48	0.254 48	0.228 71	0.201 97	0.177 81	0.158 90	40.02

Table A.8.1 *Variable definitions of standard temperature and pressure.*

Temperature (°C)	Absolute pressure (kPa)	Publishing or establishing entity
0	100.000	International Union of Pure and Applied Chemistry
0	101.325	National Institute of Standards and Technology International Organization for Standardization
15	101.325	ICAO's International Standard Atmosphere International Organization for Standardization European Environment Agency Electricity and Gas Inspection Act of Canada
20	101.325	U.S. Environmental Protection Agency National Institute of Standards and Technology
25	101.325	U.S. Environmental Protection Agency
25	100.000	Standard Ambient Pressure and Temperature
20	100.000	Compressed Air and Gas Institute
15	100.000	Society of Petroleum Engineers

References

- Achenbach, J.D., 1984. *Wave Propagation in Elastic Solids*. Amsterdam: Elsevier Science Publication.
- Aki, K. and Richards, P.G., 1980. *Quantitative Seismology: Theory and Methods*. San Francisco, CA: W. H. Freeman and Co.
- Aleksandrov, K.S. and Ryzhova, T.V., 1961a. Elastic properties of rock-forming minerals II. Layered silicates. *Bull. Acad. Sci. USSR, Geophys. Ser.* English translation no. **12**, 1165–1168.
- Alexandrov, K.S. and Ryzhova, T.V., 1961b. The elastic properties of crystals. *Sov. Phys. Crystallogr.*, **6**, 228–252.
- Alexandrov, K.S., Ryzhova, T.V., and Belikov, B.P., 1964. The elastic properties of pyroxenes. *Sov. Phys. Crystallog.*, **8**, 589–591.
- Alkalifah, T. and Tsvankin, I., 1995. Velocity analysis for transversely isotropic media. *Geophys.*, **60**, 1550–1566.
- Anderson, O.L. and Liebermann, R.C., 1966. Sound velocities in rocks and minerals. *VESIAC State-of-the-Art Report No. 7885-4-x*, University of Michigan.
- Angel, Y.C. and Achenbach, J.D., 1985. Reflection and transmission of elastic waves by aperiodic array of cracks. *J. Appl. Mech.*, **52**, 33–41.
- Archie, G.E., 1942. The electrical resistivity log as an aid in determining some reservoir characteristics. *Trans. Am. Inst. Mech. Eng.*, **146**, 54–62.
- Auld, B.A., 1990. *Acoustic Fields and Waves in Solids*, vols. 1, 2. Malabar, FL: Robert E. Krieger Publication Co.
- Backus, G.E., 1962. Long-wave elastic anisotropy produced by horizontal layering. *J. Geophys. Res.*, **67**, 4427–4440.
- Bakulin, A., 2003. Intrinsic and layer-induced vertical transverse isotropy. *Geophys.*, **68**, 1708–1713.
- Bakulin, A. and Grechka, V., 2003. Effective anisotropy of layered media. *Geophys.*, **68**, 1817–1821.
- Bakulin, A., Grechka, V., and Tsvankin, I., 2000. Estimation of fracture parameters from reflection seismic data – Part I: HTI model due to a single fracture set. *Geophys.*, **65**, 1788–1802.
- Bakulin, V. and Bakulin, A., 1999. Acoustopolarizational method of measuring stress in rock mass and determination of Murnaghan constants. In *69th Annual International Meeting, SEG, Expanded Abstracts*, pp. 1971–1974.
- Banik, N.C., 1987. An effective anisotropy parameter in transversely isotropic media. *Geophys.*, **52**, 1654.
- Banik, N.C., Lerche, I., and Shuey, R.T., 1985. Stratigraphic filtering, Part I: Derivation of the O'Doherty–Anstey formula. *Geophys.*, **50**, 2768–2774.
- Bardis, S.C., Lumsden, A.C., and Barton, N.L., 1983. Fundamentals of rock joint deformation. *Int. J. Rock Mech.*, **20**, 249–268.

- Bass, J.D., 1984. Elasticity of single-crystal orthoferrosilite. *J. Geophys. Res.*, **89**, 4359–4371.
- Batzle, M. and Wang, Z., 1992. Seismic properties of pore fluids. *Geophys.*, **57**, 1396–1408.
- Bear, J., 1972. *Dynamics of Fluids in Porous Media*. Mineola, NY: Dover Publications, Inc.
- Belikov, B.P., Alexandrov, T.W., and Rysova, T.W., 1970. *Elastic Properties of Rock Minerals and Rocks*. Moscow: Nauka.
- Beltzer, A.I., 1988. *Acoustics of Solids*. Berlin: Springer-Verlag.
- Ben-Menahem, A. and Singh, S., 1981. *Seismic Waves and Sources*. New York: Springer-Verlag.
- Beran, M.J., 1968. *Statistical Continuum Theories*. New York: Wiley Interscience.
- Beran, M.J. and Molyneux, J., 1966. Use of classical variational principles to determine bounds for the effective bulk modulus in heterogeneous media. *Quart. Appl. Math.*, **24**, 107–118.
- Berge, P.A., Fryer, G.J., and Wilkens, R.H., 1992. Velocity–porosity relationships in the upper oceanic crust: theoretical considerations. *J. Geophys. Res.*, **97**, 15239–15254.
- Berge, P.A., Berryman, J.G., and Bonner, B.P., 1993. Influence of microstructure on rock elastic properties. *Geophys. Res. Lett.*, **20**, 2619–2622.
- Bergmann, L., 1954. *Der Ultraschall und seine Anwendung in Wissenschaft und Technik*. Zurich: S. Hirzel.
- Berlincourt, D., Jaffe, H., and Shiozawa, L.R., 1963. Electroelastic properties of the sulfides, selenides, and tellurides of Zn and Cd. *Phys. Rev.*, **129**, 1009–1017.
- Bernal, J.D. and Mason, J., 1960. Coordination of randomly packed spheres. *Nature*, **188**, 910–911.
- Bernstein, B.T., 1963. Elastic constants of synthetic sapphire at 27 degrees Celsius. *J. Appl. Phys.*, **34**, 169–172.
- Berryman, J.G., 1980a. Confirmation of Biot's theory. *Appl. Phys. Lett.*, **37**, 382–384.
- Berryman, J.G., 1980b. Long-wavelength propagation in composite elastic media. *J. Acoust. Soc. Am.*, **68**, 1809–1831.
- Berryman, J.G., 1981. Elastic wave propagation in fluid-saturated porous media. *J. Acoust. Soc. Am.*, **69**, 416–424.
- Berryman, J.G., 1983. Dispersion of extensional waves in fluid-saturated porous cylinders at ultrasonic frequencies. *J. Acoust. Soc. Am.*, **74**, 1805–1812.
- Berryman, J.G., 1992a. Effective stress for transport properties of inhomogeneous porous rock. *J. Geophys. Res.*, **97**, 17409–17424.
- Berryman, J.G., 1992b. Single-scattering approximations for coefficients in Biot's equations of poroelasticity. *J. Acoust. Soc. Am.*, **91**, 551–571.
- Berryman, J.G., 1993. Effective stress rules for pore-fluid transport in rocks containing two minerals. *Int. J. Rock Mech.*, **30**, 1165–1168.
- Berryman, J.G., 1995. Mixture theories for rock properties. In *Rock Physics and Phase Relations: a Handbook of Physical Constants*, ed. T.J. Ahrens. Washington, DC: American Geophysical Union, pp. 205–228.
- Berryman, J.G., 2008. Exact seismic velocities for transversely isotropic media and extended Thomsen formulas for stronger anisotropies. *Geophys.*, **73**, D1–D10.
- Berryman, J.G. and Milton, G.W., 1988. Microgeometry of random composites and porous media. *J. Physics D*, **21**, 87–94.
- Berryman, J.G. and Milton, G.W., 1991. Exact results for generalized Gassmann's equation in composite porous media with two constituents. *Geophys.*, **56**, 1950–1960.
- Berryman, J.G., Pride, S.R., and Wang, H.F., 1992. A differential scheme for elastic properties of rocks with dry or saturated cracks. In *Proc. 15th ASCE Engineering Mechanics Conference*.
- Berryman, J.G., Grechka, V.Y., and Berge, P., 1999. Analysis of Thomsen parameters for finely layered VTI media. *Geophys. Prospect.*, **47**, 959–978.

- Bhalla, A.S., Cook, W.R., Hearmon, R.F.S., *et al.*, 1984. Elastic, piezoelectric, pyroelectric, piezooptic, electrooptic constants, and nonlinear dielectric susceptibilities of crystals. In *Landolt-Börnstein: Numerical Data and Functional Relationships in Science and Technology. Group III: Crystal and Solid State Physics*, vol. 18 (supplement to vol. III/11), ed. K.-H. Hellwege and A.M. Hellwege. Berlin: Springer-Verlag.
- Bhimasenacher, J., 1945. Elastic constants of calcite and sodium nitrate. *Proc. Ind. Acad. Sci. A*, **22**, 199–207.
- Bilodeaux, B., 1997. *Shaley Sand Evaluation*, course notes. Stanford University.
- Biot, M.A., 1956. Theory of propagation of elastic waves in a fluid saturated porous solid. I. Low frequency range and II. Higher-frequency range. *J. Acoust. Soc. Am.*, **28**, 168–191.
- Biot, M.A., 1962. Mechanics of deformation and acoustic propagation in porous media. *J. Appl. Phys.*, **33**, 1482–1498.
- Biot, M.A. and Willis, D.G., 1957. The elastic coefficients of the theory of consolidation. *J. App. Mech.*, **24**, 594–601.
- Birch, F., 1960a. Elastic constants of rutile – a correction to a paper by R.K. Verma, “Elasticity of some high-density crystals.” *J. Geophys. Res.*, **65**, 3855–3856.
- Birch, F., 1960b. The velocity of compressional waves in rocks to 10 kilobars. *J. Geophys. Res.*, **65**, 1083–1102.
- Birch, F., 1961. The velocity of compressional waves in rocks to 10 kilobars, Part 2. *J. Geophys. Res.*, **66**, 2199–2224.
- Birch, F., 1966. Compressibility; elastic constants. In *Handbook of Physical Constants*, ed. S.P. Clark, Geolog. Soc. Am., Memoir, vol. **97**, pp. 97–174.
- Bishop, C.M., 2006. *Pattern Recognition and Machine Learning*. New York: Springer-Verlag.
- Blair, D.P., 1990. A direct comparison between vibrational resonance and pulse transmission data for assessment of seismic attenuation in rock. *Geophys.*, **55**, 51–60.
- Blakslée, O.L., Proctor, D.G., Seldin, E.J., Sperce, G.B., and Werg, T., 1970. Elastic constants of compression-annealed pyrolytic graphite. *J. Appl. Phys.*, **41**, 3373–3382.
- Blangy, J.P., 1992. *Integrated Seismic Lithologic Interpretation: the Petrophysical Basis*. Ph.D. dissertation, Stanford University.
- Boggs, S., 2001. *Principles of Sedimentology and Stratigraphy*. Upper Saddle River, NJ: Prentice-Hall.
- Born, M. and Wolf, E., 1980. *Principles of Optics*, 6th edn. Oxford: Pergamon Press.
- Bortfeld, R., 1961. Approximation to the reflection and transmission coefficients of plane longitudinal and transverse waves. *Geophys. Prospecting*, **9**, 485–503.
- Bourbié, T., Coussy, O., and Zinszner, B., 1987. *Acoustics of Porous Media*. Houston, TX: Gulf Publishing Co.
- Bowers, G.L., 1995. Pore pressure estimation from velocity data: accounting for pore pressure mechanisms besides undercompaction. *SPE Drilling and Completion* (June), 89–95.
- Boyse, W.E., 1986. *Wave Propagation and Inversion in Slightly Inhomogeneous Media*. Ph.D. dissertation, Stanford University.
- Bracewell, R., 1965. *The Fourier Transform and Its Application*. New York: McGraw-Hill Book Co.
- Bradford, I.D.R., Fuller, J., Thompson, P.J., and Walsgrove, T.R., 1998. *Benefits of assessing the solids production risk in a North Sea reservoir using elastoplastic modeling: SPE/ISRM 47360*. Papers presented at the *SPE/ISRM Eurock '98*, Trondheim, Norway, 8–10 July, pp. 261–269.
- Bradley, W.B., 1979. Failure of inclined boreholes. *J. Energy Resources Tech., Trans., ASME*, **101**, 232–239.

- Brandt, H., 1955. A study of the speed of sound in porous granular media. *J. Appl. Mech.*, **22**, 479–486.
- Bratli, R.K., Horsrud, P., and Risnes, R., 1983. Rock mechanics applied to the region near a wellbore. *Proc. 5th Int. Congr. Rock Mechanics*, F1–F17. Melbourne: International Society for Rock Mechanics.
- Brevik, I., 1995. Chalk data, presented at workshop on effective media, Karlsruhe.
- Brie, A., Pampuri, F., Marsala, A.F., and Meazza, O., 1995. Shear sonic interpretation in gas-bearing sands. *SPE*, **30595**, 701–710.
- Brisco, B., Pultz, T.J., Brown, R.J., *et al.*, 1992. Soil moisture measurement using portable dielectric probes and time domain reflectometry. *Water Resources Res.*, **28**, 1339–1346.
- Bristow, J.R., 1960. Microcracks, and the static and dynamic elastic constants of annealed heavily coldworked metals. *Brit. J. Appl. Phys.*, **11**, 81–85.
- Brito Dos Santos, W.L., Ulrych, T.J., and De Lima, O.A.L., 1988. A new approach for deriving pseudovelocity logs from resistivity logs. *Geophys. Prospecting*, **36**, 83–91.
- Brocher, T., 2005. Relations between elastic wavespeeds and density in the Earth's crust. *Bull. Seismol. Soc. Amer.*, **95**, 6, 2081–2092.
- Brown, G.G., 1966. *Unit Operations*. New York: J. Wiley.
- Brown, R. and Korringa, J., 1975. On the dependence of the elastic properties of a porous rock on the compressibility of the pore fluid. *Geophys.*, **40**, 608–616.
- Brown, S.R. and Scholz, C.H., 1986. Closure of random elastic surfaces: I. Contact. *J. Geophys. Res.*, **90**, 5531–5545.
- Bruggeman, D.A.G., 1935. Berechnung verschiedener physikalischer Konstanten von heterogenen Substanzen. *Ann. Phys., Lpz*, **24**, 636–679.
- Budiansky, B., 1965. On the elastic moduli of some heterogeneous materials. *J. Mech. Phys. Solids*, **13**, 223–227.
- Budiansky, B. and O'Connell, R.J., 1976. Elastic moduli of a cracked solid. *Int. J. Solids Structures*, **12**, 81–97.
- Cadoret, T., 1993. *Effet de la Saturation Eau/Gaz sur les Propriétés Acoustiques des Roches*. Ph.D. dissertation, University of Paris, VII.
- Carcione, J.M., Ursin, B., and Nordskog, J.I., 2007. Cross-property relations between electrical conductivity and the seismic velocity of rocks. *Geophysics*, **72**, E193–E204.
- Carman, P.C., 1961. *L'écoulement des Gaz à Travers les Milieux Poreux*, Bibliothèque des Sciences et Techniques Nucléaires, Presses Universitaires de France, Paris.
- Carmichael, R.S., 1989. *Practical Handbook of Physical Properties of Rocks and Minerals*. Boca Raton, FL: CRC Press.
- Castagna, J.P., 1993. AVO analysis-tutorial and review. In *Offset Dependent Reflectivity – Theory and Practice of AVO Analysis*. ed. J.P. Castagna and M. Backus. *Investigations in Geophysics*, No. 8, Society of Exploration Geophysicists, Tulsa, Oklahoma, pp. 3–36.
- Castagna, J.P., Batzle, M.L., and Eastwood, R.L., 1985. Relationships between compressional-wave and shear-wave velocities in clastic silicate rocks. *Geophys.*, **50**, 571–581.
- Castagna, J.P., Batzle, M.L., and Kan, T.K., 1993. Rock physics – The link between rock properties and AVO response. In *Offset-Dependent Reflectivity – Theory and Practice of AVO Analysis*, ed. J.P. Castagna and M. Backus. *Investigations in Geophysics*, No. 8, Society of Exploration Geophysicists, Tulsa, Oklahoma, pp. 135–171.
- Chang, C., Zoback, M.D., and Khaksar, A., 2004. Rock strength and physical property measurements in sedimentary rocks. *SRB Annual Report*, vol. **96**, paper G4.
- Chapman, M., 2003. Frequency-dependent anisotropy due to meso-scale fractures in the presence of equant porosity. *Geophys. Prosp.*, **51**, 369–379.

- Chapman, M., Zatsepin, S. V., and Crampin, S., 2002. Derivation of a microstructural poroelasticity model. *Geophys. J. Int.*, **151**, 427–451.
- Chapman, M., Liu, E., and Li, X-Y., 2006. The influence of fluid-sensitive dispersion and attenuation on AVO analysis. *Geophys. J. Int.*, **167**, 89–105.
- Chelam, E. V., 1961. *Thesis*, Indian Institute of Science, Bangalore.
- Chen, W., 1995. *AVO in Azimuthally Anisotropic Media: Fracture Detection Using P-wave Data and a Seismic Study of Naturally Fractured Tight Gas Reservoirs*. Ph.D. dissertation, Stanford University.
- Cheng, C.H., 1978. *Seismic Velocities in Porous Rocks: Direct and Inverse Problems*. Sc.D. thesis, MIT, Cambridge, Massachusetts.
- Cheng, C.H., 1993. Crack models for a transversely anisotropic medium. *J. Geophys. Res.*, **98**, 675–684.
- Choy, M.M., Cook, W.R., Hearmon, R.F.S., *et al.*, 1979. Elastic, piezoelectric, pyroelectric, piezooptic, electrooptic constants, and nonlinear dielectric susceptibilities of crystals. In *Landolt-Börnstein: Numerical Data and Functional Relationships in Science and Technology. Group III: Crystal and Solid State Physics*, vol. 11 (revised and extended edition of vols. III/1 and III/2), ed. K.-H. Hellwege and A.M. Hellwege. Berlin: Springer-Verlag.
- Christensen, N.I., 1972. Elastic properties of polycrystalline magnesium, iron, and manganese carbonates to 10 kilobars. *J. Geophys. Res.*, **77**, 369–372.
- Christensen, N.I. and Wang, H.F., 1985. The influence of pore pressure and confining pressure on dynamic elastic properties of Berea Sandstone. *Geophysics*, **50**, 207–213.
- Christensen, N.I. and Mooney, W.D., 1995. Seismic velocity structure and composition of the continental crust: a global view. *J. Geophys. Res.*, **100**, 9761–9788.
- Christensen, R.M., 1991. *Mechanics of Composite Materials*. Malabar, FL: Robert E. Krieger Publication Co.
- Christensen, R.M., 2005. *Mechanics of Composite Materials*. New York: Dover Publications.
- Ciz, R. and Shapiro, S., 2007. Generalization of Gassmann equations for porous media saturated with a solid material. *Geophysics*, **72**, A75–A79.
- Ciz, R., Siggins, A.F., Gurevich, B., and Dvorkin, J., 2008. Influence of microheterogeneity on effective properties of rocks. *Geophysics*, **73**, E7–E14.
- Claerbout, J.F., 1985. *Fundamentals of Geophysical Data Processing*. Palo Alto, CA: Blackwell Scientific Publications.
- Claerbout, J.F., 1992. *Earth Sounding Analysis: Processing versus Inversion*. Boston, MA: Blackwell Scientific Publications.
- Clark, V.A., Tittmann, B.R., and Spencer, T.W., 1980. Effect of volatiles on attenuation (Q^{-1}) and velocity in sedimentary rocks. *J. Geophys. Res.*, **85**, 5190.
- Clavier, C., Coates, G., and Dumanoir, J., 1984. Theoretical and experimental bases for the dual-water model for interpretation of shaley sands. *Soc. Pet. Eng. J.*, **24**, 153–168.
- Cleary, M.P., Chen, I-W., and Lee, S.-M., 1980. Self-consistent techniques for heterogeneous media. *Am. Soc. Civil Eng. J. Eng. Mech.*, **106**, 861–887.
- Cole, K.S. and Cole, R.H., 1941. Dispersion and absorption in dielectrics I. Alternating current characteristics. *J. Chem. Phys.*, **9**, 341–351.
- Connolly, P., 1998. Calibration and inversion of non-zero offset seismic. *Soc. Expl. Geophys.*, 68th Annual Meeting, Expanded Abstracts. Tulsa, OK: Society of Exploration Geophysicists.
- Connolly, P., 1999. Elastic impedance. *The Leading Edge*, **18**, 438–452.
- Corson, P.B., 1974. Correlation functions for predicting properties of heterogeneous materials. *J. Appl. Phys.*, **45**, 3159–3179.

- Cruts, H. M. A., Groenenboom, J., Duijndam, A. J. W., and Fokkema, J. T., 1995. Experimental verification of stress-induced anisotropy. *Expanded Abstracts, Soc. Expl. Geophys.*, 65th Annual International Meeting, pp. 894–897.
- Cumberland, D. J. and Crawford, R. J., 1987. The packing of particles. In *Handbook of Powder Technology*, vol. 6. New York: Elsevier.
- Dagan, G., 1993. Higher-order correction for effective permeability of heterogeneous isotropic formations of lognormal conductivity distribution. *Transp. Porous Media*, **12**, 279–290.
- Dandekar, D. P., 1968. Pressure dependence of the elastic constants of calcite. *Phys. Rev.*, **172**, 873.
- Darcy, H., 1856. *Les Fontaines Publiques de la Ville de Dijon*. Paris: Dalmont.
- Debye, P., 1945. *Polar Molecules*. Mineola, NY: Dover.
- de la Cruz, V. and Spanos, T. J. T., 1985. Seismic wave propagation in a porous medium. *Geophysics*, **50**, 1556–1565.
- Delameter, W. R., Hermann, G., Barnett, D. M., 1974. Weakening of an elastic solid by a rectangular array of cracks. *J. Appl. Mech.*, **42**, 74–80.
- Dellinger, J. and Vernik, L., 1992. Do core sample measurements record group or phase velocity? *Soc. Expl. Geophys.* 62nd Annual International Meeting, Expanded Abstracts, pp. 662–665.
- Dellinger J., Vasicek D., and Sondergeld, C., 1998. Kelvin notation for stabilizing elastic-constant inversion. *Rev. IFP*, **53**, 709–719.
- Denton, W. H., 1957. The packing and flow of spheres. *AERE Report E/R 1095*.
- Desbrandes, R., 1985. *Encyclopedia of Well Logging*. Houston, TX: Gulf Publishing Company.
- Digby, P. J., 1981. The effective elastic moduli of porous granular rocks. *J. Appl. Mech.*, **48**, 803–808.
- Dix, C. H., 1955. Seismic velocities from surface measurements. *Geophys.*, **20**, 68–86.
- Domenico, S. N., 1976. Effect of brine-gas mixture on velocity in an unconsolidated sand reservoir. *Geophys.*, **41**, 882–894.
- Doraiswami, M. S., 1947. Elastic constants of magnetite, pyrite, and chromite. *Proc. Ind. Acad. Sci., A*, **25**, 414–416.
- Duda, R. O., Hart, P. E., and Stork, D. G., 2000. *Pattern Classification*. New York: John Wiley & Sons.
- Duffaut, K., Alsos, T., Landrø, M., Rognø, H., and Al-Najjar, N. F., 2000. Shear-wave elastic impedance. *Leading Edge*, **19**, 1222–1229.
- Dullien, F. A. L., 1991. One and two phase flow in porous media and pore structure. In *Physics of Granular Media*, ed. D. Bideau and J. Dodds. New York: Science Publishers Inc., pp. 173–214.
- Dullien, F. A. L., 1992. *Porous Media: Fluid Transport and Pore Structure*. San Diego, CA: Academic Press.
- Dutta, N. C. and Odé, H., 1979. Attenuation and dispersion of compressional waves in fluid-filled porous rocks with partial gas saturation (White model) – Part 1: Biot theory, Part II: Results. *Geophys.*, **44**, 1777–1805.
- Dutta, N. C. and Seriff, A. J., 1979. On White's model of attenuation in rocks with partial gas saturation. *Geophysics*, **44**, 1806–1812.
- Dvorkin, J. and Nur, A., 1993. Dynamic poroelasticity: a unified model with the squirt and the Biot mechanisms. *Geophys.*, **58**, 524–533.
- Dvorkin, J. and Nur, A., 1996. Elasticity of high-porosity sandstones: theory for two North Sea datasets. *Geophys.*, **61**, 1363–1370.
- Dvorkin, J., Nolen-Hoeksema, R., and Nur, A., 1994. The squirt-flow mechanism: macroscopic description. *Geophys.*, **59**, 428–438.

- Dvorkin, J., Mavko, G., and Nur, A., 1995. Squirt flow in fully saturated rocks. *Geophys.* **60**, 97–107.
- Dvorkin, J.P. and Mavko, G., 2006. Modeling attenuation in reservoir and nonreservoir rock. *Leading Edge*, **25**, 194–197.
- Eastwood, R.L. and Castagna, J.P., 1986. Interpretation of V_P/V_S ratios from sonic logs. In *Shear Wave Exploration, Geophysical Developments*, no. 1, ed. S.H. Danbom and S.N. Domenico. Tulsa, OK: Society of Exploration Geophysicists.
- Eaton, B.A., 1975. The equation for geopressure prediction from well logs. *Paper SPE 5544*. Houston, TX: Society of Petroleum Engineers.
- Eberhart-Phillips, D.M., 1989. *Investigation of Crustal Structure and Active Tectonic Processes in the Coast Ranges, Central California*. Ph.D. dissertation, Stanford University.
- Efron, B. and Tibshirani, R.J., 1993. *An Introduction to the Bootstrap*. New York: Chapman and Hall.
- Eimer, C., 1967. Stresses in multi-phase media. *Arch. Mech. Stos.*, **19**, 521.
- Eimer, C., 1968. The boundary effect in elastic multiphase bodies. *Arch. Mech. Stos.*, **20**, 87.
- Einspruch, N.G. and Manning, R.J., 1963. Elastic constants of compound semi-conductors ZnS, PbTe, GaSb. *J. Acoust. Soc. Am.*, **35**, 215–216.
- Eissa, E.A. and Kazi, A., 1988. Relation between static and dynamic Young's moduli of rocks. *Int. J. Rock Mech.*, **25**, 479–482.
- Ellis, D., Howard, J., Flaum, C., *et al.*, 1988. Mineral logging parameters: Nuclear and acoustic. *Tech. Rev.*, **36**(1), 38–55.
- Elmore, W.C. and Heald, M.A., 1985. *Physics of Waves*. Mineola, NY: Dover Publications, Inc.
- Elrod, H.G., 1979. A general theory for laminar lubrication with Reynolds roughness. *J. Lubr. Tech.*, **101**, 8–14.
- Endres, A.L. and Knight, R., 1992. A theoretical treatment of the effect of microscopic fluid distribution on the dielectric properties of partially saturated rocks. *Geophys. Prospecting*, **40**, 307–324.
- Epstein, P.S., 1941. On the absorption of sound waves in suspensions and emulsions. In *Theodore Von Karmen Anniversary Volume*, pp. 162–188.
- Epstein, P.S. and Carhart, R.R., 1953. The absorption of sound in suspensions and emulsions: I. Water fog in air. *J. Acoust. Soc. Am.*, **25**, 553–565.
- Eshelby, J.D., 1957. The determination of the elastic field of an ellipsoidal inclusion, and related problems. *Proc. Royal Soc. London A*, **241**, 376–396.
- Fabricius, I.L., 2003. How burial diagenesis of chalk sediments controls sonic velocity and porosity. *AAPG Bull.*, **87**, 1755–1778.
- Faust, L.Y., 1953. A velocity function including lithologic variation. *Geophys.*, **18**, 271–288.
- Finney, J.L., 1970. Random packings and the structure of simple liquids – I. The geometry of random close packing. *Proc. Roy. Soc. London A*, **319**, 479–493.
- Fjaer, E., Holt, R.M., Horsrud, P., Raaen, A.M., and Risnes, R., 2008. *Petroleum Related Rock Mechanics*. Amsterdam: Elsevier.
- Florez, J.-M., 2005. *Integrating Geology, Rock Physics, and Seismology for Reservoir Quality Prediction*. Ph.D. dissertation, Stanford University.
- Focke, J.W. and Munn, D., 1987. Cementation exponents (m) in Middle Eastern carbonate reservoirs. *Soc. Pet. Eng., Form. Eval.*, **2**, 155–167.
- Folk, R.L. and Ward, W., 1957. Brazos river bar: a study in the significance of grain-size parameters. *J. Sedim. Petrol.*, **27**, 3–26.
- Formation Evaluation Data Handbook*, 1982. Fort Worth, TX: Gearhart Industries, Inc.
- Frazer, L.N., 1994. A pulse in a binary sediment. *Geophys. J. Int.*, **118**, 75–93.

- Freyburg, E., 1972. Der Untere und mittlere Buntsandstein SW-Thuringen in seinen gesteintechnischen Eigenschaften. *Ber. Dte. Ges. Geol. Wiss. A*, **176**, 911–919.
- Fukunaga, K., 1990. *Introduction to Statistical Pattern Recognition*. Boston, MA: Academic Press.
- Gammon, P.H., Kieft, H., and Clouter, M.J., 1980. Elastic constants of ice by Brillouin spectroscopy. *J. Glaciol.*, **25**, 159–167.
- Gangi, A.F. and Carlson, R.L., 1996. An asperity-deformation model for effective pressure. *Tectonophysics*, **256**, 241–251.
- Garcia, X. and Medina, E.A., 2006. Hysteresis effects studied by numerical simulations: cyclic loading-unloading of a realistic sand model. *Geophysics*, **71**, F13–F20.
- Gardner, G.H.F., 1962. Extensional waves in fluid-saturated porous cylinders. *J. Acoust. Soc. Am.*, **34**, 36–40.
- Gardner, G.H.F., Gardner, L.W., and Gregory, A.R., 1974. Formation velocity and density – the diagnostic basics for stratigraphic traps. *Geophys.*, **39**, 770–780.
- Gassmann, F., 1951. Über die Elastizität poröser Medien. *Vier. der Natur. Gesellschaft Zürich*, **96**, 1–23.
- Geertsma, J., 1961. Velocity-log interpretation: the effect of rock bulk compressibility. *Soc. Pet. Eng. J.*, **1**, 235–248.
- Geertsma, J. and Smit, D.C., 1961. Some aspects of elastic wave propagation in fluid-saturated porous solids. *Geophys.*, **26**, 169–181.
- Gelinsky, S. and Shapiro, S., 1997a. Poroelastic Backus averaging for anisotropic layered fluid- and gas-saturated sediments. *Geophys.*, **62**, 1867–1878.
- Gelinsky, S. and Shapiro, S., 1997b. Dynamic equivalent medium model for thickly layered saturated sediments. *Geophys. J. Int.*, **128**, F1–F4.
- Gelinsky, S., Shapiro, S., Muller, T., and Gurevich, B., 1998. Dynamic poroelasticity of thinly layered structures. *Int. J. Solids Struct.*, **35**, 4739–4751.
- Gibiansky, L.V. and Torquato S., 1996. Bounds on the effective moduli of cracked materials. *J. Mech. Phys. Solids*, **44**, 233–242.
- Gibson, R.L. and Toksöz, M.N., 1990. Permeability estimation from velocity anisotropy in fractured rock. *J. Geophys. Res.*, **95**, 15 643–15 656.
- Glover, P.W.J., Hole, M.J., and Pous J., 2000. A modified Archie's law for two conducting phases. *Earth Planet. Sci. Lett.*, **180**, 369–383.
- Goddard, J.D., 1990. Nonlinear elasticity and pressure-dependent wave speeds in granular media. *Proc. R. Soc. A*, **430**, 105–131.
- Godfrey, J.J., Beaudoin, B.C., and Klemperer, S.L., 1997. Ophiolitic basement to the Great Valley forearc basin, California, from seismic and gravity data: implications for crustal growth at the North American continental margin. *Geol. Soc. Amer. Bull.*, **109**, 1536–1562.
- Gold, N., Shapiro, S., Bojinski, S., and Muller, T.M., 2000. An approach to upscaling for seismic waves in statistically isotropic heterogeneous elastic media. *Geophys.*, **65**, 1837–1850.
- Golubev, A.A. and Rabinovich, G.Y., 1976. Resultaty primeneia apparturny akusticeskogo karotasa dlja predeleina proconstykh svoistv gornych porod na mestorosdeniiaach tverdykh isjopaemykh. *Priklad. Geofizika Moskva*, **73**, 109–116.
- González, E.F. 2006. *Physical and Quantitative Interpretation of Seismic Attributes for Rocks and Fluids Identification*. Ph.D. dissertation, Stanford University.
- Goodman, R.E. 1976. *Methods of Geological Engineering in Discontinuous Rocks*. New York: West Publishing.
- Gorjainov, N.N. and Ljachowickij, F.M., 1979. *Seismic Methods in Engineering Geology*. Moscow: Nedra.

- Graham, E.K., Jr. and Barsch, G.R., 1969. Elastic constants of single-crystal forsterite as a function of temperature and pressure. *J. Geophys. Res.*, **74**, 5949–5960.
- Gray, D., Goodway, B., and Chen, T., 1999. Bridging the gap: AVO to detect changes in fundamental elastic constants. In *Expanded Abstract, SEG International Meeting*. Tulsa, OK: Society of Exploration Geophysicists.
- Grechka, V. and Tsvankin, I., 1998. 3-D description of normal moveout in anisotropic inhomogeneous media. *Geophys.*, **63**, 1079–1092.
- Greenberg, M.L. and Castagna, J.P., 1992. Shear-wave velocity estimation in porous rocks: theoretical formulation, preliminary verification and applications. *Geophys. Prospect.*, **40**, 195–209.
- Greenhalgh, S.A. and Emerson, D.W., 1986. Elastic properties of coal measure rock from the Sydney Basin, New South Wales. *Expl. Geophys.*, **17**, 157–163.
- Greenwood, J.A. and Williamson, J., 1966. Contact of nominally flat surfaces. *Proc. R. Soc., London A*, **295**, 300–319.
- Gubernatis, J.E. and Krumhansl, J.A., 1975. Macroscopic engineering properties of polycrystalline materials: elastic properties. *J. Appl. Phys.*, **46**, 1875.
- Guéguen, Y. and Palciauskas, V., 1994. *Introduction to the Physics of Rocks*. Princeton, NJ: Princeton University Press.
- Gurevich, B., 2004. A simple derivation of the effective stress coefficient for seismic velocities in porous rocks. *Geophys.*, **69**, 393–397.
- Gurevich, B. and Lopatnikov, S.L., 1995. Velocity and attenuation of elastic waves in finely layered porous rocks. *Geophys. J. Int.*, **121**, 933–947.
- Gutierrez, M.A., Braunsdorf, N.R., and Couzens, B.A., 2006. Calibration and ranking of pore-pressure prediction models. *Leading Edge*, **25**(12), 1516–1523.
- Gvirtzman, H. and Roberts, P., 1991. Pore-scale spatial analysis of two immiscible fluids in porous media. *Water Resources Res.*, **27**, 1165–1176.
- Hacikoylu, P., Dvorkin, J., and Mavko, G., 2006. Resistivity–velocity transforms revisited. *Leading Edge*, **25**, 1006–1009.
- Han, D.-H., 1986. *Effects of Porosity and Clay Content on Acoustic Properties of Sandstones and Unconsolidated Sediments*. Ph.D. dissertation, Stanford University.
- Han, D.-H., Nur, A., and Morgan, D., 1986. Effects of porosity and clay content on wave velocities in sandstones. *Geophys.*, **51**, 2093–2107.
- Hanai, T., 1968. Electrical properties of emulsions. In *Emulsion Science*, ed. P. Sherman. New York: Academic Press, pp. 353–478.
- Hashin, Z. and Shtrikman, S., 1962. A variational approach to the theory of effective magnetic permeability of multiphase materials. *J. Appl. Phys.*, **33**, 3125–3131.
- Hashin, Z. and Shtrikman, S., 1963. A variational approach to the elastic behavior of multiphase materials. *J. Mech. Phys. Solids*, **11**, 127–140.
- Hastie, T., Tibshirani, R., and Freidman, J., 2001. *The Elements of Statistical Learning: Data Mining, Inference, and Prediction*. New York: Springer-Verlag.
- Hearmon, R.F.S., 1946. The elastic constants of anisotropic materials. *Rev. Mod. Phys.*, **18**, 409–440.
- Hearmon, R.F.S., 1956. The elastic constants of anisotropic materials II. *Adv. Phys.*, **5**, 323–382.
- Hearmon, R.F.S., 1979. The elastic constants of crystals and other anisotropic materials. In *Landolt–Börnstein Tables, III/11*, ed. K.H. Hellwege and A.M. Hellwege. Berlin: Springer-Verlag, pp. 1–244.
- Hearmon, R.F.S., 1984. The elastic constants of crystals and other anisotropic materials. In *Landolt–Börnstein Tables, III/18*, ed. K.H. Hellwege and A.M. Hellwege. Berlin: Springer-Verlag, pp. 1–154.

- Helbig, K., 1994. *Foundations of Anisotropy for Exploration Seismics*. Tarrytown, NY: Pergamon.
- Helbig, K., 1998. A formalism for the consistent description of non-linear elasticity of anisotropic media. *Rev. Inst. Français Pétrole*, **53**, 693–708.
- Helbig, K. and Schoenberg, M., 1987. Anomalous polarizations of elastic waves in transversely isotropic media. *J. Acoust. Soc. Am.*, **81**, 1235–1245.
- Helgerud, M.B., 2001. *Wave Speeds in Gas Hydrate and Sediments Containing Gas Hydrate: a Laboratory and Modeling Study*, Ph.D. dissertation, Stanford University.
- Hermance, J.F., 1979. The electrical conductivity of materials containing partial melt, a simple model from Archie's law. *Geophys. Res. Lett.*, **6**, 613–616.
- Herrick, D.C., 1988. Conductivity models, pore geometry, and conduction mechanisms. *Trans. Soc. Prof. Well Log Analysts, 29th Annual Logging Symposium*, San Antonio, TX. Paper D.
- Hicks, W.G. and Berry, J.E., 1956. Application of continuous velocity logs to determination of fluid saturation of reservoir rocks. *Geophys.*, **21**, 739.
- Hill, R., 1952. The elastic behavior of crystalline aggregate. *Proc. Phys. Soc., London A*, **65**, 349–354.
- Hill, R., 1963. Elastic properties of reinforced solids: some theoretical principles. *J. Mech. Phys. Solids*, **11**, 357–372.
- Hill, R., 1965. A self-consistent mechanics of composite materials. *J. Mech. Phys. Solids*, **13**, 213–222.
- Hilterman, F., 1989. Is AVO the seismic signature of rock properties? *Expanded Abstracts, Soc. Expl. Geophys., 59th Annual International Meeting*. Tulsa, OK: Society of Exploration Geophysicists, p. 559.
- Hoffmann, R., Xu, X., Batzle, M., *et al.*, 2005. Effective pressure or what is the effect of pressure? *Leading Edge*, December, 1256–1260.
- Horsrud, P., 2001. Estimating mechanical properties of shale from empirical correlations. *SPE Drilling Completion*, **16**, 68–73.
- Hottman, C.E. and Johnson, R.K., 1965. Estimation of formation pressures from log derived shale properties. *J. Petrol. Tech.*, **17**, 717–722.
- Hovem, J.M. and Ingram, G.D., 1979. Viscous attenuation of sound in saturated sand. *J. Acoust. Soc. Am.*, **66**, 1807–1812.
- Hudson, J.A., 1980. Overall properties of a cracked solid. *Math. Proc. Camb. Phil. Soc.*, **88**, 371–384.
- Hudson, J.A., 1981. Wave speeds and attenuation of elastic waves in material containing cracks. *Geophys. J. R. Astron. Soc.*, **64**, 133–150.
- Hudson, J.A., 1990. Overall elastic properties of isotropic materials with arbitrary distribution of circular cracks. *Geophys. J. Int.* **102**, 465–469.
- Hudson, J.A. and Liu, E., 1999. Effective elastic properties of heavily faulted structures. *Geophys.*, **64**, 479–485.
- Hudson, J.A., Liu, E., and Crampin, S., 1996. The mechanical properties of materials with interconnected cracks and pores. *Geophys. J. Int.*, **124**, 105–112.
- Huffman, D.F. and Norwood, M.H., 1960. Specific heat and elastic constants of calcium fluoride at low temperatures. *Phys. Rev.*, **117**, 709–711.
- Humbert, P. and Plicque, F., 1972. Propriétés élastiques de carbonate rhomboédriques monocristallins: calcite, magnésite, dolomie. *C. R. Acad. Sci., Paris B*, **275**, 391–394.
- Huntington, H.B., 1958. The elastic constants of crystals. In *Solid State Physics*, vol. 7, ed. F. Seitz and D. Turnbull. New York: Academic Press, pp. 213–351.
- Jackson, J.D., 1975. *Classical Electrodynamics*, 2nd edn. New York: John Wiley and Sons.

- Jackson, P.D., Taylor-Smith, D., and Stanford, P.N., 1978. Resistivity–porosity–particle shape relationships for marine sands. *Geophys.*, **43**, 1250–1262.
- Jaeger, J., Cook, N.G., and Zimmerman, R., 2007. *Fundamentals of Rock Mechanics*, 4th edn. Malden, MA: Blackwell Ltd.
- Jaeger, J.C. and Cook, N.G.W., 1969. *Fundamentals of Rock Mechanics*. London: Chapman and Hall Ltd.
- Jakobsen, M., Hudson, J.A., Minshull, T.A., and Singh, S.C., 2000. Elastic properties of hydrate-bearing sediments using effective medium theory. *J. Geophys. Res.*, **105**, 561–577.
- Jakobsen, M., Hudson, J.A., and Johansen, T.A., 2003a. *T*-matrix approach to shale acoustics. *Geophys. J. Int.*, **154**, 533–558.
- Jakobsen, M., Johansen, T.A., and McCann, C., 2003b. The acoustic signature of fluid flow in a complex porous media. *J. Appl. Geophys.*, **54**, 219–246.
- Jenkins, G.M. and Watts, D.G., 1968. *Spectral Analysis and Its Applications*. San Francisco, CA: Holden-Day.
- Jenkins, J., Johnson, D., La Ragione, L., and Makse, H., 2005. Fluctuations and the effective moduli of an isotropic, random aggregate of identical, frictionless spheres. *J. Mech. Phys. Solids*, **53**, 197–225.
- Jílek, P., 2002a. *Modeling and Inversion of Converted-wave Reflection Coefficients in Anisotropic Media: a Tool for Quantitative AVO Analysis*. Ph.D. dissertation, Center for Wave Phenomena, Colorado School of Mines.
- Jílek, P., 2002b. Converted PS-wave reflection coefficients in weakly anisotropic media. *Pure Appl. Geophys.*, **159**, 1527–1562.
- Jizba, D.L., 1991. *Mechanical and Acoustical Properties of Sandstones and Shales*. Ph.D. dissertation, Stanford University.
- Johnson, D.L. and Plona, T.J., 1982. Acoustic slow waves and the consolidation transition. *J. Acoust. Soc. Am.*, **72**, 556–565.
- Johnson, D.L., Koplic, J., and Dashen, R., 1987. Theory of dynamic permeability and tortuosity in fluid-saturated porous media. *J. Fluid Mech.*, **176**, 379–400.
- Johnson, D.L., Schwartz, L.M., Elata, D., *et al.*, 1998. Linear and nonlinear elasticity of granular media: stress-induced anisotropy of a random sphere pack. *Trans. ASME*, **65**, 380–388.
- Johnson, P.A. and Rasolofosaon, P.N.J., 1996. Nonlinear elasticity and stress-induced anisotropy in rock. *J. Geophys. Res.*, **100**(B2), 3113–3124.
- Joshi, S.K. and Mitra, S.S., 1960. Debye characteristic temperature of solids. *Proc. Phys. Soc., London*, **76**, 295–298.
- Juhász, I., 1981. Normalised Q_v – The key to shaley sand evaluation using the Waxman–Smits equation in the absence of core data. *Trans. Soc. Prof. Well Log Analysts, 22nd Annual Logging Symposium*, Paper Z.
- Kachanov, M., 1992. Effective elastic properties of cracked solids: critical review of some basic concepts. *Appl. Mech. Rev.*, **45**, 304–335.
- Kan, T.K. and Swan, H.W., 2001. Geopressure prediction from automatically derived seismic velocities. *Geophys.*, **66**, 1937–1946.
- Katahara, K., 2004. Fluid substitution in laminated shaly sands. *SEG Extended Abstracts 74th Annual Meeting*. Tulsa, OK: Society of Exploration Geophysicists.
- Keller, J.B., 1964. Stochastic equations and wave propagation in random media. *Proc. Symp. Appl. Math.*, **16**, 145–170.
- Kelvin, W. Thomson, Lord, 1856. *Phil. Trans. R. Soc.*, **166**, 481.
- Kendall, K. and Tabor, D., 1971. An ultrasonic study of the area of contact between stationary and sliding surfaces. *Proc. R. Soc., London A*, **323**, 321–340.

- Kennett, B.L.N., 1974. Reflections, rays and reverberations. *Bull. Seismol. Soc. Am.*, **64**, 1685–1696.
- Kennett, B.L.N., 1983. *Seismic Wave Propagation in Stratified Media*. Cambridge: Cambridge University Press.
- King, M.S., 1983. Static and dynamic elastic properties of rocks from the Canadian Shield. *Int. J. Rock Mech.*, **20**, 237–241.
- Kjartansson, E., 1979. Constant Q wave propagation and attenuation. *J. Geophys. Res.*, **84**, 4737–4748.
- Klimentos, T. and McCann, C., 1990. Relationships among compressional wave attenuation, porosity, clay content, and permeability in sandstones. *Geophys.*, **55**, 998–1014.
- Knight, R. and Dvorkin, J., 1992. Seismic and electrical properties of sandstones at low saturations. *J. Geophys. Res.*, **97**, 17425–17432.
- Knight, R. and Nolen-Hoeksema, R., 1990. A laboratory study of the dependence of elastic wave velocities on pore scale fluid distribution. *Geophys. Res. Lett.*, **17**, 1529–1532.
- Knight, R.J. and Nur, A., 1987. The dielectric constant of sandstones, 60kHz to 4MHz. *Geophys.*, **52**, 644–654.
- Knopoff, L., 1964. *Q. Rev. Geophys.*, **2**, 625–660.
- Knott, C.G., 1899. Reflection and refraction of elastic waves, with seismological applications. *Phil. Mag., London*, **48**(64–97), 567–569.
- Koesoemadinata, A.P. and McMechan, G.A., 2001. Empirical estimation of viscoelastic seismic parameters from petrophysical properties of sandstone. *Geophys.*, **66**, 1457–1470.
- Koesoemadinata, A.P. and McMechan, G.A., 2003. Correlations between seismic parameters, EM parameters, and petrophysical/petrological properties for sandstone and carbonate at low water saturations. *Geophys.*, **68**, 870–883.
- Koga, I., Aruga, M., and Yoshinaka, Y., 1958. Theory of plane elastic waves in a piezoelectric crystalline medium and determination of elastic and piezo-electric constants of quartz. *Phys. Rev.*, **109**, 1467–1473.
- Korringa, J., 1973. Theory of elastic constants of heterogeneous media. *J. Math. Phys.*, **14**, 509.
- Krief, M., Garat, J., Stellingwerff, J., and Ventre, J., 1990. A petrophysical interpretation using the velocities of P and S waves (full-waveform sonic). *Log Analyst*, **31**, November, 355–369.
- Krishnamurty, T.S.G., 1963. Fourth-order elastic coefficients in crystals. *Acta Cryst.*, **16**, 839–840.
- Kröner, E., 1967. Elastic moduli of perfectly disordered composite materials. *J. Mech. Phys. Solids*, **15**, 319.
- Kröner, E., 1977. Bounds for effective elastic moduli of disordered materials. *J. Mech. Phys. Solids*, **25**, 137.
- Kröner, E., 1986. Statistical modeling. In *Modeling Small Deformations of Polycrystals*, ed. J. Gittus and J. Zarka. New York: Elsevier, pp. 229–291.
- Kumazawa, M. and Anderson, O.L., 1969. Elastic moduli, pressure derivatives, and temperature derivative of single-crystal olivine and single-crystal forsterite. *J. Geophys. Res.*, **74**, 5961–5972.
- Kuperman, W.A., 1975. Coherent components of specular reflection and transmission at a randomly rough two-fluid interface. *J. Acoust. Soc. Am.*, **58**, 365–370.
- Kuster, G.T. and Toksöz, M.N., 1974. Velocity and attenuation of seismic waves in two-phase media. *Geophys.*, **39**, 587–618.
- Lal, M., 1999. Shale stability: drilling fluid interaction and shale strength. SPE 54356, presented at *SPE Latin American and Caribbean Petroleum Engineering Conference*, Caracas, Venezuela, 21–23 April. Tulsa, OK: Society of Exploration Geophysicists.
- Lamb, H., 1945. *Hydrodynamics*. Mineola, NY: Dover.

- Landau, L.D. and Lifschitz, E.D., 1959. *Theory of Elasticity*. Tarrytown, NY: Pergamon.
- Landauer, R., 1952. The electrical resistance of binary metallic mixtures. *J. Appl. Phys.*, **23**, 779–784.
- Lashkaripour, G.R. and Dusseault, M.B., 1993. A statistical study on shale properties; relationship among principal shale properties. *Proceedings of the Conference on Probabilistic Methods in Geotechnical Engineering*, Canberra, Australia, Rotterdam: Balkema, pp. 195–200.
- Lawn, B.R. and Wilshaw, T.R., 1975. *Fracture of Brittle Solids*. Cambridge: Cambridge University Press.
- Lazarus, D., 1949. The variation of the adiabatic elastic constants of KCl, NaCl, CuZn, Cu, and Al with pressure to 10000 bars. *Phys. Rev.*, **76**, 545–553.
- Levin, F.K., 1971. Apparent velocity from dipping interface reflections. *Geophys.*, **36**, 510–516.
- Levin, F.K., 1979. Seismic velocities in transversely isotropic media. *Geophys.*, **44**, 918–936.
- Liebermann, R.C. and Schreiber, E., 1968. Elastic constants of polycrystalline hematite as a function of pressure to 3 kilobars. *J. Geophys. Res.*, **73**, 6585–6590.
- Liu, H.P., Anderson, D.L., and Kanamori, H., 1976. Velocity dispersion due to anelasticity: implications for seismology and mantle composition. *Geophys. J. R. Astron. Soc.*, **47**, 41–58.
- Lockner, D.A., Walsh, J.B., and Byerlee, J.D., 1977. Changes in velocity and attenuation during deformation of granite. *J. Geophys. Res.*, **82**, 5374–5378.
- Log Interpretation Charts*, 1984. Publication SMP-7006. Houston, TX: Schlumberger Ltd.
- Lucet, N., 1989. *Vitesse et Atténuation des Ondes Élastiques Soniques et Ultrasoniques dans les Roches sous Pression de Confinement*. Ph.D. dissertation, University of Paris.
- Lucet, N. and Zinszner, B., 1992. Effects of heterogeneities and anisotropy on sonic and ultrasonic attenuation in rocks. *Geophys.*, **57**, 1018–1026.
- Ludwig, W.J., Nafe, J.E., and Drake, C.L., 1970. Seismic refraction. In *The Sea*, ed. A.E. Maxwell. New York: Wiley-Interscience, vol. 4, pp. 53–84.
- Makse, H.A., Gland, N., Johnson, D.L., and Schwartz, L.M., 1999. Why effective medium theory fails in granular materials. *Phys. Rev. Lett.*, **83**, 5070–5073.
- Makse, H.A., Johnson, D.L., and Schwartz, L.M., 2000. Packing of compressible granular materials. *Phys. Rev. Lett.*, **84**, 4160–4163.
- Makse, H.A., Gland, N., Johnson, D.L., and Schwartz, L.M., 2004. Granular packings: nonlinear elasticity, sound propagation, and collective relaxation dynamics. *Phys. Rev. E*, **L70**, 061302.1–061302.19.
- Mallick, S., 2001. AVO and elastic impedance. *Leading Edge*, **20**, 1094–1104.
- Manegold, E. and von Engelhardt, W., 1933. Über Kapillar-Systeme, XII, Die Berechnung des Stoffgehaltes heterogener Gerutstrukturen. *Koll. Z.*, **63**(2), 149–154.
- Marion, D., 1990. *Acoustical, Mechanical and Transport Properties of Sediments and Granular Materials*. Ph.D. dissertation, Stanford University.
- Marion, D. and Nur, A., 1991. Pore-filling material and its effect on velocity in rocks. *Geophys.*, **56**, 225–230.
- Marion, D., Nur, A., Yin, H., and Han, D., 1992. Compressional velocity and porosity in sand–clay mixtures. *Geophys.*, **57**, 554–563.
- Marle, C.M., 1981. *Multiphase Flow in Porous Media*. Houston, TX: Gulf Publishing Company.
- Marple, S.L., 1987. *Digital Spectral Analysis with Applications*. Englewood Cliffs, NJ: Prentice-Hall.
- Mason, W.P., 1943. Quartz crystal applications. *Bell Syst. Tech. J.*, **22**, 178.
- Mason, W.P., 1950. *Piezoelectric Crystals and Their Application to Ultrasonics*. New York: D. Van Nostrand Co., Inc.

- Mavko, G., 1980. Velocity and attenuation in partially molten rocks. *J. Geophys. Res.*, **85**, 5173–5189.
- Mavko, G. and Bandyopadhyay, K., 2008. Approximate fluid substitution in weakly anisotropic VTI rocks. *Geophys.*, in press.
- Mavko, G. and Jizba, D., 1991. Estimating grain-scale fluid effects on velocity dispersion in rocks. *Geophys.*, **56**, 1940–1949.
- Mavko, G. and Mukerji, T., 1995. Pore space compressibility and Gassmann's relation. *Geophys.*, **60**, 1743–1749.
- Mavko, G. and Nolen-Hoeksema, R., 1994. Estimating seismic velocities in partially saturated rocks. *Geophys.*, **59**, 252–258.
- Mavko, G. and Nur, A., 1975. Melt squirt in the asthenosphere. *J. Geophys. Res.*, **80**, 1444–1448.
- Mavko, G. and Nur, A., 1978. The effect of nonelliptical cracks on the compressibility of rocks. *J. Geophys. Res.*, **83**, 4459–4468.
- Mavko, G. and Nur, A., 1997. The effect of a percolation threshold in the Kozeny–Carman relation. *Geophys.*, **62**, 1480–1482.
- Mavko, G., Kjartansson, E., and Winkler, K., 1979. Seismic wave attenuation in rocks. *Rev. Geophys.*, **17**, 1155–1164.
- Mavko, G., Chan, C., and Mukerji, T., 1995. Fluid substitution: estimating changes in V_p without knowing V_s . *Geophys.*, **60**, 1750–1755.
- Mavko, G., Mukerji, T., and Godfrey, N., 1995. Predicting stress-induced velocity anisotropy in rocks. *Geophys.*, **60**, 1081–1087.
- Mazáč, O., Císlerová, M., Kelly, W.E., Landa, I., and Venhodová, D., 1990. Determination of hydraulic conductivities by surface geoelectrical methods. In *Geotechnical and Environmental Geophysics*, vol. II., ed. S.H. Ward. Tulsa, OK: Society of Exploration Geophysicists, pp. 125–131.
- McCann, D.M. and Entwisle, D.C., 1992. Determination of Young's modulus of the rock mass from geophysical well logs. In *Geological Applications of Wireline Logs II*, ed. A. Hurst, C.M. Griffiths, and P.F. Worthington. Geological Society Special Publication, vol. 65. London: Geological Society, pp. 317–325.
- McCoy, J.J., 1970. On the displacement field in an elastic medium with random variations in material properties. In *Recent Advances in Engineering Science*, vol. 2, ed. A.C. Eringen. New York: Gordon and Breach pp. 235–254.
- McGeary, R.K., 1967. Mechanical packing of spherical particles. *J. Am. Ceram. Soc.*, **44**(10), 513–522.
- McNally, G.H., 1987. Estimation of coal measures rock strength using sonic and neutron logs. *Geoexploration*, **24**, 381–395.
- McSkimin, H.J. and Bond, W.L., 1972. Elastic moduli of diamond as a function of pressure and temperature. *J. Appl. Phys.*, **43**, 2944–2948.
- McSkimin, H.J., Andreatch, P., Jr., and Thurston, R.N., 1965. Elastic moduli of quartz vs. hydrostatic pressure at 25 and 195.8 degrees Celsius. *J. Appl. Phys.*, **36**, 1632.
- Meador, R.A. and Cox, P.T., 1975. Dielectric constant logging: a salinity independent estimation of formation water volume. *Soc. Petrol. Eng.*, Paper 5504.
- Mehrabadi, M.M. and Cowin, S., 1989. Eigentensors of linear anisotropic elastic materials. *Q.J. Mech. Appl. Math.*, **43**, 15–41.
- Mehta, C.H., 1983. Scattering theory of wave propagation in a two-phase medium. *Geophys.*, **48**, 1359–1372.
- Mese, A. and Dvorkin, J., 2000. Static and dynamic moduli, deformation, and failure in shaley sand. *DOE report*, unpublished.

- Midya, T.R. and Basu, A.N., 1986. Self-consistent T -matrix solution for the effective elastic properties of noncubic polycrystals. *J. Appl. Phys.*, **59**, 2368–2375.
- Milholland, P., Manghnani, M.H., Schlanger, S.O., and Sutton, G.H., 1980. Geoacoustic modeling of deep-sea carbonate sediments. *J. Acoust. Soc. Am.*, **68**, 1351–1360.
- Militzer, H. and Stoll, R., 1973. Einige Beitrageder geophysics zur primadatenerfassung im Bergbau: neue Bergbautechnik. *Lipzig*, **3**, 21–25.
- Milton, G.W., 1981. Bounds on the electromagnetic, elastic and other properties of two-component composites. *Phys. Rev. Lett.*, **46**, 542–545.
- Mindlin, R.D., 1949. Compliance of elastic bodies in contact. *J. Appl. Mech.*, **16**, 259–268.
- Moos, D., Zoback, M.D., and Bailey, L., 1999. Feasibility study of the stability of openhole multilaterals, Cook Inlet, Alaska. Presentation at 1999 *SPE Mid-Continent Operations Symposium*, Oklahoma City, OK, 28–31 March, SPE 52186.
- Mukerji, T. and Mavko, G., 1994. Pore fluid effects on seismic velocity in anisotropic rocks. *Geophys.*, **59**, 233–244.
- Mukerji, T., Berryman, J.G., Mavko, G., and Berge, P.A., 1995a. Differential effective medium modeling of rock elastic moduli with critical porosity constraints. *Geophys. Res. Lett.*, **22**, 555–558.
- Mukerji, T., Mavko, G., Mujica, D., and Lucet, N., 1995b. Scale-dependent seismic velocity in heterogeneous media. *Geophys.*, **60**, 1222–1233.
- Mukerji, T., Jørstad, A., Mavko, G., and Granli, J.R., 1998. Near and far offset impedances: seismic attributes for identifying lithofacies and pore fluids. *Geophys. Res. Lett.*, **25**, 4557–4560.
- Müller, G., Roth, M., and Korn, M., 1992. Seismic-wave traveltimes in random media. *Geophys. J. Int.*, **110**, 29–41.
- Muller, T.M. and Gurevich, B., 2005a. A first-order statistical smoothing approximation for the coherent wave field in porous random media. *J. Acoust. Soc. Am.*, **117**, 1796–1805.
- Muller, T.M. and Gurevich, B., 2005b. Wave-induced fluid flow in random porous media: attenuation and dispersion of elastic waves. *J. Acoust. Soc. Amer.*, **117**, 2732–2741.
- Muller, T.M. and Gurevich, B., 2006. Effective hydraulic conductivity and diffusivity of randomly heterogeneous porous solids with compressible constituents. *Appl. Phys. Lett.*, **88**, 121924.
- Muller, T.M., Lambert, G., and Gurevich, B., 2007. Dynamic permeability of porous rocks and its seismic signatures. *Geophys.*, **72**, E149–E158.
- Mura, T., 1982. *Micromechanics of Defects in Solids*. The Hague: Kluwer.
- Murnaghan, F.D., 1951. *Finite Deformation of an Elastic Solid*. New York: John Wiley.
- Murphy, W.F., III, 1982. *Effects of Microstructure and Pore Fluids on the Acoustic Properties of Granular Sedimentary Materials*. Ph.D. dissertation, Stanford University.
- Murphy, W.F., III, 1984. Acoustic measures of partial gas saturation in tight sandstones. *J. Geophys. Res.*, **89**, 11549–11559.
- Murphy, W.F., III, Winkler, K.W., and Kleinberg, R.L., 1984. Contact microphysics and viscous relaxation in sandstones. In *Physics and Chemistry of Porous Media*, ed. D.L. Johnson and P. N. Sen. New York: American Institute of Physics, pp. 176–190.
- Murphy, W.F., Schwartz, L.M., and Hornby, B., 1991. Interpretation physics of V_P and V_S in sedimentary rocks. *Trans. SPWLA 32nd Ann. Logging Symp.*, 1–24.
- Myer, L., 2000. Fractures as collections of cracks. *Int. J. Rock Mech.*, **37**, 231–243.
- Nishizawa, O., 1982. Seismic velocity anisotropy in a medium containing oriented cracks – transversely isotropic case. *J. Phys. Earth*, **30**, 331–347.
- Nolet, G., 1987. Seismic wave propagation and seismic tomography. In *Seismic Tomography*, ed. G. Nolet. Dordrecht: D. Reidel Publication Co., pp. 1–23.

- Norris, A.N., 1985. A differential scheme for the effective moduli of composites. *Mech. Mater.*, **4**, 1–16.
- Norris, A.N. and Johnson, D.L., 1997. Nonlinear elasticity of granular media. *ASME J. Appl. Mech.*, **64**, 39–49.
- Norris, A.N., Sheng, P., and Callegari, A.J., 1985. Effective-medium theories for two-phase dielectric media. *J. Appl. Phys.*, **57**, 1990–1996.
- Nur, A., 1971. Effects of stress on velocity anisotropy in rocks with cracks. *J. Geophys. Res.*, **76**, 2022–2034.
- Nur, A. and Byerlee, J.D., 1971. An exact effective stress law for elastic deformation of rocks with fluids. *J. Geophys. Res.*, **76**, 6414–6419.
- Nur, A. and Simmons, G., 1969a. Stress-induced velocity anisotropy in rocks: an experimental study. *J. Geophys. Res.*, **74**, 6667.
- Nur, A. and Simmons, G., 1969b. The effect of viscosity of a fluid phase on velocity in low-porosity rocks. *Earth Planet. Sci. Lett.*, **7**, 99–108.
- Nur, A., Marion, D., and Yin, H., 1991. Wave velocities in sediments. In *Shear Waves in Marine Sediments*, ed. J.M. Hovem, M.D. Richardson, and R.D. Stoll. Dordrecht: Kluwer Academic Publishers, pp. 131–140.
- Nur, A., Mavko, G., Dvorkin, J., and Gal, D., 1995. Critical porosity: the key to relating physical properties to porosity in rocks. In *Proc. 65th Ann. Int. Meeting, Soc. Expl. Geophys.*, vol. 878. Tulsa, OK: Society of Exploration Geophysicists.
- O'Connell, R.J. and Budiansky, B., 1974. Seismic velocities in dry and saturated cracked solids. *J. Geophys. Res.*, **79**, 4626–4627.
- O'Connell, R.J. and Budiansky, B., 1977. Viscoelastic properties of fluid-saturated cracked solids. *J. Geophys. Res.*, **82**, 5719–5735.
- O'Doherty, R.F. and Anstey, N.A., 1971. Reflections on amplitudes. *Geophys. Prospect.*, **19**, 430–458.
- Ohno, I., Yamamoto, S., and Anderson, O.L., 1986. Determination of elastic constants of trigonal crystals by the rectangular parallelepiped resonance method. *J. Phys. Chem. Solids*, **47**, 1103–1108.
- Olhoeft, G.R., 1979. Tables of room temperature electrical properties for selected rocks and minerals with dielectric permittivity statistics. *US Geological Survey Open File Report* 79–993.
- Osborn, J.A., 1945. Demagnetizing factors of the general ellipsoid. *Phys. Rev.*, **67**, 351–357.
- Ozkan, H. and Jamieson, J.C., 1978. Pressure dependence of the elastic constants of nonmetamict zircon. *Phys. Chem. Minerals*, **2**, 215–224.
- Paillet, F.L. and Cheng, C.H., 1991. *Acoustic Waves in Boreholes*. Boca Raton, FL: CRC Press, p. 264.
- Papadakis, E.P., 1963. Attenuation of pure elastic modes in NaCl single crystals. *J. Appl. Phys.*, **34**, 1872–1876.
- Paterson, M.S. and Weiss, L.E., 1961. Symmetry concepts in the structural analysis of deformed rocks. *Geolog. Soc. Am. Bull.*, **72**, 841.
- Pedersen, B.K. and Nordal, K., 1999. Petrophysical evaluation of thin beds: a review of the Thomas–Stieber approach. Course 24034 Report, Norwegian University of Science and Technology.
- Peselnick, L. and Robie, R.A., 1963. Elastic constants of calcite. *J. Appl. Phys.*, **34**, 2494–2495.
- Pickett, G.R., 1963. Acoustic character logs and their applications in formation evaluation. *J. Petrol. Technol.*, **15**, 650–667.
- Ponte-Castaneda, P. and Willis, J.R., 1995. The effect of spatial distribution on the effective behavior of composite materials and cracked media. *J. Mech. Phys. Solids*, **43**, 1919–1951.

- Postma, G.W., 1955. Wave propagation in a stratified medium. *Geophys.*, **20**, 780–806.
- Poupon, A. and Leveaux, J., 1971. Evaluation of water saturations in shale formations. *Trans. Soc. Prof. Well Log Analysts, 12th Annual Logging Symposium*, Paper O.
- Prasad, M. and Manghnani, M.H., 1997. Effects of pore and differential pressure on compressional wave velocity and quality factor in Berea and Michigan sandstones. *Geophys.*, **62**, 1163–1176.
- Prioul, R. and Lebrat, T., 2004. Calibration of velocity–stress relationships under hydrostatic stress for their use under non-hydrostatic stress conditions. *SEG Expanded Abstracts 74th International Meeting*, October 2004.
- Prioul, R., Bakulin, A., and Bakulin, V., 2004. Nonlinear rock physics model for estimation of 3D subsurface stress in anisotropic formations: theory and laboratory verification. *Geophys.*, **69**, 415–425.
- Pšenčík, I. and Martins, J.L., 2001. Weak contrast PP wave displacement *R/T* coefficients in weakly anisotropic elastic media. *Pure Appl. Geophys.*, **151**, 699–718.
- Pšenčík, I. and Vavryčuk, V., 1998. Weak contrast PP wave displacement *R/T* coefficients in weakly anisotropic elastic media. *Pure Appl. Geophys.*, **151**, 699–718.
- Pyrak-Nolte, L.J., Myer, L.R., and Cook, N.G.W., 1990. Transmission of seismic waves across single natural fractures. *J. Geophys. Res.*, **95**, 8617–8638.
- Rafavich, F., Kendal, C.H.St.C., and Todd, T.P., 1984. The relationship between acoustic properties and the petrographic character of carbonate rocks. *Geophys.*, **49**, 1622–1636.
- Ransom, R.C., 1984. A contribution towards a better understanding of the modified Archie formation resistivity factor relationship. *Log Analyst*, **25**, 7–15.
- Rasolofosaon, P., 1998. Stress-induced seismic anisotropy revisited. *Rev. Inst. Français Pétrole*, **53**, 679–692.
- Raymer, L.L., Hunt, E.R., and Gardner, J.S., 1980. An improved sonic transit time-to-porosity transform. *Trans. Soc. Prof. Well Log Analysts, 21st Annual Logging Symposium*, Paper P.
- Renshaw, C.E., 1995. On the relationship between mechanical and hydraulic apertures in rough-walled fractures. *J. Geophys. Res.*, **100**, 24629–24636.
- Resnick, J.R., Lerche, I., and Shuey, R.T., 1986. Reflection, transmission, and the generalized primary wave. *Geophys. J. R. Astron. Soc.*, **87**, 349–377.
- Reuss, A., 1929. Berechnung der Fließgrenzen von Mischkristallen auf Grund der Plastizitätsbedingung für Einkristalle. *Z. Ang. Math. Mech.*, **9**, 49–58.
- Risnes, R., Bratli, R., and Horsrud, P., 1982. Sand stresses around a borehole. *J. Soc. Petr. Eng.*, **22**, 883–898.
- Riznichenko, Y.V., 1949. On seismic quasi-anisotropy. *Izv. Akad. Nauk SSSR, Geograf. Geofiz.*, **13**, 518–544.
- Rosenbaum, J.H., 1974. Synthetic microseismograms: logging in porous formations. *Geophys.*, **39**, 14–32.
- Roth, M., Müller, G., and Sneider, R., 1993. Velocity shift in random media. *Geophys. J. Int.*, **115**, 552–563.
- Rüger, A., 1995. P-wave reflection coefficients for transversely isotropic media with vertical and horizontal axis of symmetry. *Expanded Abstracts, Soc. Expl. Geophys., 65th Annual International Meeting*. Tulsa, OK: Society of Exploration Geophysicists, pp. 278–281.
- Rüger, A., 1996. Variation of P-wave reflectivity with offset and azimuth in anisotropic media. *Expanded Abstracts, Soc. Expl. Geophys., 66th Annual International Meeting*. Tulsa, OK: Society of Exploration Geophysicists, pp. 1810–1813.
- Rüger, A., 1997. P-wave reflection coefficients for transversely isotropic models with vertical and horizontal axis of symmetry. *Geophys.*, **62**, 713–722.
- Rüger, A., 2001. *Reflection Coefficients and Azimuthal AVO Analysis in Anisotropic Media*. Tulsa, OK: Society of Exploration Geophysicists.

- Rumpf, H. and Gupte, A.R., 1971. Einflüsse der Porosität und Korngrößenverteilung im Widerstandsgesetz der Porenströmung. *Chem-Ing.-Tech.*, **43**, 367–375.
- Ryzhova, T.V., Aleksandrov, K.S., and Korobkova, V.M., 1966. The elastic properties of rock-forming minerals, V. Additional data on silicates. *Bull. Acad. Sci. USSR, Earth Phys.*, no. 2, 111–113.
- Rzhevsky, V. and Novick, G., 1971. *The Physics of Rocks*. Moscow: MIR Publishing.
- Sahay, P.N., 1996. Elastodynamics of deformable porous media. *Proc. R. Soc., London A*, **452**, 1517–1529.
- Sahay, P.N., 2008. On Biot slow S-wave. *Geophys.*, **72**, N19–N33.
- Sahay, P.N., Spanos, T.J.T., and de la Cruz, V., 2001. Seismic wave propagation in inhomogeneous and anisotropic porous media. *Geophys. J. Int.*, **145**, 209–222.
- Sahimi, M., 1995. *Flow and Transport in Porous Media and Fractured Rock*, VCH Verlagsgesellschaft mbH, Weinheim, 482 pp.
- Sarkar, D., Bakulin, A., and Kranz, R., 2003. Anisotropic inversion of seismic data for stressed media: theory and a physical modeling study on Berea sandstone. *Geophys.*, **68**, 690–704.
- Sayers, C.M., 1988a. Inversion of ultrasonic wave velocity measurements to obtain the microcrack orientation distribution function in rocks. *Ultrasonics*, **26**, 73–77.
- Sayers, C.M., 1988b. Stress-induced ultrasonic wave velocity anisotropy in fractured rock. *Ultrasonics*, **26**, 311–317.
- Sayers, C.M., 1995. Stress-dependent seismic anisotropy of shales. *Expanded Abstracts, Soc. Expl. Geophys., 65th Annual International Meeting*. Tulsa, OK: Society of Exploration Geophysicists, pp. 902–905.
- Sayers, C.M., 2004. Seismic anisotropy of shales: What determines the sign of Thomsen delta parameters? *Expanded A&b Abstract, SEG 74th International Exposition*. Tulsa, OK: Society of Exploration Geophysicists.
- Sayers, C.M. and Kachanov, M., 1991. A simple technique for finding effective elastic constants of cracked solids for arbitrary crack orientation statistics. *Int. J. Solids Struct.*, **12**, 81–97.
- Sayers, C.M. and Kachanov, M., 1995. Microcrack-induced elastic wave anisotropy of brittle rocks. *J. Geophys. Res.*, **100**, 4149–4156.
- Sayers, C.M., Van Munster, J.G., and King, M.S., 1990. Stress-induced ultrasonic anisotropy in Berea sandstone. *Int. J. Rock Mech. Mining Sci. Geomech. Abstracts*, **27**, 429–436.
- Schlichting, H., 1951. *Grenzschicht-Theorie*. Karlsruhe: G. Braun.
- Schlumberger, 1989. *Log Interpretation Principles/Applications*. Houston, TX: Schlumberger Wireline & Testing.
- Schlumberger, 1991. *Log Interpretation Principles/Applications*. Houston, TX: Schlumberger Wireline & Testing.
- Schmitt, D.P., 1989. Acoustic multipole logging in transversely isotropic poroelastic formations. *J. Acoust. Soc. Am.*, **86**, 2397–2421.
- Schoenberg, M., 1980. Elastic wave behavior across linear slip interfaces. *J. Acoust. Soc. Amer.*, **68**, 1516–1521.
- Schoenberg, M. and Douma, J., 1988. Elastic wave propagation in media with parallel fractures and aligned cracks. *Geophys. Prospect.*, **36**, 571–590.
- Schoenberg, M. and Muir, F., 1989. A calculus for finely layered anisotropic media. *Geophys.*, **54**, 581–589.
- Schoenberg, M. and Protázio, J., 1992. “Zoeppritz” rationalized and generalized to anisotropy. *J. Seismic Explor.*, **1**, 125–144.
- Schön, J.H., 1996. *Physical Properties of Rocks*. Oxford: Elsevier.

- Schwerdtner, W.M., Tou, J.C.-M., and Hertz, P.B., 1965. Elastic properties of single crystals of anhydrite. *Can. J. Earth Sci.*, **2**, 673–683.
- Scott, G.D. and Kilgour, D.M., 1969. The density of random close packing of spheres. *Brit. J. Appl. Phys. (J. Phys. D)*, **2**(2), 863–866.
- Segel, L.A., 1987. *Mathematics Applied to Continuum Mechanics*. Mineola, NY: Dover.
- Sen, P.N. and Goode, P.A., 1988. Shaley sand conductivities at low and high salinities. *Trans. Soc. Prof. Well Log Analysts, 29th Annual Logging Symposium*, Paper F.
- Sen, P.N., Scala, C., and Cohen, M.H., 1981. A self-similar model for sedimentary rocks with application to the dielectric constant of fused glass beads. *Geophys.*, **46**, 781–795.
- Seshagiri Rao, T., 1951. Elastic constants of barytes and celestite. *Proc. Ind. Acad. Sci. A*, **33**, 251–256.
- Shapiro, S.A. and Hubral, P., 1995. Frequency-dependent shear-wave splitting and velocity anisotropy due to elastic multilayering. *J. Seismic Explor.*, **4**, 151–168.
- Shapiro, S.A. and Hubral, P., 1996. Elastic waves in thinly layered sediments: the equivalent medium and generalized O'Doherty–Anstey formulas. *Geophys.*, **61**, 1282–1300.
- Shapiro, S.A. and Hubral, P., 1999. *Elastic Waves in Random Media: Fundamentals of Seismic Stratigraphic Filtering*. Berlin: Springer-Verlag.
- Shapiro, S.A. and Zien, H., 1993. The O'Doherty–Anstey formula and localization of seismic waves. *Geophys.*, **58**, 736–740.
- Shapiro, S.A., Hubral, P., and Zien, H., 1994. Frequency-dependent anisotropy of scalar waves in a multilayered medium. *J. Seismic Explor.*, **3**, 37–52.
- Sharma, M.M. and Tutuncu, A.N., 1994. Grain contact adhesion hysteresis: a mechanism for attenuation of seismic waves. *Geophys. Res. Lett.*, **21**, 2323–2326.
- Sharma, M.M., Garrouch, A., and Dunlap, H.F., 1991. Effects of wettability, pore geometry, and stress on electrical conduction in fluid-saturated rocks. *Log Analyst*, **32**, 511–526.
- Sharma, M.M., Tutuncu, A.N., and Podia, A.L., 1994. Grain contact adhesion hysteresis: a mechanism for attenuation of seismic waves in sedimentary granular media. In *Extended Abstracts, Soc. Expl. Geophys., 64th Annual International Meeting*, Los Angeles. Tulsa, OK: Society of Exploration Geophysicists, pp. 1077–1080.
- Shen, L.C., 1985. Problems in dielectric-constant logging and possible routes to their solution. *Log Analyst*, **26**, 14–25.
- Sheriff, R.E., 1991. *Encyclopedic Dictionary of Exploration Geophysics*, 3rd edn. Tulsa, OK: Society of Exploration Geophysics.
- Sherman, M.M., 1986. The calculation of porosity from dielectric constant measurements: a study using laboratory data. *Log Analyst*, Jan.–Feb., 15–24.
- Sherman, M.M., 1988. A model for the frequency dependence of the dielectric permittivity of reservoir rocks. *Log Analyst*, Sept.–Oct., 358–369.
- Shuey, R.T., 1985. A simplification of the Zoeppritz equations. *Geophys.*, **50**, 609–614.
- Siggins, A.F. and Dewhurst, D.N., 2003. Saturation, pore pressure and effective stress from sandstone acoustic properties. *Geophys. Res. Lett.*, **30**, 1089 doi:10.1029/2002GL016143.
- Simandoux, P., 1963. Dielectric measurements on porous media: application to the measurement of water saturations: study of the behavior of argillaceous formations. *Rev. Inst. Français Petrole*, **18**, supplementary issue, 193–215.
- Simmons, G., 1965. Single crystal elastic constants and calculated aggregate properties. *J. Grad. Res. Center, SMU*, **34**, 1–269.
- Simmons, G. and Birch, F., 1963. Elastic constants of pyrite. *J. Appl. Phys.*, **34**, 2736–2738.
- Skelt, C., 2004. Fluid substitution in laminated sands. *Leading Edge*, **23**, 485–489.

- Smith, G.C. and Gidlow, P.M., 1987. Weighted stacking for rock property estimation and detection of gas. *Geophys. Prospect.*, **35**, 993–1014.
- Smith, W.O., Foote, P.D., and Busand, P.G., 1929. Packing of homogeneous spheres. *Phys. Rev.*, **34**(2), 1271–1274.
- Sneddon, I.N. and Lowergrub, M., 1969. *Crack Problems in the Classical Theory of Elasticity*. New York: John Wiley and Sons.
- Soga, N., 1967. Elastic constants of garnet under pressure and temperature. *J. Geophys. Res.*, **72**, 4227–4234.
- Spangenburg, K. and Haussuhl, S., 1957. Die elastischen Konstanten der Alkalihalogenide. *Z. Kristallogr.*, **109**, 422–437.
- Spanos, T.J.T., 2002. *The Thermophysics of Porous Media*. Boca Raton, FL: Chapman & Hall/CRC.
- Spratt, R.S., Goins, N.R., and Fitch, T.J., 1993. Pseudo-shear – the analysis of AVO. In *Offset Dependent Reflectivity – Theory and Practice of AVO Analysis*, ed. J.P. Castagna and M. Backus, *Invest. Geophys.*, No. 8. Tulsa, OK: Society of Exploration Geophysicists, pp. 37–56.
- Stoll, R.D., 1974. Acoustic waves in saturated sediments. In *Physics of Sound in Marine Sediments*, ed. L.D. Hampton. New York: Plenum, pp. 19–39.
- Stoll, R.D., 1977. Acoustic waves in ocean sediments. *Geophys.*, **42**, 715–725.
- Stoll, R.D., 1989. *Sediment Acoustics*. Berlin: Springer-Verlag, p. 154.
- Stoll, R.D. and Bryan, G.M., 1970. Wave attenuation in saturated sediments. *J. Acoust. Soc. Am.*, **47**, 1440–1447.
- Stoner, E.C., 1945. The demagnetizing factors for ellipsoids. *Philos. Mag.*, **36**, 803–821.
- Strandenes, S., 1991. *Rock Physics Analysis of the Brent Group Reservoir in the Oseberg Field*. Stanford Rockphysics and Borehole Geophysics Project, special volume.
- Sumino, Y., Kumazawa, M., Nishizawa, O., and Pluschkell, W., 1980. The elastic constants of single-crystal Fe_{1-x}O , MnO , and CoO , and the elasticity of stoichiometric magnesiowüstite. *J. Phys. Earth*, **28**, 475–495.
- Tang, X.-M. and Cheng, A., 2004. *Quantitative Borehole Acoustic Methods*. Amsterdam: Elsevier.
- Tang, X.-M., Cheng, A., and Toksöz, M.N., 1991. Dynamic permeability and borehole Stoneley waves: a simplified Biot–Rosenbaum model. *J. Acoust. Soc. Am.*, **90**, 1632–1646.
- Thomas, E.C. and Stieber, S.J., 1975. The distribution of shale in sandstones and its effect upon porosity. In *Trans. 16th Annual Logging Symposium of the SPWLA*, paper T.
- Thomas, E.C. and Stieber, S.J., 1977. Log derived shale distributions in sandstone and its effect upon porosity, water saturation, and permeability. In *Trans. 6th Formation Evaluation Symposium of the Canadian Well Logging Society*.
- Thomsen, L., 1986. Weak elastic anisotropy. *Geophys.*, **51**, 1954–1966.
- Thomsen, L., 1993. Weak anisotropic reflections. In *Offset Dependent Reflectivity – Theory and Practice of AVO Analysis*, ed. J.P. Castagna and M. Backus, *Invest. Geophys.*, No. 8. Tulsa, OK: Society of Exploration Geophysicists, pp. 103–111.
- Thomson, W., 1878. Mathematical theory of elasticity. *Elasticity, Encyclopedia Britannica*, **7**, 819–825.
- Timoshenko, S.P. and Goodier, J.N., 1934. *Theory of Elasticity*. New York: McGraw-Hill.
- Tixier, M.P. and Alger, R.P., 1967. Log evaluation of non-metallic mineral deposits. *Trans. SPWLA 8th Ann. Logging Symp.*, Denver, June 11–14, Paper R.
- Todd, T. and Simmons, G., 1972. Effect of pore pressure on the velocity of compressional waves in low porosity rocks. *J. Geophys. Res.*, **77**, 3731–3743.
- Topp, G.C., Davis, J.L., and Annan, A.P., 1980. Electromagnetic determination of soil water content: measurements in coaxial transmission lines. *Water Resource Res.*, **16**, 574–582.

- Tosaya, C.A., 1982. *Acoustical Properties of Clay-bearing Rocks*. Ph.D. dissertation, Stanford University.
- Tosaya, C.A. and Nur, A., 1982. Effects of diagenesis and clays on compressional velocities in rocks. *Geophys. Res. Lett.*, **9**, 5–8.
- Truesdell, C., 1965. *Problems of Nonlinear Elasticity*. New York: Gordon and Breach.
- Tsvankin, I., 1997. Anisotropic parameters and P-wave velocity for orthorhombic media. *Geophys.*, **62**, 1292–1309.
- Tsvankin, I., 2001. *Seismic Signatures and Analysis of Reflection Data in Anisotropic Media*. New York: Pergamon.
- Tucker, M.E., 2001. *Sedimentary Petrology*, 3rd edn. Oxford: Blackwell Science.
- Tutuncu, A.N., 1992. *Velocity Dispersion and Attenuation of Acoustic Waves in Granular Sedimentary Media*. Ph.D. dissertation, University of Texas, Austin.
- Tutuncu, A.N. and Sharma, M.M., 1992. The influence of grain contact stiffness and frame moduli in sedimentary rocks. *Geophys.*, **57**, 1571–1582.
- Urmos, J. and Wilkens, R.H., 1993. *In situ* velocities in pelagic carbonates: new insights from ocean drilling program leg 130, Ontong Java. *J. Geophys. Res.*, **98**(B5), 7903–7920.
- Vaughan, M.T. and Guggenheim, 1986. Elasticity of muscovite and its relationship to crustal structure. *J. Geophys. Res.*, **91**, 4657–4664.
- Vavryčuk, V. and Pšenčík, I., 1998. PP-wave reflection coefficients in weakly anisotropic elastic media. *Geophys.*, **63**(6), 2129–2141.
- Verma, R.K., 1960. Elasticity of some high-density crystals. *J. Geophys. Res.*, **65**, 757–766.
- Vernik, L., Bruno, M., and Bovberg, C., 1993. Empirical relations between compressive strength and porosity of siliciclastic rocks. *Int. J. Rock Mech. Min. Sci. Geomech. Abstracts*, **30**(7), 677–680.
- Vernik, L., Fisher, D., and Bahret, S., 2002. Estimation of net-to-gross from P and S impedance in deepwater turbidites. *Leading Edge*, **21**, 380–387.
- Voigt, W., 1890. Bestimmung der Elastizitätskonstanten des brasilianischen Turmalines. *Ann. Phys. Chem.*, **41**, 712–729.
- Voigt, W., 1907. Bestimmung der Elastizitätskonstanten von Eisenglanz. *Ann. Phys.*, **24**, 129–140.
- Wachtman, J.B., Jr., Tefft, W.E., Lam, D.G., Jr., and Strinchfield, R.P., 1960. Elastic constants of synthetic single crystal corundum at room temperature. *J. Res. Natl. Bur. Stand.*, **64A**, 213–228.
- Waddell, H., 1932. Volume, shape and roundness of rock particles. *J. Geol.* **40**, 443–451.
- Wadsworth, J., 1960. Experimental examination of local processes in packed beds of homogeneous spheres. *Nat. Res. Council of Canada, Mech. Eng. Report MT-41* February.
- Walls, J., Nur, A., and Dvorkin, J., 1991. A slug test method in reservoirs with pressure sensitive permeability. *Proc. 1991 Coalbed Methane Symp.*, University of Alabama, Tuscaloosa, May 13–16, pp. 97–105.
- Walsh, J.B., 1965. The effect of cracks on the compressibility of rock. *J. Geophys. Res.*, **70**, 381–389.
- Walsh, J.B., 1969. A new analysis of attenuation in partially melted rock. *J. Geophys. Res.*, **74**, 4333.
- Walsh, J.B., Brace, W.F., and England, A.W., 1965. Effect of porosity on compressibility of glass. *J. Am. Ceramic Soc.*, **48**, 605–608.
- Walton, K., 1987. The effective elastic moduli of a random packing of spheres. *J. Mech. Phys. Solids*, **35**, 213–226.
- Wang, H.F., 2000. *Theory of Linear Poroelasticity*. Princeton, NJ: Princeton University Press.

- Wang, Z., 2000a. Dynamic versus static properties of reservoir rocks, in seismic and acoustic velocities in reservoir rocks. *SEG Geophysics Reprint Series*, **19**, 531–539.
- Wang, Z., 2002. Seismic anisotropy in sedimentary rocks, Parts I and II. *Geophys.*, **67**, 1415–1440.
- Wang, Z. and Nur, A., 1992. *Seismic and Acoustic Velocities in Reservoir Rocks*, vol. 2, *Theoretical and Model Studies*, Soc. Expl. Geophys., *Geophysics Reprint Series*. Tulsa, OK: Society of Exploration Geophysicists.
- Wang, Z. and Nur, A. (eds.), 2000. *Seismic and Acoustic Velocities in Reservoir Rocks*, vol. 3, *Recent Developments*, Geophysics Reprint Series, no. 19. Tulsa, OK: Society of Exploration Geophysicists.
- Ward, S.H. and Hohmann, G.W., 1987. Electromagnetic theory for geophysical applications. In *Electromagnetic Methods in Applied Geophysics*, vol. I, *Theory*, ed. M.N. Nabighian. Tulsa, OK: Society of Exploration Geophysicists, pp. 131–311.
- Watt, J.P., Davies, G.F., and O'Connell, R.J., 1976. The elastic properties of composite materials. *Rev. Geophys. Space Phys.*, **14**, 541–563.
- Waxman, M.H. and Smits, L. J. M., 1968. Electrical conductivities in oil-bearing shaley sands. *Soc. Petrol Eng. J.*, **8**, 107–122.
- Weidner, D.J. and Carleton, H.R., 1977. Elasticity of coesite. *J. Geophys. Res.*, **82**, 1334–1346.
- Weidner, D.J. and Hamaya, N., 1983. Elastic properties of the olivine and spinel polymorphs of Mg_2GeO_4 and evaluation of elastic analogues. *Phys. Earth Planetary Interiors*, **33**, 275–283.
- Weidner, D.J., Bass, J.D., Ringwood, E., and Sinclair, W., 1982. The single-crystal elastic moduli of stishovite. *J. Geophys. Res.*, **87**, 4740–4746.
- Weingarten, J.S. and Perkins, T.K., 1995. Prediction of sand production in wells: methods and Gulf of Mexico case study. *J. Petrol. Tech.*, 596–600.
- Whitcombe, D.N., 2002. Elastic impedance normalization. *Geophys.*, **67**, 59–61.
- Whitcombe, D.N., Connolly, P.A., Reagan, R.L., and Redshaw, T.C., 2002. Extended elastic impedance for fluid and lithology prediction. *Geophys.*, **67**, 63–67.
- White, J.E., 1975. Computed seismic speeds and attenuation in rocks with partial gas saturation. *Geophys.*, **40**, 224–232.
- White, J.E., 1983. *Underground Sound: Application of Seismic Waves*. New York: Elsevier.
- White, J.E., 1986. Biot–Gardner theory of extensional waves in porous rods. *Geophys.*, **51**, 742–745.
- Widmaier, M., Shapiro, S.A., and Hubral, P., 1996. AVO correction for a thinly layered reflector overburden. *Geophys.*, **61**, 520–528.
- Wiggins, R., Kenny, G.S., and McClure, C.D., 1983. A method for determining and displaying the shear-velocity reflectivities of a geologic formation. European Patent Application 0113944.
- Williams, D.M., 1990. The acoustic log hydrocarbon indicator. *Soc. Prof. Well Log Analysts*, *31st Ann. Logging Symp.*, Paper W.
- Willis, J.R., 1977. Bounds and self-consistent estimates for the overall properties of anisotropic composites. *J. Mech. Phys. Solids*, **25**, 185–202.
- Winkler, K., 1986. Estimates of velocity dispersion between seismic and ultrasonic frequencies. *Geophys.*, **51**, 183–189.
- Winkler, K.W., 1983. Contact stiffness in granular porous materials: comparison between theory and experiment. *Geophys. Res. Lett.*, **10**, 1073–1076.
- Winkler, K.W., 1985. Dispersion analysis of velocity and attenuation in Berea sandstone. *J. Geophys. Res.*, **90**, 6793–6800.
- Winkler, K.W. and Murphy, W.F., III, 1995. Acoustic velocity and attenuation in porous rocks. In *Rock Physics and Phase Relations, A Handbook of Physical Constants*, AGU Reference Shelf 3. Washington, DC: American Geophysical Union.

- Winkler, K.W. and Nur, A., 1979. Pore fluids and seismic attenuation in rocks. *Geophys. Res. Lett.*, **6**, 1–4.
- Woerber, A.F., Katz, S., and Ahrens, T.J., 1963. Elasticity of selected rocks and minerals. *Geophys.*, **28**, 658–663.
- Wong, S.W., Kenter, C.J., Schokkenbroek, H., van Regteren, J., and De Bordes, P.F., 1993. Optimising shale drilling in the Northern North Sea; borehole stability considerations. SPE paper 26736, *Offshore Europe Conference*, Aberdeen, 7–10 September.
- Wood, A.W., 1955. *A Textbook of Sound*. New York: McMillan Co.
- Worthington, P.F., 1985. Evolution of shale sand concepts in reservoir evaluation. *Log Analyst*, **26**, 23–40.
- Wu, T.T., 1966. The effect of inclusion shape on the elastic moduli of a two-phase material. *Int. J. Solids Structures*, **2**, 1–8.
- Wyllie, M.R.J. and Gregory, A.R., 1953. Formation factors of unconsolidated porous media: influence of particle shape and effect of cementation. *Trans. Am. Inst. Mech. Eng.*, **198**, 103–110.
- Wyllie, M.R.J., Gregory, A.R., and Gardner, L.W., 1956. Elastic wave velocities in heterogeneous and porous media. *Geophys.*, **21**, 41–70.
- Wyllie, M.R.J., Gregory, A.R., and Gardner, G.H.F., 1958. An experimental investigation of factors affecting elastic wave velocities in porous media. *Geophys.*, **23**, 459–493.
- Wyllie, M.R.J., Gardner, G.H.F., and Gregory, A.R., 1963. Studies of elastic wave attenuation in porous media. *Geophys.*, **27**, 569–589.
- Xu, S. and White, R.E., 1994. A physical model for shear-wave velocity prediction. In *Expanded Abstracts, 56th Eur. Assoc. Expl. Geoscientists Meet. Tech. Exhib.*, Vienna, p. 117.
- Xu, S. and White, R.E., 1995. A new velocity model for clay–sand mixtures. *Geophys. Prospect.*, **43**, 91–118.
- Yale, D.P. and Jameison, W.H., Jr., 1994. Static and dynamic rock mechanical properties in the Hugoton and Panoma fields. Kansas Society of Petroleum Engineers, Paper 27939. *Society of Petroleum Engineers Mid-Continent Gas Symposium*, Amarillo, TX, May.
- Yamakawa, N., 1962. Scattering and attenuation of elastic waves. *Geophys. Mag., Tokyo*, **31**, 63–103.
- Yeganeh-Haeri, A., Weidner, D.J., and Ito, E., 1989. Single-crystal elastic moduli of magnesium metasilicate perovskite. In *Perovskite: a Structure of Great Interest to Geophysics and Materials Science, Geophysics Monograph Series*, vol. 45. Washington, D.C.: American Geophysical Union, pp. 13–25.
- Yeganeh-Haeri, A., Weidner, D.J., and Parise, J.B., 1992. Elasticity of α -cristobalite: a silicon dioxide with a negative Poisson's ratio. *Science*, **257**, 650–652.
- Yin, H., 1992. *Acoustic Velocity and Attenuation of Rocks: Isotropy, Intrinsic Anisotropy, and Stress-Induced Anisotropy*. Ph.D. dissertation, Stanford University.
- Yoneda, A., 1990. Pressure derivatives of elastic constants of single crystal MgO, MgAl₂O₄. *J. Phys. Earth*, **38**, 19–55.
- Yoon, H.S. and Newnham, R.E., 1969. Elastic properties of fluorapatite. *Amer. Mineralog.*, **54**, 1193–1197.
- Yoon, H.S. and Newnham, R.E., 1973. The elastic properties of beryl. *Acta Cryst.*, **A29**, 507–509.
- Young, H.D., 1962. *Statistical Treatment of Experimental Data*. New York: McGraw-Hill.
- Yu, G., Vozoff, K., and Durney, W., 1993. The influence of confining pressure and water saturation on dynamic properties of some rare Permian coals. *Geophys.*, **58**, 30–38.
- Zamora, M. and Poirier, J.P., 1990. Experimental study of acoustic anisotropy and birefringence in dry and saturated Fontainebleau sandstone. *Geophys.*, **55**, 1455–1465.

- Zarembo, I.K. and Krasil'nikov, V.A., 1971. Nonlinear phenomena in the propagation of elastic waves in solids. *Sov. Phys. Usp.*, **13**, 778–797.
- Zeller, R. and Dederichs, P.H., 1973. Elastic constants of polycrystals. *Phys. Stat. Sol. b*, **55**, 831.
- Zener, C., 1948. *Elasticity and Anelasticity of Metals*. Chicago, IL: University of Chicago Press.
- Zhao, Y. and Weidner, D.J., 1993. The single-crystal elastic moduli of neighborite. *Phys. Chem. Minerals*, **20**, 419–424.
- Zimmerman, R.W., 1984. The elastic moduli of a solid with spherical pores: new self-consistent method. *Int. J. Rock Mech., Mining Sci. Geomech. Abstracts*, **21**, 339–343.
- Zimmerman, R.W., 1986. Compressibility of two-dimensional cavities of various shapes. *J. Appl. Mech. Trans. Am. Soc. Mech. Eng.*, **53**, 500–504.
- Zimmerman, R.W., 1991a. *Compressibility of Sandstones*. New York: Elsevier.
- Zimmerman, R.W., 1991b. Elastic moduli of a solid containing spherical inclusions. *Mech. Mater.*, **12**, 17–24.
- Zoback, M.D., 2007. *Reservoir Geomechanics*, Cambridge: Cambridge University Press.
- Zoeppritz, K., 1919. Erdbebenwellen VIII B, On the reflection and propagation of seismic waves. *Göttinger Nachr.*, **I**, 66–84.

Index

- Aki–Richards approximation, 100
 - see also* AVO
- analytic signal, 6–7
 - see also* Hilbert transform
- anellipticity, 37
- anisotropy, elastic
 - anellipticity, 37
 - Backus average, 138, 179, 210–218
 - coordinate transformation, 18–20, 26
 - dispersion, 138–146
 - displacement discontinuity model, 219, 223
 - Eshelby–Cheng model, 203–205
 - fluid substitution, anisotropic, 284–286
 - frequency-dependent, 138–146
 - group, phase, energy velocities, 83–86
 - Hooke’s law, 23–35
 - Hudson’s model, 152, 194–203
 - layered media, 37–38, 138–146
 - ordered sphere packing, effective moduli, 264
 - squirt, anisotropic, 306–309
 - stiffness tensor, 23–35
 - stress-induced anisotropy, 43–47
 - T*-matrix inclusion models, 205–210
 - see also* AVO; effective medium models, elastic;
 - elasticity; NMO; granular media; Thomsen’s
 - weak anisotropy; Tsvankin’s parameters
- API gravity, 344
- Archie’s law, 425
 - cementation exponent, 425
 - saturation exponent, 425
 - second law, 425
- attenuation electromagnetic, 418–419
- attenuation, seismic, 332
 - Biot model, 143–146, 157, 266–271
 - BISQ model, 302–303
 - Chapman *et al.* squirt model, 304–305
 - characteristic frequency, 311
 - comparison among fluid-related mechanisms, 310–315
 - Dvorkin–Mavko attenuation model, 315
 - empirical relation, 384
 - Kennett algorithm, 130
 - Kennett–Frazer theory, 134
 - layered media, *see* stratigraphic filtering
 - O’Doherty–Anstey formula, 136
 - squirt model, 297–301, 304–309
 - stratigraphic filtering, 134–137
 - viscous fluid
 - see also* borehole; scattering; viscoelasticity and *Q*
- autocorrelation, 2
- AVO, 93–115
 - Aki–Richards approximation, 100
 - anisotropic, 105–115
 - arbitrary anisotropy, 114
 - Bortfield approximation, 100
 - Gardner’s equation, 102
 - gradient, 102
 - Hilterman’s equation, 103
 - isotropic, 96–105
 - orthorhombic, 111
 - Poisson’s ratio trace (Hilterman’s), 103
 - Shuey’s approximation, 102
 - Smith and Gidlow’s formula, 102
 - transversely isotropic, 108, 110
 - Zoeppritz equations, 98
- AVOA, *see* AVO, anisotropic
- Backus average, 138, 179, 210–218
 - arbitrarily anisotropic layers, 215
 - fractures, parallel, 219
 - isotropic layers, 211
 - poroelastic layers, 216
 - transversely isotropic layers, 211
 - uniform shear modulus, 213
- BAM, *see* bounding average method
- bar resonance, *see* cylindrical rods
- Batzle–Wang relations, 341–346
- Bayes decision theory, 17
- Berryman self-consistent model, *see* self-consistent approximation
- binary mixture of spheres, *see* granular media
- binomial coefficients, 12
- binomial distribution, 12
- Biot coefficient, 45, 58, 280
- Biot model, 143–146, 157, 266–271
 - Geertsma–Smit approximation, 272
 - partial saturation, 327–332
 - slow P-wave, 267–268

- Biot model (cont.)
 slow S-wave, 269–271
 see also Gassmann's equations
- Biot–Rosenbaum theory, 164
- Biot–White–Gardner effect in resonant bars, 157
- BISQ model, 302–303
- Bond coordinate transformation, 19, 26
- bootstrap, 16
- borehole,
 Biot–Rosenbaum theory, 164
 permeable formation, 164
 pseudo-Rayleigh in borehole, 160
 Stoneley waves, 160, 167
 stress and deformation, 70–76
 waves, 160–168
- Bortfield's AVO formula, *see* AVO
- bound water, 428
- bounds, cross-property
 Berryman–Milton bounds, 432
 Gibiansky–Torquato bound, 432
 Milton bounds, 432
- bounds elastic, 169–175
 bound-filling models, 224–228
 bounding average method, 225, 295–296
 Hashin–Shtrikman, 169–228, 258, 260
 Hashin–Shtrikman–Walpole, 169–174, 224
 isoframe model, 225
 modified Hashin–Shtrikman bound, 224
 modified Voigt bound, 348
 Reuss, 172, 174–177, 224, 324
 Voigt, 174–175, 177, 224, 347
 Voigt–Reuss–Hill average, 177, 225
- bounds electrical, 414
- bound-filling models, 224–228
- bounding average method, 225, 295–296
- Bower's relation, 383
- Bragg scattering, 137
- Brandt model, 252
- Brie mixing equation, 327
- Brinkman's equation, 394
- Brocher's empirical relations, 359
- Brown and Korringa equation, 210, 290
 anisotropic form, 285
 mixed mineralogy, 282–284
- Buckley–Leverett equation, 390
- bulk modulus, *see* elasticity, effective medium models, elastic
- Burger's vector, 65
- capillary forces, 396–400
- capillary pressure, 398
 Laplace equation, 398
- carbon dioxide, properties, 474
- Castagna's empirical relations, 358
- cation exchange capacity, 427
- Cauchy's formula, 76
- causality, 8
- cavities in elastic solid, 57–76
 Biot coefficient, 58
 circular hole, 70–76
 crack closing stress, 48, 61, 219
 cylindrical shell, 70
 ellipsoidal with finite thickness, 68
 elliptical borehole, 72
 needle-shaped (prolate spheroid), 61
 nonelliptical, 67, 220
 penny-shaped crack (oblate spheroid), 60
 spherical cavities, 59, 151
 spherical shells, 68
 three-dimensional ellipsoidal cavities, 59
 two-dimensional cavities, 62–67
 see also borehole; effective medium theories, elastic; inclusion models
- cementation models, 255
- Chapman *et al.* squirt model, 304–305
- classification, 17
 Bayes decision theory, 17
 discriminant analysis, 18
 Mahalanobis distance, 18
- Clausius–Mossotti formula, 415
- clay
 Castagna's velocity relations, 358
 electrical conductivity, 426
 Han's velocity relations, 355
 mudrock line, 366
 Tosaya's velocity relations, 357
 V_P – V_S relations, 363–379
- closing stress, *see* crack closing stress
- coal, V_P – V_S relations, 369
- Coates equation, 407
- Coates–Dumanoir equation, 407
- coefficient of determination, 10
- coherent potential approximation, 209
- Cole–Cole dielectric model, 419
- complex dielectric constant, *see* dielectric constant, attenuation electromagnetic
- complex modulus, *see* viscoelasticity and Q
- compliance tensor, *see* elasticity
- compressibility
 cavities in elastic solid, 57–76
 definitions and pitfalls, 179–183
 reservoir fluids, 341–346
 see also elasticity; effective medium models, elastic; bounds, elastic
- compressive strength, *see* unconfined compressive strength
- constant Q model, 126
 see also viscoelasticity and Q
- contact angle, 398
- contact stiffness, *see* Hertz–Mindlin–model
- conversion tables, 452–456
- convolution, 2
- coordinate transformation, 18–20, 26
- coordination number, *see* granular media
- correlation coefficient, 9

- covariance, 10, 12
- cracks, 57–76
 - Chapman *et al.* squirt model, 304–305
 - crack closing stress, 48, 61, 219
 - deformation under stress, *see* cavities in elastic solid
 - displacement discontinuity model, 219, 223
 - Eshelby–Cheng model, 203–205
 - fracture compliance, 219–223
 - fractures, flow in, 410–411
 - Hudson model, 152, 194–203
 - Kuster–Toksöz model, 183–185
 - seismic response, 219–223
 - self-consistent approximation, 185–188
 - squirt model, 297–301, 304–309
 - stress-induced anisotropy, 43–47
 - T*-matrix inclusion models, 205–210
 - see also* cavities in elastic solid; effective medium models, elastic; scattering
- creeping flow, 396
- CRIM formula, 421
- critical porosity, 347
 - modified DEM model, 192
 - modified Hashin–Shtrikman bound, 224
 - modified Voigt bound, 347–348
 - V_P – V_S relations, 369
- cross-correlation, 2
- cross-property relations, 429–435
- crystallographic third order constants, 42
- curvilinear coordinates, 55–56
- cylindrical rods, 155–159
 - flexural waves, 156
 - longitudinal waves, 156
 - Pochhammer equation, 156–157
 - porous, saturated, 157
 - torsional waves, 155
- cylindrical shell, 70
- Darcy, unit, 389
- Darcy's law, 389
 - Brinkman's equation, 394
 - Forchheimer's relation, 394
- dead oil, 345
- Debye dielectric model, 419
- DEM model, 190–194, 415
- density–velocity relations, *see* empirical velocity relations
- depolarizing factors, dielectric, 416
- dielectric constant, 418–419
- dielectric permittivity, 414–417
- dielectric susceptibility, 418
- differential effective medium model, *see* DEM
- diffusion, 391–392, 411–413
- diffusion equation hyperbolic, 412
- diffusion equation nonlinear, 411
- diffusion scattering, 150
- Digby model, 249
- discriminant analysis, 18
- dislocation theory, 66
- dispersion, *see* velocity dispersion
- displacement discontinuity model, *see* cracks
- dissipation, *see* attenuation
- distributions,
 - binomial coefficients, 12
 - binomial distribution, 12
 - logistic distribution, 15
 - lognormal distribution, 14
 - normal (Gaussian) distribution, 13
 - Poisson distribution, 13–14
 - truncated exponential distribution, 14
 - uniform distribution, 13
 - Weibull distribution, 15
- Dix equation, 88
 - see also* NMO
- drainage, 400
- dual water model, 426
- Dutta–Odé model, 327–332
- Eaton's pore-pressure relation, 383
- Eberhart–Phillips (Han) velocity relations, 355
- effective electrical properties, 414–435
- effective fluid, 323
- effective medium models, dielectric
 - bounds, 414
 - Clausius–Mossotti formula, 415
 - coherent potential approximation, 415
 - Cole–Cole model, 419
 - Debye model, 419
 - DEM model, 415
 - ellipsoidal inclusions, 416
 - Lorentz–Lorenz equation, 415
 - Maxwell–Garnett equation, 415
 - self-consistent approximation, 415
- effective medium models, elastic, 169–228
 - BISQ model, 302–303
 - bound-filling models, 224–228
 - bounding average method, 225
 - Brandt model, 252
 - cavities in elastic solid, 57–76
 - cementation models, 255
 - Chapman *et al.* squirt model, 304–305
 - comparison among fluid-related dispersion mechanisms, 310–315
 - compressibility and pitfalls, 179–183
 - contact stiffness, grain, *see* Hertz–Mindlin model
 - coordination number, 232, 245
 - DEM model, 190–194
 - Digby model, 249
 - Eshelby–Cheng model, 203–205
 - granular media, 245–265
 - Hashin–Shtrikman bounds, *see* bounds, elastic
 - Hertz (–Mindlin) model, 220, 246–248, 252, 258
 - Hudson model, 152, 194–203
 - isoframe model, 225
 - Jenkins, *et al.* model, 251

effective medium models, elastic (cont.)

- Johnson *et al.* model, 253
 - Kuster–Toksöz model, 183–185
 - O’Connell–Budiansky model, 186
 - ordered sphere packing, effective moduli, 264
 - self-consistent approximation, 185–188
 - squirt, anisotropic, 306–309
 - squirt model, 297–301, 304–305
 - stiff sand model, 260
 - stress-induced anisotropy, 43–47
 - T*-matrix inclusion models, 205–210
 - uniform shear modulus (Hill), 178
 - Walton model, 248
 - Wood’s formula, 175
 - Xu–White model, 377
 - see also* bounds, elastic
- effective stress properties, 43–47
- eigensensors and eigenvalues, 32
- elastic compliance, *see* elasticity
- elastic impedance, 115–121
- isotropic, 118
 - orthorhombic, 120
 - transversely isotropic, 119
- elastic moduli, *see* elasticity
- elasticity
- anelasticity, 37
 - anisotropic, 23–40, 43–47
 - Biot coefficient, 58
 - bulk modulus, 21
 - cavities in elastic solid, 57–76
 - compliance tensor, 24
 - compressibility, 21, 179–183
 - cubic, 27, 264
 - effective stress properties, 43–47
 - eigensensors and eigenvalues, 32
 - hexagonal, 27, 264
 - Hooke’s law, 21, 23–35
 - isotropic, 24, 26
 - Kelvin notation, 30–32, 207
 - Lame’s constant, 22
 - moduli, elastic, 21, 79, 80
 - monoclinic, 28
 - nonlinear elasticity, 40–47
 - orthorhombic, 28, 39–40, 47
 - P-wave modulus, 22
 - Poisson’s ratio, 22, 33
 - shear modulus, 22
 - Skempton coefficient, 58
 - static and dynamic moduli, 79
 - stiffness tensor, 25–35
 - stress-induced anisotropy, 43–47
 - third-order elasticity, 40–43, 53
 - Thomsen parameters, 35–39
 - transversely isotropic, 27, 35–39, 41, 210–218
 - triclinic, 24
 - Tsvankin’s parameters, 39–40
 - Voigt notation, 24–28, 35, 207
 - Young’s modulus, 22

- see also* AVO; bounds, elastic; effective medium models, elastic; phase velocity
- electrical conductivity, 424–429
- Archie’s law, 425
 - dual water model, 426
 - Indonesia formula, 426
 - Sen and Goode model, 428
 - shaley sands, 426
 - Simandoux equation, 426
 - Waxman–Smits model, 426
 - Waxman–Smits–Juhász model, 426
- electromagnetic waves, 418
- reflection coefficients, 420
 - transmission coefficients, 420
- ellipsoidal cavities, 57–76
- see also* cavities in elastic solid; effective medium models, elastic
- empirical electrical property relations, 421–429
- Archie’s law, 425
 - CRIM formula, 421
 - cross-property relations, 429–435
 - Faust’s relation, 429
 - hydraulic conductivity, 423
 - Knight and Nur relation, 423
 - Koeseomadinata and McMechan relations, 423
 - Lichtnecker–Rother formula, 421
 - Odelevskii formula, 422
 - Olhoeft’s relation, 422
 - Topp’s relation, 422
- empirical velocity relations
- Brocher’s compilation, 359
 - Castagna’s velocity relations, 358, 363–379
 - coal, 369
 - critical porosity model, 347–349
 - cross-property relations, 429–435
 - Eberhart–Phillips (Han) relations, 355
 - Faust’s relation, 429
 - Gardner’s velocity–density relation, 102, 381
 - Geertsma’s modulus–porosity relation, 350
 - Greenberg–Castagna relations, 374
 - Han’s velocity relations, 355
 - Krief’s relation, 372
 - Pickett’s relation, 363
 - Raymer–Hunt–Gardner velocity relations, 353
 - static and dynamic moduli, 79
 - Tosaya’s velocity relations, 357
 - velocity–density relations, 359, 380
 - velocity–strength relations, 386
 - Vernik’s relations, 376
 - V_P – V_S relations, 361, 363–379
 - Williams’s relation, 377
 - Wyllie’s time average, 350
- energy spectrum, 2
- energy velocity, 84
- envelope, *see* Hilbert transform
- equations of state fluids, *see* Batzle–Wang relations
- Eshelby–Cheng model, 203–205

- exponential distribution, 14
- eye, gnat's, *see* gnat's eye
- fast path effect, 147
- Faust's relation, 429
- FFT, *see* Fourier transform
- flexural waves
bar, 156
- Floquet solution, 137
- fluid
Batzle–Wang relations for physical properties, 341–346
nonwetting, 398
wetting, 398
- fluid flow
Brinkman's equation, 394
creeping flow, 396
Darcy's law, 389
diffusion equation nonlinear, 411
diffusivity, 391
drainage, 400
Forchheimer's relation, 394
fractured formation, 410–411
imbibition, 400
Kozeny–Carman relation, 401–406
multiphase flow, 390
pipe, 395
relative permeability, 390–391
viscous flow, 394–396
- fluid substitution, 274, 279, 284–286
Batzle–Wang relations for fluid properties, 341–346
bounding average method, 225, 295–296
Brown and Korringa equations, 210, 282–285
Gassmann's equations, 273–281, 284–285
partial saturations, 320–332
thinly laminated sands, 292
- Fontainebleau sandstone, 407
- Forchheimer's relation, 394
- formation factor, 424
- Fourier transform, 1–6
- fractures, *see* cracks
- Fresnel's equations, electromagnetic, 420
- Gardner's equation, 102, 381
- gases, properties, 468–474
- Gassmann equations, 273–281, 290
anisotropic form, 284–285
Batzle–Wang relations for fluid properties, 341–346
Biot coefficient form, 280
bounding average method, 295–296
compressibility form, 275
dry rock caveat, 273, 320
generalized form for composite porous media, 287–289
linear form, 276
P-wave modulus form, 277
partial saturations, 320–332
pore stiffness interpretation, 278
Reuss average form, 276
solid pore-filling material, 290–291
thinly laminated sands, 292
velocity form, 277
 V_P -only form (no V_S), 281
see also Brown and Korringa equations
- Gaussian distribution, 13
- Geertsma's modulus–porosity relations, 350
- Geertsma–Smit approximation to the Biot model, 272
- gnat's eye, 453
- granular media, 229–265
binary mixtures, 234–236, 238
Brandt model, 252
cementation models, 255
coefficient of variation (sorting), 244
coordination number, 232
Digby model, 249
effective moduli, 245–265
see also effective medium models, elastic
energy of deposition, 236
Hertz (–Mindlin) model, 220, 246–248, 252, 258
Jenkins *et al.* model, 251
Johnson *et al.* model, 253
ordered sphere packing, effective moduli, 264
packing and sorting of spheres, 229–237
packing of identical spheres, 229–234
particle shape, 236
particle size, 236, 242
phi-scale, 242–243
phi standard deviation, 244
psi-scale, 242
random packing of spheres, 229
sorting, 242–244
stiff sand model, 260
Thomas–Stieber model for sand–shale systems, 237–242
Udden–Wentworth scale, 242
uncemented (soft) sand model, 258
Walton model, 248
- gravity, API, 344
- Greenberg–Castagna V_P – V_S relations, 374
- group velocity, 83–86
see also velocity
- Han's velocity relations, 355
- Hashin–Shtrikman bounds, *see* bounds, elastic, bounds, electrical
- Hertz (–Mindlin) model, 220, 246–248
- hexagonal symmetry, *see* elasticity, transverse isotropy
- Hilbert transform, 6–9
analytic signal, 6–7
instantaneous envelope, 8
instantaneous frequency, 8
instantaneous phase, 8
- Hill relations
uniform shear modulus, 178
Voigt–Reuss–Hill average, 177

- Hilterman's AVO formulas, 103
 Hooke's law, *see* elasticity
 Hudson's crack model, 38, 194–203
 scattering attenuation, 152
 HTI, *see* AVO, elasticity, phase velocity, reflectivity,
 transverse isotropy
 hydrate, methane, 457
 hydraulic aperture, fractures, 411
 hyperelastic, 43
 see also nonlinear elasticity
- ice, properties, 457
 imbibition, 400
 impedance, seismic, 93–115
 see also elastic impedance; AVO
 impulse response, 8
 inclusion models, dielectric
 Clausius–Mossotti formula, 415
 coherent potential approximation, 415
 DEM model, 415
 depolarizing factors, 416
 ellipsoidal inclusions, 416
 Lorentz–Lorenz equation, 415
 Maxwell–Garnett equation, 415
 self-consistent approximation, 415
 inclusion models, elastic
 DEM model, 190–194
 Eshelby–Cheng model, 203–205
 Hudson's model, 194–203
 Kuster–Toksöz model, 183–185
 self-consistent approximation, 185–188
 T-matrix inclusion models, 205–210
 Xu–White model, 377
 Indonesia formula, 426
 instantaneous envelope, 8
 see also Hilbert transform
 instantaneous frequency, 8
 see also Hilbert transform
 instantaneous phase, 8
 see also Hilbert transform
 interfacial tension, *see* surface tension
 invariant imbedding, *see* Kennett algorithm
 irreducible water saturation, 400, 407
 Coates equation, 407
 Coates–Dumanoir equation, 407
 permeability relations, 407–409
 Timur equation, 407
 Tixier equation, 407
 isoform model, 225
 isostrain average, *see* Voigt average
 isostress average, *see* effective fluid, Reuss average,
 Wood's formula
- Jenkins *et al.* model, 251
 Johnson *et al.* model, 253
- Kelvin notation, 30–32, 207
 Kennett algorithm, 130, 134
 Kennett–Frazer theory, 134
 Klinkenberg effect, 394
 Knight and Nur relation, 423
 Knott–Zoeppritz equations, 98
 see also AVO
 Koesoemadinata and McMechan relations, 423
 Kozeny–Carman relation, 401–406
 Kramers–Kronig relations, 127
 Krief's relation, 372
 Kuster–Toksöz model, 183–185
- Lamé's constant, *see* elasticity
 Landau's third-order constants, 42
 Laplace equation for capillary pressure, 398
 layered media, 129–146
 anisotropy and dispersion, 138–146
 Bragg scattering, 137
 dielectric constant, 417
 electromagnetic waves, 421
 Floquet solution, 137
 Kennett algorithm, 130
 Kennett–Frazer theory, 134
 O'Doherty–Anstey formula, 136
 periodic, 137
 poroelastic, 143–146
 synthetic seismograms, 129
 uniform shear modulus, 179
 see also Backus average; stratigraphic filtering;
 velocity dispersion
 Lichtnecker–Rother formula, 421
 linear regression, 10
 live oil, 344
 local flow model, *see* squirt model
 logarithmic decrement, 123
 see also viscoelasticity and Q
 logistic distribution, 15
 lognormal distribution, 14
 longitudinal waves, 156
 see also cylindrical rods
 Lorentz–Lorenz formula, 415
- Mahalanobis distance, 18
 Maxwell solid, *see* viscoelasticity and Q
 Maxwell–Garnett equation, 415
 mean, 9
 mean deviation, 9
 median, 9
 methane hydrate, 457
 Mie scattering, 150
 Mindlin model
 mineral property tables, 457
 minimum phase, 3
 modified Hashin–Shtrikman, *see* bounds, elastic;
 effective medium models, elastic
 modified Voigt, *see* bounds, elastic;
 effective medium models, elastic
 moduli, *see* elasticity
 modulus defect, 126, 310

- see also* viscoelasticity and Q
 Mohr's circles, 76–79
 monoclinic symmetry, *see* elasticity
 Monte Carlo simulations, 15
 mudrock line, 366
 Murnaghan third-order constants, 42

 Navier–Stokes equations, 395
 nearly constant Q model, 126
 see also viscoelasticity and Q
 Newtonian flow, 394–396
 NMO, 86–93
 anisotropic, 88–93
 Dix equation, 88
 elliptical anisotropy, 90–91
 interval velocity, 88
 isotropic, 86
 orthorhombic, 92–93
 transversely isotropic, 89–90
 nonlinear elasticity, 40–43
 normal distribution, 13
 Nyquist frequency, 3

 O'Connell–Budiansky model, 186
 Odelevskii formula, 422
 O'Doherty–Anstey formula, 136
 oil properties
 Batze–Wang relations, 341–346
 dead oil, 345
 live oil, 344
 Olhoeft's relation, 422
 optical potential approximation, 208
 orthorhombic symmetry, *see* AVO, elasticity, phase velocity, reflectivity

 packing, 320–327, *see* granular media
 partial saturations, 320–327
 Brie mixing equation, 327
 effective fluid, 323
 patchy saturation, 325
 relaxation scale, 324
 relaxation time, 324
 Reuss average mixing, 324
 Voigt average mixing, 327
 White–Dutta–Odé model, 327–332
 see also fluid substitution; Gassmann's equations; Biot model
 patchy saturation, 325, 327–332
 see also partial saturations
 pdf, *see* probability distributions
 pendular ring, 398
 penny-shaped crack, *see* cavities in elastic solid, cracks, effective medium models, elastic
 percolation porosity for flow, 403
 permeability, 389
 Coates equation, 407
 Coates–Dumanoir equation, 407
 dynamic, 332, 338
 fractured formations, 410–411
 irreducible water saturation relations, 407–409
 Klinkenberg correction, 394
 Kozeny–Carman relation, 401–406
 relative, 390–391
 Timur equation, 407
 Tixier equation, 407
 phase spectrum, 3
 minimum phase, 3
 zero phase, 3
 phase velocity, 82–86
 anisotropic, 28–30
 electromagnetic, 419
 isotropic, 28
 orthorhombic, 29
 transversely isotropic, 28, 36
 phi-scale, 242
 see also granular media
 physical constants, tables, 456
 Pickett's relation, 363
 pipe, flow in
 circular pipe, 395
 elliptical pipe, 395
 rectangular pipe, 395
 triangular pipe, 396
 Pochhammer equation, 156–157
 Poisson distribution, 13–14
 Poisson's ratio, *see* AVO, effective medium models, elastic, elasticity
 population variance, *see* variance
 pore compressibility, *see* compressibility, cavities in elastic solid
 pore pressure, empirical relations, 383–384
 Bower's relation, 383
 Eaton's relation, 383
 pore pressure, stress-induced, *see* Skempton's coefficient
 poroelasticity, *see* Biot model
 porosity, *see* empirical velocity relations, effective medium models, elastic
 probability, *see* statistics and probability
 probability distributions, *see* distributions
 propagator matrix, 129, 421
 psi-scale, 242
 see also granular media
 P-wave modulus, *see* effective medium models, elastic, elasticity

 Q , 123
 see also viscoelasticity and Q
 quality factor, 123
 see also viscoelasticity and Q

 ray parameter, 93, 98
 Rayleigh scattering, 150
 Rayleigh wave velocity, 82
 pseudo-Rayleigh in borehole, 160
 Raymer form, V_S relation, 379

- Raymer–Hunt–Gardner velocity relations, 353
 reflectivity, electromagnetic, 420
 reflectivity, seismic, 93–115
 see also AVO
 regression, 9
 residual oil, 400
 resistivity, electrical, 424–429
 see also electrical conductivity
 resonant bar, *see* cylindrical rod
 Reuss average, *see* bounds, elastic, Reuss
 reverberation operator, 133
 Reynolds number, 393, 396
 RMS velocity, *see* NMO
 rock property tables, 437–450

 sample covariance, *see* covariance
 sample mean, *see* mean
 sample variance, *see* variance
 sampling theorem, 3
 saturation
 see also partial saturations
 scattering
 attenuation, 150–155
 Bragg scattering, 137
 diffusion scattering, 150
 Hudson's model, 152, 194–203
 Kuster–Toksöz model, 183–185
 Mie scattering, 150
 Rayleigh scattering, 150
 self-consistent approximation, 185–188
 spherical inclusions, 151–152
 stochastic (Mie) scattering, 150
 T-matrix inclusion models, 205–210
 see also layered media
 seismic impedance, *see* impedance, seismic
 seismic velocity, *see* velocity
 self-consistent approximation, 185–188
 Sen and Goode model, 428
 shaley sands
 Castagna's velocity relations, 358
 electrical conductivity, 426
 Han's velocity relations, 355
 mudrock line, 366
 Tosaya's velocity relations, 357
 V_P – V_S relations, 363–379
 shear modulus, *see* effective medium models, elastic, elasticity
 Shuey's approximation, 102
 signal velocity, 83–86
 Simandoux equation, 426
 Skempton's coefficient, 58
 see also cavities in elastic solid
 skin depth electromagnetic, 418
 slow P-wave, Biot, 267–268
 see also Biot model
 slow S-wave, 269–271
 slowness, 83
 see also velocity; stratigraphic slowness

 Smith and Gidlow's AVO formula, 102
 see also AVO
 Snell's law
 sorting, *see* granular media
 specific surface area, 229, 402
 spectral ratio, 124
 see also viscoelasticity and Q
 spectrum, 2
 sphere packs, *see* granular media
 spherical inclusions, *see* cavities in elastic solid, effective medium models, elastic, scattering
 spherical shells, 68
 squirt model, 297–298, 304–305
 anisotropic, 306–309
 Chapman *et al.* squirt model, 304–305
 extended to all frequencies, 298–301
 standard deviation, 9
 standard linear solid, *see* viscoelasticity and Q
 standard temperature and pressure (STP), 474
 statistical classification, 17
 statistics and probability, 9–18
 see also distributions; Monte Carlo; bootstrap; classification; Bayes
 stiff sand model, 260
 stiffness tensor, *see* elasticity
 stochastic (Mie) scattering, 150
 Stoneley waves in borehole, 160, 167
 stratigraphic filtering, 134–137
 Floquet solution, 137
 O'Doherty–Anstey formula, 136
 stratigraphic slowness, 134
 strength, *see* unconfined compressive strength
 stress-induced anisotropy, 43–47
 surface tension, 396
 contact angle, 398
 Young's relation, 397
 suspensions, *see* Wood's formula
 synthetic seismograms, 129–146
 see also Kennett algorithm; layered media

 tensor transformation, *see* coordinate transformation
 third-order elasticity, 40–43, 53
 Thomas–Stieber model for sand–shale systems, 237–242
 Thomsen's weak anisotropy, 35–39
 time-average equation, 350
 time-domain reflectometry (TDR)
 Timur equation, 407
 Tixier equation, 407
T-matrix inclusion models, 205–210
 coherent potential approximation, 209
 optical potential approximation, 208
 self-consistent approximation, 209
 Topp's relation, 422
 torsional waves, 155
 see also cylindrical rods
 tortuosity, 267, 402
 Tosaya's velocity relations, 357
 transfer function, 8

- transmissivity
 - electromagnetic, 420
 - seismic, 93–115
 - see also* AVO
- transverse isotropy, *see* AVO, elasticity, NMO, phase velocity, reflectivity
- truncated exponential distribution, 14
- Tsvankin's parameters, 39–40
- Udden–Wentworth scale, 242
- uncemented (soft) sand model, 258
- unconfined compressive strength (UCS), empirical relations, 386
- uniform distribution, 13
- variance, 9
- variogram, 12
- velocity, dispersion, 84, 134–146, 332
 - anomalous normal
 - Biot model, 143–146, 157, 266–271
 - BISQ model, 302–303
 - Bragg scattering, 137
 - Chapman *et al.* squirt model, 304–305
 - characteristic frequency, 311
 - comparison among fluid-related mechanisms, 310–315
 - cylindrical rods, 155–159
 - Dvorkin–Mavko attenuation model, 315
 - electromagnetic, 418
 - fast path effect, 147
 - Floquet solution, 137
 - group, phase, energy velocities, 83–86
 - heterogeneous media, 146–150
 - layered poroelastic, 143–146
 - O'Doherty–Anstey formula, 136
 - resonant bar, *see* cylindrical bar
 - saturation-related, 320–332
 - scattering attenuation, 150–155
 - squirt model, 297–301, 304–309
 - stratigraphic filtering, 134–137
 - stratigraphic slowness, 134
 - three-dimensional heterogeneous media, 147
 - waves in pure viscous fluid, 339
 - see also* layered media; viscoelasticity and Q
- velocity, electromagnetic, 418
- velocity, seismic, 81–83
 - cylindrical rods, 155–159
 - dispersion, 84
 - group, phase, energy velocities, 83–86
 - isotropic, 81
 - phase velocity, 36
 - Rayleigh wave, 82
 - RMS, *see* NMO
 - signal velocity, 86
 - stratigraphic filtering, 134–137
 - viscous fluid, in, 339
 - see also* anisotropy; empirical velocity relations; velocity dispersion
- velocity–density relations, 359, 380
- velocity–porosity relation, *see* empirical velocity relations
- Vernik's V_P – V_S relations, 376
- viscoelasticity and Q , 121–129, 138–146, 332
 - characteristic frequency, 311
 - comparison among fluid-related mechanisms, 310–315
 - constant Q model, 126
 - dispersion, 84
 - Dvorkin–Mavko attenuation model, 315
 - group, phase, energy velocities, 83–86
 - logarithmic decrement, 123
 - Maxwell solid, 122
 - modulus defect, 126, 310
 - nearly constant Q model, 126
 - quality factor (Q), 123
 - saturation-related, 320–332
 - spectral ratio, 124
 - standard linear solid, 122, 124
 - Voigt solid, 122
 - see also* Kramers–Kronig relations; velocity dispersion
- viscosity of reservoir fluids, 341–346
- viscous flow, 394–396
 - circular pipe, 395
 - elliptical pipe, 395
 - parallel plate, 395
 - rectangular pipe, 395
 - triangular pipe, 396
- viscous fluid
 - scattering from spheres, 152
 - wave velocity in, 339
- Voigt average, *see* bounds, elastic, Voigt
- Voigt notation, 24–28, 207
- Voigt–Reuss–Hill average, 177, 225
- Voigt solid, *see* viscoelasticity and Q
- V_P – V_S relations, 361, 363–379
- VTI, *see* AVO, elasticity, NMO, phase velocity, reflectivity, transverse isotropy
- Walton model, 248
- Waxman–Smits equations, 426
- Waxman–Smits–Juhász model, 426
- Weibull distribution, 15
- White–Dutta–Odé model, 327–332
- Williams V_P – V_S relation, 377
- Wood's formula, 175
- Wyllie's time-average equation, 350
- Xu–White model, 377
- Young's modulus, 22
- Young's relation, 397
- zero phase, 3
- Zoeppritz equations, *see* AVO